СБОРНИК МАТЕРИАЛОВ

III Международной школы-конференции молодых ученых
«Динамика сложных сетей и их применение в интеллектуальной робототехнике»

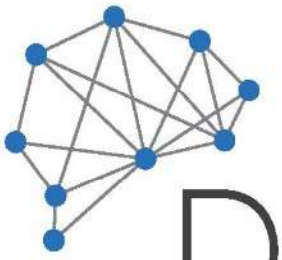

DCNAIR

Лаборатория нейронауки и когнитивных технологий

г. Иннополис
с 9 по 11 сентября 2019 года

УДК 004.896
ББК 32.813
Д46

Динамика сложных сетей и их применение в интеллектуальной робототехнике (Dynamics of Complex Networks and their Application in Intellectual Robotics).
Сборник материалов III Международной школы-конференции молодых учёных – Москва: ООО «Издательство «Перо»», – 2019, 208 с.

Материалы III Международной школы-конференции молодых учёных «Динамика сложных сетей и их применение в интеллектуальной робототехнике» содержат тезисы докладов ученых и специалистов в области интеллектуальных технологий, инженерного образования, исследования и проектирования мехатронных и робототехнических систем, сложных сетей.

Школа-конференция стала международной площадкой для обмена образовательными, научными и техническими идеями и достижениями между специалистами, в особенности молодыми учёными и студентами, работающими в области изучения сложных сетей и интеллектуальной робототехники, способствует коллаборации и взаимодействию специалистов в области сложных сетей и робототехники как на всероссийском, так и на международном уровне.

Материалы конференции предназначены для широкого круга научных и инженерно-технических работников, преподавателей ВУЗов, средних специальных учебных заведений, аспирантов и студентов.

Работа школы-конференции и настоящее издание осуществлено при поддержке Российского научного фонда (проект №17-72-30003), IEEE Russia Section C Chapter.

Part Number: CFP19O96-USB
ISBN: 978-1-7281-2469-8

CONFERENCE ORGANISERS

Innopolis University, Innopolis, Russia

Universidad Politécnica de Madrid,
Centre for Biobedical Technology, Spain

ANO “Research Center
“Education. Quality. Industry””

Industry Union Neuronet

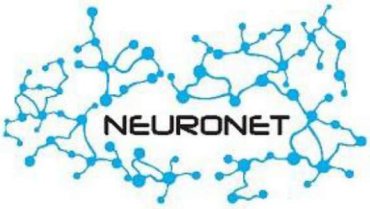

IEEE Russia Section C Chapter

CONFERENCE SPONSORS

Russian Science Foundation

Innopolis University, Innopolis, Russia

PROGRAMME COMMITTEE

Chair:
Prof. Alexander Hramov, Head of Neuroscience and Cognitive Technology Lab, Professor in Institute of Robotics (Innopolis University, Russia)

Members:
Prof. Alexander Tormasov (Rector of Innopolis University, Russia)
Prof. Iskander Bariev (Vice-Rector of Innopolis University, Russia)
Prof. Alexander Divin (Tambov State Technical University, Tambov)
Prof. Alexander Klimchik (Innopolis University, Russia)
Prof. Alexey Pavlov (Yuri Gagarin State Technical University of Saratov, Russia)
Prof. Alexander Pisarchik (Universidad Politécnica de Madrid, Centre for Biomedical Technology, Spain)
Prof. Grigory Osipov (Lobachevsky State University of Nizhni Novgorod, Russia)
Prof. Leonid Savin (Orel State University named after I.S. Turgenev, Russia)
Prof. Mikhail Prokhorov (Saratov Branch of the Institute of Radio Engineering and Electronics of Russian Academy of Science, Russia)
Dr. Petr Storozhev (RPE Fort XXI, Ltd., Russia)
Prof. Semen Kurkin (Innopolis University, Russia)
Prof. Stefano Boccaletti (ISC-Institute for Complex Systems, Italy)
Prof. Syamal K. Dana (CSIR - Indian Institute of Chemical Biology, India)
Prof. Victor Kazantsev (Vice-Rector for Research of Lobachevsky State University of Nizhni Novgorod, Russia)

ORGANISING COMMITTEE

Chair: Prof. Alexander Hramov
Conference secretary: Mr. Andrey Andreev

Members:
Dr. Alexander Klimchik
Prof. Semen Kurkin
Mr. Artem Badarin
Ms. Elena Pitsik
Ms. Nataliya Malova
Dr. Nikita Frolov
Dr. Vadim Grubov
Dr. Vladimir Maksimenko

CONTENTS

The program of The Third School for Young Scientists "Dynamics of Complex Networks and their Application in Intellectual Robotics" (DCNAIR 2019)

September 9, Monday		
9.00-9.30 – Opening of the School Room 107		
Time, Room	**Speaker**	**Title of talk**
9.30-10.15, **Room 107**	**Prof. Jürgen Kurths** *Humboldt University, Berlin, Germany*	**Lecture** Predictability of extreme climate events via a complex network approach
10.15-11.00, **Room 107**	**Prof. Claudio Franceschi** *IRCCS Institute of Neurological Sciences Bologna and University of Bologna, Italy*	**Lecture** Systems biology of ageing: dynamics, nonlinearity, and stochasticity
11:00-11:30	*Coffee Break*	
11.30-12.15, **Room 107**	**Prof. Stefano Boccaletti** *ISC-Institute for Complex Systems, Italy*	**Lecture** Collective states of networked phase oscillators: explosive synchronization, dynamically interdependent networks and Bellerophon states
12:15-13:45, Room 320	**Section 1 of the Young Scientists** *Dr. Nikita Frolov*	
12:15-12:25	V.V. Skazkina, E.N. Mureeva, A.S. Karavaev, A.R. Kiselev, E.I. Borovkova, O.S. Panina, Yu.M. Ishbulatov, Y.V. Popova	Choosing parameters for the analysis of synchronization of the autonomic regulatory contours of blood circulation in newborns
12:25-12:35	V.V. Skazkina, Yu.M. Ishbulatov, E.I. Borovkova, B.P. Bezruchko, A.R. Kiselev, A.S. Karavaev	Slow trends in the degree of synchronization of the elements of autonomous control of blood circulation in healthy subjects
12:35-12:45	E.I. Borovkova, Yu.M. Ishbulatov, A.R. Kiselev, A.V. Tankanag, G.V. Krasnikov, A.S. Karavaev	Synchronization of the process of autonomous regulation of blood circulation with low-frequency components of the laser Doppler flowmetry signal
12:45-12:55	E.I. Borovkova, E.P. Chernets, Yu.M. Ishbulatov, V.V. Skazkina, A.S. Karavaev	Experimental observation of Arnold tongues in the analysis of the signal from contour of the autonomous regulation of heart rate and respiration

12:55- 13:05	Yu.M. Ishbulatov, E.I. Borovkova, A.S. Karavaev, A.R. Kiselev, B.P. Bezruchko	Comparing methods for extraction of autonomic control signals from electrocardiogramm
13:05- 13:15	E.V. Navrotskaya, M.V. Sinkin, A.N. Khramkov, D.M. Yezhov, B.P. Bezruchko	Development of a method for coupling detection based on the phase dynamics modeling for analyzing EEG rhythms during an epileptic seizure in patients with a reduced level of consciousness
13:15- 13:25	A. Badarin	Development of a digital software platform for the study of nonlinear dynamics of electronic systems
13:25- 13:35	S. Kurkin	Investigation of complex nonlinear processes in systems with intense relativistic electron beams
13:35- 13:45	V.B. Baiburin, A.S. Rozov	Poisson equation numerical solution method based on bidirectional multiple passage of grid cells and parallel computations
12:15- 13:55, Room 305	**Section 2 of the Young Scientists** *Prof. Semen Kurkin*	
12:15- 12:25	V. Khorev, E. Borovkova, Yu. Ishbulatov, V. Gridnev, A. Karavaev	Asymmetry of coupling between the P3 and P4 electroencephalographic leads during the motions
12:25- 12:35	A.V. Kochetkov, D.R. Malakhov, O.V. Zakharov	Optimization approach for inverse kinematic problem for manipulator with redundant degrees of freedom
12:35- 12:45	A.V. Kochetkov, P.M. Salov, O.V. Zakharov	Route optimization in measuring surfaces on coordinate measuring machines
12:45- 12:55	E. Pitsik, N. Frolov	Time-frequency and recurrence quantification analysis detect limb movement execution from EEG data
12:55- 13:05	A.R. Miftahova, A.E. Hramov	Reccurence plot analysis of functional brain connectivity during bistable visual perception
13:05- 13:15	A.A. Grishchenko, T.M. Medvedeva, C.M. van Rijn, M.V.Sysoeva, I.V. Sysoev	Application of directed connectivity measures for identifying the evolution of the interaction structure in WAG/Rij rats brain at absence epilepsy
13:15- 13:25	A. Kuc, V. Nedaivozov	Influence of the sensory information ambiguity on the brain state during the decision-making task
13:25- 13:35	A. Andreev, A. Pisarchik	Modeling of a brain neuronal network under visual stimulation
13:35- 13:45	A. Andreev, V. Makarov, A. Balanov, A. Hramov	Chaos and hyperchaos in a chain of coupled Rydberg atoms
13:45-	O.N. Pavlova, N.M. Kupriyashkina,	Characterization of intermittent dynamics

13:55	A.N. Pavlov	from experimental data with DFA
12:15-13:15, Room 308	**Section 3 of the Young Scientists** *Prof. Mikhail Prokhorov*	
12:15-12:30	M.D. Prokhorov, D.D. Kulminskiy, V.I. Ponomarenko	Controlling Synchronization in Networks of Nonidentical Neuronlike Oscillators
12:30-12:45	V.I. Ponomarenko, A.S. Karavaev, Yu.M. Ishbulatov, A.R. Kiselev, E.I. Borovkova, V.V. Skazkina, M.D. Prokhorov	Interaction of slow oscillatory processes in the human cardiovascular system and their mathematical modeling
12:45-13:00	A. Karavaev, E. Borovkova, A. Kiselev, A. Runnova, V. Prokhorov, V. Ponomarenko, A. Hramov, V. Gridnev, B. Bezruchko	Interactions between the processes of regulation of the cardiovascular system and the brain structures
13:00-13:15	A. Karavaev, A. Kiselev, E. Borovkova, Y. Popova, V. Gridnev, O. Posnenkova	Dynamics of low-frequency components of photoplethysmogram signals in hypertension
13.15-14.45	*Lunch*	
14:45-15:45, Room 305	**Section 4 of the Young Scientists** *Dr. Vladimir Maksimenko*	
14:45-14:55	N. Frolov, A. Hramov	**Invited Talk** Multilayer perceptron reveals functional connectivity structure in thalamo-cortical brain network
14:55-15:05	A.K. Alimuradov, A.Yu. Tychkov, P.P. Churakov	A novel approach to speech signal segmentation based on empirical mode decomposition to assess human psycho-emotional state
15:05-15:15	A. Tychkov, A. Alimuradov, P. Churakov	The empirical mode decomposition for ECG signal preprocessing
15:15-15:25	A. Petukhov	Modeling the distortions of public opinion under conditions of external influence using differential stochastic equations
15:25-15:35	A.K. Alimuradov, A.Yu. Tychkov, P.P. Churakov	A method for noise-robust speech signal processing to assess human psycho-emotional state
15:35-15:45	V. Khorev	Mean phase coherence modified for piecewise constant phase difference data
14:45-15:30, Room 308	**Section 5 of the Young Scientists** *Prof. Mikhail Prokhorov*	
14:45-15:00	M.A. Simonyan, A.S. Karavaev, Y.M. Ishbulatov, V.V. Skazkina, V.I. Gridnev, B.P. Bezruchko, A.R. Kiselev	Directional coupling between the low-frequency control of heart rate and vessels tone in myocardial infarction patients

15:00- 15:15	S. Salem, V. Tuchin	Theoretical study for a mixture from magnetic microcapsule suspensions and blood under magnetic field effect
15:15- 15:30	S. Salem, V. Tuchin	Numerical simulation for blood flow in a tube under magnetic field effect
September 10, Tuesday		
9.00- 9.45, **Room 107**	**Prof. Vladimir Nekorkin** *Inst. Of Appl. Phys., Nizhny Novgorod, Russia*	**Lecture** Dynamics of oscillatory networks: from simple to complex links
9.45- 10.30, **Room 107**	**Prof. Alexander Fradkov** *Inst. for Problems of Mech. Eng., St. Petersburg, Russia*	**Lecture** Cybernetical physics and cyber-physical systems
10:30- 11:00	*Coffee Break*	
11.00- 11.45, **Room 107**	**Prof. Ulrike Feudel** *Carl von Ossietzky Universität Oldenburg, Oldenburg, Germany*	**Lecture** Tipping phenomena and resilience: two sides of the same coin?
11:45- 12:45, **Room 107**	**Prof. Eugene Postnikov** *Kursk State University, Kursk, Russia*	**Lecture** Spectral and wavelet approaches for revealing state transitions from individual trajectories
12.45- 14.00	Lunch	
14:00- 14:15, **Room 107**	**Dr. Vasiliy Kuznetsov,** *Goethe-Institut, Moscow, Russia*	**Lecture** Philosophical Aspects of Artificial Intelligence
14.15- 14.45, **Room 107**	**Prof. Leonid Savin,** **Prof. Alexey Kornaev** *Orel State University, Orel, Russia*	**Lecture** Application of machine learning to modeling of nonlinear hydromechanical systems
14.45- 15.15, **Room 107**	**Prof. Yury Poduraev** *Moscow State University of Technology "STANKIN", Moscow, Russia*	**Lecture** Intellectual collaborative robotics in medicine: problems and solutions
September 11, Wednesday		
9.00- 9.45, **Room 107**	**Prof. Eckehard Schöll** *Technische Universität, Berlin, Germany*	**Lecture** Partial synchronization patterns in complex networks - interplay of dynamics, time delay, and network topology

9.45-10.30, **Room 107**	**Dr. Annika Lüttjohann** *University of Münster, Münster, Germany*	**Lecture** Development of brain computer interfaces for the interruption and prevention of epileptic seizures
10:30-11:00	Coffee Break	
11:00-13:15, Room 421	**Section 6 of the Young Scientists** *Dr. Annika Lütjohann*	
11:00-11:30	**Prof. Mikhail Lebedev** *Higher School of Economics, Moscow, Russia* *Duke University, Durham, USA*	**Invited Talk** Expansion of brain functions and neurorehabilitation using neurocomputer interfaces
11:30-11:45	P. Chholak, A.N. Pisarchik, S.A. Kurkin, V.A. Maksimenko, A.E. Hramov	**Invited Talk** Phase-amplitude coupling between mu- and gamma-waves to carry motor commands
11:45-12:00	V. Maksimenko, V. Grubov	Cognitive interaction during a collaborative attentional task
12:00-12:15	V. Grubov, V. Maksimenko, V. Makarov	Features of brain activity in children during cognitive tasks of different types
12:15-12:30	V. Grubov, N. Frolov, E. Pitsik, A. Badarin	Features of real and imaginary motor activity on EEG and fNIRS signals for neurorehabilitation
12:30-12:45	E. Pitsik, N. Frolov, A. Hramov	Network analysis of brain activity during real motor actions execution using recurrence-based measure of dependence
12:45-13:00	A. Hramov, A. Kiselev, N. Schykovskii	Post-stroke rehabilitation with the help of brain-computer interface
13:00-13:15	A. Hramov, A. Pisarchik	Kinesthetic and visual modes of imaginary movement: MEG studies for BCI development
11:00-13:40, Room 107	**Section 7 of the Young Scientists** *Prof. Vladimir Ponomarenko*	
11:00-11:10	A. Kornaev, R. Zaretsky, S. Egorov	Simulation of deep learning control systems to reduce energy loses due to vibration and friction in rotor bearings
11:10-11:20	M.V. Bobyr, A.S. Yakushev, N.A. Milostnaya	Three-coordinate definition of color mark and distance to objects according to stereo image
11:20-11:30	N. Fadeeva, A. Gulai, S. Astakhov	Amplitude-phase dynamics of the three-mode cross-coupled generator
11:30-11:40	D. Artyukhov, I. Artyukhov, V. Alekseev, I. Burmistrov	Using thermoelectrics for power supplying of wireless sensors network
11:40-	A. Makashov	The network layer model of the wireless

11:50		sensor network acting under the influence of interferences
11:50- 12:00	A. Kirpichnikov, A. Titovtsev	Practical recommendations on the application of Markov queuing models with a restricted queue
12:00- 12:10	V.A.-jr. Krysko, T.V. Yakovleva, V.A. Krysko	Theory of contact interaction of inhomogeneous beam-lamellar nanostructures taking into account the connectivity of the temperature and deformation fields
12:10- 12:20	I.V. Papkova, A.V. Krysko, E.Yu. Krylova	Mathematical modeling of NEMS elements in the form of flexible round plates under the Casimir's force action
12:20- 12:30	E.Yu. Krylova, I.V. Papkova, O.A. Saltykova, V.A. Krysko	Mathematical modeling of the behavior of flexible micropolar mesh cylindrical panels with two sets of mutually orthogonal rods
12:30- 12:40	O.A. Saltykova, V.A. Krysko	Nonlinear dynamics of a flexible closed cylindrical size-dependent shell under the action of a band load
12:40- 12:50	M. Bolotov, T. Levanova, L. Smirnov, A. Pikovsky	Dynamics of disordered heterogeneous chains of phase oscillators
12:50- 13:00	A.M. Vaskovsky, M.S. Chvanova	Designing the neural network for personalization of food products for persons with genetic president of diabetic sugar
13:00- 13:10	A. Kuc, V. Maksimenko	Spatio-temporal cortical activity during a visual task accomplishing
13:10- 13:20	S. Kurkin, P. Chholak, V. Maksimenko, A. Pisarchik	Machine learning approaches for classification of imaginary movement type by MEG data for neurorehabilitation
13:20- 13:30	A. Badarin	The control of the dynamics of intense electron beams coupled through a common field
13:30- 13:40	S. Kurkin, V. Maksimenko, E. Pitsik	Approaches for the improvement of motor-related patterns classification in EEG signals
13.00- 14.30	Lunch	
14:30- 16:30 Room 305	**Section 8 of the Young Scientists** *Prof. Mikhail Ivanchenko*	
14:30- 14:45	**Prof. Viktor Kazantsev** *Lobachevsky State University of Nizhni Novgorod, Russia*	**Invited Talk** To be announced
14:45- 15:00	S. Jalan, V. Rathore, A.D. Kachhvah, A. Yadav	Multiplexing with inhibitory layer leading to explosive synchronization in multiplex networks
15:00-	I.P. Mariño, L. Lacasa, J. Míguez,	Identifying the hidden multiplex

15:15	V. Nicosia, É. Roldán, A. Lisica, S.W. Grill, J. Gómez-Gardeñes	architecture of biological processes
15:15-15:30	S. Makovkin, M. Ivanchenko, A. Zaikin, S. Jalan	Investigating multiplex models of neuron-glial systems: small-world topology and inhibitory coupling
15:30-15:45	M. Krivonosov, M. Ivanchenko, S. Jalan, M.G. Bacallini, C. Franceschi	Parenclitic analysis of high-dimensionality DNA methylation data
15:45-16:00	O. Vershinina, S. Denisov, M. Ivanchenko	Quasi-stationary oscillations in game-driven evolutionary dynamics
16:00-16:15	A. Makeeva, A. Dmitrichev, V. Nekorkin	Torus canards in the ensemble synaptically related neurons Fitzhugh-Nagumo
16:15-16:30	T. Nazarenko, M. Krivonosov, A. Zaikin	Analysis of longitudinal high-dimensional medical data with parenclitic networks
14:30-16:40, Room 421	**Section 9 of the Young Scientists** *Dr. Anatoly Karavaev*	
14:30-14:40	M. Rassabin, R. Yagfarov, S. Gafurov	Approaches for road lane detection
14:40-14:50	S. Mikhel	State-based velocity profile for manipulator
14:50-15:00	V. Skvortsova, D. Popov	Design of the parallel spherical manipulator for wrist rehabilitation
15:00-15:10	R. Khusainov, S. Mamedov, P. Dmitry	Trajectory planning for biped walk with non-instantaneous double support phase
15:10-15:20	A. Evlampev, M. Ostanin	Obstacle avoidance for robotic manipulator using mixed reality glasses
15:20-15:30	P. Khakimov, S. Savin, A. Klimchik	Trajectory optimization for underactuated systems using reinforcement learning: cart-pole problem
15:30-15:40	I.D. Galushko, G.M. Makaryants, S.A. Gafurov	Mathematical modeling of changes in geometric parameters of pneumatic muscles
15:40-15:50	A. Kurbanov, S. Grebennikov, S. Gafurov, A. Klimchik	Vulnerabilities in the vehicle's electronic network equipped with ADAS system
15:50-16:00	R. Yagfarov, V. Ostankovich, S. Gafurov	Augmentation-based object detection for winter time applications
16:00-16:10	G.Y. Prokudin, N.G. Sharonov, E.S. Briskin	Optimal control of orthogonal-rotary movers of walking robot with an excessive number of drives
16:10-16:20	T.I. Muftakhov, V.M. Giniyatullin, D.V. Shekhovtsov	Interpretation of the results of the neural network after the substitution of continuous activation function on the threshold function
16:20-16:30	N. Stankevich, E. Volkov, E. Hellen	Self-organized quasiperiodicity and multistability in dynamical systems of different nature

16:30-16:40	E. Bagautdinova, S. Kuznetsov, E. Seleznev, N. Stankevich	Circuit simulation of a blue sky catastrophe in the context of bursting dynamics occurrence
16:30-17:00	Coffee Break	
17:00-18:00, Room 421	**Section 10 of the Young Scientists** *Dr. Vadim Grubov*	
17:00-17:10	S. Savin	Detecting changes in contact interaction regime with a reaction predictor and a linear contact model
17:10-17:20	D. Popov, A. Klimchik	Identification stiffness model parameter for bipedal robots
17:20-17:30	D. Popov, A. Klimchik	Multiple collision detection for a collaborative robot
17:30-17:40	P. Kozlov, A. Klimchik	Automated robotic assembly of complex workpieces from regular components
17:40-17:50	E.A. Marchuk, A.P. Fedin, Ya.V. Kalinin	Neuro-fuzzy anti-block braking system of the vehicle
17:50-18:00	T.A. Tarasova, I.A. Tarasova, A.V. Maloletov, Ya.V. Kalinin	Application of systems of stochastic differential equations for modeling transport processes
18.00-18.30, Room 107	**Closing ceremony**	

A method for noise-robust speech signal processing to assess human psycho-emotional state

Alan K. Alimuradov
Research Institute for Fundamental and Applied Studies
Penza State University
Penza, Russia
alansapfir@yandex.ru

Alexander Yu. Tychkov
Research Institute for Fundamental and Applied Studies
Penza State University
Penza, Russia
tychkov-a@mail.ru

Pyotr P. Churakov
Data Measuring Equipment and Metrology Department
Penza State University
Penza, Russia
churakov-pp@mail.ru

***Abstract*—The nature of the noise-robust processing method consists in decomposing a speech signal into informative noise and signal frequency components using the improved complete ensemble empirical mode decomposition with adaptive noise, and selection of the component containing the pitch with the subsequent determination of frequency features. A simplified block diagram of the method with a brief mathematical description is presented. A study was conducted using a verified base of pure and noisy speech signals recorded from a group of subjects with signs of psycho-emotional disorders. In accordance with the results of the study, the method provides good robustness to noise of various intensities (signal-to-noise ratio is from 0 dB to 30 dB), and can be successfully tested in actual conditions of an "aggressive" noise environment to assess a person's psycho-emotional state.**

Keywords—noise robustness, speech signal, empirical mode decomposition, psycho-emotional state

I. INTRODUCTION

In the last decade, an automated assessment of human psycho-emotional state by speech has been actively developed. Speech is very sensitive to disorders of the nervous system and depending on the psychological situation it "encodes" the emotional state of a person into certain relevant informative parameters [1]. In the conditions of free human activity and current "aggressive" noise environment, all speech signals are to some degree noisy. To improve noise robustness, it is urgent to create novel speech processing methods that are adaptive to modern noise environments. The article presents a method for noise-robust processing of speech signals, applicable in systems for assessing a psycho-emotional state in conditions of noisy environment. In particular, the method is designed to determine frequency features of speech, and is based on empirical mode decomposition (EMD) [2].

II. MATERIALS AND METHODS

A. Frequency Features of Speech

A speech signal is a complex acoustic oscillation. Frequency features give necessary and sufficient information on a person with a minimum time of perception. Frequency features used in the method that most fully reflect information on psycho-emotional state of a person include [2]: minimum, average and maximum values of pitch frequency (PF); standard PF deviation; range of background frequencies; mean absolute value of jitter; relative average PF perturbation; pitch perturbation quotient.

B. Empirical Mode Decomposition

The principle of empirical mode decomposition (EMD) consists in decomposing a signal into a sum of functions with a limited band, called intrinsic mode functions (IMF), or modes [3]:

$$x(n) = \sum_{i=1}^{I} IMF_i(n) + r_I(n) \quad (1)$$

where $x(n)$ is an original signal; $IMF_i(n)$ is an IMF; $r_I(n)$ is a residue, $i = 1, 2, \ldots, I$ is the IMF number, n is discrete timing.

During decomposition, the signal model is not specified in advance, and an IMF is calculated during the sifting procedure, taking into account local features (such as extremes and signal zeros), and the internal structure of each particular signal. The results of detailed studies of decomposition technologies have revealed the promise of using the improved complete ensemble empirical mode decomposition with adaptive noise (CEEMDAN) [4], based on the classic EMD.

III. DESCRIPTION OF THE METHOD

Currently, lots of filtering methods based on classical approaches have been developed, for example, enhancing clarity (adjustment) of speech, well known as spectrum subtraction methods, Wiener filters, cepstral mean subtraction (CMS), cepstral variance normalization (CVN), and others. However, in conditions of aggressive noise environment with signal-to-noise ratio (SNR) values of 10 dB, 5 dB and 0 dB, the known methods do not provide the required noise suppression.

The nature of the proposed method consists in decomposing a signal into informative noise and signal frequency components, and the selection of the component containing the pitch (P) followed by the determination of frequency features. Decomposition by the improved CEEMDAN is the basis of the method, which allows filtering a noisy speech signal If we assume that the noise component of the signal has the highest frequency, then it will be extracted into the first IMF, which can be eliminated at subsequent processing steps. An idea of noise robustness is based on this principle of the improved CEEMDAN technology. Determination of the informative signal mode, containing the pitch, consists in sequent modulo calculating the difference between the values of the energy logarithms of the current and subsequent modes [2].

To determine the PF value, the method uses the function of the Teager operator. The use of this function in speech

signal processing is justified by the efficiency, simplicity of calculations, and good susceptibility to a sharp change in the amplitude of the signal:

$$T(n) = \left(IMF_{i,PF}(n)\right)^2 - IMF_{i,PF}(n-1) \times IMF_{i,PF}(n-1) \quad (2)$$

where $T(n)$ is the function of the Teager operator; $IMF_{i,PF}(n)$ is the IMF, containing the pitch.

Having calculated the values of the Teager operator function, the P period is determined by closely located maxima (in one) in milliseconds, and then the PF is determined in Hz:

$$P_0 = \frac{T_{max}(n+2) - T_{max}(n)}{f_d} \quad (3)$$

$$f_0 = \frac{1}{P_0} \quad (4)$$

where P_0 is the pitch; f_0 is the PF; $T_{max}(n)$, $T_{max}(n+2)$ are the maxima of the Teager operator function; f_d is the sampling rate.

IV. Investigation of the Method

To test the developed method, a group of subjects was formed with the support of K.R. Evgrafov Regional Psychiatric Hospital, and Medical Institute of Penza State University (Penza, Russian Federation). The group comprised 220 male and female subjects, aged 18 to 79 years with signs of psycho-emotional disorders. A control group of 220 conditionally healthy subjects was formed from the staff and lecturers of Penza State University. In accordance with the method developed by the authors, a database of speech signals was registered. To determine the assessment effectiveness of a psycho-emotional state, errors of the first and second kind were used. Noisy speech signals (signal-to-noise ratio is 30 dB, 20 dB, 10 dB, and 0 dB) were generated by imposing white noise with different amplitudes to pure speech signal. Table 1 presents the results of determination of a human psycho-emotional state for pure and noisy speech signals.

TABLE I. Results of Determination of Psycho-Emotional States

Predictable result	Determination result, pers.		Errors, %	
	Pathology	*Norm*		
Pure speech signal				
Pathology	184	36	1st, α	16.36
Norm	18	202	2nd, β	8.19
Noisy signal, SNR = 30 dB				
Pathology	182	38	1st, α	17.27
Norm	22	198	2nd, β	10.00
Noisy signal, SNR = 20 dB				
Pathology	168	52	1st, α	19.10
Norm	31	189	2nd, β	14.09
Noisy signal, SNR = 10 dB				
Pathology	154	66	1st, α	30.00
Norm	45	202	2nd, β	20.45
Noisy signal, SNR = 0 dB				
Pathology	121	99	1st, α	45.00
Norm	58	157	2nd, β	26.36

V. Discussion and Results

The obtained results show that the values of the 1st (α) and 2nd (β) kind errors are within acceptable limits (< 25% and < 20%) for noisy signals, including high values of noise intensity (SNR is 10 dB and 0 dB). Fig. 1 (left column) shows oscillograms of noisy voiced sections of a speech signal. The reliability of α and β error values obtained is confirmed by an analysis of the power spectral density of the IMFs, containing the pitch, derived from the decomposition of pure and noisy speech signals (Fig. 1, right column).

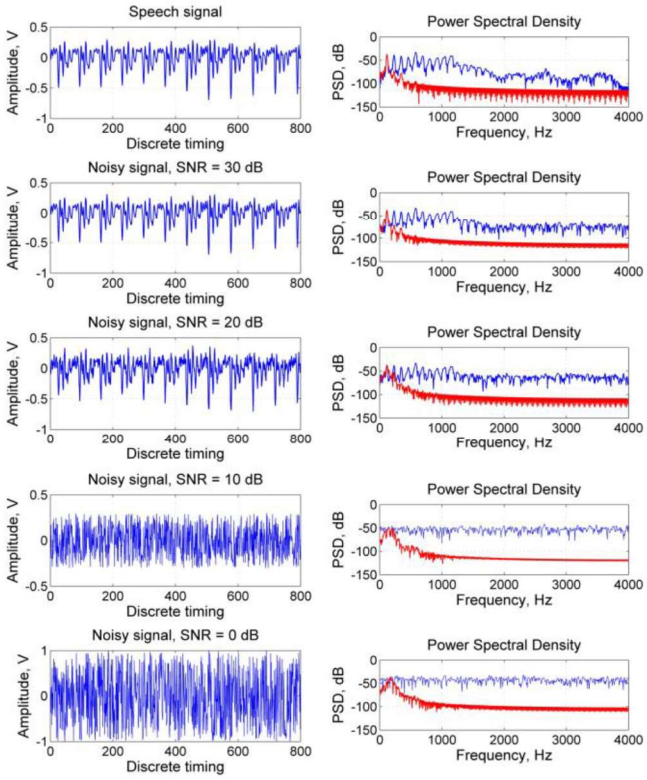

Fig. 1. Oscillograms of noisy voiced sections of the speech signal (left column); power spectral densities (right column) of noisy voiced speech signal sections (blue color), and extracted IMFs containing the pitch (red color).

Based on the obtained results, we can conclude that the developed method for determining frequency features of speech signals provides a fairly good stability even at very high values of noise intensity. Thus, the method can be successfully tested under the conditions of a modern "aggressive" noise environment in systems for assessing human psycho-emotional state.

Acknowledgment

Funded by the Council for Grants of the President of the Russian Federation, project No. SP-246.2018.5, 2018-2020.

References

[1] B.W. Schuller and A.M. Batliner, Computational Paralinguistics: Emotion, Affect and Personality in Speech and Language Processing. New York: Wiley, 2013.

[2] A.K. Alimuradov, A.Yu. Tychkov, A.V. Kuzmin, P.P. Churakov, A.V. Ageykin, and G.V. Vishnevskaya, "Improved CEEMDAN based speech signal analysis algorithm for mental disorders diagnostic system. Pitch frequency detection and measurement," International Journal of Embedded and Real-Time Communication Systems (IJERTCS), 2019, vol. 10, no. 1, pp. 22-47.

[3] N.E. Huang, Sh. Zheng, and R.L. Steven, "The empirical mode decomposition and the Hilbert spectrum for nonlinear and non-stationary time series analysis," Proc. R. Soc. Lond., vol. A454, pp. 903-995, 1998.

[4] M.A. Colominasa, G. Schlotthauera, and M.E. Torres, "Improved complete ensemble EMD: A suitable tool for biomedical signal processing," Biomedical Signal Processing and Control, 2014, vol.14, pp. 19-29.

A novel approach to speech signal segmentation based on empirical mode decomposition to assess human psycho-emotional state

Alan K. Alimuradov
Research Institute for Fundamental and Applied Studies
Penza State University
Penza, Russia
alansapfir@yandex.ru

Alexander Yu. Tychkov
Research Institute for Fundamental and Applied Studies
Penza State University
Penza, Russia
tychkov-a@mail.ru

Pyotr P. Churakov
Data Measuring Equipment and Metrology Department
Penza State University
Penza, Russia
churakov-pp@mail.ru

***Abstract*—A novel technology for speech signal segmentation into voiced, unvoiced and pause sections has been developed. It is based on the adaptive decomposition of short-time fragments of speech signals with a subsequent analysis of the parameters of empirical modes. A segmentation method based on a novel technology with a brief mathematical description is presented. The research has been conducted using the formed base of speech signals, recorded from 220 male and female subjects with signs of psycho-emotional disorders. In accordance with the obtained results, it was concluded that the method based on the developed technology determines the boundaries of informative sections more accurately, and it can be successfully tested at the preprocessing stages in the systems for detection and assessment of human psycho-emotional disorder.**

Keywords—speech signal processing, empirical mode decomposition, voiced and unvoiced speech, psycho-emotional state assessment

I. INTRODUCTION

To control a psycho-emotional state is very important in those branches of human activity that are associated with an increased risk of man-made and biogenic accidents [1]. This is especially relevant for operators of control systems with a high degree of responsibility: pilots, astronauts, airport dispatchers, and dispatchers of hazardous production facilities (e.g., nuclear power plants, thermal power plants, chemical and nuclear industries).

Currently, research in the field of detection and assessment of human psycho-emotional disorder by speech is actively supported by grants of large companies and international technological funds:

- Industry Cooperation with BMW AG, project "Sentiment Analyses", May 1, 2018 - May 31, 2021.
- EU H2020 Marie Sklodowska-Curie Innovative Training Networks European Training Networks (MSCA-ITN-ETN: ENG), project "Training Network on Automatic Processing of Pathological Speech" (#766287), November 1, 2017 - October 31, 2021.

The greatest interest in this field belongs to new approaches and technologies for speech signal processing, but due to trade secret this information is not provided. That is why, modernization of existing methods and development of speech processing technologies remains in the focus of researchers in solving problems of detecting and assessing human psycho-emotional disorder.

This article presents a novel technology for speech signal segmentation into informative sections, based on the empirical mode decomposition method (EMD) [2]. The article is the development of the previously published works of the authors [3, 4].

II. MATERIALS AND METHODS

A. Speech Signal

A speech signal is a complex acoustic signal whose characteristics change rapidly in time. Depending on the degree of involvement of the vocal cords, human speech is divided into voiced and unvoiced speech, and pauses [5]. In accordance with the physiological aspect of the formation of speech, a person makes an initial short pause from 200 to 500 ms before pronunciation, corresponding to silence.

The speech apparatus is extremely sensitive to disorders of the nervous system. Duration, rate, acceleration and entropy of the distribution of the time intervals of voiced, unvoiced and pause sections characterize the operation of the speech apparatus [6].

B. Segmentation into Informative Sections

Segmentation into informative sections is a process of determining the exact boundaries of voiced, unvoiced and pause sections in continuous speech. Correct determining the boundaries of informative sections of speech not only increases the efficiency of detection and assessment of human psycho-emotional disorder, but also reduces the number of computational operations.

At present, there are many different approaches to the segmentation of speech signals. Among the most known methods are the ones based on:

- The analysis of short-time energy (STE) and zero-crossing rate (ZCR).
- The analysis of statistical properties of the background noise and the one-dimensional Mahalanobis distance.

C. Empirical Mode Decomposition

The empirical mode decomposition (EMD) method was developed by Norden Huang in 1998, and was intended to decompose non-stationary signals arising in nonlinear systems [2]. The EMD provides decomposition of a signal into high frequency and low frequency components, called intrinsic mode functions (IMFs). During decomposition, the

signal model is not set in advance, the IMFs are calculated during the sifting procedure taking into account local features (extremes and zeros of the signal), and the internal structure of a particular signal. Thus, IMFs do not have a rigorous analytical description:

$$x(n) = \sum_{i=1}^{I} IMF_i(n) + r_I(n) \quad (1)$$

where $x(n)$ is an original signal; $IMF_i(n)$ is an IMF; $r_I(n)$ is a residue, $i = 1, 2, \ldots, I$ is the IMF number, n is discrete timing.

An improved complete ensemble empirical mode decomposition with adaptive noise (CEEMDAN) is the most adaptive to complex non-stationary speech signals [7]. The emergence of the improved CEEMDAN made it possible to solve a number of problems inherent in other types of decomposition: mixing the IMFs that are incommensurable in amplitude and frequency scales; the presence of residual noise in IMFs; the presence of parasitic IMFs in the early stages of decomposition.

A characteristic feature of the improved CEEMDAN is the addition of controlled noise to the original signal to create new extremes:

$$x_j(n) = x(n) + w(n) \quad (2)$$

$$x_j(n) = \sum_{i=1}^{I} IMF_{ji}(n) + r_{jI}(n) \quad (3)$$

$$IMF_i(n) = \sum_{j=1}^{J} \frac{IMF_{ji}(n)}{J} \quad (4)$$

$$r_I(n) = \sum_{j=1}^{J} \frac{r_{jI}(n)}{J} \quad (5)$$

where $j = 1, 2, \ldots, J$ is the amount of white noise realizations; $x_j(n)$ are noise copies of a speech signal; $w_j(n)$ are white noise realizations.

III. Brief Description of a Novel Segmentation Technology

Fig. 1 structurally presents a method for speech signal segmentation based on the proposed technology. Blocks 1-3 represent the first stage of the method in which the following steps are carried out: the linear division of a speech signal into short-term fragments of 30 ms duration; decomposition of fragments into IMFs; determination of IMF parameters. In the framework of the second stage (blocks 4, 5), direct segmentation is carried out: the formation of threshold values for the parameters of IMF fragments corresponding to the initial pause; determination of voiced, unvoiced and pause sections.

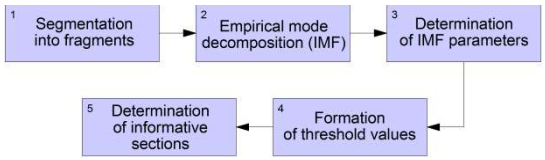

Fig. 1. The structure of the segmentation method of speech signals into informative sections.

Fig. 2 shows an example of the functioning of the segmentation method based on the proposed technology. In accordance with the novel approach, each short-term fragment of a speech signal is represented by a set of IMFs obtained by the improved CEEMDAN method (Fig. 2c, 2e, 2g). A special feature of the novel segmentation technology is that the correlation of the analyzed signal fragment to voiced, unvoiced speech or pause is carried out by examining the properties of each IMF fragment separately. Given that each IMF has certain parameters, a comparative analysis of the IMFs increases the efficiency of determining the boundaries of voiced, unvoiced sections and pauses during unstable operation of the speech apparatus.

The studied parameters of IMF speech signal fragments are:

- Logarithm of energy:

$$LE_{s,i} = log_2\left(\sum_{n=1}^{N}\left(IMF_{s,i}(n)\right)^2\right) \quad (6)$$

where $LE_{s,i}$ is IMF energy logarithm of the speech signal fragment; s is the fragment number;

- The ratio of the IMF short-term energy to the zero-crossing rate of the IMF signal:

$$Z_{s,i} = \frac{\sum_{n=1}^{N}\left(IMF_{s,i}(n)\right)^2}{ZCR_{s,i}} \quad (7)$$

$$ZCR_{s,i} = 0{,}5\sum_{n=1}^{N-1}\left|sgn\left(IMF_{s,i}\left((n-1)N+n+1\right)\right) - sgn\left(IMF_{s,i}\left((n-1)N+n\right)\right)\right| \quad (8)$$

where $ZCR_{s,i}$ is the zero-crossing rate of the IMF signal; sgn is the sign function ($sgn(x) = 1$, if $x \geq 0$ and $sgn(x) = -1$, if $x < 0$).

Applying the averaged values of IMF parameters LE and Z for fragments of the initial pause (200 ms), one can determine the threshold values of $LE_{tresh.}$ and $Z_{tresh.}$. Fig. 2h and 2i (left column) present a graphical interpretation for determination of threshold values for the first six modes. Dashed red lines indicate the values of the IMF parameters of the initial pause, and the averaged threshold values of the IMF parameters are marked with a thick red solid line. Fig. 2h and 2i (right column) provide a graphical interpretation for threshold processing. A thick solid green line indicates the IMF parameters of the voiced speech fragment, and a thick blue line is for the unvoiced fragment.

Fig. 3 shows the result of speech signal segmentation into information sections (pauses are in red colour; voiced and unvoiced speech are in green and blue colour, respectively).

IV. Research and Segmentation Results

To study the novel segmentation technology, a group of subjects has been formed with the participation of K.R. Evgrafov Regional Psychiatric Hospital (Penza, Russian Federation). The group included 220 men and women with signs of psycho-emotional disorders. A database of speech signals, consisting of phonetically balanced words, phrases, and sentences has been registered. The segmentation efficiency was estimated by the detection rate (DR) [8], being a dimensionless quantity equal to the ratio of correctly defined fragments to the total number of fragments. Speech signal segmentation was used as a reference in a manual mode of a specialized sound editor.

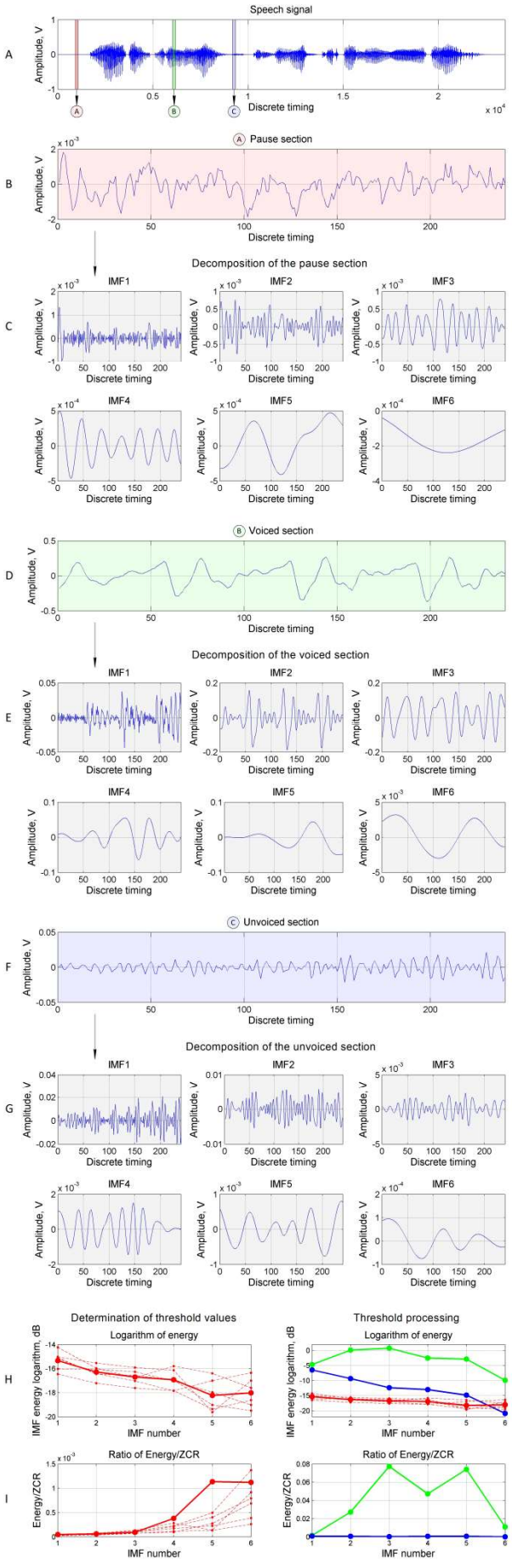

Fig. 2. Operation of the segmentation method based on the proposed technology.

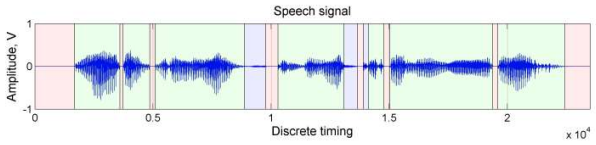

Fig. 3. Speech signal segmentation.

Table 1 presents the averaged results of speech signal segmentation into voiced, unvoiced speech and pauses in comparison with other methods.

TABLE I. SEGMENTATION RESULTS

Segmentation methods	DR, %		
	Voiced speech	*Unvoiced speech*	*Pauses*
Method based on the analysis of STE+ZCR	88.6	46.4	78.5
Method based on the analysis of the Mahalanobis distance	78.5	90.2	58.6
Method based on the novel technology	97.5	77.3	91.4

In accordance with the obtained DR values, it can be concluded that the method based on the novel technology provides the best results for the segmentation of speech signals recorded with signs of psycho-emotional disorders. These results are achieved through the study of each IMF features of the analyzed fragment, which allows you to accurately determine the boundaries of informative speech sections during unstable operation of the speech apparatus. Thus, the proposed novel segmentation technology can be successfully tested at the preprocessing stages in the systems for detecting and evaluating human psycho-emotional disorder.

ACKNOWLEDGMENT

This work was financially supported by the Russian Foundation for Basic Research according to the research project No. 18-37-00256.

REFERENCES

[1] B.W. Schuller and A.M. Batliner, Computational Paralinguistics: Emotion, Affect and Personality in Speech and Language Processing. New York: Wiley, 2013.

[2] N.E. Huang, Sh. Zheng, and R.L. Steven, "The empirical mode decomposition and the Hilbert spectrum for nonlinear and non-stationary time series analysis," Proc. R. Soc. Lond., 1998, vol. A454, pp. 903-995.

[3] A.K. Alimuradov, A.Yu. Tychkov, and P.P. Churakov, "Increasing detection efficiency of psycho-emotional disorders based on adaptive decomposition and cepstral analysis of speech signals," Proc. 2019 International Youth Conference on Radio Electronics, Electrical and Power Engineering (REEPE), March 14-15, 2019, Moscow, Russia, 5 p.

[4] A.K. Alimuradov, A.Yu. Tychkov, and P.P. Churakov, "Formant analysis of speech signals based on empirical mode decomposition to detect human psycho-emotional disorder," Proc. 2019 IEEE Conference of Russian Young Researchers in Electrical and Electronic Engineering (EIConRus), Jan. 28-31, 2019, Saint Petersburg; Moscow, Russia, pp. 1123-1128.

[5] G.K. Fant, Acoustic Theory of Speech Formation. Moscow: Nauka, 1964.

[6] J. Hlavnička, R. Čmejla, T. Tykalová, K. Šonka, E. Růžička, and J. Rusz, "Automated analysis of connected speech reveals early biomarkers of Parkinson's disease in patients with rapid eye movement sleep behaviour disorder," Scientific Reports, 2017, vol. 7, no.12, 13 p.

[7] M.A. Colominasa, G. Schlotthauera, and M.E. Torres, "Improved complete ensemble EMD: A suitable tool for biomedical signal

processing," Biomedical Signal Processing and Control, 2014, vol. 14, pp. 19-29.

[8] X. Huang, A. Acero, and H.-W. Hon, Spoken Language Processing. Guide to Algorithms and System Development. Prentice Hall, 2001.

Chaos and hyperchaos in a chain of coupled Rydberg atoms

Andrey Andreev
Neuroscience and Cognivite Technology Lab, Center for Technologies in Robotics and Mechatronics Components
Innopolis University
Innopolis, Russia
andreevandrei1993@gmail.com

Vladimir Makarov
Neuroscience and Cognivite Technology Lab, Center for Technologies in Robotics and Mechatronics Components
Innopolis University
Innopolis, Russia
vladmak404@gmail.com

Alexander Balanov
Department of Physics,
Loughborough University,
Loughborough, United Kingdom
A.Balanov@lboro.ac.uk

Alexander Hramov
Neuroscience and Cognivite Technology Lab, Center for Technologies in Robotics and Mechatronics Components
Innopolis University
Innopolis, Russia
hramovae@gmail.com

***Abstract*—Partially quantum coherent arrays of artificial atoms (e.g., superconducting qubits) may be used as analogue simulators of other quantum systems, when the behaviour of the latter cannot be directly observed or modeled by classical means. Here we show that a chain of superconducting qubits can simulate the chaotic behaviour predicted in chains of Rydberg atoms. We investigate the transition from periodic to chaotic dynamics and show the increase of the number of positive Lyapunov exponents as the number of atoms grows. The possibility of an external control and suppression of hyperchaos in the chain is demonstrated.**

Keywords—Rydberg atoms, chaos, hyperchaos, qubits, nonlinear dynamics.

I. INTRODUCTION

Current progress in fabrication and experimental techniques allows creation of large, partially quantum coherent arrays of "artificial atoms" (e.g., superconducting qubits), which allow a degree of control over their quantum state. When fully developed, such devices can find numerous applications, ranging from quantum sensing and communications to universal quantum computing [1,2]. A straightforward application of such structures is the simulation of other quantum systems, which are too big or too complex for simulation by classical computers. The digital quantum simulation is based on mimicking the action of the evolution operator of the simulated system with a sequence of elementary transformations realized by timely changing the Hamiltonian of the simulator. While providing scalability, versatility and controlled accuracy, this approach imposes practically as strict requirements on the hardware as a universal quantum computation. On the contrary, the analogue quantum simulation is less demanding, because it uses the natural evolution of the simulator and thus does not require a precise control over its Hamiltonian. The downside is the loss of universality and controlled precision. This approach has already provided interesting results within the current experimental capabilities [3].

In this paper we discuss the possibility of simulating a chain of Rydberg atoms with qubits. Rydberg atoms are a topic of active research in quantum technologies and many-body physics because of their strong dipole-dipole interactions allowing long-range entanglement, leading to a rich physics, and also, as we shall see, they are a natural choice for analogue quantum simulation.

II. MODEL

The standard description of a set of interacting qubits is based on the Ising Hamiltonian,

$$H = \sum_j H_j + \sum_{j<k} U_{jk}, \qquad (1)$$

with

$$H_j = -\frac{1}{2}\left[\epsilon_j \sigma_j^z + \delta_j \sigma_j^x\right], \quad U_{jk} = J_{jk}\sigma_j^z \sigma_k^z. \qquad (2)$$

Here the Pauli operators, σ_j^α, describe the transitions between qubit states, ϵ_j and δ_j are, respectively, the bias and the tunneling matrix element in the *j*-th qubit, and J_{jk} is the qubit-qubit coupling. Expressing the Pauli matrices in terms of projectors to ground and excited states of the qubits, $|g\rangle$, $|e\rangle$,

$$\sigma_j^z \equiv |g\rangle\langle g|_j - |e\rangle\langle e|_j \equiv \hat{1}_j - 2|e\rangle\langle e|_j;$$
$$\sigma_j^x \equiv |e\rangle\langle g|_j + |g\rangle\langle e|_j; \hat{1}_j \equiv |g\rangle\langle g|_j + |e\rangle\langle e|_j \qquad (3)$$

we can rewrite (2) as

$$H_j = -\frac{1}{2}\epsilon_j \hat{1}_j + \epsilon_j |e\rangle\langle e|_j - \frac{1}{2}\delta_j\left[|e\rangle\langle g|_j + |g\rangle\langle e|_j\right],$$
$$H_{jk} = \left[\hat{1}_j - 2|e\rangle\langle e|_j\right] \otimes \left[\hat{1}_k - 2|e\rangle\langle e|_k\right]. \qquad (4)$$

The resulting form of the Hamiltonian (1),

$$H = \sum_j \left\{ \left[\epsilon_j - 2\sum_k J_{jk} \right] |e\rangle\langle e|_j - \frac{1}{2}\delta_j \left[|e\rangle\langle g|_j + |g\rangle\langle e|_j \right] \right\}$$

$$+4\sum_{jk} J_{jk}\, |e\rangle\langle e|_j \otimes |e\rangle\langle e|_k + \left[-\frac{1}{2}\sum_j \epsilon_j + \sum_{jk} J_{jk} \right].$$

Up to the irrelevant total energy shift, $\Delta E = \left[-\frac{1}{2}\sum_j \epsilon_j + \sum_{jk} J_{jk} \right]$, and parameter relabeling, this Hamiltonian is just an inhomogeneous version of the interaction-representation Hamiltonian of a system of Rydberg atoms in a laser field [4,5].

$$H = \sum_{j=1}^{N} \left[-\widetilde{\Delta} |e\rangle\langle e|_j + \frac{\widetilde{\Omega}}{2} \left(|e\rangle\langle g|_j + |g\rangle\langle e|_j \right) \right] + \frac{V}{N-1} \sum_{j<k} |e\rangle\langle e|_j \otimes |e\rangle\langle e|_k \qquad (5)$$

where $\widetilde{\Delta} = w_l - w_o$ is the detuning between the laser and transition frequencies, and $\widetilde{\Omega}$ is the Rabi frequency (tuned by the laser field amplitude). Therefore, one can directly model the behavior of Rydberg atoms by using a set of qubits, thus realizing an instance of analogue quantum simulation.

Further, introducing appropriate Lindblad operators responsible for relaxation and pure dephasing, we obtain for the matrix elements $w_j = (\rho_j)_{11} - (\rho_j)_{00}$ (population inversion of the *j*-th qubit) and $q_j = (\rho_j)_{10} = (\rho_j)^*_{01}$ (its coherence) the following set of equations

$$\dot{w}_j = -2\Omega\, \mathrm{Im} q_j - (w_j + 1)$$

$$\dot{q}_j = i\left[\Delta - c\sum_{k\neq j} (w_j + 1) \right] q_j - \frac{1}{2} q_j + i\frac{\Omega}{2} w_j \qquad (6)$$

where w_j is the inversion, q_j is off-diagonal element, $\Omega = \widetilde{\Omega}/\gamma$, $\Delta = \widetilde{\Delta}/\gamma$, $c = dV/\gamma$, where *d* is the lattice dimension.

III. Results

We study the dynamics of ring lattices consisting of different number of Rydberg atoms as it is schematically shown in Fig. 1. We investigate the dynamics of the system using Lyapunov exponents calculation and bifurcation diagrams plotting. Authors of [4] found that there are 3 possible regimes of the dynamics: uniform, antiferromagnetic and oscillatory and no chaos. But we found chaos and hyperchaos in the system, and hyperchaos characterized by different number of positive Lyapunov exponents that depends of control parameters value and number of atoms in the system [6]. We analyse the region of control parameters Ω and Δ using Lyapunov exponents calculation.

We started our consideration with studying the dynamics of two coupled atoms. Previously, it has been shown [4] that interplay between the energy pumping and dissipation can eventually evoke self-sustained oscillations of the populations in this system, and even lead to emergence of bistability, when homogeneous and antiferromagnetic states coexist at the same time. Our analysis revealed another interesting phenomenon associated with onset of deterministic chaos, which is realized via a cascade of period-doubling bifurcation for periodic oscillations. We found out that the discovered chaos is a robust phenomenon existing in ranges of parameters, which for certain parameter values can coexist with the antiferromagnetic steady state [12].

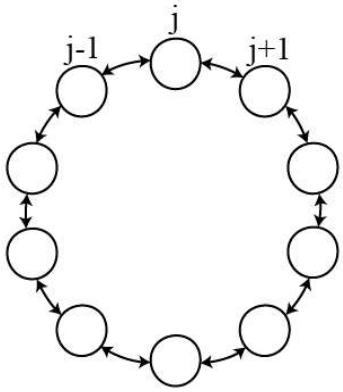

Fig. 1. The model of circular chain of 10 Rydberg atoms.

Analysis of the chains with even larger *N* revealed that hyperchaos is not only preserved in the system, but becomes more complicated as more Lyapunov exponents become positive. The result of our analysis in summarized in Fig. 2, where the dependence of the number of positive Lyapunov exponents *M* on the number of the atoms in the chain is depicted. The graphs demonstrates almost linear growth when inclusion of two-three additional atoms leads to appearance of one more positive Lyapunov exponent. This phenomenon takes place due to almost no correlation between the oscillations in distant atoms, which creates the condition, when an inclusion of a subsystem of coupled atoms, able to demonstrate chaotic dynamics, simply adds one more positive value in the spectrum of the Lyapunov exponents.

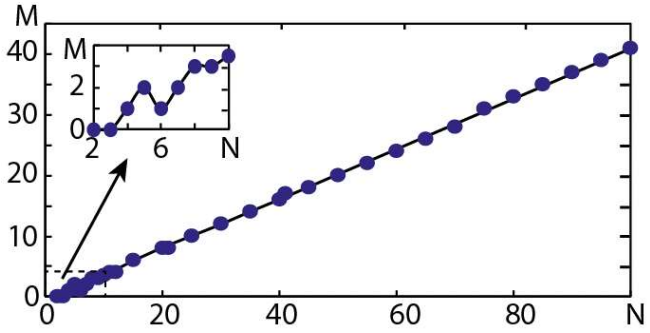

Fig. 2. The dependance of maximum number of positive Lyapunov exponents for Rydberg atom chains from chain length.

For the chain of 5 atoms we also plotted a regime map. It was found that there are a lot of different regimes such as hyperchaos, chaos, quasiperiodic, periodic and stationary regimes. The area of parameters Ω and Δ of oscillatory dynamics for chain of 5 atoms are bigger that one for 2 atoms. Investigating the transition to chaos in the system we calculated bifurcation diagram. As in system of 2 atoms there is a transition from periodic regime to chaos occurs through a direct cascade of period doubling bifurcations. But the first one is arising from a periodic window of quasiperiodic regime.

IV. Conclution

In conclusion we discovered that an interplay between dissipation and energy pumping in the quantum coherent systems can evoke very non-trivial emergent phenomena associated with onset of complex stable chaotic and even

hyperchaotic oscillations. The complexity of the hyperchaos increases with the size of the chain.

REFERENCES

[1] M. Walport, P. Knight, The quantum age: Technological opportunities. Government Office for Science, 2016.

[2] de Touzalin, C. Marcus, F. Heijman, I. Cirac, R. Murray, T. Calarco, Quantum manifesto. a new era of technology, 2016.

[3] M. Zagoskin, "Analogue simulation with the use of artificial quantum coherent structures," Reviews in Physics, V. 3, pp. 1-14, 2018.

[4] T. Lee, H. Haffner, M. Cross, "Antiferromagnetic phase transition in a nonequilibrium lattice of Rydberg atoms," Phys. Rev. A, vol. 84, p. 031402(R), 2011.

[5] T. E. Lee, H. Haffner, M. C. Cross, "Collective quantum jumps of Rydberg atoms," Physical review letters, V. 108, no. 2, p. 023602, 2012.

[6] O. E. Rossler, "An equation for hyperchaos," Physics Letters A, V. 71, no. 2-3, pp. 155-157, 1979.

[7] V. Andreev, O. I. Moskalenko, A. A. Koronovskii, A. E. Hramov. "Chaos and its suppression in a system of two coupled Rydberg atoms," Bulletin of the Russian Academy of Sciences: Physics, vol. 79, no. 12, pp. 1432-1434, 2015.

Modeling of a brain neuronal network under visual stimulation

Andrey Andreev
Neuroscience and Cognivite Technology Lab, Center for Technologies in Robotics and Mechatronics Components
Innopolis University
Innopolis, Russia
andreevandrei1993@gmail.com

Alexander Pisarchik
Center for Biomedical Technology
Technical University of Madrid
Madrid, Spain
alexander.pisarchik@ctb.upm.es

***Abstract*—We numerically simulate a network of coupled Hodgkin-Huxley neurons for modulating a processing visual perception by the brain. On a part of the network, we apply an external current of constant amplitude modulating visual information entering the brain. We analyze the influence of the external stimulus amplitude on the dynamics of the system. We discover coherent resonance phenomenon when for certain area of external stimulus amplitude both signal-to-noise ratio and characteristic correlation time are maximal.**

Keywords—Hodgkin-Huxley neuron, neural network, biological neuron, visual stimulus, coherent resonance.

I. INTRODUCTION

Investigations of neuronal models subjected to different types of perturbations have received significant attention in the last years [1-3]. It is widely acknowledged that signal processing in neural systems takes place in a noisy environment. Hence, it is of interest to understand the statistical properties of stochastic neuronal systems. Investigation of the influence of noise on spike generation in the presence of some external forcing signals is particularly important because noise plays a significant role in the detection, transmission, and encoding of such signals [4].

The investigation of multilayer networks is of interest because the networks of brain have a multilayer structure [5-8]. The studies help to understand how the brain works.

Coherence resonance is an important finding emerging in many fields of science, including complex neuronal systems [9-11]. The phenomenon of coherence resonance was first discussed in a simple autonomous system in the vicinity of the saddle-node bifurcation. The nonuniform noise-induced limit cycle leads to a peak at a definite frequency in the power spectrum. The signal-to-noise ratio (SNR) increases first to a maximum and then decreases when the intensity of noise increases, showing the optimization of the coherent limit cycle to the noise.

In this paper, we numerically simulate a two-layer network of coupled Hodgkin-Huxley neurons for modulating a processing visual perception by the human brain [12-14]. The first and the second layers of the network consist of 5 and 50 neurons and represent a visual area of the thalamus and visual cortex respectively. As a model neuron, we chose the Hodgkin-Huxley neuron. We simulate visual stimulus by adding some external stimulus of constant amplitude to the neurons in the first layer connected to the neurons in the second one unidirectionally. We investigate the influence of the external stimulus amplitude on the dynamics of second layer neurons. We calculate power spectra of signal averaged over all neurons in the second layer and then we calculate signal-to-noise ratio and characteristic correlation time. As a result, we discover coherent resonance phenomenon in the system: there is an area of external stimulus amplitude when both SNR and characteristic correlation time are maximal.

II. MODEL

The system under study represents the networks of N^{ex}=5 and N=50 Hodgkin-Huxley neurons (Fig. 1). Inside each network, all elements are connected to each other, and there is a probability p=0.3 of making a one-way connection between a neuron from the first network to a neuron from the second one. To all N^{ex} neurons from the first network, we inject the external current I^{ex} of constant amplitude simulating the visual stimulus.

The time evolution of the transmembrane potential of each HH neuron is given by

$$C_m \frac{dV}{dt} = -g_{\mathrm{Na}} m^3 h (V - V_{\mathrm{Na}}) - g_{\mathrm{K}} n^4 (V - V_{\mathrm{K}}) - g_{\mathrm{L}} (V - V_{\mathrm{L}}) + I^{\mathrm{ex}} + I^{\mathrm{syn}} \quad (1)$$

where $C_m = 1\mu F/cm^3$ is the capacity of cell membrane, I^{ex} is an external bias current injected into a neuron, V is the membrane potential of a neuron, $g_{\mathrm{Na}} = 120\, mS/cm^2$, $g_{\mathrm{K}} = 136\, mS/cm^2$ and $g_{\mathrm{L}} = 0.3\, mS/cm^2$ receptively denote the maximal sodium, potassium and leakage conductance when all ion channels are open. $V_{\mathrm{Na}} = 50\, mV$, $V_{\mathrm{K}} = -77\, mV$ and $V_{\mathrm{L}} = -54.4\, mV$ are the reversal potentials for sodium, potassium and leak channels respectively. m, n and h represent the mean ratios of the open gates of the specific ion channels. n^4 and m^3h are the mean portions of the open potassium and sodium ion channels within a membrane patch. The dynamics of gating variables (x=m,n,h) depending on rate functions $\alpha_x(V)$ and $\beta_x(V)$ are given:

$$\frac{dx}{dt} = \alpha_x(V)(1-x) - \beta_x(V)x + \xi_x(t),$$
$$x = m, n, h \qquad (2)$$

$\xi_x(t)$ is independent zero mean Gaussian white noise sources whose autocorrelation functions are given as below

$$\langle \xi_m(t)\xi_m(t')\rangle = \frac{2\alpha_m\beta_m}{N_{Na}(\alpha_m+\beta_m)}\delta(t-t') \qquad (3)$$

$$\langle \xi_h(t)\xi_h(t')\rangle = \frac{2\alpha_h\beta_h}{N_{Na}(\alpha_h+\beta_h)}\delta(t-t') \qquad (4)$$

$$\langle \xi_n(t)\xi_n(t')\rangle = \frac{2\alpha_n\beta_n}{N_{K}(\alpha_n+\beta_n)}\delta(t-t') \qquad (5)$$

where N_{Na} and N_{K} represent the total number of sodium and potassium channels within a membrane patch, and are calculated as $N_{\mathrm{Na}} = \rho_{\mathrm{Na}}S$, $N_{\mathrm{K}} = \rho_{\mathrm{K}}S$ where $\rho_{\mathrm{Na}} = 60\,\mu m^{-1}$ and $\rho_{\mathrm{K}} = 18\,\mu m^{-1}$ are the sodium and potassium channel densities, respectively. S is the membrane patch area of each neuron.

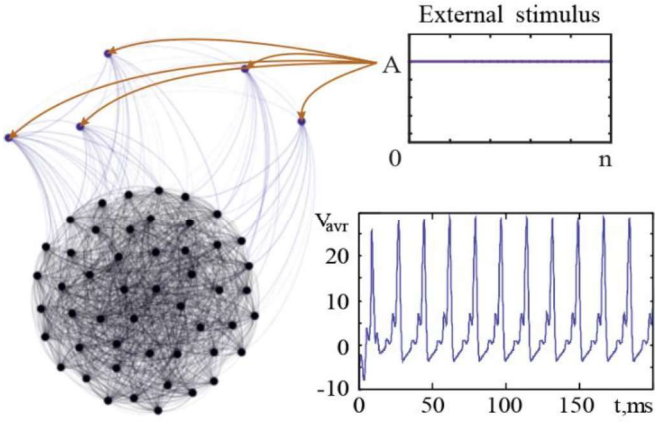

Fig. 1. Network model. The external stimulus with amplitude A is applied to N^{ex}=5 neurons in the first network. Each neuron in this network is connected to each neuron in the second network with a probability p = 0.3. From the system we signal V_{avr} averaged aver all these neurons. Each element has its own Gaussian noise.

I_i^{syn} is the total synaptic current received by i-th neuron. We consider coupling via chemical synapses. The synaptic current takes the form

$$I_i^{\mathrm{syn}} = \sum_{j\in \mathrm{neight}(i)} g_c e^{-(t-t_0^j)/\tau_{\mathrm{syn}}}(E_{\mathrm{rev}} - V_i) \qquad (6)$$

where the alpha function $\alpha(t)$ describes the temporal evolution of the synaptic conductance, g_c is the maximal conductance of the synaptic channel, t_0^j is the time at which presynaptic neuron j fires, $\tau_{\mathrm{syn}} = 3\, ms$.

III. Results

We analyze the signal averaged over all N neurons from the second network $V_{\mathrm{avr}} = \sum_{i=1}^{N} V_i/N$. The example of characteristic neuron dynamics one can on the Fig.1.

To investigate the dynamics of the system we analyze the coherence of a signal. For that, we can calculate the signal-to-noise ratio (SNR) derived from the energy spectrum using the Fourier transform.

The maximum energy in the spectrum $E_{\max}$ appears at the average frequency of spiking neurons f_s. Therefore, this spectral component reflects the contribution of regular behavior, while the noise contributes mainly to the background component E_{N} at the same frequency f_s. The signal-to-noise ratio can be calculated from the power spectra as $\mathrm{SNR} = E_{\max}^2 - E_{\mathrm{N}}^2$ (dB) at the dominant frequency f_s.

Another way to measure of coherence of the system is the calculation of characteristic correlation time defined as

$$\tau_c = \sum_{n_0}^{T} C(\tau)^2, \qquad (7)$$

where t_0 is the transient time, T is the total time, $C(\tau)$ is the autocorrelation function given as

$$C(\tau) = \frac{\langle (x_{avr}(n) - \langle x_{avr}\rangle)(x_{avr}(n+\tau) - \langle x_{arv}\rangle)\rangle}{\langle (x_{avr}(n) - \langle x_{avr}\rangle)^2\rangle}, \qquad (8)$$

where $\langle ... \rangle$ is the time average after transients. The larger the correlation time, the better the coherence.

In this work, we calculate the dependencies of signal-to-noise ratio and characteristic correlation time from external stimulus amplitude (Fig. 2). They both have the same dynamics: at low external stimulus amplitude all neurons are in "silent" regime and there is no spikes generation. Increasing the stimulus amplitude leads to increasing the signal-to-noise ratio and characteristic correlation time. After I^{ex}=10.0 $\mu A/sm^2$ they start to decrease, so the dependencies have resonance at this amplitude value.

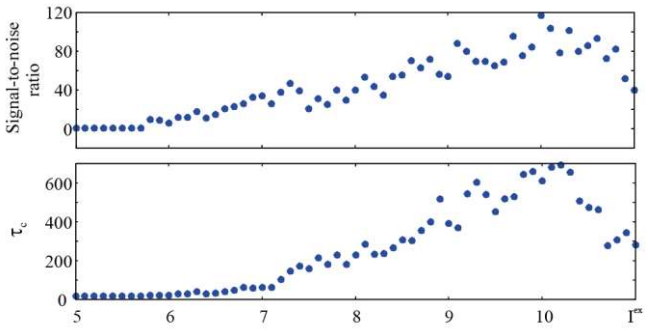

Fig. 2. The dependencies of signal-to-noise ratio and characteristic correlation time from external stimulus amplitude for ξ=0.1.

IV. Conclution

We have numerically simulated the dynamics of the brain under visual perception using 2-layer Hodgkin-Huxley neuron network. We have calculated characteristic correlation time and signal-to-noise ratio from power spectra of signal averaging over all neurons in the second layer to

measure the coherence of the system. Analyzing the influence of amplitudes of internal noise and external stimulus on system dynamics we found that the coherence is maximal on the certain value of stimulus intensity. It means that the network processes visual information better for some values of external stimulus amplitude.

ACKNOWLEDGMENT

This work has been supported by Russian Science Foundation (Grant 19-12-00050).

REFERENCES

[1] M. Uzuntarla, J. J. Torres, A. Calim, E. Barreto, "Synchronization-induced spike termination in networks of bistable neurons," Neural Networks, V.110, pp.131–140, 2019.

[2] V. Andreev, E. N. Pitsik, V. V. Makarov, A. N. Pisarchik, A. E. Hramov, "Dynamics of map-based neuronal network with modified spike-timing-dependent plasticity," Eur. Phys. J. Special Topics, vol.227, no.10-11, pp.1029–1038, 2018.

[3] V. Makarov, D. Kirsanov, M. Goremyko, A. Andreev, A. E. Hramov, "Nonlinear dynamics of the complex multi-scale network," Proc. SPIE, V. 10717, p. 1071729, 2018.

[4] E. Runnova, A. E. Hramov, V. V. Grubov, A. A. Koronovskii, M. K. Kurovskaya, A. N. Pisarchik "Theoretical background and experimental measurements of human brain noise intensity in perception of ambiguous images," Chaos, Solitons & Fractals, V. 93, pp. 201-206,

[5] A. Maksimenko, A. Lüttjohann, V. V. Makarov, M. V. Goremyko, A. A. Koronovskii,, A. E. Runnova, G. van Luijtelaar, A. E. Hramov, S. Boccaletti "Macroscopic and microscopic spectral properties of brain networks during local and global synchronization," Physical Review E, V. 96, no. 1, p. 012316, 2017.

[6] Maksimenko, A. Badarin, V. Nedaivozov, D. Kirsanov, A. Hramov, "Brain-computer interface on the basis of EEG system Encephalan," Proc. SPIE, V. 10717, p. 107171R, 2018.

[7] V. Makarov, A. A. Koronovskii, V. A. Maksimenko, A. E. Hramov, O.I. Moskalenko, J.M. Buldúc, S. Boccaletti, "Emergence of a multilayer structure in adaptive networks of phase oscillators," Chaos, Solitons & Fractals, V. 84, pp. 23-30, 2016.

[8] V. V. Makarov, D. Kirsanov, M. Goremyko, A. Andreev, A. E. Hramov, "Nonlinear dynamics of the complex multi-scale network," Proc. SPIE, V. 10717, p. 1071729, 2018.

[9] V. A. Maksimenko, A. E. Hramov, V. V. Grubov, V. O. Nedaivozov, V. V. Makarov, A. N. Pisarchik, "Nonlinear effect of biological feedback on brain attentional state," Nonlinear Dynamics, V. 95, no. 3, pp. 1923-1939, 2019

[10] V Andreev, A. N Pisarchik "Mathematical simulation of coherent resonance phenomenon in a network of Hodgkin-Huxley biological neurons," Proc. SPIE, V. 11067, p. 1106708, 2019. A. V. Andreev, V. V. Makarov, A. E. Runnova, A. N. Pisarchik, A. E. Hramov, "Coherence resonance in stimulated neuronal network," Chaos Solitons & Fractals, vol.106, pp.80–85, 2018.

[11] V. Andreev, A. E. Runnova, A. N. Pisarchik, "Numerical simulation of coherent resonance in a model network of Rulkov neurons," Proc. SPIE, V. 10717, p. 107172E, 2018.

[12] V. A. Maksimenko, A. E. Runnova, N. S. Frolov, V. V. Makarov, V. Nedaivozov, A. A. Koronovskii, A. Pisarchik, A. E. Hramov, "Multiscale neural connectivity during human sensory processing in the brain," Physical Review E. V. 97, no. 5, p. 052405, 2018.

[13] E. Hramov, V. A. Maksimenko, S. V. Pchelintseva, A. E. Runnova, V. V. Grubov, V. Y. Musatov, M. O. Zhuravlev, A. A. Koronovskii, A. N. Pisarchik, "Classifying the perceptual interpretations of a bistable image using eeg and artificial neural networks," Frontiers in neuroscience, V. 11, p. 674, 2017.

[14] E. Runnova, A. E. Hramov, V. V. Grubov, A. A. Koronovskii, M. K. Kurovskaya, A. N. Pisarchik, "Theoretical background and experimental measurements of human brain noise intensity in perception of ambiguous images," Chaos, Solitons & Fractals, V. 93, pp. 201–206, 2016.

Using thermoelectrics for power supplying of wireless sensors network

Denis Artyukhov, Igor Burmistrov
Department of Chemistry and Materials Chemistry
Yuri Gagarin State Technical University of Saratov
Saratov, Russia
mr.tokve@gmail.com, glas100@yandex.ru

Ivan Artyukhov, Vadim Alekseev
Department of Power Supply and Electrotechnologies
Yuri Gagarin State Technical University of Saratov
Saratov, Russia
ivart54@mail.ru, alekseevvs_sstu@mail.ru

***Abstract*—Nowadays, energy harvesting is an emerging topic that electronic researchers are increasingly interested in. It is based on collecting very small amounts of energy from the environment using small scale transducers. The harvested energy is used in order to feed low power circuits such as wireless sensors. This paper presents a sensor power supply system in which thermo-electrochemical cells are used to convert heat into electrical energy.**

Keywords— energy harvesting, thermo-electrochemical cell, wireless sensors

I. INTRODUCTION

Wireless Sensor Networks (WSNs) are widely used in industry, automotive, construction, medicine, scientific research, security systems. These networks perform a variety of useful functions including factory automation, measurement, and control; control of lighting, heating, and cooling in residential and commercial buildings; structural health monitoring of bridges, commercial buildings, aircraft, and machinery [1]. WSNs have been considered as a promising communication technology for the monitoring and control of Smart Grid operation [2].

The use of batteries to power wireless sensors is in many cases difficult. Due to the remoteness of the objects on which the sensors are located, or the difficult conditions of their operation, replacing batteries is a big problem. Therefore, the actual task of supplying these sensors with energy, which can be harvested and stored at the sensor installation site, has arisen and needs to be addressed.

There are various sources for energy harvesting [3]: solar, organic, vibration, thermal, near field electromagnetic and far-field electromagnetic (or Radio-Frequency).

Researchers pay much attention to utilizing low-potential heat energy using thermoelectric generators. Typical applications are heat radiators or pipes with hot fluids. Also heat from mechanical or electrical equipment is a potential energy source, e.g. industrial drives. The conversion process is based on the Seebeck effect. The output voltage is proportional to the temperature difference.

As ultra-low power wireless sensors are increasingly being proposed for many applications, there is a tremendous need for micro-energy harvesting techniques to provide power to the sensors. However, power management technology for micro-energy harvesting offers big challenge on energy storage and management because the delivered voltage from extreme environment condition is much lower than the threshold voltage of standard electronic devices, so it is often unsuitable for standard power management chips.

II. Characteristics of a Thermo-Electrochemical Cells

The thermoelectric effect, also known as the Seebeck effect, is an observable property of various metals and chemical solutions. It represents direct conversion of heat to electricity. If the temperature difference ΔT between the two ends is small, then the thermoelectric voltage ΔU at the terminals is defined as:

$$\Delta U = -S_e \cdot \Delta T , \quad (1)$$

where S_e is the Seebeck coefficient.

There are two major types of thermoelectric cells: solid-state and liquid electrochemical. A solid-state thermoelectric cell is a traditional thermoelectric conversion device where an applied temperature difference between P and N type materials results in electron flow and electricity generation. The typical Bismuth Telluride solid-state thermoelectrics boasts a Seebeck coefficient of up to 230 μV/K.

In an effort to maximize the output voltage and power, and to overcome the material constraints, cost ineffectiveness, and lack of reliability of current thermoelectric cells, new attempts have been made to produce improved alternatives that focus on higher Seebeck coefficients. These new alternatives are liquid thermo-electrochemicals cells (TECs) [4].

TECs take advantage of the temperature dependence of electrochemical redox potentials to transfer electrons and produce electric power. Until relatively recently, the commercial viability of TECs was limited by their low power output and conversion efficiency. However, there have lately been significant advances in TEC performance as a result of improvements to the electrode materials, electrolyte and redox chemistry and various features of the cell design.

Developed cells [5] have a Seebeck coefficient up to 1.4 mV/K. Fig. 1 shows the TEC's scheme. Cell body consists of hot and cold plates made of stainless steel to ensure the best thermal conductivity. These plates contact with the electrodes, the distance between them is provided by the distance frame. The electrodes size was 10 × 10 mm with the thickness of 0.34 mm. Titanium foils (Ti – 99.9%) with a deposited layer of oxidized multi-walled carbon nanotubes were studied as an electrode material. The thickness of the cover layer was 1-2 μm.

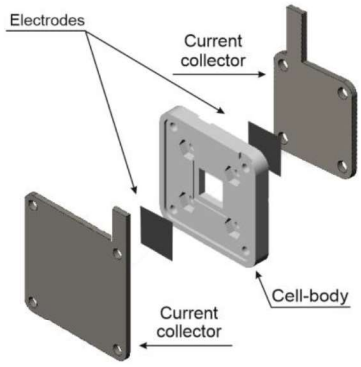

Fig. 1. Schematic representation of TEC

I-V curves of TEC for different values of electrolyte concentration and electrode's temperature difference were obtained. Fig. 2 shows the I-V curves of TEC with an electrolyte concentration of 0.3 mol/l.

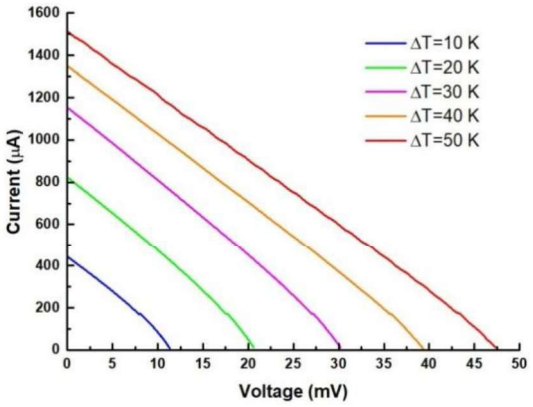

Fig. 2. I-V curves at the electrolyte concentration of 0.3 mol/l

Analysis of the I-V curves showed that they are shifted almost in parallel when the temperature difference ΔT on the electrodes is changed. The open-circuit voltage U_{OC} and, accordingly, the slope of the curves depend on the electrolyte concentration. This allows us to represent the cell as an equivalent two-terminal circuit, in which the EMF of E_{TEC} is equal to the open-circuit voltage U_{OC}, and the internal resistance is determined by the formula

$$R_{SOURCE} = U_{OC} / I_{SC} , \quad (2)$$

where I_{SC} is short-circuit current.

III. Design of the Wireless Sensors Power Supply System

The delivered voltage from thermoelectric energy harvesting is very low under small temperature difference, and can vary greatly as the ambient temperature.

In [6], a DC converter is presented that can boost very low voltages to the typical supply voltages of current integrated circuits. The converter is based on a hybrid inductive and capacitive architecture and it is suitable for power harvesting applications too. The prototype can supply 1.2 V by converting an input voltage of 200 mV delivered by a thermopile exposed to a 5 K thermal gradient.

Special DC boost converters with ultra-low initial voltage are presented in [7-9] and in a number of other articles.

Fig. 3 shows diagram of the wireless sensors power supply system. The input voltage is provided by a TEC. The step-up DC-DC converter is needed to convert the ultra-low voltage of TEC into a usable voltage level for sensors and embedded systems (microprocessor, RF link). It should be able to start up and operate efficiently at voltages from 20 mV.

Step-up converter is based on the chip LTC3108 [10]. The converter has two stages. The first stage is used to start up the converter from low input voltages. The second stage provides the charge of the supercapacitor and generates voltages that are necessary for the operation of sensors, a microprocessor and a radio transmitter.

The LTC3108 utilizes a MOSFET switch to form a resonant step-up oscillator using an external small step-up transformer T and a coupling capacitor C2. The step-up transformer turns ratio determines how low the input voltage can be for the converter to start. Using a 1:100 ratio can yield start-up voltages as low as 20 mV.

Other factors that affect performance are the DC resistance of the transformer windings and the inductance of the windings. Higher DC resistance will result in lower efficiency.

The secondary winding inductance L2 determines the resonant frequency of the oscillator, according to the following formula

$$f = \frac{1}{2\pi\sqrt{L_2 C}}, \tag{3}$$

where C is the load capacitance on the secondary winding. This is comprised of the input capacitance C2 at pin 14 in parallel with the transformer secondary winding's shunt capacitance.

AC voltage produced on the secondary winding of the transformer is boosted and rectified using an external charge pump capacitor C1 (from the secondary winding to pin 13) and rectifiers internal to the LTC3108. The rectifier circuit feeds current into pin 2, providing charge to the external capacitor C_{AUX} and the other capacitors.

The capacitor's C_{OUT} value is dictated by the load current, duration of the load pulse, and the voltage droop the circuit can tolerate. The capacitor C_{STORE} may be a very large value (thousands of microfarads or even Farads) to provide holdup at times when input power may be lost.

In the experimental sample of the power supply system, a small step-up transformer LPR6235-752SMR was applied [11]. Capacitors in fig. 3 had the following parameters: C_{in} = 220 µF, C1 = 1 nF, C2 = 330 pF, C_{LDO} = 2.2 µF, C_{AUX} = 1 µF, C_{OUT} = 470 µF. The two series connected supercapacitors ESHSR-0005C0-002R7 are used as an energy storage unit C_{STORE}.

The power supply system of wireless sensors at several voltage values U_{in} was studied. Fig. 4 shows oscillograms of voltages on the secondary winding of the transformer and on the input of the rectifier in the LTC3108 chip (pin13). The voltage diagrams were experimentally taken with digital memory oscilloscope Fluke 196C with two galvanic isolated channels.

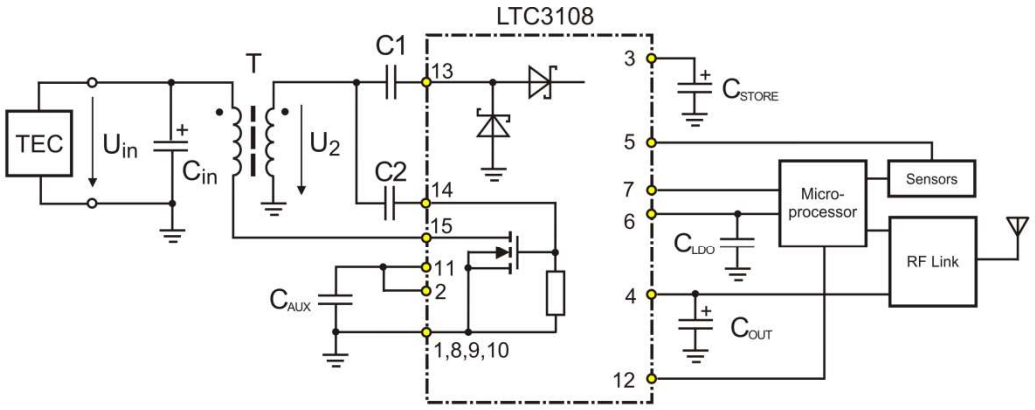

Fig. 3. Block diagram of the developed wireless sensors power supply system

During the experiment, it was found that the boost converter starts at an input voltage of 22 mV. However, the operation of the generator at this voltage is unstable. Frequency deviation and amplitude voltage modulation are observed on the secondary winding of the transformer.

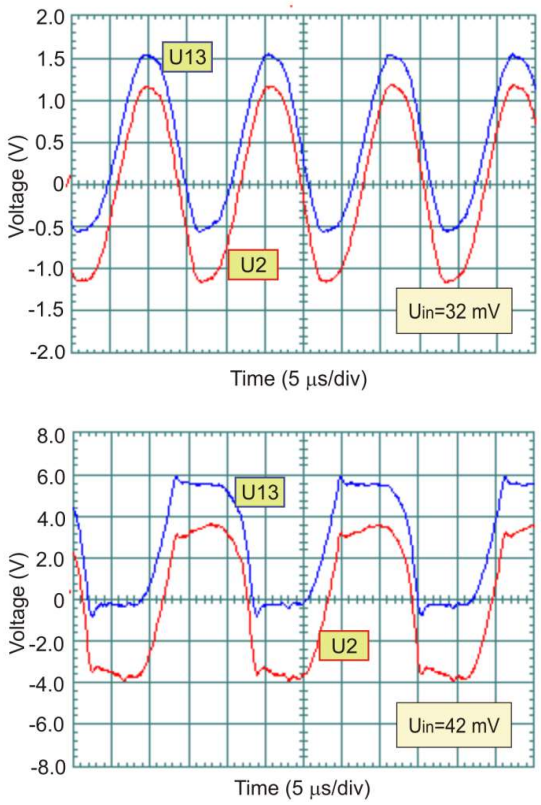

Fig. 4. Voltages oscillograms

In the voltage range U_{in} up to 40 mV, the voltages U2 and U13 are sinusoidal. With a further increase in the input voltage, the U13 voltage is limited to 5.52 V. In this case, an increase in the input voltage is accompanied by a decrease in the oscillation frequency of the generator from 62.3 to 34.9 kHz.

It is important that the design of the LTC3108 is such that as U_{in} drops, the input resistance increases. This feature allows the LTC3108 to adapt reasonably well to TECs with different source resistances.

IV. Conclusion

Supplying wireless sensors with energy that can be harvested and stored at the sensor installation site is an actual task. Promising devices for harvesting waste heat for the sustainable energy production are thermoelectrochemical cells used the working fluid with the ferri/ferrocyanide salts. A prototype of the power supply system of wireless sensors using an LTC3108 chip and a supercapacitor was developed and experimentally investigated.

Acknowledgment

This research was financially supported by the Ministry of Education and Science of the Russian Federation (project 10.1434.2017/4.6).

References

[1] J. Weiss, R. Yu. Wireless Sensor Networking for the Industrial Internet of Things. Available: www.linear.com/smartmesh

[2] S. Rekik, N. Baccour, M. Jmaiel, and K. Drira. Wireless Sensor Network Based Smart Grid Communications: Challenges, Protocol Optimizations, and Validation Platforms. Wireless Personal Communications, Springer Verlag, 2017, 95 (4), pp.4025-4047.

[3] M.F. Dupont, D.R. MacFarlane, and J.M. Pringle. Thermo-electrochemical cells for waste heat harvesting - progress and perspectives, Chem. Commun, vol. 53, 2017, pp. 6288-6302.

[4] Burmistrov, N. Kovyneva, N. Gorshkov, A. Gorokhovsky, A. Durakov, D. Artyukhov, and N. Kiselev, "Development of new electrode materials for thermo-electrochemical cells for waste heat harvesting," Renewable Energy Focus, vol. 29, pp. 42-48, 2019.

[5] Shindrov, D. Artyukhov, M. Vikulova, N. Spirin, N. Nikitina, N. Savin, N. Gorshkov, and I. Burmistrov, "Thermo-electrochemical cells based on polymer and mineral hydrogels for low-grade waste heat conversion, " AIP Conference Proceedings 1899, 020016, 2017.

[6] Richelli, L. Colalongo, and S. Tonoli, "A 0.2-1.2V DC/DC boost converter for power harvesting applications," IEEE Trans. on Power Electronics, vol. 24, nr. 6, pp.1541-1546, 2009.

[7] Carlson, K. Strunz, and B. Otis. 20mV Input Boost Converter for Thermoelectric Energy Harvesting. 2009 Symposium on VLSI Circuits Digest of Technical Papers, pp. 162-163.

[8] Hua Yu, Hanzhong Wu, Yumei Wen, and Li Ping. An Ultra-low Input Voltage DC-DC Boost Converter for Micro-energy Harvesting System. The 2nd International Conference on Information Science and Engineering, 2010. DOI: 10.1109/ICISE.2010.5691809.

[9] J.-M. Gruber, and S. Mathis. Efficient Boost Converter for Thermoelectric Energy Harvesting, AMA Conferences 2017 – SENSOR 2017 and IRS2 2017. DOI 10.5162/sensor2017/P3.6.

[10] Ultralow Voltage Step-Up Converter and Power Manager LTC3108. Available: http://www.linear.com/LTC3108

[11] Coupled Inductors LPR6235. Available: http://www.coilcraft.com

Development of a digital software platform for the study of nonlinear dynamics of electronic systems

Artem Badarin
Neuroscience and Cognivite Technology Lab, Center for Technologies in Robotics and Mechatronics Components
Innopolis University
Innopolis, Russia
Badarin.a.a@mail.ru

***Abstract*— The paper presents the results of applied research on the design and application of an integrated platform for solving applied problems of developing, studying and optimizing high-power electron-plasma devices from the centimeter to THz range based on the results of previous fundamental and exploratory research.**

Keywords— PIC, non-stationary processes of electron-wave interaction; numerical simulation; optimization; digital platform; electron-plasma devices.

I. INTRODUCTION

The development and optimization of efficient high-power generators and amplifiers are one of the most important and rapidly developing areas of modern applied physics. The promise and relevance of advancing microwave devices and devices to a higher frequency region, as well as creating new generators of terahertz (THz) radiation, is due to the fact that currently the THz range (especially the interval 0.2-3 THz) is one of the least mastered in radio physics and electronics [1]. Being outside the modes of operation of traditional microwave (microwave) and optical devices, it belongs to the so-called "technological gap". And although currently there are devices capable of generating terahertz radiation, for example, gyrotrons , free-electron lasers (FEL), quantum-cascade lasers, Gunn diodes, etc. [2-5] due to difficulties in operation, low efficiency and / or lack of reliability, their use is often limited to scientific research, and thus this range is still not readily available for wide use in high-tech industries.

Another important task is the development of power generators and amplifiers of the microwave and sub-THz ranges, without which modern radiophysics, microwave electronics, and plasma physics are inconceivable [6-9]. The need for such devices is due to a number of applied problems and fundamental applications: problems of plasma and solid physics, nanotechnology and spectroscopy, tasks related to information transfer and radiolocation, synthesis of new materials, development of non-destructive testing and security systems, turbulent state of liquids, tasks of biophysics and medicine, etc.

Thus, the obvious need for the development, research, and optimization of powerful devices that can generate and amplify electromagnetic radiation in a wide range.

The solution of the above-described complex scientific and technical problems is almost impossible without the use of modern methods and means of numerical modeling and computational technologies. In particular, this is due to the high cost and high complexity of carrying out field studies and experiments with similar electronics systems, as well as with a low speed of performing such work. This is especially true when new equipment is being optimized or new devices and units are being developed, which is undoubtedly associated with a large volume of measurements when various parameters of such systems are changed. In a full-scale experiment, it is usually not possible to ensure that even the minimum required an array of parameters of the device under investigation is enumerated. Another drawback of experimental studies of electronics systems is often the inability to measure the characteristics of interest due to the limited capabilities of the experimental tools.

An effective method for studying systems of sub-THz and THz electronics, devoid of the above disadvantages, is numerical simulation using modern computing technologies. The most advanced and popular at the moment here are three-dimensional fully electromagnetic codes in which Maxwell's equations are numerically solved to find self-consistent electromagnetic fields in the system, and the large particles method (PIC method) is used to simulate the dynamics of charged particles [10]. This approach well complements and to some extent replaces experimental research, especially during the development stages of prototypes of new devices, as well as the optimization of existing ones.

Currently, a number of commercial three-dimensional electromagnetic PIC codes are widely known for the numerical study of electronics and radiophysics systems: Magic (USA), CST Particle Studio (Germany / France), VSim (USA), Neptune (USA), WARP (USA), KARAT (Russia) and others. At the same time, all the listed software products have a number of consumer and technical shortcomings, namely: extremely high cost; the difficulty of using most of them; the high degree of universality of these software products and their proximity to the real experiment (especially CST Particle Studio) to the detriment of the possibility of simplifying the models and taking into account the principal features of the sub-THz and THz electronics systems. The latter is most clearly expressed in that, in fact, most commercial codes are a “black box”, where it is impossible to disable functions that are not needed at the moment, approximations and modeling capabilities, as well as connect the necessary new ones, remove the required non-standard for this software product characteristics and etc. A critical problem here is also the inability to eliminate, on its own, various numerical nonphysical effects inherent in such PIC codes.

II. RESULTS

In the developed code, the basic mathematical model is the system of equations often used in electronics and plasma physics, consisting of the Vlasov kinetic equation for the electron distribution function and the Maxwell equations for finding self-consistent electromagnetic fields:

$$\frac{\partial f}{\partial t} + \vec{v}\frac{\partial f}{\partial \vec{r}} + e\left(\vec{E} + \frac{1}{c}\left[\vec{v}, \vec{H}\right]\right)\frac{\partial f}{\partial \vec{p}} = 0,$$

$$\rho = e\int f\, d\vec{p}, \qquad \vec{j} = e\int f\vec{v}\, d\vec{p},$$

$$rot\ \vec{E} = -\frac{1}{c}\frac{\partial \vec{H}}{\partial t},$$

$$rot\ \vec{H} = -\frac{1}{c}\frac{\partial \vec{E}}{\partial t} + \frac{4\pi}{c}\vec{j},$$

$$\mathrm{div}\ \vec{E} = 4\pi\rho,$$

$$\mathrm{div}\ \vec{H} = 0$$

here $f = f(\vec{r}, \overrightarrow{p, t})$– is the electron distribution function, ρ and $\vec{j}$ – re the charge and current densities of the electron beam, $\vec{E}$ and $\vec{H}$ – are the electric and magnetic fields, respectively, c – is the speed of light, e – is the electron charge, , $\vec{r}$, $\vec{v}$ and $\vec{p}$ – are the radius-vector, velocity and momentum of electrons, respectively, t – is time.

The Vlasov equation is valid when the condition of the collisionlessness of charged particles is satisfied when the collision integral in the kinetic equation tends to zero. This requirement is fulfilled for the electron flow in the range of spatial and temporal scales of the processes occurring in it that are of interest within the framework of this research. Indeed, the plasma frequency of an intense electron beam, which is the main time scale during the development of various instabilities in it, is significantly greater than the frequency of pair collisions of particles in the beam, and the mean free path of electrons is greater than the characteristic spatial scale of the systems under consideration. with the

collective interaction of the electromagnetic field and particles.

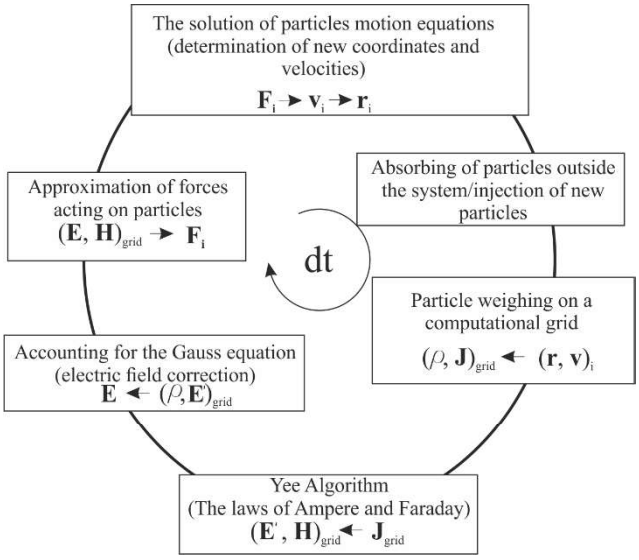

Fig. 1. The algorithm of the method "particle in a cell" at one time step.

To solve this system of equations, the "particle in a cell" method is used. The essence of the method consists of dividing the problem into two parts: the solution of the kinetic equation is modeled using a large number N of "large" particles with the same charge-to-mass ratio; The solution of the field part of the problem is carried out using the Yi algorithm. In this case, the transition to the integral values of the charge density and current from the distribution of particles occurs by weighing the latter on the computational grid. The algorithm for finding the evolution of matched fields at one time step is presented in Figure 1.

Note that when using the concept of "large" particles, such characteristic parameters of the electron flow as the plasma frequency ω_p and the Debye distance λ_d do not change in the model system compared to the real one, which indicates that the proposed mathematical model can correctly reproduce collective phenomena. However, the mean free path and the Debye number (the number of particles in the sphere of the Debye length radius) in the model are reduced, and the frequency of collisions of "large" particles increases in proportion to the weight factor Z, which can distort pair interactions. In order to avoid this, the developed model uses two approaches.

The first is to increase the number of "large" particles so that their number is much larger than the Debye number n_d: $N \gg n_d \gg 1$. The second approach is based on a sharp decrease in the near (pair) interactions of "large" particles due to the transition to particles of finite own volume (finite size) in terms of computational grid. In this case, each particle is a "cloud" of a volume charge with a certain density distribution. With the approach of remote clouds, the interaction force between them first increases, and then, with the beginning of the interpenetration of clouds, weakens. With a full match, the clouds do not interact. This means a decrease in short-range interactions, i.e. collisional effects. The role of the Debye number in this case is played by the number of cloud overlaps $n_m = n_0 d_p^3$, where n_0 is the concentration of "large" particles, dp is the length of "large" particles. Thus, the longer the cloud length d_p, the easier it is to satisfy the condition nm 1 with the same number of particles N.

ACKNOWLEDGMENT

This work has been supported by Russian Foundation for Basic Research (Project 18-32-20135).

REFERENCES

[1] J.H. Booske, "Plasma physics and related challenges of millimeter-wave-to-terahertz and highpower microwave generation," Physics of Plasmas, V. 15, p. 055502, 2008.

[2] M.Yu. Glyavin, A.G. Luchinin, G.Yu. Golubiatnikov, "Generation of 1.5-kW, 1-THz Coherent Radiation from a Gyrotron with a Pulsed Magnetic Field," Phys. Rev. Lett., V. 100, p. 015101, 2008.

[3] G.L. Carr, M.C. Martin, W.R. McKinneyetal, "High-power terahertz radiation from relativistic electrons," Nature, V. 420. pp. 153–156, 2002.

[4] R. Köhler, A. Tredicucci, F. Beltrametal, "Terahertz semiconductor-heterostructure laser", Nature, V. 417, pp. 156-159, 2002.

[5] N. S. Frolov, Kurkin, S. A., Khramova, M. V., Badarin, A. A., Koronovskii, A. A., Pavlov, A. N., Hramov, A. E. Perspective sub-THz powerful microwave generator" nanovircator" for T-rays biomedical diagnostics. In Saratov Fall Meeting 2015: Third International Symposium on Optics and Biophotonics and Seventh Finnish-Russian Photonics and Laser Symposium (PALS), International Society for Optics and Photonics, V. 9917, p. 991721, 2016.

[6] A. Badarin, S. A. Kurkin, A. E. Hramov, "Multistability in a relativistic electron beam with an overcritical current," Bulletin of the Russian Academy of Sciences: Physics, V. 79, no. 12, pp. 1439-1442, 2015.

[7] A. Badarin, S. A. Kurkin, A. V. Andreev, A. A. Koronovskii, N. S. Frolov, A. E. Hramov, "Virtual cathode oscillator with elliptical resonator," In 2017 Eighteenth International Vacuum Electronics Conference (IVEC), IEEE, pp. 1-2, 2017.

[8] A. Badarin, S. A. Kurkin, A. A. Koronovskii, A. E. Hramov, A. O. Rak, "Processes of virtual cathodes interaction in multibeam system," Physics of Plasmas, V. 25, no. 8, p. 083110, 2018.

[9] C.K. Birdsall, A.B. Langdon, "Plasma physics via computer simulation," Taylor and Francis Group, 2005.

[10] S. A. Kurkin, A. A. Badarin, A. A. Koronovskii, N. S. Frolov, A. E. Hramov, "Modeling instabilities in relativistic electronic beams in the CST particle studio environment," Mathematical Models and Computer Simulations, V. 10, no. 1, pp. 59-68, 2018.

Circuit simulation of a blue sky catastrophe in the context of bursting dynamics occurrence

Elmira Bagautdinova
Dept. of Dynamic Modeling and Biomedical Engineering
Chernyshevsky State University of Saratov
Saratov, Russia
infinitum13@mail.ru

Nataliya Stankevich
Dept. of Radio-Engineering and Telecommunications
Yuri Gagarin State Technical University of Saratov
Saratov, Russia
e- stankevichnv@mail.ru

Sergey Kuznetsov
Dept. of Theoretical Nonlinear Dynamics
Kotel'nikov's Institute of Radio-Engineering and Electronics RAS
Saratov, Russia
spkuz@yandex.ru

Evgeny Seleznev
Dept. of Modelling in Nonlinear Dynamics
Kotel'nikov's Institute of Radio-Engineering and Electronics RAS
Saratov, Russia
evgenii_seleznev@mail.ru

***Abstract*—We present a study of a model with bifurcation associated with blue sky catastrophe. Circuit simulation is implemented in the software package MultiSim.**

Keywords— blue sky catastrophe, bursting dynamics, circuit simulation

I. INTRODUCTION

Bursting dynamics is typical behavior for neurons [1-2]. One of the scenarios of transition from spiking to bursting dynamics in neurons is associated with blue sky catastrophe [3-4]. Originally, the bifurcation of the blue sky catastrophe was described in [5]. In the simplest case it can be explained as follows. The phase trajectory departs from a vicinity of a semi-stable limit cycle existing at the threshold of the saddle-node bifurcation, goes near a large-size loop along an unstable manifold, and turns back to the limit cycle from the other side. At varying a control parameter in one direction, the semi-stable cycle transforms into a pair of cycles, a stable and an unstable one. If we vary the control parameter in opposite direction, two cycles collide forming the semi-stable cycle, then disappear, while the large-size limit cycle emerges in the domain containing the helical coils [6-7].

The catastrophe of the blue sky turned out to be a typical phenomenon in fast-slow systems. In the fast-slow Hodgkin-Huxley model of computational neuroscience, the blue catastrophe describes a continuous and reversible transition between bursting and tonic spiking dynamics [3-4].

In papers [8-10], a set of mathematical models was proposed in which hyperbolic chaos, or quasiperiodic oscillations are possible as a result of a bifurcation associated with a blue sky catastrophe. In the present paper we implement circuit simulation of such system with hyperbolic chaos in the software package Multisim. First, we describe mathematical model which can demonstrate hyperbolic chaos occurring via blue sky catastrophe and give some typical illustrations. Then, we present results of circuit simulations.

II. NUMERICAL SIMULATION OF MODEL WITH BLUE SKY CATASTROPHE

A. Mathematicla model

In our paper we consider a model with hyperbolic chaos. The model can be written as follows:

$$
\begin{aligned}
\dot{x}_1 &= \omega_0 y_1 + [1-(x_2^2+y_2^2)+\tfrac{1}{2}(x_1^2+y_1^2) \\
&\quad -\tfrac{1}{50}(x_1^4+2x_1^2y_1^2+y_1^4)]x_1 + \varepsilon x_2 y_2, \\
\dot{y}_1 &= -\omega_0 x_1 + [1-(x_2^2+y_2^2)+\tfrac{1}{2}(x_1^2+y_1^2) \\
&\quad -\tfrac{1}{50}(x_1^4+2x_1^2y_1^2+y_1^4)]y_1, \\
\dot{x}_2 &= \omega_0 y_2 + [(x_1^2+y_1^2)-\mu+\tfrac{1}{2}(x_2^2+y_2^2) \\
&\quad -\tfrac{1}{50}(x_2^4+2x_2^2y_2^2+y_2^4)]x_2 + \varepsilon x_1, \\
\dot{y}_2 &= -\omega_0 x_2 + [(x_1^2+y_1^2)-\mu+\tfrac{1}{2}(x_2^2+y_2^2) \\
&\quad -\tfrac{1}{50}(x_2^4+2x_2^2y_2^2+y_2^4)]y_2,
\end{aligned}
\qquad (1)
$$

where x_1, x_2 and y_1, y_2 are dynamical variables representing the real and imaginary parts of complex variables a_1 and a_2. The papers [8-10] presented the corresponding interpretation of the model. ε is a coupling coefficient, ω_0 is basic frequency of the self-oscillations and the parameter μ responsible for the transition through the blue sky bifurcation.

B. Numerical Simulations

Let us turn to numerical simulation of model (1). In [10] the structure of the parameters plane and typical dynamical behavior were described. It was shown, that in the parameter plane (ω_0, μ) there is line of the blue sky bifurcation: μ^C=3.125. Firstly we chose parameters before bifurcation of blue sky catastrophe: ε=0.5, ω_0=2π, μ=3.12. Fig. 1a shows the corresponding two-dimensional projection of phase portraits on the plane of real and imaginary parts of the amplitude of the first oscillator.

As one can see phase portrait has form of a limit cycle. This limit cycle is cycle of period-two. Periods each of them

are close to each other, but zoomed fragment shows structure of the phase portrait.

Then we fixed parameter μ greater then bifurcation: ε=0.5, $\omega_0=2\pi$, μ=3.15. In Fig.1b corresponding phase portrait is depicted. After bifurcation amplitude of oscillations increased in 50 times. For model (1) it is character formation of hyperbolic chaos via blue sky catastrophe. Attractor in Fig. 1b is hyperbolic chaotic attractor. In [10] verification of hyperbolicity was carried out.

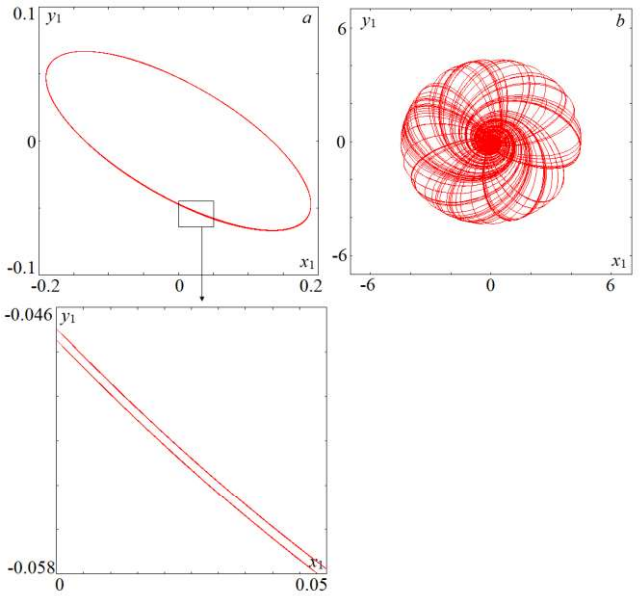

Fig. 1. Phase portraits of model (1) before and after the blue sky catastrophe in phase space of real and imaginary parts of complex variables, a) ε = 0.5, $\omega_0 = 2\pi$, μ = 3.12; b) ε = 0.5, $\omega_0 = 2\pi$, μ = 3.15.

III. CIRCUIT SIMULATION

Then let us turn to development and study circuit, model of this generator. With this aim we can write equations (1) in integral form:

$$
\begin{aligned}
x_1 &= \int \{\omega_0 y_1 + [1-(x_2^2+y_2^2)+\tfrac{1}{2}(x_1^2+y_1^2) \\
&\quad -\tfrac{1}{50}(x_1^4+2x_1^2y_1^2+y_1^4)]x_1 + \varepsilon x_2 y_2\}dt, \\
y_1 &= \int \{-\omega_0 x_1 + [1-(x_2^2+y_2^2)+\tfrac{1}{2}(x_1^2+y_1^2) \\
&\quad -\tfrac{1}{50}(x_1^4+2x_1^2y_1^2+y_1^4)]y_1\}dt, \\
x_2 &= \int \{\omega_0 y_2 + [(x_1^2+y_1^2)-\mu+\tfrac{1}{2}(x_2^2+y_2^2) \\
&\quad -\tfrac{1}{50}(x_2^4+2x_2^2y_2^2+y_2^4)]x_2 + \varepsilon x_1\}dt, \\
y_2 &= \int \{-\omega_0 x_2 + [(x_1^2+y_1^2)-\mu+\tfrac{1}{2}(x_2^2+y_2^2) \\
&\quad -\tfrac{1}{50}(x_2^4+2x_2^2y_2^2+y_2^4)]y_2\}dt,
\end{aligned}
\qquad (2)
$$

and use typical circuits on operational amplifiers to implement the full scheme the corresponding system of equations. Electron scheme also contains analog amplifiers, analog adder, integrating amplifier. The full electron scheme is complex, and very big and will be presented on the conference. The role of the control parameter μ of system (2) in the circuit is played by the source, the voltage of which is regulated with potentiometer *R*.

When the resistance of the potentiometer *R* changes, various periodic and chaotic oscillatory regimes are observed. In Fig.2 an examples of attractors obtained in MultiSim are shown. When voltage on the source *V* = 6V, a cycle of period 2 is observed in the dynamics of the system (see Fig. 2a). It corresponds situation before blue sky catastrophe. With an increase in the parameter at *V* = 7.4V, a blue sky catastrophe is observed in the system, while the system moves for a long time in the vicinity of cycle 2, then runs away from it and returns to it, and so on to infinity.

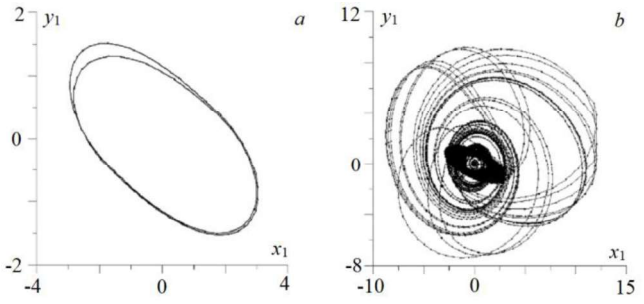

Fig. 2. Phase portaraints in Poincarè section and basins of attraction for co-existing limit cycle of period-7 and two-frequency quasiperiodic regime. μ=0.7, *a*: ω_0=2.7761; *b*: ω_0=2.8083.

The form of attractors in circuit model and in numerical simulations are similar. Thus, our circuit model are in a good agreemnt with mathemetaical model and can be used for study properties of blue sky catastrophe in experiments.

ACKNOWLEDGMENT

The work was carried out with the financial support of the Russian Scientific Foundation, grant No. 17-12-01008.

REFERENCES

[1] E.M. Izhikevich. “Neural excitability, spiking and bursting,” Int. J. Bif. Chaos, vol.10, No. 6, 2000, pp. 1171-1266.

[2] E.V. Izhikevich, Dynamical systems in neuroscience. MIT press, 2007.

[3] Shilnikov and G. Cymbalyuk, “Transition between Tonic Spiking and Bursting in a Neuron Model via the Blue-Sky Catastrophe,” Phys. Rev. Lett., vol. 94, No.4, 2005, pp. 048101.

[4] Shilnikov, “Complete Dynamical Analysis of a Neuron Model”, Nonlinear Dynam., vol.68, No.3, 2012, pp.305–328.

[5] J. Palis, and C.C. Pugh, “Fifty Problems in Dynamical Systems, in Dynamical Systems,” Proc. Sympos. Appl. Topology and Dynamical Systems (Univ. Warwick, Coventry, 1973/1974): Presented to E.C.Zeeman on His Fiftieth Birthday, Lecture Notes in Math., vol.468, Berlin: Springer, 1975, pp. 345–353.

[6] D.V. Turaev and L.P. Shil’nikov, “Blue Sky Catastrophes”, Dokl. Math., vol.51, 1995, pp.404–407; see also: Dokl. Akad. Nauk, vol.342, No.5, 1995, pp.596–599.

[7] L.P. Shilnikov and D.V. Turaev, “A New Simple Bifurcation of a Periodic Orbit of Blue Sky Catastrophe Type,” Methods of Qualitative Theory of Differential Equations and Related Topics, Amer. Math. Soc. Transl. Ser. 2, vol.200, Providence,R.I.: AMS, 2000, pp.165–188.

[8] S.P. Kuznetsov, “Example of blue sky catastrophe accompanied by a birth of Smale - Williams attractor,” Regular and Chaotic Dynamics, vol. 15, No. 2-3, 2010, pp. 348-353.

[9] A.P. Kuznetsov, S.P. Kuznetsov, N.V. Stankevich, “Four-dimensional system with torus attractor birth via saddle-node bifurcation of limit cycles in context of family of blue sky catastrophes,” Izvestiya Vysshikh Uchebnykh Zavedeniy. Prikladnaya Nelineynaya Dinamika, vol. 23, No.4, 2015, pp. 63-70.

[10] P.V. Kuptsov, S.P. Kuznetsov, N.V. Stankevich, “A Family of Models with Blue Sky Catastrophes of Different Classes,” Regular and Chaotic Dynamics, vol. 22, No 5, 2017, pp. 551–565

Poisson equation numerical solution method based on bidirectional multiple passage of grid cells and parallel computations

Vil B Baiburin
School of Applied Information Technology and Communications
Yuri Gagarin Saratov State Technology University
Saratov, Russian Federation
baiburinvb@rambler.ru

Alexander S. Rozov
School of Applied Information Technology and Communications
Yuri Gagarin Saratov State Technology University
Saratov, Russian Federation
fog545@mail.ru

***Abstract*—This article is devoted to the numerical solution of Poisson equation. The main method of the work based on the assumption of the monotony of unknown function. A an algorithm for numerical solution of the Dirichlet problem for the Poisson equation for a complex domain is shown, the idea of the method is that, the values in the internal grid nodes are searched as arithmetic averages over three neighboring nodes, taking into account the known function. It is shown that the proposed method can be implemented in parallel computing. As a result, a comparison is made with the finite element method.**

Keywords—Poisson equation; approximation; net; parallel calculations; cell

The need to solve the Poisson equation arises in many areas of science and technology: electrodynamics, microwave, and solid-state mechanics [1, 2].

Typically known methods for solving Poisson's equation are reduced to solving systems of linear algebraic equations [3], in the best case, tridiagonal, requiring at the same time-consuming system resources and computer time in the calculations, especially when a large number of grid points.

In [4], authors has presented a method for solving the Laplace equation that does not require a transition to systems of algebraic equations. In this paper, this method has developed to solve the Poisson equation.

Consider the Poisson equation in the two-dimensional case:

$$\partial^2 U(x,y)/\partial x^2 + \partial^2 U(x,y)/\partial y^2 = f(x,y) \qquad (1)$$

Where $U(x, y)$ – unknown function, $f(x, y)$ – known function. The proposed numerical algorithm based on the assumption that the unknown function $U(x, y)$ is monotonous. Hence, with a sufficiently small grid cell size covering a given area, the values of $U(x, y)$ in nearby nodes will differ slightly.

Upgrade proposed in [4] a method for solving the equation (1) with respect to the domain in Fig. 1. Let the U values on the boundary correspond to the values of $\phi(x, y)$.

$$U(x_i,y_i) = U_{i,j},\ f(x_i,y_i)=f_{i,j},\ \phi_c(x_i,y_i) = \phi_{c\,i,j} \qquad (2)$$

The essence of the algorithm can be described by the example of the grid shown in Fig. 1, where the centers of the cells are their numbers, as well as the coordinates of the corresponding nodes.

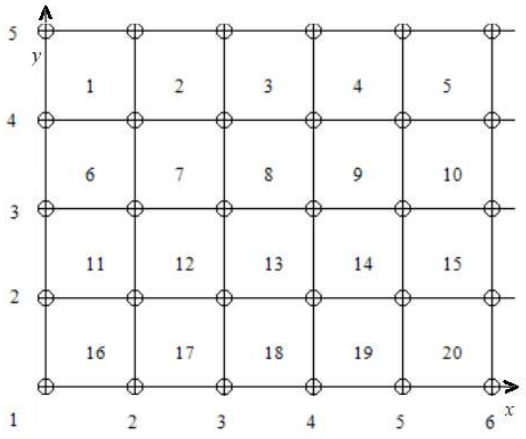

Fig. 1. Example domain

Consider cell number 1. We calculate U_{24} and define it as the average value of the known values at the boundary nodes U_{15}, U_{25}, U_{14}:

$$U_{24} = (U_{15} + U_{25} + U_{14})/3 \qquad (3)$$

Next, we will clarify the value of the function U^*_{24}, as the average value, taking into account f_{24}:

$$U^*_{24} = (U_{24} + f_{24})/2 \qquad (4)$$

As a result, we obtain:

$$U^*_{24} = (U_{15} + U_{25} + U_{14} + 3 f_{24})/6 \qquad (5)$$

Next, moving from left to right, go to cell number 2 and knowing the values U_{25}, U_{35}, U^*_{24} we find U^*_{34}:

$$U^*_{34} = (U_{25} + U_{35} + U^*_{24} + 3f_{34})/6 \qquad (6)$$

Repeat this algorithm until cell number 5.

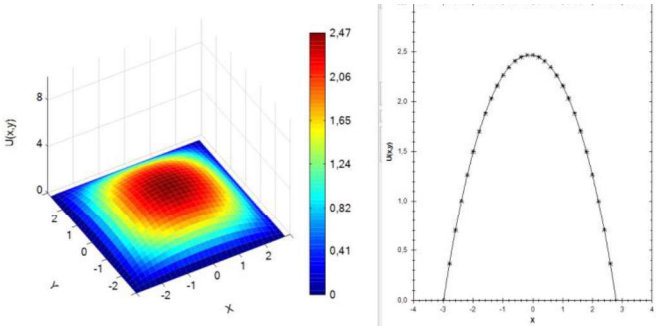

Fig. 2. Surface and cross-section of the analytical and numerical solutions in the X-Z plane, with y = 0, the solid line shows the analytical solution, numerical asterisks

Note, that the algorithm described above allows for parallel computations, namely, moving “from right to left” from cell number 5 to cell number 1 and also “from left to right” from cell number 16 to cell number 20, as well as from top to bottom from cell number 1 to cell number 16 and "bottom-up." from cell number 16 to cell number 1 in several threads. At the same time, the values of the function at the nodes can calculated as an average value, in two directions.

It makes sense to compare the proposed algorithm with the well-known analytical solution and the results of numerical calculations using finite element method (FEM), applied to a rectangular area in Fig. 1, with $f_{i,j} = f_0 = const.$ The analytical solution of the Dirichlet problem for the Poisson equation has the form [5].

$$U(x,y) = \frac{16 f_0 a^2}{\pi^3} \sum_{i=0}^{n} \frac{1}{(2n+1)^3} \left[1 - \frac{ch(2n+1)(b-y)\pi/2a)}{ch(2n+1)b\pi/2a)}\right] \cdot \sin\left[\frac{(2n+1)\pi}{2a}\right] x \quad (7)$$

Where a and b are size of the domain.

Numerical calculations and an analytical solution were carried out for a grid of 1000000 * 1000000 cells with $a = b = 6$. When we use an analytical solution, it was possible to limit to $n = 10$ and calculations showed that taking into account the higher terms of the series is comparable to the computational error. Fig. 2 shows the surface of the sought-for function $U(x, y)$, and the section of the analytical and numerical solutions for $y = 0$. As can be seen, the solutions in Fig. 2 almost coincide.

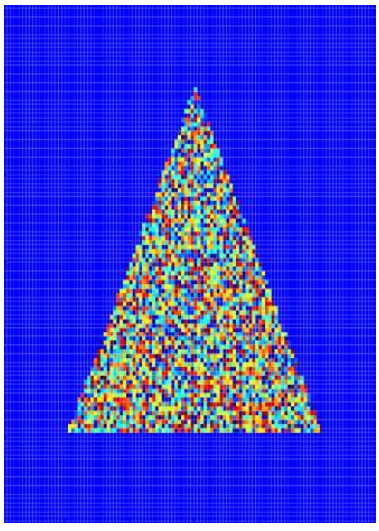

Fig. 3. Domain with random numbers in internal nodes

TABLE I. COMPARASION BETWEEN METHODS

Time of solution in sec		
Domain dimension	Proposed method	FEM
1000000*1000000	0.376	0.56

Next, we compare the results of the calculations proposed in the work of the algorithm and finite element method (FEM). Consider an area with the dimension of 1000000 * 1000000 cells and zero values of unknown function on the border. In this case, the nonzero values of $f_{i,j}$ bounded by a triangular region were specified using a pseudo-random number generator in the range of 1 - 100. Fig. 3.

Below in Fig. 4, the solution surface of the sought-for function $U(x, y)$ is shown, and the sections of numerical solutions obtained by the method considered in the paper and FEM with $y = 0$.

The table 1 has shown compares the speed of the proposed numerical solution of equation (1) for the domain in Fig. 3 compared with FEM.

It should also be noted that the proposed algorithm has an extremely simple implementation (see formula (5)), which makes the most efficient use of RAM and the processor's cache memory, which is extremely critical for parallel implementation of numerical algorithms, and as a result determines the gain of the proposed algorithm.

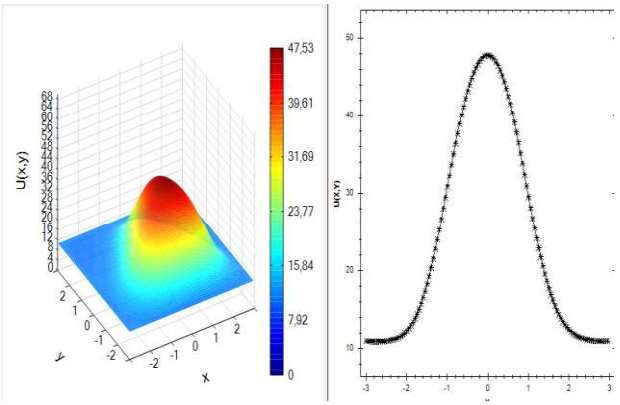

Fig. 4. Surface and cross-section of numerical solutions by proposed method and FEM in the X-Z plane, with y = 0, the solid line shows the solution by proposed numerical solution, FEM asterisks

REFERENCES

[1] Feynman, R.P., Leighton, R.B. and Sands M.L. The Feynman Lectures on Physics. Addison-Wesley, Redwood City, CA. 1989.

[2] Landau, L. D., Lifshitz, E. M. Classical Theory of Fields, 4th rev. Eng. ed., Oxford: Pergamon, 1975.

[3] David E. Potter Computational physics Wiley-Interscience Publications , 1988,

[4] Baiburin V B., Rozov A S Kolomin A.M. Parallel method for the numerical solution of the Laplace equation using multiprocessor systems/ 2018 2nd School on Dynamics of Complex Networks and their Application in Intellectual Robotics (DCNAIR 2018)., pp 240-244.

[5] Yu.V. Egorov Partial Differential Equations IV (Encyclopaedia of Mathematical Sciences). Springer Verlag, 1992.

Three-coordinate definition of color mark and distance to objects according to strereo image

Bobyr M.V.
Department of computer engineering
Southwest State University
Kursk, Russian federation
fregat_mn@rambler.ru
Orcid:0000-0002-5400-6817

Yakushev A.S.
Department of computer engineering
Southwest State University
Kursk, Russian federation
alekseyakushev@yandex.ru
Orcid:0000-0002-6214-3563

Milostnaya N.A.
Department of computer engineering
Southwest State University
Kursk, Russian federation
Orcid:0000-0002-3779-9165

***Abstract* – This article discusses the determination of distances to objects in three coordinates. To determine the distance of objects, a depth map is constructed using the SAD algorithm; to determine the offset, a color mark is determined and its movement in the frame is calculated by calculating the coordinates of the center of gravity of the color mark on two frames.**

Keywords – color shading, RGB model, HSV model, depth map, fuzzy logic.

I. INTRODUCTION

Technical vision systems are used to recognize symbols and colors, as well as to perform various measurements. They are applied to ensure road safety and to monitor and control complex dynamic systems. Nowadays, in the process of image processing, the following algorithms are used: selection of the boundaries of objects, recognition of color shades, image filtering, determining the distance to objects [1-3]. Increasing the speed of processing one pixel per unit of time is one of the tasks that needs to be solved when creating technical vision systems. In some real time systems, the frame is processed for a long time (more than 100 ms), then the control signal arrives at the actuator with a delay. Various intelligent algorithms are used to solve this problem, for example, neural networks, genetic algorithms, multi-agent and probabilistic systems, fuzzy logic. When using neural networks or genetic algorithms, it is necessary to have basic knowledge of the control object. Therefore, in the case of using uncertain information, it is rational to use the apparatus of fuzzy logic. [4-6].

II. DETERMINATION OF DISTANCE TO OBJECTS USING 3D DEPTH MAP

Two methods are combined to build 3D depth maps. First, a depth map must be constructed using a modified SAD algorithm. Second, an algorithm for color recognition must be created to determine movements along the longitudinal axis relative to the location of stereo cameras.

Using the modified SAD algorithm and depth map the distance from the stereo cameras to distant objects is determined. Thus, coordinates in area YZ are determined. Then, using one of the stereo cameras, a fuzzy color recognition model defines the color labels on the stereo images. After that, to determine the movement of the actuators along the XY axis, a proportional relationship between the center of gravity of the color mark and the sizes of the stereo image is calculated.

Thus, the combination of these two methods of processing stereo images allows calculating distances to objects in a three-dimensional area. Taking into account changes in brightness and contraction in real time on stereo images, the authors propose to use a fuzzy logic apparatus.

To construct a depth map using stereo images, it is required for each pixel with coordinates (x; y) of the left stereo image to calculate the difference of intensity levels in the window (for example, 3x3 pixels size) of the left and right stereo images. After that, on the right stereo image, the window is shifted by one pixel and the difference between the intensity levels of the left and right stereo images is re-calculated. The shift of the pixels in the right image and the calculation of the level difference continue until the value is reached d= 0…d_{max}:

$$SAD(x,y,d)=\sum_{m=-b\,n=-b}^{m=b\,n=b} R \sum_{m=-b\,n=-b}^{m=b\,n=b} G \sum_{m=-b\,n=-b}^{m=b\,n=b} B\left|I_l(x+m,y+n)-I_r(x+m+d,y+n)\right|,$$

where I_l, I_r are color intensity on left and right stereo images; x, y – coordinates on stereo images; b – window size calculated by the formula 2b+1, when b=1 window size is equal 3×3 pixels; R, G, B – three-channel color model components (if YUV-model is used, then transformation is carried out by the formula Y=0,299R+0,587G+0,114B).

After calculating the absolute difference of intensity levels for an array of values from 0 to the threshold value d_{max}, in the modified SAD algorithm finds the minimum value of $D(x, y)_{SAD}$:

$$D(x,y)_{SAD}=\arg\min_{d\in[0\ldots d_{max}]} SAD(x,y,d). \qquad (1)$$

The value of D (x, y) SAD is the offset value that forms the depth map for a pixel with YZ coordinates.

One of the main problems in the SAD model is the search and the ratio of identical points on the left and right stereo images. Due to the presence on the images of the same areas of a large area, white artifacts appear. The input variables of the fuzzy method for constructing a depth map using stereo images are three intensity levels calculated by the formula *SAD*(*x,y,d*): at the starting point with coordinates (*x*, *y*) – *SAD*(*x*, *y, d*); at a point offset from the starting point by 3 pixels to the left – *SAD*(*x–3*, *y, d*); at a point offset from the starting point by 3 pixels to the right – *SAD*(*x+3*, *y, d*). The output value is the disparity value $D(x, y)_{SAD}$. In addition, for

each pixel of the depth map, a fuzzy output is calculated for an array of values in the range from 0 to d_{max}. The variable disparity $D(x, y)$ is assigned the minimum value from this range of values. By completing the depth map using the SAD algorithm, you can determine the distance from research object to the stereo cameras. To determine the amount of movement of actuators along the x-axis, the following procedure is performed. A color mark is set on the actuator (see Fig. 1 - pink rectangle). Then the first image is taken. After that using the recognition algorithm coordinates of the center point of the color mark are determined using the center of gravity method. After this, the movement of the actuator begins. In the process of moving the camera constantly takes pictures and calculates the distance from the starting point to the current point where the actuator is located in real time.

To recognize the color mark, the conversion from the RGB color model to the HSV color model is used as follows:

$$MAX = \max(R, G, B);$$

$$MIN = \min(R, G, B);$$

$$H = \begin{cases} undefined, & if\ MAX = MIN; \\ 60 \times \dfrac{G-B}{MAX-MIN} + 0^0, & if\ MAX = R\ and\ G \geq B; \\ 60 \times \dfrac{G-B}{MAX-MIN} + 360^0, & if\ MAX = R\ and\ G < B; \\ 60 \times \dfrac{B-R}{MAX-MIN} + 120^0, & if\ MAX = G; \\ 60 \times \dfrac{R-G}{MAX-MIN} + 240^0, & if\ MAX = B; \end{cases}$$

$$S = 256 \cdot \frac{MAX - MIN}{1 - |1 - (MAX + MIN)|};$$

where R, G, B are values ranging from 0 to 256; MAX is the maximum value of the three components of the RGB; MIN is the minimum value of the three components of the RGB; H is hue value ranging from 0 to 360; S is saturation value ranging from 0 to 256; 256 is normalization factor.

After that, the binarization and filtration of the color mark are performed. And then the coordinates of the center of gravity of the color mark are calculated as follows:

$$\text{if } I_F = 1 \quad \text{then } X = \frac{\sum_{i=1}^{w} l_i}{\text{count}},$$

$$\text{if } I_F = 1 \quad \text{then } Y = \frac{\sum_{j=1}^{h} l_j}{\text{count}},$$

where I_f is brightness value after filtering; X, Y are the coordinates of the center of gravity of the color mark on the x-axis and y-axis; l is the distance from the begin of the frame to the binarized point along the x-axis; *count* is total number of binarized points; w is frame width in pixels; h is frame height in pixels.

After that distances between the coordinates of the centers of gravity of the beginning color mark and the monitored at the current time is determined by the following formula:

$$\text{length} = \frac{X \cdot w_{real}}{w}, \quad (2)$$

where w_{real} is real frame width in centimeters.

As soon as these steps are performed, we recognize the color mark and then determine the distances of the actuators moving from the beginning point to the current point in real time mode.

III. Experiment

The method for recognizing color marks and determining distances between objects proposed by the authors was investigated during the operation of a mechatronic complex for sorting parts (see Fig. 1) and moving a mobile robot in a labyrinth (see Fig. 2).

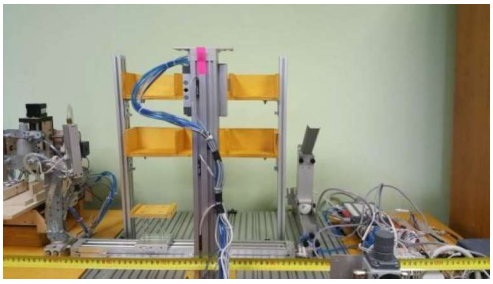

Fig. 1. Mechatronic complex for sorting parts

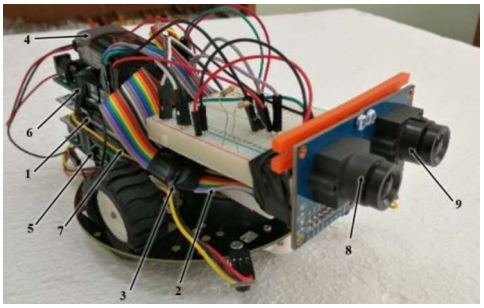

Fig. 2. Mobile robot to move into the labyrinth

To calculate the offset value of the actuators of the mechatronic complex for sorting the parts (see. Fig. 1), the algorithm to recognize color marks and formula (2) were used. To calculate the distance from the mobile robot (see Fig. 2) to the object (see Fig. 3), the method of constructing a depth map and formula (1) were used. The results of determining the offset distance of the actuators of the mechatronic complex for sorting parts and the accuracy of their calculations are presented in Table 1. The results of determining the distance from the camera of the mobile robot to the objects and the accuracy of their calculations are presented in Table 2.

TABLE I. Result definition of distance using the recognition of color marks

Real size, sm	10	20	30	35
Calculated size, sm	10.03	20.07	30.08	35.15
Accuracy, %	99.47	99.68	99.88	99.76

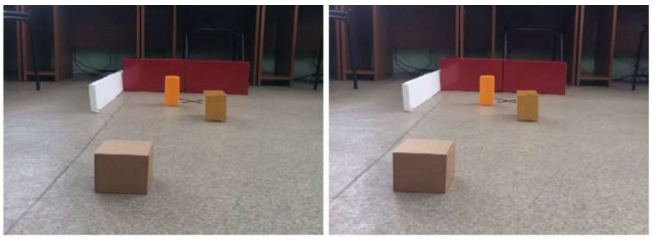

Fig. 3. Stereo images before depth mapping

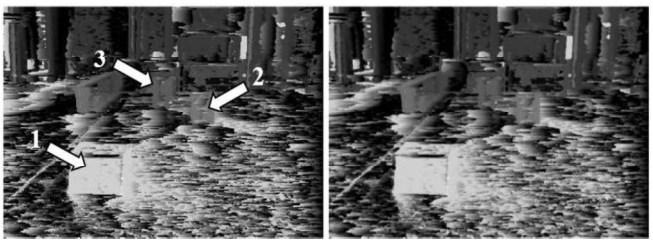

Fig. 4. Stereo images after depth mapping

TABLE 2. RESULT DETERMINATIONS OF DISTANCES FROM THE CAMERA TO OBJECTS

	REAL SIZE, SM	CALCULATED SIZE, SM	ACCURACY, %
1 OBJECT	73	73,5	99.4
2 OBJECT	146	148.7	98
3 OBJECT	178	188.6	94

IV. CONCLUSION

As a result of the research conducted on the method of recognizing color marks and determining the offset value of the actuators of the mechatronic complex for sorting parts, it was found that the average accuracy of calculations is equal to 99.7%.

As a result of the research conducted by the method of constructing depth maps and determining the distances from the camera of a mobile robot to obstacles, it was found that the average accuracy of calculations is equal to 99.7%.

ACKNOWLEDGMENTS

This work was supported by the Goszadanie under the project №2.3440.2017/4.6 and by the Russian Science Foundation under the project No16-19-00186.

REFERENCES

[1] K. Patle, D. R. K. Parhi, A. Jagadeesh, Sunil Kumar Kashyap, Application of probability to enhance the performance of fuzzy based mobile robot navigation, Applied Soft Computing, 2019, 75, pp. 265-283 (DOI: 10.1016/j.asoc.2018.11.026)

[2] Chaki, J., Dey, N., Moraru, L., & Shi, F., Fragmented plant leaf recognition: Bag-of-features, fuzzy-color and edge-texture histogram descriptors with multi-layer perceptron, Optik, 2019, 181, pp. 639–650. (DOI: 10.1016/j.ijleo.2018.12.107)

[3] Boukezzoula, R., Coquin, D., Nguyen, T. L., & Perrin, S., Multi-sensor information fusion: Combination of fuzzy systems and evidence theory approaches in color recognition for the NAO humanoid robot. Robotics and Autonomous Systems, 2018. 100, pp. 302–316. (DOI: 10.1016/j.robot.2017.12.002)

[4] Bobyr, M., Luneva, M., & Yakushev, A. An algorithm for controlling of cutting speed based on soft calculations. MATEC Web of Conferences, 2017. 129, 01064. (DOI: 10.1051/matecconf/201712901064)

[5] Bobyr, M.V., Kulabukhov, S.A. Simulation of control of temperature mode in cutting area on the basis of fuzzy logic, Journal of Machinery Manufacture and Reliability, 2017, №3 (46), pp. 288-295. (DOI: 10.3103/S1052618817030049)

[6] M.V. Bobyr, N.A. Milostnaya, S.A.Kulabuhov A method of defuzzification based on the approach of areas ratio, Applied soft computing, 2017, pp. 19-32 (DOI: 10.1016/j.asoc.2017.05.040).

Experimental observation of Arnold tongues in the analysis of the signal from contour of the autonomous regulation of heart rate and respiration

Ekaterina Borovkova
Saratov Branch of the Institute of RadioEngineering and Electronics of Russian Academy of Sciences, Saratov State Medical University named after V. I. Razumovsky, Saratov State University
Saratov, Russia
0000-0002-9621-039X

Viktoriia Skazkina
Saratov Branch of the Institute of RadioEngineering and Electronics of Russian Academy of Sciences, Saratov State Medical University named after V. I. Razumovsky, Saratov State University
Saratov, Russia
0000-0001-9380-8292

Elena Chernets
Saratov State University
Saratov, Russia
chernets-elena@mail.ru

Anatoly Karavaev
Saratov Branch of the Institute of RadioEngineering and Electronics of Russian Academy of Sciences, Saratov State Medical University named after V. I. Razumovsky, Saratov State University
Saratov, Russia
0000-0003-4678-3648

Yurii Ishbulatov
Saratov Branch of the Institute of RadioEngineering and Electronics of Russian Academy of Sciences, Saratov State Medical University named after V. I. Razumovsky, Saratov State University
Saratov, Russia
0000-0003-2871-5465

Abstract—**We proposed a method of experimental observation of the Arnold tongues in the study of the synchronization of the contours of autonomic regulation of the heart rate with a characteristic frequency of about 0.1 Hz and respiration. The formulation of a special active experiment made it possible to determine the boundaries of synchronization tongues in 3 subjects. The method allows non-invasive research. The basic idea is to influence the contours of heart rate regulation with a respiratory signal, which has respiratory frequency varying linearly about 0.1 Hz according to the sound signal generated by a special device. The amplitude of the breath is changed by the subjects at the command of the researcher. The study is important for understanding the features of complex multichannel systems of biological nature and their mathematical modeling.**

Keywords—phase locking, frequency locking, synchronization, active experiment, Arnold, sympathetic regulation of heart rate, 0.1 Hz, cardiointervalogram, respiration

I. INTRODUCTION

Systems of biological nature are prime example of complex dynamic systems. Biological nature of systems characterized by complex multi-component structure with a large number of structural elements connected in a complex way and strong instability (variability of parameters over time). Signals of systems biological nature have complex shape, wide range, they are noisy and non-stationary. One way to study such systems is to set up a special active experiment with an impact on the system under investigation by a known external signal that causes changes in the dynamics of the system. In turn, the use of radiophysical methods to study biological systems in such experiments, allows to obtain additional information on the investigated objects.

A typical example is the study of interactions between respiration and contour of the sympathetic regulation of heart rate (HR), which have frequencies of about 0.1 Hz in the spectrum from cardiointervalogram signals [1].

It is known that the contour is under the influence of the respiration, demonstrating synchronization [2,3]. By synchronization we mean the phase locking and frequency locking of interacting objects in a certain range of detuning and coupling coefficients [4]. The use of radiophysical methods for studying the contour of the regulation of heart rate in well-known papers [5, 6] made it possible to refine the mathematical models of the cardiovascular system, resulting in a number of important results for fundamental physiology and the development of medical diagnostic methods in cardiology.

The purpose of this study was to develop a methodology for assessing the boundaries of the Arnold tongues due to analyzing the contour of autonomous regulation of heart rate and respiration during an experimental study.

II. EXPERIMENT

The study involved 3 subjects, who simultaneously recorded signals of electrocardiogram (ECG) and respiration. Three series of active breathing experiments were conducted for each subject. In the first and second series of experiments, the respiratory frequency of the subjects linearly increased from 0.05 to 0.25 Hz during 25 minutes, following the sound signals generated by the special device, similarly to [7]. In the first series of experiments, the subject was asked to maintain a comfortable respiratory depth. In the second series of experiments, the subject performed forced deeper breaths. In the third series of experiments to assess the characteristic frequency of the studied contour of the regulation of heart rate, the signals were recorded at the natural respiration rate of the subjects. The recording time was 20 minutes.

III. METHODS

RR interval sequence was preliminarily extracted from the ECG and interpolated by cubic splines and re-sampling at regular intervals of time with a frequency of 5 Hz. Oscillations reflecting the activity of the regulation contour of the heart rate were extracted from signals of equidistant RR interval sequence using band-pass filtering in the band of 0.05-0.25 Hz and were re-selected to the sampling frequency of 5 Hz. The instantaneous phases of signal are extracted by the Hilbert transform. [8]. The instantaneous frequencies were determined based on the calculation of the continuous wavelet transform [9]. Figure 1 shows the Morlet wavelet spectrum of the experimental RR interval sequence and signals of respiration for the three experimental series.

Then we studied the frequency locking and phases locking of spectral components with a characteristic frequency of about 0.1 Hz, observed in the RR intervals and signal of respiration.

The frequency locking of low-frequency oscillations due to respiration signal with a frequency f_r was diagnosed by evaluating the corresponding $f(f_r)$ dependence, similar to [10]. When the fundamental frequency f of the RR interval sequence oscillations coincided with the instantaneous frequency of oscillations of the affecting respiration signal f_r, frequency synchronization boundaries were detected with a spectral resolution accuracy and quantitative conclusions were made about the duration of the synchronization intervals.

The instantaneous phases synchronization was diagnosed by calculating the coefficient of phase coherence ρ in sliding windows [11]. The calculation of ρ was carried out in windows with a duration of 100 seconds, the offset step was 10 seconds. Statistical significance was monitored by comparing ρ values with a full 95% significance level, constructed by generating pairs of surrogate AAFT (Amplitude Adjusted Fourier Transform) signals [12]. When ρ exceeded the full level of significance ($p=0.05$), phase synchronization boundaries were detected and quantitative conclusions were drawn about the duration of the phase synchronization intervals.

IV. RESULTS

It turned out that in the first and second series of experiments it was possible to identify long-term sections of the synchronization for all subjects (Fig. 2). Moreover, in a typical case, the methods of analysis give close results of determining the boundaries of the synchronization interval of the order of 1:1. The coefficient ρ increases sharply within the interval of synchronous behavior, remaining close to 1 and significant (Fig. 2(a)). The fundamental frequency of RR interval sequence dependence of the frequency of breathing in the spectrum (Fig. 2 (b)) demonstrates the classic picture of the frequency synchronization of a non-autonomous oscillator due to an external variable frequency signal, typical, for example, to radiophysical oscillators [4].

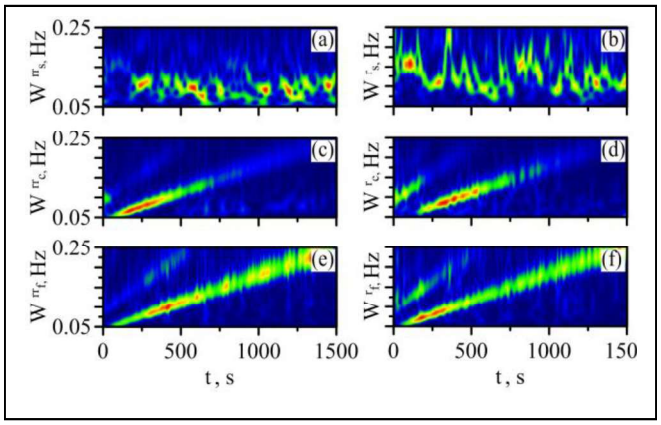

Fig. 1. Morlet wavelet spectrum of the experimental RR interval sequence (left) and respiration (r) (on right) signals of subject #1. (a, b) – breathing with the normal frequency. (c, d, e, f) – the frequency varies linearly from 0.05 to 0.25 Hz during the experiment. (c, d) – comfort depth of breath. (e, f) – forced depth of breath.

This behavior corresponds to the dynamics within the Arnold tongues between its boundaries. [4].

Figure 3 presents the results of the analysis of the phase synchronization of 0.1 Hz of RR interval sequence oscillations with a comfortable and forced depth of breathing for 3 subjects. Arnold tongues are marked for different subjects. It can noticed that on Figure 3 the synchronization boundaries in both experiments are asymmetrically shifted relative to the typical frequency of the studied regulation contour – 0.1 Hz and during forced breathing, the synchronization interval is shifted to the left. This can serve as an argument in favor of the hypothesis that the interaction of the studied contours and respiration is fundamentally nonlinear.

In the course of quantitative analysis, a comparison was made of the durations of the phase synchronization intervals of the order of 1:1 in first and second series of experiments.

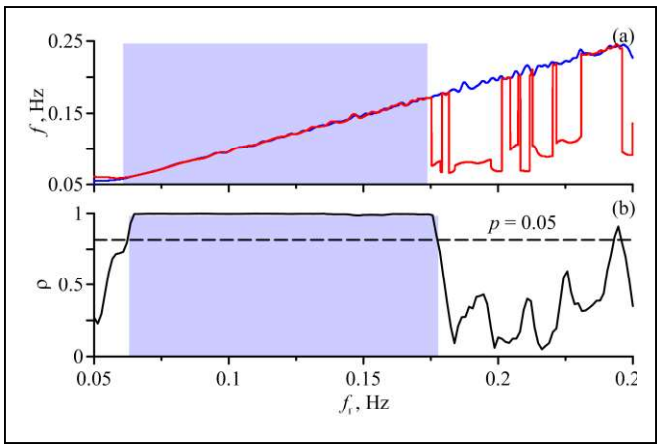

Fig. 2. The results of the analysis of the phase and frequency locking between 0.1 Hz oscillations of RR interval sequences and signal of respiration with a frequency linearly increasing with time. (a) – Dependence of the fundamental frequency *f* in the spectrum of 0.1 Hz RR interval sequences oscillations on the respiration rate *f*r. (b) – Dependence of the phase coherence coefficient on the respiration rate *f*r, the horizontal line marks the p=0.05 significance level. The vertical dashed lines indicate the diagnosed synchronization interval near the natural frequency, where ρ remains above the level of significance. The dashed line indicates the corresponding respiration rates.

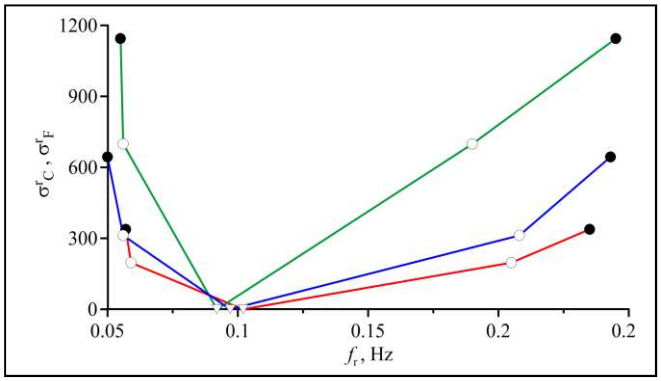

Fig. 3. Arnold tongues based on the analysis of phase synchronization of 0.1-Hz oscillations of RR interval sequence with a breathing signal at a comfortable and forced depth of breathing for 3 subjects. On the y axis is inspiratory amplitude standard deviation, on the x axis – frequency of respiration. White dots mark the beginning and end of synchronization with a comfortable depth of breathing, black dots mark the beginning and end of synchronization with a forced depth of breathing. Triangles mark the characteristic oscillation frequency of the studied processes.

The average duration of synchronization intervals of low-frequency rhythm in CIG with a comfortable depth of breathing was 1120±322 s (mean ± standard deviation), with a forced depth of breathing was 1234±260 s. An analysis of the ensemble of experimental data of 3 subjects allowed us to conclude that the longest synchronization intervals are observed in 2 series of active experiments with increasing amplitude of external influence. Apparently, such results are due to the fact that with an increase in the depth of respiration, the coupling coefficient between respiration and the studied contours increases.

As a result of the study, we proposed a technique of experimental observation of the Arnold tongue for analyzing the contour of autonomous regulation of heart rate and respiration. The technique was used to analyze the signals of 3 subjects and allowed to determine the boundaries of the Arnold tongues. It was reveal that the interaction of the contours and breathing under consideration is fundamentally non-linear. Proof of this is the non-linear and asymmetrical form of the beak. It was concluded that the longest synchronization intervals are observed during forced deep breathing.

The Arnold tongues of contour of autonomic regulation of heart rate and respiration are of fundamental interest for modeling the cardiovascular system and applied interest for the development of non-invasive diagnostic methods and require further study [5, 6, 7].

ACKNOWLEDGMENT

The work was carried out within the framework of the state task (development of the method), as well as with financial support МД-2202.2019.8 (registration, preliminary analysis and processing of experimental data, synchronization diagnostics).

REFERENCES

[1] Yu.M. Ishbulatov, A.S Karavaev, V.I. Ponomarenko, M.D. Prokhorov, B.P. Bezruchko, "Model of cardiovascular system autonomic regulation with a circuit of baroreflectory control of mean arterial pressure in the form of delayed-feedback oscillator," Izvestiya of Saratov University. New series. Series: Physics, vol. 15, N. 2, pp. 32-38, 2015.

[2] A.R. Kiselev, A.S. Karavaev, V.I. Gridnev, M.D. Prokhorov, V.I. Ponomarenko, E.I. Borovkova, V.A. Shvartz, Yu.M. Ishbulatov, O.M.

Posnenkova, B.P. Bezruchko, "Method of estimation of synchronization strength between low-frequency oscillations in heart rate variability and photoplethysmographic waveform variability," Russian Open Medical Journal, vol. 5, N. 1, pp. 0101, 2016.

[3] Y.I. Borovkova, A.S. Karavaev, B.P. Bezruchko, V.I. Ponomarenko, M.D. Prokhorov, "Uncovering frequency locking for systems affected by chirping," Bulletin of the Russian Academy of Sciences: Physics, vol. 75, N. 12, pp. 1601-1604, 2011.

[4] Pikovsky, M. Rosenblum, J. Kurths, Synchronization, "A Universal Concept in Nonlinear Sciences," Cambridge University Press, 2001.

[5] A.R. Kiselev, V.A. Shvartz, S.A. Mironov, A.S Karavaev., D.D. Kulminskiy, M.D. Prokhorov, V.V. Skazkina, E.I. Borovkova, V.I. Ponomarenko, "A comprehensive assessment of cardiovascular autonomic control using photoplethysmograms recorded from the earlobe and fingers," Physiological Measurement, vol. 37, N. 4, pp. 580-595, 2016.

[6] A.R. Kiselev, V.I. Gridnev, O.M. Posnenkova, M.D. Prokhorov, A.S. Karavaev, V.I. Ponomarenko, B.P. Bezruchko, "Effects of antihypertensive treatment on cardiovascular autonomic control: a prospective study," Anadolu Kardiyoloji Dergisi, vol. 14, N. 8, pp. 701-710, 2014.

[7] A.S. Karavaev, A.R. Kiselev, V.I. Gridnev, E.I. Borovkova, M.D. Prokhorov, O.M. Posnenkova, V.I. Ponomarenko, B.P. Bezruchko, V. A. Shvartz, "Phase and Frequency Locking of 0.1 Hz Oscillations in Heart Rhythm and Baroreflex Control of Arterial Pressure by Respiration with Linearly Varying Frequency in Healthy Subjects," Human Physiology, vol. 39, N. 4, pp. 93–104, 2013.

[8] Gabor, "Theory of communication. Part 1: The analysis of information," Journal of the Institution of Electrical Engineers - Part III: Radio and Communication Engineering, vol. 93, iss. 26, pp. 429-441, 1946.

[9] J.C. Van den Berg, "Wavelets in Physics," Cambridge: Cambridge University Press, 1998.

[10] I.I. Blekhman, "Synchronization in Science and Technology," ASME Press, 1988.

[11] F. Mormann, K. Lehnertz, P. David, C.E. Elger, "Mean phase coherence as a measure for phase synchronization and its application to the EEG of epilepsy patients," Physica D, vol. 144, iss. 3-4, pp. 358-369, 2000.

[12] T. Schreiber, A. Schmitz, "Improved Surrogate Data for Nonlinearity Tests," Phys. Rev. Lett, vol. 77, N. 4, pp. 635-638, 1996.

Synchronization of the process of autonomous regulation of blood circulation with low-frequency components of the laser Doppler flowmetry signal

Ekaterina Borovkova
Saratov Branch of the Institute of RadioEngineering and Electronics of Russian Academy of Sciences, Saratov State Medical University named after V. I. Razumovsky, Saratov State University
Saratov, Russia
0000-0002-9621-039X

Yurii Ishbulatov
Saratov Branch of the Institute of RadioEngineering and Electronics of Russian Academy of Sciences, Saratov State Medical University named after V. I. Razumovsky, Saratov State University
Saratov, Russia
0000-0003-2871-5465

Anton Kiselev
Saratov State Medical University named after V. I. Razumovsky, Saratov State University
Saratov, Russia
0000-0003-3967-3950

Arina Tankanag
Institute of Cell Biophysics Russian Academy of Science
Pushchino, Moscow
0000-0002-9538-1939

Gennady Krasnikov
Tula State Lev Tolstoy Pedagogical University
Tula, Russia
0000-0003-0943-6727

Anatoly Karavaev
Saratov Branch of the Institute of RadioEngineering and Electronics of Russian Academy of Sciences, Saratov State Medical University named after V. I. Razumovsky, Saratov State University
Saratov, Russia
0000-0003-4678-3648

***Abstract*— The features of the individual dynamics and interaction of the elements of the autonomous regulation of blood circulation and blood flow fluctuations in the microvasculature of the skin were investigated. Phase synchronization of the laser Doppler flowmetry signal with processes of autonomic regulation is revealed. This may indicate the effect of vegetative regulation on the myogenic range of laser Doppler flowmetry.**

Keywords — Laser Doppler flowmetry, 0.1 Hz, heart rate variability, blood pressure variability, cardiointervalogram, photoplethysmogram, phase capture, statistical significance

I. INTRODUCTION

The purpose of this study was to study the characteristics of individual dynamics and the interaction of elements of the cardiovascular system (CVS). The problem of studying the mechanisms of oscillation with a characteristic frequency of 0.1 Hz in laser Doppler flowmetry (LDF) signals was considered.

Despite the fairly widespread use of LDF signals, the question of the physiological interpretation of spectral components in the frequency range of 0.04–0.15 Hz, which traditionally refers to the sympathetic regulation of heart rhythm and the regulation of arterial vascular tone, remains controversial [1-4]. In [5,6] it was noted that the oscillations

of the LDF signal in the frequency range of 0.04–0.15 Hz correspond to the local regulation of muscle tone, determined by smooth muscle fibers of precapillaries.

Also in a number of works [2, 3] it was noted that oscillations of blood flow in the microvasculature with a frequency close to 0.1 Hz do not reflect information about the sympathetic baroreflex regulation of arterial vascular tone.

Earlier, we demonstrated the importance of studying the interaction of elements of the autonomous regulation of blood circulation [7,8]. In the works [9,10] it was shown that the rhythms of the contours of the regulation of the heart rate and the contour of the regulation of arterial vascular tone, which have natural oscillation frequencies of about 0.1 Hz, can demonstrate irregularly alternating phase synchronization intervals during spontaneous breathing.

In the present work, we studied the synchronization of the elements of the autonomous regulation of blood circulation and blood flow oscillations with a frequency close to 0.1 Hz in the microvasculature of the skin.

II. Experiment

The study involved 30 subjects. Simultaneous recording of electrocardiograms (ECG), photoplethysmogram (PPG) and laser Doppler flowmetry (LDF) signals was carried out during spontaneous breathing. Registration duration was 20 minutes.

Registration of an ECG was carried out in the I standard lead. The respiration signal was recorded by an abdominal strain gauge sensor. The LDF signal was recorded from the index fingers of the right (LDFR) and left hand (LDFL). The PPG signal was recorded from the middle finger of the right hand. Signals were recorded using standard certified equipment with a quantization width of 16 bits and a sampling rate of 120 samples per second per channel. The bandwidth of the filter of the recorded signals is 0.003-60 Hz.

III. Methods

Cardiointervalogram was preliminarily extracted from the ECG and interpolated by cubic splines and re-sampling at regular intervals of time with a frequency of 5 Hz. Oscillations of the contours of the autonomic regulation of HRV and the contour of the regulation of arterial vascular tone were distinguiextracted from signals of the equidistant CIG and PPG using band-pass filtering in the band of 0.04–0.15 Hz and were reselected to the sampling frequency of 5 Hz. LDF signals were also filtered in the band of 0.04–0.15 Hz and were reselected to a sampling frequency of 5 Hz. The instantaneous phases of the signals were distinguished using the Hilbert transform [11].

We stadyed the phase locking of HRV, PPG, LDFL and LDFR processes in pairs.

We used the integral indicator of the summary percentage of phase synchronization *S*, which is the sum of the lengths of the synchronization intervals, referred to the duration of the entire record and expressed as a percentage [12]. The boundaries of synchronous intervals were diagnosed by the signal of the phase difference using the previously proposed algorithm [9].

The algorithm is based on a piecewise linear approximation of the instantaneous phase difference in a sliding window with a length b and control of the slope of the approximating straight line α. The areas of phase synchronization in which the dependence $\Delta\varphi(t)$ has an almost horizontal view should correspond to areas with a small value of $|\alpha|\leq a$, where a is the threshold value of the slope α, equal to $\pm a$. The duration of synchronous sections must be at least l.

The values of the method parameters: l=22 s, $|a|$=0.004, b=10 s were selected in accordance with [9]. Such a set of parameters provides sensitivity (the probability of detecting the synchronization interval where it is actually present) at the level of 0.93, the specificity (the probability of detecting a false synchronization interval) at the level of 0.36.

The statistical significance of the analysis results was estimated at the level of p=0.05 using the formation of the AAFT ensemble (Amplitude Adjusted Fourier Transform) of surrogate data [13].

For the quantitative analysis, only statistically significant indicators *S* were used.

IV. Results

Figure 1(a) shows the characteristic power spectra of time series. Oscillatory activity is seen in the signal spectra in the frequency range of 0.04–0.15 Hz. In the LDF signals recorded from the right and left hands, the spectral component at a frequency of 0.1 Hz is less pronounced compared to the HRV and PPG signals (Fig. 1(a)).

Figure 1(b) shows the result of the bandpass filtering of the corresponding time series in the 0.04–0.15 Hz band. A visual analysis shows a correlation of 0.1 Hz oscillations, extracted from the PPG and LDF signals. The result of HRV filtering demonstrates excellent oscillation dynamics, unlike PPG and LDF signals.

Figure 2 shows the result of the study of the phase locking of the low-frequency components of the HRV and PPG (a), HRV and LDFL (b), HRV and LDFR (c) by the 10-minute time intervals. The plots show the phase difference signals as a function of time. The time intervals corresponding to the phase capture are highlighted in blue. It turned out that in a typical case it is possible to identify long-term areas of phase capture between the studied processes. Moreover, the intervals of phase capture of low-frequency components of signals HRV and PPG (Fig. 1(a)), HRV and LDFL (Fig. 1(b)), HRV and LDFR (Fig. 1(c)) are diagnosed simultaneously.

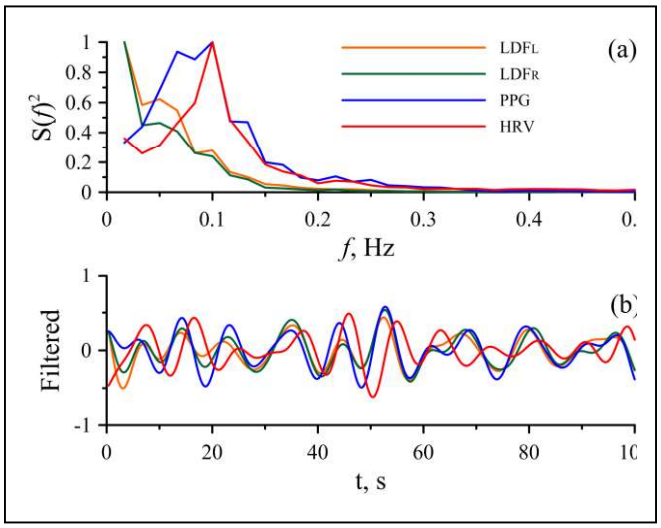

Fig. 1. (a) - Power spectra of time series recorded in the experiment for the subject # 1. The plots are normalized maximum power in the spectrum. (b) - Filtered time series in the frequency range 0.04–0.15 Hz band. Time series normilized to unit variance.

For all pairs of signals, a statistically significant synchronization was detected (Fig. 3).

An analysis of the ensemble of experimental data allows us to conclude that the longest synchronization intervals are observed between the LDF signals recorded from different hands (Fig. 3 (column 6)). The *S* score between the LDF and PPG signals is lower than that between the LDFR and LDFL signals (Fig. 3 (4-5 columns)). The *S* score between HRV and PPG is higher than for HRV and LDF from different hands (Fig. 3 (columns 1-3)).

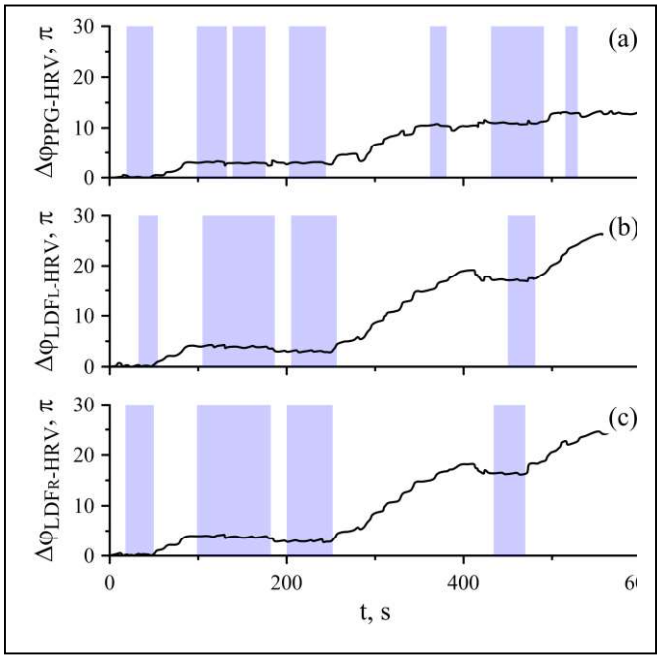

Fig. 2. The result of the study of the phase capture of low-frequency components: (a) - CIG-FIG, (b) - CIG-LDFL, (c) - CIG-LDFpr. The solid line is a graph of the phase difference versus time. The time points corresponding to the phase capture are highlighted in blue.

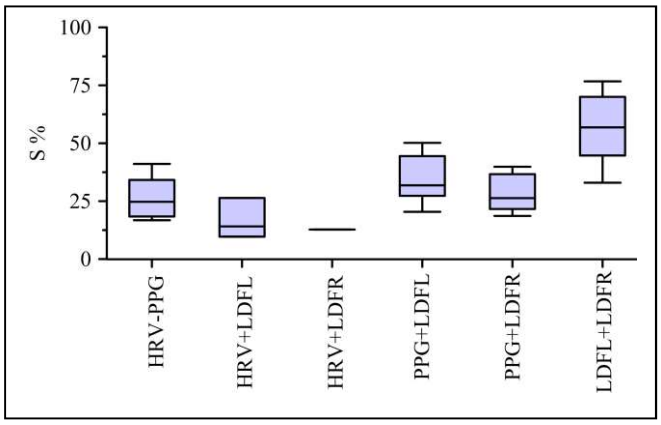

Fig. 3.Statistics of the distribution of indicators *S* (p = 0.05), estimated for the low-frequency components of the PPF, LDF and HRV signal. Box-first, second, third quartiles, whiskers - min and max values S, estimated for the ensemble of experimental data.

When observing the statistical significance of synchronization between HRV and LDF, a statistically significant synchronization between HRV and PPG was diagnosed. From which it follows that in the frequency range of 0.04–0.15 Hz, the LDF signal is a passive reflection of the PPG signal.

So, according to the results of the conducted research, phase synchronization of LDF signals with processes having a central nature in the frequency range of 0.04–0.15 Hz was revealed. This, in turn, led to the conclusion that in the frequency range of 0.04–0.15 Hz, in addition to myogenic oscillations, the signal of the LDF contains information on the processes of sympathetic baroreflex regulation of arterial vascular tone. In all likelihood, the same processes are observed in the LDF signal as in the FPG signal.

ACKNOWLEDGMENT

This work was supported by the Russian Science Foundation, Grant № 19-12-00201.

REFERENCES

[1] "Heart rate variability. Standards of measurement, physiological interpretation, and clinical use. Task Force of the European Society of Cardiology the North American Society of Pacing Electrophysiology," Circulation, vol. 93, pp. 1043-1065, 1996.

[2] A.I. Krupatkin, "Blood flow oscillations at a frequency of about 0.1 hz in skin microvessels do not reflect the sympathetic regulation of their tone," Human Physiology, vol. 35, N. 2, pp. 183-191, 2009.

[3] A.I. Krupatkin, "The influence of the sympathetic innervation on the skin microvascular tone and blood flow oscillations," Human Physiology, vol. 32, N. 5, C. 584-592, 2006.

[4] Г.М. Пискунова, Н.К. Чемерис, Г.В. Красников, А.В. Танканаг, Т.В. Кирилина, "Пространственная синхронизация колебаний кровотока в системе микроциркуляции кожи человека," Регионарное кровообращение и микроциркуляция, N. 3, pp. 32-36, 2009. T.V Kirilina, G.V. Krasnikov, A.V. Tankanag, G.V. Krasnikov, G.M. Piskinova, N.K. Chemeris, "Spatial synchronization of the blood flow oscillations in human skin microcirculation," Region. Blood Circ. Microcirc, vol. 8, pp. 32-36, 2009.

[5] Stefanovska, M. Bracic, "Wavelet analysis of oscillations in the peripheral blood circulation measured by laser Doppler technique," IEEE Transactions on Biomedical Engineering, vol. 46, iss. 10, pp. 1230-1239, 1999.

[6] M.F. Meyer, C.J. Rose, J.O. Halsmann, H. Schatz, M. Pfohl, "Impaired 0.1-Hz vasomotion assessed by laser Doppler anemometry as an early index of peripheral sympathetic neuropathy in diabetes," Microvascular Research, vol. 65, iss. 2, pp. 88-95, 2003.

[7] A.R. Kiselev, V.I. Gridnev, O.M. Posnenkova, M.D. Prokhorov, A.S. Karavaev, V.I. Ponomarenko, B.P. Bezruchko, "Effects of antihypertensive treatment on cardiovascular autonomic control: a prospective study," Anadolu Kardiyoloji Dergisi,2014, vol. 14, N. 8, pp. 701-710, 2014.

[8] Yu.M. Ishbulatov, A.R. Kiselev, A.S. Karavaev, "Numerical modeling of dynamics of heart rate and arterial pressure during passive orthostatic test", Proceedings of SPIE, 2018, vol. 10717, pp. 1071726-1.

[9] A.S. Karavaev, M.D. Prokhorov, V.I. Ponomarenko, A.R. Kiselev, V.I. Gridnev, E.I. Ruban, B.P. Bezruchko , "Synchronization of low–frequency oscillations in the human cardiovascular system," CHAOS, vol. 19. pp. 33112, 2009.

[10] B.P. Bezruchko ,V.I.Gridnev, A.S. Karavaev , A.R. Kiselev, V.I. Ponomarenko, M.D. Prokhorov, E.I. Ruban, "Technique of investigation of synchronization between oscillatory processes with the frequency of 0.1 Hz in the human cardiovascular system," Proceedings of higher educational institutions. Applied nonlinear dynamics, vol. 17, N. 6, pp. 44-56, 2009.

[11] Gabor, "Theory of communication. Part 1: The analysis of information," Journal of the Institution of Electrical Engineers - Part III: Radio and Communication Engineering, vol. 93, iss. 26, pp. 429-441, 1946.

[12] A.R. Kiselev, A.S. Karavaev, V.I. Gridnev, M.D. Prokhorov, V.I. Ponomarenko, E.I. Borovkova, V.A Shvartz., Yu.M. Ishbulatov, O.M. Posnenkova, B.P. Bezruchko, "Method of estimation of synchronization strength between low-frequency oscillations in heart rate variability and photoplethysmographic waveform variability," Russian Open Medical Journal, vol. 5, N. 1, pp. 0101, 2016.

[13] T. Schreiber, A. Schmitz, "Improved Surrogate Data for Nonlinearity Tests", Phys. Rev. Lett, vol. 77, N. 4, pp. 635–638, 1996.

Phase-amplitude coupling between mu- and gamma-waves to carry motor commands

Parth Chholak
Centro de Tecnología Biomédica
Universidad Politécnica de Madrid
Madrid, Spain
https://orcid.org/0000-0002-6437-7750

Alexander N. Pisarchik
Centro de Tecnología Biomédica
Universidad Politécnica de Madrid
Madrid, Spain
https://orcid.org/0000-0003-2471-2507

Semen A. Kurkin
Center for Technologies in Robotics and Mechatronics Components, Innopolis University
Innopolis, Russia
https://orcid.org/0000-0002-3438-5717

Vladimir A. Maksimenko
Center for Technologies in Robotics and Mechatronics Components, Innopolis University
Innopolis, Russia
https://orcid.org/0000-0002-4631-6896

Alexander E. Hramov
Center for Technologies in Robotics and Mechatronics Components, Innopolis University
Innopolis, Russia
https://orcid.org/0000-0003-2787-2530

***Abstract*—The development of brain computer interfaces, especially the ones related to controlling exoskeletons and neurorehabilitation of stroke patients, strongly relies on our understanding of motor system and its neuronal mechanism. Motor imagery (MI) has turned out to be one of the most popular experimental regimes to study this system. Kinesthetic imagery (KI) is a kind of MI which shares a large portion of its neuronal pathway with real movements, except for having an additional inhibitory mechanism to prevent movement execution. Our magnetoencephalographic (MEG) experiments with ten untrained subjects revealed that this inhibitory control implied local neuronal desynchronization. We found that the motor-related communication between the inferior parietal cortex and the prefrontal cortex was carried out using the mu-frequency range. Additionally, three gamma frequencies were also pinpointed that encode the motor command specifics. Using artificial neural networks (ANNs) we classified left- and right-hand MI which reached maximal accuracy when we included these three gamma frequencies in the input signal for ANN. We suggest that mu-activity acts as a carrier of gamma-activity between inferior and parietal areas utilising phase-amplitude coupling.**

Keywords—brain-computer interface, motor imagery, inhibition, neuronal communication, phase-amplitude coupling, artificial neural network, magnetoencephalography (MEG)

I. INTRODUCTION

Brain-computer interfaces (BCIs) aim to control external devices using the operator's brain activity [1]. The BCI systems can be classified into two general categories [1]. In the first category, feedforward brain activity is used to control external devices and in the second category, a closed-loop feedback control is applied for neural rehabilitation.

The important task of BCIs is the pattern recognition of neurophysiological brain activity associated with motor imagery (MI) defined as a mental simulation of overt actions in the absence of any muscle movements. This bears crucial importance for brain-controlled exoskeletons, bioprosthesis and neurorehabilitation of amputee and post-stroke patients. The scientists distinguish two types of MI, visual imagery (VI) and kinesthetic imagery (KI) [2]. While in VI subjects MI activates visual cortex, in KI subjects the activity is detected in the same motor areas as in the case of real movements [2] with an additional mechanism for inhibiting motor commands to avoid overt actions [1], [3]–[5]. Functional magnetic resonance imaging (fMRI) studies evidence the involvement of motor associated areas and inferior parietal (IP) cortex for KI subjects, in contrast to VI subjects, who exhibit the involvement of visual and superior parietal cortices [6]. Moreover, transcranial magnetic stimulation (TMS) experiments suggest that the IP area participates in the inhibitory control of the primary motor cortex (M1) during KI-dominated MI [7]. However, despite extensive research on MI, no clear experimental evidence of the underlying KI mechanism has yet been provided.

One of the most popular experimental paradigms for MI studies is based on sensorimotor rhythms (SMR) [1], which

involves KI of large body parts, such as whole limbs, to modulate neural activity [8]. At the same time, alpha- and beta-rhythms are crucial and ubiquitous in most studies on MI [9]. For example, in 1991 the alpha-rhythm was used to control the cursor position on a computer screen in one-dimensional space [10]. Later, more advanced and sophisticated methods, such as linear regression, logistic regression, and artificial neural networks (ANNs), were applied to control the cursor position in three-dimensional space [11]–[13], prosthetics [14]–[16], robots [17]–[21], and for stroke rehabilitation [16], [22], [23] (for review see [1], [24]).

Among a significant amount of literature on the BCI development using MI, electroencephalography (EEG) is found to be the most popular noninvasive technique [25]–[32] for controlling wheelchairs [25], communication aid systems [33], assistive and rehabilitative devices for healthy [34] and disabled people, stroke patients and people with other neurological deficits [26], [27], [35]–[37]. In addition, a fair amount of papers were devoted to magnetoencephalography (MEG) studies on MI [38]–[42], which has the advantage of a higher spatial resolution and better resilience against artifacts as compared to EEG, although some advantages of EEG, such as low cost and portability, are crucial for BCI development, but can be kept aside while understanding the fundamental activity underlying MI.

The aim of this study is to analyse MEG signals, especially in alpha- and beta-frequency bands associated with MI in the SMR paradigm. We focus on the inhibitory mechanism to avoid overt action during KI, that was previously investigated using other neuroimaging techniques, such as TMS. Subsequently, we perform various validation tests along the way using methods based on the power spectrum anaslysis, coherence and ANNs, and suggest a model which explains empirical observations related to KI and real movements (overt actions).

II. Materials and Methods

The neurophysiological data were acquired using the Vectorview MEG system (Elekta AB) with 306 channels (102 magnetometers and 204 planar gradiometers) placed inside a magnetically shielded room (Vacuum Schmelze GmbH). Three fiducial points (nasion, left and right preauricular) were acquired for each subject.

The experimental study consisted of ten (nine right-handed, eight males) untrained volunteers between the age of 20 and 31. The subjects sat in a comfortable reclining chair with their legs straight, shoes off, and arms resting on an armrest in front of them. All of them provided a written informed-consent before the experiment commencement. The experimental studies were performed in accordance with the Declaration of Helsinki.

Spatiotemporal signal space separation [43] was used to separate neuronal signals from nearby electromagnetic interference. The signals from bad MEG channels were replaced with spatially-averaged signals of the nearby well-functioning MEG channels. The software used for this preprocessing task was MaxFilter that came along with the Elekta-Neuromag machine. The sampling frequency was 1000 Hz and an online anti-alias [0.1–330] Hz bandpass filter was utilised.

The experimental protocol was designed as shown in Fig. *1*. Resting-state recordings were performed at the start and at the end of each experiment with open eyes (OE) and closed eyes (CE), respectively. OE recordings were later discarded because all data during MI were recorded with closed eyes. The duration of CE recordings was different for each subject and ranged from 40 to 280 s.

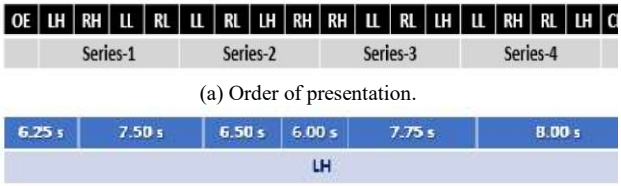

(a) Order of presentation.

(b) MI trials for left hand.

Fig. 1. Experimental protocol.

All MI recordings were divided into four sets of time series. Every set contained the MEG data of MI of each of four limbs in a random order, i.e., left hand (LH), right hand (RH), left leg (LL), and right leg (RL). The order of presentation shown in Fig. *1*(a) displays one of such protocols, which was different for each subject. Before MI of each limb, a visual message appeared on the screen to ask the subject close eyes and imagine the movement of the indicated limb as soon as a beep sounds. The subsequent beeps were given after a random time interval between 6 and 8 seconds. Each imaginary movement between the beeps was counted as one trial. Fig. *1*(b) shows a model example of the beep presentation for LH MI-trials. The number of trials for each limb was varied among subjects between 4 and 7 in each series. After every series, the subjects had a 40-s rest during which they listened to a relaxing music.

The experiments were programmed using software provided by the Cogent 2000 team at the Functional Imaging Laboratory and the Institute of Cognitive Neuroscience and Cogent Graphics developed by John Romaya at the Laboratory of Neurobiology at the Wellcome Department of Imaging Neuroscience. A MATLAB code was used to produce all audio and visual commands (Cogent) as well as to log the time at the beginning of each MI-trial in a protocol file (in .txt format). The protocol file was later used to mark all events manually when analysing the MEG file (in .fif format). A part of the data analysis was performed with Brainstorm [44] documented and freely available for downloading under the GNU general public license (http://neuroimage.usc.edu/brainstorm). Once the events were marked at the beginning of each limb's MI using the protocol file, 5-s trials were extracted immediately after these marks. Similarly, 10-s trials from CE-recordings were also marked and extracted as the background activity for every subject.

The time-frequency structure of the MEG signals was analysed using the wavelet approach, widely acceptable for the analysis of nonstationary biological and medical data [45]. For each limb, we used Morlet wavelets with f0 = 1 Hz central frequency and a 3-s full width at half maximum (FWHM) to evaluate time-frequency spectrograms (TFSs) for all extracted 5-s MEG-trials of each limb, and then averaged the TFSs over all trials for that limb. Then, the TFS was also averaged over desired frequency ranges of delta (1–

5 Hz) and mu (8–30 Hz). The same process was repeated for background 10-s trials using the same parameters. To

evaluate ERS/ERD, we took the difference between the spectrogram for the MI-trials and the time-averaged spectrogram of the background and then normalized it to the background. This normalized difference was assumed to be positive for ERS and negative for ERD.

ANNs were used in the later stages for validation purposes. Multilayer perceptron (MLP) was chosen as the network architecture to classify between LH and RH MI-trials. The input data for the ANN were taken from MEG time series from all 102 magnetometers, after bandpass filtering with a 10-Hz passing window. This passing window was varied from 5-60 Hz in steps of 5 Hz, i.e., (5-15), (10-20), (15-25), ..., and (50-60) Hz. The input layer containing 102 neurons was followed by three hidden layers having 30, 15, and 5 neurons, respectively. The output layer consisted of a single neuron. Scaled conjugate gradient training algorithm was used. The training stopped as soon as the batch training with all input data ran for at least 5000 times. To improve the efficiency of machine learning, we randomly mixed the input signal maintaining the correspondence to the MI-type, either LH or RH. Therefore, to classify MI of LH and RH, we mixed the MEG time series of all collected trials related to LH and RH for each channel without losing their corresponding targets (0 for LH and 1 for RH). The ANN classification was carried out using Neural Network Toolbox of MATLAB (R2017a; Mathworks Inc., MA, USA).

III. Results and Discussion

Based on differential mu-activity of the cortex, we first segregated the subjects into two groups, six KI subjects (Sub 1, 2, 4, 5, 9, and 10) and four VI subjects (Sub 3, 6, 7, and 8). The differentiation was performed according to ERD/ERS in the mu-frequency range. Specifically, the KI subjects exhibited ERD in the aforementioned associated cortical sites (**Ошибка! Источник ссылки не найден.**(a)), while the VI subjects showed ERS.

Curiously, the authors of [46] reported event-related desynchronisation (ERD) of mu-rhythms in the sensorimotor cortex during MI in the SMR paradigm and ERS for resting. Although the subjects in our study were instructed to perform KI, only some of them could successfully achieve this goal, because of the absent of preliminary traning.

The obtained results are in agreement with the previous study [46], where KI subjects (successful-SMR) exhibited ERD in mu-band, while VI subjects (failed-SMR) showed ERS, similar to the resting state of SMR. In the delta-range, all KI subjects exhibited either ERS or ERD in the prefrontal cortex (PF) and insignificant activty in the posterior parts of the brain (**Ошибка! Источник ссылки не найден.**(b)). In addition, the VI subjects exhibited the distributed non-uniform activity without any preference for a particular region. The method used to evaluate ERS/ERD was as explained in section II.

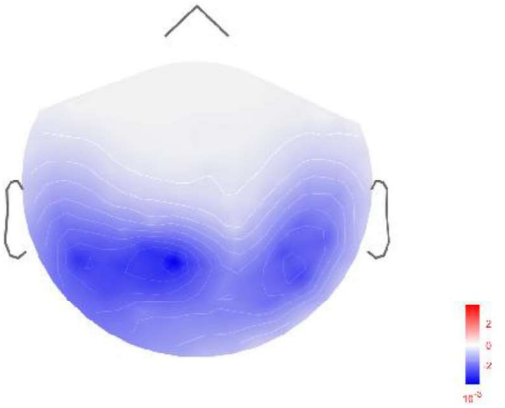

(a) ERS/ERD distribution for mu-frequency range averaged over all trails and trial time.

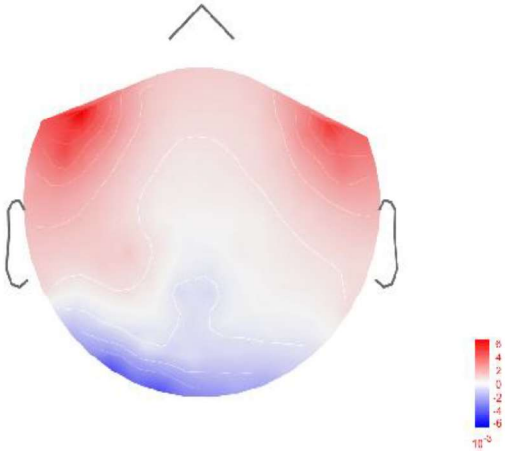

(b) ERS/ERD distribution for delta-frequency range averaged over all trails and trial time.

Fig. 2. Event-related wavelet energy for subject-2 (KI).

As discussed in section I, KI and real movements share a common neuronal network, distinctly to KI which involves an additional mechanism for inhibiting overt movement that is likely to be situated in the IP. The coincidence of finding ERD for the KI subjects in mu-band at the same site as the one that is responsible for inhibitory control (i.e., IP) instils curiosity and deems to be further looked upon. In order to reveal the mechanism underlying this inhibitory control, we suppose that desynchronised activity of neurons near the IP disrupts signal propagation that passes from IP to M1, as hinted by TMS studies.

The PF is also known to be involved in inhibition of movements [47], more specifically in choosing between brain responses [48]. The authors of [49] showed that when subjects were asked to predict beforehand the time necessary to perform motor tasks, the subjects with lesions in the posterior parietal cortex typically underestimated/ overestimated the time. This strongly contrasted with subjects having dysfunctional motor regions, who exhibited impaired movements, but retained the ability to estimate motor performance times [50]. In order to predict motor performance times, the subject needs to simulate the entire repertoire of the act from long-term memory. This function is perhaps localised in the posterior parietal cortex. Conveniently, nearby temporal lobe has been implicated to play a role in long-term memory function, especially the medial temporal lobe [51].

Before the actual execution of motor commands by M1, aided by its associated areas like premotor cortex (PM) and supplementary motor area (SMA), passable responses are likely to be chosen at PF. As most of the conscious processing is performed in the frontal cortex, PF being the point hosting this decision-making process is amenable. We therefore propose the following neuronal pathway for motor signals (**Ошибка! Источник ссылки не найден.**). Motor commands are generated in the posterior parietal cortex and need to travel to PF before being relayed to motor associated areas for final execution. ERD centred around IP disrupts the communication of motor commands from the posterior parietal cortex to PF in order to avoid any overt movement during KI.

The authors of [52] showed that bilateral lesions in the parietal cortex led to the execution of motor commands during MI experiments without the patient realising it. The patient with lesions at IP may not have ERD in IP at mu-frequency and would pass the signal to the PF region, not expecting an input from IP during KI and thus leading to actual execution without the subject's knowledge. We used coherence as a measure of connectivity between two parts of the brain. The results indicate uninhibited communication in the mu-band between IP and PF for all VI subjects, whereas KI subjects exhibit a clearly compromised connectivity between these areas.

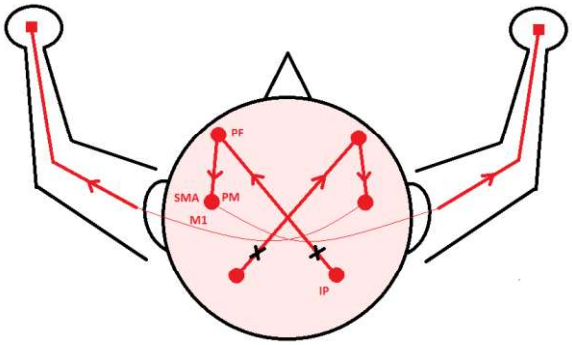

Fig. 3. Neuronal pathway for KI. During KI, inhibition is manifested in the vicinity of IP in the form of ERD which prevents propagation of motor signal towards PF. The rest of the neural circuitry remains the same for MI and actual execution of motor commands

In Fig. *4* we plot the mean-squared coherence of the MEG signals collected from IP and PF versus frequency (in Hz). The strength of connectivity between these areas was found to be suppressed for KI subjects as compared to the VI subjects and exhibit peaks at 10 (mu range), 32 (gamma range), 45 (gamma range), and 48 Hz (gamma range) for both groups of subjects.

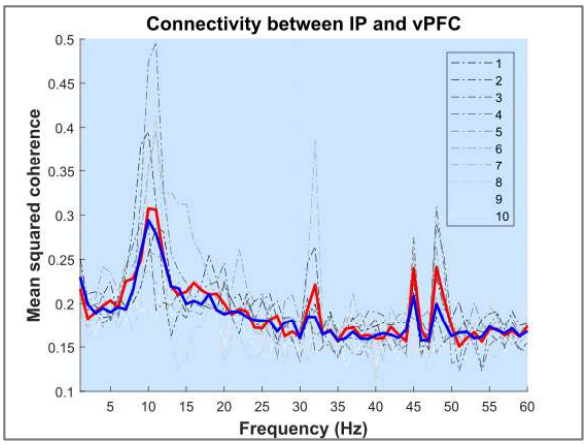

Fig. 4. Connectivity (mean squared coherence) between IP and PF for all 10 subjects. Peaks obtained at 10 Hz (mu), 32 Hz (gamma), 45 Hz (gamma), and 48 Hz (gamma). The thick red and blue lines represent average connectivity of VI and KI subjects, respectively.

The authors of [53] discussed about a theta-gamma neural code for multi-message communication during memory processes. They prescribed phase-amplitude coupling between the phase of theta-waves and the amplitude of gamma-waves and envisaged upon the extension of their model to sensory processes if theta-waves are replaced by alpha-waves. The studies provide evidences of this phase-amplitude coupling in humans [54]–[[54]–[61].

During each gamma-cycle, a set of neurons or neural ensemble fire concurrently, forming a spatial pattern on the cortex that corresponds to the object being represented by that gamma-cycle. The authors of [62]–[65] showed that a sequence of generated information in the form of gamma-cycles gets mapped to different phases of theta-wave, maintaining the same order of information generation. Furthermore, the authors of [60] reported shifts in gamma phase-amplitude coupling frequency from theta to alpha during visual tasks. Similarly, we expect a phase-amplitude coupling between gamma and alpha/mu-waves for MI tasks.

We therefore suggest that motor commands involve mu-waves as general carriers of motor related activity. These carrier waves carry gamma-waves containing specifics of motor activity from IP to PF, which acts as a relay junction and transfers the information to motor related areas such as M1, PM, and SMA. The authors of [66]–[69] also evidence that the coherence in gamma-band between two points of the brain can be used to control neural communication between them.

Our ANN classification study designed in an unconventional but appropriate way, supports the hypothesis so far. The study was designed to find what frequency component of the MEG signal generates higher ANN accuracy in order to gauge the kind of ANN classification-task related information carried by that component.

As already mentioned in section II, the bandpass filtering in a 10-Hz window was used for preprocessing MEG data before the ANN classification of LH and RH MI. The classification accuracy was found to be independent of the type of MI. **Ошибка! Источник ссылки не найден.** shows the ANN classification accuracy averaged over all subjects versus the bandpass frequency range. Each data point in this figure represents a centre of the corresponding

bandpass frequency range. Thus, the points at the two local maxima represent 25–35 Hz and 45–55 Hz windows, respectively, as marked in **Ошибка! Источник ссылки не найден.**. Observing these two maxima in the frequency ranges which include the gamma frequencies shown in Fig. *4* confirms our hypothesis that the MI specification (e.g., hand movement) is encoded in the gamma-wave. On the other hand, the mu-band played a general role in this motor task and did not contribute as much in differentiating two hands.

The amplitude of intracellular spiking in gamma-band in the directionality specific (LH or RH) neurons is codependent on the phase of the 10-Hz mu-band signal which acts as an envelope for motor-related activity between these regions.

In the very recent systematic and extensive review [9], only eight papers were mentioned in which authors employed MLP for deep neural network classification using EEG, and only three of which were focussed on MI. Only one of these MI studies utilised MEG time series as inputs for ANN [70] with a 75% accuracy, whereas other two studies [71], [72] used different forms of frequency transformations on the input signal and achieved up to 85% accuracy. The maximum accuracy obtained in our study, utilising MEG signals as input, was about 85% in the 40–50 Hz range.

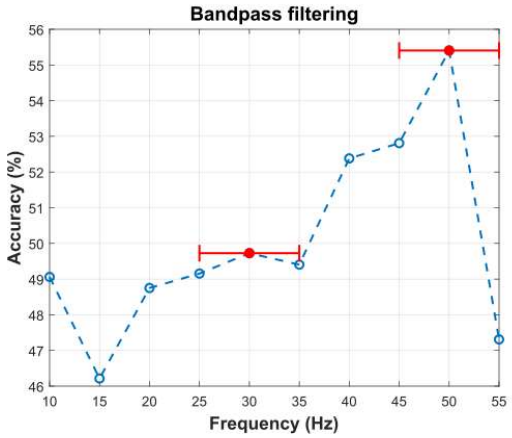

Fig. 5. ANN accuracy in classification between LH and RH MI averaged over all subjects, versus bandpass frequency range on the input MEG signal to ANN. Each data point on the x-axis represents a central frequency of the 10-Hz bandpass frequency range.

IV. Conclusions

In this work we identified a neuronal pathway for motor command propagation during both kinesthetic imagery (KI) and real movements. We also revealed parts of the encoding details and signal disruption to avoid overt action. During KI, desynschronised neurons prevent brain activity in gamma (32, 45, and 48 Hz) carrying specifics of the movement to propagate from inferior parietal lobe to the prefrontal cortex which can blindly relay the signal to the motor areas for execution. All motor related communications are performed in the mu (10-Hz) frequency range using phase-amplitude coupling. Delta waves also participate in this circuit and definitely play an important role in the prefrontal cortex. We aspire that the identification of these motor related frequencies and the areas where they communicate through will turn out to be radical in developing BCIs henceforth. The insights about neural communication and inhibition may benefit research on controlling human inhibition towards harmful substances or preventing the propagation of undesirable sensations, such as pain.

Acknowledgment

This work was supported by the Spanish Ministry of Economy and Competitiveness (project SAF2016-80240) in the part of data acquisition and processing and by the President Program (projects NSH-2737.2018.2) in the part of method development.

References

[1] R. Abiri, S. Borhani, E. W. Sellers, Y. Jiang, and X. Zhao, “A comprehensive review of EEG-based brain–computer interface paradigms,” J. Neural Eng., vol. 16, no. 1, p. 011001, Feb. 2019.

[2] P. Chholak et al., “Visual and kinesthetic modes affect motor imagery classification in untrained subjects,” Sci. Reports 2019 91, vol. 9, no. 1, p. 9838, Jul. 2019.

[3] A. Solodkin, P. Hlustik, E. E. Chen, and S. L. Small, “Fine Modulation in Network Activation during Motor Execution and Motor Imagery,” Cereb. Cortex, vol. 14, no. 11, pp. 1246–1255, Nov. 2004.

[4] T. Hanakawa, M. A. Dimyan, and M. Hallett, “Motor Planning, Imagery, and Execution in the Distributed Motor Network: A Time-Course Study with Functional MRI,” Cereb. Cortex (New York, NY), vol. 18, no. 12, p. 2775, 2008.

[5] A. Guillot, F. Di Rienzo, T. Macintyre, A. Moran, and C. Collet, “Imagining is Not Doing but Involves Specific Motor Commands: A Review of Experimental Data Related to Motor Inhibition.,” Front. Hum. Neurosci., vol. 6, p. 247, 2012.

[6] A. Guillot, C. Collet, V. A. Nguyen, F. Malouin, C. Richards, and J. Doyon, “Brain activity during visual versus kinesthetic imagery: An fMRI study,” Hum. Brain Mapp., vol. 30, no. 7, pp. 2157–2172, Jul. 2009.

[7] F. Lebon, W. D. Byblow, C. Collet, A. Guillot, and C. M. Stinear, “The modulation of motor cortex excitability during motor imagery depends on imagery quality,” Eur. J. Neurosci., vol. 35, no. 2, pp. 323–331, Jan. 2012.

[8] V. Morash, O. Bai, S. Furlani, P. Lin, and M. Hallett, “Classifying EEG signals preceding right hand, left hand, tongue, and right foot movements and motor imageries,” Clin. Neurophysiol., vol. 119, no. 11, pp. 2570–2578, Nov. 2008.

[9] A. Craik, Y. He, and J. L. Contreras-Vidal, “Deep learning for electroencephalogram (EEG) classification tasks: a review,” J. Neural Eng., vol. 16, no. 3, p. 031001, Jun. 2019.

[10] J. R. Wolpaw, D. J. McFarland, G. W. Neat, and C. A. Forneris, “An EEG-based brain-computer interface for cursor control,” Electroencephalogr. Clin. Neurophysiol., vol. 78, no. 3, pp. 252–259, Mar. 1991.

[11] J. R. Wolpaw and D. J. McFarland, “Control of a two-dimensional movement signal by a noninvasive brain-computer interface in humans,” Proc. Natl. Acad. Sci., vol. 101, no. 51, pp. 17849–17854, Dec. 2004.

[12] J. R. Wolpaw and D. J. McFarland, “Multichannel EEG-based brain-computer communication,” Electroencephalogr. Clin. Neurophysiol., vol. 90, no. 6, pp. 444–449, Jun. 1994.

[13] D. J. McFarland, W. A. Sarnacki, and J. R. Wolpaw, “Electroencephalographic (EEG) control of three-dimensional movement,” J. Neural Eng., vol. 7, no. 3, p. 036007, Jun. 2010.

[14] A. R. Murguialday et al., “Brain-Computer Interface for a Prosthetic Hand Using Local Machine Control and Haptic Feedback,” in 2007 IEEE 10th International Conference on Rehabilitation Robotics, 2007, pp. 609–613.

[15] C.-W. Chen, C.-C. K. Lin, and S. J Ming, “Hand Orthosis Controlled Using Brain-computer Interface,” J Med Biol Eng, vol. 29, pp. 234–241, 2008.

[16] A. Ramos-Murguialday et al., “Brain-Machine-Interface in Chronic Stroke Rehabilitation: A Controlled Study,” Ann. Neurol., vol. 74, no. 1, p. 100, 2013.

[17] G. R. Müller-Putz, R. Scherer, G. Pfurtscheller, and R. Rupp, "EEG-based neuroprosthesis control: A step towards clinical practice," Neurosci. Lett., vol. 382, no. 1–2, pp. 169–174, Jul. 2005.

[18] Kai Keng Ang et al., "A clinical study of motor imagery-based brain-computer interface for upper limb robotic rehabilitation," in 2009 Annual International Conference of the IEEE Engineering in Medicine and Biology Society, 2009, pp. 5981–5984.

[19] M. Sarac, E. Koyas, A. Erdogan, M. Cetin, and V. Patoglu, "Brain Computer Interface based robotic rehabilitation with online modification of task speed," in 2013 IEEE 13th International Conference on Rehabilitation Robotics (ICORR), 2013, pp. 1–7.

[20] B. S. Baxter, A. Decker, and B. He, "Noninvasive control of a robotic arm in multiple dimensions using scalp electroencephalogram," in 2013 6th International IEEE/EMBS Conference on Neural Engineering (NER), 2013, pp. 45–47.

[21] K. LaFleur, K. Cassady, A. Doud, K. Shades, E. Rogin, and B. He, "Quadcopter control in three-dimensional space using a noninvasive motor imagery-based brain-computer interface.," J. Neural Eng., vol. 10, no. 4, p. 046003, Aug. 2013.

[22] T. Ono et al., "Brain-computer interface with somatosensory feedback improves functional recovery from severe hemiplegia due to chronic stroke," Front. Neuroeng., vol. 7, p. 19, Jul. 2014.

[23] S. M. Rayegani et al., "Effect of Neurofeedback and Electromyographic-Biofeedback Therapy on Improving Hand Function in Stroke Patients," Top. Stroke Rehabil., vol. 21, no. 2, pp. 137–151, Mar. 2014.

[24] K. K. Ang and C. Guan, "EEG-Based Strategies to Detect Motor Imagery for Control and Rehabilitation," IEEE Trans. Neural Syst. Rehabil. Eng., vol. 25, no. 4, pp. 392–401, Apr. 2017.

[25] L. Bi, X.-A. Fan, and Y. Liu, "EEG-Based Brain-Controlled Mobile Robots: A Survey," IEEE Trans. Human-Machine Syst., vol. 43, no. 2, pp. 161–176, Mar. 2013.

[26] S. Machado, L. F. Almada, and R. N. Annavarapu, "Progress and Prospects in EEG-Based Brain-Computer Interface: Clinical Applications in Neurorehabilitation," J. Rehabil. Robot., vol. 1, no. 1, pp. 28–41, Jun. 2013.

[27] S. Moghimi, A. Kushki, A. Marie Guerguerian, and T. Chau, "A Review of EEG-Based Brain-Computer Interfaces as Access Pathways for Individuals with Severe Disabilities," Assist. Technol., vol. 25, no. 2, pp. 99–110, Apr. 2013.

[28] T. M. Vaughan, J. R. Wolpaw, and E. Donchin, "EEG-based communication: prospects and problems," IEEE Trans. Rehabil. Eng., vol. 4, no. 4, pp. 425–430, 1996.

[29] H.-J. Hwang, S. Kim, S. Choi, and C.-H. Im, "EEG-Based Brain-Computer Interfaces: A Thorough Literature Survey," Int. J. Hum. Comput. Interact., vol. 29, no. 12, pp. 814–826, Dec. 2013.

[30] F. Lotte, M. Congedo, A. Lécuyer, F. Lamarche, and B. Arnaldi, "A review of classification algorithms for EEG-based brain–computer interfaces," J. Neural Eng., vol. 4, no. 2, pp. R1–R13, Jun. 2007.

[31] "Encyclopedia of Biomedical Engineering," 1st ed., vol. 2, New Jersey: John Wiley and Sons, 2006, pp. 1156–1166.

[32] S. Machado et al., "EEG-based brain-computer interfaces: an overview of basic concepts and clinical applications in neurorehabilitation.," Rev. Neurosci., vol. 21, no. 6, pp. 451–68, 2010.

[33] N. Birbaumer et al., "A spelling device for the paralysed," Nature, vol. 398, no. 6725, pp. 297–298, Mar. 1999.

[34] J. Meng, S. Zhang, A. Bekyo, J. Olsoe, B. Baxter, and B. He, "Noninvasive Electroencephalogram Based Control of a Robotic Arm for Reach and Grasp Tasks," Sci. Rep., vol. 6, no. 1, p. 38565, Dec. 2016.

[35] J. J. Daly and J. R. Wolpaw, "Brain–computer interfaces in neurological rehabilitation," Lancet Neurol., vol. 7, no. 11, pp. 1032–1043, Nov. 2008.

[36] N. Birbaumer and L. G. Cohen, "Brain-computer interfaces: communication and restoration of movement in paralysis," J. Physiol., vol. 579, no. 3, pp. 621–636, Mar. 2007.

[37] N. Birbaumer, "Breaking the silence: Brain?computer interfaces (BCI) for communication and motor control," Psychophysiology, vol. 43, no. 6, pp. 517–532, Nov. 2006.

[38] R. Salmelin and R. Hari, "Spatiotemporal characteristics of sensorimotor neuromagnetic rhythms related to thumb movement," Neuroscience, vol. 60, no. 2, pp. 537–550, May 1994.

[39] A. Schnitzler, S. Salenius, R. Salmelin, V. Jousmäki, and R. Hari, "Involvement of Primary Motor Cortex in Motor Imagery: A Neuromagnetic Study," Neuroimage, vol. 6, no. 3, pp. 201–208, Oct. 1997.

[40] L. Kauhanen, P. Rantanen, J. A. Lehtonen, I. Tarnanen, H. Alaranta, and M. Sams, "'Sensorimotor cortical activity of tetraplegics during attempted finger movements' intention and imagery," Biomed. Tech., vol. 49, pp. 59–60, 2004.

[41] H.-L. Halme and L. Parkkonen, "Comparing Features for Classification of MEG Responses to Motor Imagery," PLoS One, vol. 11, no. 12, p. e0168766, 2016.

[42] H.-L. Halme and L. Parkkonen, "Across-subject offline decoding of motor imagery from MEG and EEG," Sci. Rep., vol. 8, no. 1, p. 10087, Dec. 2018.

[43] S. Taulu and R. Hari, "Removal of magnetoencephalographic artifacts with temporal signal-space separation: Demonstration with single-trial auditory-evoked responses," Hum. Brain Mapp., vol. 30, no. 5, pp. 1524–1534, May 2009.

[44] F. F. Tadel, S. Baillet, J. C. Mosher, D. Pantazis, and R. M. Leahy, "Brainstorm: A user-friendly application for MEG/EEG analysis," Comput. Intell. Neurosci., vol. 2011, p. 879716, Apr. 2011.

[45] P. C. Ivanov, A. L. Goldberger, S. Havlin, C.-K. Peng, M. G. Rosenblum, and H. E. Stanley, "Wavelets in medicine and physiology," in Wavelets in Physics, J. C. van den Berg, Ed. Cambridge: Cambridge University Press, 1999, pp. 391–420.

[46] G. Pfurtscheller and F. H. Lopes da Silva, "Event-related EEG/MEG synchronization and desynchronization: basic principles," Clin. Neurophysiol., vol. 110, no. 11, pp. 1842–1857, Nov. 1999.

[47] M. Krams, M. F. S. Rushworth, M.-P. Deiber, R. S. J. Frackowiak, and R. E. Passingham, "The preparation, execution and suppression of copied movements in the human brain," Exp. Brain Res., vol. 120, no. 3, pp. 386–398, May 1998.

[48] J. Duque, L. Labruna, S. Verset, E. Olivier, and R. B. Ivry, "Dissociating the role of prefrontal and premotor cortices in controlling inhibitory mechanisms during motor preparation.," J. Neurosci., vol. 32, no. 3, pp. 806–16, Jan. 2012.

[49] A. Sirigu, J. R. Duhamel, L. Cohen, B. Pillon, B. Dubois, and Y. Agid, "The mental representation of hand movements after parietal cortex damage," Science (80-.)., vol. 273, pp. 1564–1568, 1996.

[50] A. Sirigu et al., "Congruent unilateral impairments for real and imagined hand movements," Neuroreport, vol. 6, pp. 997–1001, 1995.

[51] A. Jeneson and L. R. Squire, "Working memory, long-term memory, and medial temporal lobe function.," Learn. Mem., vol. 19, no. 1, pp. 15–25, Jan. 2012.

[52] J. Schwoebel, C. B. Boronat, and H. Branch Coslett, "The man who executed ``imagined'' movements: evidence for dissociable components of the body schema," Brain Cogn., vol. 50, pp. 1–16, 2002.

[53] J. E. Lisman and O. Jensen, "The θ-γ neural code.," Neuron, vol. 77, no. 6, pp. 1002–16, Mar. 2013.

[54] R. Llinás and U. Ribary, "Coherent 40-Hz oscillation characterizes dream state in humans.," Proc. Natl. Acad. Sci. U. S. A., vol. 90, no. 5, pp. 2078–81, Mar. 1993.

[55] F. Mormann et al., "Phase/amplitude reset and theta-gamma interaction in the human medial temporal lobe during a continuous word recognition memory task," Hippocampus, vol. 15, no. 7, pp. 890–900, Jan. 2005.

[56] R. T. Canolty et al., "High gamma power is phase-locked to theta oscillations in human neocortex.," Science, vol. 313, no. 5793, pp. 1626–8, Sep. 2006.

[57] T. Demiralp et al., "Gamma amplitudes are coupled to theta phase in human EEG during visual perception," Int. J. Psychophysiol., vol. 64, no. 1, pp. 24–30, Apr. 2007.

[58] P. Sauseng et al., "Brain Oscillatory Substrates of Visual Short-Term Memory Capacity," Curr. Biol., vol. 19, no. 21, pp. 1846–1852, Nov. 2009.

[59] N. Axmacher, M. M. Henseler, O. Jensen, I. Weinreich, C. E. Elger, and J. Fell, "Cross-frequency coupling supports multi-item working memory in the human hippocampus.," Proc. Natl. Acad. Sci. U. S. A., vol. 107, no. 7, pp. 3228–33, Feb. 2010.

[60] B. Voytek, R. T. Canolty, A. Shestyuk, N. E. Crone, J. Parvizi, and R. T. Knight, "Shifts in Gamma Phase–Amplitude Coupling Frequency

from Theta to Alpha Over Posterior Cortex During Visual Tasks," Front. Hum. Neurosci., vol. 4, 2010.

[61] E. Maris, M. van Vugt, and M. Kahana, "Spatially distributed patterns of oscillatory coupling between high-frequency amplitudes and low-frequency phases in human iEEG.," Neuroimage, vol. 54, no. 2, pp. 836–50, Jan. 2011.

[62] W. E. Skaggs, B. L. McNaughton, M. A. Wilson, and C. A. Barnes, "Theta phase precession in hippocampal neuronal populations and the compression of temporal sequences," Hippocampus, vol. 6, no. 2, pp. 149–172, Jan. 1996.

[63] K. D. Harris, J. Csicsvari, H. Hirase, G. Dragoi, and G. Buzsáki, "Organization of cell assemblies in the hippocampus," Nature, vol. 424, no. 6948, pp. 552–556, Jul. 2003.

[64] G. Dragoi and G. Buzsáki, "Temporal Encoding of Place Sequences by Hippocampal Cell Assemblies," Neuron, vol. 50, no. 1, pp. 145–157, Apr. 2006.

[65] A. S. Gupta, M. A. A. van der Meer, D. S. Touretzky, and A. D. Redish, "Segmentation of spatial experience by hippocampal θ sequences.," Nat. Neurosci., vol. 15, no. 7, pp. 1032–9, Jun. 2012.

[66] S. L. Bressler, "Large-scale cortical networks and cognition," Brain Res. Rev., vol. 20, no. 3, pp. 288–304, Mar. 1995.

[67] F. Varela, J.-P. Lachaux, E. Rodriguez, and J. Martinerie, "The brainweb: Phase synchronization and large-scale integration," Nat. Rev. Neurosci., vol. 2, no. 4, pp. 229–239, Apr. 2001.

[68] P. Fries, "A mechanism for cognitive dynamics: neuronal communication through neuronal coherence," Trends Cogn. Sci., vol. 9, no. 10, pp. 474–480, Oct. 2005.

[69] M. Siegel, T. H. Donner, and A. K. Engel, "Spectral fingerprints of large-scale neuronal interactions," Nat. Rev. Neurosci., vol. 13, no. 2, pp. 121–134, Feb. 2012.

[70] I. Sturm, S. Lapuschkin, W. Samek, and K.-R. Müller, "Interpretable deep neural networks for single-trial EEG classification," J. Neurosci. Methods, vol. 274, pp. 141–145, Dec. 2016.

[71] S. A. C. Yohanandan, I. Kiral-Kornek, J. Tang, B. S. Mshford, U. Asif, and S. Harrer, "A Robust Low-Cost EEG Motor Imagery-Based Brain-Computer Interface," in 2018 40th Annual International Conference of the IEEE Engineering in Medicine and Biology Society (EMBC), 2018, pp. 5089–5092.

[72] Q. She, B. Hu, Z. Luo, T. Nguyen, and Y. Zhang, "A hierarchical semi-supervised extreme learning machine method for EEG recognition," Med. Biol. Eng. Comput., vol. 57, no. 1, pp. 147–157, Jan. 2019.

Obstacle avoidance for robotic manipulator using mixed reality glasses

A. Evlampev, M. Ostanin
Center for Technologies in Robotics and Mechatronics Components,
Innopolis University,
Innopolis, Russia
a.evlampev@innopolis.ru

A. Evlampev, M. Ostanin
Center for Technologies in Robotics and Mechatronics Components,
Innopolis University,
Innopolis, Russia
m.ostanin@innopolis.ru

***Abstract*—The problem of finding the shortest path for manipulators with obstacle avoidance has many solutions. The paper presents the usage of well-known methods for solving that problem using mixed reality glasses. Glasses contain the Spatial mapping module, presented in the form of an continuously updating mesh. Analyzing space through mixed reality glasses, we have developed algorithms for obtaining the shortest path in the Cartesian and Joint spaces. In the beginning, we implement A* simple algorithm and then realized the improved RRT algorithm. The approaches were verified using Unity, Microsoft HoloLens and 6 DOF robot UR10e.**

***Keywords* —Shortest path; obstacle avoidance; robotic manipulator; path planning; mixed reality; RRT algorithm**;

I. INTRODUCTION

Many real-world tasks, ranging from opening doors and pushing carts to align beams for construction and removing rubble, exhibit workspace constraints. In these circumstances, the robot must not only preserve the task constraint but also detect obstacles, avoid collisions and joint limits throughout a planned motion [1]. Jen-Hao Chen and Kai-Tai Song showed with practical experiments that the 6-DOF robot arm can effectively avoid an obstacle in a constrained environment and complete the original task [2].

Recently a lot of research was done in the field of collaborative robotics [3]. Collaborative robots are working with a human in dynamic unstructured environment. Path-planning becomes an important problem since different obstacles can exist in the workspace of robot and robot path is required to obey workspace constraints. Obstacles are defined as any portion of an object with which contact is undesirable [4].

Detecting obstacles can be done with Mixed reality (MR) glasses. MR is an incorporated of the real world and virtual environment [5]. MR glasses provide a direct connection between 2 worlds. In our research, we use Microsoft HoloLens holographic device. HoloLens has Spatial mapping module that represents the real environment, in other words, obstacles.

In recent years there have been many developments in field MR and Robotic. In 2015, Hoenig et al. [6] defined benefits of using MR in various applications of robotics. Other researches proposed the system for interactive programming of industrial robots based on Mixed Reality

[7]-[9]. We use this kind of systems to set tasks for the robot [7].

The goal task is to find a shortest path with obstacle avoidance. It is a problem of a graph theory and it has a lot of solutions. In our research we used the A* for find path in Cartesian space and Rapidly-exploring Random Tree (RRT) for robot Joint space. RRT is a randomized algorithm that used to perform path-planning with obstacle avoidance [10] [11] that have been widely used in autonomous robotic motion planning. In our research we implemented this algorithm to work with mixed reality and discovered efficiency of this approach. Details of RRT implementation well described in paper Wei K, Ren B [12]. They tested algorithm with UR robot and used Kinect as main sensor.

II. System overview

System consists of 3 main parts: mixed reality glasses, robot controller and robot. We use HoloLens as example of MR glasses. Robot controller based on ROS realised a connection between glasses and robot. MR glasses application has some modules: Interface, Path Planner, Spatial mapping and Robot model. External computer runs ROS Kinetic and controls robot. Controller receives commands from HoloLens, transforms them in required format and sends to robot.

Fig. 1. Mixed reality based robots control system architecture

Application for HoloLens was developed in Unity 2018 with help of Mixed Reality Toolkit for Unity. Integrated part of HoloLens application is the Spatial mapping which geometrically represents a real environment. Core of the system is Path planner module, because it generates path with obstacles avoidance. For connection to ROS we used Ros-Sharp library for UWP (Universal Windows Platform) and Rosbridge.

Interaction script is following: user specifies start and final points. The path that satisfies all constraint is generated between these points. After that user can run virtual simulation or execute path on real robot.

Path planning can be performed in 2 coordinate systems: Cartesian space and Joint space. For each of it, we have implemented own path construction algorithm. To find the shortest path in the Cartesian coordinate system, we used the algorithm A*. We used RRT to find the path in the joints space. Let's consider it in more detail.

III. Shortest path in Cartesian space

Finding the shortest path in Cartesian space is necessary to simplify and speed up the process of manipulator programming since the user only sets the start and final position of the tool. Such a method will be especially useful for pick and place operations. We realize a A* algorithm for finding shortest path in 3D space. It was implemented in Unity/C#.

Before starting the search for a path, it is necessary to tune the system, namely, indicate the model of the manipulator and determine the position of the base operation. Determining the position and orientation of the robot for such systems is described in detail in [13]. Below the pseudo code of the path finding algorithm is presented.

Input: *isObstacleCollider, ControlPoints, CellSize, Workspace Radius*
Output: *Path*
Initialisation :
1: *Path* ← *Ø*
2: *N* ← *WorkspaceRadius * 2 / Cellsize*
Fill environment map
3: **for** *every cell in 3D area* **do**
4: **if** *CurrentCell inside workspace and isObstacleCollider(CurrentCell)* **then**
5: *EnvMap(CurrentCell)* ← 1
6: **else**
7: *EnvMap(CurrentCell)* ← −1
8: **end if**
9: **end for**
Build path
10: **for** *i* = 0 *to size(ControlPoints)* − 1 **do**
11: *LocalPath* ← *Astar*(*ControlPoints*[i], *ControlPoints*(i + 1))
12: *Path* ← *Path* + *LocalPath*
13: **end for**
14: **return** *Path*

For each robot model we know the robot work-space, therefor in the beginning we divided it into small cells. After that each cell checked by Unity tools whether it contains obstacle or not, results collected into boolean array. Finally, A* algorithm runs.

We verified our algorithm based on the Microsoft HoloLens and the UR10e robotic manipulator. By the HoloLens interface we set 2 point in different sides of the wall and build a shortest path. The result of the work is represented by the figure 2.

IV. Shortest path in Joint space

Shortest path in Cartesian space is helpful in the robot programming process, but it has the main drawback - corresponding method cannot detect a collision of robot links with obstacles. Therefore we developed the path planning algorithm which takes to account a robot structure. our algorithm is based on RRT and works in joint space.

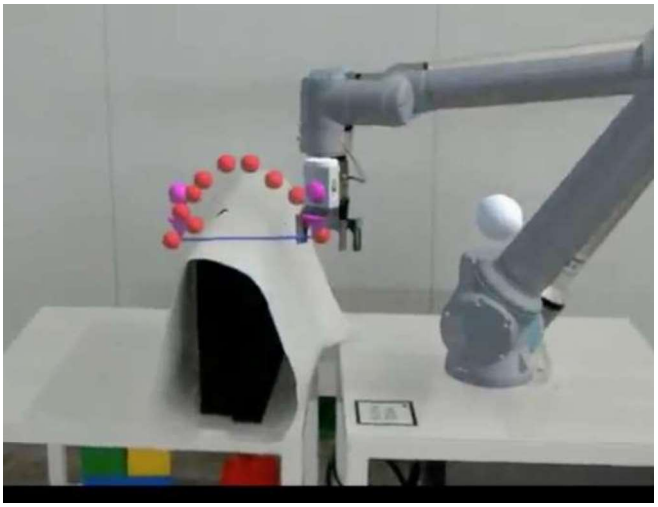

Fig. 2. Path for end-effector created by A* algorithm

The basic idea of the RRT algorithm is to explore space in the form of the tree from the initial state of the manipulator and to generated samples randomly to extend the branches and leaves until the exploring tree covers the target region. Search performed for first 3 joints because a motion space of last 3 joints we can define as a part of third link. RRT search can be performed in high-dimension spaces but our assumption help us to minimize the search space. Start and finish points should be specified with joint angles. Pseudo code of developed algorithm is presented bellow.

Input: *qInit*
Output: *Tree*

1: *initializeTreeRoot(Tree, qInit)*
2: **while** not reached goal **do**
3: *qRand ← RandomState()*
4: *Extend(Tree, qRand)*
5: **end while**

Each new node should be reached without collisions. To verify this, robot motion is simulated each time between old and new configuration. Unity has methods for collision detection. Also, we implemented forward kinematics for the robot to know the position of links.

RRT method should know how far one point from another to find the nearest neighbor. We used Euclidean vector norm to handle this.

After reaching the goal point it is easy to reconstruct the path because each node has a link to its parent. A resulting path generated by RRT contains many redundant nodes. We remove them by applying pruning technique that described in [12].

We verified our algorithm based on the Microsoft HoloLens, Unity Editor and the UR10e robotic manipulator. The results presented in figure 3.

V. Algorithms Comparison

To compare A* based and RRT based path planning algorithms we had run them in simulation. A virtual environment

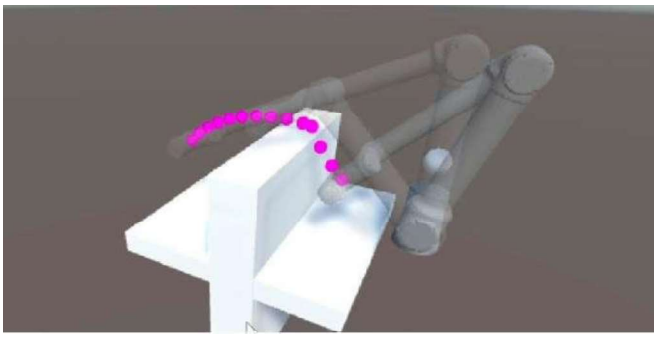

Fig. 3. One of paths generated by RRT algorithm

is a Unity scene that contains room mesh and UR10e model. Robot should avoid contact with mesh. All experiments were run on MacBook Pro 2014 with 2.6 GHz Intel Core i5 CPU, OS Windows. Microsoft Hololens has weaker cpu, 1,04 GHz Intel Atom.

In figure 4 we can see paths generated by both algorithms. Pink balls represent the position of robot end-effector for path generated by RRT and white balls represent A* path. With this configuration of initial and final points, we had run 10 experiments with RRT. Average time of execution was 200ms. It had some variation because the algorithm relies on randomness. The fastest search was done in 83ms with 560 iterations.

Most time-consuming operations for RRT are collision detection and nearest neighbor search (NNS). Generally, NNS search took 10 times more CPU time than collision detection. NNS search is so slow because it just linearly checks all nodes. It can be optimized in further research.

A* algorithm is more stable and in most experiments, it completed in 400ms. As we mentioned before it builds an internal 3D grid to detect obstacles and free spaces. Grid size is 30 and totally it does 27000 calls to check collisions. The path generated by A* tends to be straight in Cartesian space, it should be smoothed.

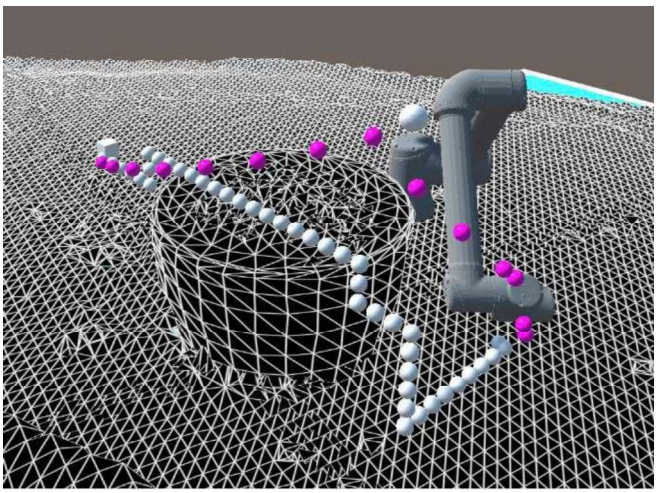

Fig. 4. Both algorithms in virtual environment with mesh

VI. Conclusion

This paper proposes a collision-free path planning for robotic manipulators with using mixed reality and describes 2 methods with different approaches.

Experiments showed that joint space space method based on RRT works faster than method based on A* and also generated trajectory with arbitrary shape. Searching for nearest neighbor is most time-consuming path here. Method works in joint space, however inverse kinematics still needed to provide initial and final state.

Cartesian space method gives path for end-effector without considering robot body so it does not depend on robot structure. But additional effort needed to do inverse kinematics for all points. We used A* algorithm which is deterministic and result always can be repeated in the exact same way.

ACKNOWLEDGMENT

The work presented in this paper was supported by the grant of Russian Science Foundation 17-19-01740.

REFERENCES

[1] M. Stilman, "Global manipulation planning in robot joint space with task constraints," IEEE Transactions on Robotics, vol. 26, no. 3, pp. 576-584, 2010.

[2] J.-H. Chen and K.-T. Song, "Collision-free motion planning for human- robot collaborative safety under cartesian constraint," 2018 IEEE International Conference on Robotics and Automation (ICRA), pp. 1-7, 2018.

[3] L. W. Abdullah Mohamme, Bernard Schmidt, "Active collision avoidance for humanrobot collaboration driven by vision sensors," International Journal of Computer Integrated Manufacturing, vol. 30, no. 9, pp. 970-980, 2017.

[4] A. A. Maciejewski and C. A. Klein, "Obstacle avoidance for kinematically redundant manipulators in dynamically varying environments," International Journal of Robotics Research, vol. 4, no. 3, pp. 109-117, 1985.

[5] P. Milgram and F. Kishino, "A taxonomy of mixed reality visual displays," IEICE Trans. Information Systems, vol. vol. E77-D, no. 12, pp. 1321-1329, 12 1994.

[6] W. Hoenig, C. Milanes, L. Scaria, T. Phan, M. Bolas, and N. Ayanian, "Mixed reality for robotics," pp. 5382-5387, 2015.

[7] M. Ostanin and A. Klimchik, "Interactive robot programing using mixed reality," IFAC-PapersOnLine, vol. 51, pp. 50-55, 01 2018.

[8] J. Guhl, S. Tung, and J. Kruger, "Concept and architecture for programming industrial robots using augmented reality with mobile devices like microsoft hololens," pp. 1-4, 2017.

[9] J. W. S. Chong, S. Ong, A. Y. Nee, and K. Youcef-Youmi, "Robot programming using augmented reality: An interactive method for planning collision-free paths," Robotics and Computer-Integrated Manufacturing, vol. 25, no. 3, pp. 689-701, 2009.

[10] S. M. LaValle, "Rapidly-exploring random trees: A new tool for path planning," 1998.

[11] J. J. LaValle, Steven M.;Kuffner Jr., "Randomized kinodynamic planning," The International Journal of Robotics Research, vol. 20, no. 5, pp. 378-400, 2001.

[12] R. B. Wei K, "A method on dynamic path planning for robotic manipulator autonomous obstacle avoidance based on an improved rrt algorithm," 2018.

[13] M. Ostanin, R. Yagfarov, and A. Klimchik, "Interactive robot programing using mixed reality," ACCEPTED, Manufacturing Modelling, Management and Control - 9th MIM 2019.

Amplitude-phase dynamics of the three-mode cross-coupled generator

Natalia Fadeeva
School of Applied Information Technology and Communication Yuri Gagarin State Technical University of Saratov
Saratov, Russia
n.krakhovskaya@mail.ru

Artem Gulai
School of Electrical and Mechanical Engineering Yuri Gagarin State Technical University of Saratov
Saratov, Russia
gulai.artem@gmail.com

Sergey Astakhov
Quantum Technology Centre Lomonosov Moscow State University
Moscow, Russia
s.v.astakhov@icloud.com

Амплитудно-фазовая динамика трехмодового генератора с перекрестной связью

Фадеева Наталья Сергеевна
Институт прикладных информационных технологий и телекоммуникаций СГТУ имени Гагарина Ю.А.
Саратов, Россия
n.krakhovskaya@mail.ru

Гулай Артем Петрович
Институт электронной техники и машиностроения СГТУ имени Гагарина Ю.А.
Саратов, Россия
gulai.artem@gmail.com

Астахов Сергей Владимирович
Центр квантовых технологий МГУ имени М.В. Ломоносова
Москва, Россия
s.v.astakhov@icloud.com

***Abstract*—The van der Pol generator with two additional oscillators in the feedback loop is investigated. We applied the methods of slowly-varying amplitudes to obtain the shortened system of equations describing the amplitude-phase dynamics of this system. Bifurcation analysis allowed us to determine the mechanisms underlying the transitions between the quasiperiodic modes observed in the complete system. Also, we present here the results of the bifurcation analysis of the transition to chaos.**

Keywords—stability analysis, bifurcations, oscillations, three-mode generator

***Аннотация*—Исследуемая в данной работе модель представляет собой генератор Ван дер Поля с двумя дополнительными колебательными контурами в цепи обратной связи. Методом медленно меняющихся амплитуд получена укороченная система уравнений, описывающих амплитудно-фазовую динамику данной системы. Бифуркационный анализ системы позволил установить механизмы, лежащие в основе переходов между квазипериодическими режимами, наблюдаемыми в полной системе. Описаны особенности перехода к хаосу.**

Ключевые слова—анализ устойчивости, бифуркации, колебания, трехмодовый генератор

I. Введение

Исследование динамических механизмов возникновения нелинейных явлений, характерных для систем, состоящих из автогенераторов и пассивных осцилляторов, играет важную роль в понимании закономерностей, лежащих в основе поведения широкого спектра систем [1]. В том числе, одним из наиболее исследуемых эффектов, является управление хаосом.

Недавно нами была исследована полная система, описывающая генератор Ван дер Поля с двумя дополнительными линейными колебательными контурами, включенными в цепь обратной связи [1]. Было показано, что в данной системе при вариации управляющих параметров могут быть реализованы мультистабильность и переход к хаосу через каскад бифуркаций удвоения двумерных торов. В настоящей работе методом медленно меняющихся амплитуд мы выводим укороченную систему уравнений. Данный подход позволяет исследовать бифуркации устойчивых и седловых двумерных торов в исходной системе. С помощью бифуркационного анализа укороченной модели мы установили механизмы, лежащие в основе качественных переходов между квазипериодическими режимами, наблюдаемыми в полной системе. В частности, в укороченной системе в явном виде показаны бифуркации удвоения периода предельных циклов, а также бифуркации Андронова-Хопфа, соответствующие бифуркациям удвоения торов и бифуркациям Неймарка-Сакера полной системы уравнений.

II. Исследуемая система

A. Модель

Исследуемая в данной работе динамическая система представляет собой генератор Ван дер Поля, в цепь обратной связи которого внесены два дополнительных колебательных контура. Данная модель может быть реализована в виде электронной схемы, представленной на Рис.1. После перехода к нормированным фазовым переменным и нормированному времени, методом медленно меняющихся амплитуд для данной схемы получим систему дифференциальных уравнений (1).

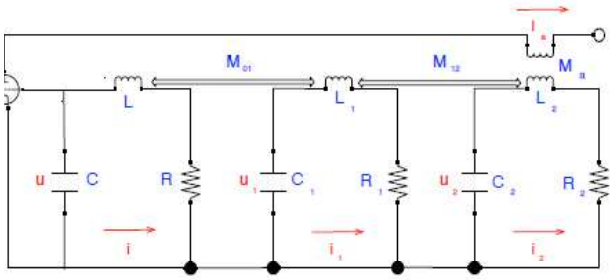

Рис.1. Электронная схема исследуемого генератора. Здесь символами i обозначены токи в колебательных контурах, u – напряжения на конденсаторах C. L - индуктивность цепей, M – взаимоиндукция, R – омические сопротивления.

$$
\begin{cases}
\dot{\phi} = \frac{p^2 m}{2w} - yp^2\left[\frac{\alpha r}{2 r_1}\sin(-\phi) - \frac{m}{2w r_1}r\cos(-\phi) + \frac{\alpha r_2}{2 r_1}\sin(-\delta) - \frac{m}{2w r_1}r_2\cos(-\delta) - \frac{\lambda r}{2 r_1}\sin(-\phi) + \frac{\beta r^3}{8 r_1}\sin(-\phi)\right] - (1-\gamma^2 p^2)\frac{m}{2w} \\
\quad + yp\left(\frac{\alpha r_1}{2 r}\sin(\phi) - \frac{pm r_1}{2w r}\cos(\phi)\right) - \gamma^2 p^2\left[\frac{m r_1}{2w r}r\cos(\phi-\delta) - \frac{\alpha r_2}{2 r}\sin(\phi-\delta)\right] \\
\dot{\delta} = \frac{p^2 m}{2w} - yp^2\left[\frac{\alpha r}{2 r_1}\sin(-\phi) - \frac{m}{2w r_1}r\cos(-\phi) + \frac{\alpha r_2}{2 r_1}\sin(-\delta) - \frac{m}{2w r_1}r_2\cos(-\delta) - \frac{\lambda r}{2 r_1}\sin(-\phi) + \frac{\beta r^3}{8 r_1}\sin(-\phi)\right] \\
\quad + \left(\gamma^2 p^2 - 1\right)\left[\frac{m}{2w} + \frac{\lambda r}{2 r_1}\sin(\delta-\phi) - \frac{\beta r^3}{8 r_1}\sin(\delta-\phi)\right] - yp\left(-\frac{\alpha r_2}{2 r_2}\sin(\delta) + \frac{pm r_2}{2w r_2}\cos(\delta)\right) \\
\quad - \gamma^2 p^2\left(-\frac{\alpha r}{2 r_2}\sin(\delta-\phi) + \frac{m r}{2w r_2}\cos(\delta-\phi)\right) \\
\dot{r} = \left(\gamma^2 p^2 - 1\right)\left(\frac{\alpha}{2}r\right) - yp\left(\frac{\alpha}{2 r_2}r_1\cos(\phi) + \frac{pm}{2w}r_1\sin(\phi)\right) - \gamma^2 p^2\left[\frac{\alpha r_2}{2}\cos(\phi-\delta) + \frac{m}{2w}r_2\sin(\phi-\delta) - \frac{\lambda}{2}r + \frac{\beta}{8}r^3\right] \\
\dot{r}_1 = -\frac{p\alpha}{2}r_1 - yp^2\left[\frac{\alpha}{2}r\cos(-\phi) + \frac{m}{2w}r\sin(-\phi) + \frac{\alpha}{2}r_2\cos(-\delta) + \frac{m}{2w}r_2\sin(-\delta) - \frac{\lambda}{2}r\cos(-\phi) + \frac{\beta}{8}r^3\cos(-\phi)\right] \\
\dot{r}_2 = \left(1-\gamma^2 p^2\right)\left[-\frac{\alpha}{2}r_2 + \frac{\lambda}{2}r\cos(\delta-\phi) - \frac{\beta}{8}r^3\cos(\delta-\phi)\right] + yp\left(-\frac{\alpha}{2}\cos(\delta) - \frac{pm}{2w}r_2\sin(\delta)\right) \\
\quad + \gamma^2 p^2\left[-\frac{\alpha}{2}r\cos(\delta-\phi) - \frac{m}{2w}r\sin(\delta-\phi)\right]
\end{cases}
$$

Б. Динамические режимы в системе

Рассмотрим бифуркационную диаграмму, представленную на Рис.2.

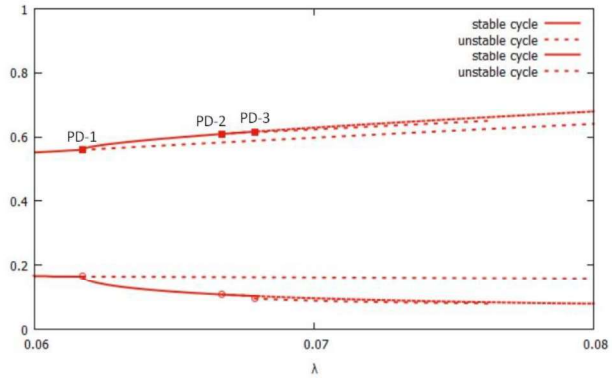

Рис.2. Однопараметрическая диаграмма исследуемой системы. Устойчивый цикл претерпевает последовательность бифуркаций удвоения периода (PD) при значении параметра p=2. Сплошными линиями обозначены устойчивые циклы, пунктирными – неустойчивые.

При малом значении параметра λ в системе существует устойчивый предельный цикл. При увеличении параметра λ цикл претерпевает последовательность бифуркаций удвоения периода, что ведет к возникновению хаотических колебаний. Подобная картина наблюдалась с каскадом бифуркаций удвоения двумерных торов в полной системе, завершающуюся формированием хаотического аттрактора [2].

При этом данная система демонстрирует развитую мультистабильность (Рис.3). В ее фазовом пространстве

могут сосуществовать устойчивые предельные циклы и даже хаотические аттракторы.

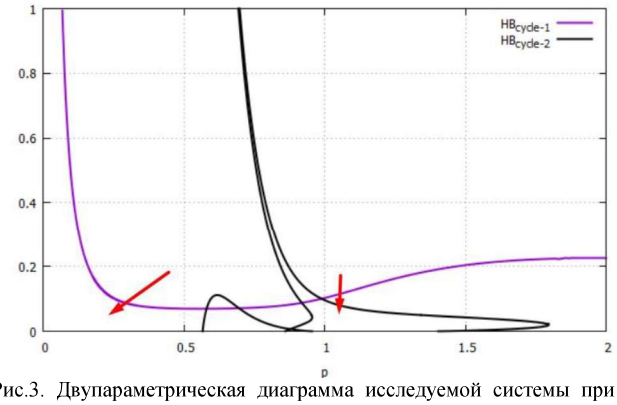

Рис.3. Двупараметрическая диаграмма исследуемой системы при значении параметра λ=0.05. Области, отмеченные указателями, отвечают областям существования устойчивого состояния равновесия. HB – линии бифуркаций Андронова-Хофа первого устойчивого состояния равновесия и второго.

III. Заключение

Сравнивая результаты бифуркационного анализа системы укороченных уравнений трехмодового осциллятора с перекрестной обратной связью с результатами, полученными ранее для полной системы, можно сделать следующие выводы.

В исследованной укороченной системе уравнений были выявлены бифуркации Андронова-Хопфа и бифуркации удвоения предельных циклов, соответствующие бифуркациям Неймарка-Сакера и бифуркациям удвоения торов полной системы.

Благодарности

Работа выполнена при поддержке гранта Российского научного фонда № 17-72-30003.

Ссылки

[1] Anishchenko V., Astakhov V., Neiman A., Vadivasova T., Schimansky-Geier L. Nonlinear Dynamics of Chaotic and Stochastic Systems. Tutorial and Modern Developments. Second Edition. - Berlin: Springer Publ., 2007. - 446 p.

[2] Н.С. Краховская, С.В. Астахов, “Квазипериодические колебания и эффект мультистабильности в модели центрального генератора ритма,” Динамика сложных сетей и их применение в интеллектуальной робототехнике. Сборник материалов I Международной школы-конференции молодых ученых, Саратов, p. 108, 2017.

Applying UML modeling techniques on the domain of product lifecycle management

Alena V.Fedotova
Robotics and complex automation faculty
Bauman Moscow State Technical University
Moscow, Russia
afedotova.bmstu@gmail.com

Применение концептуальных методов моделирования UML в области управления жизненным циклом изделия

Федотова Алена Валериевна
Факультет робототехники и комплексной автоматизации
Московский Государственный Технический Университет им.Н.Э.Баумана
Москва, Россия
afedotova.bmstu@gmail.com

***Abstract*—The problem of ontological modeling with applying UML modeling techniques on the domain of product lifecycle management is considered in the mainstream of the machine-building corporation engineering. Simple ontologies are developed on the basis of nesting and overlapping relationships. A set of ontologies for a typical enterprise of the corporation has been built, which ensures the coordination of various enterprises activities. The main classes and subclasses of the enterprise ontology, diagrams of the composite structure of the lifecycle, products and enterprise (UML diagrams) are presented.**

Keywords—enterprise engineering, ontology, product lifecycle management, UML modeling.

***Аннотация*—Рассмотрена задача онтологического моделирования с применением концептуальных методов моделирования UML в области управления жизненным циклом изделия в русле инжиниринга машиностроительной корпорации. Разработаны простые онтологии на основе отношений вложенности и перекрытия. Построен ряд онтологий типового предприятия корпорации, обеспечивающий согласование работ различных предприятий. Представлены основные классы и подклассы онтологии предприятия, диаграммы составной структуры жизненного цикла, изделия и предприятия (UML диаграммы).**

Ключевые слова — инжиниринг предприятий, онтология, управление жизненным циклом изделия, UML моделирование.

I. Введение

В работе главное внимание уделено интеллектуализации методов инжиниринга предприятия с помощью онтологического моделирования в интересах разработки эффективных методов и технологий управления жизненным циклом продукции, а в результате, создании PLM-систем нового поколения – интегрированных интеллектуальных систем IIPLM [1,2]. В работе построена система онтологий типового машиностроительного предприятия – корпорации. Эта задача является крупномасштабной, междисциплинарной и весьма важной для различных отраслей высокотехнологичного производства.

Для построения системы онтологий использованы концептуальные методы моделирования UML: Диаграмма составной структуры (Composite Structure Diagram), диаграммы классов (Static Structure Diagram), а также язык описания OWL.

II. Онтология машиностроительного предприятия

Машиностроительная корпорация – это единая система конструкторских бюро, опытных и серийных заводов, обеспечивающая весь жизненный цикл изделия (его разработку, производство, испытания, послепродажное обслуживание, ремонт, модернизацию и утилизацию). Онтологическое моделирование предметной области и задач необходимо для повышения эффективности совместной работы различных предприятий в рамках единой корпорации.

Общая онтология машиностроительного предприятия построена в формате .owl и представлена на рис. 4. Её более подробная визуализация имеется на ресурсе [3]. Файл в формате .owl и сопутствующие файлы можно получить по ссылке [4].

A. Создание онтологии

Машиностроительные онтологии предназначены для управления корпоративной информацией об организации и организационных структурах, необходимых для поддержания жизненного цикла продукции. Здесь онтология включает универсальное ядро многократного использования, которое может быть расширено или специализировано для использования в конкретных ситуациях [5, 6]. Базовыми понятиями являются: организация, изделие, жизненный цикл (ЖЦ), персонал (распределённый человеческий капитал), процесс (распределенные бизнес процессы) [7]. Каждый из перечисленных классов подразделяется на подклассы.

Б. Диаграмма составной структуры жизненного цикла, изделия и предприятия

Диаграмма составной структуры (Composite Structure Diagram) – статическая структурная диаграмма, которая демонстрирует внутреннюю структуру классов и, по возможности, взаимодействие элементов (частей) внутренней структуры класса. Они удобны при моделировании шаблонов проектирования. Диаграммы композитной структуры могут использоваться совместно с диаграммами классов.

Основные диаграммы классов предприятия представлены на рис.1-3.

На рис. 1 показана диаграмма составной структуры ЖЦ. Она делится на стадии: проектирование, производство и эксплуатация. Каждая из них состоит из этапов.

Рис. 1. Диаграмма составной структуры ЖЦ.

Изделие делится на отсеки, которые состоят из сборочных единиц, а сборочные единицы – из деталей. Каждый из классов имеет свои атрибуты (рис. 2).

Рис. 2. Диаграмма составной структуры изделия.

Также была составлена диаграмма составной структуры предприятия (рис. 3в). Предприятие имеет множество подразделений, в которых работают сотрудники. Каждый класс также имеет ряд атрибутов. Например, для класса “Предприятие” это – название (тип string) и тип (тип string).

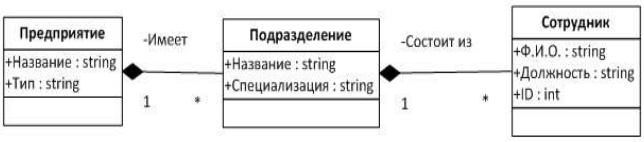

Рис. 3. Диаграмма составной структуры предприятия.

В. Основные классы и подклассы онтологии предприятия

После изучения деятельности и структуры предприятия были выделены сначала простые онтологии, затем составлены аксиомы, которые описаны правилами на языке дескриптивной логики. В результате разработки простых онтологий были составлены онтологии: ЖЦ изделия, Оргструктура, Процессы, Персонал.

Класс «ЖЦ» содержит следующие подклассы: изделие; заказчик; объем и стоимость производства; техническое задание; техническое предложение;

концептуальный проект; эскизный проект; технический проект; рабочий проект; технологическое оборудование; организационно-техническая документация; опытный образец; серийный экземпляр; технологическое оснащение; оснастка; эксплуатация; техническое обслуживание; капитальный ремонт; утилизация.

Класс «Оргструктура предприятия» подразделяется на следующие подклассы: архив, бухгалтерия (Б), дирекция заказчика(ДЗ), опытное конструкторское бюро (ОКБ), отдел главного технолога (ОГТ), отдел по составлению договоров, отдел технического контроля(ОТК), отдел экономики и труда (ОЭТ), правовой департамент (ПД), профком, производственно-техническое управление (ПТУ), секретариат, служба качества(СК), управление финансами (УФ), управление охраны труда (УОТ), центр информационных технологий (ЦИТ), эксплуатационно-ремонтный отдел (ЭРО), цеха.

Класс «Персонал» включает подклассы: генеральный директор, заместитель генерального директора, ведущий конструктор, главный конструктор, инженер-конструктор, инженер-технолог, техник-конструктор, техник-технолог, начальник отдела, начальник цеха, заместитель начальника отдела, заместитель начальника цеха, начальник бригады, контролер, программист, системный администратор, обслуживающий персонал, экономист, рабочий.

Класс «Процессы» подразделяется на подклассы: изготовление деталей, написание программы испытаний, написание техпроцесса, настройка программного обеспечения (ПО), обучение сотрудников, проведение испытаний, проверка конструкторской документации (КД), разработка КД, расчет на прочность, расчеты по материальным, трудовым и финансовым затратам, ремонтные работы, сборка изделий, создание извещений, согласование КД, сопровождение КД, составление отчета о работе бригады, цеха и отдела, составление плана работ, составление технического задания(ТЗ), учет КД.

Г. Примеры правил на основе простых онтологий

В виде простых онтологий [8] вышеописанные классы и отношения между ними записываются следующим образом: Изготовление деталей $\subseteq$ Процессы, Написание программы испытаний $\subseteq$ Процессы, Написание техпроцесса $\subseteq$ Процессы, Настройка ПО $\subseteq$ Процессы, Архив $\subseteq$ Оргструктура, Бухгалтерия $\subseteq$ Оргструктура, Оргструктура $\subseteq$ Предприятие, ЖЦ изделия $\subseteq$ Предприятие, Персонал $\subseteq$ Предприятие, Процессы $\subseteq$ Предприятие, Написание технологического процесса Инженер – технолог $\neq\varnothing$, Написание технологического процесса $\cap$ Техник – технолог $\neq\varnothing$, Изготовление деталей $\cap$ Рабочий $\neq\varnothing$ и др.

Далее на основе написанных правил строятся онтологии: ЖЦ изделия, Оргструктура предприятия, Процессы, Персонал в системе моделирования онтологий Protégé. Затем полученные онтологии с помощью правил и ограничений объединяются в единую онтологию машиностроительного предприятия (рис. 4). Со всеми правилами и ограничениями можно ознакомиться на ресурсе [4].

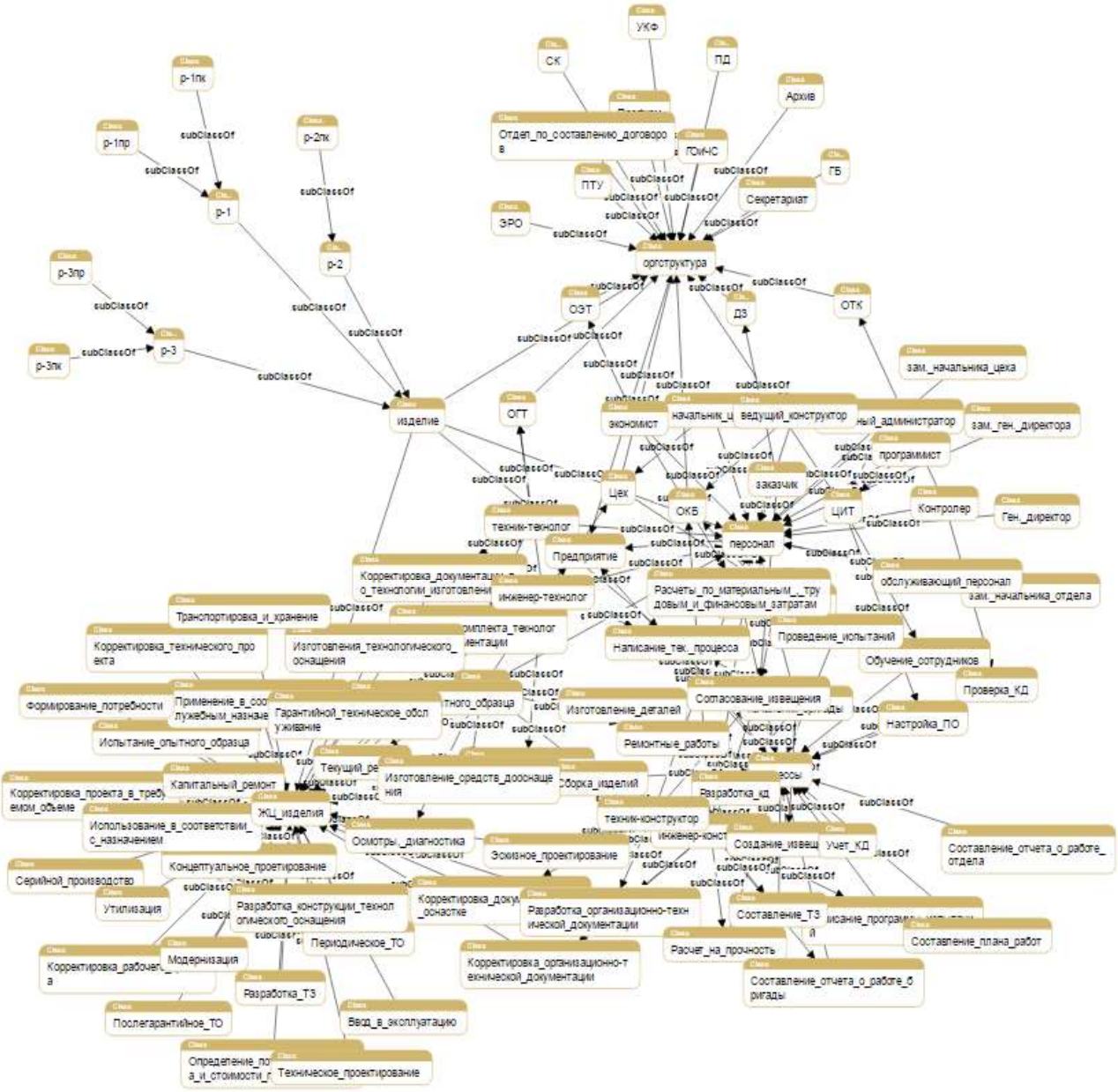

Рис. 4. Диаграмма составной структуры предприятия.

III. Заключение

В настоящей статье рассмотрена задача онтологического моделирования с применением концептуальных методов моделирования UML в области управления жизненным циклом изделия в русле инжиниринга машиностроительной корпорации. Пример онтологического инжиниринга предприятия дает возможность повышения эффективности управления жизненным циклом продукции за счет систематизации знаний предприятия и о предприятии в виде системы взаимосвязанных онтологий, а также проведения автоматизированного анализа общего состояния предприятия. Данная работа представляет собой первый шаг на пути создания полномасштабной интеллектуальной системы управления жизненным циклом сложных технических систем.

Благодарности

Работа выполнена при финансовой поддержке DAAD и Минобрнауки шифр 2.13444.2019/13.2.

Ссылки

[1] A.V. Fedotova, I.T. Davydenko, A. Pförtner, “Design Intelligent Lifecycle Management Systems Based on Applying of Semantic Technologies”, in Proceedings of the First Inter-national Scientific Conference “Intelligent Information Technologies for Industry” (IITI’16, Sochi, Russia, May 16-21), Springer International Publishing Switzerland, vol. 1, 2016, pp. 251–260.

[2] A.B. Petrochenkov, Bochkarev S.V., M.V. Ovsyannikov, S.A. Bukhanov, “Construction of an Ontological Model of the Life Cycle of Electrotechnical Equipment”, in Russian Electrical Engineering, vol.86, Issue 6, 2015, pp. 320-325.

[3] Enterprise Ontology [Электронный ресурс]. – Режим доступа: http://app.ontodia.org/diagram?sharedDigram=d7h87avp22ehbcionnp9p61pcn. – Дата доступа: 20.06.2019.

[4] Enterprise Ontology [Электронный ресурс]. – Режим доступа: https://archive.org/details/EnterpriseOntology – Дата доступа: 20.06.2019.

[5] S.M. Kovalev, V.B. Tarassov, M.N. Koroleva et al., "Towards Intelligent Measurement in Railcar On-Line Diagnostics: From Measurement Ontologies to Hybrid Information Gran-ulation System", in: Proceedings of the 2nd International Scientific Conference «Intelligent Information Technologies for Industry» (IITI'17, Varna, September 14-16, 2017). Ed. by A.Abraham, S.Kovalev, V.Tarassov et al. Advances in Intelligent Systems and Computing, vol.679, Cham, Switzerland: Springer International Publishing, 2018, pp.169-181.

[6] V.V. Kuzenov, S.V. Ryzhkov, "Numerical modeling of laser target compression in an external magnetic field", in Mathematical Models and Computer Simulations, vol. 10, 2018, pp. 255–264.

[7] A.V. Fedotova, V.V. Tabakov, M.V. Ovsyannikov, J. Bruening: "Ontological Modeling for Industrial Enterprise Engineering", in Proceedings of the Third International Scientific Conference "Intelligent Information Technologies for Industry" (IITI'18, Sochi, Russia, September 17-21). A. Abraham et al. (Eds.), IITI 2018, AISC 874, Springer International Publishing Switzerland, 2019, pp. 182–189.

[8] Г.С. Плесневич "Анализ простых онтологий" в Интеллектуальные системы. Коллективная монография под ред. В.М. Курейчика. Москва: Физматлит, 2010, сс. 206-221.

Ann in car antilock braking systems modeling

Alexey Fedin
Volgograd State Technical University
Volgograd, Russia
falexey2005@yandex.ru

Yaroslav Kalinin
Volgograd State Technical University
Volgograd, Russia
jkv83@mail.ru

Evgeniy Marchuk
Volgograd State Technical University
Volgograd, Russia
marocci@bk.ru

***Abstract*— this article presents the rationale for using ANN in car antilock braking system models.**

Keywords — ANN, wavelet, control, identification, ABS, car, braking

I. INTRODUCTION

The existing descriptions of the braking process of land transport wheels use the formula of dependence of the coefficient of longitudinal traction φ with the road on the coefficient of longitudinal slippage S. The greatest efficiency of the anti-lock braking system (ABS) is achieved if the argument S corresponds to the maximum of the function $\varphi = f(s)$. Compliance is achieved through the control action by applying or reducing the braking force to the wheel of the vehicle [1].

II. MATHEMATICAL MODELING OF ABS

Currently, several representations of this dependence are used, which necessarily include tabular values of the coefficients for different types of road surface in addition to the value of the longitudinal slip coefficient changing over time. This process has a pronounced nonlinear dependence. As examples, we indicate two typical formulas in which the nonlinear functional dependence can be represented either by Weierstrass – using polynomials (A. A. Revin's formula):

$$\varphi = \frac{f_0 * S}{a * S^2 + b * S + c}, \quad (1)$$

where the coefficients a, b, c, f_0 are tabular values defined for each particular type of road surface, or Fourier – using harmonic functions (Pacejka's formula):

$$\mu(S) = C_1 * \sin x * (C_2 * tan^{-1}(C_3 * S_x - C_4 * (C_3 * S_x - tan^{-1}(C_3 * S_x))) \quad (2)$$

where the coefficients $C_1 \dots C_4$ are also tabular values defined for a particular type of road surface [2].

In the case of creating a strict mathematical model of the braking process of the car wheel in real time (for all four wheels) the task is much more complicated since the need for rapid and accurate integration and differentiation (the model must be ahead and predict the course of the real process) is added to the need to accurately determine and account for the characteristics of the road surface and synchronize data processing [3]. The solution of such problems becomes possible either with graphics processors using or with ANN using, which also allow simultaneous processing of parallel information flows in real time. As suitable methods for approximating nonlinear processes, we indicate the possibility of describing a nonlinear function by means of fuzzy logic (Kosko's theorem) [4], or by using artificial neural networks (Hornik's and Cybenko's theorems) [5], [6]. Let us consider in more detail the artificial neural network (ANN) as a universal approximator of a function of several variables.

III. ANN IN CAR ABS MODELING

When modeling the ABS of the car using ANN two current tasks are indicated: identification of the road surface and control of the braking process. Here, ANN will be on the one hand a nonlinear model of the process that provides the development of the corresponding control action and on the other hand act as a cotrolling system that adapts to changing environmental conditions [7]. The choice of the sigmoid network "multilayer perceptron" seems adequate. The use of wavelets is seen as the main principle of road surface identification. The use of ANN as a control system ensures the stability of the ACS, which is also an undeniable advantage of ANN in comparison with classical regulators.

IV. SUMMARY

A new approach to the simulation of vehicle braking ABS using ANN will significantly simplify and improve the reliability of the automated control system in comparison with the classical methods using numerical methods in the integration and control PID type regulators.

ACKNOWLEDGMENT

The project was implemented with the support of RFBR (19-48-340016)

REFERENCES

[1] K. Reif, “Brakes, Brake Control and Driver Assistance Systems”. BOSCH professional automotive information. / KonradReif. - Springer, 2014. - 275 p.

[2] H.B. Pacejka, I.Y. Besselink, “Magic Formula Tyre Model with Transient Properties”. Supplement to Vehicle System Dynamics, 1997, vol. 27, pp. 234–249.

[3] E.A. Marchuk, “The development of recommendations for optimization of car wheel movement computer simulation in real-time braking mode”, MSc Thesis, Volgograd, VSTU, 2019, pp. 17-19

[4] Kosko, “Fuzzy Systems as Universal Approximators” / Bart Kosko // IEEE Trans. on Computers. - 1994. – Vol.43. - №11.- p. 1153-1162

[5] K. Hornik, “Multilayer Feedforward Networks are Universal Approximators” , Neural Networks, Vol. 2, pp. 359-366, 1989.

[6] G. Cybenko, “Approximation by Superpositions of a Sigmoidal Function”, Math. ControlSignalsSystems (1989) 2; pp. 303-314.

[7] S. Osowski, “Sieci neuronowe do przetwarzania informacji”, Warszawa, 2000, 344 p.

Multilayer perceptron reveals functional connectivity structrure in thalamo-cortical brain network

Nikita S. Frolov
Neuroscience and Cognitive Technology Laboratory, Center for Technologies in Robotics and Mechatronics Components
Innopolis University
Innopolis, Russia
0000-0002-2788-1907

Alexander E. Hramov
Neuroscience and Cognitive Technology Laboratory, Center for Technologies in Robotics and Mechatronics Components
Innopolis University
Innopolis, Russia
0000-0003-2787-2530

***Abstract*— Artificial neural networks (ANNs) are known to be a powerful tool for big data analysis. They are widely used in computer science, nonlinear dynamics, robotics, and neuroscience for solving tasks of classification, forecasting, pattern recognition, etc. In neuroscience ANNs allow recognizing specific forms of brain activity from multichannel electro- (EEG) or magnetoencephalographic (MEG) data and, therefore, widely used as a computational core in various brain-computer interfaces. Another challenging problem is the analysis of connectivity structures in big multivariate data. In neuroscience restoring the functional brain network using multichannel EEG/MEG signals uncovers mechanisms of neuronal interaction during various physiological or cognitive processes. In this report we use recent advances in the area of machine learning known as feed-forward artificial neuronal network to formulate a method for detecting functional dependence in unidirectionally and bidirectionally coupled systems without additional information about them. We apply our method for the first time to reveal functional connectivity structure in the thalamo-cortical network of epileptic brain based on a rodent electrocorticography (ECoG) data set.**

Keywords—functional connectivity, synchronization, artificial neural network, EEG, brain

I. INTRODUCTION

Brain, being one of the most complex systems in nature, exhibits well-pronounced network properties on both anatomical and functional levels [1]. The latter implies the existence of functional dependence between the states of remote brain areas, which is believed to provide mechanisms for neuronal. communication and information transfer within a distributed brain network. According to the recent theories [2-4], neural interaction between distant brain regions through emergent functional connectivity structures determines normal brain functioning, including cognitive, motor-related activity etc.

At the same time, abnormalities in functional brain networks stand behind various types of brain disorders like epilepsy, Parkinson’s and Alzheimer’s diseases, brain tumors etc. [5,6].

Thus, restoration of functional connectivity between brain areas is a crucial approach for brain functioning diagnostics in modern neuroscience [7].

In nonlinear dynamics, the presence of a functional relation between the dynamics of coupled chaotic systems is known as a particular type of synchronous behavior called generalized synchronization (GS) [8]. This relation may be very complicated, and its explicit form cannot be found in most cases. The definition of the GS regime in the case of unidirectional coupling accepted hitherto is the presence of a functional relation

$$\mathbf{y}(t) = \mathbf{F}[\mathbf{x}(t)] \quad (1)$$

between the drive x(t) and response y(t) oscillator states. This definition has been generalized on mutual coupling systems as:

$$\mathbf{F}[\mathbf{x}(t), \mathbf{y}(t)] = 0 \quad (2)$$

The concept of generalized synchronization may be essentially applied in neuroscience for data-driven functional connectivity restoration based on multichannel EEG/MEG data. However, it has not been systematically used in this context so far. In this context, machine learning, which has already become a useful tool in nonlinear dynamics and

neuroscience [9-11], to infer functional links in terms of GS. In this study, we use our feed-forward artificial neural network (FANN) to analyze functional connectivity in small thalamo-cortical network during the onset of epileptic seizure in WAG/Rij rats with genetic predisposition to absence epilepsy. Such seizures manifest as a hyper synchronization of brain activity in thalamo-cortical network, thus they are extremely suitable for demonstration of FANN approach applied for experimental data. We show the emergence of functional interdependence between cortical layers and thalamic nuclei after epileptic discharge onset.

II. Method

ANN is known to be a biologically inspired computational system, whose main purpose is to fit unknown and usually complex relationship between input and output data32. Since functional connectivity in coupled systems implies the existence of functional dependence between them, ANN seems to be an essential tool in this context.

Considering two coupled processes, whose dynamics is represented by multivariate signals $\mathbf{x}(t)$ and $\mathbf{y}(t)$, functional connectivity implies $\mathbf{y}(t) = \mathbf{F}[\mathbf{x}(t)]$. Since from a mathematical point of view ANN defines a function f: $\mathbf{x} \rightarrow \mathbf{y}$, one may use ANN to build a model of the unknown relation $\mathbf{F}[\bullet]$ and predict the $\mathbf{y}$ state based on the $\mathbf{x}$ state. Thus, if a true functional relation $\mathbf{y}(t) = \mathbf{F}[\mathbf{x}(t)]$ exists, ANN is able to approximate it and give a precise prediction $\mathbf{y}'(t)$ of the $\mathbf{y}(t)$ state based on $\mathbf{x}(t)$. On the contrary, if functional dependence is not established, ANN fails to learn it and therefore is not able to predict the $\mathbf{y}$-state accurately enough. Summarizing the above, the criterion for functional connectivity inference is equality of predicted and actual values of y processes: $\mathbf{y}'(t) = \mathbf{y}(t)$.

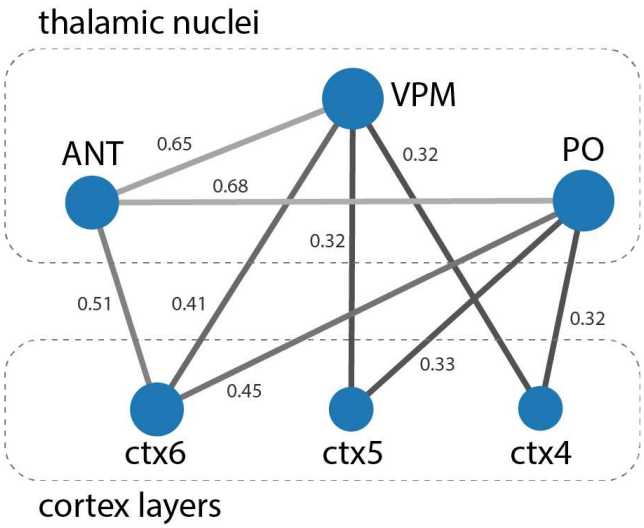

Fig. 1. For all presented plots, t is time, sec, with audio command placed in 0 and marked with red line. (a) Raw EEG signal corresponding to the movement; (b) wavelet surface of corresponding EEG signal; (c) averaged mu-rhythm energy W_μ; (d) recurrence plot of considering time series; (e) matched EMG signal; (f) RQA metrics.

We use the traditional FFANN architecture – multilayer perceptron – to build an ANN-model of functional dependence $\mathbf{F}[\bullet]$ between interacting systems. MLP consists of 2 hidden layers, each containing 10 softmax units. The number of both inputs and outputs is determined by the embedding dimensions of coupled systems. Output artificial neurons have a linear activation function. To build a proper ANN-model of relationship between $\mathbf{x}$ and $\mathbf{y}$ we normalize the data in range [0;1], shuffle it and keep 50% of the dataset to train ANN and the other 50% to validate prediction accuracy. To train the network we use a popular and efficient Adam optimizer with learning rate 0.001 implemented in Keras API33. To quantify the degree of functional dependence establishment we use a metric called R^2-score (coefficient of determination).

III. Results

We analyzed a multichannel set of ECoG recordings taken from Wistar Albino Glaxo from Rijswijk (WAG/Rij) rats – a genetic animal model giving rise to spontaneous absence seizures [12]. In the experiments 6-month-old WAG/Rij rats were chronically implanted with stainless steel electrodes in layer 4 to 6 of the somatosensory cortex (ctx4–6), as well as in the (i) posterior (PO), (ii) ventral-postero-medial (VPM), and (iii) anterior thalamic nucleus (ANT), respectively. Two weeks after surgery, ECoG signals were recorded from these structures in freely moving animals. Signals were filtered by a band pass filter with cut-off points at 1(HP) and 100(LP) and a 50 Hz Notch filter and digitized by WINDAQ-recordingsystem (DATAQ-Instruments Inc., Akron, OH, USA) with a constant sampling rate of 2048 Hz. Experiments were carried out in accordance with the Ethical Committee on Animal Experimentation of University of Münster.

Based on the considered approach for functional connectivity diagnostics in experimental time series identified on a pair of ECoG channels, we have reconstructed the structure of functional links in the thalamo-cortical network during background (3 s prior SWD onset) and pathological (1 s after SWD onset) activity. To reveal the functional network, we considered changes in $R2$-score in pathological activity with respect to background via t-test for related samples with Bonferroni correction (critical α-level = 0.003). One can see that the pathological activity shown in Fig. 1 is accompanied primarily by the appearance of functional links between between the thalamic nuclei and cortical layers (ctx4-PO, ctx4-VPM, ctx5-PO, ctx5-VPM, ctx6-PO, ctx6-VPM, ctx6-ANT). Notable, intra-thalamic functional connectivity intensifies as well (ANT-PO, ANT-VPM).

Conclusion

In conclusion, we have proposed a machine learning based method for detecting functional connectivity in unidirectionally and mutually coupled systems without additional information about analyzed systems.

Acknowledgment

This work has been supported by Russian Science Foundation (Grant 17-72-30003).

References

[1] O. Sporns, "Structure and function of complex brain networks," Dialogues in clinical neuroscience, vol. 15, no. 3, p. 247, 2013.

[2] Schnitzler and J. Gross, "Normal and pathological oscillatory communication in the brain," Nature reviews neuroscience, vol. 6, no. 4, p. 285, 2005.

[3] P. Fries, "Rhythms for cognition: communication through coherence," Neuron, vol. 88, no. 1, pp. 220-235, 2015.

[4] V.A. Maksimenko, A.E. Runnova, N.S. Frolov, V.V. Makarov, V. Nedaivozov, A.A. Koronovskii, A. Pisarchik and A.E. Hramov,

"Multiscale neural connectivity during human sensory processing in the brain," Physical Review E, vol. 97, no. 5, p.052405, 2018.

[5] Lüttjohann and G. van Luijtelaar, "Dynamics of networks during absence seizure's on-and offset in rodents and man," Frontiers in physiology, vol. 6, p. 16, 2015.

[6] C.J. Stam, "Modern network science of neurological disorders," Nature Reviews Neuroscience, vol. 15, no. 10, p. 683, 2014.

[7] Bastos and J.-M. Schoffelen, "A tutorial review of functional connectivity analysis methods and their interpretational pitfalls," Frontiers in systems neuroscience, vol. 9, p. 175, 2016.

[8] N.F. Rulkov, M.M. Sushchik, L.S. Tsimring, and H.D.I. Abarbanel, "Generalized synchronization of chaos in directionally coupled chaotic systems," Physical Review E, vol. 51, no. 2, p. 980, 1995.

[9] J. Pathak, B. Hunt, M. Girvan, Z. Lu and E Ott, "Model-free prediction of large spatiotemporally chaotic systems from data: A reservoir computing approach," Physical review letters, vol. 120, no. 2, p. 024102, 2018.

[10] J. Pathak, Z. Lu, B.R. Hunt, M. Girvan and E. Ott, "Using machine learning to replicate chaotic attractors and calculate Lyapunov exponents from data," Chaos: An Interdisciplinary Journal of Nonlinear Science, vol. 27, no. 12, p.121102, 2017.

[11] A.E. Hramov, N.S. Frolov, V.A. Maksimenko, V.V. Makarov, A.A. Koronovskii, J. Garcia-Prieto, L.F. Antón-Toro, F. Maestú and A.N. Pisarchik, "Artificial neural network detects human uncertainty," Chaos: An Interdisciplinary Journal of Nonlinear Science, vol. 28, no. 3, p. 033607, 2018.

[12] A.M.L. Coenen and E.L.J.M. van Luijtelaar, "Genetic animal models for absence epilepsy: a review of the WAG/Rij strain of rats," Behavior genetics, vol. 33, no. 6, pp. 635-655, 2003.

Mathematical modeling of changes in geometric parameters of pneumatic muscle

Ilya D. Galushko
Department of Automatic Systems of Power Plants
Samara National Research University
Samara, Russian Federation
neeva2804@gmail.com

Georgy M. Makaryants:
Department of Automatic Systems of Power Plants
Samara National Research University
Samara, Russian Federation
georgy.makaryants@gmail.com

Salimzhan A. Gafurov
Center for Technologies of Robotics and Mechatronics Components: Innopolis University
Innopolis, Russian Federation
s.gafurov@innopolis.ru

***Abstract*—Today, this type of actuators as pneumatic muscles has wide application. Pneumatic muscle is a one-way actuator and has such advantages as the developed force, as well as speed. Pneumatic muscles, compared to pneumatic cylinders, have a non-linear structure that needs to be correctly identified. In this paper, we study the dynamic processes of pressure change in the working cavity of a pneumatic muscle in order to build a mathematical model, which can later be used to develop control systems, where the main actuator is pneumatic muscle. As well as in order to accurately describe and predict the geometric parameters of pneumatic muscles on pressure of compressed air in the working cavity.**

I. INTRODUCTION

To ensure the quality of the automatic control system (ACS), the main executive element of which is such a type of actuator as a pneumatic muscle, a mathematical model of its dynamic processes is necessary. In previous studies [1,2], static characteristics were identified in the form of functional dependencies describing the relative contraction, as well as the diametric expansion of the pneumatic muscle, depending on the pressure applied to the working cavity. In work [3], non-linear characteristics of pneumatic muscles were determined by the method of parametric excitation; in works [4,5], characteristics of pneumatic muscles were studied in an opposite pair configuration, such as stiffness, as well as fundamental dependencies defined for a pneumatic muscle with two degrees of freedom are considered in [6]. However, these studies do not reveal the full mathematical model that describes the dynamics of contraction of the pneumatic muscle, taking into account such parameters as the value of the developed force, as well as the movement depending on the input pressure [7]. In order to obtain a complete linearized mathematical model of pneumatic muscles, it is necessary to know the force developed by the drive, which depends directly on the magnitude of the working pressure, as well as on the cross-sectional area. Knowing the force being developed, it is possible to make a transition to a mathematical model that describes the dynamic process of contraction of a pneumatic muscle rather fully [7, 8]. Thus, to develop a complete mathematical model of the drive, it is necessary to accurately describe the dynamic process of pressure change in its working cavity.

II. ASSUMPTIONS AND METHODS

In studies [6, 9, 10], dynamic processes of pressure change in the working cavities of pneumatic muscles were presented at an input pressure of 0.6 MPa. In this work, it is assumed that the dynamic process of pressure change in the working cavity of the considered actuator can be described by a typical first-order aperiodic link, the temporary implementation of which has the form (1), and the transfer function W is (2):

$$P(t) = k\left[1 - e^{-\frac{t}{T}}\right], \quad (1)$$

$$W(s) = \frac{k}{Ts + 1}, \quad (2)$$

where k-gain and T-time response of the transition process, s-Laplace operator and t - time. It is also assumed in the work that the gain coefficient k and the transient time constant T are functions of the drive output pressure. Then the proposed mathematical model will have the form, as shown in Fig.1

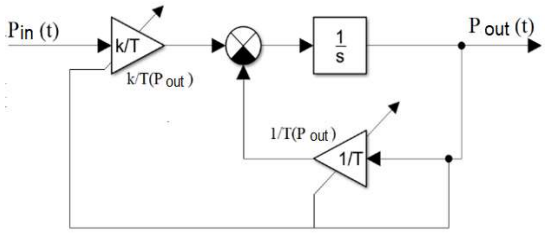

Fig. 1. Type of proposed mathematical model

III. EXPERIMENTAL SETUP

To identify the dynamic processes of pressure change in the working cavity of the pneumatic muscle, an experimental setup was made, shown in Fig. 2.

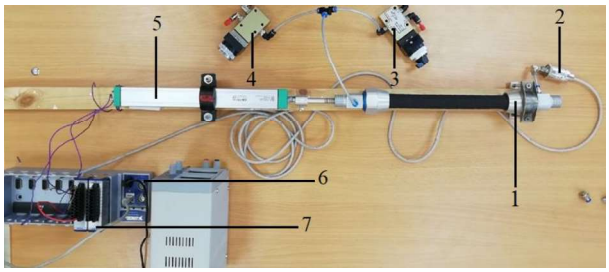

Fig. 2. Experimental setup

Compressed air enters the working cavity of the pneumatic muscle (1) through pneumatic directional valves (3) and (4). Pneumatic muscle movements are measured using a displacement sensor (5). Data from the pressure sensor (2) went to the NI 9203 input module (7) located on the NI DAQ FPGA (6) connected to a PC via an Ethernet cable. The processing and recording of data on the dynamic processes of pressure change in the working cavity of the pneumatic muscle (1) was performed using the NI LabView software package.

The pneumatic circuit of the experimental setup, presented in Figure 3. It includes a compressed air source (1), a preparation unit, which consists of filter (2), a pressure reducing valve (3) and a pressure gauge (4), a pressure reducing valve (5), a pressure gauge (6), two pneumatic directional valves (7) and (8), a pneumatic pressure test muscle PM and pressure sensor recording the dynamic process of pressure change in the working cavity of the pneumatic muscle. Pressure reducing valves (3) and (5) are adjusted so that a constant pressure drop of 0.1 MPa in the interval from 0 to 0.6 MPa is created in the pressure line of the pneumatic muscle PM, that is, the first experiment is carried out with the pressure reducing valves (3) and (5) installed 0.1 MPa, in the second experiment, the valves are adjusted to a pressure of 0.1 and 0.2 MPa, respectively, etc. Thus, six independent experiments were carried out, as a result of which, by means of a pressure sensor, transient changes of pressure were recorded in the working cavity of the investigated pneumatic muscle PM.

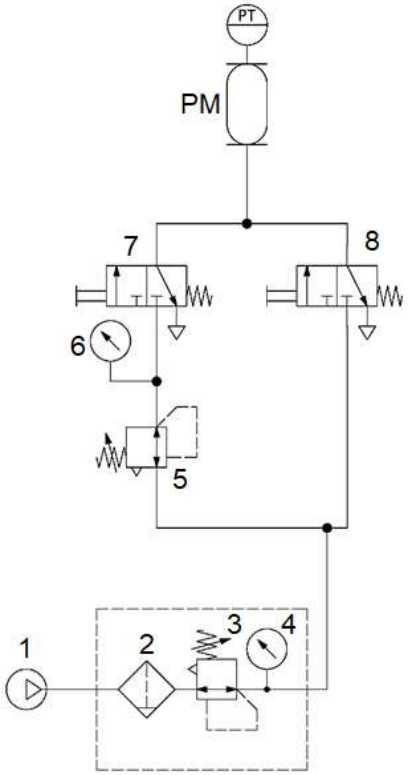

Fig. 3. Pneumatic circuit

IV. THE APPROXIMATION OF THE EXPERIMENTAL DATA

As mentioned earlier, in this paper it is assumed that the obtained dynamic processes of pressure change in the working cavity of a pneumatic muscle can be approximated by a function of the time realization of an aperiodic type element of the first order. Initially, for each of the six transient processes obtained experimentally, the gain coefficient k and the time response T were determined, after which the functions of the time realization for the aperiodic type element of the first order were derived, after which the results of the approximation were verified. The verification of the obtained mathematical dependences of the output pressure on time with the corresponding average approximation errors A is presented in Fig. 4.

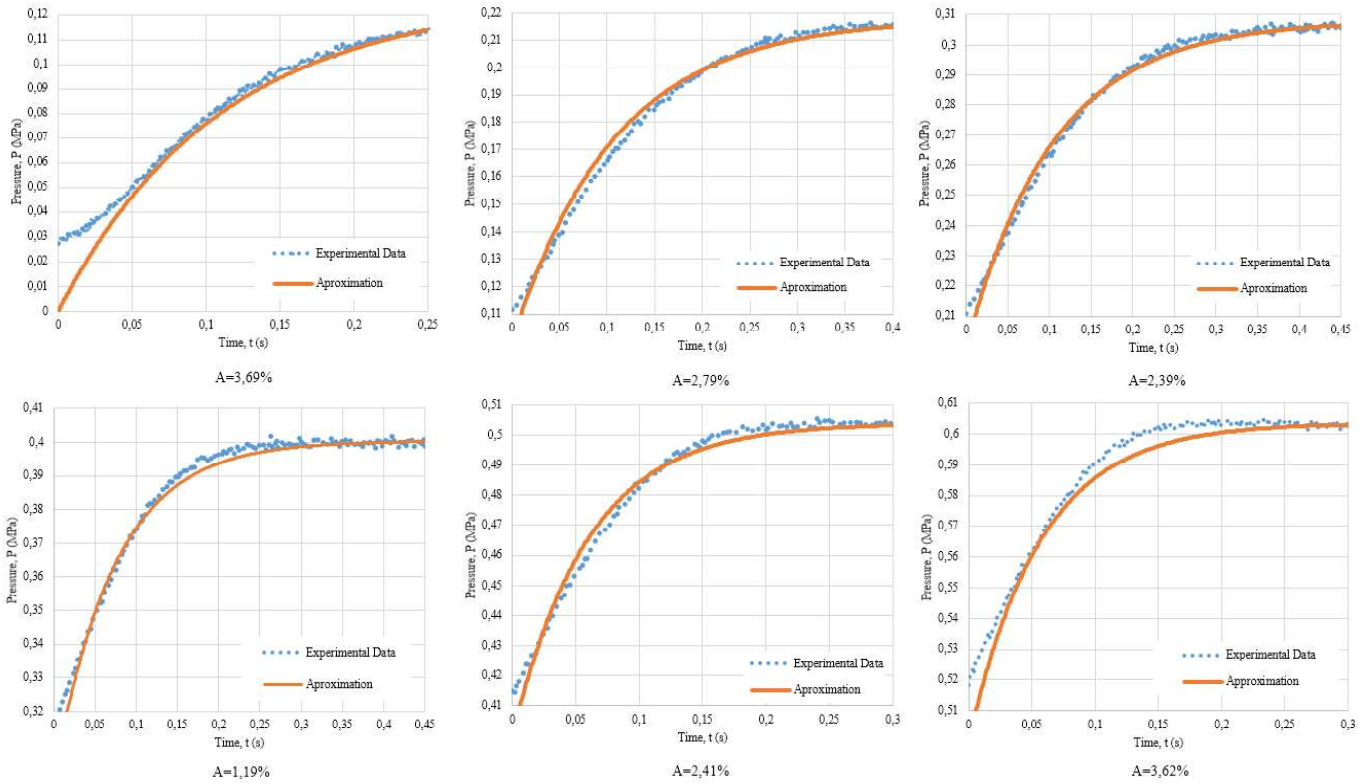

Fig. 4. The results of the approximation of experimental data

As a result of the approximation produced, the transfer functions for each interval were obtained and are summarized in Table 1.

TABLE I. THE RESULTING TRANSFER FUNCTIONS

Interval	Transfer Function
0…0,1 MPa	$W(s) = \frac{1,27}{0,110s + 1}$
0,1…0,2 MPa	$W(s) = \frac{1,18}{0,109s + 1}$
0,2…0,3 MPa	$W(s) = \frac{1,08}{0,106s + 1}$
0,3…0,4 MPa	$W(s) = \frac{1,005}{0,074s + 1}$
0,4…0,5 MPa	$W(s) = \frac{1,039}{0,064s + 1}$
0,5…0,6 MPa	$W(s) = \frac{1,036}{0,057s + 1}$

As can be seen from the obtained transfer functions, the gain k and the time response T really have a functional dependence on the output pressure of the pneumatic muscle. Moreover, the function describing the dependence of the time response T on the output pressure is monotonously decreasing.

V. MATHEMATICAL MODELING

The development of the mathematical model was made in the software package Matlab Simulink. The resulting mathematical model is presented in Fig. 5.

The Lookup Table blocks indicated the values of the functional dependences of the ratio of the gain factor k to the time response T, as well as the time response T itself, on the output pressure Pout, as shown in Fig. 6.

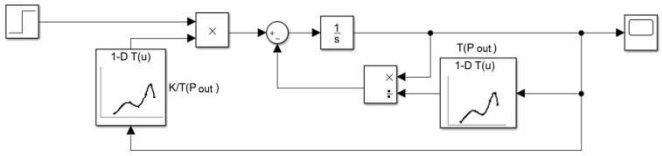

Fig. 5. Mathematical model of pneumatic muscle in Matlab Simulink

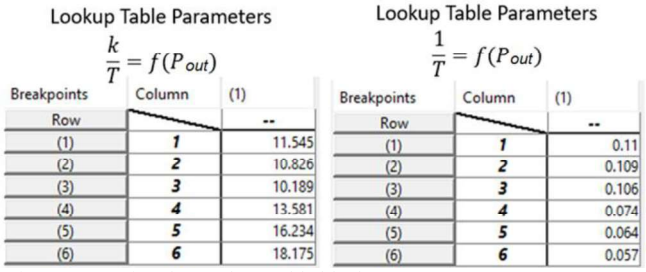

Fig. 6. Setting the Lookup Table blocks

VI. VERIFICATION OF THE MATHEMATICAL MODEL

After building a mathematical model, its verification was performed. The simulation results were compared with the data obtained experimentally. It should be noted that the simulation results are different from the results of the approximation of the dynamic processes of pressure change in the working cavity of the pneumatic muscle, which is associated with setting the cubic algorithm of the interpolation and extrapolation dependencies of the ratio of the gain k to the time response T as well as the time response T itself in the Lookup Table blocks. on the output pressure Pout. The verification results for each interval with the corresponding average errors A are presented in Fig. 7.

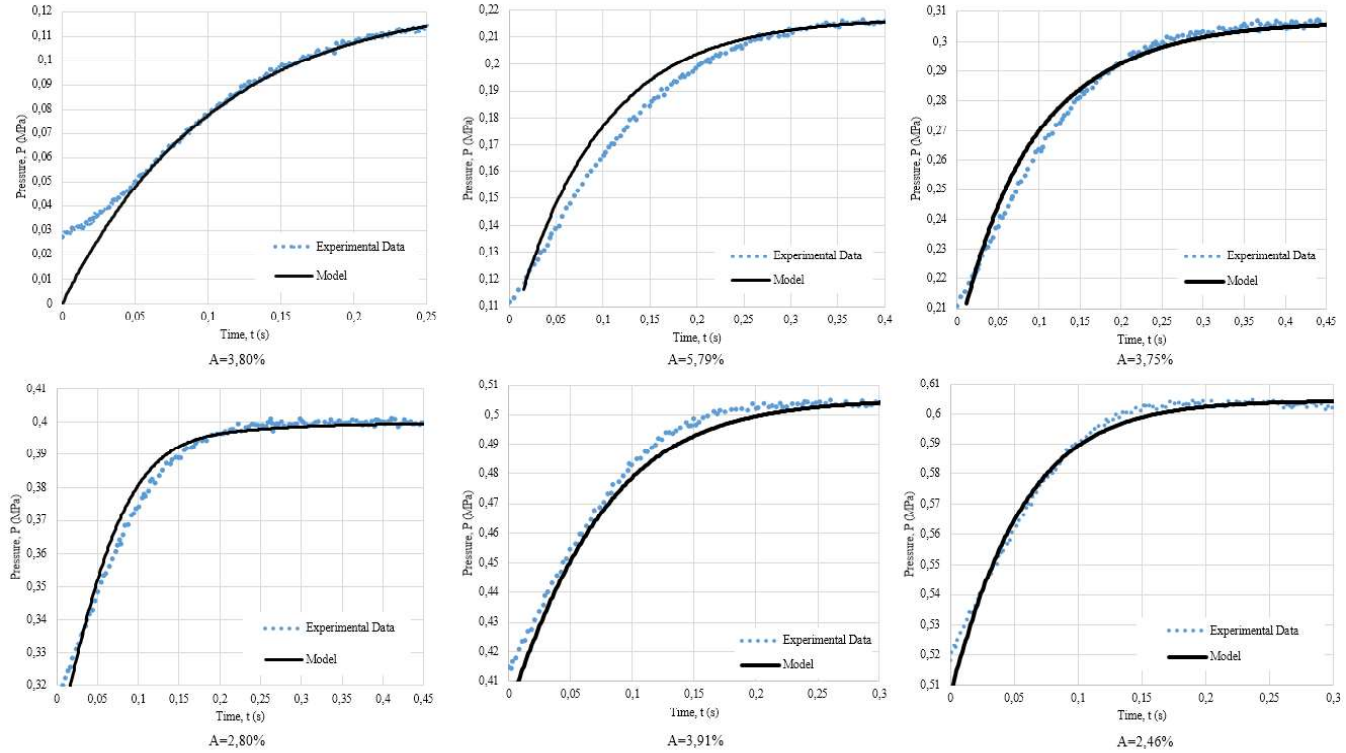

Fig. 7. Verification of the resulting mathematical mode

Thus, the obtained mathematical model provides acceptable accuracy, but this applies only to those cases in which a small signal is sent to the input of the mathematical model, corresponding to the pressure in the working cavity of the pneumatic muscle of about 0.1 MPa. When a mathematical model is applied to the input, the signal corresponds to the maximum pressure in the working cavity of the pneumatic muscle, there is a significant discrepancy between the simulation data and the real data obtained experimentally. In this case, the average error A was 37.5%. Verification data are presented in Fig. 8.

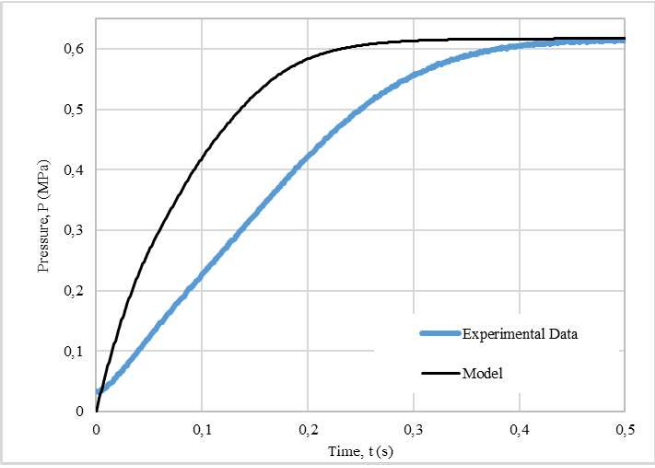

Fig. 8. Pneumatic circuit

VII. CONCLUSION

Mathematical model of the pneumatic muscle was developed. The average error in the simulation was 5.79%. The resulting mathematical model of the pneumatic muscle ensures acceptable accuracy only when a low-level pressure is applied to the input.

When applying a high-level pressure to the input, there is a large deviation of the simulation data from the real data obtained experimentally, which is presumably associated with the manifestation of the integrating properties of the object of study. The average error was 37.5%.

To build a complete mathematical model that provides sufficient accuracy for any input pressure in the range from 0 to 0.6 MPa, it is necessary to have a large experimental data base, as well as more sophisticated modeling approaches that will provide a variable structure of the transfer function of the pneumatic muscle as object modeling.

ACKNOWLEDGMENT

This work was supported by the Ministry of Education and Science of the Russian Federation (Grant # 1.7914.2017/8.9). This research has been also supported by Russian Ministry of Education and Science within the Federal Target Program grant (research grant ID RFMEFI60917X0100).

REFERENCES

[1] Galushko I.D., Gafurov S.A., Salmina V.A., etc. Experimental test bench for investigation of flow control around unmanned underwater robot // IFAC-PapersOnLine. – 2018. V. 51. № 30. - pp. 604-609.

[2] Galushko I.D., Gafurov S.A., Salmina V.A., etc. Approach of Flow Control Around Unmanned Underwater Robot // IFAC-PapersOnLine. - 2018. V. 51. № 30. — pp. 452-457.

[3] Bhaben K., Dwivedy S. K. Nonlinear dynamics of a parametrically excited pneumatic artificial muscle (PAM) actuator with simultaneous resonance condition // Mechanism and Machine Theory. – 2019. V. 135. – pp. 281-297.

[4] Chan C.Y., Chong S.H., Tan M.H., Tang T.F., Sato K. Characterization of pneumatic artificial muscle system in an opposing

pair configuration // Journal of Telecommunication, Electronic and Computer Engineering. - 2016. – V.8. - pp. 73-77.

[5] Chen Y.C., Chiang C.J., Neural network fuzzy sliding mode control of pneumatic muscle actuators // Engineering Applications of Artificial Intelligence. - 2017.V. 65. - pp. 68-86.

[6] Biro I., Cveticanin L., Nemeth J., Sarosi J. Dynamic modeling of a pneumatic muscle actuator with two-direction motion // Mechanism and Machine Theory. - 2015.V. 85. – pp. 25-34

[7] Doumit M. D., Pardoel S. Dynamic contraction behaviour of pneumatic artificial muscle // Mechanical Systems and Signal Processing. - 2017.V. 91. - pp. 93-110.

[8] Wang S., Sato K. High-precision motion control of a stage with pneumatic artificial muscles//Precision Engineering. – 2016. V. 43. - pp. 448-461.

[9] Guerra Tsuzuki M.D.S., Horikawa O., Scaff W. Pneumatic Artificial Muscle Optimal Control with Simulated Annealing // IFAC-PapersOnLine. – 2018.V. 51. № 30. — pp. 333-338.

[10] Leephakpreeda T., Wickramatunge K.C. Empirical modeling of dynamic behaviors of pneumatic artificial muscle actuators // ISA Transactions.- 2013. V. 52. № 6. - pp. 825-834.

Application of directed connectivity measures for identifying the evolution of the interaction structure in WAG/Rij rats brain at absence epilepsy

A.A. Grishchenko
Saratov State University
Russia, Saratov
vili_von@mail.ru

T.M. Medvedeva
Saratov State University
Institute of higher nervous activity and neurophysiology of RAS
Russia, Moscow

C.M. van Rijn
Donders Centre for Cognition, Radboud University
Nijmegen, Netherlands

M.V.Sysoeva
Saratov State Technical University
Saratov Branch of Kotel'nokov's Institute of Radioengineering and Electronics of RAS
Russia, Saratov

I.V. Sysoev
Saratov State University
Saratov Branch of Kotel'nokov's Institute of Radioengineering and Electronics of RAS
Russia, Saratov

***Abstract*—In this article EEG from 5 rats were analyzed by three different methods: the linear Granger causality method, the nonlinear adapted Granger causality method, entropy transfer method.**

Keywords—EEG, WAG Rij rats, coupling estimation, Granger causality, transfer entropy

I. INTRODUCTION

Absence epilepsy is a widespread form of epilepsy among children and adolescents (up to 50% of cases [1]). The main manifestations of this epilepsy are partial or complete loss of consciousness for a short time - the duration of the attack is, as a rule, about 5-10 s [2,3].

II. EXPERIMENTAL DATA

The 130-minute records of intracranial EEG (signals of local field potentials) from 5 male WAG Rij rats were analyzed, with 28 seizures (L = 28) in each animal. All discharges were spontaneous.

Each animal was considered individually. The length of the selected seizures was at least 6 s, and it was taken five seconds before and after the seizure. Each seizure was divided into six intervals, at which the measures were calculated. For convenience, the seizure onset is taken as 0 and the seizure termination is taken as T. Then, the studied intervals, selected in accordance with the results of the work [4], can be designated as follows:

1) [−5; −3] s before the seizure onset (background activity);

2) [−2; 0] s before the seizure onset (preictal activity); at this time, as a rule, changes in connectivity leading to seizure initiation are detected already [5,6];

3) [0; 2] s after the seizure onset (decoupling); this interval corresponds mainly to the moment of decoupling found in [4];

4) [2; 4] s after the seizure onset (seizure maintenance);

5) [T-2; T] s before the seizure termination;

6) [T; T + 2] s after the seizure termination (postictal stage).

III. COUPLING ANALYSIS METHODS

Data was analyzed by three different methods:

- the linear Granger causality method [7],
- the nonlinear adapted Granger causality method [8],
- entropy transfer method [9].

To test the results for significance, surrogate time series for each animal were built separately by permuting realizations [10]. 27· 28 = 756 pairs.

It is combinations of all possible episodes for a channel pairs, except when they are from one episode. This number of surrogates allows us to get a high confidence level of 99.87% (p-value is equal to 0.0013), which is important because there is multiple testing.

IV. Comparison of Three Coupling Measures

Consider the results of the coupling estimations in the same animal. In figure 1, the calculation results of all three coupling measures are shown: red color shows the transfer entropy, blue color shows linear Granger causality, gray color shows nonlinear Granger causality. The effect of which brain area on which ones was evaluated is shown in the title above each subplot. The studied intervals are shown along the X-axis. The total number of seizures for which the conclusion about coupling on this interval were significant is shown on the Y-axis on the left. The same number, but as a percentage of the total seizure number (28 for all cases considered) is shown on the right.

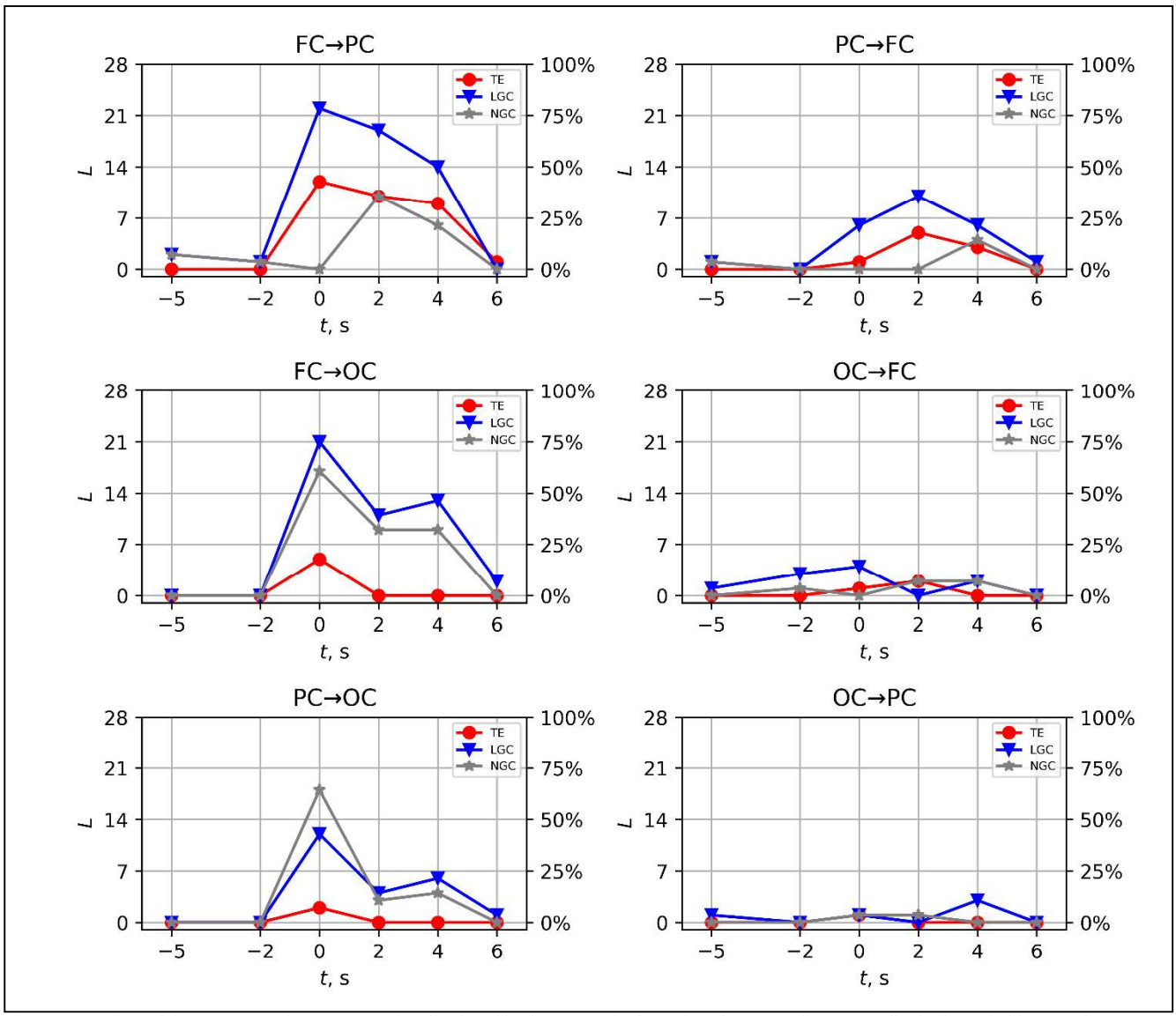

Fig. 1 Comparison of three measures for rat No. 27, for all pairs of leads; entropy is shown in red, Granger linear causality is shown in blue, non-linear Granger causality is shown in gray.

Acknowledgment

The reported study was funded by Russian Science Foundation, project No 19-12-00201.

References

[1] Megiddo I., Colson A., Chisholm D., Dua T., Nandi A., Laxminarayan R. Health and economic benefits of public financing of epilepsy treatment in India: An agent-based simulation model. Epilepsia. 2016. V. 57. No. 3. P. 464–474. doi: 10.1111/epi.13294

[2] Holmes G.L., McKeever M., Adamson M. Absence seizures in children: Clinical and electroencephalographic features. Annals of Neurology. 1987. V. 21. No. 3. P. 268–273.

[3] Bosnyakova D., Gabova A., Zharikova A., Gnezditski V., Kuznetsova G., van Luijtelaar G. Some peculiarities of time-frequency dynamics of spike-wave discharges in humans and rats. Clinical Neurophysiology. 2007. V. 118. No. 8. P. 1736–1743.

[4] Sysoeva M.V., Lüttjohann A., van Luijtelaar G., Sysoev I.V. Dynamics of directional coupling underlying spike-wave discharges. Neuroscience. 2016. V. 314. P. 75–89.

[5] Lüttjohann A., van Luijtelaar G. The dynamics of cortico-thalamo-cortical interactions at the transition from pre-ictal to ictal LFPs in absence epilepsy. Neurobiology of Disease. 2012. V. 47. P.47–60.

[6] Sysoeva M.V., Sitnikova E., Sysoev I.V., Bezruchko B.P., van Luijtelaar G. Application of adaptive nonlinear Granger causality: Disclosing network changes before and after absence seizure onset in a genetic rat model. J. Neurosci Methods. 2014. V. 226. P. 33–41.

[7] Clive WJ Granger. Investigating causal relations by econometric models and cross-spectral methods. Econometrica: Journal of the Econometric Society. 1969. P. 424–438.

[8] Maksim V. Kornilov, Tatiana M. Medvedeva, Boris P. Bezruchko, Ilya V. Sysoev. Choosing the optimal model parameters for Granger causality in application to time series with main timescale. Chaos, Solitons & Fractals, 82. 2016. 11-21.

[9] Schreiber, T. Measuring Information Transfer. Physical Review Letters 85. 2000. 461–464.

[10] Theiler J., Eubank S., Longtin A., Galdrikian B., Farmer J.D. Testing for nonlinearity in time series: the method of surrogate data. Physica D. 1992. V. 58. P. 77–94.

Features of brain activity in children during cognitive tasks of different types

Vadim Grubov
Neuroscience and Cognitive Technology Lab, Center for Technologies in Robotics and Mechatronics Components
Innopolis University
Innopolis, Russia
v.grubov@innopolis.ru

Vladimir Maksimenko
Neuroscience and Cognitive Technology Lab, Center for Technologies in Robotics and Mechatronics Components
Innopolis University
Innopolis, Russia
v.maksimenko@innopolis.ru

Vladimir Makarov
Neuroscience and Cognitive Technology Lab, Center for Technologies in Robotics and Mechatronics Components
Innopolis University
Innopolis, Russia
vladmak404@gmail.com

***Abstract* — EEG signals of children were recorded during cognitive load of various types in accordance with proposed design of experiment. Obtained EEG data were analyzed with methods of time-frequency analysis and statistics. Differences in time-frequency structure of EEG signals and ratio between frequency ranges was shown for background activity and two types of cognitive activity.**

Keywords — cognitive task, children, electroencephalogram, continuous wavelet transform, frequency ranges, attention state

I. INTRODUCTION

One of the common ways to estimate subject's intelligence is to measure the mental speed, i.e. the speed of information processing [1]. For this purpose, elementary cognitive tasks (ECTs) are used and the reaction time to perform them is studied [2, 3]. One of the most popular types of ECT is so-called paper-and-pencil test due to simplicity of its implementation and subsequent data analysis [2]. Elementary ECTs are based on the Hick paradigm [4]: there is a linear correlation between the amount of processed information and the reaction time of the subject. The reaction time in its turn can be estimated with Sternberg memory scanning task [5], according to which the reaction time increases linearly with the memory set size. A similar idea underlies the letter matching paradigm [6] which associates reaction time with the speed of lexical access. Thus, there is a direct correlation between mental speed and mental abilities (intelligence), i.e., more intelligent individuals exhibit lower reaction time and therefore higher speed of information processing [7].

Another very promising approach to firmly extract cognitive components is the use of information about electrical brain activity. This information can be obtained using number of experimental techniques, for example, electroencephalogram (EEG) [8]. Studies suggest, that there are particular EEG features correlated with intelligence, attention and other brain characteristics [9-12]. EEG-based method for estimation of subject's intelligence and attention level would find social application, for instance, in education.

II. MATERIALS AND METHODS

A. Experiments

Seven healthy children (7-10 years), right-handed, with normal or corrected-to-normal visual acuity participated at the experiment. All of them were asked to maintain a healthy life regime with an 8-hrs night rest during 48 hrs prior the experiment. Parents of each volunteer provided informed written consent before participating in the experiment. The experimental procedure was performed in accordance with the Helsinki's Declaration.

For EEG recording we used electroencephalograph "actiCHamp" by Brain Products (Germany). EEG was recorded for 31 channels according to "10-20" system. Experiment was performed using tablet computer and design included several phases in the following order: background activity, cognitive task 2, cognitive task 1, cognitive task 2. Background activity was recorded at the start of experimental session for 90 s. During this phase subject sat still with opened eyes and without performing any task. Cognitive task 1 was to accomplish Schulte test - simplified version of Zahlen-Verbindungs-Test (ZVT), widely used in Russia. Schulte test consisted of matrices (tables) of 5 × 5 randomly arranged numbers from 1 to 25. The subject was asked to find numbers in a descending order. by pointing each found number with a pencil. All participants had to complete R = 5 tables (50-90 s for each table) under direct supervision of a professional psychologist. Between tables subject had a break for 10-20 s. Cognitive task 2 consisted of

watching a video – short cartoon with content appropriate for children. Duration of each video was ~300 s.

B. Data analysis

We analyzed time-frequency representations of EEG signals obtained via a continuous wavelet transform (CWT), which has recently become a very popular technique for studying dynamics of neurophysiological brain activity [13]. CWT is a convolution of EEG signal $x(t)$ with basic function $\psi(\eta)$ as

$$W_n(f,t) = \sqrt{f}\int_{-\infty}^{+\infty} x_n(t)\,\psi^*(f,t)dt, \quad (1)$$

where $n = 1, 2 \ldots N$ is the number of EEG channel ($N = 31$) and '*' stands for complex conjugation. As mother wavelet of CWT we used the complex Morlet wavelet

$$\psi(\eta) = \frac{1}{\sqrt[4]{\pi}} e^{j\omega_0\eta} e^{-\eta^2/2} \quad (2)$$

where $\eta = f(t - t_0)$and $\omega_0 = 2\pi$ is the wavelet central frequency.

We analyzed wavelet energy spectrum as $E^n(f,t) = \sqrt{W_n^2(f,t)}$ in number of frequency bands: delta (2-4 Hz), theta (4-8 Hz), alpha (8-13 Hz) and beta (15-30 Hz). For these particular frequency bands averaged wavelet energy was calculated as:

$$E^n_{\delta,\theta,\alpha,\beta}(t) = \frac{1}{\Delta f}\int_{f\in f_{\delta,\theta,\alpha,\beta}} E^n(f,t)df \quad (3)$$

The ratio between EEG signal energies in beta and alpha frequency bands, especially in occipital area, is often used to characterize attention and its stability. However, in some instances the ratio of EEG energy for high frequencies (HF) and low frequencies (LF) provides more evident results. For example, Liutsyuk et al. [12] found that the subjects with good working ability displayed relatively high values of HF/LF ratio. Moreover, this ratio was greater in the right hemisphere, that probably indicated stronger contribution of neuronal activity in this hemisphere to provide stability of attention.

Thus, we were interested in analysis and comparison of following frequency ranges: alpha and beta, LF ($E^n_{LF}(t) = E^n_\delta(t) + E^n_\theta(t) + E^n_\alpha(t)$) and HF ($E^n_{HF}(t) = E^n_\beta(t)$). The ratio between HF and LF was calculated for each EEG channel as following:

$$\varepsilon^n(t) = \frac{E^n_{HF}(t)}{E^n_{LF}(t)} \quad (4)$$

Then coefficients $\varepsilon^n(t)$ were averaged separately for channels in left and right hemisphere (13 channels for each hemisphere according to "10-20" system) to obtain $\varepsilon^L(t)$ and $\varepsilon^R(t)$ correspondingly. Wavelet energies for alpha and beta rhythm were averaged for EEG channels in occipital area (6 channels) to obtain $E^O_\alpha(t)$ and $E^O_\beta(t)$ correspondingly.

The wavelet analysis of EEG recordings was performed withg home written C/Cuda software for increasing computation performance [14].

III. Results

We analyzed EEG signals for each epoch in experiment separately: background activity, Schulte tables – each table as individual epoch, video watching – two separate epochs, one for each video. Corresponding EEG fragments were processed with CWT and following characteristics were calculated: $\varepsilon^L(t)$, $\varepsilon^R(t)$, $E^O_\alpha(t)$, $E^O_\beta(t)$. Examples of acquired distributions are illustrated on Fig. 1-3.

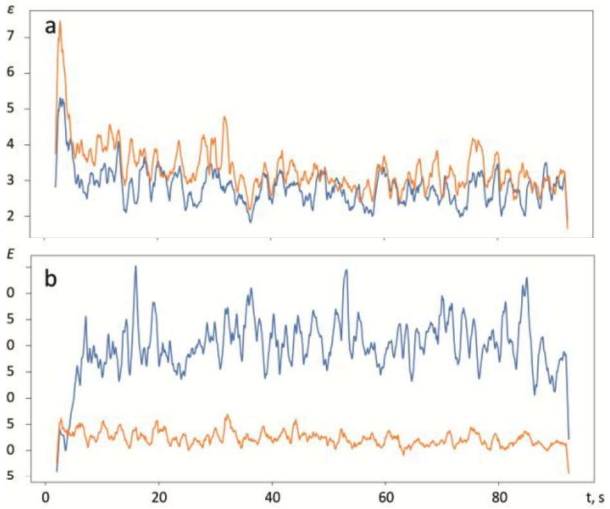

Fig. 1. Results for background epoch: (a) distributions of $\varepsilon^L(t)$and $\varepsilon^R(t)$ (blue and orange colors correspindingly); (b) distributions of $E^O_\alpha(t)$and $E^O_\beta(t)$ (blue and orange colors correspindingly)

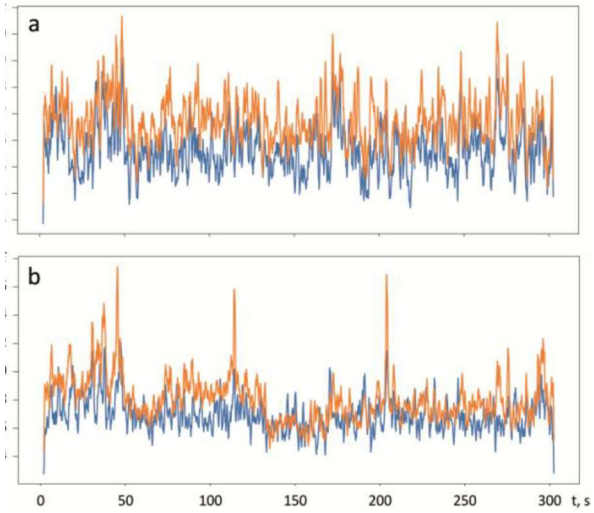

Fig. 2. Results for video watching epoch: (a) distributions of $\varepsilon^L(t)$and $\varepsilon^R(t)$ (blue and orange colors correspindingly); (b) distributions of $E^O_\alpha(t)$and $E^O_\beta(t)$ (blue and orange colors correspindingly)

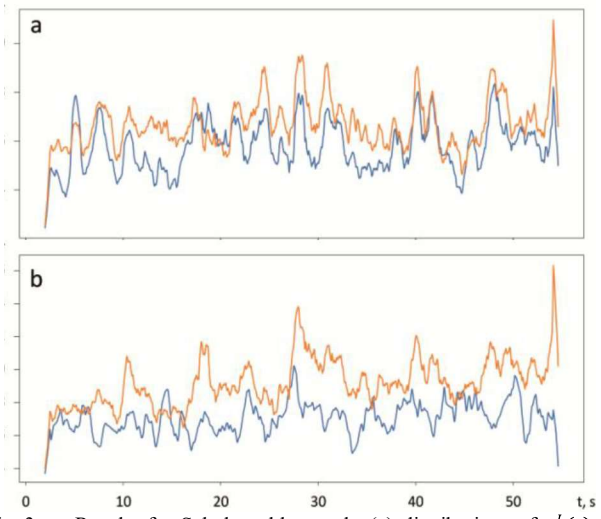

Fig. 3. Results for Schulte table epoch: (a) distributions of $\varepsilon^L(t)$and $\varepsilon^R(t)$ (blue and orange colors correspindingly); (b) distributions of $E_\alpha^O(t)$and $E_\beta^O(t)$ (blue and orange colors correspindingly)

By comparing Fig. 1 with Fig. 2 or Fig. 3 one can see, that see that during background epoch alpha rhythm is dominating (see Fig. 1b), which also leads to lower values of $\varepsilon^L(t)$ and $\varepsilon^R(t)$ (see Fig. 1a). These features can be used for simple separation of background epochs from ones with cognitive tasks.

However, this method ca not be used to distinguish Schulte table epoch from epoch with video: values of $\varepsilon^L(t)$, $\varepsilon^R(t)$, $E_\alpha^O(t)$, $E_\beta^O(t)$ on Fig. 2 are very close to corresponding ones on Fig. 3.

For better comparison of energy in different frequency ranges we calculated difference between HF/LF ratio in right and left hemisphere as $\varepsilon^{R-L}(t) = \varepsilon^R(t) - \varepsilon^L(t)$ and difference between beta and alpha rhythm in occipital area as $E_{\beta-\alpha}^O(t) = E_\beta^O(t) - E_\alpha^O(t)$. Then these characteristics were time-averaged for each epoch separately ($\langle\varepsilon^{R-L}\rangle$ and $\langle E_{\beta-\alpha}^O\rangle$). We found, that $\langle\varepsilon^{R-L}\rangle = 0.09 \div 0.1$ for Shulte tables while for epoch with video $\langle\varepsilon^{R-L}\rangle$~0.11. In terms of $\langle E_{\beta-\alpha}^O\rangle$ difference between Schulte table and watching of video is more pronounced: $1.5 \div 2.1$ and $0.6 \div 1.1$ correspondingly.

Revealed differences between background activity and cognitive tasks of different types can be used in further research on fundamental properties of brain related to cognitive activity in children, especially during educational process. It also can be used in development of EEG-based method for evaluation of intelligence and attention level.

ACKNOWLEDGMENT

This work has been supported by Russian Science Foundation (grant 19-72-10121).

REFERENCES

[1] L. D. Sheppard, P. A.Vernon, "Intelligence and speed of information-processing: A review of 50 years of research," Personality and Individual Differences, vol. 44(3), pp. 535-551, 2008.

[2] C. Neubauer, E. Knorr, "Three paper-and-pencil tests for speed of information processing: Psychometric properties and correlations with intelligence," Intelligence, vol. 26(2), pp. 123-151, 1998.

[3] L. Schubert, D. Hagemann, A. Voss, A. Schankin, K. Bergmann, "Decomposing the relationship between mental speed and mental abilities," Intelligence, vol 51, pp. 28-46, 2015.

[4] W. E. Hick, "On the rate of gain of information," Quarterly Journal of Experimental Psychology, vol. 4(1), pp. 11-26, 1952.

[5] S. Sternberg, "Memory-scanning: Mental processes revealed by reaction-time experiments," American Scientist, vol. 57(4), pp. 421-427, 1969.

[6] M. I. Posner, R. F. Mitchell, "Chronometric analysis of classification," Psychological Review, vol. 74(5), pp. 392-409, 1967.

[7] O. Jager, H. M. Suss, A. Beauducel, Berliner Intelligenzstruktur-Test: BIS-Test, Hogrefe, 1997.

[8] Niedermeyer, L. S. Fernando, Electroencephalography: Basic Principles, Clinical Applications, and Related Fields, Lippincott Williams & Wilkins, 2004.

[9] M. Houlihan, R. Stelmack, K. Campbell, "Intelligence and the effects of perceptual processing demands, task difficulty and processing speed on P300, reaction time and movement time," Intelligence, vol 26(1), pp. 9-25, 1998.

[10] M. J. Euler, T. L. McKinney, H. M. Schryver, H. Okabe, "ERP correlates of the decision time-IQ relationship: The role of complexity in task-and brain-IQ effects," Intelligence, vol. 65, pp. 1-10, 2017.

[11] A. Maksimenko et al, "Nonlinear effect of biological feedback on brain attentional state," Nonlinear Dynamics, vol. 95(3), pp. 1923-1939, 2019.

[12] E. Runnova A. E. et al, "Theoretical background and experimental measurements of human brain noise intensity in perception of ambiguous images," Chaos, Solitons & Fractals, vol. 93, pp. 201-206, 2016.

[13] N. Pavlov, A. E. Hramov, A. A. Koronovskii, E. Sitnikova, V. A. Makarov, A. A. Ovchinnikov, "Wavelet analysis in neurodynamics," Phys. Uspekhi, vol. 55, pp. 845–875, 2012.

[14] N. Lutsyuk, E. Eismont, V. Pavlenko, "Correlation of the characteristics of EEG potentials with the indices of attention in 12-to 13-year-old children," Neurophysiology, vol. 38(3), pp. 209-216, 2006.

[15] Grubov, V. Nedaivozov, "Stream processing of multichannel eeg data using parallel computing technology with nvidia cuda graphics processors," Technical Physics Letters, vol. 44, pp. 453–455, 2018.

Features of real and imaginary motor activity on EEG and fNIRS signals for neurorehabilitation

Vadim Grubov
Neuroscience and Cognitive Technology Lab, Center for Technologies in Robotics and Mechatronics Components
Innopolis University
Innopolis, Russia
v.grubov@innopolis.ru

Nikita Frolov
Neuroscience and Cognitive Technology Lab, Center for Technologies in Robotics and Mechatronics Components
Innopolis University
Innopolis, Russia
n.frolov@innopolis.ru

Elena Pitsik
Neuroscience and Cognitive Technology Lab, Center for Technologies in Robotics and Mechatronics Components
Innopolis University
Innopolis, Russia
e.pitsik@innopolis.ru

Artem Badarin
Neuroscience and Cognitive Technology Lab, Center for Technologies in Robotics and Mechatronics Components
Innopolis University
Innopolis, Russia
a.badarin@innopolis.ru

***Abstract* — Experimental design for recording of EEG and fNIRS during performance of real and imaginary movement was proposed. Set of experiments was conducted in accordance with this design and obtained EEG and fNIRS dataset was analyzed. Analysis allowed to introduce certain features in time-frequency domain that can be used to separate real motor activity from imaginary.**

Keywords — EEG, fNIRS, real and imaginary motor activity, time-frequency analysis

I. Introduction

Motor activity and related mental tasks are widely used in development of brain-computer interfaces (BCIs). BCI performs an online detection of various features of electrical signals, such as electroencephalograms (EEGs), including a transformation of certain patterns into control commands for the mechanical part, to provide special actions in the surrounding world without the use of muscles [1]. Instead of electrical processes, other sources of information about brain can also be used, for instance, functional near-infrared spectroscopy (fNIRS) [2,3].

The ultimate goal of BCI is possibility to generate control commands without any muscular activity. In this case motor imagery tasks (or imaginary movements without real neuromuscular activity) become good candidates. Motor imagery, sometimes is considered to be a conscious use of unconscious preparation for an actualmovement [4]. Previous studies outlining the similarities between real motor activity and motor imagery [5-7]. In terms of application in BCI the main question is whether motor imagery follows the same cortical layout as motor execution in the primary motor cortex (M1).

II. Materials and Methods

A. Experiments

Twenty conditionally healthy volunteers (20-40 years, men and women both), right-handed, amateur practitioners of physical exercises, and non-smokers participated at the experiment. All of them were asked to maintain a healthy life regime with an 8-hrs night rest during 48 hrs prior the experiment. Each participant provided informed written consent before participating in the experiment. The experimental procedure was performed in accordance with the Helsinki's Declaration.

In the first part of the study we recorded electroencephalogram (EEG) - sum of electrical currents generated by a small group of neurons in brain network [8]. For EEG signal recording we used electroencephalograph “Encephalan-EEG-19/26” (Medicom MTD company, Taganrog, Russian Federation). To obtain EEG signals we used “10-10” scheme for EEG electrode placement with 31 EEG channels. Before EEG recording scalp was treated with the abrasive “NuPrep” gel in order to increase skin conductivity, then cup adhesive Ag/AgCl electrodes were noninvasively placed on scalp with help of “Ten20” paste. The impedance of electrodes was monitored during the experimental procedure with typical values of 2-5 kΩ. The ground electrode N was located above the forehead near the Fpz electrode location and two referent electrodes were located on the earlobes. The EEG signals were filtered by band-pass filter (high-pass at 0.016 Hz and low-pass at 100-Hz) and by 50-Hz notch filter. Time resolution of the recorded EEG signals was 250 Hz.

In the second part we used functional near-infrared spectroscopy (fNIRS) - a noninvasive, relatively low-cost, portable optical brain-imaging technique [9]. It uses near-infrared light to measure changes in oxygenated (HbO) and deoxygenated (HbR) hemoglobin levels due to the hemodynamic response, the rapid delivery of oxygenated blood to active cortical areas through neurovascular coupling [10]. Despite lower temporal resolution and time delay of the hemodynamic response compared to EEG signals, fNIRS represents another approach to obtain information about brain activity, which can complementary to information provided by EEG analysis.

In the common configuration for fNIRS recording, light sources and detectors are placed on the scalp and two wavelengths of light are transmitted through skin, skull and top layer of the cerebral cortex. fNIRS uses light with two wavelengths: ~ 700 and ~900 nm, that can pass through skin, bone, and water, but are highly absorbed by HbO and HbR correspondingly [11]. Because HbO and HbR have different light absorption properties, the relative changes in HbO and HbR, and therefore the change in oxygenation of the tissue, can be calculated from changes in the reflected dual-wavelength light using the modified Beer-Lambert law [12]. Obtained distributions of HbO and HbR are analyzed for different cortex areas to find ones that are activated during particular real or imaginary movement. We used NIRScout device by NIRx company (Germany) with 8 sources and 8 detectors and time resolution of ~7.8 Hz.

Basic experimental design was the same for EEG and fNIRS parts: subject was sitting in a chair with hands on armrests and feee flat on the ground. The screen before subject demonstrated text command. Each experiment consisted of two parts: first, subject was asked to perform real movement with left and right hand according to the commands, then after a short rest he/she was asked to imagine the same movements after corresponding commands on the screen. In EEG experiment subject was given ~4 s to perform one real movement after text command with 4-6 s breaks between consecutive command. Time interval for imaginary movement was ~7 s with 6-8 s breaks. In fNIRS experiment subject performed or imagined movement for the same time intervals of 15 s with 15 s breaks between them. Hand movement consisted of curling the fingers towards the palm as if squeezing an imaginary ball. In both experiments subject performed 20 real and 20 imaginary movement for each hand.

B. Data analysis

For time-frequency analysis of EEG signals we used continuous wavelet transform (CWT), which has recently become a very popular technique for studying dynamics of neurophysiological brain activity [13]. CWT is a convolution of EEG signal $x(t)$ with basic function $\psi(\eta)$ as

$$W_n(f,t) = \sqrt{f}\int_{-\infty}^{+\infty} x_n(t)\,\psi^*(f,t)dt, \qquad (1)$$

where $n = 1,2 \ldots N$ is the number of EEG channel ($N = 31$) and '*' stands for complex conjugation. As mother wavelet of CWT we used the complex Morlet wavelet

$$\psi(\eta) = \frac{1}{\sqrt[4]{\pi}} e^{j\omega_0\eta} e^{-\eta^2/2} \qquad (2)$$

where $\eta = f(t - t_0)$and $\omega_0 = 2\pi$ is the wavelet central frequency.

Wavelet energy spectrum ($E^n(f,t) = \sqrt{W_n^2(f,t)}$ where n is number of EEG channels) provides information about time-frequency structure of the signal. We also analyzed wavelet energy in alpha frequency range (8-13 Hz) For this particular frequency band averaged wavelet energy was calculated as:

$$E_\alpha^n(t) = \frac{1}{\Delta f}\int_{f\in f_\alpha} E^n(f,t)df \qquad (3)$$

III. RESULTS

We processed EEG signals with CWT and computed wavelet energy spectra $E^n(f,t)$ along with wavelet energy averaged over alpha frequency range $E_\alpha^n(t)$. Fig. 1 demonstrate results for real movements of left and right hands on EEG channel C3.

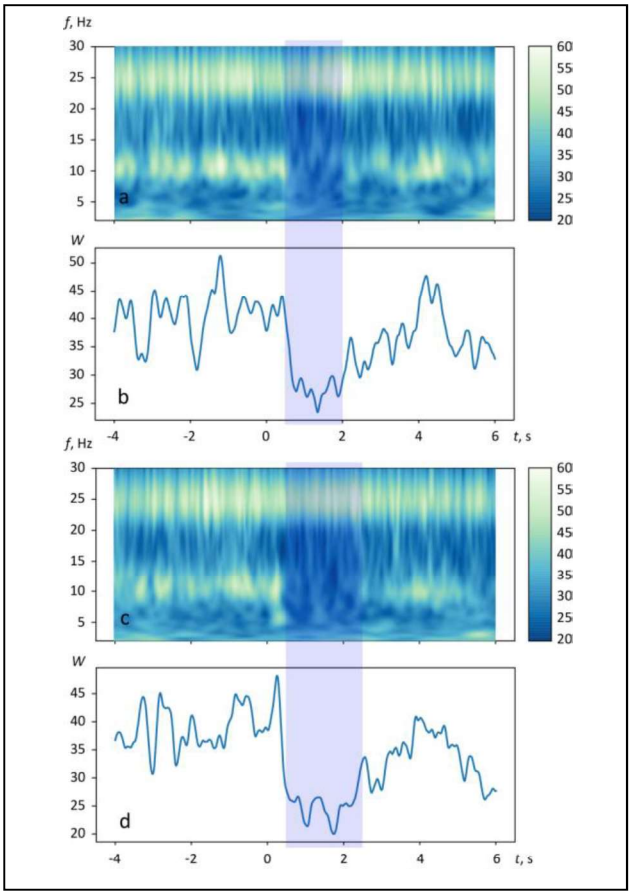

Fig. 1. Wavlet spectra for left (a) and right (c) hand movement, distributions of averaged wavelet energy for left (b) and right (d) hand movement

As one can see from Fig. 1 left and right hand movements are accompanied by pronounced decrease of wavelet energy level in alpha frequency band. This can be used to distinguish movement from background activity, however, there is no essential difference in such dynamics for left and right hand movement.

Results from fNIRS experiment are illustrated on Fig. 2 and 3. As one can see, increase in level of HbO with corresponding decrease of HbR mark each movement, real or imaginary. Moreover, this dynamics is more pronounced in right hemisphere for left hand and in left hemisphere for right hand, which opens opportunity to distinguish different types of movement. These results can be used in further research with synchronous recording of EEG and fNIRS in one experiment.

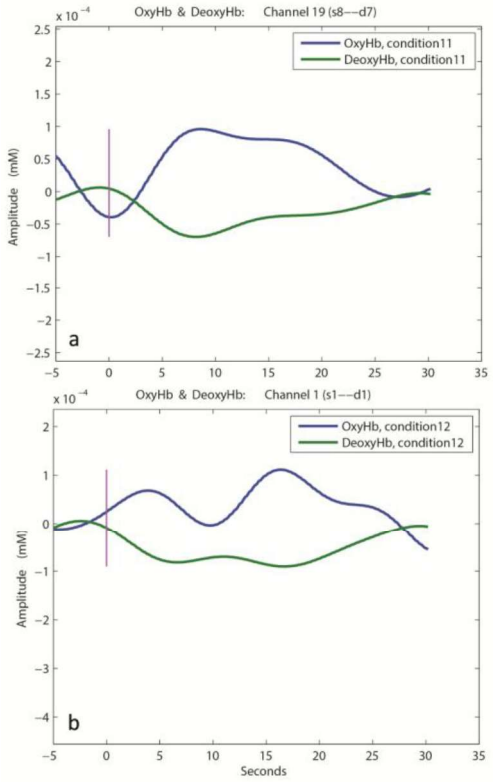

Fig. 2. Distributions of HbO (red) and HbR (blue) for real left hand movement in right hemisphere (a) and real right hand movement in left hemisphere

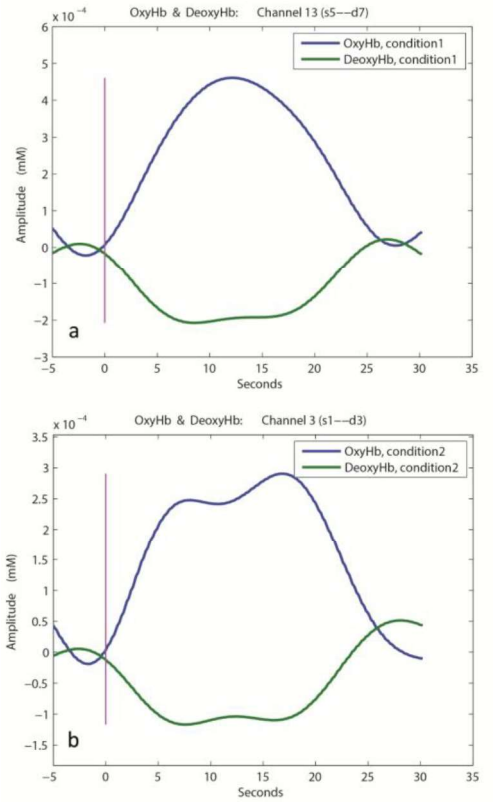

Fig. 3. Distributions of HbO (red) and HbR (blue) for imaginary left hand movement in right hemisphere (a) and imaginary right hand movement in left hemisphere (b)

ACKNOWLEDGMENT

This work has been supported by the Center for Technologies in Robotics and Mechatronics Components (Innopolis University).

REFERENCES

[1] J. R. Wolpaw, E. W. Wolpaw, Brain-computer interfaces: principles and practice. New York: Oxford University Press, 2012 .

[2] Abdalmalak et al, "Single-session communication with a locked-in patient by functional near-infrared spectroscopy," Neurophotonics, vol. 4(4), pp. 040501, 2017.

[3] Abdalmalak et al, "Can time-resolved NIRS provide the sensitivity to detect brain activity during motor imagery consistently?" Biomed Opt Express, vol. 8, pp 2162-2172, 2017.

[4] M. Jeannerod, "Mental imagery in the motor context," Neuropsychologia, vol. 33, no. 11, pp. 1419–1432, 1995.

[5] J. Munzert, B. Lorey, and K. Zentgraf, "Cognitive motor processes: the role of motor imagery in the study of motor representations," Brain Research Reviews, vol. 60, no. 2, pp. 306–326, 2009.

[6] N. Sharma, P. S. Jones, T. A. Carpenter, and J.-C. Baron, "Mapping the involvement of BA 4a and 4p during Motor Imagery," NeuroImage, vol. 41, no. 1, pp. 92–99, 2008.

[7] Solodkin, P. Hlustik, E. E. Chen, and S. L. Small, "Fine modulation in network activation during motor execution and motor imagery," Cerebral Cortex, vol. 14, no. 11, pp. 1246–1255,2004.

[8] Niedermeyer, L. S. Fernando, Electroencephalography: Basic Principles, Clinical Applications, and Related Fields, Lippincott Williams & Wilkins, 2004.

[9] H. Ayaz, B. Onaral, K. Izzetoglu, P. A. Shewokis, R. Mckendrick, and R. Parasuraman, "Continuous monitoring of brain dynamics with functional near infrared spectroscopy as a tool for neuroergonomic research: empirical examples and a technological development," Frontiers in Human Neuroscience, vol. 7, article 871, 2013.

[10] Villringer and B. Chance, "Non-invasive optical spectroscopy and imaging of human brain function," Trends in Neurosciences, vol. 20, no. 10, pp. 435–442, 1997.

[11] H. Ayaz, P. A. Shewokis, A. Curtin, M. Izzetoglu, K. Izzetoglu, and B. Onaral, "Using MazeSuite and functional near infrared spectroscopy to study learning in spatial navigation," Journal of Visualized Experiments, no. 56, pp. 1–12, 2011.

[12] M. Cope, The Development of a near Infrared Spectroscopy Systemand Its Application for Non InvasiveMonitory of Cerebral Blood and Tissue Oxygenation in the Newborn Infants, University of London, London, UK, 1991.

[13] Hramov et al, Wavelets in neuroscience, Springer Berlin Heidelberg, 2015.

Kinesthetic and visual modes of imaginary movement: MEG studies for BCI development

Alexander E. Hramov
Neuroscience and Cognitive Technology Laboratory, Center for Technologies in Robotics and Mechatronics Components
Innopolis University,
Innopolis, Russia
a.hramov@innopolis.ru

Alexander N. Pisarchik
Center for Biomedical Technology,
Technical University of Madrid,
Madrid, Spain
alexander.pisarchik@ctb.upm.es

***Abstract*— The study of neurophysiological mechanisms responsible for motor imagery is important for the development of brain-computer interfaces (BCI). Here we analyze the results of magnetoencephalographic (MEG) experiments which confirm the existence of two types of motor imagery, kinesthetic and visual imagery, distinguished by activation and inhibition of different brain areas in motor-related alpha (8-12 Hz) and beta (15-30 HZ) frequency ranges. Kinesthetic imagery implies muscular sensation when performing an imaginary moving action that leads to event-related desynchronization (ERD) of motor-associated brain rhythms. By contrast, visual imagery refers to visualization of the corresponding action that results in event-related synchronization (ERS) of alpha/beta activity. A main difference between kinesthetic and visual modes occurs in the frontal brain area. The analysis of evoked responses shows that in all kinesthetic imagery subjects the activity in the frontal cortex is suppressed during motor imagery, while in the visual imagery subjects the frontal cortex is always active. The accuracy in classification of left- and right-arm motor imagery using artificial intelligence methods is similar for kinesthetic and visual imagery modes. The possibility to increase the accuracy for visual imagery is in demand for BCIs.**

Keywords—brain-computer interface, motor imagery, bioprosthetics, MEG, machine learning

I. INTRODUCTION

The revealing features of brain activity during imagination of the movement of different limbs are very important for fundamental neuroscience and applied neurotechnologies, such as BCIs which can help in rehabilitation of patients after trauma or stroke, as well as for noninvasive brain-controlled bioprostheses and exoskeletons [1]. Mental imagination of movements referred to as motor imagery [2] manifests as a result of the rehearsal of a given motor act in the working memory without any overt movement of the corresponding muscle. It is classified into two categories, namely, visual and kinesthetic imagery [3]. While visual imagery consists of visualization of the subject moving a limb, that does not require any special training or sensing of the muscles, kinesthetic imagery is the feeling of muscle movement, that can usually be achieved by athletes or specially trained persons [4].

To understand and classify motor imagery different methods of time-frequency analyses are used, in particular, the most common techniques are using ERS and ERD, wavelet transform, empirical mode decomposition, common spatial patterns, as well as their combinations [5-8]. Due to good spatial and frequency resolution MEG was extensive used for motor imagery studies [9]. However, to the best of our knowledge, the MEG experiments with untrained subjects were not carried out for classification of different modes of imaginary movement.

Early, it was shown that kinesthetic and visual imagery modes affect the classification accuracy, e.g., the accuracy rate obtained for kinesthetic imagery were better than for visual one [10]. In this context, taking into account that untrained subjects often demonstrate the visual imagery mode, the possibility to increase the accuracy rate for visual imagery is in demand for BCI applications.

II. EXPERIMENTS AND METODS

The experimental study consisted of ten untrained volunteers. The subjects were sat in a comfortable reclining chair with their legs straight and arms resting on an armrest in front of them. All participants were required to imagine moving their arms after being presented with audible beeps as the cue. The whole MEG experiment was divided into four series with one-fourth of the total number of trials in each series. Each series consisted of equal number of trials randomly chosen for each of two arms (left or right arm). The imaginary movement of each arm was counted as one trial. The beeps were presented with time gaps randomly varied from 6 to 8 s. The number of trials per limb was varied among the subjects from 16 to 28. All participants provided a written informed consent before the experiment commencement. The experimental studies were performed in accordance with the Declaration of Helsinki. Methods were carried out in accordance with approved guidelines. The neurophysiological data were acquired with the Vectorview MEG system (Elekta AB, Sweden) with 102 magnetometers placed inside a magnetically shielded room at the Laboratory of Cognitive and Computational Neuroscience, Center for Biomedical Technology, Technical University of Madrid, Spain. The research was approved by the Ethics Committee of the Technical University of Madrid.

The time-frequency spectrogram (TFS) of the MEG signals was analyzed using wavelet-based approach, a well-known tool for the analysis of non-stationary time series [6,7]. For each limb, we used the Morlet wavelet to evaluate the TFS for all extracted epochs, and then averaged the TFSs for the limb. Then, the TFS was also averaged over the desired motor-related frequency ranges of alpha (8–12 Hz) and beta (15–30 Hz) bands. The same process was repeated over the resting state using the same parameters. To evaluate ERS/ERD, we took the difference between the

spectrogram for the trials and the averaged-over-time spectrogram of the resting state and then normalized it to the resting state [11].

To classify MEG trials we have used two different machine learning technics. First, to perform the cluster analysis of kinesthetic and visual imagery, we applies the hierarchical cluster analysis (HCA) [12], a widely-used unsupervised machine learning technique. Using the HCA, we found the hierarchy in considered data in a greedy way, that allowed to uncover its structural properties, i.e., organize observed objects into subgroups. Second, to classify the brain states associated with motor imagery, we used such type of artificial neural network as multilayer perceptron (MLP) [13] which is often used for classification of EEG trials [14,15].

III. Results

We analyzed brain dynamics in terms of ERS/ERD in alpha (8–12 Hz) and beta (15–30 Hz) frequency bands during the motor imagery performance, which allowed us to classify the subjects into kinesthetic and visual categories. We shown that the kinesthetic imagery subjects have stronger ERD centralized near the inferior-parietal lobe, while the visual imagery subjects tend to have ERS in the superior-parietal and occipital lobes.

The obtained results of classification into kinesthetic and visual imagery groups was confirmed by the analysis of the evoked response, which is the average of time series over all trials. The subjects from the visual imagery group are characterized by neural activation of the occipital cortex in contrast to the subjects from the kinesthetic imagery group, who demonstrate activity in the premotor area, which is absent in the visual imagery group.

The HCA results are present in Fig 1, where the dendrogram with the arrangement of clusters obtained by HCA is shown. One can see that all subjects can be well separated into two large clusters with the exception of the upper row of the dendrogram marked by the dashed lines, i.e., subjects 3, 4, 5, 6, 7 and 8 are arranged into the kinesthetic imagery group, while the rest of the subjects 1, 2, 9 and 10 are arranged into the VI group. It should be noted, that the links between the subjects inside each group are much smaller than the links between the clusters. This confirms that HCA provides a good enough precision for the clustering.

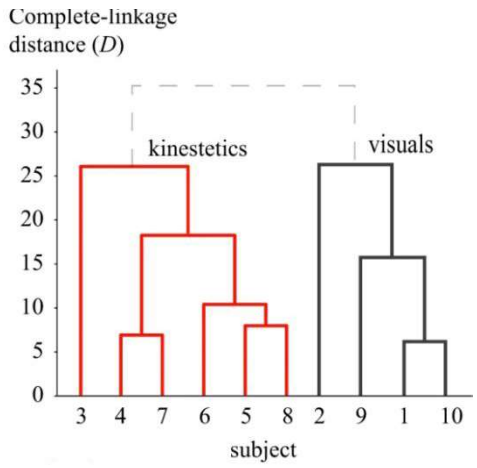

Fig. 1. Results of HCA illustrating the clustering of subjects belonging to kinesthetic and visual imagery types. Here dendrogram shows the formation of two subgroups (kinesthetic and visual imagery subjects) in terms of Euclidean distance between clusters in ERD/ERS feature space.

The brain activity during motor imagery of the kinesthetic subjects is characterized by well-pronounced ERD in both alpha and beta frequency bands. Such a behavior is similar to real movement when alpha- and beta-wave energies are suppressed in the motor brain area [16]. On the contrary, for the visual imagery subjects the motor imagery process is accompanied by ERS in the alpha and beta ranges, that determines a leading role of self-visualization of the limb movement.

A multilayer perceptron was constructed and applied to classify MEG time series trials associated with left-arm and right-arm motor imaginery in these two groups of subjects. Fig. 2 demonstrates the classification accuracy for each subject. The average classification accuracy over all subjects was about 70%. At the same time, the best accuracy reached 90% for subject 6.

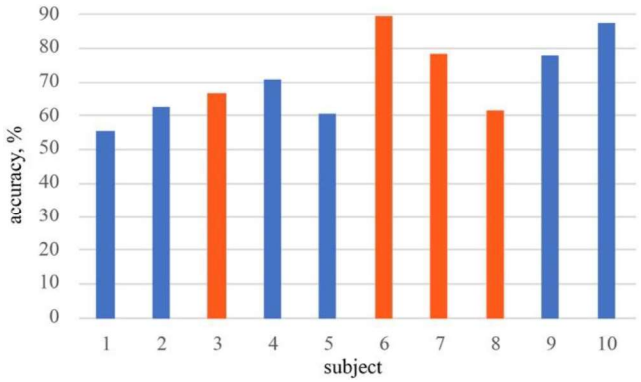

Fig. 2. Results of ANN classification accuracy of motor imagery of left and righ arm. Orange boxes correspond to visual imaginery subjects, blue boxes – kinesthetic imaginery subjects.

This is an important result, which shows that the classification accuracy does not depend on the type of imagination. We can get high classification accuracy for both kinesthetic and visual types of imagination. This opens up opportunities for improving the efficiency of the active interfaces of the brain-computer, which exploit imaginary movements as mental commands.

IV. Conclusion

We analyze the results of MEG experiments with voluntary participants which confirm the existence of two types of motor imagery, kinesthetic and visual imagery, distinguished by activation and inhibition of different brain areas in motor-related alpha and beta frequency ranges. Similar to real movement, kinesthetic imagery implies muscular sensation when performing an imaginary moving action that leads to ERD of motor-associated brain rhythms. By contrast, visual imagery refers to visualization of the corresponding action that results in ERS of alpha and beta activity. A notable difference between kinesthetic and visual modes of imagination occurs in the frontal brain area. The analysis of evoked responses shows that in all kinesthetic imagery subjects the activity in the frontal cortex is suppressed during motor imagery, while in the visual imagery subjects the frontal cortex is always active. The accuracy in classification of left-arm and right-arm motor imagery using maschine learning is similar for kinesthetic and visual imagery modes. Since untrained subjects usually demonstrate the visual imagery mode, the possibility to

increase the accuracy for visual imagery is in demand for BCIs.

ACKNOWLEDGMENT

This work has been supported by Russian Science Foundation (grant 17-72-30003).

REFERENCES

[1] S. Perrey, "Brain activation associated with eccentric movement: a narrative review of the literature," Eur. J. Sport Sci. vol. 18, pp. 75–82, 2018.

[2] M. Jeannerod, "The representing brain: neural correlates of motor intention and imagery," Behav. Brain Sci. vol. 17, pp. 187–202, 1994.

[3] P. Chholak, G. Niso, V. A. Maksimenko, S. A. Kurkin, N. S. Frolov, E. N. Pitsik, A. E. Hramov, Alexander N. Pisarchik. "Visual and kinesthetic modes affect motor imagery classification in untrained subjects," Scientific Reports. vol. 9, article number: 9838, 2019.

[4] N. Mizuguchi, H. Nakata, Y. Uchida, K. Kanosue, "Motor imagery and sport performance," J. Phys. Fit. Sports Med. vol. 1, pp. 103–111, 2012.

[5] N. Takeuchi, T. Mori, K. Nishijima, T. Kondo, S. Izumi. "Inhibitory transcranial direct current stimulation enhances weak beta event-related synchronization after foot motor imagery in patients with lower limb amputation," J. Clin. Neurophysiol. vol. 32, pp. 44–50, 2015.

[6] VV. Grubov, E. Sitnikova, A.N. Pavlov, A.A. Koronovskii, A.E. Hramov. "Recognizing of stereotypic patterns in epileptic EEG using empirical modes and wavelets," Phys. A. vol. 486, pp. 206–217, 2017.

[7] A.N. Pavlov, A.E. Hramov, A.A. Koronovskii, E.Yu. Sitnikova, V.A Makarov, and A.A. Ovchinnikov. "Wavelet analysis in neurodynamics," Physics-Uspekhi, vol. 55, pp. 845–875, 2012.

[8] A.A. Koronovskii, A.E. Hramov. "Wavelet transform analysis of the chaotic synchronization of dynamical systems," Journal of Experimental and Theoretical Physics Letters. vol. 79, pp. 316-319, 2004.

[9] H.-L. Halme, and L. Parkkonen. "Across-subject offline decoding of motor imagery from meg and eeg," Scientific Reports. vol. 8, pp. 10087, 2018.

[10] Neuper, C., Scherer, R., Reiner, M. & Pfurtscheller, G. Imagery of motor actions: Differential effects of kinesthetic and visual-motor mode of imagery in single-trial eeg. Cogn. Brain Res. 25, 668–677 (2005).

[11] G. Pfurtscheller, F.H. Lopes da Silva, "Event-related eeg/meg synchronization and desynchronization: basic principles," Clin. Neurophysiol. vol.110, pp. 1842–1857, 1999.

[12] D.S. Wilks. Cluster analysis. In International Geophysics, vol. 100, pp. 603–616 (Elsevier, 2011).

[13] S.S. Haykin, "Neural Networks and Learning Machines," vol. 3 (Pearson Upper Saddle River, NJ, USA, 2009).

[14] V.A. Maksimenko, S.A. Kurkin, E.N. Pitsik, V.Yu. Musatov, A.E. Runnova, T.Yu. Efremova, A.E. Hramov, A.N. Pisarchik. "Artificial neural network classification of motor-related eeg: an increase in classification accuracy by reducing signal complexity," Complexity. 2018 (2018).

[15] A.E. Hramov, V.A. Maksimenko, S.V. Pchelintseva, A.E. Runnova, V.V. Grubov, V.Yu. Musatov, M.O. Zhuravlev, A.A. Koronovskii, and A.N. Pisarchik. "Classifying the perceptual interpretations of a bistable image using EEG and artificial neural networks". Front. Neurosci., vol 11, p. 674, 2017.

[16] V.A. Maksimenko, A. Pavlov, A.E. Runnova, V. Nedaivozov, V. Grubov, A. Koronovslii, S.V. Pchelintseva, E. Pitsik, A.N. Pisarchik, A.E. Hramov. "Nonlinear analysis of brain activity, associated with motor action and motor imaginary in untrained subjects," Nonlin. Dyn. vol. 91, pp. 2803–2817, 2018.

Comparing methods for extraction of autonomic control signals from electrocardiogramm

Yurii M. Ishbulatov
Department of Innovative Cardiological Information Technology, Institute of Cardiological Research Saratov State Medical University
Laboratory of Nonlinear Dynamics Modelling
Saratov Branch of the Institute of RadioEngineering and Electronics of Russian Academy of Sciences
Department of Dynamic Modeling and Biomedical Engineering
Saratov State University
Saratov, Russia
ishbulatov95@mail.ru

Ekaterina I. Borovkova
Department of Innovative Cardiological Information Technology, Institute of Cardiological Research Saratov State Medical University
Laboratory of Nonlinear Dynamics Modelling
Saratov Branch of the Institute of RadioEngineering and Electronics of Russian Academy of Sciences
Department of Dynamic Modeling and Biomedical Engineering
Saratov State University
Saratov, Russia
rubanei@mail.ru

Anatoly S. Karavaev
Laboratory of Nonlinear Dynamics Modelling
Saratov Branch of the Institute of RadioEngineering and Electronics of Russian Academy of Sciences
Department of Innovative Cardiological Information Technology, Institute of Cardiological Research Saratov State Medical University
Department of Dynamic Modeling and Biomedical Engineering
Saratov State University
Saratov, Russia
karavaevas@gmail.com

Anton R. Kiselev
Department of Innovative Cardiological Information Technology, Institute of Cardiological Research Saratov State Medical University
Department of Dynamic Modeling and Biomedical Engineering
Saratov State University
Saratov, Russia
antonkis@list.ru

Boris P. Bezruchko
Laboratory of Nonlinear Dynamics Modelling
Saratov Branch of the Institute of RadioEngineering and Electronics of Russian Academy of Sciences
Department of Dynamic Modeling and Biomedical Engineering
Saratov State University
Saratov, Russia
bezruchkobp@gmail.com

***Abstract*—In present study we compared two methods for extraction of autonomic control signal from electrocardiogram. First method is based on estimation of heart rate variability and second technique is based on heterodyning. Comparison was carried out for 3 mathematical models: linear oscillator with frequency modulation; electrocardiogram signal with variability of heart rate; complex model of autonomic control; For the last two systems only the method of time intervals estimation appeared to be applicable, but it also distort phase and spectral characteristics of the control signal.**

Keywords—cardio-vascular system, autonomic control, mathematical modeling, nonlinear dynamics

I. INTRODUCTION

Extraction of signal of heart rate autonomic control from electrocardiogram (ECG) data is an important step during fundamental studies and medical diagnostics [1].

It is widely accepted that 0.05-0.4 Hz frequency band of heart rate variability signal represent the dynamics of both sympathetic and parasympathetic control of heart rate [2]. However it is unknown what distortions are introduced to the control signal during estimation of heart rate variability signal from ECG. How this method functions is also yet to be fully studied.

Autonomic control of heart rate changes its frequency therefore one can suggest this control is somewhat similar to frequency modulation. Method of heterodyning is commonly used to extract frequency modulation from signals of radiophysical generators.

In this study we applied both methods to 3 mathematical models, for which the signal of autonomic control is priory known: linear oscillator with frequency modulation; electrocardiogram signal with frequency modulation of heart rate; complex model of autonomic control;

II. DATA AND METHODS

We compared 2 methods for extraction of the autonomic control signal from ECG. Firs approach is based on estimation of heart rate variability signal which is sequence of time intervals between heart beats. Heart beats are commonly detected as R-spikes on ECG. Resulting nonequidistant time-series is then interpolated with cubic β-splines, according to the recommendations from [2].

Operation of heterodyning is based on following trigonometrical identity (1):

$$\sin(\alpha)\sin(\beta) = 0.5(\cos(\alpha-\beta) - \cos(\alpha+\beta)) \quad (1)$$

According to (1) if ECG is multiplied by sinusoidal signal with frequency of main cardiac rhythm then $\cos(\alpha-\beta)$ - is signal of heart rate frequency modulation. Second term $\cos(\alpha+\beta)$ can then be filtered by low-pass filter.

Methods were compared for 3 objects. First object was a linear oscillator with sine frequency modulation. Frequency of oscillations was set to 1.47 Hz and modulation frequency was set to 0.1 Hz to simulate the sympathetic modulation.

Second object was a modified mathematical model of ECG from [3] to which we added frequency modulation, similar to the 1 object. Heart rate was also set to 1.47 Hz.

Third object was a complex model of circulation autonomic control, based on [4]. Model consists of 5 ordinary differential equations and can simulate combination of sympathetic and parasympathetic autonomic control of heart rate and can generate ECG signals with spectral properties similar to the real data. Full description of the model and its parameters are presented elsewhere [5].

Euler method was used for numerical integration with step of 0.004 s. Time series obtained from the models were 7 000 second.

III. Results

Methods demonstrated similar results for linear oscillator with sine frequency modulation. In both extracted signals we observed multiple frequency harmonics of the modulation frequency. Those harmonics were also present in spectra of linear oscillator around its main frequency which is typical for oscillators with frequency modulation. From this one can assume that both methods are based on the same principle and extract frequency modulation of heart rate.

Approach based on heterodyning was found to be unsuitable for analysis of signals from mathematical model of ECG and from complex model of circulation autonomic control. Analysis of ECG signals from complex model demonstrated that method based on detection of time intervals between R-spikes of ECG introduced some distortions to the extracted signal: lowered spectral power density in frequency band of 0.15-0.4 Hz, which has significance for medical diagnostics [2].

Further evidences of this phenomenon were obtained from experiments with mathematical model of ECG with modulation of heart rate. We used several modulation frequencies ranging from 0 to 0.5 Hz. For modulation signal of each frequency we measured the amplitude and frequency of the extracted signal. Form this data we obtained amplitude-frequency response curve and phase-frequency response curve of the method. Both are represented in figure 1.

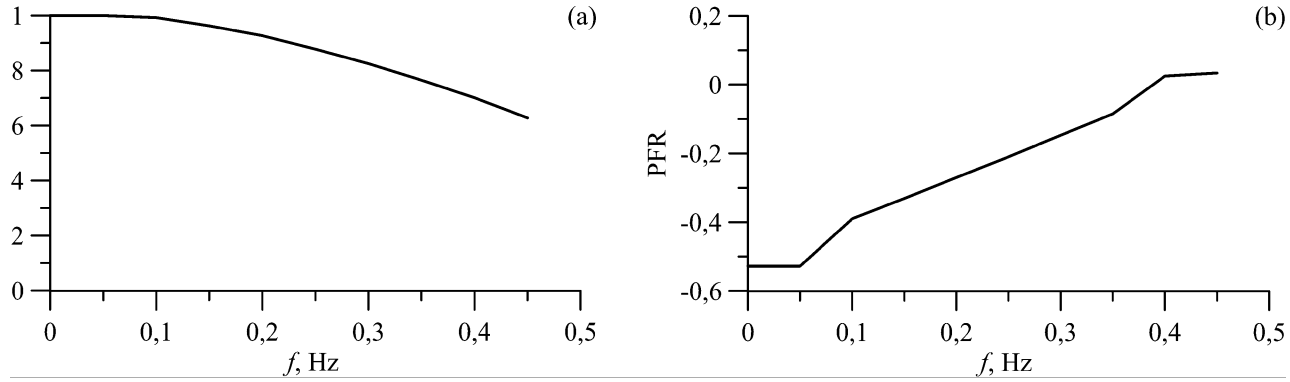

Fig. 1. a - amplitude-frequency response (AFR) and b - phase-frequency response (PFR) for method for extraction of autonomic modulation of heart rate from ECG based on time-interval detection between heart beats.

It is evident from amplitude-frequency response curve (fig. 1(a)) that for frequencies above 0.15 Hz the amplitude of extracted signal is lowered. Phase-frequency response curve (fig. 1(b)) is also deviate from linearity for modulation signals of 0.05 Hz and 0.45 Hz.

IV. Conclusion

Obtained results suggest that estimation of heart variability signal from ECG based on the same principle as extraction of frequency modulation of heart rate with heterodyning. It is evident from appearance of multiple frequency harmonics in both signals.

It was shown that estimation of heart variability signal from ECG introduces distortion to the signal of heart rate autonomic control. Power spectral density is lowered in frequency band of 0.15-0.5 Hz and phases are distorted.

Acknowledgment

This work was supported by the Russian Science Foundation, grant no. 19-12-00201.

References

[1] V.A. Shvartz, A.S., Karavaev E.I. Borovkova, S.A. Mironov, V.I. Ponomarenko, M.D. Prokhorov, Y.M. Ishbulatov, E.E. Lapsheva, V.I. Gridnev, and A.R. Kiselev, "Investigation of statistical characteristics of interaction between the low-frequency oscillations in heart rate variability and photoplethysmographic waveform variability in healthy subjects and myocardial infarction patients," RusOMJ, vol. 5, iss. 2, pp. e0203, 2016.

[2] Task Force of the European Society of Cardiology the North American Society of Pacing Electrophysiology "Heart rate variability. Standards of measurement, physiological interpretation, and clinical use," Circulation, vol. 93, pp. 354-381, 1996.

[3] P.E. McSharry, G.D. Clifford, L. Tarassenko, and L.A. Smith, "A dynamical model for generating synthetic electrocardiogram signals," IEEE trans. Biomed. Eng., vol. 50, no. 3, pp. 289-294, march 2003.

[4] H. Seidel, and H. Herzel "Bifurcations in a nonlinear model of the baroreceptor-cardiac reflex," Physica D, vol. 115, pp. 145-160, 1998.

[5] A.S. Karavaev, J.M. Ishbulatov, V.I. Ponomarenko, M.D. Prokhorov, V.I. Gridnev, B.P. Bezruchko, and A.R. Kiselev “Model of human cardiovascular system with a loop of autonomic regulation of the mean arterial pressure,” J. Am. Soc. Hypertens., vol 10, iss. 3, pp. 235-243, 2016.

[6] A.R. Kiselev, V.I. Gridnev, O.M. Posnenkova, M.D. Prokhorov, A.S. Karavaev, V.I. Ponomarenko, and B.P. Bezruchko, “Effects of antihypertensive treatment on cardiovascular autonomic control: a prospective study,” Anadolu. Kardiyoloji. Dergisi, vol. 14, no. 8, pp. 701-710, 2014.

[7] A.R. Kiselev, V.A. Shvartz, S.A. Mironov, A.S. Karavaev, D.D. Kulminskiy, M.D. Prokhorov, V.V. Skazkina, E.I. Borovkova, V.I. Ponomarenko, “A comprehensive assessment of cardiovascular autonomic control using photoplethysmograms recorded from the earlobe and fingers,” Physiol. Meas., vol. 37, no. 4, pp. 580-595, 2016.

Optimization of management of the implementation of technological processes taking into account the dynamics of multi-product manufactures

Ivanov Aleksandr Aleksandrovich
Institute of Electronic Engineering and Mechanical Engineering
Saratov State Technical University
Saratov, Russia
aleksandr.ivanov@lineate.com

Bochkarev Petr Yurievich
Institute of Electronic Engineering and Mechanical Engineering
Saratov State Technical University
Saratov, Russia
bpy@mail.ru

Оптимизация управления реализацией технологических процессов с учетом динамики многономенклатурных производств

Иванов Александр Александрович
Институт электронной техники и машиностроения
Саратовский государственный технический университет имени Гагарина Ю.А.
Саратов, Россия
aleksandr.ivanov@lineate.com

Бочкарев Петр Юрьевич
Институт электронной техники и машиностроения
Саратовский государственный технический университет имени Гагарина Ю.А.
Саратов, Россия
bpy@mail.ru

***Abstract*— A formalization procedure for realization of technological processes and a methodology for finding suboptimal decisions in system of planning for mechanical production were presented here. Was shown that presented model and methodology allow decreasing common production time.**

***Keywords*— Production scheduling, model of small-scale production of mechanoprocessing, implementation of technological processes**

***Аннотация*— Представлена формализация процедуры реализации технологических процессов и методика поиска субоптимальной реализации в системе планирования технологических процессов для управления многономенклатурным механообрабатывающим производством. Показано, что предложенные модель и метод поиска позволяют получить значительное уменьшение общего времени работы производственной системы.**

***Ключевые слова*— планирование производства, модель мелкосерийного производства механообработки, реализация технологических процессов**

I. Введение

Эффективность функционирования мелкосерийных многономенклатурных механообрабатывающих производств (ММП) в России остается еще очень низкой. Резервы повышения их эффективности помимо прочего видятся в разработке новых способов

управления производством, особенно таких, которые способны учитывать динамику производства в виде контроля изменений в производственной ситуации.

В настоящее время в наибольшей степени этой концепции удовлетворяет система автоматизированного планирования САПЛ-ТП [1], разрабатываемая на базе СГТУ. Основное ее преимущество заключается в возможности оперативного реагирования на изменение производственной ситуации за счет многовариантности решений на всех этапах планирования ТП, и едином критериальном подходе на стадии разработки и реализации.

При глубокой проработке этапа проектирования, в САПЛ-ТП не выполнена проработка задачи этапа реализации – определение оптимального управления реализацией ТП заданной номенклатуры деталей для производственной ситуации на момент запуска.

II. Постановка задачи

Качественная постановка такой задачи представляется следующим образом. На вход производственной системы, для обработки, поступает некоторый заказ из множества разнотипных деталей, объединенных в партии. ТП для каждого типа детали определяется в САПЛ-ТП, исходя из текущей производственной ситуации. ТП состоит из последовательности операций, которые должны быть полностью выполнены на конкретном типе технологического оборудования (ТО). Производственная система состоит из множества различных типов ТО, объединенных в группы. ТО одной группы в общем случае имеют разную скорость обработки. Каждой операции для обработки назначается группа или множество групп ТО. Каждая операция должна обрабатываться только одним ТО из группы. Все операции должны быть выполнены в строгой последовательности с заданным ТП. Обработка операций ТП происходит без прерываний, переналадок и перехода на другое ТО. На каждом ТО в любой момент времени должно обрабатываться не более одной детали. Каждое ТО требует время на переналадку при переходе к следующей операции, которое также зависит от последовательности и типа операций. Исходные данные для поставленной задачи формируются в САПЛ-ТП на момент запуска. Изменение производственной ситуации (поломки оборудования, изменение статуса заказа и пр.) не входит в постановку задачи, поскольку САПЛ-ТП обрабатывает такую ситуацию путем переопределения входных данных и восстановления способа реализации ТП для новой ситуации. Критерием оптимизации является минимизация общего времени работы производственной системы, т.к. она приводит к максимуму загрузки ТО, снижению себестоимости и повышению рентабельности, что до сих пор является одной из основных задач в механообрабатывающем производстве.

III. Модель управления реализацией ТП

В результате проведенной научной работы, на базе классической модели системы с «различными (фиксированными) порядками прохождения» (job-shop) была получена обобщенная модель реализации ТП, учитывающая такие ключевые особенности процесса как: группирование технологического оборудования, трудоемкость переналадок ТО при выполнении конкретного производственного задания, а также учет рециркуляции и времен загрузки/разгрузки ТО.

Полученная модель формализуется в терминах смешанного целочисленного линейного программирования следующим образом:

Целевой критерий – $C\max = x_b \to \min$

Условие соблюдения маршрута

$$x_{D.Onj} - x_{D.Oni} \geq \sum_{Tpg \in M_{D.Oni}, TOm \in Tpg} T_{\text{шт.}}(D.Oni, Tpg, TOm) z_{D.Oni}^{TOm} + \\ + \sum_{TOm \in M_{D.Oni} \cap M_{D.Onj}} T_{\text{п-з.}}(TOm, D.Oni, D.Onj) z_{D.Oni}^{TOm} z_{D.Onj}^{TOm},$$

$$\forall D \in N, \forall (D.Oni, D.Onj) \in A_D$$

Соблюдение очередности выполнения операций каждым оборудованием

$$x_{J.Onj} + H(1 - y_{D.Oni,J.Onj}) - x_{D.Oni} + H(2 - z_{D.Oni}^{TOm} - z_{J.Onj}^{TOm}) \geq$$

$$\geq \sum_{Tpg \in M_{D.Oni}, TOm \in Tpg} (T_{\text{шт.}}(D.Oni, Tpg, TOm)) z_{D.Oni}^{TOm} + T_{\text{п-з.}}(TOm, D.Oni, J.Onj),$$

$$\forall (D.Oni, J.Onj) \in B, \forall Tpg \in (M_{D.Oni} \cap M_{J.Onj}), \forall TOm \in Tpg$$

$$x_{D.Oni} + Hy_{D.Oni,J.Onj} - x_{J.Onj} + H(2 - z_{D.Oni}^{TOm} - z_{J.Onj}^{TOm}) \geq$$

$$\geq \sum_{Tpg \in M_{J.Onj}, TOm \in Tpg} (T_{\text{шт.}}(J.Onj, Tpg, TOm)) z_{J.Onj}^{TOm} + T_{\text{п-з.}}(TOm, J.Onj, D.Oni),$$

$$\forall (D.Oni, J.Onj) \in B, \forall Tpg \in (M_{D.Oni} \cap M_{J.Onj}), \forall TOm \in Tpg$$

Общее время работы системы x_b

$$x_b - x_{D.Oni} \geq \sum_{Tpg \in M_{D.Oni}, TOm \in Tpg} (T_{\text{шт.}}(D.Oni, Tpg, TOm)) z_{D.Oni}^{TOm},$$

$$\forall D \in N, \forall Oni \in O^D$$

Область определения переменных

$$y_{D.Oni,J.Onj} \in \{0,1\}, \ \forall (D.Oni, J.Onj) \in B$$

$$x_{D.Oni} \geq \sum_{Tpg \in M_{D.Oni}, TOm \in Tpg} (T_{\text{загр}}(D.Oni, Tpg, TOm)) z_{D.Oni}^{TOm},$$

$$\forall D \in N, \forall Oni \in O^D$$

$$x_b \geq 0$$

$$z_{D.Oni}^{TOm} \in \{0,1\}, \ \forall D \in N, \forall Oni \in O^D, TOm \in M_{D.Oni}$$

$$\sum_{TOm \in M_{D.Oni}} z_{D.Oni}^{TOm} = 1, \ \forall D \in N, \forall Oni \in O^D$$

Условие генерации полуактивных расписаний

Исключаются простои машины, если имеется операция, которую она, согласно всем предшествующим ограничениям, может выполнить

Здесь $N = \{D_1, D_2, .. D_n\}$ – это множество из n деталей, $M = \{TO1, TO2.., TOm\}$ – множество из m ТО, и O – множество из o операций.

$D.\text{Оп}1,\ldots,D.\text{Оп}\left|O^D\right|$ – технологический процесс детали D, где O_D – множество операций детали D.

$A_D = \left\{\left(D.\text{Оп}i, D.\text{Оп}j\right) : i < j, 1 \le i < \left|O^D\right|, 1 < j \le \left|O^D\right|\right\}$ – множество всех упорядоченных пар операций одной детали.

Тшт.(D.Опi, Гpg, TOk) > 0 – время штучное выполнения операции D.Опi на TOk.

Тп-з.(TOk, D.Опi, J.Опj) – время, затрачиваемое на переналадку TOk между операциями D.Опi и J.Опj. Каждая группа $Гpg, g = 1..r$ состоит из mg идентичных $TOk \in M$. Таким образом, $\sum_{g=1..r} m_g = \left|M\right|$.

$r^{D.Oni} \le r$ – количество (различных) групп оборудования, назначаемого операции $D.Oni$.

$g^{D.Oni} = \left\{g_q^{D.Oni} : g_q^{D.Oni} \in \left[1..r\right], \forall q = 1..r^{D.Oni}\right\}$ – множество индексов групп ТО, назначенных для операции $D.Oni$.

$$M_{D.Oni} = \left\{TOk : TOk \in Гpg_q^{D.Oni}, \forall g_q^{D.Oni} \in g^{D.Oni}\right\}.$$

B – множество неупорядоченных пар операций $\left(D.\text{Оп}i, J.\text{Оп}j\right)$, принадлежащих различным деталям и имеющих потенциально общие ТО. К переменным модели относятся:

$x_{D.Oni}$ – время начала обработки операции $Oni \in O^D$, детали $D \in N$;

$y_{D.Oni,J.Onj}$ – 1, если D.Опi обрабатывается перед J.Опj, $\left(D.Oni, J.Onj\right) \in B$; иначе – 0;

x_b – время начала обработки фиктивной операции b;

$z_{D.Oni}^{TOm}$ – 1, если D.Опi назначается на $TOm \in M$; иначе – 0.

Полученная обобщенная модель позволила оценить сложность моделируемого процесса и сформировать графоаналитический подход к ее решению. В результате был разработан специальный метаэвристический алгоритм на базе метода поиска с запретом, особенностью которого стала адаптация метода поиска с запретом к новой сложной задаче – задаче реализации ТП. Предложенный метод позволяет использовать сильные стороны известных алгоритмов ([2] и [3]), применявшихся для менее трудных задач, и скомпенсировать их недостатки. В результате были разработаны оригинальный способ построения начального расписания, оригинальный способ построения окрестности поиска допустимых реализаций ТП и специальные методики ускорения поиска.

IV. ЗАКЛЮЧЕНИЕ

Результаты промышленных экспериментов показали, что предложенные модель реализации ТП, а также метод на базе метаэвристического метода поиска с запретом, позволяют сократить время обработки поступившего в ММП заказа от 10% до 40% по сравнению с принятыми на производстве методиками планирования. Применение в САПЛ-ТП разработанных моделей и методов позволит создать более эффективную систему интеллектуальной поддержки принятия решений при реализации технологических процессов механообработки в ММП с учетом динамического состояния многономенклатурного производства.

ССЫЛКИ

[1] Автоматизация проектных процедур реализации технологических процессов в условиях многономенклатурных производственных систем механообработки/ А.А. Иванов, П.Ю. Бочкарев. – Саратов: СГТУ, 2016. – 240 с

[2] R. Burgy and H. Groflin. The blocking job shop with rail-bound transportation. Journal of Combinatorial Optimization, 31(1):152–181, 2016.

[3] M. A. Gonzalez, C. R. Vela, and R. Varela., 2015, Genetic Tabu Search for the Fuzzy Flexible Job Shop Problem, Computers and Operations Research, 54, 74–89.

Dynamics of low-frequency components of photoplethysmogram signals in hypertension

Anatoly Karavaev
Saratov Branch of the Institute of Radio Engineering and Electronics of Russian Academy of Sciences,
Saratov State Medical University,
Saratov State University
Saratov, Russia
karavaevas@gmail.com

Anton Kiselev
Saratov State Medical University,
Saratov State University
Saratov, Russia
kiselev@cardio-it.ru

Ekaterina Borovkova
Institute of Cardiological Research,
Saratov State Medical University,
Saratov State University
Saratov, Russia
rubanei@mail.ru

Yulia Popova
Saratov Branch of the Institute of RadioEngineering and Electronics of Russian Academy of Sciences,
Saratov State Medical University
Saratov, Russia
doctorup@mail.ru

Vladimir Gridnev
Saratov State Medical University,
Saratov State University
Saratov, Russia
gridnev@cardio-it.ruline

Margarita Simonyan
Saratov State Medical University,
Saratov, Russia
dr.m-simonyan@yandex.ru

Olga Posnenkova
Saratov Branch of the Institute of RadioEngineering and Electronics of Russian Academy of Sciences
Saratov State Medical University
Saratov, Russia
posnenkova@cardio-it.ru line

***Abstract* – Oscillations in the low-frequency range of heart rate variability and photoplethysmogram signals are associated with processes of autonomous control of the cardiovascular system. We have previously shown that synchronization of such processes may be a sensitive indicator of the development of certain diseases. In the course of the study it was shown that these processes are accompanied by a change in power spectral density. The work compared the dynamics of power density in healthy people and patients with hypertension.**

***Key words* – Autonomic control, spectral analysis, heart rate variability, photoplethysmogram**

I. INTRODUCTION

Heart rate variability (HRV) processes and fluctuations in the blood supply to the arterial vessels are distinguished by a complex chaotic dynamics [1]. In a number of works, the degree of irregularity of such fluctuations was associated with the state of health [1-3]. For historical and technical reasons, it was mainly the processes of heart rhythm regulation that were investigated. At the same time, fluctuations in the blood supply can carry important information about the state of the arterial vessels and the peculiarities of blood flow regulation. Such oscillations are recorded, in particular, using the method of photoplethysmography. In this case, using the open optocoupler, oscillations of the light transmission of the tissues of the limbs are recorded. This is a cheap and non-invasive method. However, the amplitude of the received signals is difficult to calibrate and its depends on many factors. At the same time, the normalization of the oscillation power to the intensity of the characteristic spectral component allows comparing the results of studies of healthy people and patients. In our works, it was previously shown that the assessment of the degree of synchronization of the low-frequency components of photoplethysmogram (PPG) and HRV makes it possible to diagnose the development of certain diseases [3], personalize the choice of therapy [4-5] and predict the survival of patients after myocardial infarction [6]. The purpose of this work is to study the dynamics of the power spectral density in the low-frequency range of the univariate signal of PPG in healthy people and patients with hypertension.

II. MATERIALS

The study analyzed 12 records of healthy subjects and 12 records of patients with hypertension. The duration of each entry was 10 minutes. The signal of PPG was recorded from a finger sensor. The sensor contained the light-emitting diode and a phototransistor which worked in the infrared range in transmitted light.

Signals were recorded with a standard instrument with a sampling rate of 250 Hz. The bandwidth for -3dB power levels was 0,016-30 Hz.

III. METHODS

In the course of data analysis, signal power spectra were estimated. The periodograms method of Welch was used for this. Time series were divided into 9 windows with a duration of 2 minutes, which shifted with an overlap of 1 minute along the signal. Periodograms were evaluated in each window, which were then averaged. Further, the power spectral density was estimated in the LF (0,04–0,15 Hz) and HF (0,15–0,4 Hz) bands. In accordance with the work of [7-8], the LF range is associated primarily with the sympathetic control of the arterial vessels, and the power in the HF range is associated mainly with parasympathetic activity and the respiratory process. Therefore, the comparison was carried out for the normalized quantities LFn=LF/HF.

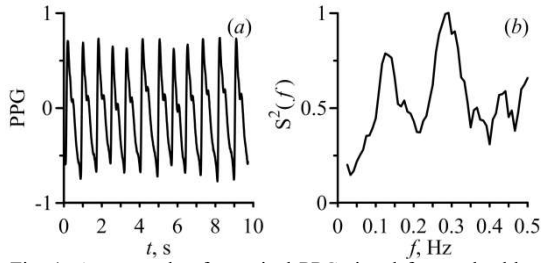

Fig. 1. An example of a typical PPG signal from a healthy subject. (a) - The time series of PPG and (b) - its power spectrum

IV. RESULTS

A typical PPG signal and power spectrum for a healthy subject are presented in Figure 1. Figure 2 shows a typical PPG signal and power spectrum for a patient with hypertension. The spectra are normalized to the maximum power in the HF band. It is seen that the patient power in the LF range is significantly lower than in healthy.

Statistical analysis of the results shows that LFn values in patients with 0,59±0,42 (mean and standard deviation) are significantly lower than in healthy 2,34±1,92. Thus, it was shown that the normalized power of LFn in the low-frequency region of the PPG spectrum is significantly reduced in patients with hypertension.

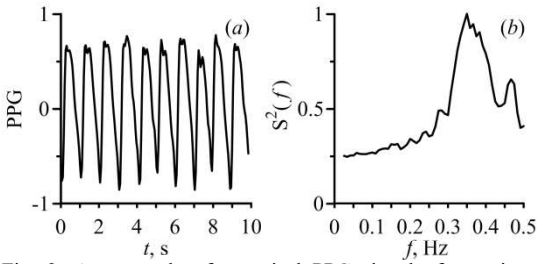

Fig. 2. An example of a typical PPG signal of a patient with arterial hypertension. (a) - The time series of PPG and (b) - its power spectrum

V. CONCLUSIONS

The obtained results are interesting from the point of view of understanding the work of a complex multicomponent object of biological nature the cardiovascular system. The results may also be relevant for the development of medical diagnostic methods.

ACKNOWLEDGEMENTS

Work was carried out within the grant of the President of RF MD-2202.2019.8 and the framework of the state task.

REFERENCES

[1] Wu, G.Q. et al. “Chaotic signatures of heart rate variability”. PLoS One, 2009, vol. 4(2), pp. e4323.

[2] Valenza, G. “Complexity variability assessment of nonlinear time-varying cardiovascular control”. Sci. Rep., 2017, vol. 7, pp. 42779.

[3] Kunz, V. C., Borges, E. N., Coelho, R. C., et al.” Linear and nonlinear analysis of heart rate variability after myocardial infarction in patients”. Braz. J. Med. Biol. Res., 2012, vol. 45(5), pp. 450-458.

[4] Kiselev, A.R., Karavaev, A.S., Gridnev, V.I., et al. “Method of estimation of synchronization strength between low-frequency oscillations in heart rate variability and photoplethysmographic waveform variability”. Russ. Open Med. J., 2016, vol. 5, pp. e0101.

[5] Kiselev, A. R., Gridnev, V. I., Prokhorov, M. D., et al. “Effects of antihypertensive treatment on cardiovascular autonomic control. Anadolu Kardiyol”. Derg., 2014, vol. 14, pp. 701-710.

[6] Kiselev, A. R., Gridnev, V. I., Prokhorov, M. D., et al. “Evaluation of 5-year risk of cardiovascular events in patients after acute myocardial infarction using synchronization of 0.1-Hz rhythms in cardiovascular system”. Ann. Noninvasive Electrocardiol., 2012, vol. 17(3), pp. 204-213.

[7] Bernardi, L., Radaelli, A., Solda, P. L., et al. “Autonomic control of skin microvessels: assessment by power spectrum of photoplethysmographic waves”. Clin. Sci. (Lond.), 1996, vol. 90, pp. 345-355.

[8] Middleton, P. M., Chan, G. S., Steel, E., et al. “Fingertip photoplethysmographic waveform variability and systemic vascular resistance in intensive care unit patients”. Med. Biol. Eng. Comput., 2011, vol. 49, pp. 859-866.

Dynamics of mathematical model of cardio-vascular system

Anatoly Karavaev
Saratov Branch of the Institute of RadioEngineering and Electronics of Russian Academy of Sciences, Department of Innovative Cardiological Information Technology, Institute of Cardiological Research, Saratov State Medical University, Saratov State University
Saratov, Russia
karavaevas@gmail.com

Anton Kiselev
Department of Innovative Cardiological Information Technology, Institute of Cardiological Research, Saratov State Medical University, Saratov State University
Saratov, Russia
kiselev@cardio-it.ru

Ekaterina Borovkova
Department of Innovative Cardiological Information Technology, Institute of Cardiological Research, Saratov State Medical University, Saratov State University
Saratov, Russia
rubanei@mail.ru

Yurii Ishbulatov
Department of Innovative Cardiological Information Technology, Institute of Cardiological Research Saratov State Medical University Saratov Branch of the Institute of RadioEngineering and Electronics of Russian Academy of Sciences
Saratov, Russia
ishbulatov95@mail.ru

***Abstract*—Complex mathematical model of cardio-vascular system was modified with addition of self-exciting time-delay nonlinear loop of heart rate and arterial pressure autonomic control. Taking into account nonlinearity of the control loop it made it possible to simulate the complex dynamics of the real system.**

Keywords—cardio-vascular system, autonomic control, mathematical modeling

I. INTRODUCTION

The Complex nonlinear dynamics is an important characteristic of cardio-vascular system (CVS) [1]. Study of this dynamics is not only important for fundamental understanding but also perspective for medical applications [2-4]. In a number of studies it was shown that development of pathologies and aging causes decrease in complexity of CVS behavior [1, 5].

Several hypothesis were proposed to explain chaotic behavior of CVS. First hypothesis present CVS as dynamic chaotic oscillator, and second hypothesis present CVS as a complex network with many subsystems and dynamical noise originated from other organs and changes in the environment.

Development of mathematical models is a promising way to obtain arguments in favor of one of the hypothesis, since mathematical modeling is widely used to study various systems of biological origin including CVS.

II. MODEL

Proposed model is based on [6], it can simulate following processes: heartbeat; autonomic control of heart rate, contractility, vascular resistance; arterial pressure forming during systolic and diastolic phases of cardiac cycle; Model also includes influence of respiration on the aforementioned processes.

Main feature of the modified model is inclusion of nonlinear autonomic control loops which can produce sustained 0.1 Hz oscillations that can be commonly observed in spectra of heart rate variability and arterial pressure. Addition of self-exciting control loops introduces the possibility to reproduce such effects as synchronization and dynamic chaos. More detailed description can be found in [7].

III. RESULTS

Projected space portraits for cc (noradrenaline concentration in cardiac wall), cv (noradrenaline concentration in vessel wall), p(t) (arterial pressure) are represented in Figure 1(a, b). They were calculated from time-series of 100 seconds long. To calculate ACF (Fig. 1 (c)) we used time-series of 100000 seconds long after transition process of 10000 s.

Complex form of the projections of the phase portrait and ACF decay argue for chaotic nature of the proposed model dynamics. Presence of less-developed dynamic noise is also affirmed by positive value of main Lyapunov exponent [8].

The proposed model is a dynamic system of 5 order, with time delay in some of equations witch complicates calculation of Lyapunov exponents. Therefore we restricted ourselves to calculation of only main Lyapunov exponent in 3d space of cc (noradrenaline concentration in cardiac wall), cv (noradrenaline concentration in vessel wall), p(t) (arterial pressure). We used Wolf method and time-series of 10000 seconds. Time interval for phase trajectories to scatter was

0.5 s. Estimated value of main Lyapunov exponent was 0.045.

Twofold increase and decrease in length of analyzed time series or time interval for phase trajectories to scatter resulted in variations in main Lyapunov exponent of ±0.02.

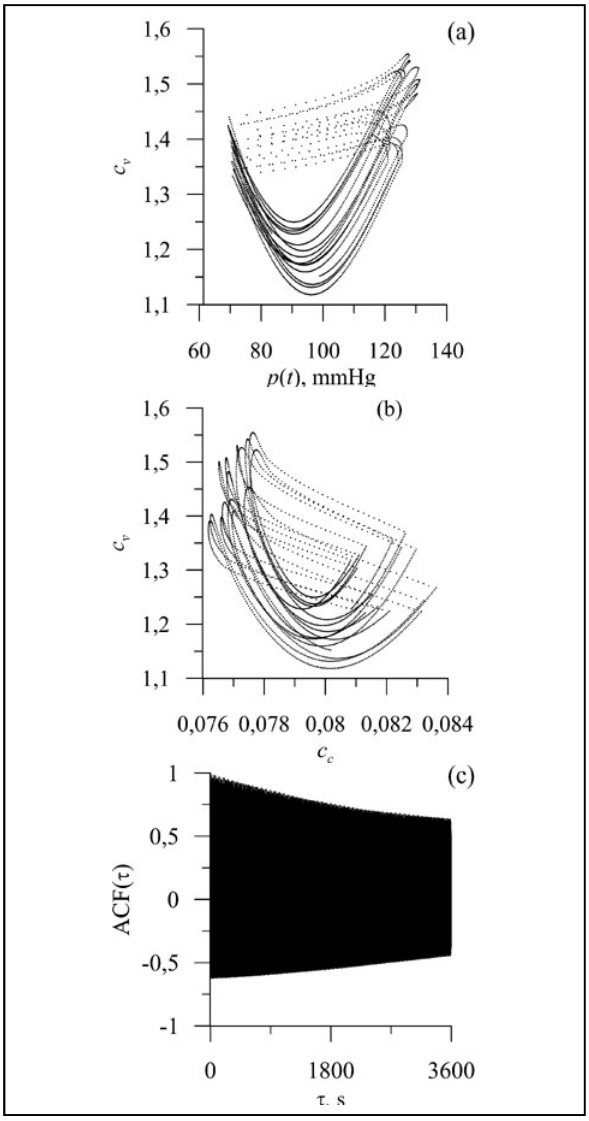

Fig. 1. (a) – projection of phase space on plane c_v-$p(t)$, (b) - on plane c_c-c_v, (c) – ACF for $p(t)$ signal.

IV. Conclusion

It was shown that adoption of the nonlinear autonomic control loops into mathematical model allows simulation of chaotic dynamic of real system within a range of physiologically grounded model parameters.

Acknowledgment

This work was supported by the Russian Science Foundation, Grant № 19-12-00201.

References

[1] A.L. Goldberger, C.-K. Peng, L.A. Lipsitz, "What is physiologic complexity and how does it change with aging and disease?," Neurobiology Aging, vol. 23, pp. 23–26, 2002.

[2] V.A. Shvartz, A.S. Karavaev, E.I. Borovkova, S.A. Mironov, V.I. Ponomarenko, M.D. Prokhorov, Y.M. Ishbulatov, E.E. Lapsheva, V.I. Gridnev, A.R. Kiselev, "Investigation of statistical characteristics of interaction between the low-frequency oscillations in heart rate variability and photoplethysmographic waveform variability in healthy subjects and myocardial infarction patients," Rusian Open Medical Journal, vol. 5, N. 2, pp. e0203, 2016.

[3] A.R. Kiselev, A.S. Karavaev, V.I. Gridnev, M.D. Prokhorov, V.I. Ponomarenko, E.I. Borovkova, V.A. Shvartz, Y.M. Ishbulatov, O.M. Posnenkova, B.P. Bezruchko, "Method of estimation of synchronization strength between low-frequency oscillations in heart rate variability and photoplethysmographic waveform variability," Russian Open Medical Journal, vol. 5, N. 1, pp. e0101, 2016.

[4] A.R. Kiselev, V.A. Shvartz, S.A. Mironov, A.S. Karavaev, D.D. Kulminskiy, M.D. Prokhorov, V.V. Skazkina, E.I. Borovkova, V.I. Ponomarenko, "A comprehensive assessment of cardiovascular autonomic control using photoplethysmograms recorded from the earlobe and fingers," Physiological Measurements, vol. 37, N. 4, pp. 580-595, 2016.

[5] A.R. Kiselev, V.I. Gridnev, O.M. Posnenkova, M.D. Prokhorov, A.S. Karavaev, V.I. Ponomarenko, B.P. Bezruchko, "Effects of antihypertensive treatment on cardiovascular autonomic control: a prospective study," Anadolu Kardiyoloji Dergisi, vol. 14, N. 8, pp. 701-710, 2014.

[6] H. Seidel, H. Herzel, "Bifurcations in a nonlinear model of the baroreceptor-cardiac reflex," Physica D, vol. 115, pp. 145-160, 1998.

[7] A.S. Karavaev, J.M. Ishbulatov, V.I. Ponomarenko, M.D. Prokhorov, V.I. Gridnev, B.P. Bezruchko, A.R. Kiselev, "Model of human cardiovascular system with a loop of autonomic regulation of the mean arterial pressure," Journal of American Soc. Hypertens, vol. 10, N. 3, pp. 235-243, 2016.

[8] Wolf, J.B. Swift, H.L. Swinney, J.A. Vastano, "Determining Lyapunov exponents from a time series," Physica D, vol. 16, N. 3, pp. 285-317, 1985.

Interactions between the processes of regulation of the cardiovascular system and the brain structure

Anatoly Karavaev
Saratov Branch of the Institute of RadioEngineering and Electronics of Russian Academy of Sciences, Department of Innovative Cardiological Information Technology, Institute of Cardiological Research, Saratov State Medical University, Saratov State University
Saratov, Russia
karavaevas@gmail.com

Ekaterina Borovkova
Department of Innovative Cardiological Information Technology, Institute of Cardiological Research, Saratov State Medical University, Saratov State University
Saratov, Russia
rubanei@mail.ru

Anton Kiselev
Department of Innovative Cardiological Information Technology, Institute of Cardiological Research, Saratov State Medical University, Saratov State University
Saratov, Russia
kiselev@cardio-it.ru

Anastasiya Runnova
Autonomous nonprofit organization of higher education Innopolis University
Innopolis, Russia
anefila@gmail.com

Mikhail Prokhorov
Saratov Branch of the Institute of RadioEngineering and Electronics of Russian Academy of Sciences
Saratov, Russia
mdprokhorov@yandex.ru

Vladimir Ponomarenko
Saratov Branch of the Institute of RadioEngineering and Electronics of Russian Academy of Sciences, Saratov State University
Saratov, Russia
ponomarenkovi@gmail.com

Alexander Hramov
Autonomous nonprofit organization of higher education Innopolis University
Innopolis, Russia
hramovae@gmail.com

Vladimir Gridnev
Department of Innovative Cardiological Information Technology, Institute of Cardiological Research, Saratov State Medical University, Saratov State University
Saratov, Russia
gridnev@cardio-it.ru

Boris Bezruchko
Saratov Branch of the Institute of RadioEngineering and Electronics of Russian Academy of Sciences, Saratov State University
Saratov, Russia
bezruchkobp@gmail.com

***Abstract*— we have developed a method for the detection of directional couplings between the respiratory process, infra-slow oscillations of electroencephalogram (EEG) and heart rate variability (HRV), having a characteristic frequency close to 0.1 Hz. The technique is tested during the analysis of the records of healthy awake subjects during spontaneous breathing. It is shown that the use of nonlinear approaches based on the analysis of phase dynamics provides a high sensitivity analysis of the coupling between the elements of a complex multichannel system of biological nature.**

Keywords—electroencephalogram, autonomic regulation, cardiovascular system, respiration process, nonlinear dynamics

I. INTRODUCTION

The study of the interaction of the infra-slow oscillations of the EEG and the signals of the Autonomic Regulation of Cardiovascular Function contours with a characteristic frequency close to 0.1 Hz is important from a fundamental and applied point of view [1, 2].

Recently we have studied the synchronisation in the infra-slow oscillations of the EEG [3, 4], the respiration process, and the signals of the Autonomic Regulation of Cardiovascular Function contours [5, 6] in awake healthy people during special active experiments.

In these studies, the respiratory frequency of healthy subjects changed according to a given law. The staging of an active experiment in combination with the use of methods for analyzing phase dynamics made it possible to detect the capture of frequencies and phases of infra-slow oscillations of EEG by breathing, to reveal signs of the presence of several self-oscillating structures in different brain regions involved in the formation of infra-slow oscillations of EEG.

In [7], an analysis of the coherence function of the studied processes was carried out.

The next step is to study the structure of the directional connections between respiration, infra-slow oscillations and elements of the vegetative regulation of the cardiovascular system.

The purpose of this study was to evaluate the opportunity of revealing the couplings between the respiratory process, infra-slow oscillations of electroencephalogram (EEG) and heart rate variability (HRV), which have a characteristic frequency close to 0.1 Hz, in awake healthy people at rest during spontaneous breathing using nonlinear methods of analysis of the phase dynamics of the studied systems.

II. EXPERIMENTS

The study involved three subjects, who simultaneously recorded signals from non-invasive scalp EEG, electrocardiograms (ECG) and respiration during spontaneous breathing. Registration duration was 30 minutes.

For non-invasive registration of 19 EEG leads, the standard "10-20" scheme was used. Simultaneously with the EEG channels, the I standard ECG lead was recorded, as well as a breathing signal by an abdominal strain gauge sensor.

Registration was carried out using a standard certified device Encephalan–EEGR–19/26 (Medicom MTD, Russia) with a quantization of 16 bits, a sampling frequency of 250 samples per second per channel. The bandwidth for the EEG channels was 0.0016-80 Hz, for the ECG channel - 0.003-80 Hz, for the breathing signal 0.003-80 Hz.

III. Methods

To increase the reliability of the analysis results, several methods of diagnosing coupling were simultaneously used.

First of all, the coupling was diagnosed using an estimate of the phase coherence coefficient □ [8].

Secondly, the coherence function C(f) was calculated, which characterizes the coupling of the spectral components of the analyzed signals using the cross-spectrum estimation [9].

Thirdly, according to the experimental data, the analysis of the directed couplings was carried out using the phase dynamics modeling method [10].

We evaluated the intensity of the impact and the analytical 95 percent confidence interval, as in [11].

In order to establish the fact of coupling, the difference between the estimates of the "strength" of coupling and, together with the 95 percent confidence interval, was verified from zero. The calculation was carried out at a time shift between rows □=10 seconds and trial lag values $\Delta_{j\to k}$ of 0-20 seconds.

IV. Results

For all subjects, an analysis of the coupling between the respiration process, infra-slow oscillations of the EEG and heart rate variability (HRV) was carried out using the methods described above. Coupling between the fluctuations of EEG leads and heart rate variability (HRV) was analyzed in the 0.04–0.15 Hz band (so-called Low Frequency – LF range [12]).

Coupling between the oscillations of EEG leads and respiration was analyzed in the 0.15–0.4 Hz band (High Frequency - HF range [12]).

It turned out that in a typical case it is not possible to identify any statistically significant values of the coefficient □ of fluctuations of EEG leads in the LF and HF ranges. For the EEG leads and respiration signal in the HF range, the average and standard deviation of the coefficient □□according to the statistics of all subjects and leads is 0.14 ± 0.08, for the EEG leads and HRV in the LF range is 0.16 ± 0.07. Coupling between HRV and respiration in the LF range is 0.18 ± 0.12, in the HF range 0.16 ± 0.02.

The coherence function C(f) significantly increases and is statistically significant at frequencies close to 0.1 Hz when analyzing the coherence of HRV and a number of EEG leads (Fig. 1 (a)), is low and is observed on the verge of significance level in the analysis of EEG with respiration at frequencies of spontaneous breathing (about 0.3 hz) (Fig. 1 (b)).

For the EEG leads and the respiration signal in the HF range, the mean and standard deviation C(f) according to the statistics of all subjects and leads is 0.59 ± 0.05, for the EEG leads and HRV in the LF range - 0.62 ± 0.08. The C(f) score between HRV and respiration in the LF range is 0.90 ± 0.04, in the HF range 0.16 ± 0.02 [17].

The distribution of the average values of the coherence function over the scalp surface is shown in Figure 2. It is seen that there is an increase in coherence in the region of the vertex.

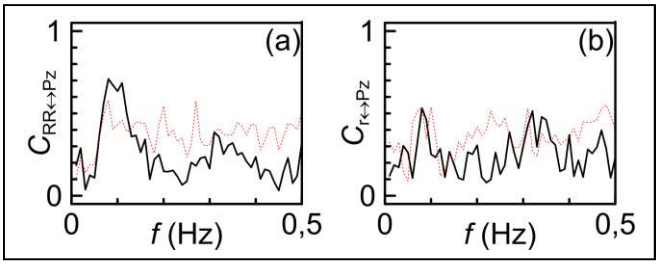

Fig. 1. The coherence function of the lead Pz EEG and (a) HRV, (b) – respiration for subject # 9. Solid line is the value of the coherence function. Dotted line is 95% significance level.

A quantitative analysis of the maximum values of the coherence function indicates that regulation processes with frequencies close to 0.1 Hz in EEG and HRV and EEG processes and spontaneous breathing with characteristic frequencies of about 0.3 Hz demonstrate high coherence, which makes it difficult to interpret the results and determine the direction of coupling, since the analytical formula for estimations of the confidence interval with strong connection does not work [9].

Therefore, the diagnosis of directional connections was accompanied by the control of statistical significance by generating surrogate data from the Amplitude Adjusted Fourier Transform ensemble [13].

Diagnostics of directional connections revealed a significant interaction of infra-slow oscillations of EEG with HRV rhythms in the LF range, which is associated mainly with the sympathetic regulation of blood circulation [7]. At the same time, the effect from HRV to EEG (Fig. 3 (b)) is most pronounced than the effect from EEG to HRV (Fig. 3 (a)).

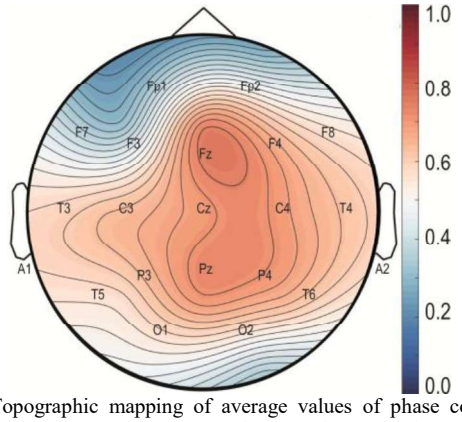

Fig. 2. Topographic mapping of average values of phase coherence coefficient during spontaneous respiration of EEG and HRV in the frequency range of 0.05-0.15 Hz. Scale in units of coherence function.

The impact of respiration on the infra-slow oscillations in the HF range that is primarily associated with the parasympathetic regulation of blood circulation is usually insignificant (Fig. 3 (c)). For most leads, it is possible to identify the pronounced significant effect of infra-slow oscillations of the EEG on the breathing process (Fig. 3 (d)).

As a result it was revealed that the interaction of the HRV components with respiration in the characteristic for respiration HF frequency range is quite strong. The most pronounced effect is from respiration to HRV in the LF frequency range.

The detected delays due to the order of a few seconds (Fig. 3 (b), Fig. 1 (d)) may indicate the complex nature of the interaction of the studied processes of the infra-slow oscillation and HRV with breathing, including temporary delays in the couplings. The technique was tested during the analysis of the records of three healthy awake subjects during spontaneous breathing in healthy people during spontaneous breathing.

The most pronounced effect of the respiration on the low-frequency components of HRV, the impact of the HRV on the low-frequency components of the infra-slow oscillations of the EEG, the impact of the low-frequency components of the infra-slow oscillations of the EEG on the respiration process. The results testify in favor of the fact that the interaction of the processes under consideration is non-linear nature and organized through a complex network structure.

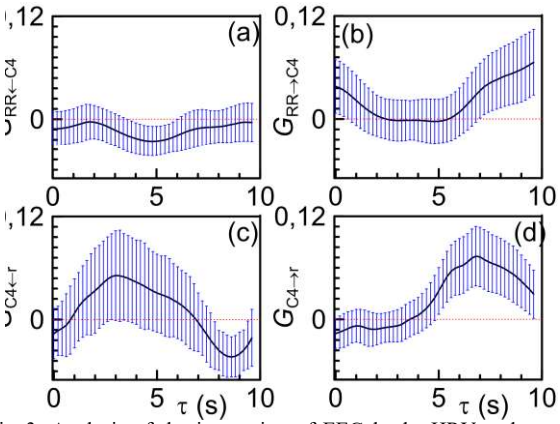

Fig. 3. Analysis of the interaction of EEG leads, HRV and respiration during the spontaneous breathing of the subject # 9. Results of diagnostics of directional coupling based on modeling the phase dynamics of the lead C4 of EEG and (a, b) - HRV, (c, d) - respiration. Solid line is the value of the G. Whiskers marks the 95% confidence interval for the difference between G and 0, calculated using an analytical formula. The arrows in the title of the vertical axis indicate the direction of the coupling being tested. A zero G value is indicated by a horizontal dotted red line. On the horisontal axes of the graphs, the tested lag between the signals was postponed.

ACKNOWLEDGMENT

This work was supported by the Russian Science Foundation, Grant № 19-12-00201.

REFERENCES

[1] N.A. Aladjalova, "Infra-Slow Rhythmic Oscillations of The Steady Potential of the Cerebral Cortex," Nature, vol. 179, pp. 957-969, 1957.

[2] R. Vandenhouten, M. Lambertz, P. Langhorst, R. Grebe, "Nonstationary time-series analysis applied to investigation of brainstem system dynamics," IEEE Trans. Biomed. Eng., vol.47, pp. 729-737, 2000.

[3] A.S. Karavaev, A.R. Kiselev, A. E. Runnova, M.O. Zhuravlev, E.I. Borovkova, M.D. Prokhorov, V.I. Ponomarenko, S.V. Pchelintseva, T.Yu. Efremova, A.A. Koronovskii, A.E. Hramov, "Synchronization of infra-slow oscillations of brain potentials with respiration," CHAOS, vol. 28, pp. 081102, 2018.

[4] A.S. Karavaev, A.E. Runnova, E.I. Borovkova, Y.M. Ishbulatov, V.S. Khorev, A.R. Kiselev, M.O. Zhuravlev, V.I. Ponomarenko, M.D. Prokhorov, B.P. Bezruchko, A.A. Koronovsky, "Synchronization of low-frequency rhythms in electroencephalogram by respiration with frequency linearly dependent from time," Physiology and Pathophysiology, vol. 12, N. 4, pp. 541-548, 2016.

[5] V.I. Ponomarenko, M.D. Prokhorov, A.S. Karavaev, A.R. Kiselev, V.I. Gridnev, B.P. Bezruchko, "Synchronization of low-frequency oscillations in the cardiovascular system: Application to medical diagnostics and treatment," The European Physical Journal Special Topics, vol. 222, pp. 2687–269, 2013.

[6] A.R. Kiselev, A.S.Karavaev, V.I. Gridnev, M.D. Prokhorov, V.I. Ponomarenko, E.I. Borovkova, V.A Shvartz, Y.M. Ishbulatov, O.M. Posnenkova, B.P. Bezruchko, "Method of estimation of synchronization strength between low-frequency oscillations in heart rate variability and photoplethysmographic waveform variability," Russian Open Medical Journal, vol. 5, iss. 1, pp. e0101, 2016.

[7] A.S. Karavaev, A.R. Kiselev, A.E. Runova, A.A. Koronovskii, "Coherence of low-frequency oscillations of electroencephalogram and the process of autonomous regulation of heart rhythm," The Second School for Young Scientists "Dynamics of Complex Networks and their Application in Intellectual Robotics", pp. 127-129, 2018.

[8] F. Mormann, K. Lehnertz, P. David, C.E. Elger, "Mean phase coherence as a measure for phase synchronization and its application to the EEG of epilepsy patients," Physica D, vol. 144, issue 3-4, pp. 358-369, 2000.

[9] J.S. Bendat, A.G. Piersol, Random data: analysis and measurement procedures. Indianapolis: Wiley, 2000.

[10] M.G. Rosenblum, A.S. Pikovsky, "Detecting direction of coupling in interacting oscillators," Phys. Rev. E., vol. 64, pp.045202, 2001.

[11] Smirnov, B. Bezruchko, "Estimation of interaction strength and direction from short and noisy time series," Phys. Rev. E., vol. 68, pp. 046209, 2003.

[12] "Heart rate variability. Standards of measurement, physiological interpretation, and clinical use. Task Force of the European Society of Cardiology the North American Society of Pacing Electrophysiology," Circulation, vol. 93, pp. 1043-1065, 1996.

[13] T. Schreiber, A. Schmitz, "Improved Surrogate Data for Nonlinearity Tests", Phys. Rev. Lett, vol. 77. N. 4. pp. 635–638, 1996.

Trajectory optimization for underactuated systems using reinforcement learning: cart-pole problem

Khakimov Pavel
Center for Technologies in Robotics and Mechatronics Components
Innopolis University
Innopolis, Russian Federation
p.khakimov@innopolis.ru

Savin Sergei
Center for Technologies in Robotics and Mechatronics Components
Innopolis University
Innopolis, Russian Federation
s.savin@innopolis.ru

Alexandr Klimchik
Center for Technologies in Robotics and Mechatronics Components
Innopolis University
Innopolis, Russian Federation
a.klimchik@innopolis.ru

Оптимизация траекторий механических систем с дефицитом управляющих воздействий с помощью обучения с подкреплением на примере задачи маятника на тележке

Хакимов Павел
Центр технологий компонентов робототехники и мехатроники
Университет Иннополис
Иннополис, Россия
p.khakimov@innopolis.ru

Савин Сергей
Центр технологий компонентов робототехники и мехатроники
Университет Иннополис
Иннополис, Россия
s.savin@innopolis.ru

Климчик Александр
Центр технологий компонентов робототехники и мехатроники
Университет Иннополис
Иннополис, Россия
a.klimchik@innopolis.ru

***Abstract*— In this article, trajectory optimization of an inverted pendulum on a cart with machine learning tools is analyzed. Reinforcement learning and Q-learning algorithm are used for searching and optimization of trajectories. Results show that combination of Monte Carlo update method with TD(0) outperforms each of them**

Keywords*— *reinforcement learning, underactuated system, cart-pole

***Аннотация*— В этой статье исследуется возможность оптимизации траектории маятника на тележке с помощью методов машинного обучения. Для поиска и оптимизации траекторий используется обучение с подкреплением и Q-learning алгоритмы. Показано, что при комбинации методов Monte-Carlo и TD(0) процесс обучения происходит быстрее, чем при использовании каждого из методов по отдельности**

Ключевые слова*— *обучение с подкреплением, система с дефицитом управляющего воздействия, маятник на тележке

I. Введение

Современная робототехника все сильнее опирается на алгоритмы машинного обучения. Достижения, полученные в областях компьютерного зрения и движения автономного транспорта дают основания полагать, что классические методы управления могут быть эффективно дополнены инструментами машинного обучения. Одним из таких подходов является обучение с подкреплением (reinforcement learning) [1]. Обучение с подкреплением — это метод машинного обучения, при котором происходит обучение агента, который не имеет сведений о среде в которой тот функционирует (модельном мире, в англ. литературе environment), но имеет возможность производить какие-либо действия в нем. Действия переводят агента в новое состояние, а модель возвращает вознаграждение, используемое в процессе обучения [2].

II. Постановка задачи

Рассматривается тележка с установленным на ней обратным однозвенным маятником и препятствие в виде стены. Стена находится ниже траектории движения тележки и является препятствием для маятника. На тележку происходит дискретное внешнее воздействие (сила, принимающая одно из нескольких возможных значений). Стена находится в начале координат, тележка на фиксированном расстоянии от стены.

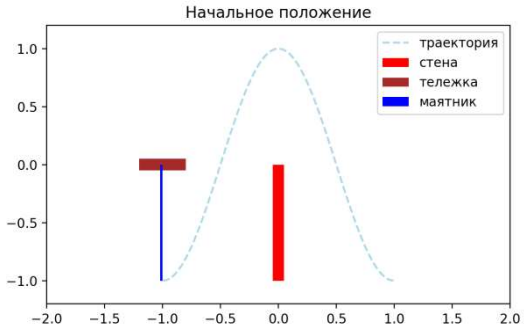

Рис. 1. Иллюстрация задачи

A. Задача

Найти закон воздействия на тележку со свободным маятником, переводящий ее из начального состояния A в симметричное относительно препятствия финальное состояние B, избегая столкновений между маятником и стеной.

Б. Модель

Для простоты вычислений примем ряд упрощений: масса тележки - 1 кг, масса стержня - 1 кг, длина маятника - 1 м, высота стены - 1 м, расстояния от стены до стержня - 1 м. Свободный конец маятника нужно перевезти из точки A(-1, -1) в точку B(1, -1).

При таких начальных условиях данная задача будет описываться следующими дифференциальными уравнениями:

$$\begin{cases} 2\ddot{x} + \ddot{\theta}\cos(\theta) - \dot{\theta}^2 \sin(\theta) = f \\ \ddot{x}\cos(\theta) + \ddot{\theta} - g\sin(\theta) = 0 \end{cases} \quad (1)$$

Где f это дискретное внешнее воздействие. Данную систему дифференциальных уравнений можно записать в векторной форме как, так называемые, манипуляторные уравнения:

$$\mathbf{M}(\mathbf{q})\ddot{\mathbf{q}} + \mathbf{C}(\mathbf{q}, \dot{\mathbf{q}})\dot{\mathbf{q}} + \mathbf{G}(\mathbf{q}) = \boldsymbol{\tau} \quad (2)$$

где $\mathbf{q} = [x \quad \theta]$ вектор обобщенных координат, $\mathbf{M}(\mathbf{q})$ - обобщенная матрица инерции, $\mathbf{C}(\mathbf{q}, \dot{\mathbf{q}})$ - матрица инерционных сил, $\mathbf{G}(\mathbf{q})$ - вектор гравитационных сил и $\boldsymbol{\tau}$ - управляющее воздействие.

Постановка задачи похожа на классическую задачу cart-pole [3], реализованную в фреймворке для тестирования алгоритмов машинного обучения OpenAI Gym [4]. Отличие состоит в том, что классическая задача cart-pole состоит в удержании маятника в положении неустойчивого равновесия, т.е. задача стабилизации. Задача перевода тележки из одной точки в другую - это задача поиска траектории. Это два разных класса задач, для которых применимы инструменты обучения с подкреплением.

Пространство состояний данной системы четырехмерное, и включает положение тележки, угол между маятником и тележкой, линейную скорость тележки и угловую скорость маятника. Пространство управляющих воздействий состоит из 3-х дискретных воздействий: -1, когда сила действует влево; 1, когда сила действует вправо; 0, когда сила не действует. Тогда решение задачи обучения с подкреплением в данном случае, это значит найти отображение $\pi: \square^4 \to \{-1 \quad 0 \quad 1\}$ из пространства состояний системы в пространство управляющих воздействий, которое бы максимизировало вознаграждение за период работы агента.

III. Q-LEARNING АЛГОРИТМ

Существует несколько подходов к поиску интересующего нас решения в виде отображения π. Одним из таких подходов является Q-learning алгоритм [5]. В своей классической форме, он применим для случаев, когда управляющее воздействие принадлежит некоторому множеству с конечным числом элементов. Это вызвано тем фактом, что в каждый момент времени алгоритм просматривает все достижимые состояния и выбирает наилучшее из возможных. Если управляющее воздействие будет непрерывным, например, принимающим любые значения из интервала [0, 1], то из теоретико-множественных соображений становится ясно, что достижимых состояний бесконечно много. В ситуациях, когда управляющее воздействие непрерывное, применяются другие алгоритмы обучения с подкреплением. Примером могут служить алгоритмы: DDPG, A3C, TRPO, PPO [6]. Они все используют глубокие нейронные сети.

Q-learning можно реализовать как через глубокие нейронные сети, как это делает так называемый DQN алгоритм, так и без них, храня статистику посещений в таблице, не тренируя при этом глубокую нейронную сеть. У каждого из подходов есть свои преимущества и недостатки. Преимущества DQN в универсальности. Алгоритм не сильно зависит от размерности пространства состояний. Нет концептуальной разницы или это вектор 4-хмерного пространства или это изображение, которое можно интерпретировать как вектор, например, 400-мерного пространства.

Преимущества обычного Q-learning в простоте реализации и в простоте интерпретации результатов. Результатом его работы является заполненная структура данных типа "массив" или "словарь". Именно из-за простоты реализации Q-learning можно рассматривать в качестве базового (baseline) алгоритма.

A. Дискретизация

Чтобы реализовать классический Q-learning алгоритм, нужно разбить пространство состояний (state space) на непересекающиеся части, и каждой из частей сопоставить число, которое можно интерпретировать как общую сумму вознаграждения, которую агент сможет накопить в будущем, начиная с этого состояния. Чем выше число, тем выше шансы успешно довезти тележку до финального состояния. Разбиение непрерывного пространства на конечное число элементов называется дискретизацией. Самый простой способ организации данных о пространстве состояний - это хранить значения в массиве.

Б. Сэмплирование

Дискретизировать есть смысл только часто посещаемые области. Для нахождения этих областей нужно выполнить множество моделирований (экспериментов). Эксперименты не обязательно должны быть успешными, их цель - получить статистику посещений и определить границы в которых каждое из состояний изменяется. Этот метод называется сэмплированием.

IV. Результаты

Для описанной выше задачи была написана среда для тестирования алгоритмов и с её помощью были проведены численные эксперименты. Первый эксперимент состоял в использовании стохастического агента со стохастическим управлением (random policy). В среднем на 1000 симуляций, только 3 симуляции завершались успешно. Второй эксперимент - это дискретизация пространства состояний и применение итеративного алгоритма Q-learning TD(0). После 10000 симуляций процесс обучения вышел на плато и показывал в среднем 1 успешную симуляцию на 10 неуспешных.

Третий эксперимент - это применение итеративного алгоритма Q-learning Monte-Carlo. Этот эксперимент показал худший результат, чем агент со стохастическим управлением. Четвертый эксперимент представлял собой комбинацию Q-learning TD(0) и Q-learning Monte-Carlo. После каждой успешной симуляции происходил пересчет значений методом Monte-Carlo, во всех других случаях пересчет значений происходил методом TD(0). Комбинация этих двух подходов дала значительный прирост в скорости обучения агента (см. рисунок 2).

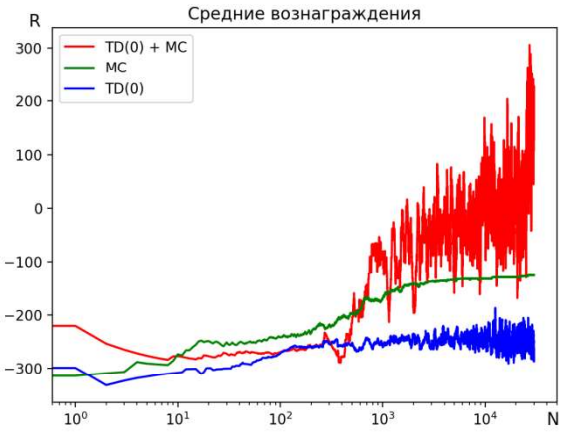

Рис. 2. Средняя величина вознаграждения агента как функция от эпохи

Как видно из рисунка с ростом числа симуляций n растет и среднее вознаграждение агента $\overline{R}$. Стоит отметить, что максимально возможное среднее вознаграждение по итогам одной симуляции не может превзойти 1000. Это означает, что с какого-то момента алгоритм выйдет на плато.

V. Заключение и дальнейшая работа

В этой статье был предложен метод обучения агента для поиска траекторий маятника на тележке с применением TD(0) и Monte-Carlo методов в рамках Q-learning и обучения с подкреплением. Предложенных подход демонстрирует устойчивый процесс обучения. В дальнейшем предполагается:

- реализовать DQN алгоритм и сравнить его результаты с результатами работы Q-learning. Можно сравнивать как скорости обучения, так и быстродействие агентов: какой из агентов переводит тележку в конечное состояние за меньшее число шагов.
- Ввести непрерывное управление. Теперь в качестве управляющего воздействия может служить любое число из отрезка [0,1]. Реализовать стохастические алгоритмы: DDPG, A3C, TRPO. Сравнить их быстродействие.
- После введения непрерывного управления можно искать решения, удовлетворяющие более сложным критериям. Например, кусочно-непрерывные управляющие сигналы или управляющие сигналы с ограничениями на скорость изменения величины сигнала. Это даст возможность использовать найденные законы управления на экспериментальной установке.

Благодарности

Эта работа была поддержана Министерством науки и высшего образования Российской Федерации, в рамках проекта «Разработка программно-аппаратного комплекса обеспечения движения по гладкой и пересеченной местности антропоморфных робототехнических комплексов с приводами переменной жёсткости» (Соглашение о предоставлении субсидии № 075-10-2019-049 (№14.606.21.0007), Уникальный Идентификатор RFMEFI60617X0007)

Ссылки

[1] Arulkumaran, K., Deisenroth, M.P., Brundage, M. and Bharath, A.A., 2017. Deep reinforcement learning: A brief survey. IEEE Signal Processing Magazine, 34(6), pp.26-38.

[2] Garcıa, J. and Fernández, F., 2015. A comprehensive survey on safe reinforcement learning. Journal of Machine Learning Research, 16(1), pp.1437-1480.

[3] Riedmiller, M., Peters, J. and Schaal, S., 2007, April. Evaluation of policy gradient methods and variants on the cart-pole benchmark. In 2007 IEEE International Symposium on Approximate Dynamic Programming and Reinforcement Learning (pp. 254-261). IEEE.

[4] Brockman, G., Cheung, V., Pettersson, L., Schneider, J., Schulman, J., Tang, J. and Zaremba, W., 2016. Openai gym. arXiv preprint arXiv:1606.01540.

[5] Watkins, C.J. and Dayan, P., 1992. Q-learning. Machine learning, 8(3-4), pp.279-292.

[6] Lillicrap, T.P., Hunt, J.J., Pritzel, A., Heess, N., Erez, T., Tassa, Y., Silver, D. and Wierstra, D., 2015. Continuous control with deep reinforcement learning. arXiv preprint arXiv:1509.02971.

Assymetry of coupling between the P3 and P4 electroencephalographic leads during the motions

Vladimir Khorev
Center for Technologies in Robotics and Mechatronics Components, Innopolis University,
Innopolis, Russia
0000-0001-6613-8940

Yuri Ishbulatov
Saratov State University, Saratov Branch of the Institute of RadioEngineering and Electronics of Russian Academy of Sciences, Saratov State Medical University named after V. I. Razumovsky
Saratov, Russia
0000-0003-2871-5465

Ekaterina Borovkova
Department of Dynamic Modeling and Biomedical Engineering
Saratov State University
Saratov, Russia
0000-0002-9621-039X

Vladimir Gridnev
Department of Innovative Cardiological Information Technology, Institute of Cardiological Research
Saratov State Medical University
Saratov, Russia
0000-0001-6807-7934

Anatoly Karavaev
Saratov branch of the Institute of *RadioEngineering and Elecrronics of Russian Academy of Sciences, Department of Innovative Cardiological Information Technology, Institute of Cardiological Research*
Saratov State Medical University,
Saratov, Russia
0000-0003-4678-3648

***Abstract* — Based on the coupling analysis we analyze electroencephalograms (EEGs) acquired in untrained humans (operators) during real and imaginary movements, and show a difference between the related EEG signals and the recordings performed during real movements or the background electrical brain activity.**

Keywords—asymmetry, EEG, connection, motion

I. INTRODUCTION

Diagnosing the connectivity parameters between leads is an important task that attracts the attention of many researchers [1-3]. However, often classical mathematical methods based on time-frequency, wave or component analysis do not allow to assess the degree of interaction between the systems [4,5] due to significant complexity, nonstationarity, noise and poorly structured data. Therefore, the application of various measures of nonlinear dynamics to these data is promising.

II. DATA AND METHODS

Specific dynamics of electrical brain activity is associated with "mental actions" being a compilation of imaginary commands. The study involved non-invasive EEG signals registered from 15 healthy subjects with (19 electrodes with a 10-20 arrangement) during special active experiments. All experimental studies were conducted in accordance with the Helsinki Declaration of the World Medical Association. Each subject participated in one experiment lasting about 30 minutes. For each subject, the active experiment was performed from 1 to 5 times. In active experiments, the special software randomly generated on the screen one of nine instructions about real or imaginary movements of the arms and legs, which the subject had to perform or imagine 10 to 15 times on commands at the moments of playing special sound signals.

The active experiment included the following instructions: "Raising the left leg with the leg locked in the upper position for 0.5 seconds", "Imagination of the left leg raising with the leg locked in the upper position for 0.5 seconds", "Raising the right leg with the leg locked in the upper position on 0.5 seconds", "Imagination of raising the right leg with fixing the leg in the upper position for 0.5 seconds", "Exercising the raising of the left hand with fixing the arm in the upper position for 0.5 seconds", "Imagination of raising the left hand with fixing the arm in the upper position on 0.5 seconds", "Raising the right hand with the fixation of the hand in the upper position for 0.5 seconds", "Imagination of raising the right hand with the fixation of the arm in the upper position for 0.5 seconds". Before and after conducting an active experiment, the background EEG recording was recorded without the subject performing special instructions. For further analysis we used theta band frequency range 3-7 Hz [6].

For data analysis we used a method based on modeling phase dynamics [7] between the signals of non-invasive scalp EEG leads P3 and P4. The main idea of the method consists in evaluating the impact measure to improve the forecast produced using a joint model of the phase dynamics of the systems under study, compared with the forecast obtained using an individual model. Exceeding the estimated coupling measure in the direction of impact from one of the systems to another can be interpreted as the direction of the prevailing influence in this case, the position of the maximum in the dependence of the impact measure estimate

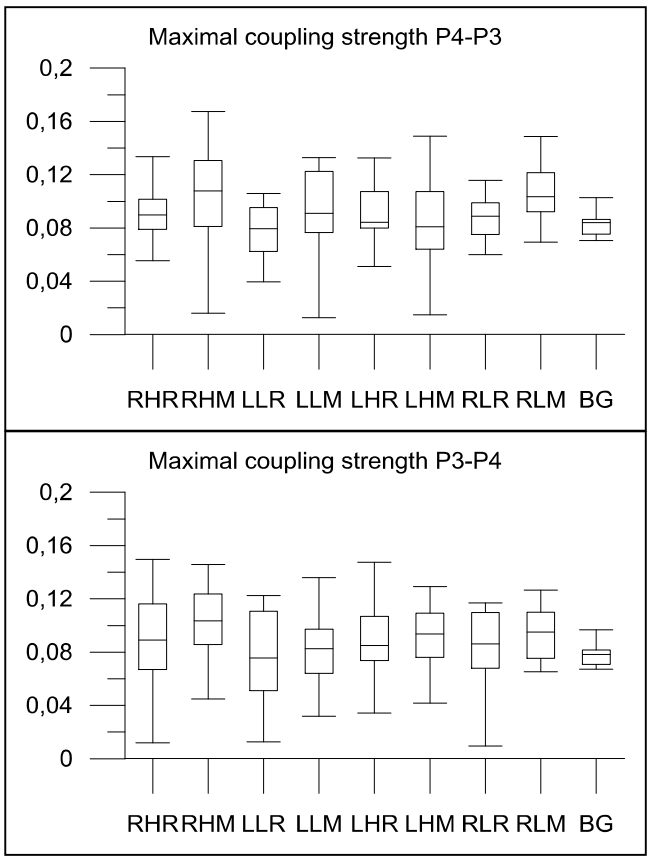

Fig. 1 Maximal observed coupling strength values for a different movement sessions. The box and whisker plot: the ends of the box are the upper and lower quartiles, so the box spans the interquartile range. the median is marked by a vertical line inside the box. the whiskers are the two lines outside the box that extend to the highest and lowest observations.

can be used to estimate the delay in connection corresponding to this direction impact. For the method of the phase dynamics analysis, the values of the delay parameters were selected equal to a single period and the range of the analyzed time shift between the rows of 1 second.

III. RESULTS

Maximal observed coupling strength values are shown in Fig. 1. In a box and whisker plot: the ends of the box are the upper and lower quartiles, so the box spans the interquartile range. the median is marked by a vertical line inside the box. the whiskers are the two lines outside the box that extend to the highest and lowest observations. The “RHR” column corresponds to the right hand real movement, RHM — right hand imaginary, LHR — left hand real, LHM — left hand imaginary, LLR — left leg real, LLM — left leg imaginary, RLR — right leg real, RLM — right leg imaginary, BG — background activity. Statistical analysis of the absolute values of the phase coupling showed that during the conduct of active movement sessions, the magnitude of the bond is equally likely to exceed or be less than the bond value in the background part of the experiment. We revealed an increase in the coupling strength force in the case of imaginary movement. Mean delays corresponding to the maximal coupling strength values are given in the Table 1. Statistical analysis of the delay values showed that during the conduct of active movement sessions mean delays are significantly lower than during background activity.

TABLE I.

Movement type	Direction P3-P4	
	Average Maximal Coupling strength delay	*Standard deviation*
Right hand real	0,145455	0,015207
Right hand imaginary	0,156842	0,036011
Left leg real	0,127273	0,027107
Left leg imaginary	0,145263	0,013518
Left hand real	0,18	0,072
Left hand imaginary	0,191579	0,109141
Right leg real	0,138182	0,009917
Right leg imaginary	0,183333	0,083704
Background activity	0,391429	0,230204
	Direction P3-P4	
	Average Maximal Coupling strength delay	*Standard deviation*
Right hand real	0,145455	0,017851
Right hand imaginary	0,184211	0,087535
Left leg real	0,154545	0,046612
Left leg imaginary	0,18	0,082105
Left hand real	0,136	0,0096
Left hand imaginary	0,224211	0,159114
Right leg real	0,127273	0,029752
Right leg imaginary	0,16	0,062222
Background activity	0,368571	0,343673

Such asymmetry in the coupling strength and delay between signals can be used to distinguish real and imaginary movements based on short fragments of experimental recordings that is important for potential application.

ACKNOWLEDGMENT

This work has been supported by the Center for Technologies in Robotics and Mechatronics Components (Innopolis University)..

REFERENCES

[1] N. Pisarchik, P. Chholak, A. E., Hramov, Brain noise estimation from MEG response to flickering visual stimulation. Chaos, Solitons & Fractals: X. 2019; vol. 1, pp. 100005.

[2] Schutter, D.J., & Hortensius, R. Brain oscillations and frequency-dependent modulation of cortical excitability. Brain Stimulation, 2011, vol. 4, pp. 97-103.

[3] T. Shibata, T. Musha, Y. Kosugi, et al. Boundary EEG Asymmetry Is Associated to Linguistic Competence in Vascular Cognitive Impairments. Front Hum Neurosci. 2018; vol. 12, pp. 170.

[4] S. Karavaev, A. R. Kiselev, A. E. Runnova, et al. Synchronization of infra-slow oscillations of brain potentials with respiration CHAOS, 2018; vol. 28, 081102.

[5] S. Karavaev, V. I. Ponomarenko, M. D. Prokhorov Reconstruction of scalar time-delay system models. Technical Physics Letters, 2001; - vol. 27. - № 5. - pp. 414-418.

[6] P. Tass, D. A. Smirnov, A. S. Karavaev, et al. The causal relationship between subcortical local field potential oscillations and Parkinsonian resting tremor. Journal of neural engineering, 2010, vol. 7. 16009.

[7] D.A. Smirnov, M. B. Bodrov, J.L. Perez Velazquez, et al. Estimation of coupling between oscillators from short time series via phase dynamics modeling: Limitations and application to EEG data. CHAOS, 2005; vol. 15, pp. 024102.

Mean phase coherence modified for piecewise constant phase difference data

Vladimir Khorev
Department of Dynamic Modeling and Biomedical Engineering
Saratov State University
Saratov, Russia
Neuroscience and Cognitive Technology Lab, Center for Technologies in Robotics and Mechatronics Components
Innopolis University
Innopolis, Russia
0000-0001-6613-8940

***Abstract* — We propose a modification of the mean phase coherence method based on the statistics arrange of phase difference data. The modification aimed towards better analysis of data of coupled oscillators under influence of strong noise inducing phase skips.**

Keywords—mean phase coherence, connection, coupling, modification.

I. INTRODUCTION

The task of determining the degree of interaction between dynamical systems is an object of interest in various fields of science[1–3]. One of the most simple and fast methods was proposed in [4]. Nevertheless, it also has limits of applicability, for the expansion of which a solution is proposed in this work. To modify the mean phase coherence index method, it is required to analyze the change in synchronization properties of interacting systems in the presence of noise. To analyze the behavior of the phase difference signal in the presence of noise, consider an example of particle motion in the presence of a potential barrier: if the noise is strong enough, or if it is Gaussian, then the particle occasionally jumps over the potential barrier and fairly quickly comes to the next state of equilibrium $\varphi_0 \pm \varepsilon$. Physically, this means that the phase point makes an extra part of the turn, as compared with the external force, along the limiting cycle. These relatively fast changes in phase difference are called phase skips [5].

In practice, there are often situations where “overshoot” is observed on a number of phase differences. In presence of weak and limited noise, the phase fluctuates around a constant value, i.e. overshoot is not observed. In presence of strong and unlimited noise, phase skips are usually observed. However, the probabilities of skipping to the right and left are now different: naturally, the particle more often jumps down than up. Therefore, although most of the time the particle fluctuates around a state of equilibrium, on average it slips down the potential. Therefore, the phase dynamics is substantially non-uniform (at least with low noise): long synchronization intervals alternate with phase skips

We now discuss the relationship between the phases of self-oscillations and strength. It was noted that the phase difference $\Delta\varphi$ can be arbitrarily large due to phase diffusion (unless the noise is limited and weak). Thus, for noise systems, generally speaking, one cannot speak of phase capture, since the phase difference is not limited. On the other hand, the particle is more often at the minimum of the potential, and therefore certain values of $\Delta\varphi$ are observed with greater probability. If we consider the phase difference on the $[0,2\pi]$ interval and construct the phase distribution density, we will see that it is not uniform, but has a pronounced maximum.

II. DATA AND METHODS

Phases are calculated by rows of initial signals. Then, the probability density in the range from 0 to 2π is calculated from the series of the wrapped phase difference. Next, the obtained values of the probability density distributions are sorted. This range of values is approximated by an exponential function in the form:

$$Z_I = a \cdot \exp(b x_i) \tag{1}$$

where x_i are the initial values of the function, a, b are the approximation coefficients determined using the least squares method, in which the Levenberg-Marquardt algorithm was used for optimization.
In the case when the synchronization level is high, the coefficient b should also take high values in the limiting cases for a series with a constant phase difference (limiting case) with a length of 100 characteristic periods a value of 7.2 was obtained. For the case of no synchronization, the coefficient b will take values close to 0.

In this modification, it we propose to calculate the distribution of phase differences and divide the distribution of phase differences into L bins. According to statistical studies, the optimal number of cells is determined by the formula:

$$L = |e^{(0.626+0.4\ln(N-1))}| \quad (2)$$

where L is the number of cells in the plot of the density of distribution of the function, N is the number of elements of the series [6]. Next is the sum of the distributions, which exceed the threshold value k, which is found by the following formula:

$$k = \varepsilon N/L \quad (3)$$

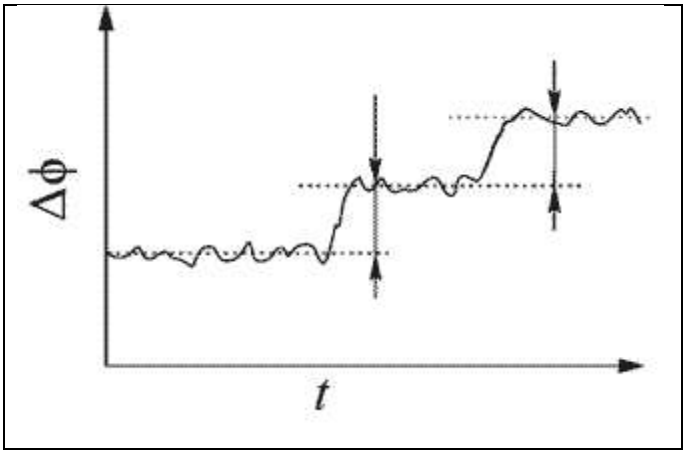

Fig. 1 An exemplary dependence of the phase difference from the time in case of switching to the synchronizatio and presence of noise when shifts occur irregularly.

It is easy to notice that in the case of constantly and monotonously increasing phase difference or if the phase difference is a random value similar to white noise, the height of all bins will tend to a constant value of N/L and for real data it is reasonably to add scaling factor ε depending on the signal/noise ratio.

III. RESULTS

We can take this value as a threshold, but due to short time series and complex properties of the dynamics of real systems requires a normalization factor. To check the performance of the modified method of calculating the mean phase coherence index using a threshold value, a system of equations describing coupled phase oscillators with coupling coefficients were taken [7].

Fig. 2 shows a graph of the phase synchronization index versus the coupling parameter of two coupled oscillators. With high noise coefficients and large lengths of series, the phase synchronization indices of the proposed method show more accurate indications for two oscillators that are not fully synchronized with each other.

From the above, it can be concluded that the method of calculating the phase synchronization index using the approximating function, is more sensitive to the coupling strength, but requires further study for application in real systems.

In the course of the work, the possibilities of estimating phase synchronization were studied, taking into account the delay in coupling between systems, estimated using the phase coherence index using the model and real data. Namely, it was found out that in some cases it is possible to recover the delay in the connection between the two systems. It was determined that taking into account the delay in case of an increase in dynamic noise allows us to obtain a higher level of the mean phase coherence.

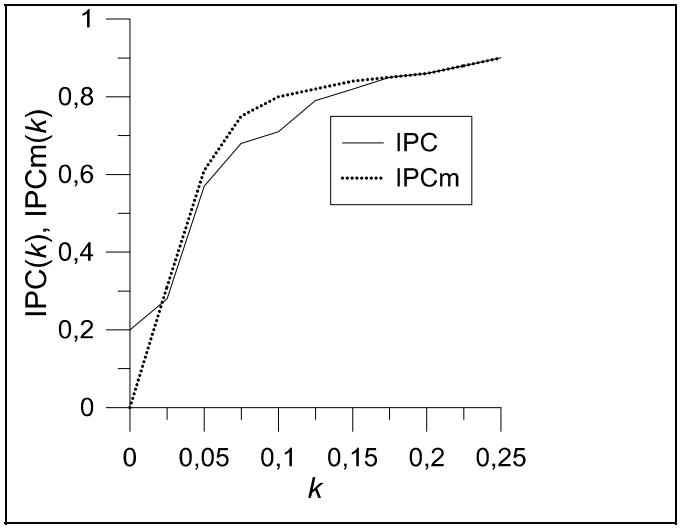

Fig. 2 The dependence of the mean phase coherence index (IPC) and modified phase coherence index (IPCm) on the coupling parameter for a number of phase difference of coupled oscillators in presence of noise.

Thus, in this work we analyzed the possibility of modifying the method of calculating the phase synchronization between two oscillatory systems using model time series for the case of a piecewise constant phase difference and proposed methods for such a modification. The performance check of the proposed modifications was implemented on model data and demonstrated the potential applicability for the analysis of time series obtained from real systems.

ACKNOWLEDGMENT

This work has been supported by the Center for Technologies in Robotics and Mechatronics Components (Innopolis University).

REFERENCES

[1] L. Cimponeriu, M. Rosenblum, A. Pikovsky, Estimation of delay in coupling from time series. Phys. Rev. E 2004. V.70 046213

[2] S. Karavaev, A. R. Kiselev, A. E. Runnova, et al. Synchronization of infra-slow oscillations of brain potentials with respiration CHAOS, 2018; vol. 28, 081102.

[3] O. I. Moskalenko, A. D. Koloskova, M. O. Zhuravlev, A. A. Koronovskii, A. E. Hramov, Intermittent phase synchronization in human epileptic brain, Proc. SPIE, 2017; 1006316-1.

[4] F. Mormann, K. Lehnertz, P. David, C. E. Elger. Mean phase coherence as a measure for phase synchronization and its application to the EEG of epilepsy patients. Physica D, 2000; vol. 144, pp. 358–369.

[5] S. Pikovsky, G. V. Osipov, M. G. Rosenblum, M. Zaks, J. Kurths, Phys. Rev. Lett., 1977; vol 79(1), pp. 47.

[6] R. Otnes and L. Enochson, Digital Time Series Analysis, New York: Wiley, 1972; pp. 112.

[7] Cumin, C. P. Unsworth, Generalising the Kuromoto model for the study of neuronal synchronisation in the brain, Physica D, 2007; vol. 226, pp. 181–196.

Practical recommendations on the application of markov queuing models with a restricted queue

Alexander Kirpichnikov
dept. of intelligent systems and information resources control
Kazan National Research Technological University
Kazan, Russia
kirpichnikov@kstu.ru

Anton Titovtsev
dept. of intelligent systems and information resources control
Kazan National Research Technological University
Kazan, Russia
notna6683@mail.ru

***Abstract*—The article provides general practical recommendations on the application of Markov queuing models in technical systems. Queuing models can be used in construction and reconstruction of various types of technical facilities operating according to the principle of queuing systems, even at the design stage. Such facilities include various telecommunication systems, objects of transport infrastructure: railway marshalling yards and freight terminals, petrol-filing stations, service stations, etc. To make such facilities work stable, it is important to compute not only the necessary number of serving channels, but also storage capacity for claims expecting service. Actually, this is the capacity of entry lines in front of automobile stations or the capacity of receiving parks of railway freight terminals and marshalling yards. Accurate computation of these parameters will avert frequent denials of service due to the system overloading and, as a result, financial costs caused by loss of customers or temporary delays in servicing.**

Keywords—queue, quality of service (QoS), queuing system (QS), service facility

I. INTRODUCTION

QS models presented in works [1-5] can be used in construction and reconstruction of various types of technical facilities operating according to the principle of queuing systems, even at the design stage. Such facilities include various telecommunication systems, objects of transport infrastructure: railway marshalling yards and freight terminals, petrol-filing stations, service stations, etc. To make such facilities work stable, it is important to compute not only the necessary number of serving channels, but also storage capacity for claims expecting service. Actually, this is the capacity of entry lines in front of automobile stations or the capacity of receiving parks of railway freight terminals and marshalling yards. Accurate computation of these parameters will avert frequent denials of service due to the system overloading and, as a result, financial costs caused by loss of customers or temporary delays in servicing.

Mathematical queuing models presented in works [1-5] allow the facilities of this sort to be described more flexibly in comparison with the well-known classical QS models since they consider the fact that claims received for service can take a different number of places in the storage due to the type of a particular claim. For example, claims that have different sizes depending on the number of carriages are trains arriving at marshalling yards. Besides, railway cargo carriages themselves have different capacities and different dimensions. Cars and trucks of different capacities also occupy a different number of places in the parking lot and on entry lines before loading /unloading. In case when the number of places for waiting of newly-arrived claims is restricted, the number of particular claims that the storage can contain will be different for each type of claims. A lot of combinations are possible here in relation to the ratio of different types of claims stream intensities. In other words, due to the limited capacity of the storage, claims of different types have different limits on the queue length which depend on the intensities of the input claim streams and are determined by the total number of claims of all types that can accommodate the storage in each specific case. Since the intensities of input streams of heterogeneous demand sare, as a rule, the initial data, then the closely related limitations on the queue length for claims of different types can also be considered as initial data.

II. RECOMMENDATIONS FOR CALCULATING THE PARAMETERS OF THE OBJECT

When computing the parameters of such a projected facility as a QS, it is necessary to determine the initial data. The intensity of input and output streams of claims are regarded as basic data. The data on the intensity of the input demand stream are collected statistically if there is such an opportunity, or they are predicted with the real need for the projected facility in view. The intensity of serviced claims stream is determined on the basis of one service facility performance which, as a rule, is known or predictable.

Further, possessing data on the intensities of the input and output streams, it is required to specify whether the mathematical QS model is suitable for describing the facility under study. The queuing models presented in works [1-5] have been obtained analytically, and they accurately describe the QS work though they are based on the assumption of a Poisson character of claim streams. Closeness of the mathematical expectation and the variance of the number of claims arriving within a certain period of time can be considered as a simple engineering criterion for the closeness

of the real claim stream to a Poisson one. In case if the given mathematical expectation and variance are commensurable, then the claim stream can be considered Poisson, and the mathematical model is suitable. Otherwise, presented mathematical models can be used only for a rough estimation of the QS performance.

Also, when collecting statistics on the number of claim sentering the system, it is significant to divide all claims into several types depending on their size, and, consequently, on the occupied place in the storage, and to collect statistics for each type of arriving claims separately. As a result, we obtain the intensities of claims streams-components of all types.

Further, based on the ratio between the intensities of the input claims stream component sand the maximum possible capacity of the storage, it is necessary to determine the limits on the queue length for each type of claims. For the unity of storage capacity one should take the capacity occupied by a claim with minimum dimensions, or the greatest common divisor between capacities occupied by claims of all types, i.e. so as to obtain an integer.

The number of service facilities should be taken equal to the ratio of the total intensity of the input stream to the intensity of service done by one channel, rounded to the integer.

Having indicated initial data, it is easy to compute the QS performance characteristics from a mathematical model and the number of service facilities necessary and sufficient for a stable operating mode of the system as well. In case of unsatisfactory results, it is possible to vary the number of service facilities and the capacity of the storage until the desired effect is achieved.

REFERENCES

[1] A. Kirpichnikov, A. Titovtsev, "Mathematical model of a queuing system with arbitrary quantity of sources and size-limited queue," International Journal of Pure and Applied Mathematics, vol. 106 (2), 2016, pp. 649–661.

[2] A. Kirpichnikov, A. Titovtsev, "Mathematical model of open queuing system with full set of memories," International Journal of Pure and Applied Mathematics, vol. 107 (1), 2016, pp. 139–143.

[3] A. Kirpichnikov, A. Titovtsev, "Physical and mathematical queues in the applied queuing theory," International Journal of Pure and Applied Mathematics, vol. 108 (2), 2016, pp. 409–418.

[4] A. Titovtsev, "The concept of higher orders queues in the queuing theory," International Journal of Pure and Applied Mathematics, vol. 109 (2), 2016, pp. 451–457.

[5] A. Kirpichnikov, A. Titovtsev, "On the problems of queues in mixed type queuing systems with random quantity of sources and size-limited queues," Communications in Computer and Information Science, vol. 800, 2017, pp. 68-82.

Optimization approach for inverse kinematic problem for manipulator with redundant degrees of freedom

Andrei V. Kochetkov
Perm National Research Polytechnic University
Perm, Russia
soni.81@mail.ru

Dmitry R. Malakhov
Yuri Gagarin State Technical University
Saratov, Russia
malax0008@mail.ru

Oleg V. Zakharov
Yuri Gagarin State Technical University
Saratov, Russia
zov20@mail.ru

***Abstract*—Manipulators of a sequential structure with redundant degrees of freedom are increasingly used in engineering. An example is an articulated robot. It has a structure similar to a human arm with three rigid links and only rotational joints. Such a structure provides greater flexibility, manageability and versatility. It is known that the inverse kinematic problem for redundant manipulator has a multivariate solution. In this case, the resulting solutions will not be equivalent. Therefore, an optimization approach is appropriate. As optimization criteria, the sum of angles, energy consumption, torques, etc. can be taken. The article describes a robot with 6 Degrees of Freedom. Mathematical dependences are obtained and software implementation in the MATLAB environment is implemented. It is proposed to use the sum of the angles of the links of the *m*anipulator as an optimization criterion. The simulation showed that the optimal solution provides for a reduction in the sum of the angles of rotation of the manipulator approximately two times. Thus, productivity increases and energy consumption decreases.**

***Keywords*—robot, manipulator, redundant robot, inverse kinematics, parametric optimization**

I. INTRODUCTION

Manipulator is a type of industrial robots. Manipulators are composed of an assembly of links and joints. Links are defined as the rigid sections that make up the mechanism and joints are defined as the connection between two links. The device attached to the manipulator which interacts with its environment to perform tasks is called the end-effector.

The combination and mutual arrangement of links and joints determines the number of Degrees of Freedom (DOF), as well as the scope of the manipulation system of the robot. Articulated robots can range from simple two-jointed structures to systems with 10 or more interacting joints. It has great amount of flexibility, manageability, and versatility.

Manipulators are extensively used in the industrial manufacturing sector and also have many other specialized applications (for example, the Canadarm was used on space shuttles to manipulate payloads). The study of robot manipulators involves dealing with the positions and orientations of the several segments that make up the manipulators. First of all, it is necessary to determine the Cartesian coordinates of the end-effector.

II. MATHEMATICAL MODEL

The kinematic problem is to calculate the Cartesian coordinates of an end-effector from its kinematic scheme and given angles of links. The well-known solving methods are constructed on coordinate transformations using the matrix of direction cosines, Euler angles, quaternion apparatus, and linear fractional transformations with Kayleigh-Klein parameters. The direct problem has an unambiguous solution and is described in sufficient detail in [1-5, 27-31]. The inverse problem is to calculate the angles of the links for a given position of the end-effector with a known scheme of its kinematics. The inverse problem, in contrast to the direct one, has many solutions, so it is advisable to solve it on the basis of parametric optimization. To do this, you need to find a set of solutions, and then choose one of them by some criterion. Thus, the inverse problem is more complex than the direct one. The actual question is the choice of criteria for optimization.

Currently, existing methods for obtaining solutions to the inverse problem can be divided into geometric, analytical, and numerical. Finding generic coordinates explicitly is a difficult task, since equations are non-linear. Therefore, an analytical solution exists only for robots with a specific design. In the Euler angle method, it is proposed to successively multiply both sides of the equation by inverse transformation matrices and determines the required angles from the matrix equations thus obtained. The method of transformations consists in transferring first one of the unknown quantities from the right to the left side of the equation, finding it and transferring it to the left side of the next unknown and repeating this procedure until all variables are found. It is also known to solve the inverse problem of kinematics in the dual Rodrig – Hamilton parameters, namely, using biquaternionic matrices [32]. The geometric approach is associated with the use of an analytical solution, taking into account the peculiarities of the kinematic scheme, which makes it possible to reduce the number of independent equations.

The disadvantages of the analytical solution include the ambiguity of the result obtained, due to the trigonometric functions used. This requires additional analysis of the choice of the correct solution. Therefore, the article proposes a new approach to solving the inverse kinematic problem based on numerical methods and parametric optimization. The mathematical model is a formula for the transformations of the Cartesian coordinates of the links of the robot, obtained for the direct kinematic problem. However, in the formulas, the angles of rotation of the links are unknown and are determined on the basis of parametric optimization. The objective function is minimized as a sum of squares of the difference between the specified and obtained Cartesian coordinates of the end-effector. The article deals with a robot manipulator with 6 DOF, which has only rotational joints.

We introduce the following coordinate systems (Fig. 1):

1) Conditionally fixed system associated with the first link of the robot – the base – (x_0, y_0, z_0);

2) Moving coordinate systems associated with the first and second links, respectively (x_1, y_1, z_1) and (x_2, y_2, z_2);

3) Moving coordinate system associated with point 0_1 – the end-effector – (x_3, y_3, z_3).

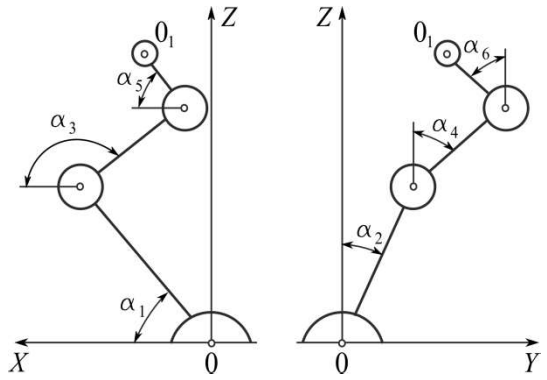

Fig. 1. Coordinate scheme of 6 DOF manipulator.

To determine the coordinates of the position of the manipulator it is necessary to consistently find the coordinates of the position of its entire links. The expressions for the Cartesian coordinates of the position of the first link will be:

$$\begin{cases} x_1 = x_0 + l_1 \cos\alpha_1 \sin\alpha_2; \\ y_1 = y_0 + l_1 \sin\alpha_1; \\ z_1 = z_0 + l_1 \cos\alpha_1 \cos\alpha_2, \end{cases} \quad (1)$$

where l_1 is the length of the first link of the robot; x_0, y_0, z_0 – coordinates of the base of the robot; α_1, α_2 – the angles of rotation of the first link around the axes Y and X, respectively.

Formulas for the Cartesian coordinates of the second link:

$$\begin{cases} x_2 = x_1 + l_2 \cos(\alpha_1 + \alpha_3)\sin(\alpha_2 + \alpha_4); \\ y_2 = y_1 + l_2 \sin(\alpha_1 + \alpha_3); \\ z_2 = z_1 + l_2 \cos(\alpha_1 + \alpha_3)\cos(\alpha_2 + \alpha_4), \end{cases} \quad (2)$$

where l_2 is the length of the second link of the robot; x_1, y_1, z_1 – coordinates of the first joint of the robot; α_3, α_4 – the angles of rotation of the second link around the Y and X axes respectively.

Formulas for the Cartesian coordinates of the third link:

$$\begin{cases} x_3 = x_2 + l_3 \cos(\alpha_1 + \alpha_3 + \alpha_5)\sin(\alpha_2 + \alpha_4 + \alpha_6); \\ y_3 = y_2 + l_3 \sin(\alpha_1 + \alpha_3 + \alpha_5); \\ z_3 = z_2 + l_3 \cos(\alpha_1 + \alpha_3 + \alpha_5)\cos(\alpha_2 + \alpha_4 + \alpha_6), \end{cases} \quad (3)$$

where l_3 is the length of the third link of the robot; x_2, y_2, z_2 – coordinates of the second joint of the robot; α_5, α_6 – the angles of rotation of the third link around, respectively, the axes Y and X.

The system of equations (3) gives a solution to the direct kinematic problem – the determination of the x, y, z coordinates for known angles α. If in these equations to set

the values of x, y, z, and the angles α are considered unknown, then we get the inverse kinematic problem.

To solve it, we use parametric optimization. The objective function is the sum of the squares of the difference between the specified and obtained Cartesian coordinates of the end-effector:

$$F(\alpha_1,\alpha_2,\alpha_3,\alpha_4,\alpha_5,\alpha_6,\beta_1,\beta_2,\beta_3,\beta_4,\beta_5,\beta_6) = \\ = \sum (X_1 - X_2)^2 + (Y_1 - Y_2)^2 + (Z_1 - Z_2)^2, \quad (4)$$

where X_2, Y_2, Z_2 – the initial coordinates of the end-effector; X_2, Y_2, Z_2 – the required coordinates of the end-effector; β_1, β_2, β_3, β_4, β_5, β_6 – the unknown angles of rotation of the links of the robot.

The software implementation is performed in the MATLAB environment (Fig. 2). The optimization method is the Nelder-Mead simplex method.

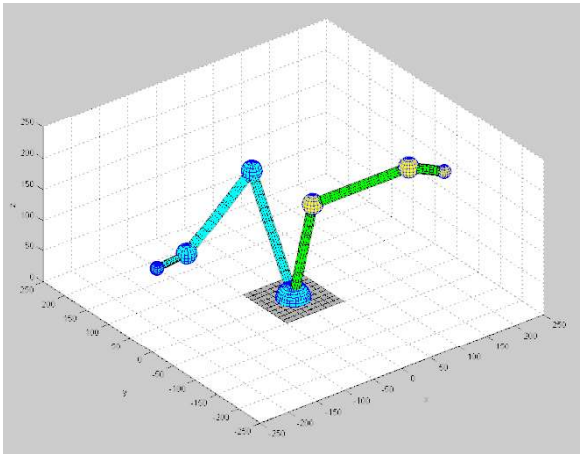

Fig. 2. Estimated movement scheme of manipulator.

III. SIMULATION RESULTS

Perform the calculation of the inverse kinematic problem for the previously considered 6 DOF robot manipulator with link lengths l_1 = 200 mm, l_2 = 150 mm, l_3 = 50 mm. Baseline data are presented in Table 1. It shows the initial values of the angles α_1, α_2, α_3, α_4, α_5, α_6 of rotation of the links, the initial and final coordinates of the end-effector X, Y, Z.

TABLE I. THE ORIGINAL COORDINATES OF THE LINKS OF THE ROBOT.

Position of the end-effector	Angles of rotation of links, degree						Coordinates, mm		
	α_1	α_2	α_3	α_4	α_5	α_6	*X*	*Y*	*Z*
Initial	50.0	20.0	120.0	20.0	5.0	40.0	-100.04	183.61	-1.00
Final	-	-	-	-	-	-	120.0	-190.0	250.0

A numerical experiment showed that the inverse kinematic problem has many solutions. All these solutions are equivalent – the objective function has a minimum close to zero (about 10^{-8}). Achievement of one or another local minimum depends on the choice of initial values of start points during optimization. The physical justification for multivariance is the excess number of degrees of freedom of the robot. Four calculation options are given in Table 2.

Data analysis of Table 2 showed that different sums of corners of the links of the robot correspond to different versions of the solution of the inverse kinematic problem. The results in the form of the angles of rotation of the first |α1-β1|+|α2-β2|, second |α3-β3|+|α4-β4|, third |α5-β5|+|α6-β6| and all links of the robot are given in Fig. 3. It can be seen from it that option 4 provides the sum of the angles of rotation of the links about two times less than option 3.

TABLE II. THE ESTIMATED COORDINATES OF LINKS OF THE ROBOT

Calculation option	Final angles of rotation of links, degree					
	β_1	β_2	β_3	β_4	β_5	β_6
1	148.97	155.14	-101.34	41.32	-0.74	-0.17
2	-65.75	16.92	141.17	98.19	110.37	202.65
3	-61.52	9.90	-160.48	-9.67	7.46	204.23
4	-53.98	-0.18	186.77	0.14	-37.56	0.19

The conducted numerical experiment showed that the solution of the inverse kinematic problem for a robot with 6 degrees of freedom is multivariate. There are many equivalent solutions with different angles of joints. Therefore, it is advisable to set an optimization problem. As a criterion, the sum of the angles of all the joints of the robot is proposed. Using the example of calculation, it is shown that the optimal solution makes it possible to reduce the sum of the angles by about 2 times and thereby to reduce move the robot links.

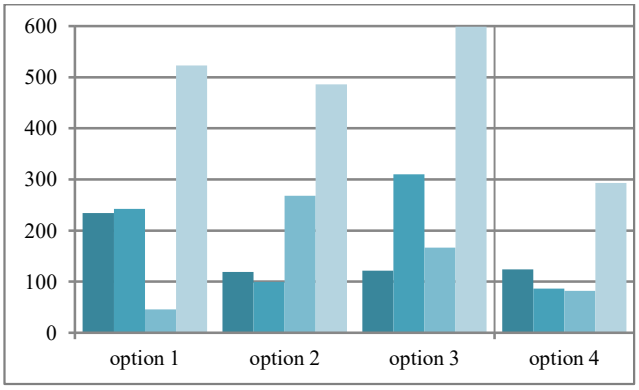

Fig. 3. Estimated sums of the angles of the manipulator links.

REFERENCES

[1] R. Manseur, and K. L. Doty, "A fast algorithm for inverse kinematics analysis of robot manipulators," International Journal of Robotics Research, vol. 7, pp. 52–63, 1988.

[2] L. T. Wang, and C. C. Chen, "A combined optimization method for solving the inverse kinematics problem of mechanical manipulators," IEEE Transactions on Robotics and Automation, vol. 7, pp. 489–499, 1991.

[3] S. Deo, and I. D. Walker, "Minimum effort inverse kinematics for redundant manipulators," IEEE Transactions on Robotics and Automation, vol. 13, pp. 767–775, 1997.

[4] Aristidou, and J. Lasenby, Inverse Kinematics: a review of existing techniques and introduction of a new fast iterative solver. London: University of Cambridge, 2009.

[5] O. V. Zakharov, I. N. Bobrovskij, and A. V. Kochetkov, "Analysis of Methods for Estimation of Machine Workpiece Roundness," Procedia Engineering, vol. 150, pp. 963–968, 2016.

[6] F. Rezchikov, A. V. Kochetkov, and O. V. Zakharov, "Mathematical models for estimating the degree of influence of major factors on performance and accuracy of coordinate measuring machines," MATEC Web of Conferences, vol. 129, pp. 01054, 2017.

[7] O. V. Zakharov, A. F. Balaev, and A. V. Kochetkov, "Modeling Optimal Path of Touch Sensor of Coordinate Measuring Machine

Based on Traveling Salesman Problem Solution," Procedia Engineering, vol. 206, pp. 1458–1463, 2017.

[8] A. Korolev, A. V. Kochetkov, and O. V. Zakharov, "Optimization of Control Points Number at Coordinate Measurements based on the Monte-Carlo Method," Journal of Physics: Conference Series, vol. 944, pp. 012061, 2018.

[9] O. A. Yalovoy, O. V. Zakharov, and A. V. Kochetkov, "The Centerless Measurement of Roundness with Optimal Adjustment," IOP Conference Series: Materials Science and Engineering, vol. 93, pp. 012024, 2015.

[10] A. Fomin, "Kinematics of surface formation in milling," Russian Engineering Research, vol. 33, pp. 660–662, 2013.

[11] S. Kiselyov, E. N. Leksin, S. A. Romanov, and O. V. Blagovski, "Hybrid machining in the creation of specified residual stress in the surface layer," Russian Engineering Research, vol. 32, pp. 504–507, 2012.

[12] A. Fomin, and V. G. Gusev, "Safe machining of blanks with nonuniform properties," Russian Engineering Research, vol. 33, pp. 602–606, 2013.

[13] A. Fomin, "Vibrational motion of a complex mill under the action of the cutting force," Russian Engineering Research, vol. 33, pp. 57–60, 2013.

[14] O. V. Zakharov, A. V. Kochetkov, N. M. Bobrovskij, I. N. Bobrovskij, and P. A. Melnikov, "Analysis of Stationary Means of Measurement Filters with Optimum Sensitivity," International Conference on Actual Problems of Electronic Instrument Engineering, vol. 1, pp. 241–244, 2016.

[15] O. V. Zakharov, and A. V. Kochetkov, "Minimization of the systematic error in centerless measurement of the roundness of parts," Measurement Techniques, vol. 58, pp. 1317–1321, 2016.

[16] N. Pavlov, A. E. Hramov, O. N. Pavlova, and A. A. Koronovskii, "Effect of measuring noise on scaling characteristics in the dynamics of coupled chaotic systems," Chaos, Solitons & Fractals, vol. 116, pp. 106–113, 2018.

[17] J. Iqbal, R. Islam, and H. Khan, "Modeling and Analysis of a 6 DOF Robotic Arm Manipulator," Canadian Journal on Electrical and Electronics Engineering ,vol. 3, pp. 300–306, 2012.

[18] Yu. N. Chelnokov, "Biquaternion solution of the kinematic control problem for the motion of a rigid body and its application to the solution of inverse problems of robot-manipulator kinematics," Mechanics of Solids, vol. 48, pp. 31–46, 2013.

[19] Jianxin Xu, Wei Wang, and Yuanguang Sun, "Two optimization algorithms for solving robotics inverse kinematics with redundancy," Journal of Control Theory and Applications, vol. 8, pp. 166–175, 2010.

[20] Srivastava, and A. Kumar, "An Optimization Technique to Solve the Inverse Kinematics of Robot Manipulator," International Conference on Manufacturing Excellence, pp. 77–83, 2013.

[21] Liao, P. Liang, and X. Yang, "Pseudoinverse-based optimization scheme for motion control of redundant robot manipulators," Information and Control, vol. 42, pp. 645–651, 2013.

[22] P. Chen, L. Liu, F. Yu, H. Li, F. Yang, and X. Wang, "A geometrical method for inverse kinematics of a kind of humanoid manipulator." Jiqiren (Robot), vol. 34, pp. 211-216, 2012.

[23] S. Chiaverini, G. Oriolo, and I. Walker, Kinematically redundant manipulators, Handbook of Robotics, Berlin: Springer, pp. 245–268, 2008

[24] Duleba, and M. Opałka, "On application of elastic band method to repeatable inverse kinematics in robot manipulators," Journal of Automation, Mobile Robotics and Intelligent Systems, vol. 7, pp. 5–12, 2013

[25] Kai Mi, Haojian Zhang, Jun Zheng, Jianhua Hu, Dengxiang Zhuang, and Yunkuan Wang, "A sampling-based optimized algorithm for task-constrained motion planning," International Journal of Advanced Robotic Systems, pp. 1–15, 2019.

Route optimization in measuring surface on coordinate measuring machines

Andrei V. Kochetkov
Perm National Research Polytechnic University
Perm, Russia
soni.81@mail.ru

Peter M. Salov
The Ulianov Chuvash State University
Cheboksary, Russia
salov-pm@yandex.ru

Oleg V. Zakharov
Yuri Gagarin State Technical University
Saratov, Russia
zov20@mail.ru

***Abstract* — One of the current problems in measuring surfaces on Coordinate Measuring Machines is currently increasing productivity. A promising way to solve this problem is to optimize the route of the touch sensor of Coordinate Measuring Machines. Currently this task has no standard mathematical solution. In this regard, we propose to optimize the route of measurement based on the spatial Traveling Salesman Problem. Traveling Salesman Problem can be solved by exact methods (for example, by the Branch and Bound Method) or by approximate methods (heuristic). It is known that optimization time for exact methods is an exponential function, and for a heuristic method it is a polynomial function. The article proposes the use of an Ant Colony algorithm. With the help of the developed program, a computer simulation of the route of the touch sensor using the branch and bound method and the adaptive Ant Colony Method was performed. The accuracy and time of the solution were investigated for a different number of measurement points on the plane, cylinder and sphere. It has been established that the Ant Colony Method gives a solution close to the optimal one and requires 5-6 times less time to search for it compared to the Branch and Bound Method.**

Keywords* — *Sphericity error; Coordinate Measuring Machines; Minimum Zone Sphere; Least Square Sphere; Maximum Inscribed Sphere

I. FORMULATION OF THE PROBLEM

For research, we chose the most commonly used surfaces as the object of measurement: plane, cylinder, and sphere. These surfaces were described by parametric equations in the Cartesian coordinate system. A uniform distribution of control points was specified with an analytical definition of the step between the nearest points. To determine the coordinates of uniformly distributed N points on a flat surface for ease of calculation, the surface was aligned with the XOY plane and bounded by four planes ($x_1 = -L/2$, $x_2 = L/2$, $y_1 = -L/2$, $y_2 = L/2$) whose intersection lines form a square with side L. The points are located on a plane with equal steps along the 0X axis and the 0Y axis, respectively, $h_x = h_y = L / N$. To determine the coordinates of uniformly distributed N points on a cylindrical surface, the axis of the cylinder was aligned with the axis 0Z, and the surface was bounded by the planes $z_1 = -L/2$, $z_2 = L/2$. The points on the cylindrical surface are distributed with an angular step $d\varphi=2\pi/N$ in the X0Y plane and a linear step $h_z = L/N$ along the 0Z axis. The points on the sphere were distributed with zenith $d\theta=2\pi/N$ and azimuth $d\varphi=2\pi/N$ angular steps.

The length of the sensor path for each surface depends on the sequence of control points. For complete information on the location of all points on the surface, it is enough that the sensor touches each control point at least once. After completing the full surface cycle, the sensor returns to the starting point. In this case, the sensor path is a closed polyline. The sensor route is represented as a graph, the vertices of which are control points, and the edges of the graph are trajectories of movement between two points. Then the problem of route optimization is reduced to the search for a Hamiltonian cycle having a minimum length, and is a well-known Traveling Salesman Problem.

We describe the traveling salesman problem as an integer linear programming problem. Imagine the movement of the probe from the i-th control point to the j-th in the form of a matrix of displacements $L_{i,j}$, where $i, j \in \overline{1,n}$ for a certain number of control points $n \in \mathbf{N}$. Imagine the direction of the transition from the i-th point to the j-th in the form of a matrix of numbers $l_{ij} \in \{0,1\}$ for $i, j \in \overline{1,n}$, where $l_{ij} = 1$, if the bypass route contains an edge (i, j), and $l_{ij} = 0$ otherwise. Then the problem is reduced to finding such a solution l, in which the route will be the smallest:

$$G(\bar{x}) = \sum_{i=1}^{n} \sum_{j=1}^{n} L_{ij} l_{ij} \to \min. \qquad (1)$$

At the same time, it is necessary to take into account that from each vertex of the graph represented by a control point, only one edge leaves and only one edge belongs to each vertex:

$$\begin{cases} \sum_{j=1}^{n} l_{ij} = 1, \ i = \overline{1,n} \\ \sum_{i=1}^{n} l_{ij} = 1, \ j = \overline{1,n} \end{cases} \qquad (2)$$

Depending on the surface, the elements of the $L_{i,j}$ displacement matrix will be determined by the expressions:

- for the plane:

$$L_{ij} = \sqrt{(x_j - x_i)^2 + (y_j - y_i)^2 + (z_j - z_i)^2} \ ; \qquad (3)$$

- for cylinder:

$$L_{ij} = \sqrt{(R \cdot \varphi_{ij})^2 + (z_j - z_i)^2} \ ; \qquad (4)$$

- for the sphere:

$$L_{ij} = R \cdot ar\cos \frac{x_i x_j + y_i y_j + z_i z_j}{R^2}, \qquad (5)$$

where (x_i, y_i, z_i) and (x_j, y_j, z_j) are the coordinates of the i-th and j-th control points of the surface.

Currently, various methods of solving the traveling salesman problem are developed, which are classified according to the method of finding a solution into exact and approximate (heuristic). In comparison with approximate ones, exact methods allow finding the best solution, but at the same time they require more time for calculation. Approximate methods require less time to calculate, but only give an approximate, often local, solution. The problem of the choice of methods and the appropriateness of their use for searching the route of a CMM sensor is to establish how significant the influence of the route difference on the measurement performance is. To solve this problem, the branch and bound method was chosen, attributable to exact methods, and the ant colony method, attributed to heuristic methods. Both of these methods are widely known and fairly well studied [12-14].

II. COMPUTER SIMULATION

For computer simulation, the following initial conditions were specified. Surface areas are equal to $S = 40000$ mm^2 for any number of points. This condition corresponds to: a) the side of the square bounding the plane is $L = 200$ mm2; b) cylinder length – R = 31.8mm, cylinder height – $L = 200$ mm; c) sphere radius – $R = 56.4$ mm. The radius of the sensor is assumed to be $r = 2$ mm. The value of the approach of the sensor is $2r$. The minimum number of measurement points for each surface is determined from the geometry: for the plane – 3 points; for the cylinder – 5 points; for the sphere – 4 points. The maximum number of points for the plane and the cylinder is 256 points, for the sphere – 266 points.

To determine the values of the parameters of the Ant Colony algorithm, preliminary testing was carried out. As a result, the following initial conditions were accepted: the number of iterations 50; pheromone evaporation rate of 0.3; the degree of influence on the choice of pheromone route 7; degree of wagging on the choice of route distance to the

nearest point 6; the number of ants is equal to the number of control points. The program for searching the sensor route using the Ant Colony algorithm was launched five times for each value of the number of points. From the obtained results the smallest route was chosen.

An illustration of the trajectories obtained for 64 control points is shown in Fig. 1 for a plane, Fig. 2 – for the cylinder, Fig. 3 – for the sphere. Dotted line corresponds to the base route.

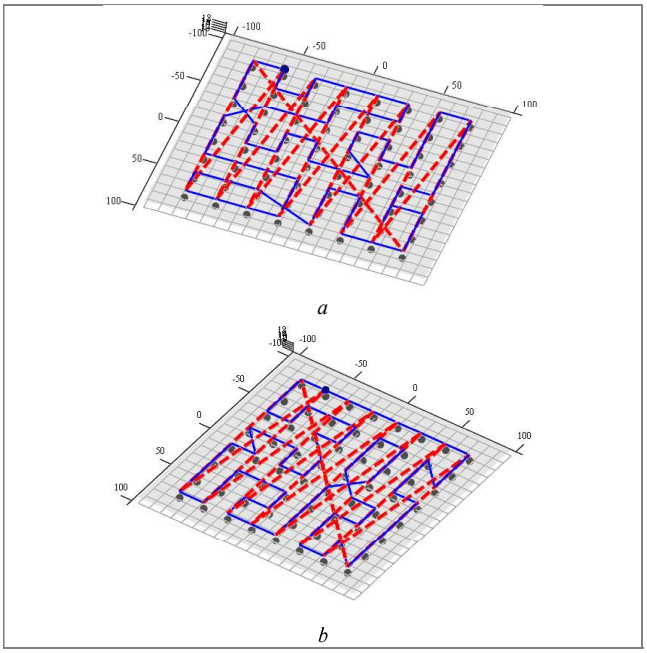

Fig. 1. Sensor path for the plane: a – Ant Colony algorithm; b – Branch and Bound algorithm.

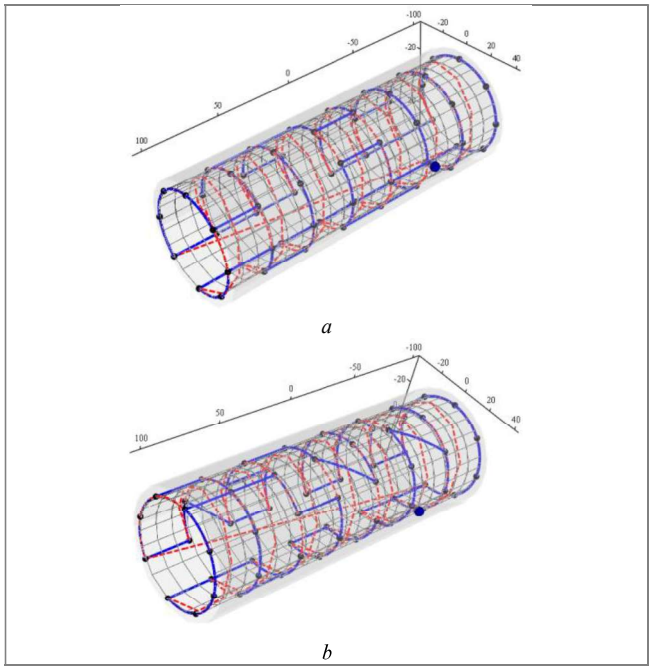

Fig. 2. Sensor path for the cylinder: a – Ant Colony algorithm; b – Branch and Bound algorithm.

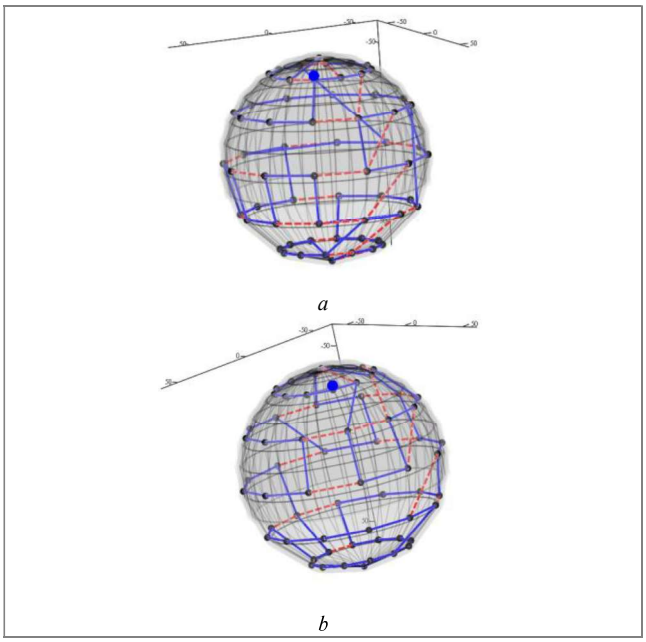

Fig. 3. Sensor path for the sphere: a – Ant Colony algorithm; b – Branch and Bound algorithm.

As a result of the simulation, the dependences of the path length of the touch sensor and the duration of the calculation on the number of control points for the plane (Fig. 4), for the cylinder (Fig. 5) and for the sphere (Fig. 6).

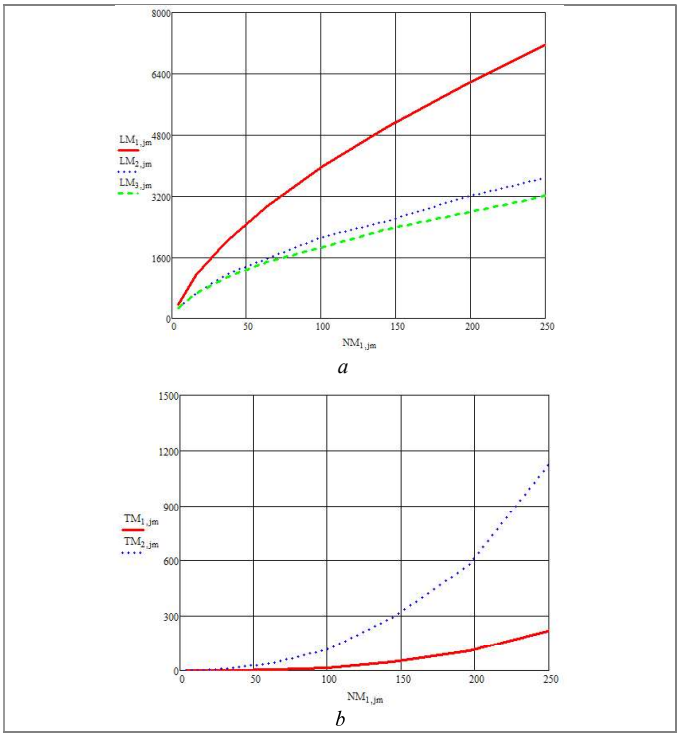

Fig. 4. The length of the path of the touch sensor (a) and the calculation time (b) on the number of control points for the plane: a – Ant Colony algorithm; b – Branch and Bound algorithm.

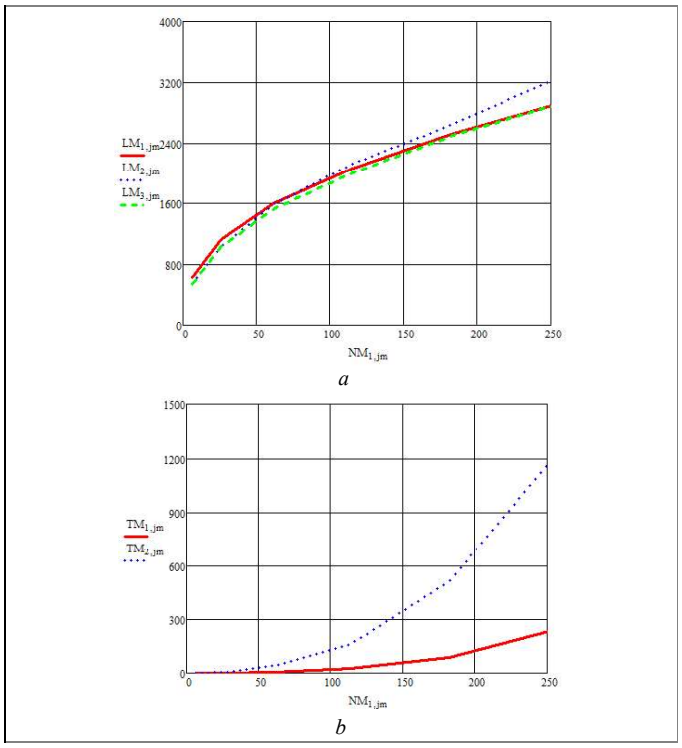

Fig. 5. The length of the path of the touch sensor (a) and the calculation time (b) on the number of control points for the cylinder: a – Ant Colony algorithm; b – Branch and Bound algorithm.

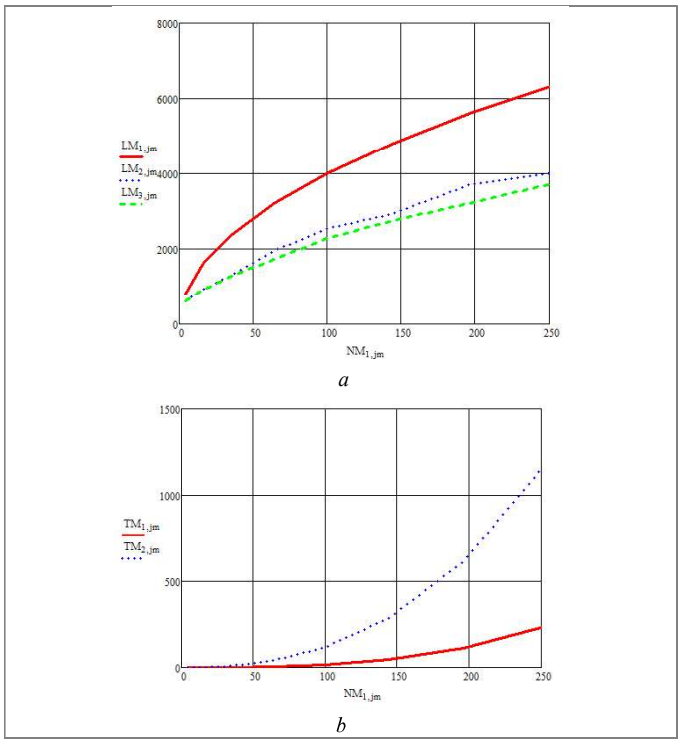

Fig. 6. The length of the path of the touch sensor (a) and the calculation time (b) on the number of control points for the sphere: a – Ant Colony algorithm; b – Branch and Bound algorithm.

As can be seen from the graph in Fig. 4-6 implementation of search algorithms allows finding a route 2 times shorter than the base one. At the same time, the solution obtained using the Ant Colony algorithm is worse than the solution found using the branch and bound algorithm by no more than 10%. Starting from 30 points, there is a significant decrease in the calculation time for the Ant Colony.

CONCLUSIONS

The possibility of improving the measurement performance by reducing the path of the CMM sensor path is investigated. Based on computer simulations, it was found that the sensor route is a Hamiltonian cycle, and the task minimum Hamilton cycle is the traveling salesman problem. This problem can be solved by exact and approximate methods. Comparison of the exact Branch and Bound method and the approximate method of the Ant Colony showed that the Ant Colony method allows finding a solution that is no more than 10% worse than the optimal one, requiring 5-6 times less time to search for a solution.

REFERENCES

[1] S.D. Jones, and A. Galip Usloy, An Optimization Strategy for Maximizing Coordinate Measuring Machines Productivity. Part 2: Problem Formulation, Solution and Experimental Results, J. Eng. Ind, vol. 117, pp. 610–618, 1995.

[2] V.A. Pechenin, M.A. Bolotov, and N.V. Ruzanov, Development of a method of ICP algorithm accuracy improvement during shaped profiles and surfaces control, International Journal of Engineering and Technology, vol. 6, 2229–2235, 2014.

[3] O.V. Zakharov, I.N. Bobrovskij, and A.V. Kochetkov, Analysis of Methods for Estimation of Machine Workpiece Roundness, Procedia Engineering, vol. 150, pp. 963–968. 2016.

[4] A.F. Rezchikov, A.V. Kochetkov, and O.V. Zakharov, Mathematical models for estimating the degree of influence of major factors on performance and accuracy of coordinate measuring machines, MATEC Web Conf, vol. 129, pp. 01054, 2017.

[5] O.V. Zakharov, A.F. Balaev, and A.V. Kochetkov, Modeling Optimal Path of Touch Sensor of Coordinate Measuring Machine Based on Traveling Salesman Problem Solution, Procedia Engineering, vol. 206, pp. 1458–1463, 2017.

[6] A.A. Korolev, A.V. Kochetkov, and O.V. Zakharov, Optimization of Control Points Number at Coordinate Measurements based on the Monte-Carlo Method, Journal of Physics: Conf. Series, vol. 944, pp. 012061, 2018.

[7] A.A. Fomin, Kinematics of surface formation in milling, Russian Engineering Research, vol. 33, pp. 660–662, 2013.

[8] A.A. Fomin, and V.G. Gusev, Safe machining of blanks with nonuniform properties, Russian Engineering Research, vol. 33, pp. 602–606, 2013.

[9] I.N. Khaimovich, and A.I. Khaimovich, Computer-Aided Engineering of the Process of Injection Molding Articles Made of Composite Materials, Key Engineering Materials, vol. 746, pp.269–274, 2017.

[10] I.V. Shrubchenko, A.V. Hurtasenko, R.R. Sharapov, T.A. Duyun, and N.A. Shchetinin, Investigation of Characteristics of Contact Bandages and Support Rollers of Rotating Technological Drums, Modern Applied Science, vol. 9, pp. 195–203, 2014.

[11] E.G. Demyanenko, and I.P. Popov, Investigation of forming method based on flanging process, IOP Conf. Series: Earth and Environmental Science, vol. 87, pp. 082010, 2017.

[12] S.D. Shtovba, Ant algorithms: Theory and applications, Programming and Computer Software, vol. 31, pp. 167–178, 2005.

[13] M. Dorigo, M. Birattari, and T. Stutzle, Ant colony optimization - Artificial ants as a computational intelligence technique, IEEE Computational Intelligence Magazine, vol. 1, pp. 28–39, 2006.

[14] A.A. Kazharov, and V.M. Kureichik, Ant colony optimization algorithms for solving transportation problems, Journal of Computer and Systems Sciences International, vol. 49, pp. 30–43, 2010.

Simulation of deep learning control systems to reduce energy loses due to vibration and friction in rotor bearings

Alexey Kornaev
dept. of Mechatronics, Mechanics and Robotics
Orel State University named after I.S. Turgenev
Orel, Russian Federation
rusakor@inbox.ru

Roman Zaretsky
dept. of Mechatronics, Mechanics and Robotics
Orel State University named after I.S. Turgenev
Orel, Russian Federation
kogots@bk.ru

Sergey Egorov
dept. of Computer-Aided Systems in Mechanical Engineering
Tambov State Technical University
Tambov, Russian Federation
egorovsy@yandex.ru

Моделирование систем управления с глубоким обучением для снижения потерь энергии на вибрации и трение в подшипниковых опорах роторных машин

А.В. Корнаев
кафедра мехатроники, механики и робототехники
Орловский государственный университет имени И.С. Тургенева
Орел, Российская Федерация
rusakor@inbox.ru

Р.К. Зарецкий
кафедра мехатроники, механики и робототехники
Орловский государственный университет имени И.С. Тургенева
Орел, Российская Федерация
kogots@bk.ru

С.Я. Егоров
кафедра компьютерно-интегрированных систем в машиностроении
Тамбовский государственный технический университет
Тамбов, Россия
egorovsy@yandex.ru

***Abstract* — the paper considers a simulation model of a rotor-bearing complex with a bearing geometry control system based on reinforcement learning algorithm. The simulation results showed that reinforcement learning allowed to reduce friction and vibration losses in a rotary machine by directly controlling the clearance in the bearings and indirectly controlling the resulting hydrodynamic force and the trajectory of the rotor.**

Keywords — rotor dynamics, journal bearing, control system, artificial neural network

***Аннотация* — в работе рассмотрена имитационная модель роторно-опорного комплекса с системой управления геометрией подшипника на основе обучения с подкреплением. Результаты расчета показали, что обучение с подкреплением позволяет снизить потери на трение и вибрации в роторной машине за счет непосредственного управления зазором в подшипники и опосредованного управления результирующей гидродинамической силой и траекторией движения ротора.**

Ключевые слова — роторная динамика, подшипник жидкостного трения, система управления, искусственная нейронная сеть

I. Введение

Подшипники жидкостного трения являются одним из четырех основных видов опор роторов и одним из двух видов опор, реализующих режим трения без соприкосновения трущихся поверхностей [1]. Процесс гидродинамической смазки является сложным для управления, так как некоторые внешние воздействия на гидромеханическую систему способны вывести ее из состояния равновесия, инициировать возрастающие колебания, и даже вывести из строя роторную машину [1, 2]. В данной работе предложена вычислительная имитационная модель роторной установки с подшипниками жидкостного трения с управляемой величиной среднего зазора. Величина среднего зазора связана с толщиной смазочного слоя и, следовательно с действующей гидродинамической силой, жесткостью и демпфированием. Имитационное моделирование выполнялось на трех уровнях: модель подшипника жидкостного трения с переменным средним зазором, модель жесткого ротора и модель системы управления.

II. Моделирование подшипника жидкостного трения

В подшипнике жидкостного трения ротор и опора разделяются тонким смазочным слоем за счет возникающей гидродинамической силы. Поэтому математическая модель подшипника жидкостного трения определяется моделью течения жидкости в зазоре между шипом и подшипником (рис. 1). Обычно результирующая гидродинамическая сила находится из численного решения уравнения Рейнольдса [1,2]. Решение такой задачи вычислительно сложно, поэтому в задачах расчета траекторий колебаний роторов часто используется метод линеаризации реакции смазочного слоя вблизи положения равновесия как функции перемещения и скорости поперечных колебаний ротора. В таком случае вместо расчета реакции смазочного слоя на каждом шаге по времени выполняется расчет в нескольких точках в окрестности равновесного положения ротора, затем реакция линеаризуется с использованием матриц жесткости и демпфирования. В данной работе, как и в работе [3] вместо линеаризации используется аппроксимация гидродинамической реакции с использованием искусственной нейронной сети (ИНС).

Рассматривалась модель ротора массой *0.65* кг, длиной *0.35* м и диаметром *40* мм, вращающегося с постоянной частотой *3000* об/мин. Гладкий радиальный подшипник длиной *20* мм смазывается водой. Для численного решения уравнения Рейнольдса методом конечных разностей использовалась сетка размером $m = [11\ \ 21\ \ 11]$ Для аппроксимации результирующей гидродинамической силы и момента силы жидкостного трения в подшипнике использовались две ИНС прямого распространения с пятью входными нейронами (по две компоненты перемещения и скорости колебаний ротора, а также средний зазор подшипника), одним скрытым слоем с логистической функцией активации и двумя или одним выходным нейроном с линейной функцией активации [4]. В качестве обучающей выборки использовались результаты расчета колебаний ротора при различных значениях среднего зазора (*50, 100, 150 и 200* мкм). Результаты расчета траекторий представлены на рис. 1 (б). Данные расчета были использованы для обучения ИНС и аппроксимации компонент результирующей гидродинамической силы момента силы жидкостного трения, которые были затем использованы при разработке имитационной модели ротора с подшипниками жидкостного трения

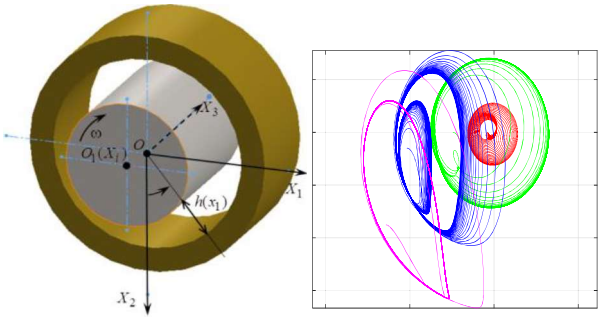

а б

Рис. 1. Моделирование подшипника жидкостного трения: расчетная схема шипа в подшипнике (а), результаты расчета траекторий колебаний ротора при различных значениях среднего зазора (б)

III. Моделирование ротора с опорами

Модель жесткого несимметричного ротора с идеальным шарнирным закреплением с одного конца и 6-степенным сопряжением, имитирующим подшипник жидкостного трения с другого конца была разработана с использованием специализированного программного обеспечения расчета динамики системы твердых тел. Силы, действующие на ротор в подшипнике рассчитываются с помощью разработанных ранее ИНС (раздел II). Также учитывается действие на ротор периодической силы, имитирующей центробежную силу с постоянным дисбалансом *5e-5* кг·м и рандомизированной внешней силы, не превосходящей по модулю веса ротора. Основным результатом расчета является траектория поперечных колебаний ротора. Кроме того, рассчитывается величина мощности движения ротора, которая в последствии должна быть минимизирована.

IV. Моделирование системы управления

Система управления траекторией движения ротора предназначена для обеспечения минимума потерь мощности на вращение ротора. Потери мощности происходят из-за потерь на трение и вибрацию. Управление зазором позволяет регулировать положение равновесия, упругие и демпфирующие свойства смазочного слоя. Минимизация потерь затруднительна для системы управления в связи с нелинейностью реакции смазочного слоя подшипника, нестационарностью состояния роторной системы и действием внешних сил случайного характера. Применение в таких условиях пропорционально-интегрально-дифференциального (ПИД) регулятора не позволило добиться положительных результатов, в отличие от ИНС, действующих по принципу обучения с подкреплением.

В качестве системы управления зазором используется агент типа DDPG (от англ. Deep Deterministic Policy Gradient). В его основе Марковский процесс, в котором регулируются отношения между состоянием, наблюдением и действием. Обучение агента производилось на имитационной модели ротора с подшипником жидкостного трения. Минимизировалась результирующая мощность движения ротора. Накладывались ограничения на его виброперемещения для предотвращения контакта шипа и подшипника. Обучение совершилось за 1700 эпизодов. Результаты расчета траекторий ротора с управлением и без представлены на рис. 2. На рис. 3 приведено сравнение мощностей вращения ротора с управлением и без. Из результатов видно, что управление зазором позволяет существенно снизить потери мощности и уровень вибраций в роторно-опорной системе. В среднем снижение мощности составило 19 %.

а б

Рис. 2. Результаты расчета траекторий ротора под действием периодической и случайной сил: движение без управления зазором (а) и с управляемым зазором (б)

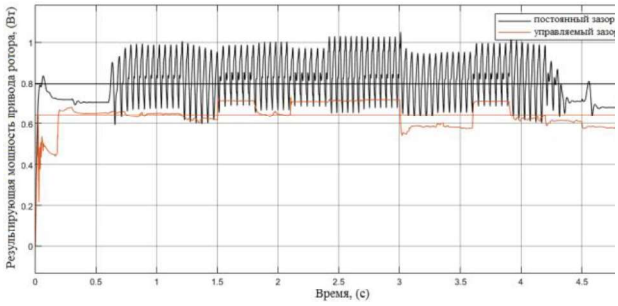

Рис. 3. Результаты расчета мощности движения ротора под действием периодической и случайной сил: движение без управления зазором (а) и с управляемым зазором (б)

Полученные результаты создают предпосылки разработки интеллектуальных роторных машин, в которых система управления в виде обученного агента может быть интегрирована в контроллер. Однако предварительно необходимо апробировать теоретические результаты в условиях реальной роторно-опорной машины или лабораторной установки.

Благодарности

Работа подготовлена в рамках выполнения проекта по гранту №16-19-00186 Российского научного фонда.

Авторский вклад

А.В. Корнаев разработал имитационную модель ротора и подшипника жидкостного трения, провел серию вычислительных экспериментов по расчету траекторий и разработал ИНС расчета гидродинамических сил. Р.К. Зарецкий разработал и протестировал систему управления зазором подшипника роторно-опорного комплекса на основе обучения с подкреплением. С.Я. Егоров разработал концепцию задачи управления.

Ссылки

[1] Л.А. Савин, О.В. Соломин. Моделирование роторных систем с опорами жидкостного трения: монография. М.: Машиностроение-1, 2006.

[2] Y. Hori. Hydrodynamic Lubrication. Yokendo Ltd, Tokyo, 2006.

[3] A.V. Kornaev, N.V. Kornaev, E.P. Kornaeva, L.A. Savin, “Application of artificial neural networks to calculation of oil film reaction forces and dynamics of rotors on journal bearings” Int. J. of Rotating Machinery, vol. 2017, 11 p, 2017 [https://doi.org/10.1155/2017/9196701].

[4] Goodfellow, Yo. Bengio, A. Courville. Deep Learning. MIT Press, 2016.

Mathematical modeling of the behavior of flexible micropolar mesh cylindrical panels with two sets of mutually orthogonal rods

Krylova E.Yu.
dept. of Mathematical and Computer Modeling
Saratov State University
Saratov, Russia
kat.krylova@bk.ru

Papkova I.V.
department of Mathematical and Modelling
Yuri Gagarin State Technical University of Saratov of organization
Saratov, Russia
Ikravzova@mail.ru

Saltykova O.A.
department of Mathematical and Modelling
Yuri Gagarin State Technical University of Saratov of organization
Saratov, Russia
olga_a_saltykova@mail.ru

Krysko V.A.
department of Mathematical and Modelling
Yuri Gagarin State Technical University of Saratov of organization
Saratov, Russia
tak@san.ru

***Abstract*— Micro- and nano-sized panels and casings are widely used in electromechanical systems, in medicine for the manufacture of biologically compatible implants, venous shunts. This leads to the need to create reliable mathematical models of the behavior of such mechanical objects, based on theories taking into account scale effects. Currently, there are few works on this subject [1-4].**

Keywords*— *micropolar mesh cylindrical panels, mathematical model

I. INTRODUCTION

In this paper, a mathematical model of the behavior of a shallow cylindrical panel, rectangular in plan, is constructed under the action of transverse distributed pressure, which occupies a region R^3 in space $\Omega = \left\{ -c \le x \le c; -b \le y \le b; -\frac{h}{2} \le z \le \frac{h}{2} \right\}$. The panel consists the sets of densely arranged edges of the same material, which allows the use the G.I.Pshenichniy continuum model [5]. The paper considers a nonclassical continual model based on a Cosserat environment, where, along with the usual stress field, momentary stresses are also taken into account. It is assumed that the fields of displacements and rotations are not independent.

II. EQUILIBRIUM EQUATIONS

The equilibrium equations of the element of a smooth panel, equivalent to the grid, the boundary and initial conditions are obtained from the Lagrange energy principle based on the Kirchhoff-Love hypotheses and Karman theory. The stresses arising in the equivalent smooth panel, associated with the stresses in the ribs making up the angles with the x-axis, will be:

$$\sigma_{xy} = \sum_{j=1}^{n} \frac{\sigma_x^j \delta_j Cos\varphi_j Sin\varphi_j}{a_j}, \ \sigma_{xx} = \sum_{j=1}^{n} \frac{\sigma_x^j \delta_j Cos^2\varphi_j}{a_j},$$

$$m_{xy} = \sum_{j=1}^{n} \frac{m_x^j \delta_j Cos\varphi_j Sin\varphi_j}{a_j}, \qquad m_{xx} = \sum_{j=1}^{n} \frac{m_x^j \delta_j Cos^2\varphi_j}{a_j},$$

$$m_{yy} = \sum_{j=1}^{n} \frac{m_x^j \delta_j Sin^2\varphi_j}{a_j}, \qquad m_{xz} = \sum_{j=1}^{n} \frac{m_{zx}^j \delta_j Cos\varphi_j}{a_j},$$

$$m_{yz} = \sum_{j=1}^{n} \frac{m_{zx}^j \delta_j Sin\varphi_j}{a_j},$$

where a_j - distance between edges of the j-th sets, δ_j - edge thickness, stresses with index j refer to rods. The physical relationships for the mesh plate are determined based on the Lagrange multipliers method:

$\sigma_x^j = \sigma_{xx} \mathrm{Cos}^2 \varphi_j + \sigma_{yy} \mathrm{Sin}^2 \varphi_j + \sigma_{xy} \mathrm{Cos}\varphi_j \mathrm{Sin}\varphi_j$;

$\tau^j = \sigma_{xz} \mathrm{Cos}\varphi_j + \sigma_{yz} \mathrm{Sin}\varphi_j$;

$m_x^j = m_{xx} \mathrm{Cos}^2 \varphi_j + m_{yy} \mathrm{Sin}^2 \varphi_j + m_{xy} \mathrm{Cos}\varphi_j \mathrm{Sin}\varphi_j$;

$m_z^j = m_{xz} \mathrm{Cos}\varphi_j + m_{yz} \mathrm{Sin}\varphi_j$.

In the future we will consider the panel with two families of edges $\varphi_1 = 0^o, \varphi_2 = 90^o$, $\delta_1 = \delta_2 = \delta$, $a_1 = a_2 = a$. Equilibrium equations in this case will take the form:

$$v\frac{\partial^2 v}{\partial x \partial y} + \frac{\partial^2 v}{\partial x^2} + k_y v\frac{\partial w}{\partial x} + v\frac{\partial w}{\partial y}\frac{\partial^2 w}{\partial x \partial y} + \frac{\partial w}{\partial x}\frac{\partial^2 w}{\partial x^2} - \frac{l^2(v-1)}{8} \cdot$$
$$\cdot \left(-\frac{\partial^4 u}{\partial y^4} + \frac{\partial^4 v}{\partial x \partial y^3} - \frac{\partial^4 u}{\partial x^2 \partial y^2} + \frac{\partial^4 v}{\partial x^3 \partial y} \right) = 0;$$

$$\frac{\partial^2 v}{\partial y^2} + v\frac{\partial^2 u}{\partial x \partial y} + k_y \frac{\partial w}{\partial y} + v\frac{\partial w}{\partial x}\frac{\partial^2 w}{\partial x \partial y} + \frac{\partial w}{\partial y}\frac{\partial^2 w}{\partial y^2} - \frac{l^2(v-1)}{8} \cdot$$
$$\cdot \left(\frac{\partial^4 u}{\partial x \partial y^3} - \frac{\partial^4 v}{\partial x^2 \partial y^2} + \frac{\partial^4 u}{\partial x^3 \partial y} - \frac{\partial^4 v}{\partial x^4} \right) = 0;$$

$$\frac{h^2}{12}\frac{\partial^4 w}{\partial y^4} + \frac{h^2 v}{6}\frac{\partial^4 w}{\partial x^2 \partial y^2} + \frac{h^2}{12}\frac{\partial^4 w}{\partial x^4} + 2l^2(1-v)\frac{\partial^4 w}{\partial x^2 \partial y^2} +$$
$$+ k_y^2 w - k_y \frac{\partial v}{\partial y} - v k_y \frac{\partial u}{\partial x} + \frac{k_y}{2}\left(\frac{\partial w}{\partial y}\right)^2 +$$
$$+ \frac{\partial w}{\partial y}\frac{\partial^2 v}{\partial y^2} + k_y w\frac{\partial^2 w}{\partial y^2} + \frac{\partial v}{\partial y}\frac{\partial^2 w}{\partial y^2} - \frac{3}{2}\left(\frac{\partial w}{\partial y}\right)^2 \frac{\partial^2 w}{\partial y^2} -$$
$$- v\frac{\partial^2 w}{\partial y^2}\frac{\partial u}{\partial x} + \frac{v k_y}{2}\left(\frac{\partial w}{\partial y}\right)^2 + \frac{v}{2}\frac{\partial^2 w}{\partial y^2}\left(\frac{\partial w}{\partial y}\right)^2 -$$
$$- v\frac{\partial w}{\partial y}\frac{\partial^2 u}{\partial x \partial y} + v\frac{\partial w}{\partial x}\frac{\partial^2 v}{\partial x \partial y} - 2v\frac{\partial w}{\partial y}\frac{\partial w}{\partial x}\frac{\partial^2 w}{\partial x \partial y} -$$
$$- \frac{\partial w}{\partial y}\frac{\partial^2 u}{\partial x^2} + v k_y w\frac{\partial^2 w}{\partial x^2} - v\frac{\partial v}{\partial y}\frac{\partial^2 w}{\partial x^2} -$$
$$- \frac{v}{2}\left(\frac{\partial w}{\partial y}\right)^2 \frac{\partial^2 w}{\partial x^2} - \frac{\partial u}{\partial x}\frac{\partial^2 w}{\partial x^2} - \frac{3}{2}\left(\frac{\partial w}{\partial x}\right)^2 \frac{\partial^2 w}{\partial x^2} = \frac{a(1-v^2)}{Eh\delta} q.$$

Boundary conditions - rigid termination at all ends of the panel:

$$u = v = w = 0, \quad \frac{\partial w}{\partial x} = 0, \quad \frac{\partial w}{\partial y} = 0, \quad npu \quad x = \pm c, \quad y = \pm b.$$

Initial conditions are zero.

The differential problem is reduced to a dimensionless form as follows: $u = \frac{h^2}{2c}\bar{u}$, $v = \frac{h^2}{2b}\bar{v}$, $k_y = \frac{h}{(2b)^2}\overline{k_y}$, $q = \frac{Eh^4}{(2c)^2(2b)^2}\overline{q}$, $x = 2c\bar{x}$, $y = 2b\bar{y}$, $w = h\bar{w}$, $\delta = h\bar{\delta}$, $a = h\bar{a}$, $l = h\bar{l}$, where u, v, w - axial displacement of the middle surface of the plate in the directions x, y, z, respectively, k_y - geometric curvature parameter, E - Young's modulus, ν - Poisson's ratio, $q = q_0$ - external normal uniformly distributed load, q_0 - its intensity.

To reduce the partial differential problem to a system of algebraic equations, we use the Bubnov – Galerkin method:

$$u(x,y) = ASin(\pi x)Sin(\pi y);$$
$$v(x,y) = BCos\left(\frac{\pi x}{2}\right)Cos\left(\frac{\pi y}{2}\right);$$
$$w(x,y) = CSin^2(\pi x)Sin^2(\pi y).$$

A study was conducted of the effect of the distance between the grid edges a, the value of the additional independent length parameter l, and the panel curvature

parameter k_y on the deflection at the center point of the panel.

III. Experiment

Experiment parameters: $c = b = 1$, $h = 0.02$, $\nu = 0.3$, $\delta = h$, $q_0 \in [0; 450000]$. A further increase in curvature leads to the more pronounced "slamming" of the panel. Increasing the distance between the ribs reduces the stiffness of the system. Increasing the parameter l increases the stiffness.

IV. Conclusion

In this paper, a mathematical model of the behavior of a micropolar mesh cylindrical panel consisting of two sets of mutually perpendicular ribs under the action of a normal distributed static load is constructed. Panel stability tested.

Acknowledgment

The work was carried out with the financial support of RFBR № 18-01-11351a, № 18-41-700001r_a

References

[1] V.A. Eremeev On a nonlinear model of the retina. News of the Russian Academy of Sciences. Solid mechanics, 2018, vol. 4, pp. 127-133.

[2] E.Yu.Krylova, I.V.Papkova, O.A.Saltykova, A.O.Sinichkina, V.A.Krysko Mathematical model of oscillations of size-dependent cylindrical shells of the net structure taking into account the Kirchhoff-Love deviations. Nonlinear world, 2018, vol. 16, 4, pp. 17-28.

[3] F.dell'Isola, D.Steigman A Two-dimensional Gradient-Elasticity Theory for Woven Fabrics J. Elast, 2015, vol. 118. N. 1. P. 113–125.

[4] E Yu Krylova, I V Papkova, A O Sinichkina, T B Yakovleva, V A Krysko-yang Mathematical model of flexible dimension-dependent mesh plates IOP Conf. Series: Journal of Physics: Conf. Series 1210 (2019) 012073 doi:10.1088/1742-6596/1210/1/012073

[5] G.I. Pshenichnov Theory of thin elastic mesh shells and plates. M .: Nauka, 1982. 352 p.

Theory of contact interaction of inhomogeneous beam-lamellar nanostructures taking into account the connectivity of the temperature and deformation fields

Krysko V.A.-jr
Department of "Mathematics and Modeling"
SSTU
Saratov, Russia
vadimakrysko@gmail.com

Yakovleva T.V.
Department of "Mathematics and Modeling"
SSTU
Saratov, Russia
yan-tan1987@mail.ru

Krysko V.A.
Department of "Mathematics and Modeling"
SSTU
Saratov, Russia
tak@san.ru

***Abstract*—In this paper, a theory of nonlinear dynamics and contact interaction of a plate-beam nanostructure was constructed taking into account the connectivity of the temperature and deformation fields under the conditions of external dynamic effects. The sought equations are derived from the Hamilton-Ostrogradsky principle. Nanoscale is taken into account by the modified couple stress theory. There are no restrictions on the temperature distribution on the plate-beam nanostructure. This is one of the key hypotheses. This mathematical model is a system of integral-differential equations of hyperbolic-parabolic type of different dimensions. The constructed mathematical model describes the operation of the constituent elements of the NEMS. Algorithms for calculating plate-beam nanostructures have been created, which are based on applying the Faedo-Galerkin method in higher approximations, reducing partial differential equations to the Cauchy problem, which is solved by Runge-Kutta-type methods.**

Keywords— coherence of temperature and strain fields, contact interaction, plate-beam nanostructures, Faedo-Galerkin method, Runge-Kutta-type methods.

I. Introduction

Nanobeams and nanoplates are components of NEMS. The presence of small gaps between the elements of such systems under the dynamic effects of various type (thermal and mechanical loads) causes chaotic oscillations in the system. At the same time, it is important to take into account the contact interaction of elements. In [1, 2], a theory of connectedness of temperature and strain fields for full-size mechanical structures was constructed. In this paper, a generalization of this theory is made taking into account nanoscale parameters according to the modified couple stress theory [3].

II. Formulation of the problem

In this paper, a theory of nonlinear dynamics and contact interaction of a nanoplate and a nanobeam with the connection of the temperature and strain fields is constructed. The nanostructure consists of a nanoplate, supported by the center of the nanobeam, between them there is a small gap, they are connected only through the boundary conditions. For the nanoplate, the Kirchhoff kinematic model was adopted, and for the nanobeam, Euler-Bernoulli. The sought equations are derived from the Hamilton-Ostrogradsky

principle. There are no restrictions on the temperature distribution on the plate-beam nanostructure. This is one of the key hypotheses. To take into account nanoscale parameters, a modified couple stress theory proposed by Young was applied. The relationship between stresses and strains in the nanoplate (β = 1) and nanobeam (β = 0) is represented in the form:

$$\varepsilon_1^z = \frac{1}{E}(\sigma_1 - \beta_1 \nu \sigma_2) + \alpha_T T_m \quad \varepsilon_{12}^z = \beta_1 2\frac{1+\nu}{E}\sigma_{12} \quad \overleftrightarrow{(1,2)} \tag{1}$$

here, E и ν are not constants in Hooke's law for a plane stress state, but functions $E = E(x, \beta y, z, \varepsilon_0, \varepsilon_i, \theta), \nu = \nu(x, \beta y, z, \varepsilon_0, \varepsilon_i, \theta)$. The method of variable parameters of elasticity of Birger I.A. [4] ε_0- volumetric deformation, ε_i- strain rate, α_T- linear thermal expansion coefficient, $\theta(x, \beta y, z)$– temperature increment for nanoplate (β=1) and for nanobeam (β=0).

To obtain the initial differential equations for the nanoplate and nanobeam, we use the variational principle:

$$\delta V + \delta D^* - \delta K^* = \iint_A (\overline{F_0}\delta\overline{u_0} - \theta\overline{n}\delta\overline{S})dA \tag{2}$$

where $\delta V, \delta D^*, \delta K^*$- variations of the generalized free energy, dissipative function and kinetic energy, respectively, F_0, u_0 - surface force and displacement, n is the external normal, and A is the surface bounding the body. The entropy displacement vector S is associated with the increment of the entropy s per unit volume according to the law: $s = -div\overline{S}$, where k_T - thermal conductivity, the dot denotes time differentiation, Ω is the volume occupied by the body (nanoplate or nanoscale), T_0 is the initial temperature.

On the right side of the first addend in the variation principle (2), the damping coefficient of the medium ε and q will appear - the intensity of the transverse load. After appropriate transformations according to the calculus of variations from (2), we obtain the system of differential equations for a two-layer nanostructure (3):

$$\begin{cases} \left\{\frac{p_1}{12\gamma_1^2} + \frac{p_2}{2}\frac{\gamma_2^2}{\gamma_1^2}\right\}\{\frac{\partial^2}{\partial x^2}[I_{1x} - \alpha_1 M_{1t}] + \frac{\partial^2}{\partial y^2}[I_{1y} - \alpha_1 M_{1t}] - 2\frac{\partial^2}{\partial x \partial y}(I_{1xy}\frac{\partial^2 w_1}{\partial x \partial y})\} + \\ + q_1 - \frac{\gamma}{g}h\frac{\partial^2 w_1}{\partial t^2} - \varepsilon\frac{\gamma}{g}h\frac{\partial w_1}{\partial t} - q_k = 0, \\ \nabla^2(\theta) = \frac{T_0}{K_T}\frac{\partial}{\partial t}(\frac{c\theta}{T_0} + G^*\alpha_T e_1), \quad (\beta_1 = 1), \\ -\left\{\frac{p_1}{12\gamma_1^2} + \frac{p_2}{2}\frac{\gamma_2^2}{\gamma_1^2}\right\}\frac{\partial^2}{\partial x^2}(I_2) - \frac{\partial^2 M_t}{\partial x^2} + q_2 - \frac{\gamma}{g}h\frac{\partial^2 w_2}{\partial t^2} - \varepsilon\frac{\gamma}{g}h\frac{\partial w_2}{\partial t} + q_k = 0, \\ \nabla^2(\theta) = \frac{T_0}{K_T}\frac{\partial}{\partial t}(\frac{c\theta}{T_0} + G^*\alpha_T e_2), \quad (\beta_1 = 0), \end{cases} \tag{3}$$

where $\gamma_1 = \frac{a}{h}, \gamma_2 = \frac{l}{h}$ $p_1 = \frac{1-\nu}{(1+\nu)(1-2\nu)}, p_2 = \frac{1}{2(1+\nu)}$,

$$I_{1x} = -\int_{-h/2}^{h/2}\frac{E_1 z^2}{1-\nu^2}(\frac{\partial^2 w_1}{\partial x^2} + \nu\frac{\partial^2 w_1}{\partial y^2})dz \quad I_{1xy} = \int_{-h/2}^{h/2}\frac{E_1 z^2}{1+\nu}dz$$

$$I_{1y} = -\int_{-h/2}^{h/2}\frac{E_1 z^2}{1-\nu^2}(\frac{\partial^2 w_1}{\partial y^2} + \nu\frac{\partial^2 w_1}{\partial x^2})dz \quad I_2 = \int_{-h/2}^{h/2}E_2 z^2 dz\frac{\partial^2 w_2}{\partial x^2}$$

$$M_{1t} = \int_{-h/2}^{h/2}\theta\, z(1+\nu)dz \quad M_t = \alpha_2\int_{-h/2}^{h/2}E_2\theta_2 z dz$$

$$q_k = K(w_1 - w_2 - h_k)\Psi \qquad \Psi = \frac{1}{2}[1 + sign(w_1 - h_k - w_2)],$$

$$e_1 = \varepsilon_{11}^z + \beta_1\varepsilon_{22}^z.$$

Contact interaction is taken into account according to the Winkler model [5]. If there is contact between the plate and the beam, then $\Psi = 1$, otherwise$\Psi = 0$. The ratio q_k represents the Winkler connection between compression and contact pressure. In system (3), w_1 and w_2 are the functions of the deflections of the nanoplate and nanobeam, respectively, K is the stiffness coefficient of transversal compression of the nanoplate in the contact zone, h_k is the gap between the elements, g is the acceleration of gravity, γ is the specific weight of the material G* - bulk compression module. The thickness of the nano-plate h and the height of the nanoplate h are the same, the width of the nanoplate is 1, a is the length of the nanoplate and nanobeam, b is the width of the nanoplate,$q(x, \beta y, t)$ – transverse loads acting on the nanoplate and applied to the nanobeam. There are no restrictions on the temperature distribution over the thickness of the nano-plate and the height of the nanobeam. It is possible to view different charts.$\sigma_i(\varepsilon_i, \theta)$, describing the dependence of stress for a number of materials on deformation and temperature. To system (3) one should add boundary conditions of the 1, 2, 3, and 4 kinds and initial conditions for the heat conduction equations. Here we give the equation only 1, 2 and 3 kind:

Boundary conditions of the first kind. Sets the temperature distribution over the body surface.

$$(0 \le x \le a), (-h/2 \le z \le h/2)\ \theta = \varphi(x, z, t) : (x, z) \in S \tag{4}$$

Boundary conditions 2 kinds. Sets the distribution of the density of the heat flux on the surface of the body as a function of the coordinates (x, z) and time Using the law of thermal conductivity of Fourier, we write in the form

$$\lambda_q\frac{\partial\theta}{\partial n} = \psi(x, z, t) : (x, z) \in S \tag{5}$$

Boundary conditions 3 kinds. On the body surface S, the distribution of the heat flux density is specified, depending on the temperature on the body surface and the temperature of the medium

$$\lambda_q\frac{\partial\theta}{\partial n} = Z(\theta - \theta_{cp}) \tag{6}$$

As the initial conditions we take the distribution of the deflections, the rates of the deflection and the temperature increment at the initial moment of time t=0.

Also, the boundary conditions for nanoplates and nanobeam:

contour hinge support for the nanoplate and at the ends of the nanobeam: $w_{\bar{n}} = M_{\bar{n}} = 0$ (7)

pinching along the contour for the nanoplate and at the ends of the nanobeam: $w_{\bar{n}} = w'_{x\bar{n}} = 0$ (8)

System (3) and boundary conditions (4-8) is a system of integral-differential equations of different dimensions, describing nonlinear oscillations and contact interaction of coupled deformation fields and structure temperature with physical nonlinearity, as well as temperature dependence of material properties.

III. ALGORITHM SOLUTIONS

Equations (3-8) are reduced to a system of ordinary integral-differential equations using the Faedo-Galerkin method in higher approximations. For this, the required functions $w_1, w_2, \theta_1, \theta_2$ are represented as follows:

$$w_1 = \sum_{i=1}^{N} A_i(t)\varphi_i(x,y)\ w_2 = \sum_{i=1}^{N} B_i(t)\psi_i(x)$$
$$\theta_1 = \sum_{i=1}^{N} C_i(t)\xi_i(x,y,z)\ \ \theta_2 = \sum_{i=1}^{N} D_i(t)f_i(x,z) \quad (9)$$

Equations (9) are substituted into the desired system (3-8) and after the orthogonalization procedure, we obtain a system of ordinary integral-differential equations with a variable coefficient and contact interaction. In this case, at the previous time step, the obtained temperature values are substituted for the integral sign as a known function from the previous step. The obtained Cauchy problem is also solved by numerical methods of the Runge-Kutta type. The convergence of the methods is investigated depending on the number of members of the series (9) and the time step.

The constructed mathematical model is the most common, since it takes into account contact interaction, the relationship of temperature fields and deformations, physical nonlinearity and the dependence of material properties on temperature.

ACKNOWLEDGMENT

This work was supported by the grant of the RSF No. 16-11-10138-П.

REFERENCES

[1] Yakovleva T.V., Krysko V.A.-jr. Contact interaction of a physically nonlinear three-layer lamellar-beam structure in a temperature field. // Deformation and destruction of materials. 2017. № 6. P. 9-14.

[2] Krysko V.A.-Jr., Awrejcewicz J., Yakovleva T.V., Kirichenko A.V., Szymanowska O., Krysko V.A. Mathematical modeling of MEMS elements subjected to external forces, temperature and noise, taking account of coupling of temperature and deformation fields as well as a nonhomogenous material structure. // Commun Nonlinear Sci Numer Simulat 72 (2019) 39–58.

[3] Yang J. , Ono T. , Esashi M. Energy dissipation in submicron thick single-crystal silicon cantilevers. J Microelectromech Sys 2002;11(6):775–83 .

[4] Birger I.A . Some general methods for solving problems in the theory of elasticity. Appl Math Mech 1951;15:6–14 .

[5] Kantor B.Y . Contact problems of the nonlinear theory of shells of revolution. Kiev: Ukrainian Academy of Sciences; 1990.

Spatio-temporal cortical activity during a visual task accomplishing

Alexander Kuc
Patent and license department,
Saratov State Technical University,
Saratov, Russia,
kuc1995@mail.ru

Vladimir Maksimenko
Neuroscience and Cognitive Technology Laboratory, Center for Technologies in Robotics and Mechatronics Components
Innopolis University,
Innopolis, Republic of Tatarstan, Russia
maximenkovl@gmail.com

***Abstract*— It is known that neuronal populations of cortical brain network are involved in the processes, related to accomplishing of different tasks, e.g. processing of sensory information and making decisions. Each particular type of tasks is characterized by the specific features of neuronal activity both in time-frequency and spatio-temporal domains. These features of neuronal activity reflect the structure of electrical activity signals (EEG) registered from the head surface via noninvasive electrodes. EEG signals are composed of the different rhythms of neuronal activity. While some studies relate these rhythms to the particular basic brain functions, other studies demonstrate that specific scenarios of EEG rhythms dynamics can be associated with accomplishing of cognitive task and affect human behavioral performance. With this in mind we analyze the spatio-temporal dynamics of alpha and beta rhythms of cortical activity during processing visual task and relate the features of rhythms dynamics to human's behavioral performance.**

Keywords—cortical network, visual task, reaction time, wavelet analysis, spatio-temporal activity.

I. INTRODUCTION

Modern concepts in neuroscience implies the key role of the whole cortical network in accomplishing of cognitive tasks [1]. For instance, it is known that remote cortical regions can interact during processing high amount of sensory information [2]. Moreover, depending on human's condition, the same task can be accomplished via involving neuronal populations in different cortical areas [3].

Activity of the neuronal population, belonging to the particular cortical region can be captured by recording electrical signal (EEG) from the corresponding area of the head surface. The recorded EEG signals are composed of different rhythms of neuronal activity e.g. delta (1-5 Hz), theta (5-8 Hz), alpha (8-12 Hz), beta (15-30 Hz) and gamma (50-100 Hz).

According to recent experimental works [4], while the spiking activity of individual neurons in a particular area appears in the high-frequency gamma-band, the low-frequency activity modulates activity of single neurons and serves for a communication between distant brain regions. Thus, increase of the EEG spectral energy in particular frequency bands in particular areas can be associated with the involvement of these areas in cognitive process.

In this paper we consider the spatio-temporal neuronal activity during visual task accomplishing by analyzing time-

frequency structure of EEG signals. We focus on alpha and beta frequency bands since they are related to visual information processing [5]. For instance, it is known that changes in alpha-band activity are associated with the visual attention [6] and changes of beta-band activity - with the stimuli processing [7] and shift of the brain to an attention state [8].

II. Materials and Methods

A. Participants

Twenty healthy unpaid volunteers, 11 males and 9 females, between the ages of 26 and 35 with normal or corrected-to-normal visual acuity participated in the experiments. All of them provided informed written consent before participating. The experimental studies were performed in accordance with the Declarationof Helsinki and approved by the local research Ethics Committee of the Innopolis University.

B. Visual task

The visual task was the classification of consistently presented ambiguous Necker cubes as left- or right-oriented [9]. The Necker cube is a 2D-image which looks like a cube with transparent faces and visible ribs (Fig. 1).

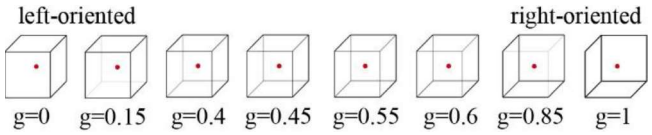

Fig.1. The examples of presented Necker cube images with different values of control parameter *g*

An observer without any perception abnormalities perceives the Necker cube as a bistable 3D-object due to the specific position of the inner ribs. The value g defining a contrast of the three middle ribs is usually used as a control parameter. The values g=1 and g=0 correspond, respectively, to 0 (black) and 255 (white) pixels' luminance of the middle lines. Each Necker cube image drawn by black and gray lines was located at the center of the computer screen on a white background. A red dot drawn at the center of the Necker cube was used to attract the attention of subjectsand prevent possible perception shifts due to eye movements while observing the image. To demonstrate a stimulus, we used a 24" BenQ LCD monitor with a spatial resolution of 1920-1080 pixels and a refresh rate of 60Hz. The subjects were located at a distance of 70–80 cm from the monitor with a visual angle of approximately 0.25 rad. The Necker cube size on the monitor was 14.2 cm. Bistability in the cubeperception consists in its interpretation as to be either left- or right-oriented depending on the inner ribs contrast.

The subject was instructed to press left or right button on the joystick depending on the interpretation of the current image (left- or right-oriented). The reaction time was estimated for each stimulus as the time interval between image presentation and button pressing moment.

C. Continuous wavelet transform

To analyze time-frequency structure of EEG signals we used continuous wavelet analysis. Wavelet coefficients were calculated via equation

$$W(f,t_0) = \sqrt{f}\int_{-\infty}^{+\infty} x(t)\varphi^*\big(f(t-t_0)\big)dt, \qquad (1)$$

where the mother wavelet function φ was used to be Morlet wavelet.

To analyze network activity in alpha and beta frequency bands, we calculated wavelet coefficients averaged over the corresponding frequency ranges (8-12 Hz and 15-30 Hz)

$$W_{\alpha,\beta}(t) = \int_{f\epsilon f_{\alpha,\beta}} W(f,t)df. \qquad (2)$$

For these bands we considered the values of wavelet spectral energy:

$$E_{\alpha,\beta}(t) = \sqrt{W_{\alpha,\beta}}(t), \qquad (3)$$

calculated for 1-s. EEG-trials, associated with processing of visual stimulus.

III. Results

We have recorded 31 EEG signals via noninvasive electrodes, arranged according to 10-10 layout (Fig. 2, a). At the first stage, EEG-trials associated with visual stimulus processing were divided into two groups according to subject's reaction times. Group S1 included trials with long reaction time and S2 – with short reaction time (Fig. 2, b). Each group contained 20 trials.

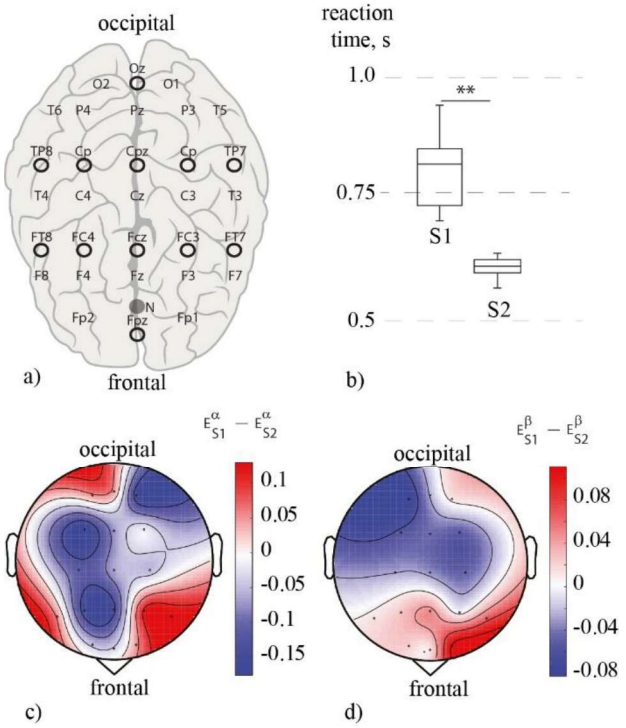

Fig.2. (a) 10-10 electrode layout; (b) Reaction times for two groups of trials; Differences between EEG spectral energy related to processing S1 and S2 stimuli in alpha (c) and beta (d) frequency bands

For groups S1 and S2 EEG spectral energy was averaged over 20 trials. Then, for each channel the difference between values, obtained for S1 and S2 was calculated and visualized by a color map over the head surface. Results are presented in Fig. 2 for alpha (c) and beta (d) frequency bands. One can see that in both bands the obtained difference exhibits negative value. It evidences higher value of spectral energy for S2 trials, where the reaction time is small. It can be seen that S2 is characterized by increase of beta-band energy in parietal area (Fig. 2, d). According to works [10, 11], this area is associated with the center of visual attention exciting in beta-band frequencies. Along with the beta-band, the

spectral energy in alpha-band exhibits increase in fronto-parietal area (Fig. 2, c). It can be associated with establishing neuronal functional interaction between these remote cortical regions for speeding up stimuli processing.

IV. CONCLUSION

We have analyzed the time-frequency and spatio-temporal neural activity during processing of visual sensory stimuli. Analysis of the behavioral data has revealed, that processing of each stimulus takes either long or short time. The short time of stimulus processing is achieved when EEG spectral energy increases in beta-band in parietal region and in alpha-band in parieto-frontal region.

ACKNOWLEDGMENT

This work is supported by Russian Science Foundation (grant 19-12-00050).

REFERENCES

[1] S. Smith, "Linking cognition to brain connectivity" in Nature neuroscience, vol. 19, 2016, p. 7.

[2] K. Finc, K. Bonna, M. Lewandowska, T. Wolak, J. Nikadon, J. Dreszer et al. "Transition of the functional brain network related to increasing cognitive demands" in Human brain mapping, vol 38, 2017, pp. 3659–3674.

[3] V.A. Maksimenko, A.E. Runnova, M.O. Zhuravlev et al, "Human personality reflects spatio-temporal and time-frequency EEG structure" in PloS one, vol. 13(9), 2018, e0197642.

[4] R.T. Canolty, E. Edwards, S.S. Dalal, M. Soltani, S.S. Nagarajan, H. E. Kirsch, M.S. Berger, N.M. Barbaro, R.T. Knight, "High Gamma Power Is Phase-Locked to Theta Oscillations in Human Neocortex" in Science , vol. 313, 2006, pp. 1626–1628.

[5] V.A. Maksimenko, A.E. Runnova, M.O. Zhuravlev, et al. "Visual perception affected by motivation and alertness controlled by a noninvasive brain-computer interface" in PloS one, vol. 12, 2017, e0188700.

[6] P. Sauseng, W. Klimesch, W. Stadler, M. Schabus, M. Doppelmayr, S. Hanslmayr, et al. "A shift of visual spatial attention is selectively associated with human eeg alpha activity" in European Journal of Neuroscience, vol. 22, 2005, pp. 2917–2926.

[7] P. Sehatpour, S. Molholm, T.H. Schwartz, J.R. Mahoney, A.D. Mehta, D.C. Javitt, et al. "A human intracranial study of long-range oscillatory coherence across a frontal–occipital–hippocampal brain network during visual object processing" in Proceedings of the National Academy of Sciences, vol. 105, 2008, pp. 4399–4404.

[8] M. Gola, M. Magnuski, I. Szumska, A. Wrobel. "EEG beta band activity is related to attention and attentional deficits in the visual performance of elderly subjects" in International Journal of Psychophysiology, vol. 89, 2013, pp. 334–341.

[9] J. Kornmeier, M. Pfaffle, M. Bach, "Necker cube: stimulus-related (low-level) and percept-related (high-level) EEG signatures early in occipital cortex" in Journal of vision, vol. 11, 2011, p. 12.

[10] H. Laufs, J.L. Holt, R. Elfont, M. Krams, J.S. Paul, K. Krakow, A. Kleinschmidt, "Where the BOLD signal goes when alpha EEG leaves". In Neuroimage, vol. 31(4), 2006, pp.1408-1418.

[11] V.A. Maksimenko, A.E. Runnova, N.S. Frolov, V.V. Makarov, V. Nedaivozov, A.A. Koronovskii, et al "Multiscale neural connectivity during human sensory processing in the brain" in Physical Review E vol. 97, 2018, 052405.

Controlling synchronization in networks of nonidentical neuronlike oscillators

Danil Kulminskiy
Saratov Branch of the Institute of Radio Engineering and Electronics of Russian Academy of Sciences
Saratov, Russia
kulminskydd@gmail.com

Mikhail Prokhorov
Saratov Branch of the Institute of Radio Engineering and Electronics of Russian Academy of Sciences
Saratov, Russia
mdprokhorov@yandex.ru

Vladimir Ponomarenko
Saratov Branch of the Institute of Radio Engineering and Electronics of Russian Academy of Sciences
Saratov, Russia
ponomarenkovi@gmail.com

***Abstract*—We study the synchronization in a network of delay-coupled nonidentical neuronlike oscillators described by the FitzHugh–Nagumo equations. The cases of constant strength of couplings and adaptively controlled couplings between the oscillators are considered. For the experimental study and control of synchronization in the network of neuronlike oscillators, we construct a radio engineering setup in which it is possible to specify an arbitrary architecture and type of couplings between the oscillators. It is shown that the using of an adaptively controlled delayed coupling allows one to achieve the in-phase synchronization of all oscillators in the network even in the case of a large parameter mismatch.**

Keywords— Adaptive control, network synchronization, delayed couplings.

I. INTRODUCTION

The study of synchronization processes and their control in networks of coupled oscillators is an important task for various scientific disciplines, which attracts the attention of many researchers [1–7]. In recent years, when solving the problem of controlling the collective dynamics in networks, the emphasis has shifted towards considering large networks with complex topologies and adaptive dynamical networks, which are characterized by own dynamics in both nodes and couplings. A lot of methods for adaptive control of synchronization have been proposed that allow for tuning the coupling parameters over time [8–13]. Such methods take into account the plasticity of couplings between oscillators, adjusting the coupling strength.

However, most of the methods for adaptive control of synchronization have been applied to model networks of coupled identical oscillators. In this paper, we experimentally and numerically investigate the synchronization in a network of delay-coupled nonidentical neuronlike oscillators. The case of adaptively controlled coupling leading to the in-phase synchronization of all oscillators in the network is considered. A scheme is proposed that allows one to study the synchronization in complex networks of neuronlike oscillators in a physical experiment with electronic oscillators.

II. Object of Investigation

We consider a network consisting of delay-coupled neuronlike oscillators, the dynamics of each of which is described by the simplified FitzHugh–Nagumo equations [9]:

$$\begin{aligned} \varepsilon\dot{u}_i(t) &= u_i(t) - \frac{u_i^3(t)}{3} - v_i(t) + C_i(t)\sum_{j=1}^{N} G_{i,j}\left(u_j(t-\tau) - u_i(t)\right), \\ \dot{v}_i(t) &= u_i(t) + a_i, \end{aligned} \quad (1)$$

where $i=1,\ldots,N$, with N being the number of oscillators, $u_i(t)$ and $v_i(t)$ denote the activator and inhibitor variables, respectively, ε is the time-scale parameter, a_i are the threshold parameters, τ is the delay time, which characterizes the time the signal needs to propagate between the nodes i and j, $C_i(t)$ describes the coupling strength, and $\mathbf{G}=\{G_{i,j}\}$ denotes the coupling matrix that determines the topology of the network. The matrix $\mathbf{G}$ is constructed by setting the entry $G_{i,j}$ equal to 1, if the j-th node is coupled to the i-th node, and equal to 0, if there is no coupling between the nodes j and i. In general case, all oscillators of the network are nonidentical.

For a large number of oscillators in the network and a large number of couplings between them, it is rather difficult to construct such a network in a physical experiment. The task is even more complicated if it is necessary to define complex functional couplings between the network elements. To solve the nontrivial problem of experimental study of the system (1), we constructed an original radio engineering setup, which allows us to specify an arbitrary architecture of couplings between the oscillators and ensure the adaptive adjustment of couplings during the experiment.

III. Results

First, we consider the case of two bidirectionally coupled FitzHugh–Nagumo systems. Both for the model and experimental coupled systems, we construct the partition of the parameter plane (a_1, a_2) into the regions of existence of typical oscillation regimes. It is shown that in the case of constant strength of couplings $C_1(t)$ and $C_2(t)$, the oscillators exhibit anti-phase oscillations with close amplitudes at $a_1<1$ and $a_2<1$. To achieve the in-phase synchronization of oscillators, we use the adaptively controlled couplings.

Then we consider a ring network consisting of 10 unidirectionally coupled nonidentical FitzHugh–Nagumo systems. Figs. 1(a) and (b) show the time series of $u_i(t)$ and $v_i(t)$, respectively, for all oscillators of the model system with the constant delayed couplings $C_1(t)=\ldots=C_N(t)=0.3$, $\varepsilon=0.1$, $\tau=1.5$, and $a_i=0.1+0.05i$. In this case, the oscillations of both $u_i(t)$ and $v_i(t)$ have close amplitudes, but they are not synchronized in phase.

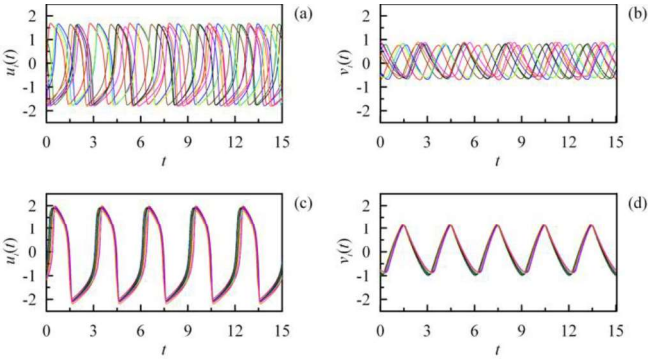

Fig. 1. Time series of $u_i(t)$ and $v_i(t)$ in the model ring system of 10 nonidentical FitzHugh–Nagumo systems for the cases of constant delayed coupling (a) and (b) and adaptively controlled delayed coupling (c) and (d).

The in-phase synchronization of oscillators cannot be achieved even with large values of $C_i(t)$. Figs. 1(c) and (d) show the in-phase synchronization of oscillators, achieved with the adaptively tuned strength of couplings.

For the same parameter values, we carried out the experimental investigation of synchronization in the ring of 10 unidirectionally coupled nonidentical FitzHugh–Nagumo electronic oscillators for the cases of constant and adaptively controlled delayed coupling. Fig. 2 illustrates the change in the experimental time series of $u_i(t)$ at the transition from the constant delayed coupling to the adaptive coupling. The oscillators exhibit non-phase oscillations at $t<2$ ms. After the switching of the delayed coupling from the constant to adaptive, a transient process is observed in the network. After the completion of the transition process, all oscillators in the ring show the in-phase oscillations.

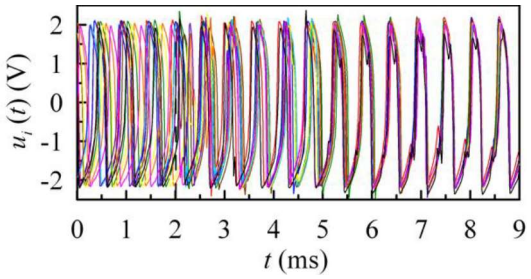

Fig. 2. Experimental time series of $u_i(t)$ in the ring of 10 nonidentical FitzHugh–Nagumo electronic oscillators with the constant delayed coupling at $t<2$ ms and adaptively controlled delayed coupling at $t\geq 2$ ms. The moment of switching of coupling from the constant to adaptive is shown by vertical dash line.

IV. Conclusion

We have experimentally and numerically investigated synchronization in the networks of delay-coupled nonidentical neuronlike oscillators. It is shown that the using of the adaptively controlled delayed coupling allows one to pass from non-phase oscillations of nonidentical oscillators to their in-phase synchronization.

Acknowledgment

This work was supported by the Grant of the President of Russian Federation for Young Scientists, project MK-1199.2019.8 (design of the experimental setup).

References

[1] Pikovsky, M. Rosenblum, and J. Kurths, Synchronization: A Universal Concept in Nonlinear Sciences, Cambridge: Cambridge University Press, 2001.

[2] S. Boccaletti, V. Latora, Y. Moreno, M. Chavez, and D.-U. Hwang, "Complex networks: structure and dynamics," Phys. Rep., vol. 424, pp. 175–308, 2006.

[3] J. Q. Sun and G. Ding, Advances in Analysis and Control of Time-Delayed Dynamical Systems, Singapore: World Scientific, 2013.

[4] V. Klinshov and V. I. Nekorkin, "Synchronization of delay-coupled oscillator networks," Phys. Usp., vol. 56, pp. 1217–1229, 2013.

[5] P. Bezruchko, M. D. Prokhorov, and Ye. P. Seleznev, "Oscillation types, multistability, and basins of attractors in symmetrically coupled period-doubling systems," Chaos, Solitons & Fractals, vol. 15, pp. 695–711, 2003.

[6] X. Mao and Z. Wang, "Stability, bifurcation, and synchronization of delay-coupled ring neural networks," Nonlinear Dyn., vol. 84, pp. 1063–1078, 2016.

[7] I. Ponomarenko, D. D. Kulminskiy, and M. D. Prokhorov, "Chimeralike states in networks of bistable time-delayed feedback oscillators coupled via the mean field," Phys. Rev. E, vol. 96, 022209, 2017.

[8] J. Lehnert, P. Hövel, A. Selivanov, A. L. Fradkov, and E. Schöll, "Controlling cluster synchronization by adapting the topology," Phys. Rev. E, vol. 90, 042914, 2014.

[9] S. A. Plotnikov, J. Lehnert, A. L. Fradkov, and E. Schöll, "Adaptive control of synchronization in delay-coupled heterogeneous networks of FitzHugh-Nagumo nodes," Int. J. Bifurcat. Chaos, vol. 26, 1650058, 2016.

[10] O. V. Maslennikov and V. I. Nekorkin, "Adaptive dynamical networks," Phys. Usp., vol. 60, pp. 694–704, 2017.

[11] W.-J. Yuan, J.-F. Zhou, I. Sendiña-Nadal, S. Boccaletti, and Z. Wang, "Adaptive control of dynamical synchronization on evolving networks with noise disturbances," Phys. Rev. E, vol. 97, 022211, 2018.

[12] Novičenko and I. Ratas, "In-phase synchronization in complex oscillator networks by adaptive delayed feedback control," Phys. Rev. E, vol. 98, 042302, 2018.

[13] Fan, L. Zhang, and Q. Wang, "Transition dynamics and adaptive synchronization of time-delay interconnected corticothalamic systems via nonlinear control," Nonlinear Dyn., vol. 94, pp. 2807–2825, 2018.

Approaches for the Improvement of motor-related patterns classification in EEG signals

Semen Kurkin
Neuroscience and Cognitive Techology Lab. Center for Technologies in Robotics and Mechatronics Components
Innopolis University
Innopolis, Russia
kurkinsa@gmail.com

Vladimir Maximenko
Neuroscience and Cognitive Techology Lab, Center for Technologies in Robotics and Mechatronics Components
Innopolis University
Innopolis, Russia
maximenkovl@gmail.com

Elena Pitsik
Neuroscience and Cognitive Techology Lab, Center for Technologies in Robotics and Mechatronics Components
Innopolis University
Innopolis, Russia
pitsikelena@gmail.com

***Abstract*—We apply artificial neural network (ANN) for recognition and classification of electroencephalographic (EEG) patterns associated with motor imagery for untrained subjects. Classification accuracy is optimized by reducing complexity of input experimental data. For multichannel EEG recorded by the set of 31 electrodes, we select an appropriate type of ANN which reaches 80±10% accuracy for single trial classification. We analyze the time-frequency structure of EEG signals and find that motor-related features associated with left- and right-leg motor imagery, are more pronounced in the mu (8-13 Hz) and delta (1-5 Hz) brainwaves. Based on the obtained results, we propose the optimization approach by pre-processing the EEG signals with a low-pass filter with different cutoffs. We demonstrate that the filtration of high-frequency spectral components significantly enhances the classification performance: up to 90±5% using 8 electrodes only.**

Keywords—EEG analysis, motor-related patterns, artificial neural network, classification accuracy

I. INTRODUCTION

EEG is a wide-spread inexpensive method for brain research which gives a deep insight into brain functionality related to various human activities. However, the treatment of multichannel EEG signals is a very sophisticated task because they are non-stationary, high-dimensional and extremely noisy. All these factors make difficult the recognition and classification of specific motor-related or percept-related patterns in a single-trial mode [1,2] and require extensive statistical measures.

Among existing approaches for EEG data analysis, the most promising and effective tools for classification of single EEG trials are based on artificial neural networks (ANNs) [3]. The successful application of ANNs requires careful selection of their parameters which can significantly vary depending on a particular task and different subjects [4]. The optimization of EEG input data and channel selection are key problems for the development of efficient ANN-based brain-computer interfaces (BCIs). Traditional methods of dimensionality reduction include principal component analysis (PCA) and linear discriminant analysis (LDA). However, such methods are non-generic and require the input data optimization for every subject due to strong inter-subject variability [5] and a lack of association of on-going optimization with physiological processes in the brain. These problems are particularly relevant for untrained subjects [5,6]. Indeed, many BCI studies involve specially trained subjects, since the classification of brain activity patterns

during motor imagery of untrained subjects is significantly more difficult and hence poorly studied [7,8].

A promising approach to solving the above problems is the optimization of the input data set based on the knowledge of the laws of the processes occurring in the brain when making some action, such as motor imagery. The simplest and intuitively clear method for the feature space reduction is a decrease of the number of EEG channels, basing on the time-frequency analysis.

Here, we propose an approach for optimization of input dataset based on the low-pass filtration of input EEG data with different cut-off values and the selection of particular EEG channels, with the aim to detect the most effective spatial EEG configuration to obtain maximum classification accuracy.

II. Experiment and Methods

A. Design of the Experiment

The main part of experimental work involved 12 subjects, both males (8 persons) and females (4 persons). Each subject participated in one experiment lasting about 30 minutes during which he/she had to perform two types of tasks: 1) real movement of left/right leg (raising a leg in a hip); 2) imaginary movement of left/right leg. The real movements in the first task were performed in order to make the subjects clearer how exactly they should imagine the movement by performing the second task. Each task proceeded by a whistle signal and followed by pauses of random durations (5-10 seconds).

The multichannel EEG were recorded at a 250-Hz sampling rate from P = 31 electrodes with two reference electrodes placed at the standard ears positions of the extended 10–10 international system. To register the EEG data, we used a cup with Ag/AgCl electrodes placed on the "TIEN–20" paste. The EEGs were recorded with the electroencephalograph "BE Plus LTM".

B. ANNs Application

Training and testing of the ANN were performed for every subject using two datasets containing 6000 points each for imaginary movements of the left and right feet. Each dataset consisted of the combination of eight 3-s EEG trials. Half of the datasets, chosen at random, were used to train the ANN based on backpropagation algorithm, and the remaining half – to test it. For each subject, the ANN training process was carried out anew. The number of ANN inputs was equal to the number of used EEG channels. Different combinations of used channels were considered in this research. The number of neurons in the output layer was one, because the output can only be 0 or 1. The recorded data were low-pass filtered with cut-offs at f_c^1=4 Hz or f_c^2=15 Hz.

The fastest and accurate recognition of motor imagery EEG patterns can be achieved with the following machine learning approaches: 1. radial basis function (RBF) network with 251 neurons in hidden layer, 31 input and 1 output linear neurons; 2. multilayer perceptron (MLP) with one hidden layer consisted of 15 neurons with hyperbolic tangent as an activation function, 31 input linear neurons and one output neuron with logistic activation function; 3. support vector machine (SVM-RBF) with nonlinear kernel based on radial basis function with values $0.01<\gamma<0.1$ and 2000 support vectors in summary (1000 for each class). A linear network (LN) was applied for more representative results.

III. Results

The EEG trials were classified into two groups (left-leg imagery and right-leg imagery) with the help of ANNs with different configurations: SVM, MP, RBF, LN. In Fig. 1a, the classification accuracy of each network was calculated for all 31 EEG channel.

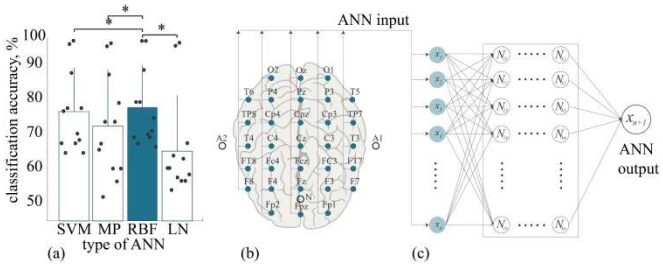

Fig. 1. (a) Classification accuracies (mean values ± SD) for SVM, MP, RBF, and LN averaged over all subjects; (b) position of electrodes according to extended 10-10 international system on human head; (c) general model of ANN, where each input neuron receives data from one of electrodes.

Having compared these ANN architectures, one can find RBF to be the most optimal architecture, which classification accuracy significantly exceeded the accuracy rates of both SVM and MLP (n = 12, $*p > 0.05$ via paired-sample t-test). The demonstrated accuracy score of 77.9% was achieved for a non-optimized input, i.e., for the whole set of EEG channels containing oscillations in a wide frequency range. However, previous studies show that if one takes into account all possible features of a multichannel EEG for the classification task, the results have an extremely high-dimensional feature space that significantly increases input complexity and decreases the accuracy rate.

In order to reduce the number of EEG channels, we analyze the RBF-based accuracy rate obtained for different predefined sets of channels. In Fig. 2a, the values of classification accuracy are shown for 9 most representative configurations. One can see that the most accurate result is obtained using combination S_1 which corresponds to full placement (31 electrodes) (see Fig. 2a). At the same time, despite the best recognition performance, we cannot consider this combination as optimal due to a large number of channels (see Fig. 2b). Let us consider S_5 corresponding to the combination of frontal and temporal lobes. One can see that among others channels' combinations (except for S_1), S_5 provides the best recognition quality.

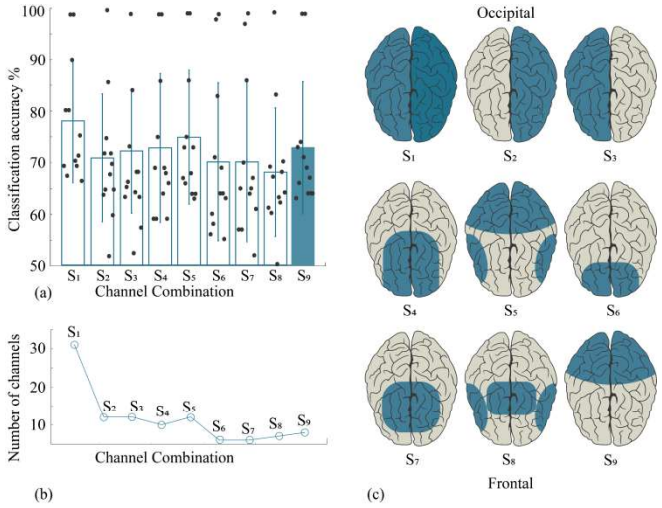

Fig. 2. (a) RBF classification performance for different brain areas, averaged over all subjects; (b) number of channels in each combination S_i (i = 1..9); (c) brain areas used for motor imagery classification.

The frontal lobe covers the largest brain area, and its combination with temporal lobes still contains too many electrodes. Considering these areas separately, we can note S_9 as the most appropriate choice due to a smaller number of channels (8 electrodes versus 12 in S_5) and about the same level of the classification score. It should be noted that frontal lobe is strongly associated with motor activity, decision-making and many others important cognitive and emotional aspects [9,10]. This result is in agreement with the previous research [10,11], where the time-frequency analysis revealed highly pronounced arm's motor imagery events in event-related desynchronization of delta band in frontal cortex.

So, by focusing on optimization of classification accuracy, we have reduced complexity of input data [12]. In the context of optimization, we have made the optimal selection of a set of EEG channels. The obtained results can be used to increase efficiency of brain-computer interfaces designed for untrained subjects or a group of subjects.

ACKNOWLEDGMENT

This work was supported by the President Program (projects NSH-2737.2018.2)..

REFERENCES

[1] V.A. Maksimenko, A.E. Runnova, M.O. Zhuravlev, et al. "Visual perception affected by motivation and alertness controlled by a noninvasive brain-computer interface," PLoS ONE, vol. 12, No. e0188700, 2017.

[2] A.E. Hramov, V.A. Maksimenko, S.V. Pchelintseva, et al. "Classifying the perceptual interpretations of a bistable image using EEG and artificial neural networks," Frontiers in Neuroscience, vol. 11, 674, 2017.

[3] J. Yang, H. Singh, E.L. Hines, et al. "Channel selection and classification of electroencephalogram signals: an artificial neural network and genetic algorithm-based approach," Artificial Intelligence in Medicine, vol. 55, pp. 117–126, 2012.

[4] H. Bashashati, R.K. Ward, G.E. Birch, A. Bashashati. "Comparing different classifiers in sensory motor brain computer interfaces," PLoS ONE, vol. 10, No. e0129435, 2015.

[5] M.C.B. Å berg, J. Wessberg. "Evolutionary optimization of classifiers and features for single-trial EEG discrimination," Biomed. Eng. Online, vol. 6, No. 32, 2007.

[6] S. Kurkin, E. Pitsik, N. Frolov. "Artificial intelligence systems for classifying EEG responses to imaginary and real movements of operators," In Saratov Fall Meeting 2018: Computations and Data Analysis: from Nanoscale Tools to Brain Functions, vol. 11067, International Society for Optics and Photonics, 2019, p. 1106709.

[7] V.A. Maksimenko, A. Pavlov, A.E. Runnova, et al. "Nonlinear analysis of brain activity, associated with motor action and motor imaginary in untrained subjects," Nonlinear Dynamics, vol. 91, pp. 2803–2817, 2018.

[8] Parth, G. Niso, V.A. Maksimenko, et al. "Visual and kinesthetic modes affect motor imagery classification in untrained subjects," Scientific reports, vol. 9, No. 1, p. 9838, 2019.

[9] P. Pressman, H.J. Rosen, "Disorders of frontal lobe function," in Neurobiology of Brain Disorders, Academic Press, San Diego, 2015, pp. 542–557.

[10] V.A. Maksimenko, A.E. Runnova, N.S. Frolov, et al. "Multiscale neural connectivity during human sensory processing in the brain," Physical Review E, vol. 97, No. 5, p. 052405, 2018.

[11] V.V. Grubov, V.Yu. Musatov, V.A. Maksimenko, et al. "Development of intelligent system for classification of multiple human brain states corresponding to different real and imaginary movements," Cybernetics and Physics, vol. 6, pp. 103–107, 2017.

[12] V.A. Maksimenko, S.A. Kurkin, E.N. Pitsik. "Artificial neural network classification of motor-related eeg: An increase in classification accuracy by reducing signal complexity," Complexity, vol. 2018, No. 9385947, 2018.

Machine learning approaches for classification of imaginary movement type by MEG data for neurorehabilitation

Semen Kurkin
Neuroscience and Cognitive Techology Lab, Center for Technologies in Robotics and Mechatronics Components
Innopolis University
Innopolis, Russia
kurkinsa@gmail.com

Alexander Pisarchik
Center for Biomedical Technology
Technical University of Madrid
Madrid, Spain
alexander.pisarchik@ctb.upm.es

Parth Chholak
Center for Biomedical Technology
Technical University of Madrid
Madrid, Spain
parth.chholak@ctb.upm.es

Vladimir Maximenko
Neuroscience and Cognitive Techology Lab, Center for Technologies in Robotics and Mechatronics Components
Innopolis University
Innopolis, Russia
maximenkovl@gmail.com

***Abstract*—The conducted magnetoencephalographic (MEG) experiments with voluntary participants confirm the existence of two types of motor imagery, kinesthetic imagery (KI) and visual imagery (VI), distinguished by activation and inhibition of different brain areas. Similar to real movement, KI implies muscular sensation when performing an imaginary moving action that leads to event-related desynchronization (ERD) of motor-associated brain rhythms. By contrast, VI refers to visualization of the corresponding action that results in event-related synchronization (ERS) of α- and β-wave activity. A notable difference between KI and VI groups occurs in the frontal brain area. The application of artificial neural networks allows us to classify MI in raising right and left arms with average accuracy of 70% for both KI and VI using appropriate filtration of input signals.**

Keywords—MEG analysis, motor-related patterns, machine learning algorithms, artificial neural network, motor imagery, kinesthetic imagery, visual imagery

I. INTRODUCTION

Mental imagination of movements referred to as *motor imagery* (MI) [1] manifests as a result of the rehearsal of a given motor act in the working memory without any overt movement of the corresponding muscle. It is classified into two categories: visual imagery (VI) and kinesthetic imagery (KI). While VI consists of visualization of the subject moving a limb, that does not require any special training or sensing of the muscles, KI is the feeling of muscle movement, that can usually be achieved by athletes or specially trained persons [2].

To understand and classify MI, many methods of time-frequency and spatio-temporal analyses are used. Among them, the most common techniques are using event-related synchronization (ERS) and event-related desynchronization (ERD) [3], power spectral density, wavelet transform, empirical mode decomposition, common spatial patterns, spatio-decomposition, as well as their combinations [4,5]. In addition, for classification of brain states associated with MI, the methods of machine learning and artificial intelligence are also applied to analyze EEG and MEG time series [6-8].

Although in the majority of papers devoted to MI the EEG approach was used, there was extensive research using MEG [9]. The advantages of MEG over EEG is that MEG provides a higher spatial resolution and less susceptibility to artifacts. In particular, a relatively good accuracy was achieved in classification between left-hand and right-hand MI and between MI and a rest state using the combination of a spatio-spectral decomposition and a common spatial patterns analysis [10]. Furthermore, both MEG and EEG were used in brain-computer interfaces (BCIs) for training MI classifiers [9]. The authors demonstrated rather efficient classification of MI even without separation of participants into KI and VI categories. At the same time, it was shown that KI and VI scenarios affect the classification accuracy, e.g., the accuracy rate obtained for KI were better than for VI [11]. In this context, taking into account that untrained subjects often demonstrate the VI imagery mode, the possibility to increase the accuracy rate for VI is in demand for BCI applications.

So, the goal of the present work is following: to obtain information about imagery-related brain activity for developing optimal strategies based on machine learning approaches which would provide maximal accuracy rate in classification between left-arm and right-arm MI in both groups of subjects.

II. EXPERIMENT AND METHODS

A. Design of the Experiment

The experimental study consisted of ten untrained volunteers, 8 males and 2 females between the ages of 20 and 31. The subjects were sat in a comfortable reclining chair (see Fig. 1). All participants were required to imagine moving their arms after being presented with audible beeps. The design of the experiment is shown in Fig. 1. The beeps were presented with time gaps randomly varied from 6 to 8 seconds. The number of trials per limb was varied among the subjects from 16 to 28. We provided a 20-s gap after finishing all trials for each arm and a resting 60-s interval between each series.

The neurophysiological data were acquired with the Vectorview MEG system (Elekta AB, Stockholm, Sweden) with 306 channels (102 magnetometers and 204 planar gradiometers) placed inside a magnetically shielded room (Vacuum Schmelze GmbH, Hanau, Germany) at the Laboratory of Cognitive and Computational Neuroscience, Center for Biomedical Technology, Technical University of Madrid, Spain.

Artifacts in the MEG recordings were removed using the temporal signal-space separation method of Taulu and Hari [12]. Once the events were marked at the beginning of each limb movement imagination, we extracted the 5-s trials just after these marks. Similarly, the 20-s trials corresponding to the resting state with closed eyes were also marked as the background activity of each subject.

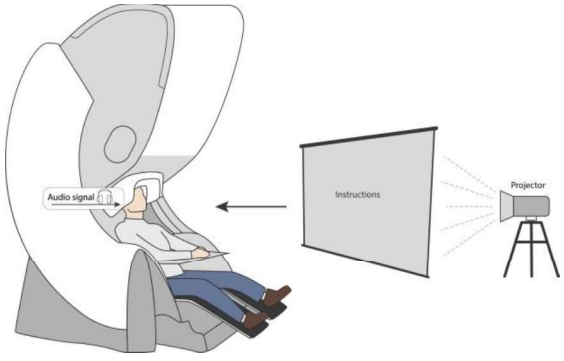

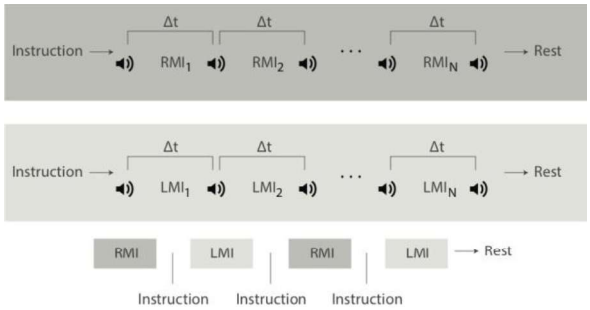

Fig. 1. Design of the MEG experiment on motor imagery. Schematic representation of experimental performance and design of the experiment. $RMI_{i\_}$ and LMI_i are time intervals corresponding to right-arm and left-arm MI, respectively.

B. *Artificial Neural Network Application*

For classification of the brain states associated with MI, we used the artificial neural network (ANNs) called multilayer perceptron (MLP). Previously, the MLP architecture was effectively used in the MEG study for detection of human decision-making uncertainty [13] and the EEG analysis of bistable image interpretations [6].

We constructed the MLP which consisted of an input layer with selected number of MEG channels for training/testing the network, followed by three hidden layers with 30, 15 and 5 neurons, respectively. The output layer comprises of a single neuron. We taught the MLP to classify the brain states of the neural ensemble through optimization of the weights of links and displacements by means of minimization of the root mean square error. We used the training algorithm called scaled conjugate gradient.

The input data were filtered by a low-pass filter of order 70 with a cutoff frequency F_c changing according to each study. Mixing the input data usually improves the efficiency of the machine learning algorithm. In this work, we used a random mixing of the input signals corresponding to a particular task. First, we trained the ANN using 75% of MEG trials and then tested it with the resting 25% trials. The ANN classification was carried out in MATLAB using the Neural Network Toolbox. We applied MLP to classify MEG time series trials associated with left-arm and right-arm MI.

III. Results

Figure 2 illustrates the variation of the maximal ANN accuracy (in %) in differentiation between MI of the left and right arms versus the cutoff frequency F_c of the low-pass filter for KI (squares) and VI (triangles) subjects. In Fig. 2a all 102 magnetometers were used for the analysis, while in Fig. 2b we only used 13 most informative channels localized near the left-parietal cortex. One can see that in the latter case the maximal classification accuracy almost does not change as compared with the case of using all 102 channels, and for some subjects (subjects 8 and 10) reaches 78%. However, the best accuracy is achieved by using all channels; it reaches 90% for subject 6. In both cases, the average classification accuracy over all subjects is about 70%. The obtained results demonstrate that high classification accuracy can be achieved for all subjects, regardless of which group they belong to, by the appropriate selection of the cutoff frequency of the low-pass filter.

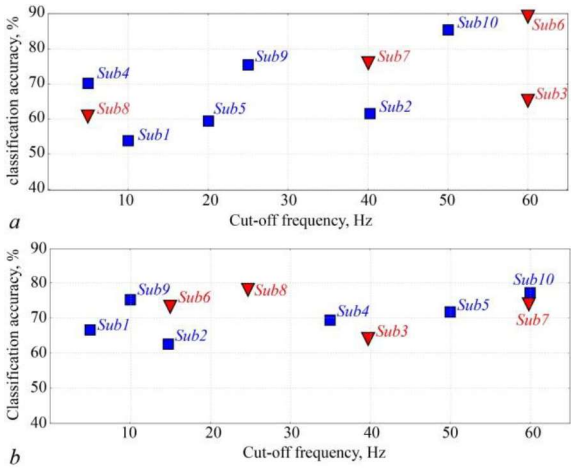

Fig. 2. ANN classification accuracy of MI of left and right arms versus cut-off frequency for KI (squares) and VI (triangles) subjects, obtained using (a) 102 and (b) 13 channels. Each data point indicates the maximal value of the classification accuracy for every subject and the corresponding cutoff frequency F_c, at which this maximal accuracy is achieved.

It should be noted that the results presented in Fig. 2 are closely related to the ANN optimization problem, important for classification of motor-related signals of electrical brain activity [7, 14, 15]. It is known that including all possible features of a multichannel neurophysiological data, e.g., EEG or, more significantly, MEG, results in an extremely large phase-space dimension, that has to be analyzed by the classifier. On one hand, this is a critical issue for BCI, where all calculations should be performed in real time by portable computers and the calculation performance is of extreme importance.

Acknowledgment

This work has been supported by the Center for Technologies in Robotics and Mechatronics Components (Innopolis University).

References

[1] M. Jeannerod. “The representing brain: Neural correlates of motor intention and imagery,” Behavioral and Brain sciences, vol. 17, No. 2, pp. 187-202, 1994.

[2] N. Mizuguchi, H. Nakata, Y. Uchida, K. Kanosue. "Motor imagery and sport performance," The Journal of Physical Fitness and Sports Medicine, vol. 1, No. 1, pp. 103-111, 2012.

[3] K. Kasahara, C.S. DaSalla, M. Honda, T. Hanakawa. "Neuroanatomical correlates of brain–computer interface performance," Neuroimage, vol. 110, pp. 95-100, 2015.

[4] V. Grubov, E. Sitnikova, A. N. Pavlov, et al. "Recognizing of stereotypic patterns in epileptic EEG using empirical modes and wavelets," Physica A: Statistical Mechanics and its Applications, vol. 486, pp. 206-217, 2017.

[5] V.A. Maksimenko, A. Pavlov, A.E. Runnova, et al. “Nonlinear analysis of brain activity, associated with motor action and motor imaginary in untrained subjects,” Nonlinear Dynamics, vol. 91, pp. 2803–2817, 2018.

[6] A.E. Hramov, V.A. Maksimenko, S.V. Pchelintseva, et al. “Classifying the perceptual interpretations of a bistable image using EEG and artificial neural networks,” Frontiers in Neuroscience, vol. 11, 674, 2017.

[7] V.A. Maksimenko, S.A. Kurkin, E.N. Pitsik. “Artificial neural network classification of motor-related eeg: An increase in classification accuracy by reducing signal complexity,” Complexity, vol. 2018, No. 9385947, 2018.

[8] S. Kurkin, E. Pitsik, N. Frolov. "Artificial intelligence systems for classifying EEG responses to imaginary and real movements of

operators," In Saratov Fall Meeting 2018: Computations and Data Analysis: from Nanoscale Tools to Brain Functions, vol. 11067, International Society for Optics and Photonics, 2019, p. 1106709.

[9] H.-L. Halme, L. Parkkonen. "Across-subject offline decoding of motor imagery from MEG and EEG," Scientific reports, vol. 8, No. 10087, 2018.

[10] H.-L. Halme, L. Parkkonen. "Comparing features for classification of MEG responses to motor imagery," PloS One, vol. 11, no. 12 (2016): e0168766.

[11] Neuper, R. Scherer, M. Reiner, G. Pfurtscheller. "Imagery of motor actions: Differential effects of kinesthetic and visual–motor mode of imagery in single-trial EEG," Cognitive Brain Research, vol. 25, No. 3, pp. 668-677, 2005.

[12] S. Taulu, R. Hari. "Removal of magnetoencephalographic artifacts with temporal signal-space separation: demonstration with single-trial auditory-evoked responses," Human Brain Mapping, vol. 30, No. 5, pp. 1524-1534, 2009.

[13] A.E. Hramov, et al. "Artificial neural network detects human uncertainty," Chaos, vol. 28, No. 033607, 2018.

[14] M.C.B. Åberg, J. Wessberg. "Evolutionary optimization of classifiers and features for single-trial EEG discrimination," Biomed. Eng. Online, vol. 6, No. 32, 2007.

[15] Parth, G. Niso, V.A. Maksimenko, et al. "Visual and kinesthetic modes affect motor imagery classification in untrained subjects," Scientific reports, vol. 9, No. 1, p. 9838, 2019.

On the movement of center-pivot irrigation machine for processing non-circeular fields

Konstantin Yu. Lepetukhin
department of Theoretical mechanics
Volgograd state technikal university
Volgograd, Russia
lepkon@gmail.com

Maria V. Miroshkina
department of Theoretical mechanics
Volgograd state technikal university
Volgograd, Russia
mariatiminen@yandex.ru

Vitaliy N. Platonov
department of Theoretical mechanics
Volgograd state technikal university
Volgograd, Russia
Platonov.Vitaliy@yandex.ru

Alexander V. Maloletov
Center for Technologies in Robotics and Mechatronics Components
University Innopolis
Innopolis, Russia
0000-0002-7312-2944

Eugene S. Briskin
department of Theoretical mechanics
Volgograd state technikal university
Volgograd, Russia
dtm@vstu.ru

***Abstract*—The movement of center-pivot irrigation machine as group of linked mobile robots is considered. Variants of increasing and decreasing radius of movement for mobile towers are presented. The algorithms needed to get to configuration needed are given.**

Keywords—Center-pivot irrigation machine, self-alignment, self-positioning, group of mobile robots, control of mobile robots.

I. INTRODUCTION

A group of robots is a complex of identical or various type robots united by main goal [1, 2]. A group of mobile robots can perform a wide range of tasks including transportation of big complex objects. The objects themselves can be of constant or of variable geometrical configuration. Center-pivot irrigation machine can be described as group of mobile robots (mobile towers) linked successively by several rigid rods (segments of pipe) with pivot in the center of field.

According to [3] one of the disadvantages of center-pivot irrigation machines is that "circular pattern leaves dry corners and potentially lower yield". To solve this problem the manufacturers of irrigation machines use corner irrigation system [4, 5].

Nevertheless the problem of processing the field of arbitrary shape is still topical. The shape of field depends on numerous factors that include location of other fields, forest, river, roads etc. The solution can be obtained if the rods can rotate one around others. According to [6] this is the first class control problem in fixed determined environment. The problem of this class can be solved.

In [7] the possibility of processing non-circular fields was shown and optimal by energy efficiency configuration was found in case of continuous curve. In [8] the effects of self-alignment and self-positioning was discovered. These effects allow to use only one drive per mobile robot to vary configuration. The main focus of [9] was on self-alignment effect. Criteria for optimizing the movement of center-pivot irrigation machine sections for processing fields of complex shape are considered in [10], and papers [11, 12] present the experience of using walking towers for such machines.

II. STATEMENT OF THE PROBLEM

Obtained in [7] solution (1) presents two possible variants of curve that depend on the sign of constant c: convex and concave.

$$\varphi_r = \frac{c}{r\cdot\sqrt{r^2\cdot(r+\mu)^2-c^2}} \quad (1)$$

where φ_r – the first derivative of angle as the function of radius, r – radius, c – constant of integration, μ – Lagrange undetermined multiplier.

In concave configuration the line that connect the most remote mobile robot with pivot is moving ahead of the machine. To get to this configuration every next robot must outrun previous one.

In convex configuration the line that connect the most remote mobile robot with pivot is moving behind of the machine. To get to this configuration every next robot must lag behind previous one.

Whatever the configuration is in steady set the machine must rotate as solid object, which means that all the mobile robots rotate around pivot with the same angular velocity ω. Equation (2) is used to calculate needed linear velocities V_i for each radius R_i.

$$V_i=\omega R_i \quad (2)$$

To achieve the needed configuration using the effects of self-alignment and self-positioning the control system of mobile robots should be able to adjust the linear speed of mobile robot.

In order to choose how to change configuration 4 cases must be considered. In each case shown on Fig. 1 the machine is undergoing planar movement, the part OK of the machine is solid, rotates around the axis through point O and the rod KM is rotating around the axis through point K. Both axes are perpendicular to the plane of movement and therefore are parallel.

I. Concave radius reduction

As shown on Fig. 1.a in order to reduce the radius OM the velocity V_{k+1} must be increased or the all the velocities

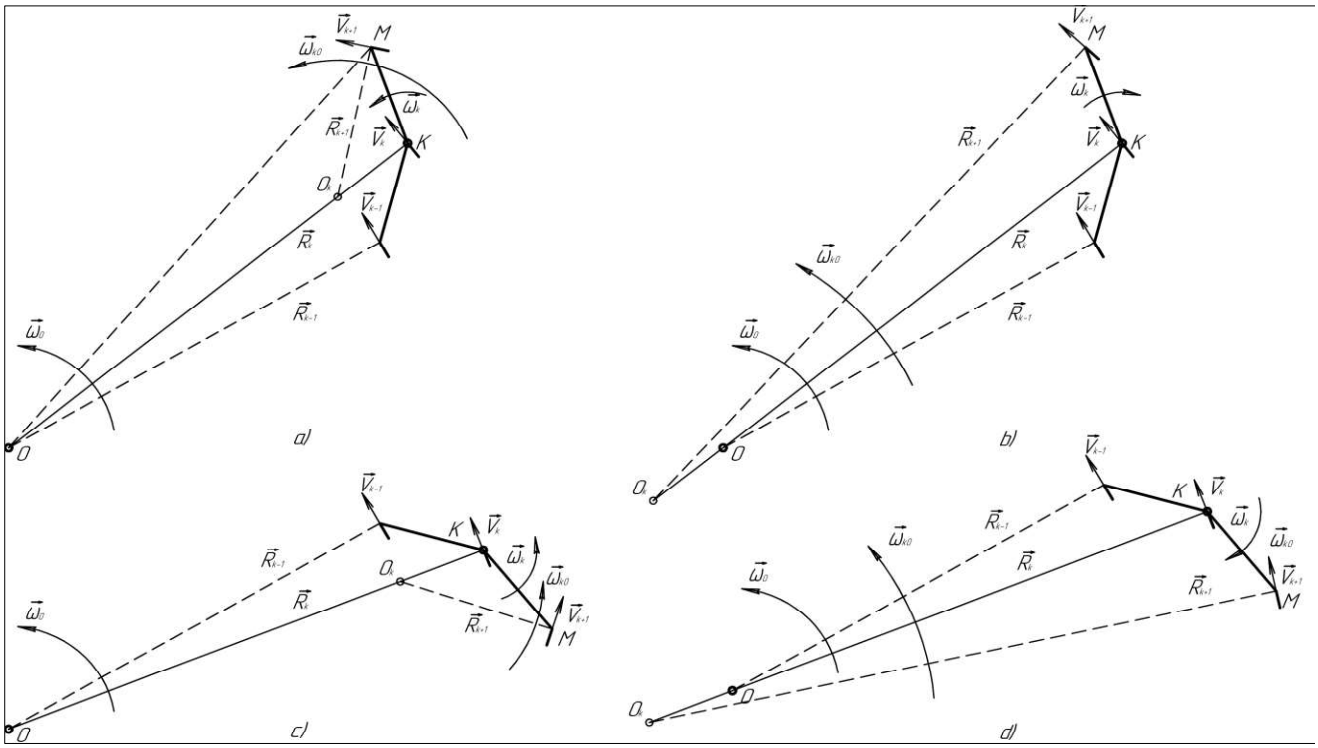

Fig. 1. The variants of mutual rods rotation

from first to K robot must be decreased. The greater the ω_K then ω_0, the more point O_K closer to the point K.

II. Concave radius incresing

As shown on Fig. 1.b in order to increase the radius OM the velocity V_{k+1} must be decreased or the all the velocities from first to K robot must be increased. All the changes in velocities must be coordinated. The closer ω_K to zero, the closer O_K to O.

III. Convex radius increasing

As shown on Fig. 1.c in order to increase the radius OM the velocity V_{k+1} must be increased or the all the velocities from first to K robot must be decreased. The greater the ω_K then ω_0, the more point O_K closer to the point K.

IV. Convex radius reduction

As shown on Fig. 1.d in order to reduce the radius the velocity V_{k+1} must be decreased or the all the velocities from first to K robot must be increased. All the changes in velocities must be coordinated. The closer ω_K to zero, the closer O_K to O.

As can be seen in concave configuration velocity of robot must be increased to reduce the radius and must be decreased to increase the radius. In convex configuration everything is more intuitive. Increasing or decreasing velocity makes accordingly change in radius. In the both cases after reconfiguration the velocities must be changed to the values matching (2).

III. THE ALGORTHMS OF RADIUS CHANGING

The variants of getting to configuration needed are presented on fig. 2. Concave configuration is presented on fig 2.a and fig 2.b. The general algorithm of radius reduction in each step (I - region) is following: until $\alpha_i < \alpha_{i0}$

$$\forall M_i\ (i \le m)\ V_i = 0; \qquad (3)$$

$$\forall M_i\ (m < i \le n)\ V_i = \omega R_{mi};$$

where α_i – current angle between M_i and M_{i+1};α_{i0} – needed angle between M_i and M_{i+1}; Mi – robot with i-number; n – quantity of robots; m – for fig 2.a – equals current step number, for 2.b – equals (n – current step number); V_{mi} – radius of M_i rotating around M_m.

In II region the velocity of machines is matched with (2).

The general algorithm of radius increasing in each step (III - region) is following: until $\alpha_i > 0$

$$\forall M_i\ (i \le m)\ V_i = \omega R_i; \qquad (4)$$

$$\forall M_i\ (m < i \le n)\ V_i = V_m;$$

where m – for fig 2.a – equals (n – current step number), for 2.b – equals current step number.

Convex configuration is presented on fig 2.c and fig 2.d. The general algorithm of radius reduction in each step (I - region) is following: until $\alpha_i < \alpha_{i0}$

$$\forall M_i\ (i \le m)\ V_i = \omega R_i; \qquad (5)$$

$$\forall M_i\ (m < i \le n)\ V_i = V_m;$$

m – for fig 2.c – equals current step number, for 2.d – equals (n – current step number).

In II region the velocity of machines is matched with (2).

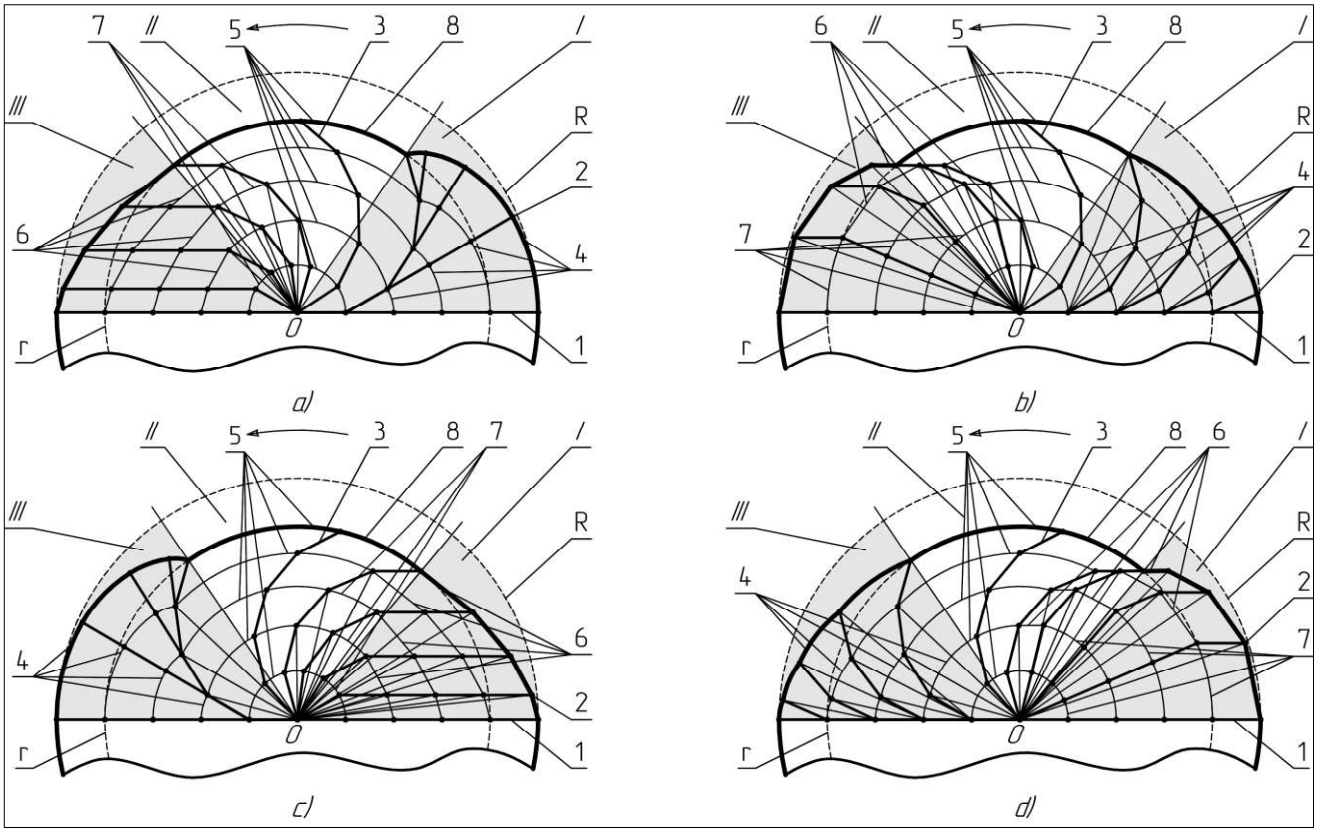

Fig. 2. The variants of getting to needed configuration

The general algorithm of radius increasing in each step (III - region) is following: until $\alpha_i > 0$

$$\forall M_i\ (i \le m)\ V_i = 0; \qquad (6)$$

$$\forall M_i\ (m < i \le n)\ V_i = \omega R_{mi};$$

where m – for fig 2.c – equals (n – current step number), for 2.d – equals current step number.

IV. Conclusion

The effects of self-alignment and self-positioning make it possible to change the configuration of center-pivot irrigation machine using only one drive per tower. Type of configuration plays a big role in control of the machine. As shown convex configuration is more intuitive. But not only that, if the velocity of any mobile robot changes the radius will change accordingly. So when the velocity return to needed value the radius will do the same.

The algorithms for both types of configuration are presented. As seen from pairs (3) - (6) and (4) - (5), the laws to calculate the velocities of machines are the same for concave and convex configuration but are implemented vice versa for increasing and decreasing of current radius.

Acknowledgment

The reported study was funded by RFBR according to the research project 18 38 00946

References

[1] Групповое управление подвижными объектами в неопределенных средах / Под ред. В.Х. Пшихопова. –М.: ФИЗМАТЛИТ, 2015. –305с.

[2] Briskin and A. Maloletov, On Optimal Laws of Groups of Walking Robots Motion while Solving Formation Task / Proceedings of the 8th ECCOMAS Thematic Conference on Multibody Dynamics 2017 (Prague, June 19-22, 2017) / Editors: M. Valasek [et al.] ; Czech Technical University in Prague, Faculty of Mechanical Engineering [et al.]. – Prague, 2017. – P. 601-605.

[3] Agricultural Irrigation Initiative: Overview of Center Pivot Irrigation Systems // https://neea.org/resources/agricultural-irrigation-initiative-overview-of-center-pivot-irrigation-systems

[4] Pat. US6085999 Corner Irrigation System / Jerry D. Gerdes, Dale A. Christensen. Valmont Industries, Inc. – 2000.

[5] Pat. US4674681A Irrigation system and apparatus / Charles H. Meis, Albion; David A. Siekmeier. Lindsay Manufacturing Co. – 1985.

[6] Каляев И.А., Гайдук А.Р., Капустян С.Г. Модели и алгоритмы коллективного управления в группах роботов. -М.: Физматлит, 2009. -280 с.

[7] Лепетухин, К.Ю. Об оптимальном управлении взаимным расположением секций дождевальной машины кругового действия при обработке некруглых полей / К.Ю. Лепетухин, А.В. Малолетов, Е.С. Брискин // Мехатроника, автоматизация, управление. - 2017. - Т. 18, № 2. - С. 103-107

[8] Об управлении движением роботизированной многозвенной дождевальной машины для орошения полей некруглой формы / Е.С. Брискин, К.Ю. Лепетухин, А.В. Малолетов, В.А. Серов, А.П. Кириллов // Экстремальная робототехника и конверсионные тенденции : тр. междунар. науч.-техн. конф. (г. Санкт-Петербург, 7-8 июня 2018 г.) - Санкт-Петербург, 2018. - С. 344-352.

[9] The concept of a bendable multi-section rainway machine of circular action = Концепция изгибаемой многосекционной дождевальной машины кругового действия / Е.С. Брискин, Я.В. Калинин, А.В. Малолетов, К.Ю. Лепетухин // Экстремальная робототехника : сб. тез. 30-й междунар. науч.-техн. конф. (International Scientific and Technological Conference «Extreme Robotics–2019») (г. Санкт-Петербург, 13-15 июня 2019 г). - Санкт-Петербург, 2019. - С. 52-53 (англ) ; С. 54-55 (рус.).

[10] Лепетухин, К.Ю. О критериях оптимизации движения секций дождевальной машины кругового действия при обработке полей сложной формы / К.Ю. Лепетухин, А.В. Малолетов, Е.С. Брискин // Известия ВолгГТУ. Сер. Актуальные проблемы управления, вычислительной техники и информатики в технических системах.-Волгоград, 2018. - № 8 (218). - С. 117-121.

[11] Briskin E.S., Chernyshev V.V., Maloletov A.V., and Zhoga V.V., The Investigation of Walking Machines with Movers on the Basis of Cycle Mechanisms of Walking / The 2009 IEEE International Conference on Mechatronics and Automation (Changchun, Jilin, August 9-12, 2009) : conf. proceedings.- [China], 2009.- P. 3631-3636.

[12] Briskin, V. Zhoga, V. Chernishev, A. Maloletov, Y. Kalinin, and N. Sharonov, Walking machines (elements of theory, experience of elaboration, application) / Emerging Trends in Mobile Robotics : proc. of the 13th Int. Conf. on Climbing and Walking Robots and the Support Technologies for Mobile Machines, 31 Aug.- 3 Sept. 2010 / Nagoya Inst. of Technology, Japan.- [Nagoya, Japan], 2010.- P. 769-776.

The network layer model of the wireless sensor network acting under the influence of interferences

Andrey Makashov
Department of Applied informatics
Moscow Aviation Institute (National Research University)
Moscow, Russia
a.a.makashov@gmail.com

***Abstract*— The paper presents a description of the network layer model of a protocol stack that allows one to implement a distributed self-organizing wireless sensor network capable of operating in the presence of interferences.**

Keywords*— *wireless sensor network, WSN, network recovery, tree topology, interference

I. INTRODUCTION

The concept of the Internet of things, including such concepts as “smart home”, “smart factory”, “smart city”, has become widespread today. The main idea is that different devices are combined to interact with each other and with users [1].

Within this concept, there are tasks of monitoring a specific area or object in order to measure a number of parameters of the physical environment and transmit this data for processing to another device. To solve these problems, wireless sensor networks (WSN) are used.

WSN is a network that consists of a set of nodes, which in the general case are composed of a processor, sensors, and a radio transmitter / receiver.

In this paper, the WSN model based on the four-tier protocol stack (physical, medium access control (MAC), network, application layers) is considered. The model of the physical and MAC is determined by the IEEE 802.15.4 standard [2], while the upper layers are not regulated by the standard, since their implementation depends on the specifics of the applied problem being solved.

WSN may have different topologies. For the network layer model considered in this paper, the tree topology was chosen based on the following considerations:

- tree topology provides good coverage and can be distributed over a large area, which allows monitoring of larger locations and objects (compared to the star topology);
- routing in the tree topology is fast and does not require auxiliary traffic (as opposed to the mesh topology), which allows you to receive data from sensor nodes more quickly and more often.

This paper solves the problem of creating a model of the network layer of the protocol stack for the tree topology. The network implemented using this model must meet the following requirements:

- distribution - according to the principle of distribution, none of the nodes should have information about the global state of the network [3];
- self-organization - the principle, which states that the network formation and recovery must be carried out without receiving commands from outside [4];
- resistance to interference - the network must ensure the preservation of health and recovery of transmission routes in noisy environments.

II. FUNCTIONAL DIAGRAM OF THE NETWORK LAYER

Consider the general functional diagram of the proposed network layer (Fig. 1). It can be divided into the following subsystems:

- MAC layer communication subsystem – this subsystem is responsible for receiving a data packet from the MAC layer of the protocol stack, as well as for transmitting the data packet to this level;
- application layer communication subsystem – this subsystem is responsible for receiving a packet from the application layer and transmitting to the application layer information about the packet with useful data destined to this node;
- message sending subsystem - is responsible for generating data for transmission to the lower level, filling in the network layer headers;
- message receiving subsystem – this subsystem is responsible for processing incoming messages from the lower level, analyzing the network layer header and redirecting the message to the processing of the corresponding subsystem;

- address assignment and routing subsystem - determines the address of the next node in the route to which this message is to be sent;
- network formation and recovery subsystem – this subsystem is responsible for scheduling the distribution of network connection invitations and keep-alive messages [5], generating the listed messages, scheduling meter checking events, and also taking measures to restore health in the event of an error.

The subsystems of routing and address assignment and the network formation and recovery are the most interesting. These systems will be discussed in detail below.

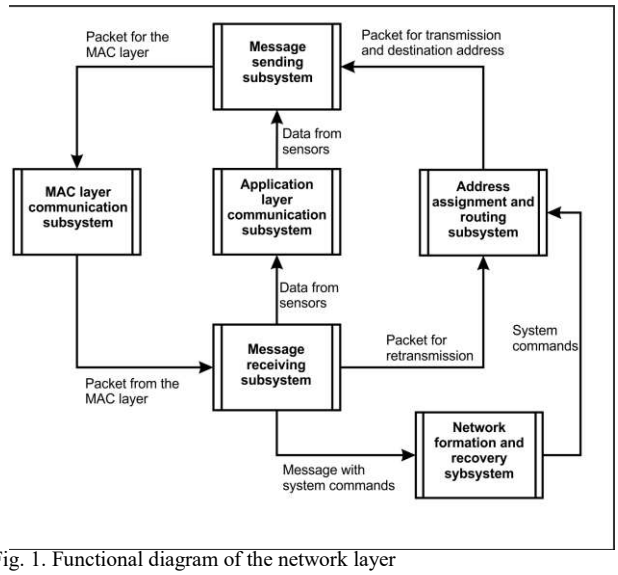

Fig. 1. Functional diagram of the network layer

III. THE SUBSYSTEM OF ROUTING AND ADDRESS ASSIGNMENT

For the model discussed in this paper, a scheme for assigning logical addresses was chosen, in which the address of each node depends on the address of the parent. The advantages of this approach are that all routes are uniquely identified, and the process of finding the address of the next node in the route requires a minimum number of elementary calculations. Also, no additional commands are required for message transmission, which significantly reduces the level of traffic on the network.

Addresses are assigned to nodes as follows: the coordinator (gateway) has the logical address "0". The address of the node *AC*, which is a descendant of node *A*, is determined by the formula:

$$AC = Am+k,\ k=1,m\ , \qquad (1)$$

where *m* is the limit number of direct descendants of each network node; *k* is the descendant number within the set of parent addresses.

A route in a tree generally consists of ascending and descending branches. In each of these cases, the address of the next node in the route can be determined by calculating the addresses of the parents for the nodes through which the route passes. Suppose we have a node with address A. Then the address AP of the parent of node A will be determined by the formula:

$$AP= [(A-1)/m], \qquad (2)$$

IV. THE SUBSYSTEM OF NETWORK FORMATION AND RECOVERY

The formation of the network, as well as its restoration after damage to existed routes due to the influence of interference, is carried out automatically by sending broadcast auxiliary messages, which are interpreted differently depending on whether this node is connected to the network.

Nodes not connected to the network perceive the message as a connection request and send a response request for connection data.

Nodes connected to the network (direct descendants of the sender) perceive the message as a keep-alive request (see below). Nodes that connected to the network, but not direct descendants of the sender ignore the message.

The coordinator sends this message periodically. When a node receives such a message, it increases the keep-alive message counter for its parent, and then sends a response to it. Upon receiving a response, the parent node increases the corresponding counter for its descendant. After processing the message, the nodes retransmit it further, launching similar broadcast messages.

After a certain time interval has expired (the period for checking keep-alive message counters), the named counters are checked for all neighboring nodes (parent and immediate descendants). If the value of the counter is equal to zero, the node is considered inoperative; if not, the node is considered operational, and the counter is reset to zero.

Thus, if a node does not hear a response from its parent for some time (the value is configured by the user when creating the network), it disconnects from the network and waits for new invitations. If the parent for some time does not hear the answer from the descendant, it excludes it from its list of descendants and releases the address for the new nodes.

The given scheme provides automatic formation and restoration of the network in cases of damage to routes due to the influence of interference or the exit of individual network nodes.

V. SIMULATION

The developed model was implemented using the ns-3 simulator and the addition to it [6]. The channel and physical layers according to the IEEE 802.15.4 standard are already implemented in the ns-3 system as a separate module. The network and application levels has implemented as a new module with support for integration with the ns-3 system.

The interference modeling subsystem consists of two parts, which are an extension of the model described above:

- model of the interference physical device;
- model of the interference application.

Interference operation is as follows: the interference device constantly transmits messages to the channel, which leads to the fact that no devices that fall within the

interference zone can access the channel (error «Channel Access Failure» [2].

The interference channel must match the channel on which the network devices operate. On one channel, several interferences can work at once.

VI. SIMULATION RESULTS

The performance of the presented model was tested on the following task: 50 nodes were located on the area of 100 meters per 100 meters. The maximum number of direct descendants for a tree was 3, the period for checking keep-alive counters was 20 seconds, messages from each node were sent to the gateway every 3 seconds, the size of one message was 30 bytes (not including headers). All nodes, as well as interference devices were located randomly.

One of the main parameters of the WSN is reliability (the ratio of the total number of delivered messages to the total number of sent messages), and this parameter is determined as a result of simulation modeling. The parameters are calculated within 800 seconds after the end of the network formation (all nodes are connected); the interference starts to work 400 seconds after the end of the network formation. The entire measurement interval is divided into segments of 20 seconds, and the reliability is calculated for each segment, which allows you to track the changes in reliability when you turn on the interference and when you rebuild the network. The study was conducted for 30 different locations. The averaged results are shown in Fig. 2

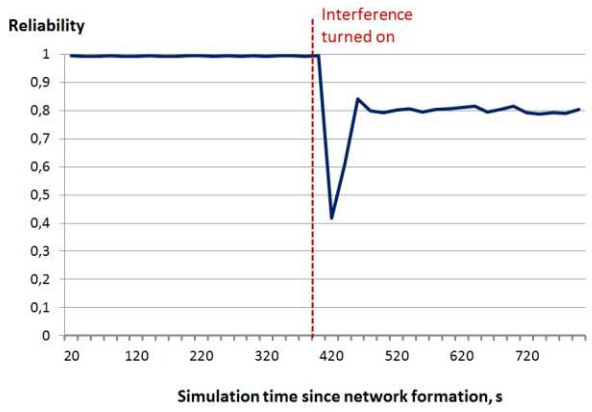

Fig. 2.Simulation results: network recovery after turning on the interference

From the above graph, it can be seen that immediately after switching on the interference, the reliability drops sharply, after which the network recovery process begins. Reliability is quickly restored to an average value of about 0.8.

The above study allows us to conclude that the network-level model does its job, quickly restoring the network in the event of route outages.

VII. CONCLUSIONS

During this work, a model of the network layer of the protocol stack for tree topology was developed and tested. This model allows you to implement the WSN, which meets the principles of distribution and self-organization, and is able to restore the network quickly in case of errors that occur during the operation of the network under the influence of interferences.

ACKNOWLEDGMENT

This research completed with the financial support of RFBR as a part of a research project № 17-08-01641a.

REFERENCES

[1] G, Jayavardhana, B. Rajkumar, S. Marusic and M. Palaniswami, “Internet of Things: a vision, architectural elements, and future directions”, Future generation computer systems, volume 29, issue 7, p. 1645-1660, 2013.

[2] “IEEE Standarts 802.15.4. Wireless medium access control (MAC) and physical layer (PHY) specifications for low-rate wireless personal area networks (LR-WPANs)”, IEEE Computer Society, 2006.

[3] Tannenbaum and M. van Steen, “Distributed systems: principles and paradigms”, Prentice-Hall Inc., 2002.

[4] Dressler, “Self-Organization in Sensor and Actor Networks”, John Wiley & Sons Ltd, 2007.

[5] R. Braden, “Requirements for Internet hosts – communication layers”, Internet Engeneering Task Force, 1989.

[6] A. Makashov, “Dopolneniye modulya LR-WPAN simulyatora ns-3 dlya provedeniya imitacionnogo modelirovaniya besprovodnyh sensorhyh setey, reshayushih prikladnye zadachi v aerokosmicheskoy oblasti”, G12 Gagarinsliye chteniya – 2018: XLIV Mezhdunarodnaya molodezhnaya nauchnaya konferenciya: Sbornik tezisov dokladov: M.; Moscow Aviation Institute (National Research University), 2018

Cognitive interaction during a collaborative attentional task

Vladimir Maksimenko
Neuroscience and Cognitive Technology Laboratory, Center for Technologies in Robotics and Mechatronics Components
Innopolis University,
Innopolis, Republic of Tatarstan, Russia
maximenkovl@gmail.com

Vadim Grubov
Neuroscience and Cognitive Technology Laboratory, Center for Technologies in Robotics and Mechatronics Components
Innopolis University,
Innopolis, Republic of Tatarstan, Russia
vvgrubov@gmail.com

***Abstract*—the modern trend in neuroscience and engineering is the developing systems allowing increase human physical and cognitive abilities through human-machine interaction. In these systems the human's condition is controlled by a brain-computer interface and assistance is activated when cognitive (or physical) performance decreases. In the current paper we consider the system, where the human's cognitive performance is enhanced due to cognitive interaction with another human. The proposed interface was tested at experimental sessions, in which the subjects were asked for a long time to solve the problem of classification of ambiguous visual stimuli of varying complexity. The proposed interface allows to increase the average productivity of a group of people due to the distribution of cognitive load between all participants.**

Keywords— brain-brain interface, workload distribution, visual task, visual attention, mental fatigue.

I. INTRODUCTION

One of the main practical tasks of modern neuroscience is the development of brain-computer interface (BCI). This interface can be used for rehabilitation medicine and for healthy subjects to enhance their cognitive abilities in solving task under high mental workload. During the last years, along with BCI, the brain-to-brain interfaces (BBI) were proposed to enable direct information transfer between the brains of interacting humans and animals.

BBI can be useful for improving the cognitive performance of a group of people subjected to a common work task that requires sustained attention and alertness. For example, pilots of military [1] or civil aircraft [2] or operators of power plants [3,4], whose work is associated with a long monotonous activity and requires high concentration of attention [5]. Brain-brain interface can help a group of people interact more effectively by assessing and controlling their physical condition. For example, as a result of the assessment of the degree of alertness by the BBI, workload can be distributed among all participants depending on their current physiological state.

In this paper, we propose a BBI to enhance human-human interaction while performing collective tasks. The proposed brain-brain interface is tested during experimental sessions in which participants perform the long task of classifying ambiguous visual stimuli with varying degrees of ambiguity.

II. MATERIALS AND METHODS

A. Participants

Twenty healthy volunteers, twelve males and eight females, between the ages of 20 and 43 with normal or corrected-tonormal visual acuity participated in the experiments. All of them provided informed written consent before participating. The experimental studies were performed in accordance with the Declaration of Helsinki and approved by the local Research Ethics Committee of the Innopolis University.

B. Visual task

Visual task consisted in classification of the sequentially presented ambiguous Necker cubes as left- or right-oriented. The Necker cube [6] is a 2D-image which looks like a cube with transparent faces and visible ribs.

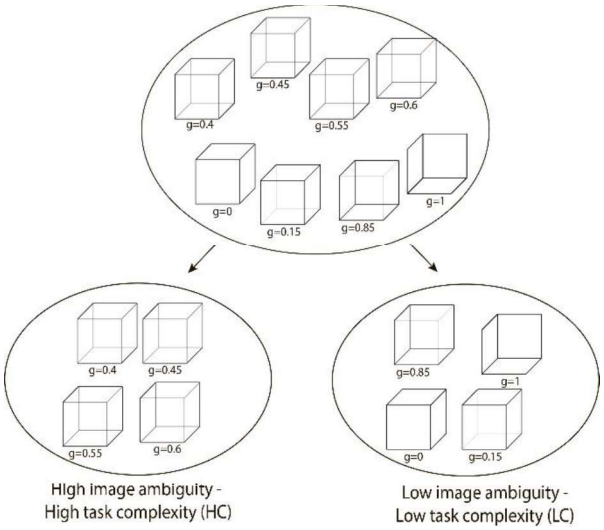

Fig.1. The examples of presented Necker cube images with different values of control parameter *g*. Two sets of visual stimuli: with a high degree of ambiguity, representing a task of high complexity (HC) and with a low degree of ambiguity, representing a task of low complexity (LC)

An observer sees the Necker cube as a 3D object because of the defined position of the cube edges. Ambiguity in the perception of this cube is to interpret it as oriented to the left (g=0) or to the right (g=1) depending on the contrast of the various internal edges of the cube. The value of g is considered as the degree of complexity of this classification. Necker cubes with a value of g close to 1 or 0 can be easily interpreted as a left- or right-oriented. the whole set of presented stimuli was divided into two subtasks: the task of

high complexity of interpretation with (HC) and the task of low complexity of interpretation with (LC) (Fig. 1) [7,8].

C. Experimental setup and design

The experimental setup is demonstrated in Fig. 2. Visual stimuli were simultaneously presented to a pair of participants (subject 1 and subject 2) using a special software running on the corresponding client personal computers. During these presentations, the EEGs of the subjects were recorded and processed. The performance of each operator was estimated using his/her stimulus-related brain response $I(i)$ to every presented i-th stimulus.

The brain responses $I_1(i)$ and $I_2(i)$ of subject 1 and subject 2, respectively, were compared. Depending on the result of this comparison, the control command, the ambiguity range of Necker cubes was corrected for each subject. For example, if $I_1(i) > I_2(i)$, then subject 1 received a stimulus with higher ambiguity, while subject 2 perceived a stimulus with weaker ambiguity.

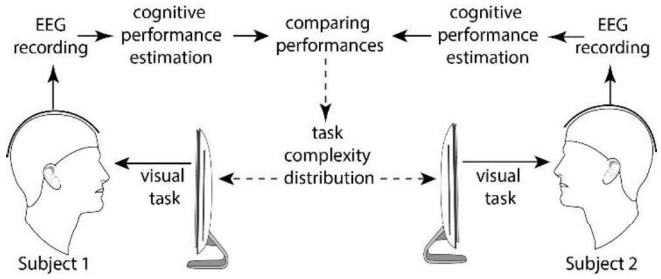

Fig.2. Schematic illustration of experimental setup

The subjects were randomly divided into 10 pairs and participated in two sets of experiments. The both sets contained two sessions, session 1 and session 2, each lasted 30 minutes. During session 1 in both experiments the cubes with different parameters g were randomly presented to the participants. Each stimulus was presented about 30 times. During the session 2 of the first experiment the cubes were demonstrated in a similar way with the session 1. During the session 2 of the second experiment, the whole set was divided into high ambiguity (HC) and low ambiguity (LC) stimuli sets (Fig. 1). These different sets of stimuli were presented to the participants according to their brain responses amplitude. Namely, a subject whose brain response amplitude exceeded one calculated for his/her partner got stimuli with higher ambiguity.

The brain response amplitude was estimated based on the spectral properties of EEG signals recorded using five electrodes located in parieto-occipital cortices [9]. EEG spectra were analyzed via the wavelet transformation [10-11]. EEG signals were analyzed in alpha and beta frequency ranges at 1 second interval preceding the stimulus presentation and following the moment of stimulus appearance. Electrical brain activity in alpha and beta bands is associated with visual attention and stimuli processing [12]. Brain response *I* was estimated for each image *i* via the ratios of wavelet energies in alpha and beta bands before and after the stimulus presentation. The high brain response amplitude was achieved when alpha rhythm energy exhibited decrease after stimulus presentation and beta rhythm energy increased.

The value of $I(i)$ calculated in real time, reflects the intensity of the brain response on the appearing visual stimuli. Large $I(i)$ is associated with a high response due to more careful image processing by the subject, whereas small $I(i)$ is associated with a low response, which takes place when the subject does not pay much attention on the classification task.

III. Results

Average individual performance $\langle I_{1,2} \rangle$ was calculated for each session. This characteristic was calculated for each subject by averaging his/her brain response $I(i)$ more than 200 demonstrations of the Necker cube. Then, individual performance $\langle I_{1,2} \rangle$ of both subjects in the pair were averaged to assess the performance of the pair $\langle I_{pair} \rangle$.

Fig. 3 presents the results of comparing the two sets of experiments. The results are presented in the form of box-and whiskers diagrams which show average performance $\langle I_{pair} \rangle$ in all pairs. It is seen that during the first experiment (a) a pair's response did not changed between sessions. However, a significant increase is observed during the session 2 of the second experimental set (b).

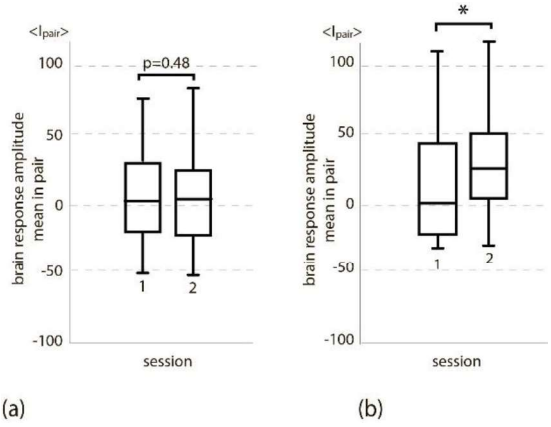

Fig.3. (a) Brain response amplitude mean in pairs $\langle I_{pair} \rangle$ during the first (a) and the second (b) experiments for session 1 and session 2. (*p < 0.05 by paired sample t-test, the compared distributions are tested with Shapiro Wilk normality test).

IV. Conclusion

In this paper, we the brain-to-brain interface in which a cognitive performance is enhanced through cognitive interaction between humans. It should be noted that the study of the possibility of human interaction through the brain-brain interface was carried out in other works [13]. It was proposed to transmit motor information registered in the cortical region directly to the motor area of the cerebral cortex of another person by means of brain stimulation [14-16]. However, this system did not improve performance, because it did not take into account the state of the brain of interacting people. The proposed system can be used in cases where cognitive or physical activity should be unevenly distributed among the participants in accordance with their current psychophysiological conditions, such as aircraft pilots or nuclear power plant operators

Acknowledgment

This work is supported by Russian Science Foundation for Basic Research (Grant 18-32-20129) and the President Programm (MK-992.2018.2).

REFERENCES

[1] Estrada, A. M. Kelley, C. M. Webb, J. R. Athy, and J. S. Crowley, "Modafinil as a replacement for dextroamphetamine for sustaining alertnessinmilitaryhelicopterpilots,"AviatSpaceEnvironMed.,vol.83, no. 6, pp. 556–564, 2012.

[2] M. Sallinen, M. Sihvola, S. Puttonen, K. Ketola, A. Tuori, M. H¨arm¨ a, G. Kecklund, and T. Akersted, "Sleep, alertness and alertness management among commercial airline pilots on short-haul and long-haul flights," Accident Analysis and Prevention, vol. 98", no. Supplement C, pp. 320–329, 2017.

[3] T. I. Baker, S. C. Campbell, K. D. Linder, and M. C. Moore-Ede, "Control-room operator alertness and performance in nuclear power plants," Report EPRI-NP–6748 United States, vol. 23, no. 13, 1990.

[4] R. C. Jensen, "Alertness-supporting activities for control room operators in automated industrial plant," Human Factors and Ergonomics Society Annual Meeting Proceedings, vol. 43, no. 12, pp. 752–756, 1999.

[5] A. Maksimenko, A. E. Runnova, N. S., Frolov, V. V. Makarov, V. Nedaivozov, A. A. Koronovskii, A. N. Pisarchik, A.E. Hramov, "Multiscale neural connectivity during human sensory processing in the brain". Physical Review E, vol. 97, no. 5, 052405, 2018.

[6] L. A. Necker Esq., "LXI. Observations on some remarkable optical phœnomena seen in Switzerland; and on an optical phœnomenon which occurs on viewing a figure of a crystal or geometrical solid," The London, Edinburgh, and Dublin Philosophical Magazine and Journal of Science, vol. 1, no. 5, pp. 329–337, 1832.

[7] A. Maksimenko, A. E. Hramov, N. S. Frolov, A. Lüttjohann, V. O. Nedaivozov, V. V. Grubov, A. E. Runnova, J. K. Kurths, A.N. Pisarchik, "Increasing human performance by sharing cognitive load using brain-to-brain interface". Frontiers in neuroscience, vol.12, 2018.

[8] A. Maksimenko, A. E. Hramov, A. E., V. V. Grubov, V. O. Nedaivozov, V. V. Makarov, A. N. Pisarchik, "Nonlinear effect of biological feedback on brain attentional state". Nonlinear Dynamics, vol. 95, no. 3, pp. 1923-1939, 2019

[9] Niedermeyer and F. L. da Silva, Electroencephalography: Basic Principles, Clinical Applications, and Related Fields, Nonlinear Dynamics. Lippincot Williams & Wilkins, 2014.

[10] E. Hramov, A. A. Koronovskii, V. A. Makarov, A. N. Pavlov, E. Sitnikova, Wavelets in Neuroscience. Springer Heidelberg New York Dordrecht London, p. 314, 2015.

[11] Sitnikova, A. E. Hramov, V. Grubov, and A. A. Koronovsky, "Time-frequency characteristics and dynamics of sleep spindles in wag/rij rats with absence epilepsy," Brain Research, vol. 1543, pp. 290–299, 2014.

[12] P.Sehatpour, S. Molholm, T. H. Schwartz, J. R. Mahoney, A. D. Mehta, D. C. Javitt, P. K.Stanton, J. J. Foxe, (2008)." A human intracranial study of long-range oscillatory coherence across a frontaloccipitalhippocampal brain network during visual object processing," Proceedings of the National Academy of Sciences, vol. 105(11), pp. 4399-4404, 2008

[13] M.Pais-Vieira,M.Lebedev,C.Kunicki,J.Wang,andM.A.L.Nicolelis, "A brain-to-brain interface for real-time sharing of sensorimotor information," Scientific Reports, vol. 3, art. no. 1319, 2013.

[14] R. P. N. Rao, A. Stocco, M. Bryan, D. Sarma, T. M. Youngquist, J. Wu, and C. S. Prat, "A direct brain-to-brain interface in humans," PLoS One, vol. 9, no. 11, art. no. e111332, pp. 1–12, 2014.

[15] S.-S. Yoo, H. Kim, E. Filandrianos, S. J. Taghados, and S. Park, "Noninvasive brain-to-brain interface (BBI): Establishing functional links between two brains," PLoS One, vol. 8, no. 4, art. no. e60410, pp. 1–8, 2013.

[16] M. E. M. Mashat, G. Li, and D. Zhang, "Human-to-human closedloop control based on brain-to-brain interface and muscle-to-muscle interface," Scientific Reports, vol. 7, no. 1, p. 11001, 2017.

Post-stroke rehabilitation with the help of brain-computer interface

Vladimir A. Maximenko
Neuroscience and cognitive technology laboratory, Center for Technologies in Robotics and Mechatronics Components
Innopolis University,
Innopolis, Russia
v.maksimenko@innopolis.ru

Anton R. Kiselev
Saratov State Medical University,
Saratov, Russia
antonkis@list.ru

Nikolay Shukovskiy
Saratov State Medical University,
Saratov, Russia
nshchukovskiy@gmail.com

Alexander N Pisarchik
Center for Biomedical Technology, Technical University of Madrid,
Madrid, Spain
alexander.pisarchik@ctb.upm.es

Elena Pitsik
Neuroscience and cognitive technology laboratory, Center for Technologies in Robotics and Mechatronics Components
Innopolis University,
Innopolis, Russia
e.pitsik@innopolis.ru

Alexander E. Hramov
Neuroscience and cognitive technology laboratory, Center for Technologies in Robotics and Mechatronics Components
Innopolis University,
Innopolis, Russia
a.hramov@innopolis.ru

***Abstract*— We considered a group of 50 patients with lateral paresis in the acute period after the first stroke. The EEG recordings in the group of post-stroke patients displayed fundamentally different brain dynamics during real movements of a conventionally healthy hand and a hand with decreased muscle strength. While for the conventionally healthy hand the brain activity in the sensory zone is quite close to the dynamics observed in the control group, for the paretic hand there is pathological activity associated with increased activity in low frequency ranges (up to 12 Hz). Meanwhile, the brain activity during imaginary motion is similar for both hands and hence to the dynamics in the control group of conditionally healthy subjects. The obtained results**

can be used in rehabilitation techniques based on imaginary motor activity with the help of brain-computer interface.

Keywords—brain-computer interface, post-stroke rehabilitation, EEG, motor imagery

I. INTRODUCTION

The rehabilitation of patients with neurological symptoms is very important for their adaptation to ordinary life. The success of neurosurgical practice and pharmacology allowed a large number of patients to return to normal conditions, that became amatter of social and medical rehabilitation services. However, no more than 20% of post-stroke patients are able to recover their mobility functions. The rest remain disabled with varying degrees of severity and need medical and social support [1–4]. The most frequent consequences of strokes are motor disorders in the form of different paresis, occurring in 80% of patients after a cerebrovascular catastrophe, in half of them the pathology persists for life [5].

In this paper, we consider the issues of primary rehabilitation in the tasks of returning the patient's motor activity and suggest the brain-computer interface for neurorehabilitation.

II. MATERIALS AND METHODS

I. Participants

Eighty subjects were involved in the experimental study and formed two groups. The 57 control group (group I) contained 30 practically healthy voluntaries selected on the base 58 of their medical records and anamnestic data. The test group consisted of 50 patients 59 with motor disorders with the first established diagnosis of "cerebral infarction, acute 60 phase" confirmed by neuroimaging data. The patients included in the test group had a 61 diagnosis of atherothrombotic cerebral infarction in the pool of the left or right middle cerebral arteries. The main neurological deficit was represented by hemiparesis on the left or right side. These patients were referred, respectively, to subgroup II and subgroup III. The time from the onset of the disease to the study was 5 ± 2 days. Motor abnormalities were assessed according to the British scale for assessing muscle strength (average score 2 ± 1). The main criterion for inclusion in the test group was the stabilityachieved by the patient in a post-stroke condition. The average age of the patients under study was 63.7 years in the range of 59–72 years. In the control group, the 69 average age of the participants was 48 years within the range between 39 and 68 years.

II. Experimental setup

The experiments were carried out with each subject independently. The electrical brain activity was recorded using a monopolar registration method based on an extended arrangement of EEG electrodes according to the "10–10" scheme which allows the evaluation of the activity of the cerebral cortex from projections of all main zones. The cup adhesive Ag/AgCl electrodes were placed on the "Ten20" paste. Before the experiment started, we performed all necessary procedures for increasing the skin conductivity and reducing its resistance using abrasive a "NuPrep" gel. The impedances were monitored after the electrodes were installed, and measured during the experiments. Usually, the impedance values varied within the 2–5 kΩ interval. The ground electrode N was located in front of the head at the Fpz electrode location. The EEG signals were filtered by a 50-Hz Notch filter and a band-pass filter with cut-off points at 1 Hz (HP) and 100 Hz (LP). The amplifier "Encephalan-EEGR-19/26" (Medicom MTD company, Taganrog, Russian Federation) was used to record bioelectric signals. This EEG recorder possesses the registration certificate of the Federal Service for Supervision in Health Care No. FCP 2007/00124 of 07.11.2014 and the European Certificate CE 538571 of the British Standards Institute (BSI).

During the experiment, each subject was sitting in a comfortable position. The experiment began with the registration of the state of passive wakefulness (rest state), 3 minutes with open eyes and 3 minutes with closed eyes. During further (active) experimental stages, the subjects were required do not close their eyes for a long time and follow instructions on the screen. The subjects were instructed to perform either real or imaginary movement of one of the hands according to the command written on the screen when they heard a beep.

III. Methods of the data analysis

Firstly, we have used empirical mode decomposition method for mitigation of artefacts on registered EEG [6,7]. Second, we have used the continuous wavelet analysis for estimation of time-frequency structure of EEG signals [8].

Standard tests were used for statistical analysis of medical data to calculate mean, median, and the range of variation for obtained assessments for the groups of subjects. The separation of the obtained classes of patients was additionally using the Wilcoxon nonparametric criterion.

III. RESULTS AND DISCUSSION

In contrast to earlier studies, in this work we consider the overall EEG activity in a wide frequency range, but not only track changes in the dynamics of a sensorimotor rhythm reflected electrical brain activity in the alpha band [9]. The analysis of the brain activity in all frequency ranges allows us to distinguish differences not only between post-stroke patients, but also in the group of healthy subjects, as well as to reveal 381 differences between EEG responses to motor imagery of the left and right paretic and healthy hands

A debatable issue is the situation in which the imagined motor activity of a paretic hand in the most acute period exhibits dynamics in the sensory region similar to healthy subjects. We considered the spatial distribution of changes in the beta and gamma ($f > 12$ Hz) and low frequency ($f < 12$ Hz) range activity, which will allow us to assess changes in the sensorimotor zone and compare them with the activity of the remaining brain areas.

The qualitative analysis of the results for real movements of the post-stroke patients allows us to treat the observed patterns as a local change in the activity characteristics during real movements, mostly the right and left hemispheres are involved near the boundaries with the sensorimotor region, close to the lesion zone visible in the MRI. This results can be correlated with the results of the assessment of the smallest fractal dimension in the lesions [10].

At the same time, the localisation of changes in motor imagery of post-stroke patients is much more complicated. These changes occur in the central, occipital and temporal areas. Whereas, in the control group of practically healthy subjects, the changes are mainly localised in the central zone,

similar to real motor activity. Such qualitatively different dynamics of motor imagery of the right and left hands is possibly associated with the activation of a compensatory mechanism for circumventing the post–stroke disturbances of conductive paths.

Thus, early rehabilitation on the basis of imaginary motor activity allows recuperating conditionally normal activation of the sensorimotor brain area as for a hand with preserving muscle strength, as for a paretic hand. Significant improvement of the rehabilitation quality, especially in clinical conditions, was obtained by using biological feedback systems.

We have suggested the brain-computer interface (BCI) developed in our group and tested during the rehabilitation activity. Fig. 1 represents a block diagram of the BCI.

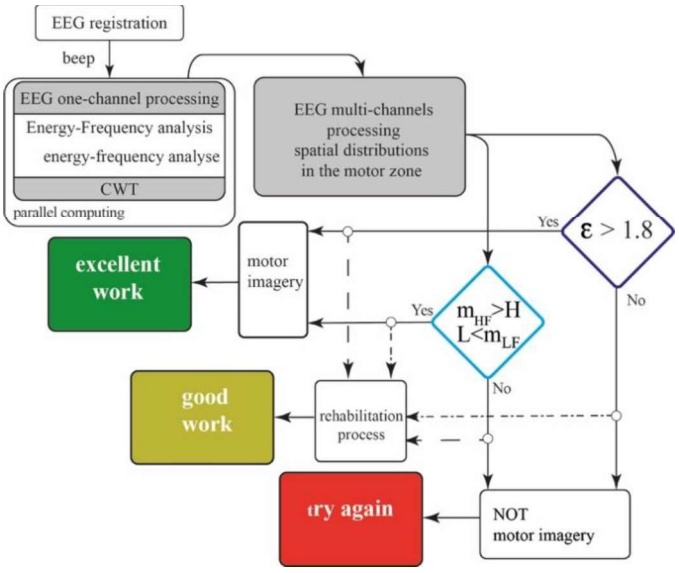

Fig. 1. Diagram of patient's work cycle during motor imagery using the brain-computer interface.

ACKNOWLEDGMENT

This work has been supported by Russian Foundation for Basic Research (grant 16-29-08221).

REFERENCES

A.G. Thrift et al, "Global stroke statistics," International Journal of Stroke. vol. 12, pp. 13–32, 2017.

Bejot Y, Bailly H, Durier J, Giroud M. Epidemiology of stroke in Europe and trends for the 21st century. La Presse Me ́dicale. 2016;45(12):e391 – e398.

E.S. Lawrence, "Estimates of the prevalence of acute stroke impairments and disability in a multiethnic population," Stroke, vol. 32, pp. 1279-1284, 2001.

F. Carod-Artal, "Determining quality of life in stroke survivors," Expert Rev Pharacoecon Outcomes Res. 2012;12:199.

P. Langhorne, J. Bernhardt, G. Kwakkel, "Stroke rehabilitation," The Lancet,vol. 377, pp. 1693–1702, 2011.

V.V. Grubov, A.E. Runnova, A.E. Hramov, "Adaptive Filtration of Physiological Artifacts in EEG Signals in Humans Using Empirical Mode Decomposition," Technical Physics, vol. 63, pp. 759-767, 2018.

A.E. Hramov et al, "Classifying the perceptual interpretations of a bistable image using EEG and artificial neural networks," Frontiers in neuroscience, vol. 11, pp. 674, 2017.

A.N. Pavlov et al, "Wavelet analysis in neurodynamics," Physics-Uspekhi, vol. 55, pp. 845-875, 2012.

V.A. Maksimenko, A. Pavlov, A.E. Runnova, V. Nedaivozov, V. Grubov, A. Koronovslii, S.V. Pchelintseva, E. Pitsik, A.N. Pisarchik, A.E. Hramov, "Nonlinear analysis of brain activity, associated with motor action and motor imaginary in untrained subjects," Nonlin. Dyn, vol. 91, pp. 2803–2817, 2018.

F. Zappasodi et al, "Fractal Dimension of EEG Activity Senses Neuronal Impairment in Acute Stroke," PLOS ONE, vol. 9, pp. 6, 2014.

Reccurence plot analysis of functional brain connectivity during bistable visual perception

Amina R. Miftahova
Innopolis University,
Innopolis, 420500, Russia
a.miftahova@innopolis.university

Alexander E. Hramov
Center for Technologies in Robotics and Mechatronics Components, Innopolis University,
Innopolis, 420500, Russia
a.hramov@innopolis.ru

***Abstract*—To develop fully-featured brain-computer interfaces it is crucial to study the behaviour of the brain in ambiguous situations. In this study, we analyzed the EEG data recorded during the perception of the bistable image - Necker's cube with the varying intensity of the lines. The image was demonstrated to the test person for one second and the person was asked to decide whether the cube is right-oriented or left-oriented and to push the corresponding data. During these actions the brain activity was recorded using 31-channel EEG, electrodes were placed according to the 10-20 system. The analysis, which was performed with the application of joint recurrence plots, suggests the existence of the synchronization between the channels of the frontal and occipital lobes. We believe that more rigorous research could reveal statistically significant brain connections and their dependence on**

physiological factors. Besides, this study may be significant for the development of the self-learning adaptive control systems.

Keywords—brain, ambiguous images, EEG, recurrence analysis

I. INTRODUCTION

The brain is by far the most complicated organ for study and yet it is one of the most important human parts that are required to be studied. Understanding what lies under the important processes happening in our brain is the key to understanding the mechanisms of particular neurological disorders. This understanding is crucial for designing the rehabilitation methods, brain-computer interfaces for helping people and, moreover, develop artificial intelligence systems with human-like reasoning.

One of the aspects that require this study is perceiving the ambiguous situations and reacting to them. We believe that the study of the perception of bistable images may bring us closer to this understanding.

We analyze the brain activity EEG recorded during the perception of the Necker's cube. Previous studies revealed the existence of two different scenarios based on the alpha- and beta- waves activity [1-2]. In this study, we are trying to find the correlation between the scenarios of brain activity and the perceived orientation of the cube. For performing the analysis we used the joint recurrence plot analysis [3-4].

II. DATA DESCRIPTION

The data was collected on three persons. It contains experimental EEG signals recorded during the perception of bistable images (the Necker's cube). The data is stored with the marks of the decision on the orientation of the cube. Signals were recorded for three seconds: one second before the demonstration of the image and two seconds after. In my analysis, I extracted one-second interval and two-second interval right after the image demonstration and choose 40 random experiments for each person.

III. METHODS

The main used method of analysis is a recurrence plot analysis. Firstly, the analysis was performed for data recorded on each person separately.

1) Extracting one-second interval and two-second interval data after the cube demonstration and performing the same action sequence for both cases.
2) Picking 40 random experiment samples.
3) Creating joint recurrence plots for each possible channel pairs. Joint recurrence plot in this case is the matrix, which is defined for channels ch1 and ch2 as $R_{i,j} = \Theta(\xi_{ch1} - |ch1_i - ch1_j|) * \Theta(\xi_{ch2} - |ch2_i - ch2_j|)$. The maximum possible recurrence rate for each of the plots was chosen to be 0.4.
4) For each channel pair calculating the sum of the recurrence rates throughout 40 experiments. The recurrence rate is defined as $RR = \frac{1}{N^2}\sum_{i,j=1}^{N} R_{i,j}$, where R is the recurrence matrix and for this case $N = 250$ for one-second interval and $N = 500$ for two-second interval.
5) Calculating the mean value and mean squared error for the recurrence rate of the channel pairs.
6) Visualizing brain networks. For the picture to be not to complicated the visualization is for the most significant connections (for ones with at least 60% of the maximum recurrence rate), where the weights of the edges are the mean recurrence rate values.

Secondly, previously analyzed data was aggregated and visualized in quite the same way as the data for each person: recurrence rates were summed up and the brain network was built for the most significant connections.

IV. RESULTS

On the cubes that were recognized as left-oriented: No apparent connections were detected.

On the cubes that were recognized as right-oriented: The connection was detected between several channels, which are capturing frontal lobe and prefrontal cortex activity. The synchronization was revealed between channels F3 and Ft8, channels Fp2 and Fcz and channels Fp1 and Ft7 (the recurrence rate is ≈0.315 when the maximum possible recurrence rate is 0.4).

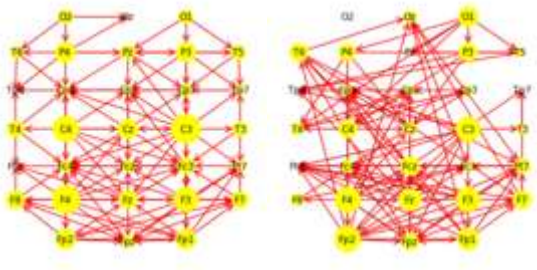

(a)Left-oriented cubes (b)Right-oriented cubes

Fig. 1. Brain connectivity map for the one-second interval combined for all three persons.
a) The strongest connections are located mainly on the frontal and central lobes (channels Fz-Fcz, F4-Fc4, F3-Fz, Fp2-Fpz, all with the recurrence rate ≈0.27 when the maximum possible recurrence rate is 0.4). b) The strongest connections are found on the frontal and central lobes (channels F3-Ft8, Fp2-Fcz, Fp1-Ft7 with the recurrence rate ≈0.29 when the maximum possible recurrence rate is 0.4) and on the temporal lobe (channel T6 connected with the channels on the frontal lobe).

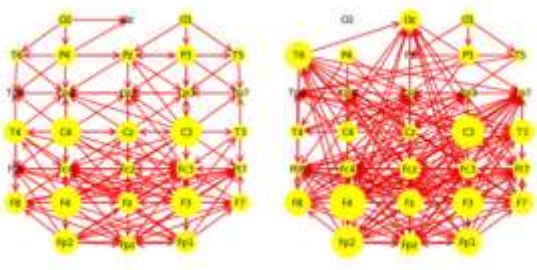

(a)Left-oriented cubes (b)Right-oriented cubes

Fig. 2. Brain connectivity map for the two-second interval combined for all three persons.
a) The strongest connections are found on the frontal and central lobes (channels Fp2-Fpz, F3-Fz, F3-Fc3, F4-Fcz, Fz-Fcz with the recurrence rate ≈0.275 when the maximum possible recurrence rate is 0.4). b) The strongest connections are found on the frontal lobe (channels Fp2-Fcz, F3-Ft8, Fp1-Ft7 with the mean recurrence rate ≈0.31 when the

maximum possible recurrence rate is 0.4), on the central lobe (C3 connected with the channels of the frontal lobe), on the temporal lobe (T6 connected with the channels of the frontal lobe) and on the occipital lobe (Oz connected with the channels of the frontal lobe).

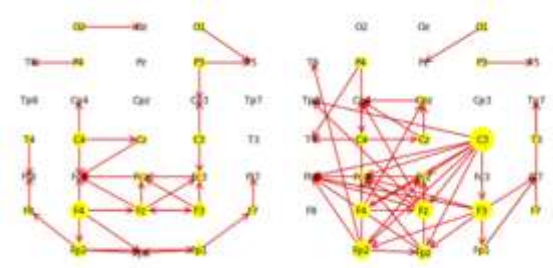

(a)Left-oriented cubes (b)Right-oriented cubes

Fig. 3. Brain connectivity map for the one-second interval for the first person.
a) The strongest connections are found on the frontal lobe. (channels F3-Fz, Fp2-Fpz, F4-Fc4 with the recurrence rate ≈ 0.3 when the maximum possible recurrence rate is 0.4).
b) The strongest connections are found in the right hemisphere: frontal and central lobes (channels F3-Ft8, Fp1-Ft7, Fp2-Fpz, Fpz-Fc4, C3-Ft8 with the recurrence rate ≈ 0.31 when the maximum possible recurrence rate is 0.4).

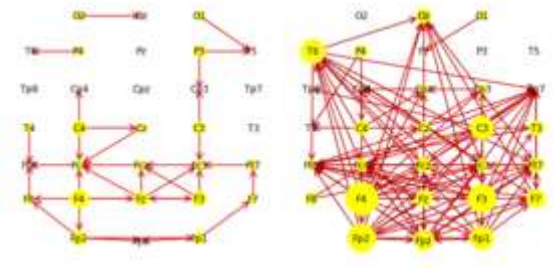

(a)Left-oriented cubes (b)Right-oriented cubes

Fig. 4. Brain connectivity map for the two-second interval for the first person.
a) The strongest connections are found on the frontal and central lobes (channels F3-Fz, Fp2-Fpz, F3-Fc3, F4-Fc4, C3-Fc3 with the recurrence rate ≈ 0.29 when the maximum possible recurrence rate is 0.4).
b) The strongest connections are found on the frontal lobe(channels Fp1-Ft7, Fp2-Fpz, Fp2-Fcz, F3-Ft8 with the recurrence rate ≈ 0.36 when the maximum possible recurrence rate is 0.4), temporal lobe (T6 connected with the channels of the frontal lobe) and occipital lobe (Oz connected with the channels of the frontal lobe).

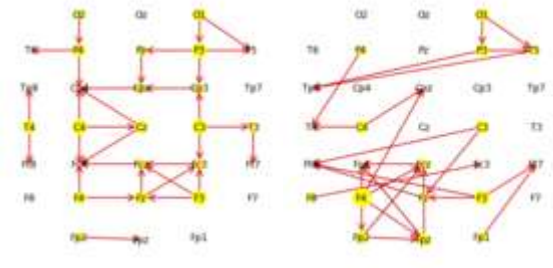

(a)Left-oriented cubes (b)Right-oriented cubes

Fig. 5. Brain connectivity map for the one-second interval for the second person.
a) There is no certain area where the strongest connections are found (the most significant are channels Fz-Fcz, C4-Cz, F4-Fc4, C3-Fc3, Pz-Cpz with the recurrence rate ≈ 0.28 when the maximum possible recurrence rate is 0.4).
b) The strongest connections are found on the frontal and parietal lobes, the most connections are located on the right hemisphere (channels Fp2-Fcz, Fpz-Fc4, F4-Fcz, F3-Ft8, P3-Tp8 with the recurrence rate ≈ 0.31 when the maximum possible recurrence rate is 0.4).

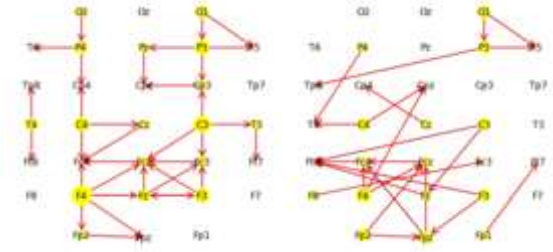

(a)Left-oriented cubes (b)Right-oriented cubes

Fig. 6. Brain connectivity map for the two-second interval for the second person.
a) The strongest connections are found on the frontal, central and parietal lobes, all, except channels Fz-Fcz, are not on the midline (channels F4-Fc4, C3-Fc3, C4-Fc4, F3-Fc3 with the recurrence rate 0.29 when the maximum possible recurrence rate is 0.4).
b) The strongest connections on the left hemisphere are found on the occipital, parietal and temporal lobes (channels C3-Ft8, P3-Tp8, C3-Fz with the recurrence rate ≈ 0.29 when the maximum possible recurrence rate is 0.4), on the right hemisphere - on the frontal and central lobes (channels Fc4-Fz, Fp2-Fcz, F4-Fcz with the recurrence rate ≈ 0.3 when the maximum possible recurrence rate is 0.4).

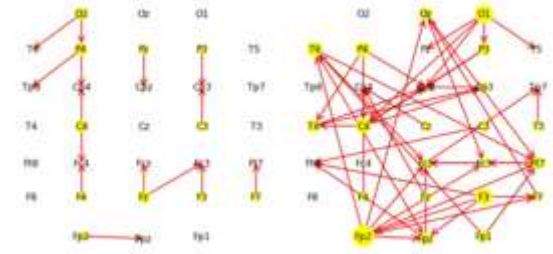

(a)Left-oriented cubes (b)Right-oriented cubes

Fig. 7. Brain connectivity map for the one-second interval for the third person.
a) There is no certain area where the strongest connections are found (the most significant are channels Pz-Cpz, P3-Cp3, F3-Fc3, O2-T6 with the recurrence rate ≈ 0.27 when the maximum possible recurrence rate is 0.4).
b) The strongest connections are found on the frontal, central and occipital lobes (channels Fp1-Ft7, C4-Cpz, Cz-Cp4, Fp2-Fcz, F3-Ft8 with the recurrence rate ≈ 0.3 when the maximum possible recurrence rate is 0.4).

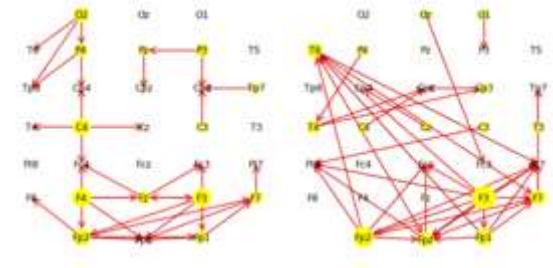

(a)Left-oriented cubes (b)Right-oriented cubes

Fig. 8. Brain connectivity map for the two-second interval for the third person.
a) The strongest connections on the right hemisphere are found on the occipital, parietal and temporal lobes (channels Pz-Cpz, F8-T6, O2-T6 with the recurrence rate ≈ 0.27 when the maximum possible recurrence rate is 0.4), on the left hemisphere - on the frontal lobe (channels F3-Fc3, F7-Ft7, Fp1-Fpz with the recurrence rate ≈ 0.27 when the maximum possible

recurrence rate is 0.4).
b) The strongest connections are found on the frontal lobe (channels Fp1-Ft7, Fp2-Fcz, F3-Ft8, F3-Fpz with the recurrence rate ≈ 0.3 when the maximum possible recurrence rate is 0.4) and on the temporal (T6-Fp1, T6-Ft7 with the recurrence rate ≈ 0.32 when the maximum possible recurrence rate is 0.4).

V. Conclusion

We analyzed the EEG data recorded during the perception of bistable images (the Necker's cube). The synchronization of the activity on the occipital and the frontal lobes was revealed. This can be explained by the receiving visual information by the occipital lobe (the cube image) and transferring it to the frontal lobe as it is responsible for the conscious decisions (in our case, whether the cube is left-oriented or right-oriented).

Just as important, we found that EEG channels with the strongest connections are the same when perceiving the cube as the right-oriented. Contrariwise, when perceiving the cube as the right-oriented, the channels with the strongest connections may vary from person to person.

However, current discoveries require an in-depth study. The next steps are: analyzing data on more people and applying the nonparametric statistical test (the permutation test) to reduce the false alarm rate. Furthermore, research should be done to reveal whether there is a correlation between the dominant eye and brain activity when perceiving bistable images.

We firmly believe that the significance of our results is not limited to the visual perception of the Necker's cube images. The studied data may be crucial when designing the self-learning adaptive control systems, particularly, when designing the behavior when coming across mixed pictures.

Acknowledgment

This work has been supported by Russian Science Foundation (Grant 19-12-00050).

References

[1] Maksimenko, V. A., Runnova, A. E., Zhuravlev, M. O., Makarov, V. V., Nedayvozov, V., Grubov, V. V., … Pisarchik, A. N. (2017). Visual perception affected by motivation and alertness controlled by a noninvasive brain-computer interface. PloS one, 12(12), e0188700. doi:10.1371/journal.pone.0188700

[2] Runnova, A & Hramov, A & Grubov, Vadim & Koronovskii, Alexey & Kurovskaya, Maria & Pisarchik, Alexander. (2016). Theoretical background and experimental measurements of human brain noise intensity in perception of ambiguous images. Chaos, Solitons & Fractals. 93. 10.1016/j.chaos.2016.11.001.

[3] Marwan, Norbert & Romano, Maria & Thiel, Marco & Kurths, Juergen. (2007). Recurrence Plots for the Analysis of Complex Systems. Physics Reports. 438. 237-329. 10.1016/j.physrep.2006.11.001.

[4] Ramos, Antônio & Builes-Jaramillo, Alejandro & Poveda, Germán & Goswami, Bedartha & Macau, Elbert & Kurths, Juergen & Marwan, Norbert. (2017). Recurrence measure of conditional dependence and applications. Phys. Rev. E. 95. 052206. 10.1103/PhysRevE.95.052206.

State-based velocity profile for manipulator

Stanislav Mikhel
Center for Technologies in Robotics and Mechatronics Components
Innopolis University
Innopolis, Russia
s.mikhel@innopolis.ru

***Abstract*— The study is focused on velocity control of a manipulator motion in the case when the precise execution of commands cannot be guaranteed because of the imperfection of the control system or interaction with the robot environment. The proposed approach combines the real-time state estimation with a trapezoidal velocity profile to optimize the performance of the linear Cartesian and point-to-point motions.**

***Keywords*— robot manipulator, trajectory, velocity profile**

I. Introduction

Manipulator trajectory often could be described as a sequence of motions in joint (point-to-point) and Cartesian (linear, circular) spaces. Because of design constraints, the robots are characterized by maximal velocities v_{max} and accelerations a_{max}. If the goal is to achieve maximal performance, the simplest strategy is to move with maximal acceleration, deceleration and velocity when it is possible (Fig. 1). Such velocity profile could be calculated in advance and then applied to the manipulator [1].

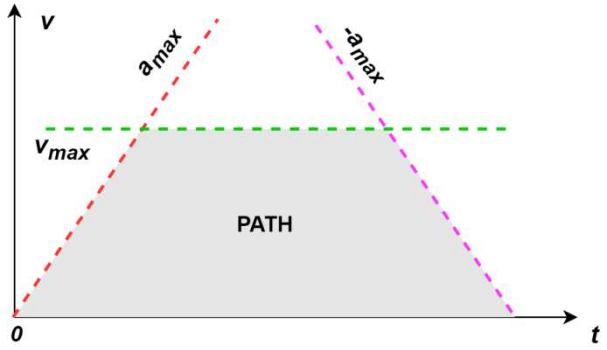

Fig. 1. Velocity profile for the performance maximization.

A trapezoidal profile is well known and widely used in the industry. First of all, it is energy efficient [2],[3]. Modification algorithms for varying the velocity profile

during execution can be found in [4]. The desired motion behavior could be achieved by the asymmetric S-curve velocity profile [5].

In some cases, an exact execution of the predefined trajectory could not be guaranteed, for example, if the controller has a big error or when the collaborative robot stops after interaction with the environment. The current command velocity, in this case, could be too big and cause the error in the controller. The problem can be solved using online parameters monitoring. However, if the current state is different from the expected one, all the rest points should be recalculated.

II. TRAJECTORY PLALLING

A. General method

Our goal is to define the method of command velocity calculation without a time reference. Assume, that we know such parameters as current state and the rest of path Δs, current velocity v and controller time step Δt. Then command velocity could be obtained from equation

$$v_{cmd} = \min\{v + a_{max}\Delta t, v_{max}, \sqrt{2a_{max}\Delta s}\} \quad (1)$$

The first element corresponds to uniformly accelerated motion (left line in Fig. 1), the second is the maximal available velocity (horizontal line). The last element describes uniformly decelerated motion with zero final speed and can be obtained by excluding the time variable from equations for velocity and path. It corresponds to the right line in Fig. 1.

B. Cartesian linear motion

First, let's consider the application of (1) for linear motion in Cartesian space, where velocity v_{max}^{cart} and acceleration a_{max}^{cart} are defined. Current cartesian velocity could be obtained using the system Jacobian $J(\boldsymbol{q})$

$$\boldsymbol{v} = J(\boldsymbol{q}) \cdot \dot{\boldsymbol{q}} \quad (2)$$

where $\boldsymbol{q}$ is joint state vector, $\dot{\boldsymbol{q}}$ is joint velocity vector [1]. Rest of the path $\Delta\boldsymbol{s}$ can be found using forward kinematics method $FK(\boldsymbol{q})$ as

$$\Delta\boldsymbol{s} = \boldsymbol{s}_{goal} - FK(\boldsymbol{q}) \quad (3)$$

Here $\boldsymbol{s}_{goal}$ is the goal point in Cartesian space. Then absolute value of command velocity can be found from application of method (1) to Eucledian norm of Cartesian velocity. The result vector can be found from projection to $\Delta\boldsymbol{s}$:

$$\boldsymbol{v}_{cmd} = v_{cmd}\frac{\Delta\boldsymbol{s}}{\|\Delta\boldsymbol{s}\|} \quad (4)$$

Finally, joint velocities could be obtained using matrix product with inverse or pseudoinverse of the robot Jacobian. If some limits are violated, joint velocities can be proportionally decreased.

C. Point-to-point motion

In the case of point to point motion in joint space we usually want the joints to start and stop execution at the same time. It makes the problem of applying the proposed approach not trivial because the independent motion of the joints does not guarantee the specified condition. The task can be solved if the motion of the joints is considered as a vector in multidimensional space. But the problem here is that the velocity and acceleration are defined for separate joints and should be mapped into the obtained space. The solution is to find such a vector that its maximal projection into joint space is inside the available limits.

First, consider the situation when the maximal velocities and accelerations for all joints are the same. If $\Delta\boldsymbol{q}$ is a path vector in joint space from current to the goal position, then maximal velocity and acceleration should be applied to that joint which has a maximal path Δq_m. Current limits can be found from projection to this axis:

$$\begin{aligned} v_{max}^{j} &= v_{max}\frac{\|\Delta\boldsymbol{q}\|}{\Delta q_m} \\ a_{max}^{j} &= a_{max}\frac{\|\Delta\boldsymbol{q}\|}{\Delta q_m} \end{aligned} \quad (5)$$

Then command velocity is calculated from (1) and can be projected back to vector $\Delta\boldsymbol{q}$ in a way similar to (4).

In general, each joint has its own limits, but the problem could be reduced to the previous case by stretching joint angle difference proportional to velocity (or acceleration) ratio. Weight matrix $\boldsymbol{W}$ could be obtained from the condition of time equality in original and modified spaces and is equal to a diagonal matrix such that $w_{v,ii} = v_{common}/v_i$, where index i denotes a joint number, index v means velocity weights, v_{common} is a common velocity in modified space, for example, maximal value among all the joint limits. The stretched path vector can be defined as

$$\begin{aligned} \Delta\boldsymbol{q}_v &= \boldsymbol{W}_v \cdot \Delta\boldsymbol{q} \\ \Delta\boldsymbol{q}_a &= \boldsymbol{W}_a \cdot \Delta\boldsymbol{q} \end{aligned} \quad (6)$$

i.e. the "slow" joints are stretched less than the "fast" ones. Limits in such modified space can be obtained from equation (5), where parameters v_{max} and a_{max} become equal to v_{common} and a_{common} consequently. If the obtained vectors are projected back to initial space, the result could be written as

$$\begin{aligned} \boldsymbol{v}_{max}^{j} &= v_{common}\frac{\Delta\boldsymbol{q}}{\Delta q_{v,m}} \\ \boldsymbol{a}_{max}^{j} &= a_{common}\frac{\Delta\boldsymbol{q}}{\Delta q_{a,m}} \end{aligned} \quad (7)$$

MODELING

The proposed technique was verified using numerical modeling in Matlab. Trajectory for each joint in case of point-to-point motion is shown in Fig. 2. The model includes errors in the controller and the sudden stop at the 4-th

second. All joints had their own goal distances and limitations.

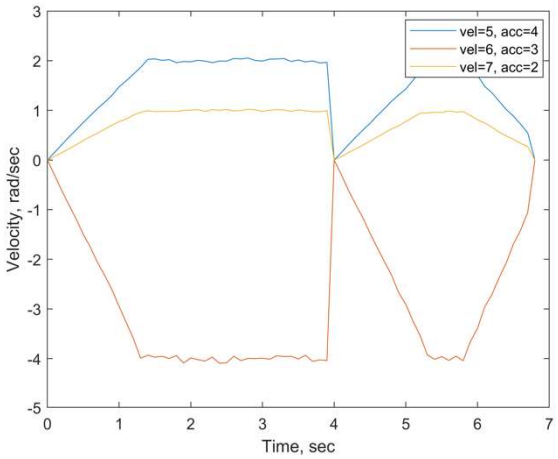

Fig. 2. Velocity profile in case on non-perfect control and sudden stop.

In general, the algorithm works correct and tries to follow the trapezoid velocity profile when it is possible.

III. Conclusion

The proposed velocity profiling technique deals with the non-perfect control system and unpredictable environment and tries to apply the trapezoidal profile for performance optimization. It was applied for the cases of linear Cartesian and point-to-point motions. Numerical modeling demonstrates the workability of the concept.

There are some limitations as well. The proposed technique considers only the simple trapeze-like velocity profiling and it is difficult to expand it for acceleration or jerk profiling. The problem can be with the division on a variable which tends to zero. It could be solved, for example, if this variable is used as the condition for evaluation braking.

Acknowledgment

This research has been supported by the grant of Russian Science Foundation 17-19-01740.

References

[1] B. Siciliano, L. Sciavicco, L. Villani, and G. Oriolo, Robotics: modelling, planning and control. Springer Science & Business Media, 2010.

[2] J. Park, "Motion profile planning of repetitive point-to-point control for maximum energy conversion efficiency under acceleration conditions," Mechatronics, vol. 6, no. 6, pp. 649–663, 1996.

[3] Z. Yu, C. Han, and M. Haihua, "A novel approach of tuning trapezoidal velocity profile for energy saving in servomotor systems," in 2015 34th Chinese Control Conference (CCC). IEEE, 2015, pp. 4412–4417.

[4] F.-Y. Luo, Y.-F. Zhou, and J. Yin, "A universal velocity profile generation approach for high-speed machining of small line segments with look-ahead," The International Journal of Advanced Manufacturing Technology, vol. 35, no. 5-6, pp. 505–518, 2007.

[5] K.-H. Rew, C.-W. Ha, and K.-S. Kim, "A practically efficient method for motion control based on asymmetric velocity profile."

Development of a method for coupling detection based on the phase dynamics modeling for analyzing EEG rhythms during an epileptic seizure in patients with a reduced level of consciousness

Navrotskaya Elena Vladimirovna
SB IRE RAS
SSU named afterN.G. Chernyshevsky
Saratov, Russia
sidakev@gmail.com

Sinkin Mikhail Vladimirovich
N.V. Sklifosovsky Research Institute of Emergency Medicine
Moscow, Russia
mvsinkin@gmail.com

Khramkov Alexey Nikolaevich
FNBMT
SSU im.NG. Chernyshevsky
Saratov, Russia
alesha.hramkov@yandex.ru

Yezhov Dmitry Maksimovich
FNBMT
SSU im.NG. Chernyshevsky
Saratov, Russia
dima6499@live.ru

Bezruchko Boris Petrovich
SB IRE RAS
SSU named afterN.G. Chernyshevsky
Saratov, Russia
bezruchkobp@gmail.com

***Abstract*—In this paper, we investigate the effectiveness of the method of coupling detection based on phase dynamics modeling in the analysis of the etalon systems whose phase dynamics properties are similar to the properties of the EEG signals from epilepsy patients who are in a coma state. On the example of the etalon model, a method of pre-filtering of signals is proposed, it provides a low level of errors while maintaining high sensitivity of the method. For the test systems, the optimal value of the method parameter and the length of the series are found.**

Keywords—EEG, coma, epileptic seizure, phase dynamics, detection of the couplings, the direction of the coupling.

I. INTRODUCTION

In neurophysiology, the study of the interaction between brain structures by EEG records is important for solving many fundamental and applied problems. In this paper, we consider the problem of analyzing the couplings between brain structures according to the EEG signals during an epileptic seizure in comatose patients. Various methods of statistical physics, information theory and nonlinear dynamics are actively used for EEG analysis [1,2]. In this paper, for the analysis of interactions between EEG oscillations we used the method based on the phase dynamics modeling [3,4]. Since the phase is a variable sensitive to the presence of influence, it can be expected that this approach will allow to identify weaker interactions. The approach is based on the construction of a phase dynamics model from the time series of phases. The model coefficients are used to estimate the intensity and direction of the interaction. The applicability of this approach was previously shown in etalon systems with different dynamics properties (small-size chaos, intense noise) and in solving real problems in climatology and medicine. But, using this method for real signals, the important question of the limits of its applicability and possible errors arises. The complexity (chaotic) and noisiness of EEG signals can prevent the identification of cause-effect relationships based on this method. Therefore, in this paper we investigate its effectiveness in the analysis of time series from test systems, which phases properties are similar to the assessment of the properties of the EEG signals from patients during an epileptic seizure in coma.

II. METHOD

To assess the presence and direction of the interaction, we used the proposed and developed in [3] method, which is based on the construction of an empirical phase dynamics model of the observed processes $x_1(t)$ and $x_2(t)$. For this, the time series of phases $\{\phi_1(t_1),\ldots,\phi_1(t_N)\}$ and $\{\phi_2(t_1),\ldots,\phi_2(t_N)\}$ are calculated using the observed time series $x_1(t)$ and $x_2(t)$, where $t_i = i\Delta t$, Δt – sampling interval, N – series length. It is assumed that the phase dynamics is adequately described by stochastic differential equations of the first order:

$$\begin{aligned} d\phi_1(t)/dt &= \omega_1 + G_1(\phi_1(t),\phi_2(t)) + \xi_1(t), \\ d\phi_2(t)/dt &= \omega_2 + G_2(\phi_2(t),\phi_1(t)) + \xi_2(t), \end{aligned} \quad (1)$$

here the parameter ω_k defines the angular oscillation frequency, $\xi_k(t)$ – white zero-mean noises with autocovariation function $\langle \xi_k(t)\xi_k(t')\rangle = D_{\xi_k}\delta(t-t')$. For the analysis of discrete time series it is convenient to consider the difference model equations corresponding to integration (1) over a finite time interval τ:

$$\phi_k(t+\tau) - \phi_k(t) = F_k(\phi_k(t),\phi_j(t)) + \varepsilon_k(t), \quad (2)$$

here $k, j = 1,2,\ j \neq k$, $\varepsilon_k(t) \approx \int_t^{t+\tau} \xi_k(t')dt'$ – are independent Gaussian zero-mean noises with variances $\sigma^2_{\varepsilon_k} \approx \sigma^2_{\xi_k}\tau$, $F_k(\phi_k,\phi_j)$ are trigonometric polynomials, whose coefficients are estimated from phase time series. Influence intensity indices $\gamma_{2\to1}$ and $\gamma_{1\to2}$ are defined as $\gamma^2_{j\to k} = \frac{1}{2\pi^2}\int_0^{2\pi}\int_0^{2\pi} \left(\partial F_k(\phi_k,\phi_j)/\partial\phi_j\right)^2 d\phi_k d\phi_j$. Here $\gamma_{2\to1}$ - index of the influence $x_2(t)$ on $x_1(t)$, and $\gamma_{1\to2}$ - conversely, index of the influence $x_1(t)$ on $x_2(t)$. In [3] for indices $\gamma_{j\to k}$ the authors proposed formulas for 95% confidence intervals based on estimates of the variance of the model $F_k(\phi_k,\phi_j)$ coefficients. The applicability of described method for assessing the presence and direction of couplings is limited by the properties of the phases. The method is effective for systems with a well-defined phase, and can give erroneous conclusions in cases where there are difficulties in phase extraction due to noise or complex spectra of the signal. In this paper we investigate the applicability of this approach to the analysis of etalon systems, phase dynamics properties of which are similar to the properties of EEG signals phases during an epileptic seizure in patients with a reduced level of the consciousness.

III. THE PROPERTIES OF EEG SIGNALS OF PATIENTS DURING AN EPILEPTIC SEIZURE

Experimental data, obtained at the N.V. Sklifosovsky Research Institute of Emergency Medicine, represent hours-long records of 8 leads of EEG according to the standard scheme of electrodes 10/20 (recorded leads: FP1, FP2, T3, T4, C3, C4, O1, O2) from patients in a coma. For several hours, while the signals were being recorded, the patients had several epileptic seizures. To analyze the properties of EEG, we considered only the parts of signals corresponding to seizures.

Figure 1.a shows the periodogram of T3 for the patient during the seizure, the main frequency is 2 Hz. For other leads of this patient periodogram similar.

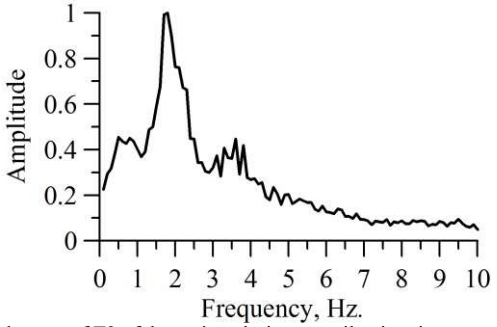

Fig.1. Periodogram of T3 of the patient during an epileptic seizure.

Also, histograms of phase increments (for the interval of one characteristic period), estimates of the varience, asymmetry and kurtosis of phase increments, phase diffusion coefficient of all leads were obtained.

IV. THE MODEL SYSTEM

The system of two linear stochastic oscillators was chosen as a test model:

$$\begin{aligned} d^2x_1/dt^2 &= -\delta_1 dx_1/dt - \omega_1^2 x_1(t) + \xi_1(t), \\ d^2x_2/dt^2 &= -\delta_2 dx_2/dt - \omega_2^2 x_2(t) + \\ &\quad + K(x_1(t) - x_2(t)) + \xi_2(t), \end{aligned} \quad (3)$$

here $\xi_k(t)$ – white zero-mean noises with autocovariation function $\langle \xi_k(t)\xi_k(t')\rangle = D_{\xi_k}\delta(t-t')$, parameters $\sqrt{D_{\xi_k}}$ determine the noise level, K - coupling coefficient, angular frequency $\omega_1 = 11.3, \omega_2 = 12$ (corresponds to the main frequencies of EEG leads of patients during seizure (1.8 and 1.9 Hz, respectively)), dissipation parameter δ_k determines the quality of oscillations and the individual width of the power spectrum. Equations (3) were integrated by the Euler technique with a step 0.0001. The signals with a sampling interval $\Delta t = 0.002$ (250 points per period) of length N=40000 points (about 150 characteristic periods) were analyzed, the phases were calculated using the Hilbert transform. The parameters δ_k and $\sqrt{D_{\xi_k}}$ in (3) were chosen so that when K=0, the periodogram and the phase increments histogram, estimates of phase diffusion coefficient, variance, asymmetry and kurtosis of phase increments, calculated from the patient's EEG were similar to the ones, calculated from the time series of the model. As a result, the parameters δ_k =3, $\sqrt{D_{\xi_k}}$ =0.2 were selected.

The effectiveness of the investigated method of coupling detection was tested as follows. We generate a 100 collection of time realizations of (3) with fixed parameters. From each time series in a collection, we estimate $\gamma_{2\to1}$ and $\gamma_{1\to2}$. Then we calculated the number of time series f, for which the estimates $\gamma_{j\to k}$ are considered significant –with the confidence interval exceed zero. In the absence of coupling f is the number of false conclusions. In $K \neq 0$ the value f is the number of correct conclusions about the presence and direction of coupling (determines the sensitivity of the method).

V. Results

Fig.2 shows the dependence of the f value on the coupling coefficient K for $\gamma_{2\to1}$ (fig.2.a) and for $\gamma_{1\to2}$ (Fig.2.b). The method demonstrates a large level of erroneous conclusions both about the presence of coupling and its direction. To reduce the number of errors, three methods of filtering of the initial time series were applied: a low-pass filter with a cutoff frequency of 5 Hz (Fig.2., dotted line), bandpass filter from 1 to 3 Hz (Fig.2., solid line with circles) and bandpass filter from 1.5 to 2.5 Hz (Fig.2., solid line with triangles).

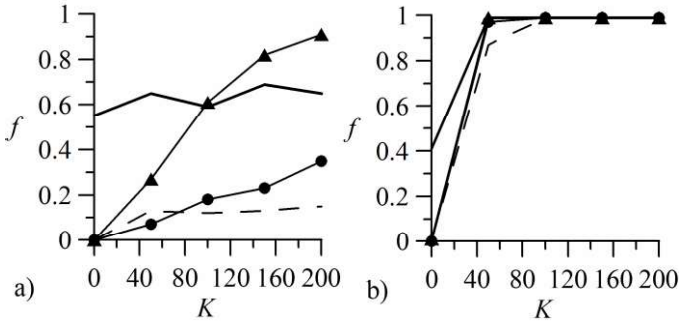

Fig.2. The frequency of positive conclusions about the presence and direction of coupling depending on the coefficient of coupling in model (3): a) for $\gamma_{2\to1}$ (here f is the number of false conclusions about the direction of coupling); b) for $\gamma_{1\to2}$ (here f is the number of correct conclusions about the coupling direction if $K \neq 0$).

The most optimal is the use of low-pass filter - with this method of filtering, the lowest level of errors is achieved, while maintaining a high sensitivity of coupling detection (fig.2.b). Also, dependences of the value f on the method parameter τ and on the time series length were obtained. The lowest level of errors, while maintaining high sensitivity of the method is achieved at τ equal to one characteristic period and at the length of a series of 40 characteristic periods.

VI. Conclusion

In this paper, we investigated the applicability of the method of coupling analysis based on the phase dynamics modeling on the example of etalon systems, the phases properties of which are similar to the properties of the phases of EEG signals in patients with reduced level of the consciousness during an epileptic seizure. It is shown that the efficiency of the method is significantly increased if one uses a low-pass filter as a preprocessing of the signals – in this case, it is possible to achieve the lowest level of errors with high sensitivity of the method. It is also shown that for the used model systems, the method parameter τ should be taken equal to the characteristic period, the minimum length of the analyzed series should be 40 characteristic periods. The obtained results are necessary for further analysis of couplings between brain structures in patients during epileptic seizure in coma.

Acknowledgment

This research was funded by Russian Foundation for Basic Research, grant No 18-29-02035 mk.

References

[1] H. Hinrichs, T. Noesselt, H.-J. Heinze “Directed information flow - a model free measure to analyze causal interactions in event related EEG-MEG-experiments”, 2008, Human Brain Mapping 29, pp.193-206.

[2] Mormann et al. “On the predictability of epileptic seizures” Clinical Neurophysiology, 2005, 116, pp.569-587.

[3] M.G. Rosenblum, A.S. Pikovsky “Detecting direction of coupling in interacting oscillators” Phys. Rev. E. 2001. V. 64. P. 045202

[4] Smirnov, B. Bezruchko “Estimation of interaction strength and direction from short and noisy time series”, Phys. Rev. E 68, 2003, 046209.

Mathematical modeling of NEMS elements in the form of flexible round plates under the Casimir's force action

I.V. Papkova
Physics and Technology Faculty
Yuri Gagarin State Technical
University of Saratov
Russia, Saratov
E-mail: ikravzova@mail.ru

A.V.Krysko
Physics and Technology Faculty
Yuri Gagarin State Technical
University of Saratov
Russia, Saratov
E-mail: anton.krysko@gmail.com

E.Yu. Krylova
Faculty of Mechanics and Mathematics
Saratov State University
Russia, Saratov
E-mail: kat.krylova@bk.ru

***Abstract*—The work is devoted to mathematical modeling of NEMS elements in the form of flexible round plates connected to the electrode. The influence of the dimension-dependent parameter on the oscillations under the action of Casimir force is investigated.**

Keywords—nanoplate, dimension-dependent parameter, modified moment theory, Casimir force

I. INTRODUCTION

In recent years, interest in physical phenomena, commonly known as the Casimir effect, has continuously increased. This effect is observed between two parallel plates, the distance between which is about 100 nm. This distance imposes a limit on the range of wavelengths, allowed wavelengths (virtual particles) inside the space between the plates. The density of energy between them falls in comparison with that in external space, where the birth of virtual particles is not limited by anything. As a result, negative pressure is created between the plates, which attracts the plates to each other. The closer surfaces to each other, then the greater the range of forbidden wavelengths of virtual particles, the greater the negative pressure and the stronger the attraction force. A literature analysis [1-4] has shown that the effect of Casimir force on the behavior of mechanical dimension dependent nanoplates is little studied

II. FORMULATION OF THE PROBLEM

In the classical theory of elasticity, the work strain and the strain energy depend on the stress tensor and do not depend on the rotation vector due to material independence. However, the gradient of the rotation vector can be a significant factor in the equations of state. Based on the modified theory of moment stresses, presented by Yang et al. [5], the strain energy density is a function of both the stress tensor (coupled with the strain tensor) and the curvature tensor (coupled with the moment stress tensor). In a deformed isotropic linear elastic material located in the Ω region, the strain energy Π is expressed by the formula

$$\Pi = \int_{\Omega} (\sigma_{ij}\varepsilon_{ij} + m_{ij}\eta_{ij}) d\Omega,\ i, j = 1, 2, 3, \qquad (1)$$

where σ_{ij} the Cauchy stress tensor, ε_{ij} is the stress tensor, m_{ij} is the deviator component of the moment stress tensor, and η_{ij} — is the symmetric curvature tensor. The scale parameter of the material length l, which is related to the material microstructures, was developed in order to interpret the size effect in the non-classical Kirchhoff-Love shell model. These tensors are determined by the formulas

$$\sigma_{ij} = \lambda tr(\varepsilon_{ij})I + 2\mu\varepsilon_{ij},\ \varepsilon_{ij} = \frac{1}{2}\left[\nabla u + (\nabla u)^T\right], \qquad (2)$$

$$m_{ij} = 2l^2\mu\chi_{ij},\ \eta_{ij} = \frac{1}{2}\left[\nabla\varphi + (\nabla\varphi)^T\right], \qquad (3)$$

where u is the displacement vector, $\lambda=E\nu/(1+\nu)(1-2\nu)$ and $\mu=E/2(1+\nu)$ — the Lame constants, E, ν are the Young modulus and the Poisson's ratio for the shell material, respectively. l is a parameter of the scale of the material length, understood as a material property, characterizing the moment strain effect, φ is the rotation vector represented as $\varphi_i = \frac{1}{2}\mathrm{rot}(u_i)$.

In a cylindrical coordinate system, the area Ω will be written as

$$\Omega = \left\{ (r, z) \middle|\ r \in [0, a], -\frac{h}{2} \le z \le \frac{h}{2} \right\}.$$

According to the Hamilton principle $\int_{t_0}^{t_1} (\delta K - \delta\Pi + \delta' W)dt = 0$. Here K, Π – kinetic and potential energy, respectively, $\delta' W$ - the work of external forces. Using the methods of calculus of variations, a differential equations system of the flexible plates theory is obtained on the basis of the moment theory of elasticity in a dimensionless form:

$$\bar{w}'' + \bar{\varepsilon}\bar{w}' = \left(1+\bar{D}_1\right)\left(-\frac{\partial^4\bar{w}}{\partial\bar{r}^4} - \frac{2}{\bar{r}}\frac{\partial^3\bar{w}}{\partial\bar{r}^3} + \frac{1}{\bar{r}^2}\frac{\partial^2\bar{w}}{\partial\bar{r}^2} - \frac{1}{\bar{r}^3}\frac{\partial\bar{w}}{\partial\bar{r}}\right) +$$

$$+\frac{\bar{\Phi}}{\bar{r}}\frac{\partial^2\bar{w}}{\partial\bar{r}^2} + \frac{1}{r}\frac{\partial\bar{\Phi}}{\partial\bar{r}}\frac{\partial\bar{w}}{\partial\bar{r}} + \frac{\bar{q}_k}{\left(1-\bar{w}\right)^4} \qquad (4)$$

$$\frac{\partial^2\bar{\Phi}}{\partial\bar{r}^2} + \frac{1}{\bar{r}}\frac{\partial\bar{\Phi}}{\partial\bar{r}} - \frac{1}{\bar{r}^2}\frac{\partial\bar{\Phi}}{\partial\bar{r}} = \frac{\partial\bar{w}}{\partial\bar{r}}\left(-\frac{1}{2\bar{r}}\frac{\partial\bar{w}}{\partial\bar{r}}\right), \Phi = \frac{\partial F}{\partial r}$$

For an axisymmetric problem the boundary conditions for a hinge-moving contour in the meridional direction will be written as follows:

$$\Phi = w = 0,\ \frac{\partial^2 w}{\partial r^2} + \frac{\nu}{a}w = 0,\ \text{with } r = a. \qquad (5)$$

Initial conditions:

$$w = 0, w' = 0, 0 \le t < \infty. \qquad (6)$$

In addition, the following relations hold in a small neighborhood of the vertex of an axisymmetric spherical shell: $\Phi \approx Ar$, $\Phi' \approx A$, $w \approx B + Cr^2$, $w' \approx 2Cr$, $w'' \approx 2C$, $w''' \approx 0$.

Dimensionless values are entered here.

$$\bar{r} = \frac{r}{a},\ \bar{w} = \frac{w}{h_0},\ \bar{F} = \frac{F}{Eh^3},\ \bar{t} = t\sqrt{\frac{D_0}{\rho h a^4}},\ \gamma^2 = \frac{l^2}{h^2},$$

$$D_0 = \frac{Eh^3\nu}{(1+\nu)(1-2\nu)},\ \bar{q}_k = \frac{\hbar c\pi^2 a^4}{240 D_0 h_0^5},\ \bar{D}_1 = \gamma^2\frac{(1-2\nu)}{2\nu},$$

t - time; w – deflection, F – effort function; h is the plate thickness; h_0 – the distance between the electrode and the nanoplate; q_0 – load amplitude, ν – the Poisson's ratio, E – the elastic modulus, l – the dimension-dependent parameter, ρ – the density of the plate material, a – radius, $\hbar$ - the Planck's constant, c – the support contour radius of the plate.

III. CALCULATION ALGORITHM

To reduce the distributed system (4) - (6) to the system with lumped parameters, we use the finite difference method with approximation $O(h^2)$. The Cauchy problem will be solved by several Runge-Kutta methods

IV. NUMERICAL EXPERIMENT

Consider the oscillations of a round nanoplate under the Casimir force. Analysis of the results shows that oscillations occur at the same frequency. With an increase in the dimension-dependent parameter, the oscillation frequency increases: for $\gamma = 0$, the frequency $\omega_0 = 4.1$; when $\gamma = 0.1$, the frequency $\omega_0 = 4.2$; when $\gamma = 0.3$, the frequency $\omega_0 = 5$; when $\gamma = 0.5$, the frequency $\omega_0 = 6.1$.

V. CONCLUSION

A mathematical model of a flexible axisymmetric round nanoplate under the action of Casimir's force was constructed. It is shown that under the action of the Casimir force the plate oscillates. The oscillation frequency of the plate increases with increasing dimension-dependent parameter.

ACKNOWLEDGMENT

The work was supported by the RNF (grant № 19-19-00215).

REFERENCES

[1] R. A. Toupin, "Elastic materials with couple-stresses", Arch. Ration. Mech. Anal. 11, 1962, pp .385–414.

[2] D.V. Scheible, A. Erbe, and R.H. Blick, "Evidence of a nanomechanical resonator being driven into chaotic response via the Ruelle–Takens route", Appl. Phys. Lett. 81, 2002, pp. 1884–1886.

[3] Fu, Y., Zhang, J.: "Electromechanical dynamic buckling phenomenon in symmetric electric fields actuated microbeams considering material damping". Acta Mech. 212, 2010, pp. 29–42

[4] X.L. Jia, J. Yang, S.Kitipornchai "Pull-in instability of geometrically nonlinear micro-switches under electrostatic and Casimir forces". Acta Mech. 218, 2011, pp. 161–174

[5] Yang, A. C. M. Chong, D. C. C. Lam, and P. Tong, "Couple stress based strain gradient theory for elasticity", Int. J. Solids Struct. 39, 2002, pp. 2731–2743

Characterization of intermittent dynamics from experimental data with DFA

Olga N. Pavlova
Physics Department
Saratov State University
Saratov, Russia
pavlov_lesha@yahoo.com

Natalia M. Kupriyashkina
Physics Department
Saratov State University
Saratov, Russia
nataliya_kupriyashkina@mail.ru

Alexey N. Pavlov
Dept. of Electrical Engineering and Electronics,
Yuri Gagarin State Technical University of Saratov
Saratov, Russia
pavlov.alexeyn@gmail.com

***Abstract*—The problem of characterizing the dynamics of nonlinear systems from experimental data is considered in the presence of switching between oscillatory processes. Errors of computing the scaling exponent of the detrended fluctuation analysis (DFA) caused by data fragments corresponding to different dynamical modes are investigated. It is shown that switching between the modes has a much stronger effect on the diagnosis of anti-correlated dynamics.**

Keywords—signal, intermittency, correlation analysis, chaotic dynamics

I. INTRODUCTION

Diagnostics of complex dynamics of nonlinear systems from experimental signals is often complicated by the presence of noise, artificial segments [1] and nonstationarity, which may include changes in control parameters and transitions between distinct types of oscillations [2]. Unlike additive fluctuations and corrupted segments of data, transitions between distinct oscillatory modes are more difficult to distinguish and exclude at the pre-processing stage. The related types of dynamics can be characterized by similar statistical properties, and the time series under study may be wrongly associated with a stationary dynamics.

In this study, we consider the effect of switching between distinct types of oscillations in two coupled Rössler systems on the correlation properties of signals reflecting their functioning.

II. MODEL AND DATA PROCESSING

A. Detrended Fluctuation Analysis

DFA is a variant of the correlation analysis of a data set, which assumes a construction of the signal profile with its further root mean square analysis [3, 4]. This method involves four steps: (1) building of the profile $y(k)$; (2) segmentation of the profile into non-overlapping parts of size n and fitting a local trend y_n (k) within each segment; (3) estimation of the root mean-square fluctuation $F(n)$; (4) performing these estimations in a wide range of n to get a power-law dependence [5, 6]

$$F(n) \sim n^{\alpha}. \qquad (1)$$

The scaling exponent α is related to quantities describing the behavior of the correlation function or the spectral power.

B. Model

We consider a model of two diffusively coupled Rössler systems, which is described by the following six ordinary differential equations

$$\frac{dx_{1,2}}{dt} = -\omega_{1,2}y_{1,2} - z_{1,2} + \gamma(x_{2,1} - x_{1,2}), \quad \frac{dy_{1,2}}{dt} = \omega_{1,2}x_{1,2} + ay_{1,2}, \qquad (2)$$
$$\frac{dz_{1,2}}{dt} = b + z_{1,2}(x_{1,2} - c), \quad \omega_{1,2} = \omega_0 \pm \Delta,$$

where ω_0=1, a=0.15, b=0.2, γ=0.02, and the remaining parameters are varied to consider switching between different types of oscillations. Analysis of intermittent dynamics was performed using sequences of return times into the Poincaré section x_1=0.

III. RESULTS AND DISCUSSION

We analyzed transitions between various types of periodic, quasi-periodic, chaotic and hyperchaotic dynamics. Consider switching between a synchronous chaotic attractor (c=6.8, Δ=0.0096) and an asynchronous chaotic attractor (c=6.8, Δ=0.0098) in model (2). These oscillatory modes represent the anti-correlated (α=0.02) and correlated (α=0.80) dynamics, respectively [5, 6]. The appearance of anti-correlations is typical for attractors appeared because of the period-doubling cascade. The chaotic oscillations arising from the destruction of quasi-periodic oscillations demonstrate a correlated structure of the sequences of return times. If the data set under study includes transitions between oscillatory modes, the offset of the scaling exponent depends on the relative duration of time, associated with each mode. In the case of similar durations, the scaling exponent approaches the value of α=0.63 (Fig. 1). Thus, the displacement of the scaling exponent is asymmetric: the anti-correlated mode changes the scaling exponent by 0.61, while the correlated mode shows the offset of 0.17. In Figure 1, the N_2/N_1 ratio characterizes the relative number of return times associated with the main process (oscillatory mode, in which the system spends most of the time, N_1) and with the additional data set (N_2).

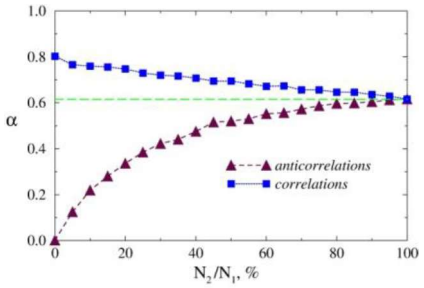

Fig. 1. The scaling exponent depending on the N2/N1 ratio related to the cases when synchromous and asynchronous chaotic oscillations are considered as the main mode, respectively.

Similar results are obtained for transitions between hyperchaotic oscillations (c=7.2, Δ=0.0094) which occur after the merging of synchronous chaotic attractors with different phase shifts between the variables, and asynchronous chaos (c=7.2, Δ=0.0098) – Figure 2.

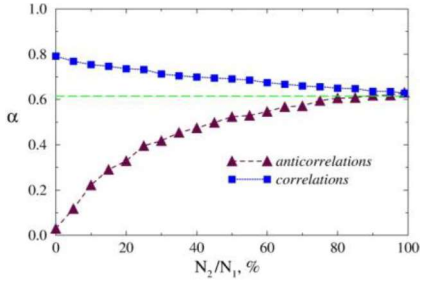

Fig. 2. The scaling exponent depending on the N2/N1 ratio related to the cases when hyperchaotic and asynchronous chaotic oscillations are considered as the main mode.

By analogy with Fig. 1, an asymmetric displacement of the scaling exponent takes place when dealing with data sets composed from segments related to both types of attractors. Analogous results are obtained for simpler dynamics – transitions between periodic and quasi-periodic oscillations (Fig. 3).

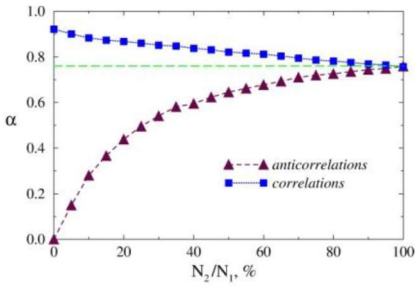

Fig. 3. The scaling exponent depending on the N_2/N_1 ratio related to the cases when periodic and quasi-periodic oscillations are considered as the main mode.

IV. Conclusion

We analyzed transitions between various types of periodic, quasi-periodic, chaotic and hyperchaotic dynamics and compared the different sensitivity of sequences of return time with power-law correlations and anti-correlations to transitions between oscillatory modes with distinct correlation properties. Based on the detrended fluctuation analysis, we compared displacement in the scaling exponent. Independently on the type of oscillations, a similar effect was established consisting in a significantly higher sensitivity of anti-correlated sequences of return times to the appearance of segments with distinct correlation properties.

Acknowledgment

This work was supported by the Russian Science Foundation (Agreement 19-12-00037).

References

[1] Q.D.Y. Ma, R.P. Bartsch, P. Bernaola-Galván, M. Yoneyama and P.Ch. Ivanov, "Effect of extreme data loss on long-range correlated and anticorrelated signals quantified by detrended fluctuation analysis," Phys. Rev. E, vol. 81, pp. 031101, 2010.

[2] J.S. Bendat and A.G. Piersol, Random Data Analysis and Measurement Procedures. Fourth edition. New Jersey: Wiley, 2010.

[3] C.-K. Peng, S.V. Buldyrev, S. Havlin, M. Simons, H.E. Stanley and A.L. Goldberger, "Mosaic organization of DNA nucleotides," Phys. Rev. E, vol. 49, pp. 1685–1689, 1994.

[4] C.-K. Peng, S. Havlin, H.E. Stanley and A.L. Goldberger, "Quantification of scaling exponents and crossover phenomena in nonstationary heartbeat time series," Chaos, vol. 5, pp. 82–87, 1995.

[5] R.M. Bryce and K.B. Sprague, "Revisiting detrended fluctuation analysis," Sci. Rep. vol. 2, pp. 315, 2012.

[6] H.E. Stanley, L.A.N. Amaral, A.L. Goldberger, S. Havlin, P.Ch. Ivanov and C.-K. Peng, "Statistical physics and physiology: monofractal and multifractal approaches," Physica A, vol. 270, pp. 309–324, 1999.

[7] A.N. Pavlov, O.N. Pavlova, A.S. Abdurashitov, O.A. Sindeeva, O.V. Semyachkina-Glushkovskaya and J. Kurths, "Characterizing scaling properties of complex signals with missed data segments using the multifractal analysis," Chaos, vol. 28, pp. 013124, 2018.

[8] O.N. Pavlova, A.S. Abdurashitov, M.V. Ulanova, N.A. Shushunova and A.N. Pavlov, "Effects of missing data on characterization of complex dynamics from time series," Commun. Nonlinear Sci. Numer. Simulat., vol. 66, pp. 31–40, 2019.

Modeling the distortions of public opinion under conditions of external influence using differential stochastic equations

Alexandr Petukhov
Research Lab. "Modeling of social and political processes"
Lobachevsky Nizhny Novgorod State University
Nizhny Novgorod, Russia
Lectorr@yandex.ru

***Abstract*— In this paper, we propose a mathematical model of public opinion, taking into account external influences, from the point of view of the author's socio-energy approach, as well as explaining its basic principles. The expression for the flow of social energy through the system is used as the basis equation, then the model is presented basing on the nonlinear dynamical system using the ideas of fractal geometry to calculate the individual elements of structures, as well as the Langevin equation (for the Wiener processes) in order to consider fluctuations in the social and political processes. With the help of this equation, the author creates the communication field model, which describes the interaction of individuals in society. This model is proposed to be used to predict structural changes in society in the conditions of information warfare.**

Keywords*— *modeling, socio-energy approach, complex social systems, nonlinear dynamical systems

I. Introduction

Even though mathematical models are so widely used in natural sciences, still they are not so applicable while conducting political, social or historical research. Nevertheless, remarkable success has been achieved in the field of creation of social and political history models [1].

The models available to date can be divided into three groups:

1) conception models, which are based on the identification and analysis of the general historical patterns and present them in the form of cognitive schemas describing logical connection between different factors affecting the historical processes (G.Goldstein, I.Wallerstein, L.N.Gumilev, N.S.Rozov et al.). These models have a high degree of generalization, but do not have a mathematical and purely logical, conceptual nature;
2) special mathematical models of simulation type, devoted to the description of specific historical events and phenomena (D.Medouz, Y.N.Pavlovsky, L.I.Borodkin, Forrester et al.). These models focus on careful consideration and description of factors and processes that influence phenomenon under consideration. Such models are usually applicable in a rather narrow space-time interval: they are «tied» to a particular historical event and cannot be extrapolated over a period of time;
3) mathematical models that are intermediate between the types mentioned above. Those models describe certain category of social processes without detailed description of peculiarities of each historical event. The task of such models is to find basic mechanisms characterizing the processes flow of the examined type. According to this, such models are called basic [2].

The socio-energy approach is based on a systematic approach and view at the state system in terms of energy. This view allows us to represent the intra and extra-systematic processes such as modification or redistribution of energy within the system and between systems. It also allows to present intra-processes through physical analogy, e.g. Weiner processes. In the theory of random processes Wiener process is a mathematical model of Brownian motion (it is described through the Langevin equation) or a random walk in continuous time [3,4].

It also introduces the concept of «social energy» or simply «energy» (E). Here, this concept means the derivative that characterizes the potential of the social system to do the work. Attempts to introduce such a concept have been made before, but without further use for the creation of a mathematical model, while limiting to general discussions [5].

II. Basis of Mathematical Model

This value, which is social energy or *E*, gives us a certain freedom in the interpretation of «not yet released energy», i.e. the work that has not been done yet, in the evaluation of potential energy of human labor, resources that have not been produced, etc. This very moment is vitaly important for model-building, because in order to evaluate the social system we must take into account all the factors, which are capable to influence it, and parameters such as, for example, human labor, are often obtain a determinative role in the system, but at the same time they are very hard to be classified in terms of standard physical concepts.

This view allows us to represent the intra and extra-systematic processes such as modification or redistribution of energy within a system and between systems. In a complex social system, there are two types of primary energy (as introduced above the notion of social energy), which includes all the others:

$$E_m = f(E_m^{sc}, E_m^{\Sigma h}, K_{sc})$$

Material energy of system, where:

E_m^{sc}- resources energy (if there is any) of social system and its material (tangible) property.

$E_m^{\Sigma h}$- energy of material savings and property of the people living in the system.

$K_{sc} = f(\vec{a}, I_I, K_s)$ - scientific and technical progress and system development.

$\overrightarrow{a}$- a number of parameters, defining scientific and technical progress in the system.

I_I- transfer function of intersystem information exchange.

$K_s = f(\vec{\beta}, I_I, N)$ - social activity coefficient of moral and ethical society condition.

Coefficients K_s and K_{sc} exist separately for each individual in the system and cumulative coefficient of the system as a whole is generated through fractal transformation of all individual values and clusters of the system.

N - number of individuals in the social system.

$\vec{\beta}$- a set of parameters that define the spiritual and moral development and moral state of society and social environment.

The labor energy of people constituting the social system:

$$E_h = f\left(K_o, E_h^{\Sigma}, K_s, K_{sc}\right)$$

E_h^{Σ} - total labor energy of the family members, which depends on *N (*number of individuals*).*

Thus, the total social energy of the system has the following formula:$\sum_{i=1}^{n} E_i = E_{\Sigma}$

Taking it into account, we obtain a model based on differential equations:

$$\sum_{i=1}^{n} \vec{P}_i = \overrightarrow{P_{\Sigma}}$$

where

$$\overrightarrow{P_{\Sigma}} = \vec{\chi} \frac{dE_{\Sigma}}{dt} \quad (1)$$

I.e. energy flow per unit of time in the system, or change the energy used, is subject to an intra-laws. In fact, we use the concept of power that considers the work (energy change), but in our case, since we are interested in the change in energy, it is the same.

$\vec{\chi}$ - unit vector of the energy flow direction.

Thus:

$$\vec{P}_\Sigma = \vec{P}_\Sigma{}^m + \vec{P}_\Sigma{}^h + \vec{P}_\Sigma{}^{out}$$

Then, taking into consideration (1):

$$\vec{j}\frac{dE_m}{dt} + \vec{k}\frac{dE_h}{dt} + \vec{\gamma}\frac{dE_{out}}{dt}$$

As a result –

$$\vec{P}_\Sigma = \vec{j}\left(\frac{dE_m{}^{\Sigma h}}{dt}K_sK_{sc} + \frac{dE_m{}^{sc}}{dt}K_dK_{sc}\right) + \vec{k}\left(\frac{dE_h{}^{\Sigma}}{dt}K_{sc}K_s\right) + \vec{\gamma}\left(\frac{dE^{\Sigma}{}_{out}}{dt}\,\xi(K_{sc}K_sI_I)\right) \quad (2)$$

Or, without external influence:

$$\vec{P}_\Sigma = \vec{j}\left(\frac{dE_m{}^{\Sigma h}}{dt}K_sK_{sc} + \frac{dE_m{}^{sc}}{dt}K_sK_{sc}\right) + \vec{k}\left(\frac{dE_h{}^{\Sigma}}{dt}K_sK_{sc}\right)$$

The expression that we get is the basic equation of the socio-energy approach, which expresses the flow of social energy passing through the system. It is assumed that it is valid for large social systems (e.g., a state), and for the smaller ones (for example, business systems). Regarding the calculation of coefficients for the social system - in other works [6].

III. Accounting Fluctuations in the Social and Political Processes

Social and political processes are characterized by the fact that they cannot be strictly specified. They are always subject to small changes and fluctuations. By resorting to analogy, the social process is similar to Brownian particles, i.e. particles move along well-defined path, but on closer inspection, the path is seen much winding, with many small breaks. These small changes (i.e. fluctuations) are explained by the random motion of other molecules. In social processes, the fluctuation can be interpreted as a manifestation of the free will of its members. [7]

Description of the social process in terms of the math is required to use a stochastic process. In mathematics the Langevin equation is used to describe the Brownian motion:

Where s(t) = (s_1(t), …, s_n(t)) is the vector field, describing social process (information exchange on this case). The Langevin equiation for s is the following:

$$\frac{ds}{dt} = -ks + \zeta \quad (3)$$

Where ζ (t) is a random power influencing the social system. It can be determined by a number of factors, such as, for example, the level of social unrest in the society (determined by the K_o and $K_н$ parameters).

The average value as follows:

$$<\zeta>(t) \equiv M\zeta(t) = \int_{E_{\zeta(t)}} [\zeta(t)](\omega)dP_{\zeta(t)}(\omega) = 0$$

$$<\zeta(t)\zeta(t')>= \delta(t-t')$$

Where $<E_{\zeta(t)}, P_{\zeta(t)}>$ is the probability space of a random variable $\zeta(t), \omega \in E_{\zeta(t)}$ is an elementary event. Then, in accordance with (3):

$$s(t) = s_0e^{-kt} + \int_0^t e^{-k(t-t')}\zeta(t')dt' \quad (4)$$

We can suppose, that the initial given value S_0 is a random value with the probability space $<E_0, P_0>$. In this case s(t)=[s(t)](ω,*v*) is a random value with a probability space $<E_{\zeta(t)} \times E_0, P_{\zeta(t)} \times P_0>$, where $v \in E_0$.

By averaging (4) we get the following formula:

$$<s>(t) = \int_{E_{\zeta(t)\times E_0}} [s(t)](\omega,v)dP_{\zeta(t)}(\omega) \times P_0(v) =$$

$$= \int_{E_0} s_0(v)e^{-kt}dP_0(v) + \int_0^t e^{-k(t-t')}\left(\int_{E_{\zeta(t')}} [\zeta(t')](\omega)dP_{\zeta(t')}(\omega)\right)dt' =$$

$$=< s_0 > e^{-kt} + \int_0^t e^{-k(t-t')} <\zeta>(t')dt' =< s_0 > e^{-kt}$$

It means that:

$$<s>(t) =< s_0 > e^{-kt}$$

Accordingly, the stochastic process s(t) with $t \to +\infty$ becomes quasi-stationary, close to balance s=0.

In general case, the Langevin equation is the following:

$$\frac{ds}{dt} = -ks + F(t) + \zeta \quad (5)$$

Where the external force F(t) can be a potential one, i.e. $F = \nabla V$, where V=V(x,t) – vector field. As we can see from this case, s=s(x,t). Thus, the social process *s* depends on additional parameters, included in the phase space [7], which are important to take into account while the process modeling.

IV. Formation of Communication Field Inside the System

Let us suppose that we have a social system A, with a determined distribution of coefficients K_o and $K_н$ (each individual *i* has a corresponding coefficient k_i). How their interaction will occur, and how the change will affect the impact on the system from the outside?

Holyst J.A., Kacperski K., Schweiter F. offered a suitable model of public opinion on the basis of representation of interaction between individuals, in the form of Brownian motion [8]. Applying this model to our case, i.e.to the coefficients, it is necessary to make some significant changes. The individuals are involved in this process by interacting through the communication field $h_k(x,t), x \in S \subset \mathbf{R}^2$

This field takes into account the spatial coefficients distribution and is distributed in a society, modeling the

transfer of information. However, we must understand that we are talking about the social space that has the physical attributes, but in terms of information means it is clear that the impact of one individual on another is not necessarily exercised while being physically close. Thus, this space is multidimensional, social and physical, characterizing the possibility of one individual «to reach out» the other by his\her communication field, that is, to influence him\her, his\her coefficients and ability to move. It is understood that, in addition to actually physical and spatial coordinates, there will be social coordinates as well (characterizing the social status of the individual).

Spatial and temporal variation of the communication field is considered by the equation:

$$\frac{\partial}{\partial t} h_k(x,t) = \sum_{i=1}^{N} f(k_i,k_n)\delta(x-x_i) + D_h \Delta h_k(x,t) \quad (6)$$

$\delta(x-x_i)$ – Dirac δ-function

$f(k_i,k_n)$ – function that determines the strength of influence of the individual on the other specific individual, depending on their coefficients.

N – the number of individuals.

D_h – the diffusion coefficient, characterizing the distribution of the communication field.

Each individual in the point x_i, constantly contributes to the development of the field $h_k(x,t)$ in accordance with the values of their coefficients (that also determine the force of influence of an individual on the surrounding individuals as well as the radius of this influence).

The field $h_k(x,t)$ influences the individual *i* in the following way. While being in the point x_i, the individual gets into the influence of the communication filed of another individual (or several of them). Depending on its difference from the coefficients and the coefficients of individuals acting on it, i-individual may react in the following ways:

1. He\she can change the value of his\her coefficients while being under influence of other individuals
2. Move towards the area where the coefficients difference is relatively minimal in the moment of action

Let us suppose that $p_{ij}(k_i,k_j,t,x_i,x_j)$ - the probability of impact on the communication field of *i*-individual (or the whole cluster of individuals) j in such a way, that can change the coefficients K_o and K_n (together or separately) in the time period *t*. Then, the probability of move of the individual-*i* to the field with relatively minimal coefficients difference in the moment of action is $1-p_{ij}(k_i,k_j,t,x_i,x_j)$.

Then the change of the given probability is the following:

$$\frac{d}{dt} p_{ij}(k_i,k_j,t,x_i,x_j) = \sum_{k_i'} \upsilon(k_i|k_i') p_{ij}(k'_i,k'_j,t,x_i,x_j)\vartheta(\Delta x_{ij}\Delta k_{ij}) - \\ - p_{ij}(k_i,k_j,t,x_i,x_j)\sum_{k_i'} \upsilon(k'_i|k_i)\vartheta(\Delta x_{ij},\Delta k'_{ij}) \quad (7)$$

$\vartheta(\Delta x_{ij}\Delta k_{ij})$ - Parameter, characterizing induction influence of the communication field.

Where $\upsilon(k_i|k_i')$ is conditional probability of coefficient change per time unit:

$$\upsilon(k_i'|k_i) = \begin{cases} k_i \neq k_i' \to \eta \exp\left\{\left[h_{k_i'}(x_i,t) - h_{k_i}(x_i,t)\right]/Q\right\} \\ k_i = k_i' \to 0 \end{cases} \quad (8)$$

Where Q is the social freedom parameter, characterizing the degree of the movement freedom of individuals in social and physical space.

The movements of individuals in social and physical space is described by the Langevin equation:

$$\frac{dx_i}{dt} = k_i \vartheta(\Delta x_{ij}\Delta k_{ij})\nabla_x h_\Sigma(x_i,t)\big|_{x_i} + \sqrt{2D_n}\zeta_i(x_i,t) \quad (9)$$

Where D_n is the spatial diffusion coefficient of individuals, $h_\Sigma(x_i,t)$ is the resulting field of communication, that impacts on individual-*i*.

Random fluctuations and impact are modeled through the stochastic force $\zeta_i(x_i,t)$, in such way that ζ_i is flat noise, which also depends on the location of the individual, (it is assumed that the influence of random external and internal factors on the social position of the individual in different parts of the system is different) with

$$<\zeta_i(x_i,t)\zeta_j(x_i,t')>=\delta_{ij}\delta(t-t')$$

Thus, this model allows the calculation of the coefficients of variation in the social system under external influence or changes the system itself and its global parameters [6].

V. Results of Computer Modeling

Initially, a system has a certain hierarchy or a certain structure that reflects its status and intra-social processes. The process of society clustering leads to the creation of certain social and political education, intra-social links in the system, in which information and energy exchange goes much faster and more often. We can assume this division as class, caste, hierarchical, stepwise divide, depending on the assessment of the state of society, which is the distribution of the individuals in their cluster must be set, so you see the changes. In some cases, certain elements of the system can be observed in chaos (for example, during the civil war or revolution), and other structures are unstable and are in constant motion, but in general, in the short term (1-2 years), long-term structural changes are shown, typically only while a strong external interference.

The method of specifying structural distribution of individuals in the society by means of fractal patterns and cognitive algorithms seems to be the most promising [6].

Eч - social energy of an individual or a single subsystem, x, y - the social and physical coordinates.

It is necessary to further clarify what are the social and physical coordinates.

Specially introduced social and physical space is a multi-dimensional one, characterizing the possibility of one individual to "reach out" by its communication field to another one, that is, to influence it, its coefficients and its ability to move.

However, how we can express it mathematically? To do this, we created an abstractive illustration of axes of social and physical space, presenting them in 3-dimensional form.

Thus, the x- and y-axis are both 3-dimensional physical coordinates, as well as two relative parameters, which are information and social permeability (I, S), which are characterized by the distance on a graph, how difficult (both in terms of energy and socio-psychology) for an individual or a subsystem to transmit information or energy to another individual or subsystem. The greater the distance is the more difficulties arise for such contact.

For simplicity, we define the axis as follows:

x is the sum of 2 physical coordinates, (x' + z' + S) and social permeability of society S.

y is the sum of information permeability and coordinate I + y' .

The main social resources are concentrated at a relatively small part of its population. Fractal type of distribution also defines the structure of a certain position in the social and physical space that allows us to make judgments about the relationships among individuals and subsystems that have significance for the entire system resources. However, the clustering of elements according to social (or class) basis is not surprising, and the fractal method allows us to demonstrate this more clearly.

However, in further calculations the fractal type of distribution of the society structure is not used because of insufficient author`s ECM capacity for its computer simulation. The fact that fractals require a huge number of iterations to reconstruct the general picture and, consequently, the numerous elements involved in the communication interactions, and the same number of intersecting communication fields.

Having such parameters, the simulation requires considerable computer power, and further optimization of the code written for the system. The author considers that it is necessary to note that this distribution is the most effective for the task and for future; hence it is supposed to work with it.

However, due to the reasons mentioned above, the so-called "peak" distribution has been used in order to demonstrate the model; it represents society in the form of several or one peak or undulating areas, whose sharpness, and quantity are highly dependent on the given initial parameters (simulation was conducted in the system MatLab 2009b) - Fig.1.

Convenience of such structural distribution also lies in the fact, that it is very clearly demonstrates changes in the general field of communication, which are demonstrated in the next section.

Graph axis remained unchanged and the location of individuals or subsystems of society are defined by points; interpolation was held to demonstrate the whole picture.

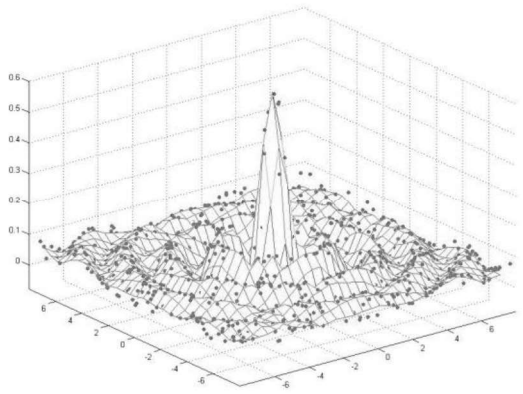

Fig.1. Peak structural distribution of coefficients and material component in general case. The z-axis – E, social energy of individual, x,y – socio-physical coordinates.

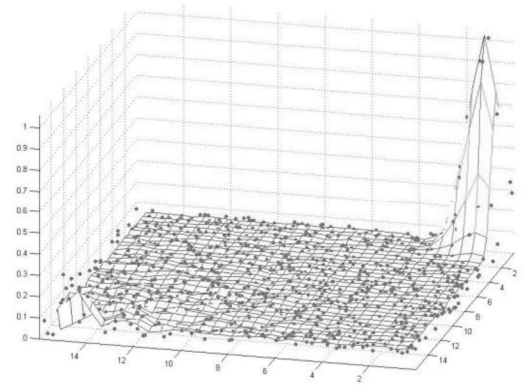

.

Fig.2. Peak structural distribution of coefficients and material component in Russia. Introduction perturbation. The z-axis – E, social energy of individual, x,y – socio-physical coordinates.

By changing the initial parameters, we can set the type of a system that is mostly correspondent to the results of political analysis.

The Fig.2 demonstrates a bit changed peak distribution. These changes are not important for structural architecture, but they can help to get rid of negative value of coordinates that exist in mathematics, but, of course, cannot exist in real life. We also displaced the peak location.

This was made exclusively for visualization, the energy and coefficients distribution do not change because of such movements, and the only thing that changes is nominal system parameters.

However in this way we can easily see the changes in the bulk of society, not fenced by peak.

E = 1, i.e.the subsystem energy that has a maximum resource relative to other subsystems in society.

Fig. 2 demonstrates perturbation that is placed in the other corner of the chart, opposite to the main peak which is the exposure of influence of the external system on the given one.

Hereby we set the parameters of interaction:

Let us suppose that the system A with coefficients K_s and K_sc that are both equal to 0.95 influences the system B with coefficients that are equal 0.80 and 0.20 respectively.

The given influence, that caused change in the coefficients, provokes the beginning of the energy redistribution. The system interaction is also based on the energy exchange, due to which the perturbation is visible on the graph. The impacting system (the subject) is used for certain spending power to influence a part of society and the impact of the object passes it.

Fig. 3. demonstrates that some sort of "ripple" is going through the society as response on the external system influence.

What does this mean in terms of policy analysis? That a number of subsystems and individuals have begun to redistribute the system energy, often spontaneously, with permanent reverse, resulting in a kind of "ripples."

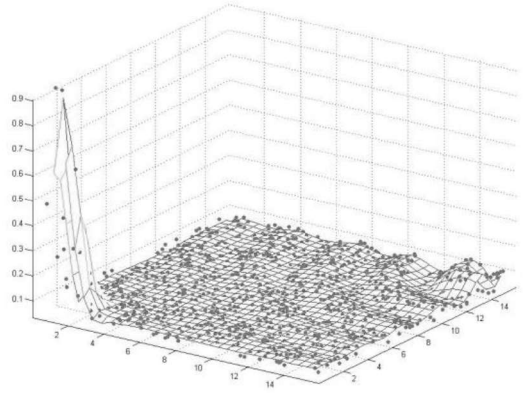

Fig.3. Peak structural distribution of coefficients and material component in Russia. Development of perturbation in the system. The z-axis – E, social energy of the individual, x, y - social and physical coordinates.

In this regard, it is also necessary to understand why the disturbance started in the opposite corner of the chart from the main peak of social energy.

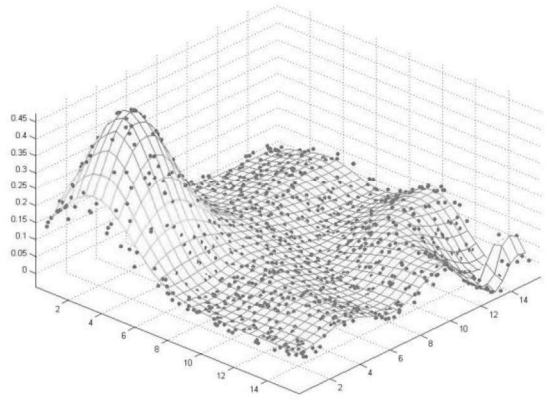

Fig. 4. Peak structural distribution of coefficients and material component in Russia. System disbalancing. Constant flow of E from one subsystem to another. The z-axis – E, social energy of individual x,y – socio-physical coordinates.

Subsystems lying there are rather distant from social and territorial or spatial perspective from controlling most of the subsystem energy (and therefore power). As a result, they are the least stable.

So, referring to the history, we can notice that often (but certainly not always) collapse of states, revolutions and chaos start from the periphery, as well as from the outskirts of states. That is especially acute today. This is the most unstable element of social system, and it is not surprising that another system seeking ways to destroy or seriously annoy another system will aim its strike at such "weak" territories or elements, trying as quickly as possible to destabilize the situation.

In many cases, Russian geopolitical opponents rely primarily on the North Caucasus separatism and anti-Caucasus reaction in Russian society in accordance with this theory. However, suddenly in 2011-2012 separatists in other regions of the country began actively express themselves, for example, in Siberia.

Further development of the disturbance in the system is evident, ref. Fig. 4.

The system comes to a condition of deterministic chaos; the system energy is lost, as well as being randomly redistributed among the rapidly emerging and endangered structures. Russia was in a very similar condition was in Russia after the collapse of the Soviet Union. However, such situation lasts for a very limited period of time, as the number of subsystems seek to control the maximum total energy of the system and try to do it by any means.

Taking our variant of modeling system is relatively stabilized in this form – Fig. 5.

There appeared several subsystems in different coordinates of social and physical space of society, which control most of the entire social energy. At the site of peak that existed prior to the impact of the external system, we can notice only a relatively small increase in energy in relation to the total weight. It is important to note that a large part of society as a result reduced its average energy level, losing it in the process of moving and energy metabolism.

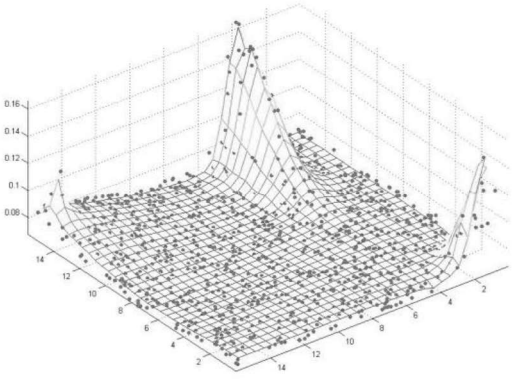

Fig. 5. Peak distribution of structural factors and the material component in Russia. The final picture of the simulation. The z-axis – E, social energy, x,y – socio-physical coordinates.

This is similar to the situation in Russia in the 90s, when the society gradually lost its last tangible savings, and basic resources accumulated in the hands of a few "clans", groups of people and subsystems.

VI. Conclusion

Thus, the current article presents the basis of the mathematical model through which the author further plans to develop the approach and model social system. It has been demonstrated that it is possible to take into account fluctuations and the factor of "accidents" in the mathematical model using the physical analogues, in particular by applying to Wiener processes through the Langevin equation.

We can calculate the general energy condition of a system by specifying parameters on the basis of this model, as well as predict the changes of its coefficients K_s and K_sc and calculate the outflow of energy from the state system or its inflow in it as well as calculate the total energy in a particular period of time. This makes it possible to determine the external influence on a given system and predict the further development of the process and change its parameters.

Computer modeling of information and energy influence of one system on another was held on the basis of the gathered data, i.e. information and psychological war in a special case.

There is also an opportunity for modeling of other types of political and social processes on the basis of this approach.

Acknowledgment

This study was funded by RFFR grant № 17-06-00640_a.

References

[1] Plotinsky Y.M. Models of Social Processes: Textbook for higher educational institutions. M. Logos. 2001.

[2] Malkov S.Y. Mathematical modeling of historical trends. Approaches and processes. Ed. MG Dmitriev - M. RSSU. 2004.

[3] Haken G. Synergetics. The hierarchy of instabilities in self-organizing systems and devices. M. Mir. 1985.

[4] Moon F. Chaotic oscillations. M. Mir. 1990.

[5] Smirnov A.V. State, society, justice: energy approach and the right philosophy. International scientific-practical conference. February 28, 2006, St. Petersburg.: Publisher SPbGUP, pp 108-110.

[6] Petukhov A. Y. Modelling of social conflict: Socio-energy approach. Global Journal of Pure and Applied Mathematics, Volume 11, Number 6, 2015, pp. 4197-4206.

[7] Guts A.K., Korobitsin V.V. et al. Mathematical models of social systems. Tutorial. - Omsk: Omsk State. University, 2000.

[8] Holyst J.A., Kasperski K., Schwei3tger F. Phase transitions in social impact models of opinion formation. Physica. 2000 v.A285. pp. 199-210.

Recurrence plot structure of motor-related human EEG

Elena Pitsik
Neuroscience and Cognivite Technology Laboratory, Center for Technologies in Robotics and Mechatronics Components
Innopolis University
Innopolis, Russia
ORCID: 0000-0003-1850-2394

Nikita Frolov
Neuroscience and Cognivite Technology Laboratory, Center for Technologies in Robotics and Mechatronics Components
Innopolis University
Innopolis, Russia
ORCID: 0000-0002-2788-1907

***Abstract*—In present paper we consider structure of recurrence plot (RP) of human motor-related electroencephalography (EEG) signal recorded in somatosensory cortex and filtered in mu-band (8-13 Hz). We show that in averaged EEG signal background activity is mostly characterized by the diagonal lines, while motor task execution is associated with increase of recurrence points density and the emergence of vertical and horizontal lines. We also demonstrate that these features of RP structure also observed in single EEG trials.**

Keywords—EEG, recurrence plots, motor-related brain activity, event-related desynchronization, single-trial analysis

I. Introduction

Neurorehabilitation of post-stroke and disabled patients based on biological feedback is a demanding technology [1]. Effective application of biological feedback requires advanced methods for precise detection and quantification of motor actions quality based on brain activity signals. Usually, brain motor activity is analyzed from multichannel magneto- and electroencephalography (M\EEG) signals by time-frequency and event-related desynchronization analysis, common spatial patterns, spatio-spectral decomposition and machine learning [2-6]. Many of the existing methods require high computational costs therefore it is hardly possible to use them in real-time applications. This problem is of strong demand and development of new methods of identification of motor-related EEG pattern is essential for effective therapy. In this context, analysis of recurrence properties of EEG signals may provide the efficient tool motor patterns recognition. This study considers features of recurrence plots (RP) structure observed in averaged EEG data as well as in single EEG trials.

Recurrent behavior is a fundamental property of dynamical systems, which can be used to distinguish between different regimes of behavior. First discussed by Poincaré, recurrences are now applied to the analysis of various processes in different areas of science and technology. One of the well-known methods is recurrence plots (RP) reconstruction – a visual representation of system recurrences obtained from nonlinear non-stationary data – which is widely used in finance and climate research [7,8], astrophysics [9,10], physiology [11] etc. In context of neuroscience, Refs. [12,13] show that RPs are quite useful in identification of N100 and P300 event-related

potentials (ERPs). Based on these results, we conclude that recurrence analysis might be extremely helpful in identification of motor-related brain activity associated with event-related desynchronization (ERD) of mu-waves (8-13 Hz) in somatosensory cortex.

With this goal in mind, we consider features of RP structure of EEG segments recorded in somatosensory cortex and related with motor executions. We demonstrate, that motor actions are accompanied by recurrence points density increase and emergence of vertical and horizontal lines, while pre-motor activity is characterized mostly by diagonal lines in RP.

II. Materials and Methods

A. Experimental data

During the experimental session subjects sat in a comfortable chair with their hands relaxingly lying on the table and squeezed their hand into fists on the audio command. We used long (1 sec) and short (0.5 sec) signals as a command to execute movement with left and right hand, respectively. Subjects were instructed to squeeze hands after the first signal and hold it until the second one (approximately 4-5 sec). Electrical brain activity was recorded by "Encephalan-EEGR-19/26" (Medicom MTD company, Taganrog, Russian Federation) with 250 Hz sampling rate using 10-10 international EEG scheme. For further analysis we used only recordings from motor cortex sensors (Cp3, Cp4, Cpz, C3, C4, Cz, Fc3, Fc4, Fcz). In order to match brain activity EEG data with motor execution, we also recorded electromyograms (EMG) on both hands.

B. Filtering and segmentation

After signals acquisition, EEG data was preliminary filtered by th 5th order band-pass Butterworths filter with lower and higher cut-off frequencies of 8 and 13 Hz respectively, which corresponds to the boundaries of mu-frequency band. EMG signals were filtered with band-pass Butterworth filter with lower and higher cut-off frequencies of 10 and 70 Hz respectively. Filtered EMG signal shows high-frequency electrical signal fluctuations associated with muscle tension during the movement execution.

Filtered multichannel EEG recordings were further cut into EEG segments in accordance with experimental protocol. In these segments time moment 0 corresponds to movement command. Also, each segment contains 2 seconds of pre-motor baseline and 6 seconds of motor-related brain activity signal after command.

Along with single trials we considered EEG segments averaged over trials, representing most pronounced motor related ERDs.

C. Recurrence quantification analysis

Recurrence plot evaluates recurrences of the phase space trajectory of the dynamical system by considering the ε-neighborhood of the current state. For each segment we reconstructed phase trajectory with embedding parameters: d=4 and T=0.03 sec.

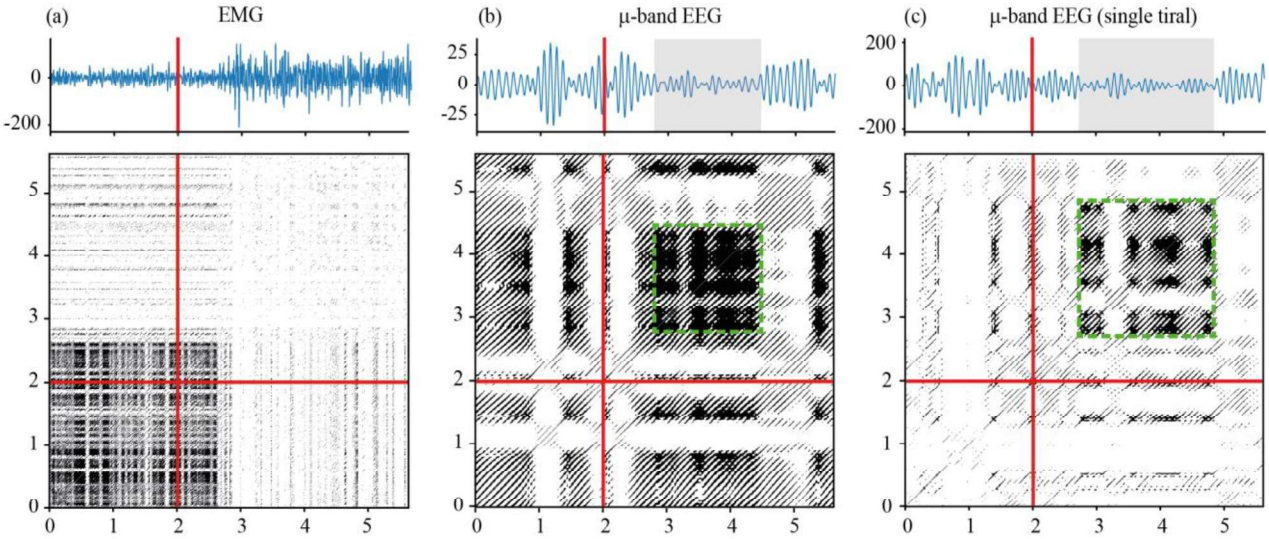

Fig. 1. Upper row represents signals of averaged filtered EMG (a), averaged mu-band filtered EEG recorded from C4 sensor (b), single mu-band filtered EEG recorded from C4 sensor (c). Lower row illustrates correspoding RP structures. Horizontal and vertiacal bold red line indicates start of the audio command, grey areas in (b,c) upper row highlight motor-related ERD, green dashed line squares in lower rows of (b,c) show RP structures associated with ERD.

Here, d is an embedding dimension and T is an embedding delay. The parameters were defined using standard methods for phase trajectory reconstruction: false nearest neighbors and mutual information.

Thus, we construct binary recurrence matrix R with ε=15 mV as follows:

$$R_{i,j} = \begin{cases} 0, if\ \varepsilon - \left|\left|\overrightarrow{x_i} - \overrightarrow{x_j}\right|\right| < 0 \\ 1, \qquad otherwise \end{cases} \quad (1)$$

where x – is a reconstructed phase trajectory of original EEG signal segment.

III. RESULTS

Fig. 1 represents the results of RP reconstruction of EMG and EEG data recorded during motor task accomplishment. Averaged filtered EMG shows start of movement execution approximately 1 sec after audio command (Fig. 1,a). It is also seen from corresponding RP, that recurrence properties of EMG signal during movement execution differ from the background – the recurrence matrix becomes sparse, which is an indicator of noisy dynamics. Note, that properties of motor-related RP block of EMG signal (1-6 sec after command) do not change in time. At the same time, RP analysis of motor-related averaged EEG trials recorded from C4 sensor in somatosensory cortex clearly indicate change of brain dynamics associated mu-rhythm suppression (ERD). It's important, that analysis of brain activity, allows direct identification of the squeezing action, which is not seen from muscle signal. One may observe, that motor-related area of RP reconstructed from averaged EEG signal has a few pronounced properties: increased recurrence points density and emergence of vertical and horizontal lines. These features of RP structure are referenced to as holding a phase point in a small volume of embedded phase space. In terms of considered EEG signal, mentioned RP properties clearly indicate suppression of mu-oscillations in somatosensory cortex, which emerges during motor task execution. Described RP features found during analysis of averaged EEG segment are observed even in single trials of motor-related EEGs (see Fig. 1,c). RPs of single EEG trial also contain a well-defined block with similar properties as observed in averaged EEG signal and allowing clear detection of motor-related ERD in mu-band.

IV. CONCLUSION

In present paper we used recurrence plots structure analysis to detect changes in motor-related EEG and EMG segments. While EMG analysis shown differences between hand movements and resting state, RP reconstruction of EEG activity in somatosensory cortex provides direct identification of motor execution. We observed, that RP of averaged EEG signal contains well-defined block associated with ERD in mu-band and characterized by increase of recurrence points density and emergence of vertical and horizontal lines. Interestingly, such properties of RP are observed even in single trials, which may clearly define the region of motor-related task accomplishment.

We believe that results presented in this study will be useful for fundamental science, as well as for the developers of EEG processing methods for brain-computer interfaces.

ACKNOWLEDGMENT

This work has been supported by Russian Science Foundation (Grant 17-72-30003).

REFERENCES

[1] M. Hamedi, S.H. Salleh and A.M. Noor, "Electroencephalographic motor imagery brain connectivity analysis for BCI: a review" in Neural computation, vol. 28(6), 2016, pp. 999-1041.

[2] V.A. Maksimenko, A. Pavlov, A.E. Runnova, V. Nedaivozov, V. Grubov, A. Koronovslii, S.V. Pchelintseva, E. Pitsik, A.N. Pisarchik and A.E. Hramov, "Nonlinear analysis of brain activity, associated with motor action and motor imaginary in untrained subjects" in Nonlinear Dynamics, vol. 91(4), 2018, pp. 2803-2817.

[3] V.A. Maksimenko, S.A. Kurkin, E.N. Pitsik, V.Y. Musatov, A.E. Runnova, T.Y. Efremova, A.E. Hramov and A.N. Pisarchik, "Artificial neural network classification of motor-related eeg: An increase in classification accuracy by reducing signal complexity" in Complexity, 2018, pp. 385947.

[4] P. Chholak, G. Niso, V.A. Maksimenko, S.A. Kurkin, N.S. Frolov, E.N. Pitsik, A.E. Hramov and A.N. Pisarchik, "Visual and kinesthetic modes affect motor imagery classification in untrained subjects" in Scientific Reports, vol. 9(1), 2019, pp. 9838.

[5] H.L. Halme and L. Parkkonen, "Across-subject offline decoding of motor imagery from MEG and EEG" in Scientific reports, vol. 8(1), 2018, p.10087.

[6] H.L. Halme and L. Parkkonen, "Comparing features for classification of MEG responses to motor imagery" in PloS one, vol. 11(12), 2016, p.e0168766.

[7] Goswami, N. Boers, A. Rheinwalt, N. Marwan, J. Heitzig, S.F. Breitenbach and J Kurths, "Abrupt transitions in time series with uncertainties" in Nature communications, vol. 9(1), 2017, p.48.

[8] S. Li, Z. Zhao, Y. Wang and Y. Wang "Identifying spatial patterns of synchronization between NDVI and climatic determinants using joint recurrence plots" in Environmental Earth Sciences, vol. 64(3), 2011, pp. 851-859.

[9] Sivaram and L.C.G. de Andrade, "Astrophysical limits on gauge invariance breaking in electrodynamics with torsion " in Astrophysics and space science, vol. 201(1), 1993, pp. 121-123.

[10] N.V. Zolotova and D.I. Ponyavin, "Phase asynchrony of the north-south sunspot activity" in Astron. Astrophys., vol. 449(1), 2006, pp. L1-L4.

[11] N. Marwan, N. Wessel, U. Meyerfeldt, A. Schirdewan and J. Kurths, "Recurrence-plot-based measures of complexity and their application to heart-rate-variability data" in Physical review E, vol. 66(2), 2002, p. 026702.

[12] N. Marwan, A. Meinke "Extended recurrence plot analysis and its application to ERP data" in International Journal of Bifurcation and Chaos, vol. 14(2), 2004, pp. 761-771.

[13] S. Schinkel, N. Marwan, J. Kurths "Brain signal analysis based on recurrences" in Journal of Physiology-Paris, vol. 103(6), 2009, pp. 315-323.

Time-frequency and recurrence quantification analysis detect limb movement execution from EEG data

Elena Pitsik
Neuroscience and cognivite technology Laboratory, Center for Technologies in Robotics and Mechatronics Components
Innopolis University
Innopolis, Russia
ORCID: 0000-0003-1850-2394

Nikita Frolov
Neuroscience and cognivite technology Laboratory, Center for Technologies in Robotics and Mechatronics Components
Innopolis University
Innopolis, Russia
ORCID: 0000-0002-2788-1907

***Abstract*— In present paper we consider application of recurrence quantification analysis (RQA) in detection of motor-related electroencephalograms (EEG). Particularly, we apply RQA to reveal transitions of mu-rhythm dynamics extracted from multichannel EEG recorded in motor cortex. The results show that the considering RQA measures of EEG in time-frequency domain one can effectively reveal dynamical features of motor-related brain activity.**

Keywords—EEG, recurrence quantification analysis, recurrence plots, continuous wavelet transform, motor-related brain activity, event-related desynchronization

I. INTRODUCTION

Analysis and accurate detection of brain motor-related activity is crucial in neurorehabilitation of post-stroke and disabled patients based on biological feedback [1]. Traditional techniques for motor activity extraction from multivariate magneto- and electroencephalography (M\EEG) include time-frequency and event-related desynchronization analysis, common spatial patterns, spatio-spectral decomposition and machine learning [2-6]. This problem is of strong demand and development of new methods of identification of motor-related EEG pattern is essential for effective therapy. In present paper we investigate the application of recurrence quantification analysis (RQA), recently used in inference of financial and climatic changes from data [7], to detect transitions of brain behavior induced by motor executions.

Recurrent behavior is a fundamental property of many dynamical systems of different nature, which can be used to distinct its different states and track its evolution in time. First discussed by Poincaré, recurrences are now studied in various areas of research. In particular, one of the well-known methods is recurrence plots (RP), which is widely used in astrophysics [8,9], physiology [10], climate research [11] and other areas, allowing to detect and visualize the repeating temporal states in nonlinear and non-stationary data. However, there is a lack of systematic studies of the biological and neurophysiological signals in terms of recurrence analysis. RQA has been predominantly used for analysis of well-pronounced patterns, such as epileptic seizures, wakefulness or sleep stages and event-related potentials during attention tasks [12-15].

However, the motor action causes less reproducible pattern on EEG highly dependent on individual characteristics of participants. With this goal in mind, we propose an approach based on combination of time-frequency and recurrence quantification analysis. RQA provides quantitative interpretations of various structures observed in RPs. By applying RQA measures to the mu-rhythm (8-13 Hz) energy time-series extracted via wavelet transform, we reveal the event-related desynchronization (ERD) in motor cortex, which is a well-known hallmark of motor-related brain activity. We show that RQA measures are highly sensitive to the start of limb movement execution.

II. MATERIALS AND METHODS

A. Experimental data

During the experimental session subjects sat in a comfortable chair with their hands relaxingly lying on the table and squeezed their hand into fists on the audio command. We used long (1 sec) and short (0.5 sec) signals as a command to execute movement with left and right hand, respectively. Subjects were instructed to squeeze hands after the first signal and hold it until the second one (approximately 4-5 sec). Electrical brain activity was recorded by "Encephalan-EEGR-19/26" (Medicom MTD company, Taganrog, Russian Federation) using 10-10 international EEG scheme. For further analysis we used only recordings from motor cortex sensors (Cp3, Cp4, Cpz, C3, C4, Cz, Fc3, Fc4, Fcz). In order to match brain activity EEG data with motor execution, we also recorded electromyograms (EMG) on both hands.

B. Continuous wavelet transform

At the first step, we applied CWT to the 14 sec trials, each corresponding to a single movement. Wavelet coefficients were calculated as follows:

$$W(f,t_0) = \sqrt{f}\int_{-\infty}^{+\infty} x(t)\varphi^*\big(f(t-t_0)\big)dt, \quad (1)$$

with Morlet wavelet as a mother wavelet function φ.

Since we were focused on the motor-related brain activity, we calculated wavelet coefficients averaged over the mu-rhythm (8-13 Hz), which contains valuable information about EEG motor-related dynamics:

$$W_\mu(t) = \int_{f\epsilon f_\mu} W(f,t)df \quad (2)$$

Obtained time series were used on the next step for RQA measures evaluation.

C. Recurrence quantification analysis

By definition recurrence plot evaluates recurrences of the phase space trajectory of the dynamical system by

considering the ε-neighborhood of the current state. Thus, we construct binary recurrence matrix R with ε=2 as follows:

$$R_{i,j} = \begin{cases} 0, if\ \varepsilon - \left|\left|\overrightarrow{x_i} - \overrightarrow{x_j}\right|\right| < 0 \\ 1, \qquad otherwise \end{cases} \quad (3)$$

As stated above, RQA allows to quantify the RP by analyzing the structures formed by vertical/horizontal and diagonal lines. In our study we use these three basic measures – determinism (DET), laminarity (LAM) and recurrence rate RR) – to evaluate the dynamics of mu-rhythm wavelet energy of motor-related EEG.

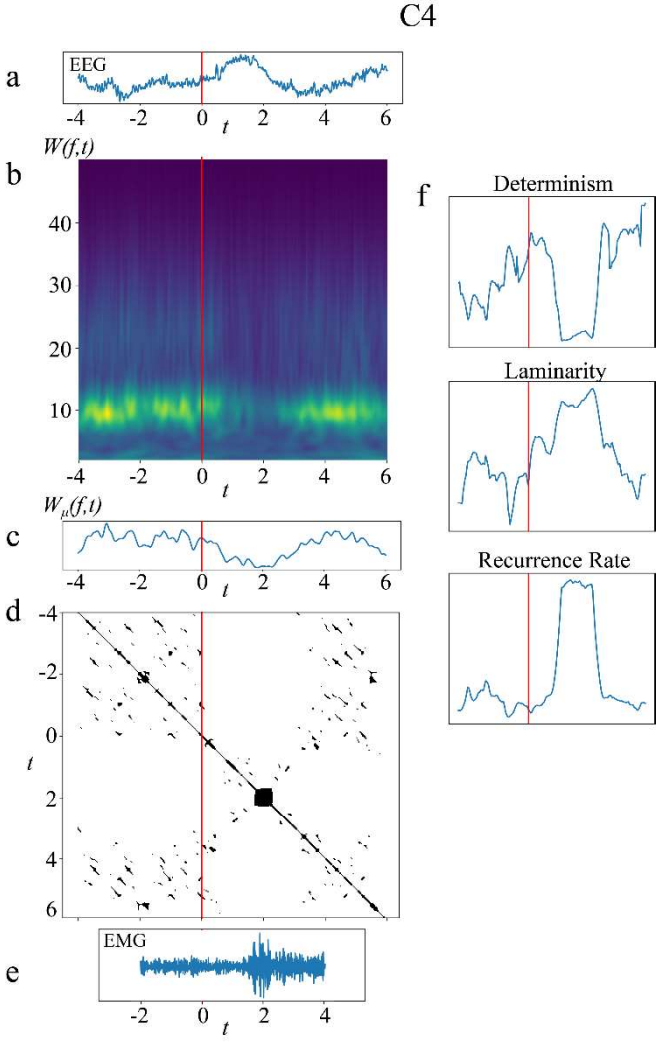

Fig. 1. For all presented plots, t is time, sec, with audio command placed in 0 and marked with red line. (a) Raw EEG signal corresponding to the movement; (b) wavelet surface of corresponding EEG signal; (c) averaged mu-rhythm energy W_μ; (d) recurrence plot of considering time series; (e) matched EMG signal; (f) RQA metrics.

RR estimates the density of recurrence points in RP:

$$RR = \frac{1}{N^2}\sum_{i,j=1}^{N} R_{I,J}(\varepsilon) \quad (4)$$

DET represents a relevant measure of signal complexity and predictability of the process. Determinism is defined as the percentage of recurrence points that form diagonal lines in RP:

$$DET = \frac{\sum_{l=l_{min}}^{N} lP(l)}{\sum_{l=1}^{N} lP(l)} \quad (5)$$

where $l_{min} = 150$ is a minimal considered length of diagonal line.

On the contrary, LAM characterizes laminar or stationary states of considered process and measures the vertical/horizontal lines ratio in RP:

$$LAM = \frac{\sum_{v=v_{min}}^{N} vP(v)}{\sum_{v=1}^{N} vP(v)} \quad (6)$$

where $v_{min} = 20$ is a minimal considered length of vertical/horizontal lines.

III. Results

Fig. 1 represents the results of CWT and RQA for one of the subjects, which has pronounced ERD of mu-rhythm corresponding to the movement execution. We show the results of left-hand movement quantification form EEG signals recorded from C4 sensor. In Fig. 1b,c,e one can see a considerable suppression of mu-rhythm during motor action execution. It is also seen from Fig. 1c, that mu-rhythm behavior preceding the audio command is characterized by the deviations of mu-rhythm oscillatory energy, while more stationary mu-rhythm behavior is peculiar to the motor-execution.

Fig. 1d shows RP constructed from time-series presented in Fig. 1c. One may notice that background activity and motor execution represent two separate blocks in RP. Fig. 1f shows corresponding quantifications of RP with RQA measures of DET, LAM and RR (top-down). Indeed, one can see that chosen measures clearly indicate start of motor-execution associated with short-term depression of mu-rhythm. Decreasing of DET, along with increase of LAM and RR is interpreted as definition of ERD in terms of RQA. A negative dynamics of determinism indicates that the system becomes less correlated and deterministic, which is consistent with the known effects of ERD. Consequently, the density of the recurrent points grows. It is notable that laminarity starts growing slightly before movement onset, which indicated that actual motor activity causes the emergence of laminar states in mu-rhythm energy, including the movement itself and short preceding period, which can also be interpreted as a preparation to the movement.

IV. Conclusion

In present paper we used recurrence quantification analysis to study mu-rhythm dynamics of motor-related EEG.

In general, obtained results are consistent with known facts about motor-related ERD in mu-rhythm. Proposed method is novel in neuroscience, which applications for brain-computer interfaces for rehabilitation is rather poorly studied. However, present paper revealed the ability of RQA to provide a deeper insight into the dynamics of EEG signal associated with motor action, which can be used for detection of motor pattern. We believe that results presented in this study will be useful for fundamental science, as well as for the developers of EEG processing methods for brain-computer interfaces.

Acknowledgment

This work was supported by the President Program (projects NSH-2737.2018.2).

References

[1] M. Hamedi, S.H. Salleh and A.M. Noor, “Electroencephalographic motor imagery brain connectivity analysis for BCI: a review” in Neural computation, vol. 28(6), 2016, pp. 999-1041.

[2] V.A. Maksimenko, A. Pavlov, A.E. Runnova, V. Nedaivozov, V. Grubov, A. Koronovslii, S.V. Pchelintseva, E. Pitsik, A.N. Pisarchik and A.E. Hramov, “Nonlinear analysis of brain activity, associated with motor action and motor imaginary in untrained subjects” in Nonlinear Dynamics, vol. 91(4), 2018, pp. 2803-2817.

[3] V.A. Maksimenko, S.A. Kurkin, E.N. Pitsik, V.Y. Musatov, A.E. Runnova, T.Y. Efremova, A.E. Hramov and A.N. Pisarchik, “Artificial neural network classification of motor-related eeg: An increase in classification accuracy by reducing signal complexity” in Complexity, 2018, pp. 385947.

[4] P. Chholak, G. Niso, V.A. Maksimenko, S.A. Kurkin, N.S. Frolov, E.N. Pitsik, A.E. Hramov and A.N. Pisarchik, “Visual and kinesthetic modes affect motor imagery classification in untrained subjects” in Scientific Reports, vol. 9(1), 2019, pp. 9838.

[5] H.L. Halme and L. Parkkonen, “Across-subject offline decoding of motor imagery from MEG and EEG” in Scientific reports, vol. 8(1), 2018, p.10087.

[6] H.L. Halme and L. Parkkonen, “Comparing features for classification of MEG responses to motor imagery” in PloS one, vol. 11(12), 2016, p.e0168766.

[7] Goswami, N. Boers, A. Rheinwalt, N. Marwan, J. Heitzig, S.F. Breitenbach and J Kurths, “Abrupt transitions in time series with uncertainties” in Nature communications, vol. 9(1), 2017, p.48.

[8] Sivaram and L.C.G. de Andrade, “Astrophysical limits on gauge invariance breaking in electrodynamics with torsion “ in Astrophysics and space science, vol. 201(1), 1993, pp. 121-123.

[9] N.V. Zolotova and D.I. Ponyavin, “Phase asynchrony of the north-south sunspot activity” in Astron. Astrophys., vol. 449(1), 2006, pp. L1-L4.

[10] N. Marwan, N. Wessel, U. Meyerfeldt, A. Schirdewan and J. Kurths, “Recurrence-plot-based measures of complexity and their application to heart-rate-variability data” in Physical review E, vol. 66(2), 2002, p. 026702.

[11] S. Li, Z. Zhao, Y. Wang and Y. Wang “Identifying spatial patterns of synchronization between NDVI and climatic determinants using joint recurrence plots” in Environmental Earth Sciences, vol. 64(3), 2011, pp. 851-859.

[12] I.H. Song, D.S. Lee and S.I. Kim “Recurrence quantification analysis of sleep electoencephalogram in sleep apnea syndrome in humans” in Neuroscience letters, vol. 366(2), 2004, pp. 148-153.

[13] U.R. Acharya, S.V. Sree, S. Chattopadhyay, W. Yu and P.C.A. Ang “Application of recurrence quantification analysis for the automated identification of epileptic EEG signals: in International journal of neural systems, vol. 21(3), 2011, pp. 199-211.

[14] N. Marwan, A. Meinke “Extended recurrence plot analysis and its application to ERP data” in International Journal of Bifurcation and Chaos, vol. 14(2), 2004, pp. 761-771.

[15] S. Schinkel, N. Marwan, J. Kurths “Brain signal analysis based on recurrences” in Journal of Physiology-Paris, vol. 103(6), 2009, pp. 315-323.

Multi-collision Detection for Collaborative Robot

Dmitry Popov
Center for Technologies in Robotics and Mechatronics Components.
Innopolis University
Innopolis, Russia
d.popov@innopolis.ru

Alexandr Klimchik
Center for Technologies in Robotics and Mechatronics Components.
Innopolis University
Innopolis, Russia
a.klimchik@innopolis.ru

Определение Множественных Коллизий для Коллаборативного Робота

Попов Дмитрий
Центр технологий компонентов робототехники и мехатроники
Университет Иннополис
Иннополис, Россия
d.popov@innopolis.ru

Климчик Александр
Центр технологий компонентов робототехники и мехатроники
Университет Иннополис
Иннополис, Россия
a.klimchik@innopolis.ru

***Abstract*—This study is focused on the problem of robot physical interaction with environment. Physical interaction in case of collaborative industrial robots means one or more physical contact with robot and work piece, robot and another robot, robot and human, robot and environment. Depending on location on the robot surface where this contact or collision happened, robot reaction should be different in order to provide safety and increase work cell performance if possible. In this work, algorithm for multiple contact point identification is presented. The algorithm is capable of running with 100 Hz loop and 1.09 cm RMSE. The approach was tested in the simulation with KUKA iiwa but can be extended to any robot with torque sensing capabilities.**

Keywords— physical human-robot interaction (pHRI), collaboration robot, collision localization, external force estimation

***Аннотация*—Данное исследование посвящено проблеме физического взаимодействия робота с окружающей средой. Физическое взаимодействие в случае коллаборативных промышленных роботов означает один или несколько физических контактов с роботом и деталью, роботом и другим роботом, роботом и человеком, роботом и окружающей средой. В зависимости от местоположения где произошел этот контакт или столкновение на поверхности робота, реакция робота**

должна быть разной, для того чтобы обеспечить безопасность и повысить производительность рабочей ячейки, если это возможно. В данной работе представлен алгоритм идентификации нескольких контактных точек. Алгоритм способен работать с частотой до 100 Гц и ошибкой в 2 см. Подход был опробован в симуляции с KUKA iiwa, но может быть распространен на любого робота с возможностью измерения усилия на суставах.

Ключевые слова— физическое взаимодействие, коллаборативный робот, локализация коллизии, определение внешней силы

I. Введение

Локализация контактов, а также оценка силы контакта могут стать тривиальной задачей с правильными вспомогательными датчиками, такими как тактильная кожа [1]. К сожалению, на практике эти датчики редки, дороги, обычно ими трудно покрыть все тело робота. Используя внешние камеры / сенсоры глубины, можно решить хотя бы часть [2], проблем локализации контакта, но только когда препятствие находится в поле зрения камеры, а условия окружающей среды, такие как освещение, благоприятные. Также, не всегда возможно покрыть все рабочее пространство камерами.

Без внешних датчиков можно использовать проприоцептивную информацию. Одним из популярных решений в области коллаборативной робототехники является использование датчика силы/момента, установленного на конечном органе робот, очевидно, что в этом случае обнаружение столкновения возможно только для инструмента робота. С другой стороны, если датчик силы крутящего момента установлен на основании робота, как в серии FANUC CR, должна быть возможность получить точку столкновения и внешнюю силу. В случае робота, оборудованного двигателями SEA / VSA, можно извлечь значение крутящего момента для соединения, оценивая деформации с известной жесткостью шарнира. Частным случаем этой установки является двигатель с гармонической передачей и двумя энкодерами, один из которых установлен со стороны двигателя, а другой со стороны нагрузки. Также требуются алгоритмы обнаружения столкновений и оценки внешней силы для отделения внешних усилий (вызванных контактом) от общего усилия двигателя. Обзор методов такого разделения можно найти в [3].

Текущие подходы рассматривают только одно столкновение, но в большинстве случаев применения коллаборативного робота-манипулятора, робот должен иметь возможность обнаруживать как минимум два столкновения. Одно столкновение - для взаимодействия, а другое - для инструмента / процесса / поднятого объекта, расположенного обычно в конечном органе робота.

II. Определение Коллизии

Основная идея состоит в том, чтобы создать сетку контрольных точек на поверхности робота, а затем применить методы оптимизации для выполнения локализации [4]. Используем предположение, что вектор F_{ext} состоит только из силы, а крутящий момент равен нулю.

На первом этапе контрольные точки должны быть равномерно распределены по поверхности манипулятора. Применение сетки позволяет упростить дальнейший поиск. Для всех точек координаты известны и контактные Якобианы $J_c(q)$ могут быть найдены. Таким образом, можно сравнить усилие, вызванное внешней силой в точке, с вектором реальных усилий в суставах.

Проблема идентификации может быть сформулирована как задача оптимизации

$$\min_{\boldsymbol{F_c},\boldsymbol{c}} \|\boldsymbol{\tau_{ext}} - \boldsymbol{J_c^T f_c}\|^2 \quad \boldsymbol{F_c} \in Fr, \boldsymbol{c} \in \boldsymbol{C} \tag{1}$$

где Fr конус трения, $\boldsymbol{C}$ – поверхность робота.

Проблема (1) является выпуклой, поскольку в каждый момент времени значения $\boldsymbol{\tau_{ext}}$ и $J_c(q)$ для фиксированной точки соприкосновения являются постоянными, а конус трения является выпуклым множеством. Если мы применим эту оптимизацию для каждой точки поверхности, то точка с наименьшим значением целевой функции является наиболее вероятным контактом, а полученная сила - наиболее вероятным внешним усилием. Конус трения можно аппроксимировать тетраэдрической пирамидой:

$$F_c = \sum_{i=1}^{4} a_i F_{ci}, \quad a_i \geq 0 \tag{2}$$

где a_iявляется вес каждого опорных векторов F_{ci}. Это позволяет переписать задачу оптимизации (1) в терминах квадратичного программирования (QP_c)для фиксированной точки контакта c:

$$QP = \min_a \left\|\tau_{ext} - J_{r,a}^T a\right\|^2 = \min_a \left(a^T J_{r,a} J_{r,a}^T a - 2a^T J_{r,a}\tau_{ext} + {\tau_{ext}}^T \tau_{ext}\right) \tag{2}$$

где $\boldsymbol{J_{c,a}} = \boldsymbol{J_c}[\boldsymbol{F_{c1}}\, \boldsymbol{F_{c2}}\, \boldsymbol{F_{c3}}\, \boldsymbol{F_{c4}}]$ - это якобиан размерностью 7 на 4 для каждого $\boldsymbol{F_c}$ в точке контакта. Поскольку $\tau_{ext}^T \tau_{ext}$ является константой, достаточно решить:

$$QP = \min_{\boldsymbol{a}\geq \boldsymbol{0}} (\boldsymbol{a}^T \boldsymbol{H} \boldsymbol{a} + \boldsymbol{g}^T \boldsymbol{a}) \tag{3}$$

где $\boldsymbol{H} = \boldsymbol{J_{c,a}} \boldsymbol{J_{c,a}^T}$ - квадрат Якобиана, переменная $\boldsymbol{a}$ - опора вектор коэффициентов размерности 4 на 1, $\boldsymbol{g} = -2\boldsymbol{J_{c,a}}\boldsymbol{r}$.

Минимальное значение QP_c равно нулю, что соответствует полному совпадению, а максимальное значение зависит от ошибки модели. Для дальнейшего анализа может быть полезно рассмотреть полученные данные как вероятность того, что фактическая внешняя сила найдена в текущей контрольной точке. Это требует отображения результата в интервале от 0 до 1. Предположим, что ошибка измерения имеет нормальное распределение с нулевым средним. Вероятность p_c может быть определена как:

$$p_c \sim \exp\left(-\frac{1}{2} QP_c\right) \tag{4}$$

Общий процесс локализации можно описать в два этапа. Первый шаг - найти значение и вероятность внешней силы для большого количества точек, что было

описано выше. Второй шаг - выбрать точку на поверхности робота с максимальной вероятностью.

Решение здесь состоит в том, чтобы оценить местоположение контакта и затем использовать локальную оптимизацию. Приблизительное местоположение столкновения может быть найдено как точка с наибольшей вероятностью (4) из набора точек, случайно или равномерно распределенных по поверхности манипулятора.

Этот подход можно расширить для случая множественных столкновений, сделав следующие предположения:

- Столкновения появляются последовательно, один за другим
- Первое столкновение не меняет своего местоположения.

Эти допущения также позволяют обнаруживать столкновения в двух случайных точках на поверхности робота, без ограничений, что одно из столкновений должно быть в конечном органе робота. Алгоритм 1 показывает эту процедуру. Функция $findFext$ находит внешнюю точку контакта c_n и внешние силы, вызванные этим контактом, в зависимости от моментов τ_{ext}, как было описано до этого. Когда внешние усилия не могут быть точно описаны только одним столкновением, следует рассмотреть возможность наличия второго столкновения. В этом случае первое столкновение считается таким же, как в предыдущем моменте времени до появления второго столкновения.

Алгоритм 1 Определение множественных коллизий

If $\tau_{ext} > \varepsilon$ **then**
  $c_1 = findFext(\tau_{ext})$
  If $\|\tau_{ext} - J_{c1}^T f_{c1}\|^2 > threshold$ **then**
    $c_1 = prev$
    $\tau_{ext} = \tau_{ext} - \tau_{prev}$
    $c_2 = findFext(\tau_{ext})$
    …
  Else
    $prev = c_1$
    $\tau_{prev} = \tau_{ext}$
  End
End

III. Результаты

Чтобы проверить алгоритм идентификации, он был реализован в MATLAB для промышленного манипулятора Kuka IIWA LBR 14. Для каждого звена была изучена тысяча случайных конфигураций с приложенным внешним усилием до 100 Нм, лежащим в конусе трения. Алгоритм идентификации столкновений позволяет оценить внешнюю точку столкновения с точностью до уровня сетки (приблизительно 0.3 см) для последних 5 звеньев и внешнюю силу с точностью менее 0.5 Нм для последних 5 звеньев (Таблица 1). Идентификация коллизий для первых двух ссылок невозможна из-за недостаточной входной информации и не будет точной. Шум от датчиков усилия и неточности внешнего наблюдателя момента в реальном роботе может снизить точность определения. Для оценки снижения точности было проведено дополнительное моделирование. Полученная точность для добавленного шума измерения амплитуды 0.3 и 0.5 Нм представлены в таблицах 2 и 3.

ТАБЛИЦА I. Точность определения коллизии: Без шума.

Звено	7	6	5	4	3
Ошибка по позиции СКО, см	0.19	0.23	0.36	0.63	0.82
Ошибка по силе СКО, %	0	0	0.3	3	11.7

ТАБЛИЦА II. Точность определения коллизии: N(0, 0.3 Нм) шум для датчиков усилия.

Звено	7	6	5	4	3
Ошибка по позиции СКО, см	0.83	1.57	2.2	5.1	10.4
Ошибка по силе СКО, %	3.9	4.1	6.3	9.1	16.6

ТАБЛИЦА III. Точность определения коллизии: N(0, 0.5 Нм) шум для датчиков усилия.

Звено	7	6	5	4	3
Ошибка по позиции СКО, см	1.05	1.89	3.1	6.4	11.6
Ошибка по силе СКО, %	7.2	5.2	6.1	12.1	16.1

Средняя ошибка оценки положения для шума 0 Нм составляет 0,44 см и 0,26 см для последних 3 звеньев. С дополнительным измерительным шумом ошибка увеличивается до 4 см и 4,8 см для шумов 0,3 и 0,5 Нм, тогда как средняя ошибка для последних 3 звеньев составляет 1,5 см и 2 см соответственно.

Разработанный алгоритм был протестирован на процессоре Intel Core i5-4210H 3 ГГц, 8 ГБ ОЗУ в качестве однопоточной программы Matlab. Типичное время выполнения алгоритма составляет около 9-11 мс или 90-110 Гц для одной коллизии.

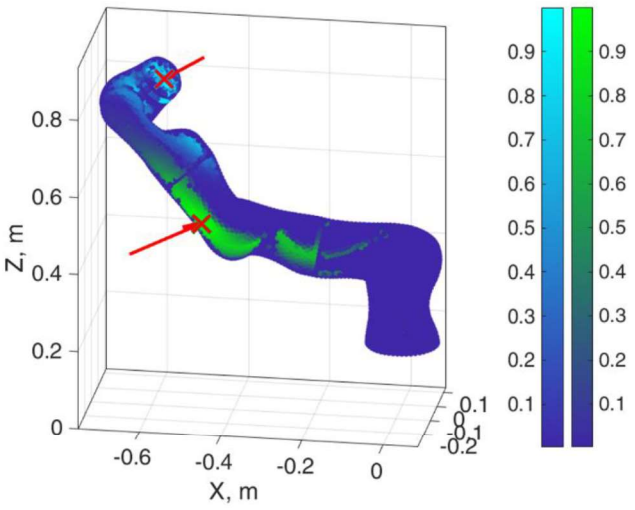

Рис. 1. Карты вероятностей для двух столкновений. Красные стрелки - внешние силы; красный крест - это предполагаемая точка контакта (наибольшая вероятность).

Поскольку мы рассматриваем каждое столкновение отдельно, точность определения множественного столкновения будет близка к значениям, упомянутым ранее. Пример оценки двух точек столкновения

представлен на рис. 1. Вероятность первого столкновения в последнем звене отмечена синим цветом, а второе столкновение, отмеченное зеленым цветом, находится в 4-й звене. Точки столкновения выбираются как точки с наибольшей вероятностью для каждой карты вероятности.

Локализация контактов - это только одна часть большего проекта, подразумевающего полный цикл обработки контактов: обнаружение, локализация, классификация, реакция [5]. Информация о позиции контакта поможет не только для безопасности, но и поможет выбрать различные сценарии для взаимодействия [6].

IV. Заключение

В данной работе был представлен метод локализации точки контакта и оценки внешней силы на основе проприоцептивных датчиков для обработки в реальном времени. Также было проверено в моделировании Matlab и на реальном манипуляторе KUKA iiwa. Достигнутая задержка между обнаружением контакта и локализацией составляет около 0,01 с, что также может быть улучшено для случаев, когда контакт продолжителен. Расчетная среднеквадратическая точность для последних 3 звеньев составляет 0,26 см для случая без учета шума при измерении усилия и 2 см с гауссовым шумом величиной 0,5 Нм. Для определения нескольких коллизий используется тот же подход что и для единичной коллизии, при этом все коллизии кроме исследуемой фиксируются. Это позволяет линейно увеличивать вычислительную сложность алгоритма с каждой последующей коллизией.

В дальнейшем этот подход будет опробован на реальном оборудовании. Оценка будет проводиться путем приложения внешней силы к датчику силы / момента с 6 степенями свободы, чтобы получить информацию о внешней силе, и использования лазерного трекера для определения точки контакта.

Благодарности

Работа выполнена при поддержке гранта РНФ 17-19-01740.

Ссылки

[1] M. Fritzsche, J. Saenz, and F. Penzlin, “A large scale tactile sensor for safe mobile robot manipulation,” in ACM/IEEE International Conference on Human-Robot Interaction, 2016, vol. 2016–April, pp. 427–428.

[2] Magrini, F. Flacco, and A. De Luca, “Control of generalized contact motion and force in physical human-robot interaction,” in Proceedings - IEEE International Conference on Robotics and Automation, 2015, vol. 2015–June, no. June, pp. 2298–2304..

[3] S. Haddadin, A. De Luca, and A. Albu-Schäffer, “Robot collisions: A survey on detection, isolation, and identification,” IEEE Trans. Robot., vol. 33, no. 6, pp. 1292–1312, 2017.

[4] Popov, Dmitry, and Alexandr Klimchik. "Real-Time External Contact Force Estimation and Localization for Collaborative Robot." In 2019 IEEE International Conference on Mechatronics (ICM), vol. 1, pp. 646-651. IEEE, 2019.

[5] Popov, Dmitry, Alexandr Klimchik, and Nikolaos Mavridis. "Collision detection, localization & classification for industrial robots with joint torque sensors." In 2017 26th IEEE International Symposium on Robot and Human Interactive Communication (RO-MAN), pp. 838-843. IEEE, 2017.

[6] Mikhel, Stanislav, Dmitry Popov, and Alexandr Klimchik. "Collision driven multi scenario approach for human collaboration with industrial robot." In Proceedings of the 2018 4th International Conference on Mechatronics and Robotics Engineering, pp. 78-84. ACM, 2018.

Stiffness Parameters Idenification for Walking Robot

Dmitry Popov
Center for Technologies in Robotics and Mechatronics Components.
Innopolis University
Innopolis, Russia
d.popov@innopolis.ru

Alexandr Klimchik
Center for Technologies in Robotics and Mechatronics Components.
Innopolis University
Innopolis, Russia
a.klimchik@innopolis.ru

Идентификации Параметров Жесткости Шагающего Робота

Попов Дмитрий
Центр технологий компонентов робототехники и мехатроники
Университет Иннополис
Иннополис, Россия
d.popov@innopolis.ru

Климчик Александр
Центр технологий компонентов робототехники и мехатроники
Университет Иннополис
Иннополис, Россия
a.klimchik@innopolis.ru

***Abstract*— This paper discusses the stiffness parameters identification for an anthropomorphic walking platform. The robot stiffness model build using a virtual joint model by introducing additional springs, then the parameters of these springs are determined using identification algorithms. Two variants of a model are considered: taking into account the links and joints compliance and only joints. Numerical experiments were performed on the AR-601M robot model.**

Keywords—biped, stiffness modeling, stiffness identification

***Аннотация*—В данной работе рассматривается идентификация параметров жесткости для антропоморфной шагающей платформы. Для построения модели жесткости робота используется модель виртуальных пружин, далее параметры этих пружин определяются с помощью алгоритмов идентификации. Рассматриваются два варианта построения модели: с учетом податливости звеньев и шарниров и только шарниров. Численные эксперименты были проведены на модели робота AR-601M.**

Ключевые слова— шагающий робот, моделирование жёсткости, идентификация жёсткости

I. Введение

Применение модели жёсткости позволяет определить ошибки податливости, возникающие в конструкции робота и в последствии компенсировать их. Данные ошибки возникают под воздействием внешних сил, вызванных нагрузкой или массой элементов робота, смещая положения рабочего органа робота относительно желаемого положения. В человекоподобных роботах ошибки податливости могут привести к снижению стабильности шага [1], в случае, когда из-за вызванной внешней силой смещения, фаза двухопорной поддержки может произойти раньше, что приведет к «спотыканию» или падению робота.

При наличии модели жесткости робота, описывающей источники податливости в системе, параметры данных податливостей должны быть определены.

II. Модель Жесткости

В данном тезисе используется метод моделирования виртуальных пружин (Virtual Joint Modeling, VJM) [2] Данный метод позволяет разработать более детальную и полную геометрическую модель манипулятора, которая обеспечивает более точную оценку положения и ориентации конечного органа робота. Согласно этому методу в исходную модель вносятся дополнительные пружины, полностью описывающие податливость того или иного элемента. Для активных шарниров может включать в себя податливость редуктора и управления, для звеньев - деформации элементов конструкции под нагрузкой.

Для шагающего робота, с учетом допущения жесткого крепления опорной ноги/ног робота к поверхности, возможны два варианта построения модели жесткости: для фазы одноопорной и двухопорной поддержки [3]. Для простоты возьмем в качестве примера типового антропоморфного робота AR-601M. В фазе одноопорной поддержки робот может быть представлен как последовательный манипулятор с 12 степенями свободы, базой в ступне, находящейся на земле и рабочим органом в свободной ступне. Для фазы с двойной опорой получаем параллельный манипулятор, состоящий из 2х последовательных цепочек с 6 степенями каждая, где ступни каждой ноги являются базой, а таз - рабочим органом.

Смещение положение рабочего органа следуя закону Гука может быть найдено как:

$$\Delta p = K_C^{-1} F \tag{1}$$

где F - внешняя сила, K_C – декартова матрица жесткости, которую можно найти как:

$$K_C = (J_\theta K_\theta^{-1} J_\theta^T)^{-1} \tag{2}$$

где $K_\theta = diag(K_\theta^1, K_\theta^2, \dots, K_\theta^n)$ – общая матрица жесткости виртуальных пружин, K_θ^i - матрица жесткости пружины соответствующего звена / шарнира, J_θ – матрица Якобиана относительно θ.

Так как жесткость шарниров как правило значительно ниже жесткости звеньев, возможно использование двух типов построения модели жесткости: с учетом только шарниров (редуцированная модель) и с учетом шарниров и звеньев (полная модель). Каждый шарнир дополняется одноосевой пружиной, расположенной вдоль оси вращения, каждое звено 6-осевой пружиной (три из которых соответствуют перемещению, а три - ориентации). Таким образом матрица жесткости для полной модели будет иметь размерность 42 на 42 и иметь более 250 независимых элементов [4], тогда как редуцированная только 6.

III. Идентификация

Идентификация заключается в определении значения податливостей. В случае полной модели идентификация может быть крайне затруднительной и требует большого количества экспериментов и пред обработки данных, поэтому идентификация будет проводится только для редуцированной модели с 6 параметрами. При этом часть податливости звеньев будет включена в податливость шарнира, тем самым увеличивая точность определения ошибки, по сравнению со случаем, когда известна только податливость одного мотора и редуктора.

Перепишем уравнение (1) связи между смещением рабочего органа робота и приложенной внешней силой через матрицу жесткости шарниров чтобы сформулировать проблему идентификации параметров. Первым этапом удобнее переписать уравнение в виде

$$\Delta p = \sum_{i=1}^{n} (J_\theta k_\theta J_\theta^T) F \tag{3}$$

где n - количество измерений, матрицы k_θ обозначают податливость звеньев/шарниров, которые необходимо найти, и J_θ обозначает Якобианы. Далее возможно переписать уравнение (3) в виде стандартном для задачи идентификации, как линейную функцию по отношению к искомым параметрам.

$$\Delta p = A_k(q, F) k + \varepsilon \tag{4}$$

где $A_k = \left[J_{\theta,1} J_{\theta,1}^T F, \dots, J_{\theta,n} J_{\theta,n}^T F \right]$ так называемая матрица наблюдений, и $k = (k_{\theta,1}, \dots, k_{\theta,n})^T$ - вектор податливостей. Уравнение 4 включает в себя шум измерения ε рассматривается как независимая одинаково распределенная случайная величина с нулевым средним значением и стандартным отклонением σ По этой причине применяется метод наименьших квадратов, который минимизирует сумму квадратов ошибок.

$$\sum_{i=1}^{m} \| \Delta p_i - A_k(q_i, F_i) \| \to \min_k. \tag{5}$$

Индекс i определяет номер конфигурации робота. Решение для уравнения (5) имеет вид

$$\hat{k} = \left(\sum_{i=1}^{m} A_i^T A_i \right)^{-1} \left(\sum_{i=1}^{m} A_i^T \Delta t_i \right) + \left(\sum_{i=1}^{m} A_i^T A_i \right)^{-1} \left(\sum_{i=1}^{m} A_i^T \varepsilon_i \right) \tag{6}$$

где второе слагаемое описывает стохастическую составляющую. Влияние ошибок измерения определяется ковариационной матрицей, которая определяет точность идентификации

$$cov(\hat{k}) = \sigma^2 \left(\sum_{i=1}^{m} A_i^T A_i \right)^{-1} \tag{7}$$

где σ - стандартное отклонение, а $\sum_{i=1}^{m} A_i^T A_i$ называется информационной матрицей. Полученная ковариационная матрица может использоваться как для оценки точности идентифицированных параметров, так и для планирования эксперимента по калибровке. Уравнение (7) предполагает, что ошибки измерения одинаковы для всех направлений и конфигураций. Если это предположение неверно, можно ввести дополнительную весовую матрицу для исправления результата.

IV. Результаты

Для численного эксперимента была использована модель антропоморфного робота AR-601M. Параметры аппроксимации звеньев ноги представлены в таблице 1, параметры затеряла из которого изготовлены звенья в таблице 2. Предполагается что звенья выполнены из полой квадратной балки.

ТАБЛИЦА I. Параметры аппроксимации звеньев

Звено	Внешний размер	Размер стенки
Бедро	125 мм	10 мм
Голень	110 мм	8 мм
Ступня	130 мм	8 мм

ТАБЛИЦА II. Параметры материала звеньев

Параметр	Значение
Модуль упругости, ГПа	70
Коэф. Пуассона	0.334
Плотность, кг/м^3	$2.7 \cdot 10^3$

Процесс идентификация состоит из двух этапов: сбор данных и обработка данных. В случае идентификации жесткости, данные представляют собой измерения смещения рабочего органа робота в различных конфигурациях под действием внешней силы различной величины и направления. В данной работе для задачи идентификации будут проводиться виртуальные эксперименты, основанные на полной геометрической и эластостатической модели робота. Таким образом, сначала мы предполагаем, что и звенья, и шарниры обладают податливостью, затем для каждой конфигурации мы вычисляем Якобиан и используем

уравнение (3) для получения вектора отклонений. Далее добавляются ошибки измерения, чтобы имитировать условия реального измерения. Эти ошибки рассматриваются как независимые идентично распределенные (то есть, случайные) значения с нулевым средним и стандартным отклонением σ. В этой статье мы принимаем σ как 100 мкм, что является типичной точностью измерительных устройств, таких как лазерный трекер FARO. Для генерации данных были использованы 100 случайных конфигураций и сил случайного направления и постоянной величины 100 Н.

Что касается обработки данных, то на этом этапе происходит подгонка данных к выбранной модели. В нашем случае модель приведена к сокращенной модели жесткости манипулятора, для которой находятся диагональные элементы матрицы жесткости. То есть, предполагая, что все отклонения как из-за шарниров, так и из звеньев, сосредоточены в суставах, находится эквивалентный манипулятор с податливыми шарнирами и жесткими звеньями, которые дали бы такое же отклонение, как полная эластостатическая модель данного манипулятора.

ТАБЛИЦА III. ПАРАМЕТРЫ СУСТАВОВ ДЛЯ РОБОТА AR-601M

Шарнир	**Изначальная податливость, м/Н**	**Идентифицированная податливость, м/Н**
1	$1 \cdot 10^{-5}$	$0.97 \cdot 10^{-5}$
2	$1 \cdot 10^{-5}$	$0.96 \cdot 10^{-5}$
3	$1 \cdot 10^{-5}$	$1.21 \cdot 10^{-5}$
4	$5 \cdot 10^{-6}$	$5.3 \cdot 10^{-6}$
5	$1.42 \cdot 10^{-5}$	$1.52 \cdot 10^{-5}$
6	$1.42 \cdot 10^{-5}$	$1.4 \cdot 10^{-5}$

В таблице 3 представлены результаты работы алгоритма. Как видно влияние звена в податливость шарнира может достигать до 20%, как в случае 3 сустава. Таким образом влияние звена в податливости шарнира может оказать существенное воздействие. Полученные результаты могут быть использованы в алгоритмах компенсации как в статике, так и в динамике [5].

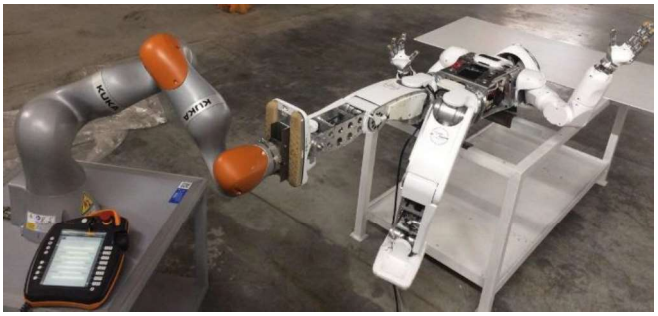

Рис. 1. Проведение эксперемента с использованием промышленного робота [6]

В дальнейшей работе предполагается произвести эксперименты на реальном роботе включающие в себя геометрическую и эластостатическую калибровку. Один из возможных способов реализации — это использование жесткой связки из ноги робота AR и промышленного робота KUKA iiwa как на рисунке 1. В данном случае постоянная внешняя сила может задаваться с помощью робота KUKA и в тоже самое время использоваться для замера отклонения рабочего органа. Альтернативным вариантом может служить крепление на ступне AR отражателя бесконтактной измерительной системы лазер трекера FARO и воздействие внешней силой путем подвеса к ноге груза. В обоих случаях робот должен крепиться в тазу, и в первом случае быть в жёсткой связке с базой робота KUKA, а во втором с базой лазер трекера.

V. ЗАКЛЮЧЕНИЕ

В работе представлены результаты численной идентификации значения податливости шарниров для антропоморфной платформы. Так как в реальном роботе определение параметров жесткости элементов из конструкторской документации может быть затруднительным, был предложен метод для идентификации параметров жесткости шарниров робота. В этом случае идентифицированная податливость будет включать в себя не только податливость шарнира, но и часть податливости звеньев. Значения податливости для изначальных и идентифицированных значений могут различаться до 20%, для робота элементы которого выполнены из алюминия.

БЛАГОДАРНОСТИ

Работа выполнена при поддержке гранта РФФИ № 18-38-00880/19.

ССЫЛКИ

[1] Popov, Dmitry, Alexandr Klimchik, and Ilya Afanasyev. "Design and Stiffness Analysis of 12 DoF Poppy-inspired Humanoid." In ICINCO (2), pp. 66-78. 2017.

[2] Pashkevich, Anatol, Alexandr Klimchik, and Damien Chablat. "Enhanced stiffness modeling of manipulators with passive joints." Mechanism and machine theory 46, no. 5 (2011): 662-679.

[3] Popov, Dmitry, and Alexandr Klimchik. "Stiffness Analysis for Anthropomorphic Platform." In 2018 2nd School on Dynamics of Complex Networks and their Application in Intellectual Robotics (DCNAIR), pp. 106-108. IEEE, 2018.

[4] Mamedov, Shamil, Dmitry Popov, Stanislav Mikhel, and Alexandr Klimchik. "Compliance Error Compensation based on Reduced Model for Industrial Robots." In ICINCO (2), pp. 190-201. 2018.

[5] Popov, Dmitry, Alexandr Klimchik, and Ilya Afanasyev. "Comprising of Elastostatic and Elastodynamic Modeling for Compliance Error Compensation in Bipedal Robot." In International Conference on Informatics in Control, Automation and Robotics, pp. 404-424. Springer, Cham, 2017.

[6] Khusainov, Ramil, Alexandr Klimchik, and Evgeni Magid. "Humanoid robot kinematic calibration using industrial manipulator." In 2017 International Conference on Mechanical, System and Control Engineering (ICMSC), pp. 184-189. IEEE, 2017.

Optimal control of orthogonal-rotary movers of walking robot with an excessive number of drives

German Y. Prokudin
Department of Theoretical Mechanics
Volgograd State Technical University
Volgograd, Russia
dtm@vstu.ru

Nikolay G. Sharonov
Department of Theoretical Mechanics
Volgograd State Technical University
Volgograd, Russia
Center for Technology Components of Robotics and Mechatronics
Innopolis University
Innopolis, Russia
0000-0002-9894-707X

Eugene S. Briskin
Department of Theoretical Mechanics
Volgograd State Technical University
Volgograd, Russia
Center for Technology Components of Robotics and Mechatronics
Innopolis University
Innopolis, Russia
0000-0002-6409-4208

Оптимальное управление ортогонально-поворотными движителями шагающего робота с избыточным количеством приводов

Прокудин Г.Ю.
Кафедра теоретической механики
Волгоградский государственный технический университет
Волгоград, Россия
dtm@vstu.ru

Шаронов Н.Г.
Кафедра теоретической механики
Волгоградский государственный технический университет
Волгоград, Россия
Центр технологий компонентов робототехники и мехатроники
Университет Иннополис
Иннополис, Россия
0000-0002-9894-707X

Е.С. Брискин
Кафедра теоретической механики
Волгоградский государственный технический университет
Волгоград, Россия
Центр технологий компонентов робототехники и мехатроники
Университет Иннополис
Иннополис, Россия
0000-0002-6409-4208

***Abstract*— The methods of operation of the orthogonal-turning mechanism of a walking mobile robot are discussed. The criteria of optimal motion are formulated. The results of design and prototyping are presented.**

Keywords*— mobile robot, walking mechanism, drive, motion control

***Аннотация*—Рассматриваются методы управления приводами ортогонально-поворотных механизмов шагания мобильного робота. Формулируются критерии оптимального движения. Приводятся результаты разработки конструкции и прототипирования.**

Ключевые слова*—мобильный робот, механизм шагания, привод, управление движением

I. Введение

Мобильные роботы с шагающими движителями, несмотря на давний и стабильный интерес со стороны исследователей [1], не обрели общепризнанных конструктивных особенностей, таких как, например, колесные и гусеничные машины. В поиске оптимальных решений разрабатываются новые схемы механизмов шагания. Отдельное внимание уделяется разработке модульных реконфигурируемых схем мобильных роботов, в качестве движителей которых используются однотипные произвольно расположенные механизмы шагания. Для подобных систем актуальной является разработка и реализация методов согласованного управления приводами движителей, обеспечивающих программные движения модульного мобильного робота произвольной конфигурации.

II. Объект исследования

В качестве движителя мобильного робота рассматриваются состоящие из нескольких идентичных по конструкции механизмов шагания, представляющих собой ортогонально расположенные в перпендикулярной раме корпуса плоскости приводы линейных перемещений: привод вертикального перемещения и привод горизонтального перемещения (рис. 1). Приводы горизонтального перемещения закреплены на поворотной направляющей в плоскости,

перпендикулярной оси вращения движителя относительно корпуса робота [2]. В зависимости от количества и взаимного расположения горизонтальных направляющих можно синтезировать движители с различными свойствами [3]. В работе рассматривается полноповоротный (относительно оси, перпендикулярной плоскости корпуса робота) движитель из трех ортогональных механизмов (рис. 2).

Принцип работы движителя основан на взаимодействии с опорой одного из трех механизмов шагания, начало которого происходит в момент времени, когда угол между вектором скорости оси вращения и продольной осью привода горизонтального перемещения взаимодействующего с поверхностью механизма. Остальные механизмы шагания с этого момента времени находятся в фазе переноса, выполняемого за счет поворота движителя в целом.

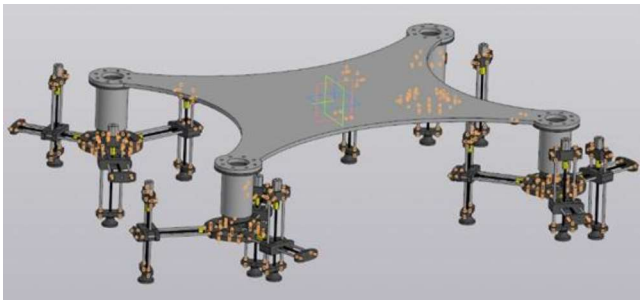

Рис. 1. Схема робота с роторно-ортогональными движителями

Возможны варианты формирования походок шагающего робота, при которых число приводов (управляющих воздействий) превышает количество степеней свободы рассматриваемой механической системы [4].

III. Управление с уравновешиванием

Рассматриваемый ортогонально-поворотный движитель при определенных алгоритмах управления, принципиально допускает возможность уравновешивания. Уравновешивание относительно корпуса достигается за счёт равномерного расположения горизонтальных направляющих в плоскости, перпендикулярной оси поворота, и согласованного режима управления приводами горизонтального перемещения, при котором находящиеся в переносе опоры телескопических опорных стоек перемещаются вместе с кареткой посредством привода горизонтального перемещения согласованно с перемещением каретки с телескопической опорной стойкой опоры, находящейся в контакте с поверхностью. Инерционные составляющие динамических нагрузок на механизмы уменьшаются, что приводит к снижению энергозатрат, требуемых для работы приводов, и позволяет достичь более высоких скоростей движения.

Критерием оптимальности по статической уравновешенности является безразмерный показатель

$$H = \frac{1}{S^2\tau}\int_0^{\tau}\sum_{j=1}^{N}\left(\rho_{Cxj}^2+\rho_{Cyj}^2\right)dt, \qquad (1)$$

где ρ_{Cxj}, ρ_{Cyj} – координаты центра масс j – го движителя в системе координат, жестко связанной с корпусом машины и началом на оси вращения движителя, S – длина шага, τ – время одного шага.

Рассматриваемый движитель может обеспечить любое плоское движение мобильного робота. Поэтому возможна задача определения оптимального программного режима движения при перемещении робота из начального положения в конечное как твердого тела, совершающего плоское движение при любом начальном положении движителей, установленных на роботе относительно его корпуса. При этом программные движения могут зависеть от различных показателей качества движения [5].

IV. Прототипирование

Разработана конструкция лабораторной модели полноповоротного движителя с тремя ортогональными механизмами, обеспечивающая физическое моделирование согласованного управления приводами (рис. 2). Линейные привода реализованы на основе передачи винт-гайка и корпусных деталей, изготовленных из пластика на 3D принтере. Согласованное управление двигателями постоянного тока реализовано на контроллере Arduino непосредственно с компьютера, с перспективой интеграции с программой расчета оптимальных законов управления.

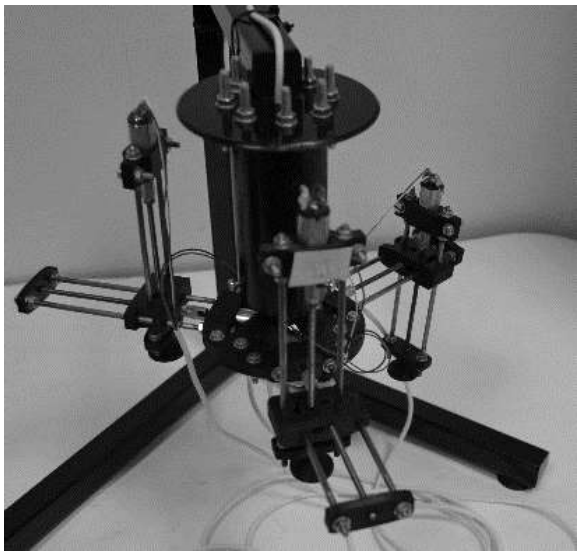

Рис. 2. Лабораторная модель полноповоротного движителя с тремя ортогональными механимами шагания

Благодарности

Исследование выполнено при финансовой поддержке РФФИ и Волгоградской области РФ в рамках научного проекта № 18-41-340014 р_ а.

Ссылки

[1] Павловский В.Е. О разработках шагающих машин // Препринты ИПМ им. М.В.Келдыша. 2013. № 101. 32 с.

[2] Development of Rotary Type Movers Discretely Interacting with Supporting Surface and Problems of Control Their Movement / E.S. Briskin, et al. // ROMANSY 21: Springer, 2016. – P. 351-359.

[3] Реконфигурируемый транспортный комплекс со сдвоенными шагающими движителями / Е.С. Брискин, Н.Г. Шаронов, С.С. Фоменко // Известия ВолгГТУ / ВолгГТУ. - Волгоград, 2013. - № 24 (127). - С. 10-15.

[4] Об управлении движением механических систем с избыточным числом управляющих воздействий / Е.С. Брискин, Н.Г. Шаронов

// Известия Российской академии наук. Теория и системы управления. - 2019. - № 3. - С. 48-54.

[5] Assessment of the performance of walking robots by multicriteria optimization of their parameters and algorithms of motion / E.S. Briskin et al. // Journal of Computer and Systems Sciences International. - 2017. - Vol. 56, No. 2. - С. 334–342.

Approaches for road lane detection

Maksim Rassabin
Laboratory of autonomous transport systems, Innopolis University,
Innopolis, Russia
rassabin@gmail.com

Rauf Yagfarov
Laboratory of autonomous transport systems, Innopolis University,
Innopolis, Russia
r.yagfarov@innopolis.ru

Salimzhan Gafurov,
Laboratory of autonomous transport systems, Innopolis University,
Innopolis, Russia
s.gafurov@innopolis.ru

***Abstract*—This article provides an overview of the three most promising methods of lane detection based on the neural network: SCNN, E-NET and LaneNET. A comparison was made based on the trained models on our own dataset to identify the robustness of these methods. Also, the evaluation of the speed of execution of the algorithm and the comparison of the masks obtained.**

Keywords — lane detection, computer vision, driverless vehicle, neural network.

I. INTRODUCTION

Nowadays the area of autonomous vehicles is one of the most promising and fast growing. A number of cars manufactures announced plans to release vehicles with built-in advanced driver assistance systems (ADAS). Such systems include a variety of modules such as adaptive cruise control, collision avoidance, traffic light, traffic signs and pedestrian detection. Lane keeping system is also a part of ADAS. This system is based on road lane marks detection. The result of lane marks detection is provided to a car's intelligent system for prediction of lane changing to maneuver efficiently as well as for informing a driver about the tendency to leave the lane.

Such a system can be built by means of cameras, GPS of LIDAR sensors. Each of these approaches have to take into account such challenges as parked and moving vehicles, shadows, bad quality of road lines, irregular lane shapes, merging lanes, bad weather conditions, illumination, snow and others. The road in most scenarios is not fully visible and is filled with other traffic users, which imposes additional issues in a lane detection task.

A wide variety of algorithms of representation, detection and tracking techniques have been proposed. There is a variety of techniques for lanes determining based on both classical computer vision methods and various structures of neural networks. Generally, there are two main computer vision approaches for lane detection: a feature-based or model-based approaches [1], [2]. The feature-based approach works with low-level features such as lane edges [3-5]. In such a manner, it is not robust as it is very sensitive to lane quality and noise. The model-based approach works with lanes representing them in the form of curves which can be determined by means of geometric parameters [6 - 10]. Such an approach is less sensitive to noise and lane quality. However, a model-based approach is not adaptive: model constructed for one image frame may not work for another one. Methods which are based on neural networks can be adopted for a wide range of road configurations and lanes quality.

Conducted literature overview as well as the results of CULane and TuSimple competition [13] we have chosen 3 most powerful approaches for lane detection which are based on neural networks: SCNN, E-NET, LaneNET. Our paper is focused on the practical aspects of each algorithm: accuracy, speed, availability, ease of use of the proposed approaches. The comparison of these methods is also provided.

II. APPROACHES DESCRIPTION

A. SCNN

Spatial convolutional neural network (SCNN), a generalization of deep convolutional neural networks to a rich spatial level [11]. In a layer-by-layer CNN, a convolution layer receives input from the former layer, applies convolution operation and nonlinear activation, and sends the result to the next layer. The main structure of this algorithm is presented on fig. 1. The algorithm won the TuSImple lane detection challenge in 2017. This algorithm is publicly available. For our comparison, we have chosen the TensorFlow implementation.

Presented SCNN model is based on developed by the author's dataset named CULane. It contains a set of 88,880 images for training, 9,675 images for validation, and 34,680 images for tests with the resolution of 1640×590.

B. E-Net

The main structure of the E-Net model is presented on fig. 2. It is heavily based on SCNN model. The main difference is in the neural network structure. E-Net model consists of five components, i.e., the binary segmentation branch (B), the drivable area detection branch (D), the lane point regression branch (P), the lane pixel embedding branch (E) and the clustering branch (C) [12]. The encoder and decoder of the first four branches are the same but only the encoder is shared. This approach is mainly focused on increasing of the multi-band algorithm speed with precision saving.

Research [12] has shown that the E-Net algorithm has the working speed in 10 times higher than SCNN model with a comparable level of accuracy (0.003% less than the SCNN). This algorithm is publicly available on Github [12].

C. LaneNet

A lane detection method called LaneNet is proposed in work [13]. This method is supposed to be more general with low computational cost, and real-time vehicle-based implantation. The proposed LaneNet breaks down the lane detection task into two stages, i.e. lane edge proposal and lane mark localization, respectively; and each involves an independent deep neural network.

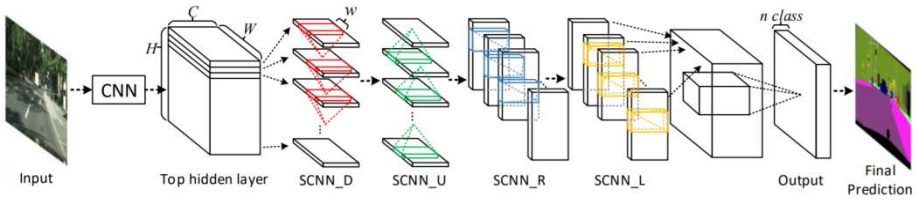

Fig. 1. SCNN structure

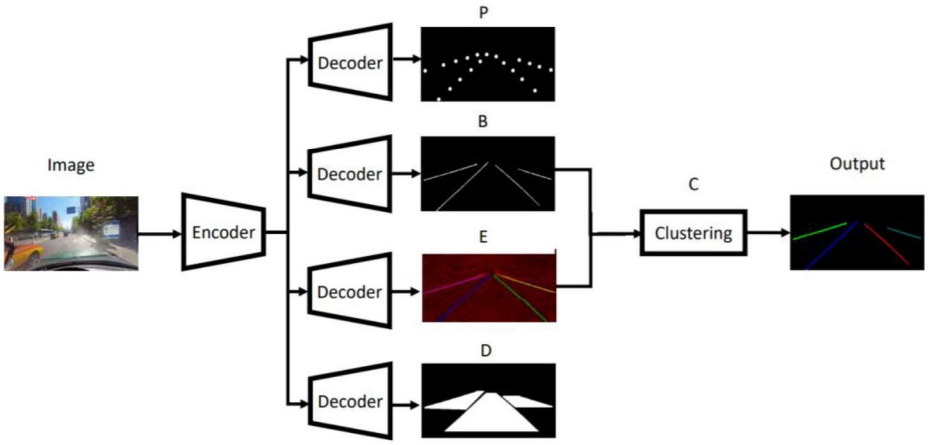

Fig. 2. E-Net main schem

On the lane edge proposal stage, the proposal network runs binary classification on every pixel of an input image for generating lane edge proposals, which are served as the input to the lane mark localization network on the second stage. This method also allows achieving high accuracy (0.001% less than that of SCNN) and high speed of work (26 fps on Jetson TX1).

This algorithm is publicly available on Github.

III. COMPASION OF ALGORITMS

A. Speed comarsion

Speed tests were conducted on the server with:

- Ubuntu 16.04.6 LTS
- CPU: Intel(R) Xeon(R) Gold 6148 CPU @ 2.40GHz
- 25GB RAM
- GPU: Nvidia Quadro P4000 with 8GB

In order to investigate the efficiency of the algorithms in case of scenarios which were not trained, we used the already trained models proposed by the authors of the method.

For this test meshing dataset was created which contains 80% of KITTI dataset images and 20% of our own images collected in the city of Innopolis (Russia). The total dataset contains 9,276 images with a resolution of 1280 x 512.

According to work [12], E-Net should be the fastest approach in terms of fitting the model. But on the practice, we are more interested in prediction speeds of algorithms. Therefore, we checked this parameter on hardware be means of datasets describing above. The result is presented in Table 1.

TABLE I. SPEED TEST RESULT

Algorithm	***Frame per second***
SCNN	16,77
E-Net	5,72
LaneNet	10

In such a manner, on practice we have not obtained the speed result for E-Net approach shown in work [12]. Moreover, this algorithm showed us the worth prediction performance. Even though low speed may be associated with implementation the method presented in [12], we consider this as the disadvantages because we could not achieve the results presented in the paper.

This also applies to the LaneNet method. According to the original research, this method should provide 26 frames

per second on Nvidia Jetson TX2. However, during our tests, we have not obtained the same results on the hardware that exceeds the performance of Jetson TX2. In such a manner, SCNN method has shown the best result in prediction speed.

B. *Accuracy*

For accuracy estimation we used the benchmark Tusimple. The results for the proposed algorithms are presented in Table 2 [13]. SCNN method is shown to be the most accurate.

Also, in our work, we conducted the comparison of 100 images from CULane dataset driver_100_30frame / 05251517_0433.MP4 parts.

TABLE II. SPEED TEST RESULT

Algorithm	***Accuracy***
SCNN	96,53%
E-Net	96,29%
LaneNet	96,4%

This part of the dataset is characterized by slightly framed images, with highlights and a fuzzy dividing strip, so that it can be classified as complex. The tests were conducted on the hardware presented in Section III A. Example is presented on fig. 3.

Fig.3. Example of sample from CULane dataset

TABLE III. F1 SCORE RESULT

Algorithm	***Precision***	***Fmeasure***	***Recall***
SCNN	0,305556	0,335512	0,371981
E-Net	0.299003	0.354331	0.434783
LaneNet	0.285714	0.331984	0.396135

Based on this dataset, an assessment was made, the results of which are presented in Table 3, where are the green best results for metrics.

As we can see, the results are rather ambiguous, according to the metric, precision is in the lead of the SCNN, and according to the metrics of recall and F1 the E-Net model.

We have also got the double training dataset as a result.

IV. RESULTS

According to our comparison, we have obtained that the SCNN algorithm is easy to set up, has an implementation on modern libraries (python and tensorflow), is quite fast in predicting the mask of road lines, and it is the most accurate in terms of benchmark TuSimple and metric precision in our tests. Thus, according to the criteria considered, the best algorithm is the one considered above.

REFERENCES

[1] J.C. McCall and M.M. Trivedi, “Video-based Lane Estimation and Tracking for Driver Assistance: Survey, System, and Evaluation”, IEEE Transactions on Intelligent Transportation Systems, vol.7, pp.20-37, 2006.

[2] Y.Wang, E. K.Teoh and D. Shen, “Lane Detection and Tracking Using B-snake,” Image and Vision Computing, vol. 22, pp. 269-280, 2004.

[3] Broggi and S. Berte, “Vision-based Road Detection in Automotive Systems: a Real-time Expectation-driven Approach”, Journal of Artificial Intelligence Research, vol.3, pp. 325-348, 1995.

[4] M. Bertozzi and A. Broggi, “GOLD: A Parallel Realtime Stereo Vision System for Generic Obstacle and Lane Detection”, IEEE Transactions of Image Processing, pp. 62-81, 1998.

[5] S.G. Jeong, C.S. Kim, K.S. Yoon, J.N. Lee, J.I. Bae, and M.H. Lee, “Real-time Lane Detection for Autonomous Navigation”,IEEE Proc. Intelligent Transportation Systems, pp. 508–513, 2001.

[6] Y.Wang, E.K. Teoh and D. Shen, “Improved Lane Detection and Tracking Using B-snake,” Image and Vision Computing, vol. 20, pp. 259-272, 2005.

[7] R. Jung and C. R. Kelber, “A Lane Departure Warning System Using Lateral Offset with Uncalibrated Camera,” Proc. IEEE Conf. on Intelligent Transportation Systems, pp.102-107, 2005.

[8] D.J. Kang, J. W. Choi and I.S. Kweon, “Finding and Tracking Road Lanes Using Line-snakes”, Proceedings of Conference on Intelligent Vehicle, pp. 189-194, 1996.

[9] Z. Kim, “Real-time lane tracking of curved local road”, Proc. IEEE Conf. on Intelligent Transportation Sys Y. Wang, D. Shen and E.K. Teoh, “Lane Detection Using Spline Model”, Pattern Recognition Letters vol.21, pp. 677-689, 2000. tem, pp. 1149-1155, 2006.

[10] Xingang Pan, Jianping Shi, Ping Luo, Xiaogang Wang, Xiaoou Tang. "Spatial As Deep: Spatial CNN for Traffic Scene Understanding", AAAI2018 J. Clerk Maxwell, A Treatise on Electricity and Magnetism, 3rd ed., vol. 2. Oxford: Clarendon, 1892, pp.68–73.

[11] Ze Wang, Weiqiang Ren, Qiang Qiu. “LaneNet: Real-Time Lane Detection Networks for Autonomous Driving”. Published in ArXiv 2018.

[12] HOU-Yuenan. “Agnostic Lane Detection”. Published in ArXiv 2018.

[13] https://paperswithcode.com/task/lane-detectio

Nonlinear dynamics of a flexible closed cylindrical size-dependent shell under the action of a band load

Saltykova O.A.
department of Mathematical and Modelling
Yuri Gagarin State Technical University of Saratov
Saratov, Russia
olga_a_saltykova@mail.ru

Krysko V.A.
department of Mathematical and Modelling
Yuri Gagarin State Technical University of Saratov
Saratov, Russia
tak@san.ru

***Abstract*—In this paper, a mathematical model of nonlinear oscillations of a closed cylindrical size-dependent shell under the action of an external band-variable alternating load is constructed. The size-dependent parameter is taken into account based on the modified moment theory. The equations of motion of the shell are obtained on the basis of the Hamilton-Ostrogradskiy variational principle based on Kirchhoff-Love kinematic hypotheses. The scenario of transition of the oscillations of the shell from harmonic to chaotic is investigated.**

Keywords—cylindrical shell, Bubnov-Galerkin method, chaos

I. INTRODUCTION

Closed cylindrical shells are widely used in various sensors and devices, which determine the relevance of this work, where the nonlinear dynamics of a flexible size-dependent closed cylindrical shell under the influence of an external band-wise alternating load is investigated [1-2]. The object of study is a closed cylindrical shell occupying a region in R^3 space $\Omega = \{x, y, z \mid (x, y, z) \in [0; L] \times [0; 2\pi] \times [-h; h]\}$. The coordinate system is entered as shown in Figure 1.

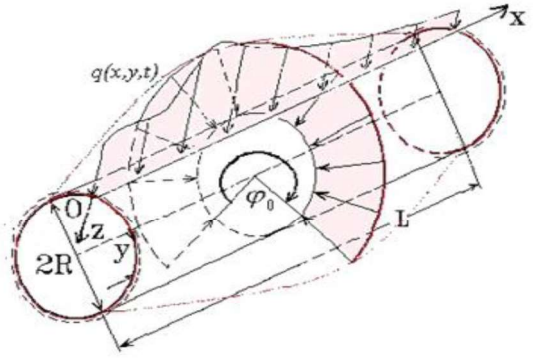

Fig. 1 Settlement scheme

The shell is isotropic and flexible. Geometric nonlinearity is taken into account according to the T. von Karman model. The shell has a distributed alternating load: $q(x, y, t) = q_0 \sin(\omega_p t)$, where q_0 - is amplitude, ω_p - frequency of load. The width of the load band is determined by φ_0.

II. EQUATIONS OF MOTION

To account for the size-dependent parameter, a modified moment theory was used.

Using the standard procedure of the calculus of variations, we obtain the equations of motion of the shell and the equation of compatibility of deformations, taking into account the Kirchhoff-Love kinematic hypotheses, in the form:

$$\left(-\frac{1}{12(1-\nu^2)}+\frac{l^2}{2(1+\nu)}\right)\cdot\left(\frac{1}{\lambda^2}\frac{\partial^2 w}{\partial x^2}\frac{\partial^2(\cdot)}{\partial x^2}+\lambda^2\frac{\partial^2 w}{\partial y^2}\frac{\partial^2(\cdot)}{\partial y^2}+\right.$$
$$\left.+2(1-\nu)\frac{\partial^2 w}{\partial x\partial y}\frac{\partial^2(\cdot)}{\partial x\partial y}+\nu\left(\frac{\partial^2 w}{\partial x^2}\frac{\partial^2(\cdot)}{\partial y^2}+\frac{\partial^2 w}{\partial y^2}\frac{\partial^2(\cdot)}{\partial x^2}\right)\right)-$$
$$-\nabla_k^2 F - L(w,F) + M\cdot q(t) - \left(\frac{\partial^2 w}{\partial t^2}+\varepsilon\frac{\partial w}{\partial t}\right)=0, \qquad (1)$$
$$\left(\lambda^2\frac{\partial^2 F}{\partial y^2}-\nu\frac{\partial^2 F}{\partial x^2}\right)\frac{\partial^2(\cdot)}{\partial y^2}+\left(\frac{1}{\lambda^2}\frac{\partial^2 F}{\partial x^2}-\nu\frac{\partial^2 F}{\partial y^2}\right)\frac{\partial^2(\cdot)}{\partial x^2}+$$
$$+2(1+\nu)\frac{\partial^2 F}{\partial x\partial y}\frac{\partial^2(\cdot)}{\partial x\partial y}+\nabla_k^2 w+\frac{1}{2}L(w,w)=0.$$

Attach to the system (1) the boundary conditions for the hinge support at the ends:

$$w=0;\frac{\partial w}{\partial x}=0;F=0;\frac{\partial^2 F}{\partial x^2}=0 \text{ for } x=0;1.$$
$$w=g(x,y,t);\frac{\partial w}{\partial y}=p(x,y,t);$$
$$\text{for } y=0;2\pi.$$
$$F=u(x,y,t);\frac{\partial F}{\partial y}=v(x,y,t)$$
$$(2)$$

In addition to the boundary conditions, we add the initial conditions to equations (1) $w\big|_{t=0}=w_0,\ \dot{w}\big|_{t=0}=0.$

Equations (1-3) are reduced to dimensionless form using the following parameters: $w=h\overline{w}$, $F=Eh^2\overline{F}$, $t=t_0\overline{t}$, $\varepsilon=\overline{\varepsilon}/\tau$, $x=L\overline{x}$, $y=R\overline{y}$, $k_y=\overline{k}_y\frac{h}{R^2}$ ($k_x=0$), $q=\overline{q}\frac{Eh^4}{L^2R^2}$, $\tau=\frac{LR}{h}\sqrt{\frac{\rho}{Eg}}$, $M=k_y{}^2$, $\lambda=\frac{L}{R}$, where L

and $R = R_y$ - shell length and radius, ν - Poisson's ratio, l - is a scale parameter of the length of the material taking into account the effect of higher order moments, w - deflection, F - function of effort, t - time, ε - the resistance coefficient of the medium in which the shell moves, $\nu = 0.3$. The bar above the dimensionless values is omitted for simplicity.

TABLE I. DYNAMIC CHARACTERISTICS AT $q_0 = 0.377$

FFT
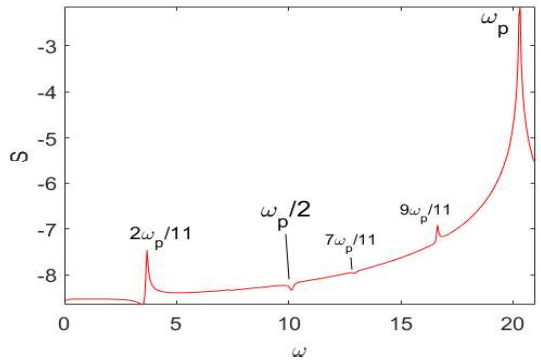
2D phase portrait
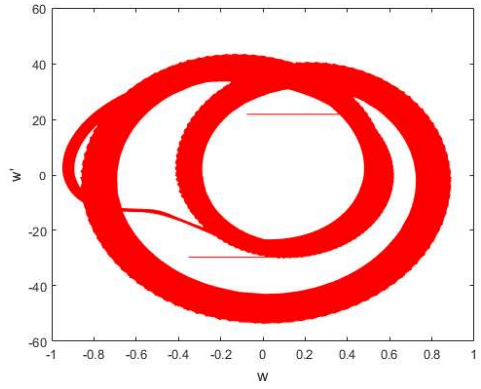
Wavelet spectrum
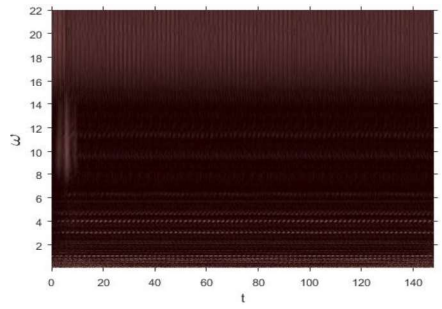

III. SOLUTIONS METHODS

For information of the obtained system of partial differential equations to the system of ordinary differential equations, the Bubnov-Galerkin method is used in higher approximations.

$$w = \sum_{i=1}^{N_1} \sum_{j=0}^{N_2} A_{ij}(t) \sin(i\pi x) \cos(jy),$$

$$F = \sum_{i=1}^{N_1} \sum_{j=0}^{N_2} B_{ij}(t) \sin(i\pi x) \cos(jy).$$

The obtained Cauchy problem is solved by Runge-Kutta-type methods with second-order approximation. The obtained results were processed by nonlinear dynamics methods, signals are built, power spectra, wavelet spectra, Poincare sections, phase portraits, signs of Lyapunov's largest indicators are determined.

TABLE II. DYNAMIC CHARACTERISTICS AT $q_0 = 0.379$

FFT
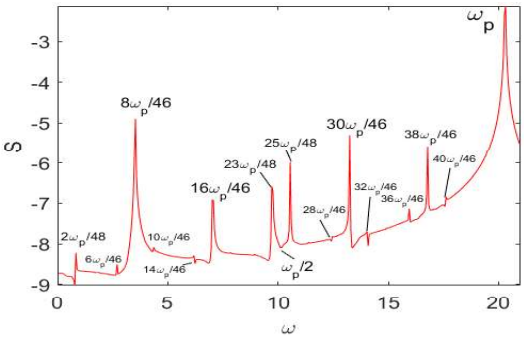
2D phase portrait
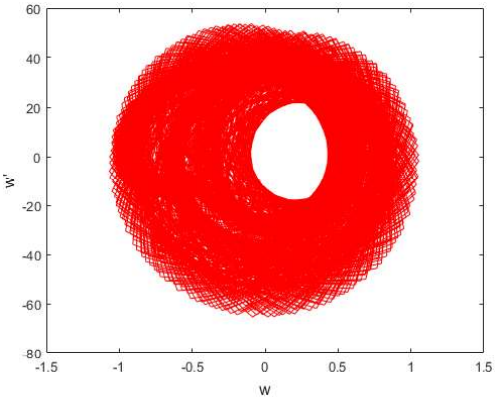
Wavelet spectrum
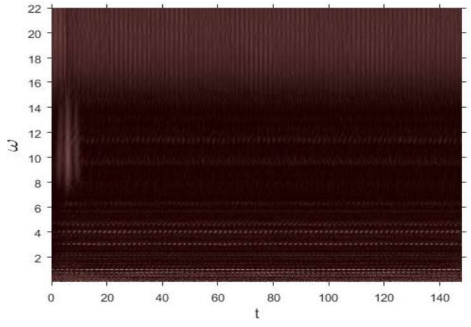

IV. NUMERICAL RESULTS

The convergence of solutions has been preliminary studied depending on the number of members of the series (N) in the Bubnov-Galerkin decomposition [3] and N = 9 for further calculations, $\lambda = \frac{L}{R} = 1$, $\omega_p = 20.3$, $\varepsilon = 1$, $\varphi_0 = 5.98$, $l = 0.5$. In table 1 we give the dynamic characteristics of the shell at $q_0 = 0.377$.

$q_0 = 0.37$ - the period's doubling $\omega_p / 2$. $q_0 = 0.376$ - appears $2\omega_p / 11$. $q_0 = 0.377$ - $7\omega_p / 11$ and $9\omega_p / 11$. In table 1 we give the dynamic characteristics of the shell at $q_0 = 0.379$.

$q_0 = 0.378$ - linear combination of frequency multiplicity 45. $q_0 = 0.379$ - frequencys multiplicity 48 and 46.

V. CONCLUSION

In this paper, the scenario of vibrations transition of a closed flexible size-dependent shell from harmonic to chaotic is studied through a combination of Feigenbaum and Ruelle-Tackens-Newhouse scenarios.

ACKNOWLEDGMENT

This work was carried out by a grant RFBR 18-41-700001 r_a

REFERENCES

[1] M.Rafiee, J.Yang , Kitipornchai S. Thermal bifurcation buckling of piezoelectric carbon nanotube reinforced composite beams, Computers and Mathematics with Applications Vol. 66, Issue 7, October 2013, pp. 1147-1160.

[2] G.G.Sheng, X.Wang The dynamic stability and nonlinear vibration analysis of stiffened functionally graded cylindrical shells, Applied Mathematical Modelling Vol. 56, April 2018, pp. 389-403.

[3] O.A.Saltykova, O.A.Afonin, T.V.Yakovleva, A.V.Krysko, Chaotic dynamics of flexible closed cylindrical nanoshells under local loading, Nonlinear world, No. 5, Vol. 16, 2018, pp. 3-15

Detecting Changes in Contact Interaction Regime with a Reaction Predictor and a Linear Contact Model

Sergei Savin
Center for Technologies in Robotics and Mechatronics Components
Innopolis University
Innopolis, Russia
0000-0001-7954-3144

***Abstract*—This paper is focused on a problem of using reaction predictors in the control pipeline of walking robots. The use of such predictors has been proposed for bipedal robots and the main advantage of this proposal is that it allows to exclude unknown reaction forces from the dynamics equations, and hence from model-based control formulations for those robots. In this paper, an additional benefit of predictor-based control formulation is discussed, namely the possibility of using it to predict changes in the contact interaction scenario, such as slipping or take off from the supporting surface.**

Keywords—walking robots, reaction forces, mechanical constraints, predictors, linearized model

I. INTRODUCTION

Walking robots are one of the most promising directions the modern robotics, aiming at solving a number of problems, from mobility over uneven and challenging terrain, to attaining biomorphic locomotion. There are bipedal, quadruped and multi-legged robot designs, crawler robots, in-pipe walking robots and even underwater walking robots [1-3]. It particular, anthropomorphic bipeds (humanoid robots) are interesting, because they should additionally provide benefits of easy integration into existing social and urban infrastructure.

In modern humanoid robotics, the issue of vertical balance of the robot remains to be important. There are classical approaches relying on assumptions about flatness of the supporting surface and the sufficient friction, such as zero-moment point (ZMP) formulation [4-5]. There are also methods that allow to directly reason about contact reaction forces, such as contact wrench cone (CWC) method [6]. Both rely on the assumption that the contact interaction regime with the supporting surface is accurately captured by the proposed model.

There had been works on introducing experimental or simulation data on the contact interaction regimes directly into the control formulation. This can be done in a variety of ways, from the use of reinforcement learning [7-8], to augmenting criteria for choosing parameters for the existing methods based on their performance in simulation [9]. The use of machine learning techniques appears especially interesting, as it allows easily integrating additional data, is flexible with respect of the types of data (experimental or based on simulation), and since it produces predictably (in

terms of computational time) operating software modules which can be analyzed with statistical tools.

In the paper [10], it was proposed to use dense neural networks to train a contact reaction forces predictor. The data for the training was collected in simulation, and the system was built using standard tool, such as Tensorflow and Keras. The trained agent was able to predict reaction forces with acceptable accuracy, allowing its use in control pipeline.

In paper [10], it was also proposed to use the agent to build a locally linear model of the robot contact interaction. The linear model can be used to substitute in place of reaction forces into the control formulations. This can allow the use of classic control algorithms designed for systems without explicit mechanical constraints for constrained systems. This allows avoiding the problems related to generating desired control actions for constrained systems, described in [11-12]. In this work, this model is additionally used to predict changes in the contact interaction regimes. That allows to predict changes in friction force mode (slipping), breaking of contact and other.

II. LINEARIZED CONTACT MODEL

Assume that the model of the robot is described by equations:

$$\mathbf{H}\ddot{\mathbf{q}} + \mathbf{c} = \boldsymbol{\tau} + \mathbf{F}^{\mathrm{T}}\boldsymbol{\lambda}, \tag{1}$$

where $\mathbf{H}$ is a generalized inertia matrix, $\ddot{\mathbf{q}}$ are generalized accelerations, $\mathbf{c}$ is a generalized bias vector, $\boldsymbol{\tau}$ are generalized torques, $\mathbf{F}$ is the constraints Jacobian, and $\boldsymbol{\lambda}$ is the vector of reaction forces.

Then a reaction predictor is given as follows:

$$\boldsymbol{\lambda} = P(\dot{\mathbf{q}}, \mathbf{q}, \boldsymbol{\tau}). \tag{2}$$

With predictor (2) we can find a linearized model about point $\mathbf{q}_0$, $\dot{\mathbf{q}}_0$, $\boldsymbol{\tau}_0$:

$$\boldsymbol{\Lambda} = \frac{1}{\alpha}[\boldsymbol{\lambda}_1 - \boldsymbol{\lambda}_0 \quad \dots \quad \boldsymbol{\lambda}_m - \boldsymbol{\lambda}_0], \tag{3}$$

$$\boldsymbol{\lambda}_0 = P(\dot{\mathbf{q}}_0, \mathbf{q}_0, \boldsymbol{\tau}_0), \tag{4}$$

$$\boldsymbol{\lambda}_i = P(\dot{\mathbf{q}}_0, \mathbf{q}_0, \boldsymbol{\tau}_0 + \alpha\delta_i), \tag{5}$$

where δ_i is a basis vector in the orthonormal basis in the space of reaction forces, α is a scalar coefficient which determines the localness of the linearization. Then a local linearized model of reaction forces is given as:

$$\boldsymbol{\lambda} = \boldsymbol{\Lambda}\mathbf{u} + \boldsymbol{\lambda}_0, \tag{6}$$

This model can be directly substituted into the model (1), effectively excluding unknown algebraic variables $\boldsymbol{\lambda}$ from the control problem based on the robot dynamics:

$$\mathbf{H}\ddot{\mathbf{q}} + \mathbf{c} = \boldsymbol{\tau} + \mathbf{F}^{\mathrm{T}}(\boldsymbol{\Lambda}\mathbf{u} + \boldsymbol{\lambda}_0), \tag{7}$$

where the resulting system of equations is no longer DAE (differential-algebraic equations), but only ODE.

III. PREDICTION OF THE CONTACT REGIME CHANGE

Observing expressions (3)-(6), we can note that the choice of α should correspond to the expected difference between $\boldsymbol{\tau}$ and $\boldsymbol{\tau}_0$. Assume that the contact regime undergoes a rapid change at a point $(\dot{\mathbf{q}}_0, \mathbf{q}_0, \boldsymbol{\tau}_0 + \alpha_c\delta_k)$, where α_c is a critical value of α. This can happen due to the crossing friction cone boundaries, for example. Then it is important to observe that for control that generates generalized torques $\boldsymbol{\tau} \geq \boldsymbol{\tau}_0 + \alpha_c\delta_k$, the correct linearization is different than for control that generates generalized torques $\boldsymbol{\tau} < \boldsymbol{\tau}_0 + \alpha_c\delta_k$.

Let us consider the problem of recognizing that scenario, naming the fact that the contact interaction model underwent a rapid change near the current point in the sate-action space. First, we produce two linearization, for two different choices of α: for $\alpha_{\min}$ and $\alpha_{\max}$. We denote linearization matrices of these models as $\boldsymbol{\Lambda}_{\max}$ and $\boldsymbol{\Lambda}_{\min}$. Then we can introduce an additive criterion σ_1 given as follows:

$$\sigma_1 = \| \boldsymbol{\Lambda}_{\max} - \boldsymbol{\Lambda}_{\min} \|_F, \tag{8}$$

where $\| \cdot \|_F$ is the Frobenius norm of a matrix.

Alternatively, a multiplicative criterion σ_2 can be used:

$$\sigma_2 = \| \boldsymbol{\Lambda}^{+}_{\max}\boldsymbol{\Lambda}_{\min} \|_F. \tag{9}$$

Values of σ_1 or σ_2 can be compared against experimentally found threshold value σ_c. Then the problem of prediction contact interaction regime change can be simplified to the problem of finding correct threshold values σ_c, which can be done experimentally, theoretically, or via simulation, using manual tuning or via machine learning.

IV. CONCLUSIONS

In this paper, a problem of using reaction predictor in order to identify the possibility of contact interaction scenario change, was discussed. The proposed idea is to measure the difference between local linearizations, as parametrized by a scalar variable, acting like a discrete step length, for different discrete steps. The difference can be measured in the additive or multiplicative sense.

This approach is simple in formulation, however it suffers from the lack of information about the direction (or location) where the change of the contact interaction scenario will occur.

ACKNOWLEDGMENT

This work is supported by the Presidential grant MK-1537.2019.8.

REFERENCES

[1] Radford, Nicolaus A., et al. "Valkyrie: Nasa's first bipedal humanoid robot." Journal of Field Robotics 32.3 (2015): 397-419.

[2] Savin, Sergei, Sergey Jatsun, and Lyudmila Vorochaeva. "Trajectory generation for a walking in-pipe robot moving through spatially

curved pipes." MATEC Web of Conferences. Vol. 113. EDP Sciences, 2017.

[3] Akizono, J., et al. "Development on walking robot for underwater inspection." Advanced Robotics: 1989. Springer, Berlin, Heidelberg, 1989. 652-663.

[4] Vukobratović, Miomir, and Branislav Borovac. "Zero-moment point—thirty five years of its life." International journal of humanoid robotics 1.01 (2004): 157-173.

[5] Kajita, Shuuji, et al. "Biped walking pattern generation by using preview control of zero-moment point." 2003 IEEE International Conference on Robotics and Automation (Vol. 2, pp. 1620-1626). IEEE.

[6] Caron, Stéphane, Quang-Cuong Pham, and Yoshihiko Nakamura. "Stability of surface contacts for humanoid robots: Closed-form formulae of the contact wrench cone for rectangular support areas." 2015 IEEE International Conference on Robotics and Automation (ICRA). IEEE, 2015.

[7] Levine Sergey, Nolan Wagener, and Pieter Abbeel. "Learning contact-rich manipulation skills with guided policy search." 2015 IEEE international conference on robotics and automation (ICRA). IEEE, 2015.

[8] Tan, Jie, et al. "Sim-to-real: Learning agile locomotion for quadruped robots." arXiv preprint arXiv:1804.10332 (2018).

[9] Savin, Sergei, Khusainov Ramil, and Klimchik Alexandr "Admissible region ZMP trajectory generation for bipedal robots walking over uneven terrain", Proceedings of 14th International Conference on Electromechanics and Robotics "Zavalishin's Readings", Springer, 2019.

[10] Savin, Sergei. "Neural Network-Based Reaction Estimator for Walking Robots." 2018 International Russian Automation Conference (RusAutoCon). IEEE, 2018.

[11] Laine, F. and Tomlin, C., 2018. Efficient Computation of Feedback Control for Constrained Systems. arXiv preprint arXiv:1807.00794.

[12] Aghili, F., 2005. A unified approach for inverse and direct dynamics of constrained multibody systems based on linear projection operator: applications to control and simulation. IEEE Transactions on Robotics, 21(5), pp.834-849.

Directional Coupling Between The Low-Frequency Control Of Heart Rate And Vessels Tone In Myocardial Infarction Patients

Margarita Simonyan
Saratov State Medical University,
Saratov, Russia
dr.m-simonyan@yandex.ru

Vladimir Gridnev
Saratov State Medical University,
Saratov State University
Saratov, Russia
gridnev@cardio-it.ru

Anatoly Karavaev
Saratov Branch of the Institute of RadioEngineering and Electronics of Russian Academy of Sciences,
Saratov State Medical University,
Saratov State University
Saratov, Russia
karavaevas@gmail.com

Boris Bezruchko
Saratov Branch of the Institute of RadioEngineering and Electronics of Russian Academy of Sciences,
Saratov State University,
Saratov, Russia
bezruchkobp@gmail.com

Yuri Ishbulatov
Saratov Branch of the Institute of RadioEngineering and Electronics of Russian Academy of Sciences,
Saratov State Medical University,
Saratov State University
Saratov, Russia
ishbulatov95@mail.ru

Anton Kiselev
Saratov State MedicalUniversity,
Saratov State University
Saratov, Russia
kiselev@cardio-it.ru

Viktoriia Skazkina
Saratov State University
Saratov, Russia
skazkinavv@yandex.ru

***Abstract* – Characteristics of directional coupling between 0,1 Hz oscillations in heart rate variability and blood filling of vascular bed are studied for healthy subjects and myocardial infarction patients at 2-5 days after acute infarction and 1 year after. It is evident that statistically significant two-directional coupling is present in healthy subjects with dominant influence of heart on vessels. It was shown that 1 week after infarction the coupling in this direction is stronger for the patients than for healthy subjects. 1 year after infarction the patients' indices approach normal healthy values.**

Keywords: time series, directional coupling, data analysis, autonomic regulation, myocardial infarction

I. Introduction

Present date data support the presence of 0,1 Hz oscillations in heart rate variability signal (HRV), arterial pressure, and blood filling of vascular bed [1-6]. Investigation of circulation autonomic control via mathematical modeling [7-9] demonstrated that 0,1 Hz oscillations in HRV and arterial pressure are caused by functional characteristics of baroreflectory control of systemic arterial pressure (response time ~2,1 s, feedback loop time-delay~2,6 s) [10].

Functional independence of 0,1 Hz oscillations in HRV and blood filling of vascular bed was also proven [11-13]. It is known that in healthy subjects the 0,1 Hz oscillations are coupled for a significant portion of time [13]. Also development of myocardial infarction (MI) correlates with significant decrease in coupling level between 0,1 Hz oscillations in HRV and blood filling of vascular bed. It increases somewhat during recuperation. Previous studies [14-15] demonstrate importance of the coupling characteristics between the 0,1 Hz oscillations for medical prognosis in patients after acute MI. However to this date there are no information on characteristics of coupling between 0,1 Hz oscillations in HRV and blood filling of vascular bed. Considering that coupling between control loops that responsible for the 0,1 Hz oscillations is present in healthy subjects [13] one can suggest that one oscillating process dominates the other, or in other words is leading and defining the dynamics of the driven oscillator. Interaction between 0,1 Hz oscillations in heart and vascular bed can be described in terms of time-delays and coupling strengths.

II. Materials and Methods

120 MI patients (70 males and 50 females) age 30-83 participated in the study. Control group consisted of 33 healthy subjects (23 males, 10 females) age 20-46 years.

The patients received full course of medical therapy, corresponding to modern recommendations for treatment of acute MI. The patients were observed for 1 year after the infarction. Checking time was set to 2-5 days after acute MI and 1 year after. During the checkups we assessed coupling strength and time-delay between 0,1 Hz oscillations in HRV and blood filling of vascular bed.

To estimate tone of circulation autonomic control we made synchronous 10 min records of electrocardiogram signals (ECG), photoplethysmogram (PPG) and respiration via strain gauge sensor in supine position.

Recording of ECG, PPG and respiration was conducted with multi-channel electroencephalograph analyzer EEGA-21/26 'Encephalan-131-03' (Medicom MTD Ltd, Taganrog, Russia) with standard set of sensors, 250 Hz sample frequency and 12 bits resolution. PPG was measured from nail bone of middle finger with transmitted light pulseoxymetry sensor.

We excluded spontaneous influence of respiration on circulation by controlling respiration: preventing forced inspirations and delays in respirations. Therefore the study was conducted in presence of relatively spontaneous respiration. Then we selected ECG and PPG without artifacts, extra systole, noticeable linear trends, and transition processes. Sequence of RR-intervals was extracted from electrocardiogram (ECG) and then extrapolated with cubic splines to create equidistant cardiointervalgram with 5Hz sample rate. The 0,1 Hz oscillations were extracted from cardiointervalgram and PPG with 0,05-0,15 Hz band-pass filters. We applied technique of phase dynamics modeling to cardiointervalgram and PPG signals to estimate the coupling strengths for various time-delays between signals. Resulted dependencies were ensemble-averaged to estimate average time-delay between 0,1 Hz oscillations in HRV and blood filling of vascular bed.

III. Results

During initial analysis of the 10 min signals it became evident that influence from heart to vessels is prevalent between 0,1 Hz oscillations in HRV and blood filling of vascular bed in healthy subjects, and also in patients 2-5 days after MI and 1 year after MI.

Analysis of the «heart → vascular bed» coupling strength in patients 2-5 days after MI resulted in the higher indices than in control group (0,36±0,06 and 0,34±0,11 respectively). However the delay-time for patients 2-5 days after MI was also higher than in healthy subjects (2,97±1,28 s and 2,7±1,1 respectively). 1 year after MI time-delay in the coupling returns to healthy values (2,73±0,86 s).

Analyzing the «vascular bed → heart» coupling strength we found differences between patients in acute period of MI and healthy subjects. In patients 1 weak after MI the coupling strength is higher than in healthy subjects (0,28±0,13 and 0,25±0,13 respectively), the time-delay is also higher, although not statistically significant (2,89±0,98 s and 2,62±1,55 s respectively).

1 year after MI the «vascular bed → heart» coupling strength tends to lower and approach healthy levels (0,25±1,15 and 0,25±0,13 respectively).

IV. Discussion

Results we obtained from initial data analysis relate to debating topic about myogenic or neurocirculatory origin of the 0,1 Hz oscillations related to autonomic control of blood filling of vascular bed.

From our study of the coupling strength in healthy subjects and patients after MI the coupling in direction «heart → vascular bed» is dominant which argues for dominant role of the 0,1 Hz oscillations in HRV. It accepted that such coupling direction typical for hemodynamic control of cardio-vascular system [16]. From this one can suggest that dominant role in cardiovascular control belongs to hemodynamic, regardless to presence or absence of the acute coronary conditions. We also concluded that in the patients in early stages of disease (2-5 days after MI) hemodynamic control is more prevalent than in healthy subjects.

From analysis of the «vascular bed → heart» coupling in the patients during acute stage of the disease the coupling strength is higher in comparison to healthy subjects. It can mean more active role of autonomic control during early stages of the disease.

Overall obtained results allow assuming activation of the nonspecific adaptation under stressing factors from cardio-vascular system in patients with developed acute coronary condition. Hemodynamic component assumes leading role. According to H. Selye concept of stress and adaptive mechanisms [17] return of the coupling-strength indices (in both directions) to healthy values after 1 year of monitoring

in conjunction with normalization of clinical score gives positive prognosis and argues for effectiveness of the adaption.

V. Conclusion

According to our results directional coupling between 0,1 Hz oscillations in HRV and blood filling of vascular bed is prevalent in direction «heart → vascular bed» regardless of presence or absence of acute myocardial infarction. In other words hemodynamic factors prevail in cardiovascular autonomic control. During acute stages of the disease activity rises for both vegetative and hemodynamic component of circulation control. It is likely due to activation of the adaptation processes in response to stressing factors from cardio-vascular system. 1 year after acute myocardial infarction the coupling strength indices return to healthy values. It can argue for effectiveness of the adaptation mechanisms and gives positive medical prognosis.

Acknowledgment

This work was supported by the Russian Science Foundation, Grant No.19-12-00201 (development of the method), as well as the grant of the President of Russian Federation, Grant MD-418.2019.7 (registration, preliminary analysis and processing of experimental data).

References

[1] L. Bernardi, C. Passino, G. Spadacini, et al. “Arterial baroreceptor as determinants of 0,1 Hz and respiration-related changes in blood pressure and heart rate spectra”. Frontiers of blood pressure and heart rate analysis, 1997, pp. 241.

[2] L. Bernardi, M. Rossi, P. Fratino, et al. “Relationship between changes in human skin blood flow and autonomic tone”. Microvasc. Res., 1989, vol. 37, pp. 16-27.

[3] L. Bernardi, M. Rossi, S. Leuzzi, et al. “Reduction of 0,1 Hz microcirculatory fluctuations as evidence of sympathetic dysfunction in insulin-dependent diabetes”. Cardiovasc. Res., 1997, vol. 34, pp. 185-191.

[4] L. Bernardi, A. Radaelli, P. L. Solda, et al. “Autonomic control of skin microvessels assessment by power spectrum of photoplethysmographic waves”. Clin. Sci., 1996, vol. 90, pp. 345-355.

[5] A. M. Whittam, R. H. Claytont, S. W. Lord, et al. “Heart rate and blood pressure variability in normal subjects compared with data from beat-to-beat models developed from de Boer’s model of the cardiovascular system”. Physiol. Meas., 2000, vol. 21, pp. 305-318.

[6] D. W. Wray, P. J. Fadel, D. M. Keller, et al. “Dynamic carotid baroreflex control of the peripheral circulation during exersice in humans”. J. Physiol., 2004, pp. 675-684.

[7] K. Kotani, Z. R. Struzik, K. Takamasu, et al. “Model for complex heart rate dynamics in health and diseases”. Phys. Rev. E, 2005, vol. 72, p. 041904.

[8] M. Ursino, E. Magosso. “Short-term autonomic control of cardiovascular function: a mini review with the help of mathematical models”. J. Integr. Neurosci., 2003 vol. 2, pp. 219-247.

[9] J. V. Ringwood, S. C. Malpas. “Slow oscillations in blood pressure via a nonlineare feedback model”. Am. J. Physiol. Regulatory Integrative Comp. Physiol., 2001, vol. 280, pp. 1105-1115.

[10] A. S. Karavaev, V. I. Ponomarenko, M. D. Prokhorov. “Reconstruction of scalar time-delay system models”. Technical Physics Letters, 2001, vol. 27, pp. 414-418.

[11] A. S. Karavaev, M. D. Prokhorov, V. I. Ponomarenko, et al. “Synchronization of low-frequency oscillations in the human cardiovascular system”. Chaos, 2009 vol. 19, p. 033112.

[12] V. A. Shvartz, A. S. Karavaev, E. I. Borovkova, et al. “Investigation of statistical characteristics of interaction between the low-frequency oscillations in heart rate variability and photoplethysmographic waveform variability in healthy subjects and myocardial infarction patients”. Russ. Open Med. J., 2016, vol. 5, p. e0203.

[13] A. R. Kiselev, V. I. Gridnev, A. S. Karavaev, et al. “The dynamics of 0,1 Hz oscillations synchronization in cardiovascular system during the treatment of acute myocardial infarction patients”. Applied Medical Informatics, 2011, vol. 28, pp. 1-10.

[14] A. R. Kiselev, A. S. Karavaev, V. I. Gridnev, et al. “Method of estimation of synchronization strength between low-frequency oscillations in heart rate variability and photoplethysmographic waveform variability”. Russ. Open Med. J., 2016, vol. 5, p. e0101.

[15] A. R. Kiselev, V. I. Gridnev, M. D. Prokhorov, et al. “Evaluation of five-year risk of cardiovascular events in patients after acute myocardial infarction using synchronization of 0.1-Hz rhythms in cardiovascular system”. Ann. Noninvasive Electrocardiol., 2012, vol. 17, pp. 204-213.

[16] V. S. Khorev, A. S. Karavaev, E. E. Lapsheva, et al. “Estimation of delay times in coupling between autonomic regulatory loops of human heart rate and blood flow using phase dynamics analysis”. The Open Hypertension Journal, 2017 , vol. 9, pp. 16-22.

[17] H. Selye. “Stress and disease”. Science, 1955, vol. 122, pp. 625-631.

Choosing parameters for the analysis of synchronization of the autonomic regulatory contours of blood circulation in newborns

Viktoriia V. Skazkina
Department of Dynamic Modeling and Biomedical Engineering
Saratov State University
Saratov, Russia
skazkinavv@yandex.ru

Elena N. Mureeva
Department of Innovative Cardiological Information Technology, Institute of Cardiological Research
Saratov State Medical University
Saratov, Russia
elena040493@mail.ru

Anatoly S. Karavaev
Laboratory of Nonlinear Dynamics Modelling
Saratov Branch of the Institute of RadioEngineering and Electronics of Russian Academy of Sciences
Department of Innovative Cardiological Information Technology, Institute of Cardiological Research
Saratov State Medical University
Department of Dynamic Modeling and Biomedical Engineering
Saratov State University
Saratov, Russia
karavaevas@gmail.com

Anton R. Kiselev
Department of Innovative Cardiological Information Technology, Institute of Cardiological Research
Saratov State Medical University
Department of Dynamic Modeling and Biomedical Engineering
Saratov State University
Saratov, Russia
antonkis@list.ru

Ekaterina I. Borovkova
Laboratory of Nonlinear Dynamics Modelling
Saratov Branch of the Institute of RadioEngineering and Electronics of Russian Academy of Sciences
Department of Innovative Cardiological Information Technology, Institute of Cardiological Research
Saratov State Medical University
Department of Dynamic Modeling and Biomedical Engineering
Saratov State University
Saratov, Russia
rubanei@mail.ru

Olga S. Panina
Department of Innovative Cardiological Information Technology, Institute of Cardiological Research
Saratov State Medical University
Saratov, Russia
olga.panina.74@mail.ru

Yurii M. Ishbulatov
Laboratory of Nonlinear Dynamics Modelling
Saratov Branch of the Institute of RadioEngineering and Electronics of Russian Academy of Sciences
Department of Innovative Cardiological Information Technology, Institute of Cardiological Research
Saratov State Medical University
Department of Dynamic Modeling and Biomedical Engineering
Saratov State University
Saratov, Russia
ishbulatov95@mail.ru

Yulia V. Popova
Laboratory of Nonlinear Dynamics Modelling
Saratov Branch of the Institute of RadioEngineering and Electronics of Russian Academy of Sciences
Department of Innovative Cardiological Information Technology, Institute of Cardiological Research
Saratov State Medical University
Saratov, Russia
doctorup@mail.ru

***Abstract*—In this paper, we studied the features of the autonomic regulatory system of the heart rate and the tone of the arteries in newborns. During the experiment, we obtained 15 records of synchronous electrocardiograms and photoplethysmograms of newborns. A spectral analysis was conducted, the results of which revealed a number of features, including the presence of an LF peak at a lower frequency than is common in adult subjects. Based on these results, we have chosen new parameters to assess the degree of synchronization of the autonomic regulatory contours of the blood circulation in newborns, which contribute to the greater significance of the results.**

***Keywords*—autonomic regulatory system, blood circulation, newborns**

I. INTRODUCTION

Recently, more and more attention has been attracted to methods of analyzing functional diagnostics of body systems. In turn, the state and degree of interaction between the subsystems of the regulation of the cardiovascular system (CVS) is a sensitive indicator, reflecting the degree of development of various pathologies both in the CVS and in the organism as a whole [1-5]. So, the method of estimating the degree of synchronization of the contours regulating blood circulation with characteristic frequencies of about 0.1 Hz has proven itself in practice [2-7]. When analyzing the state of the autonomous system of blood circulation regulation, special attention should be paid to the choice of method parameters, including the need to correctly determine the frequency ranges related to the influence of the sympathetic regulation system. This issue is important because the authors of this work, as well as other colleagues have identified features of the interaction of regulation systems in newborns, which makes it impossible to use the recommended methods of analyzing signals from adult patients with standard parameters and requires their correction in order to analyze the condition of this category of patients as newborns and children [9-10].

II. MATERIAL AND METHODS

In a study of the features of the autonomic regulation of blood circulation in newborns, we conducted a series of experiments and carried out 15 records of electrocardiogram and photoplethysmogram signals during the first 3 days after birth. The ECG was a signal recording in 1 lead, the sensor of the signal of the PPG was placed on the head of the newborn. For the analysis of heart rate variability, a sequence of RR intervals (cardiointervalogram - CIG) was extracted from the ECG signal.

Analyzing the power spectrum of CIG and PPG signals in newborns, we determined the LF-peak, mainly associated with the influence of the sympathetic system, in lower frequency range (about 0.04-0.1 Hz). In adult healthy data, the LF-peak is typically located around 0.1 Hz (the recommended range is 0.04-0.15 Hz) [8].

For the method of estimating the degree of synchronization of autonomic regulatory contours of heart rate and arterial tone of adult subjects, the experimental signals are pre-filtered by band-pass filters in the range of [0.05-0.15] Hz, which allows to select only those components that are mainly associated with the influence of the sympathetic control loop in adults.

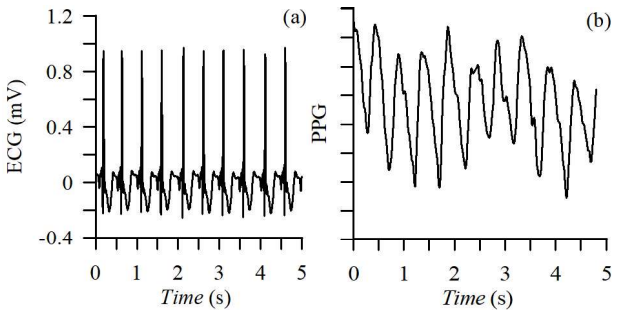

Fig. 1. The typical examples of simultaneous experimental signals for newborn A, duration 5 second: (a) — ECG, (b) — head's PPG.

However, as previously stated, in newborns the LF-peak is observed at a lower frequency than in adults. During the analysis of the degree of synchronization of the circuits of the sympathetic regulation of blood circulation in newborns, two filtration bands were chosen: 0.05-0.15 Hz and 0.04-0.1 Hz. The tables below show values of the total percentage of phase synchronization for all subjects, along with the level of

TABLE I. THE VALUES OF THE TOTAL PERCENTAGE OF PHASE SYNCHRONIZATION BETWEEN CONTOURS OF THE AUTONOMIC REGULATION OF HEART RATE AND VASCULAR TONE IN NEWBORN

№	**Filtration band [0.05-0.15] Hz**		**Filtration band [0.04-0.1] Hz**	
	S (%)	***p***	***S (%)***	***p***
1	33.16	0.06	34.30	0.81
2	25.15	0.23	40.68	0.37
3	27.37	0.46	46.18	0.35
4	14.21	0.94	31.33	0.88
5	22.80	0.83	34.29	0.90
6	19.51	0.63	50.41	0.10
7	17.22	0.82	31.55	0.65
8	13.07	0.95	28.55	1.00
9	19.97	0.86	33.14	0.76
10	24.06	0.51	**57.91**	**0.02**
11	23.03	0.53	**78.19**	**0.01**
12	18.32	0.84	20.43	0.92
13	18.40	0.74	24.84	0.89
14	16.37	0.83	**55.17**	**0.04**
15	**45.47**	**0.01**	33.26	0.59

significance for the two filtering options.

It should be noted that when selecting the shifted filtering band [0.04-0.1] Hz, the number of significant values of the total percentage of phase synchronization increases — *S* (20% significant for the [0.04-0.1] Hz band and 7% significant for the [0.05-0.15] Hz band).

The average value of *S* is equal to 40.01 at the [0.04-0.1] Hz band and 22.54 at the [0.05-0.15] Hz band.

III. RESULTS

Based on the obtained results on the shift of the LF-peak to a lower frequency range, we have chosen new parameters for estimating the degree of phase synchronization of the autonomic regulation of heart rhythm and vascular tone in newborns. The selection of new filtration band [0.04-0.1] Hz increases the significance of the results.

ACKNOWLEDGMENT

This study was funded by the Grant of President of Russian Federation for support of young scientists MK-2492.2019.8 and carried out within the framework of the state task.

REFERENCES

[1] R. Kiselev, V. I. Gridnev, M. D. Prokhorov, A. S. Karavaev, O. M. Posnenkova, V. I. Ponomarenko, and B. P. Bezruchko, "Effects of antihypertensive treatment on cardiovascular autonomic control: a prospective study", Anadolu Kardiyoloji Dergisi, vol. 14(8), pp. 701-710, 2014.

[2] R. Kiselev, V. I. Gridnev, M. D. Prokhorov, A. S. Karavaev, O. M. Posnenkova, V. I. Ponomarenko, B. P. Bezruchko, and V. A. Shvartz, “Evaluation of five-year risk of cardiovascular events in patients after acute myocardial infarction using synchronization of 0.1-Hz rhythms in cardiovascular system”, Annals of Noninvasive Electrocardiology, vol. 17(3), pp. 204-213, 2012.

[3] A. Shvartz, A. S. Karavaev, E. I. Borovkova, S. A. Mironov, V. I. Ponomarenko, M. D. Prokhorov, Yu. M. Ishbulatov, E. E. Lapsheva, V. I. Gridnev, and A. R. Kiselev, “Investigation of statistical characteristics of interaction between the low-frequency oscillations in heart rate variability and photoplethysmographic waveform variability in healthy subjects and myocardial infarction patients”, Russian Open Medical Journal, vol. 5(2), pp. e0203, 2016.

[4] R. Kiselev, V. A. Shvartz, A. S. Karavaev, S. A. Mironov, V. I. Ponomarenko, V. I. Gridnev, and M. D. Prokhorov, “Correlations between cardiovascular autonomic control indices during the two-hour immobilization test in healthy subjects”, The Open Cardiovascular Medicine Journal, vol. 10, pp. 35-43, 2016.

[5] R. Kiselev, V. I. Gridnev, M. D. Prokhorov, A. S. Karavaev, O. M. Posnenkova, V. I. Ponomarenko, and B. P. Bezruchko, “Selection of optimal dose of beta-blocker treatment in myocardial infarction patients basing on changes in synchronization between 0.1 Hz oscillations in heart rate and peripheral microcirculation”, Journal of Cardiovascular Medicine, vol. 13(8), pp. 491-498, 2012.

[6] S. Karavaev, M. D. Prokhorov, V. I. Ponomarenko, A. R. Kiselev, V. I. Gridnev, E. I. Ruban, and B. P. Bezruchko, “Synchronization of low-frequency oscillations in the human cardiovascular system”, CHAOS, vol. 19, pp. 033112, 2009.

[7] R. Kiselev, V. I. Gridnev, A. S. Karavaev, O. M. Posnenkova, M. D. Prokhorov, V. I. Ponomarenko, and B. P. Bezruchko, “The dynamics of 0.1 Hz oscillations synchronization in cardiovascular system during the treatment of acute myocardial infarction patients”, Applied Medical Informatics, vol. 28(1), pp. 1-8, 2011.

[8] “Heart rate variability: Standards of measurement, physiological interpretation and clinical use. Task Force of the European Society of Cardiology and the North American Society of Pacing Electrophysiology”, Circulation, vol. 93(5), pp. 1043-1065, 1996.

[9] Patzak, K. Lipke, W. Orlow, R. Mrowka, H. Stauss, E. Windt, P. B. Persson, and E. Schubert, “Development of heart rate power spectra reveals neonatal peculiarities of cardiorespiratory control”, Am J Physiol, vol. 271(2), pp. R1025-32, 1996.

[10] O. S. Panina, A. R. Kiselev, E. I. Borovkova, Yu.V. Chernenkov, V. V. Skazkina, V. I. Gridnev, E. N. Mureeva, and A. S. Karavaev, “Peculiarities of heart rate variability in newborns”, Rossiyskiy Vestnik Perinatologii i Pediatrii (Russian Bulletin of Perinatology and Pediatrics), vol. 63(4), pp. 52-57, 2018.

Slow trends in the degree of synchronization of the elements of autonomous control of blood circulation in healthy subjects

Viktoriia V. Skazkina
Department of Dynamic Modeling and Biomedical Engineering
Saratov State University
Saratov, Russia
skazkinavv@yandex.ru

Yurii M. Ishbulatov
Laboratory of Nonlinear Dynamics Modelling
Saratov Branch of the Institute of RadioEngineering and Electronics of Russian Academy of Sciences
Department of Innovative Cardiological Information Technology, Institute of Cardiological Research
Saratov State Medical University
Department of Dynamic Modeling and Biomedical Engineering
Saratov State University
Saratov, Russia
ishbulatov95@mail.ru

Ekaterina I. Borovkova
Laboratory of Nonlinear Dynamics Modelling
Saratov Branch of the Institute of RadioEngineering and Electronics of Russian Academy of Sciences
Department of Innovative Cardiological Information Technology, Institute of Cardiological Research
Saratov State Medical University
Department of Dynamic Modeling and Biomedical Engineering
Saratov State University
Saratov, Russia
rubanei@mail.ru

Boris P. Bezruchko
Laboratory of Nonlinear Dynamics Modelling
Saratov Branch of the Institute of RadioEngineering and Electronics of Russian Academy of Sciences
Department of Dynamic Modeling and Biomedical Engineering
Saratov State University
Saratov, Russia
bezruchkobp@gmail.com

Anton R. Kiselev
Department of Innovative Cardiological Information Technology, Institute of Cardiological Research
Saratov State Medical University
Department of Dynamic Modeling and Biomedical Engineering
Saratov State University
Saratov, Russia
antonkis@list.ru

Anatoly S. Karavaev
Laboratory of Nonlinear Dynamics Modelling
Saratov Branch of the Institute of RadioEngineering and Electronics of Russian Academy of Sciences
Department of Innovative Cardiological Information Technology, Institute of Cardiological Research
Saratov State Medical University
Department of Dynamic Modeling and Biomedical Engineering
Saratov State University
Saratov, Russia
karavaevas@gmail.com

***Abstract*—The work is devoted to the study of the dynamics of assessing the degree of phase synchronization of the contours of the autonomic regulation of blood circulation with characteristic frequencies of about 0.1 Hz using long-lasting electrocardiogram and photoplethysmogram signals of healthy subjects. The main task is to study the effect of humoral regulation and immobilization stress on the work of the studied systems.**

Keywords—phase synchronization, autonomic system, immobilization stress

I. INTRODUCTION

The study of the synchronization of biological objects attracts considerable interest of researchers. In particular, studies of the interaction and synchronization of the elements of the human cardiovascular system have fundamental interest, aimed at developing ideas about the structure of complex systems of biological nature [1-2].

Such studies have also practical importance. For example, we earlier proposed an integral numerical index (the total percentage of phase synchronization) on the basis of the method of diagnosing intervals of phase synchronization for non-stationary signals from the cardiovascular system [3-4]. It was shown that this index is important for solving problems of medical diagnostics of various pathologies [5], predicting the survival of patients after myocardial infarction [6-7], and choosing drugs for treating heart and vascular pathologies [8-9]. Moreover, due to technical, organizational and ethical limitations, most studies were carried out in the analysis of 10 minute recordings of signals from the cardiovascular system and did not consider the effect of signal's duration on the assessment of the synchronization degree of the studied regulatory contours. In our previously published work, we studied synchronous 2-hour recordings of electrocardiogram and photoplethysmogram signals of healthy subjects [10]. We studied the statistical properties of the method for estimating the degree of synchronization of the 0.1-Hz circuits of blood circulatory regulation and found some evidence of the development of immobilization stress. This work is a continuation of the study of long records. In the new series of experiments, the record duration was increased by 2 times, which made it possible to study the dynamics of the synchronization degree of the autonomic control contours at even lower frequencies.

The purpose of this work is to study the assessment of the degree of phase synchronization of the autonomic regulatory contour of heart rate and the contour of baroreflex regulation of arterial vascular tone, which controls a person's average arterial pressure, using long-term (four-hour) records of healthy subjects.

II. Material and Methods

Three conditionally healthy volunteers aged from 19 to 21 years took part in experimental studies. We carried out a simultaneous recording of the electrocardiogram (ECG) and vascular photoplethysmogram (PPG) signal with a sampling frequency of 250 Hz for each volunteer. An infrared sensor (radiation wavelength of about 960 nm) of the reflected light was applied to the distal phalanx of the test subject's right hand.

The experimental data was recorded in a calm atmosphere, the volunteer was in a prone position. The duration of each record was 240 minutes. For the analysis of heart rate variability, RR-intervals (CIG - cardiointervalogram) were isolated from the electrocardiogram signal. Typical examples of experimental signal sections are presented in Fig. 1.

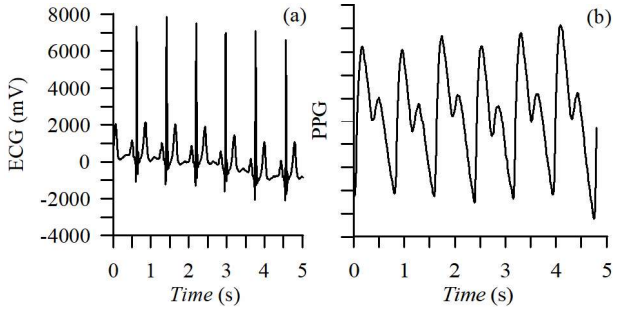

Fig. 1. Examples of the experimental signals of the subject A (a) — ECG, (b) — PPG, taken from the finger of the right hand. The signal of PPG is given in dimensionless units.

At the first stage of the analysis of the synchronization of the studied regulation processes using our developed method the intervals of phase synchronization were determined throughout the entire recording duration. In Fig. 2 shows a typical dependence of the lengths of synchronous intervals (Duration, s) on time by the example of test A and B. The maximum length of the phase synchronization interval was 108 s.

A study was conducted aimed at identifying changes in the statistical properties of the calculated values during the recording, which could lead to a potential trend of S in healthy subjects during experimental observations. To analyze the nature of the calculated S, we calculated the dependence of the averaged median values of the total percentage and the values of the first, third quartile on the recording time for all experimental data. This information is presented in Fig. 3. The values of the total percentage of phase synchronization were estimated in non-overlapping windows with a length of 1000 seconds. The graph also shows the presence of fluctuations S, a decrease and an increase in the trend value in the second part of the records (due to last 2 hours).

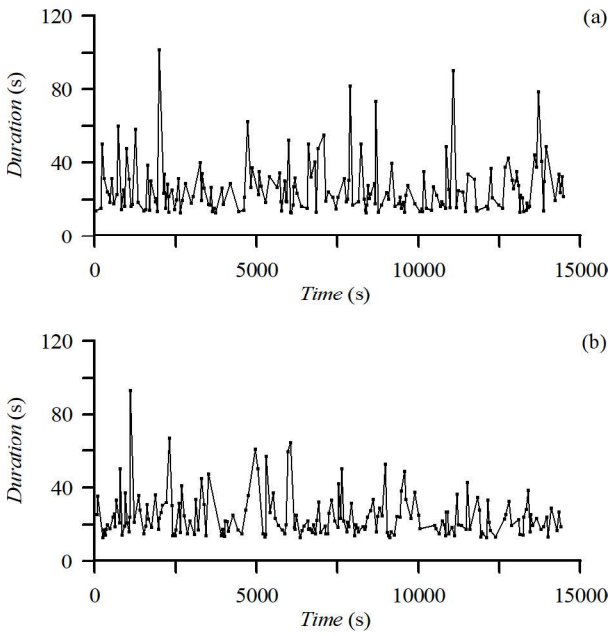

Fig. 2. The dependence of the duration of synchronous intervals on time to subjects A and B.

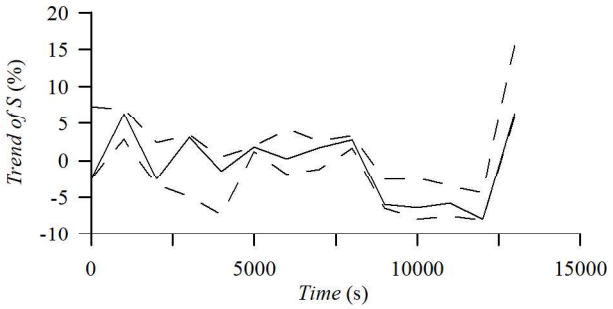

Fig. 3. Dependence of the median of the *S* values over the entire records on time (solid line) and the first and third quarters of the *S* values (dashed lines).

III. Results

The results obtained (Fig. 2) indicate that the sequence of the durations of the phase synchronization intervals show signs of a weakly correlated random process.

This also confirms the conclusions made in [10] that there are no pronounced slow periodic components depending on S.

The results of the statistical analysis of the trend S indicate that the value of S fluctuates over time, especially note a decrease, and then a sharp increase in synchronization in the fourth hour of the experiment may indicate signs of immobilization stress and confirms the results obtained in [10-11] .

Acknowledgment

This study was funded by the Russian Science Foundation, Grant No. 19-12-00201.

References

[1] M. G. Rosenblum, J. Kurths, A. Pikovsky, C. Scaefer, P. Tass, and H.-H. Abel, "Synchronization in noisy systems and cardiorespiratory interaction", Engineering in Medicine and Biology, vol. 17(6), pp. 46-53, 1998.

[2] L. Bernardi, A. Radaelli, P. L. Solda, A. J. S. Coats, M. Reeder, A. Calciati, C. S. Garrard, and P. Sleight, "Autonomic control of skin microvessels: assessment by power spectrum of photoplethysmographic waves", Clinical Science, vol. 90, pp. 345-355, 1996.

[3] S. Karavaev, M. D. Prokhorov, V. I. Ponomarenko, A. R. Kiselev, V. I. Gridnev, E. I. Ruban, and B. P. Bezruchko, "Synchronization of low-frequency oscillations in the human cardiovascular system", CHAOS, vol. 19, pp. 033112, 2009.

[4] R. Kiselev, A. S. Karavaev, V. I. Gridnev, M. D. Prokhorov, V. I. Ponomarenko, E. I. Borovkova, V. A. Shvartz, Yu. M. Ishbulatov, O. M. Posnenkova, and B. P. Bezruchko, "Method of estimation of synchronization strength between low-frequency oscillations in heart rate variability and photoplethysmographic waveform variability", Russian Open Medical Journal, vol. 5(1), pp. 0101, 2016.

[5] R. Kiselev, V. I. Gridnev, A. S. Karavaev, O. M. Posnenkova, M. D. Prokhorov, V. I. Ponomarenko, and B. P. Bezruchko, "The dynamics of 0.1 Hz oscillations synchronization in cardiovascular system during the treatment of acute myocardial infarction patients", Applied Medical Informatics, vol. 28(1), pp. 1-8, 2011.

[6] R. Kiselev, V. I. Gridnev, M. D. Prokhorov, A. S. Karavaev, O. M. Posnenkova, V. I. Ponomarenko, B. P. Bezruchko, and V. A. Shvartz, "Evaluation of five-year risk of cardiovascular events in patients after acute myocardial infarction using synchronization of 0.1-Hz rhythms in cardiovascular system", Annals of Noninvasive Electrocardiology, vol. 17(3), pp. 204-213, 2012.

[7] A. Shvartz, A. S. Karavaev, E. I. Borovkova, S. A. Mironov, V. I. Ponomarenko, M. D. Prokhorov, Yu. M. Ishbulatov, E. E. Lapsheva, V. I. Gridnev, and A. R. Kiselev, "Investigation of statistical characteristics of interaction between the low-frequency oscillations in heart rate variability and photoplethysmographic waveform variability in healthy subjects and myocardial infarction patients", Russian Open Medical Journal, vol. 5(2), pp. e0203, 2016.

[8] R. Kiselev, V. I. Gridnev, M. D. Prokhorov, A. S. Karavaev, O. M. Posnenkova, V. I. Ponomarenko, and B. P. Bezruchko, "Selection of optimal dose of beta-blocker treatment in myocardial infarction patients basing on changes in synchronization between 0.1 Hz oscillations in heart rate and peripheral microcirculation", Journal of Cardiovascular Medicine, vol. 13(8), pp. 491-498, 2012.

[9] R. Kiselev, V. I. Gridnev, O. M. Posnenkova, M. D. Prokhorov, A. S. Karavaev, V. I. Ponomarenko, and B. P. Bezruchko, "Effects of antihypertensive treatment on cardiovascular autonomic control: a prospective study", Anadolu Kardiyoloji Dergisi, vol. 14(8), pp. 701-710, 2014.

[10] S. Karavaev, V. V. Skazkina, E. I. Borovkova, A. R. Kiselev, V. I. Ponomarenko, D. D. Kulminskiy, V. I. Gridnev, M. D. Prokhorov, and B. P. Bezruchko, "Statistical properties of the phase synchronization index of cardiovascular autonomic control contours", Russian Open Medical Journal, vol.7(4), pp. e0403, 2018.

[11] R. Kiselev, V. A. Shvartz, A. S. Karavaev, S. A. Mironov, V. I. Ponomarenko, V. I. Gridnev, and M. D. Prokhorov, "Correlations between cardiovascular autonomic control indices during the two-hour immobilization test in healthy subjects", The Open Cardiovascular Medicine Journal, vol. 10, pp. 35-43, 2016.

Self-Organized Quasiperiodicity and Multistability in Dynamical Systems of different Nature

Nataliya Stankevich
Dept. of Radio-Engineering and Telecommunications
Yuri Gagarin State Technical University of Saratov
Saratov, Russia
stankevichnv@mail.ru

Evgeny Volkov
Dept. of Theoretical Physics
Lebedev Physical Institute
Moscow, Russia
volkov@td.lpi.ru

Edward Hellen
Department of Physics and Astronomy
University of North Carolina
New-York, USA
ehhellen@uncg.edu

***Abstract*—We present a study of the formation of self-organized quasiperiodicity, as well as multistability in two dynamical systems of different nature. Multistability between torus and synchronized cycles is observed.**

Keywords— quasiperiodic oscillations, multistability, gene regulatory networks

I. INTRODUCTION

Quasiperiodic oscillations represent a kind of oscillations that can be characterized by two or more incommensurable frequencies. This class of oscillations is found in many areas of science and technology [1]. It is the simplest way to implement quasiperiodic oscillations in a non-autonomous system or an ensemble of coupled oscillators. As a rule, the occurrence of quasi-periodic oscillations is associated with a non-identity in the ensemble. With a small frequency detuning or other parameter, synchronization is observed. With an increase in detuning as a result of saddle-node bifurcation limit cycles disappear and quasi-periodic modes occur. On the parameter plane, one can observe the typical Arnold tongues surrounded by quasi-periodic regimes. In systems with a large number of incommensurable frequencies, variation of the parameters responsible for nonidentity leads to the formation of the Arnold resonance web [2].

In papers [3-5], the concept of self-organized quasiperiodicity was introduced. The distinctive property of self-organized quasi-periodicity is that it occurs in ensembles of identical oscillators due to a special choice of the type of coupling. Quasiperiodic dynamics were also found in the system of identical ring oscillators (repressors), with the coupling between them constructed in the same way as the mechanism of the so-called "sense of density" (quorum sensing), which bacteria use to communicate in a growing population [6-7]. Depending on the implementation scheme, such a interaction can lead to diverse collective modes in populations of identical elements. In ensembles of synthetic genetic oscillators, this interaction leads to important applied results. Of interest is that quasiperioidcity of this type tends

to co-exist with multistable resonance cycles. The same properties were observed in a simple radio-physical model of autonomous quasiperiodic oscillations [8]. A set of autonomous quasiperiodic generators was proposed in [9]. In [8], for a generator of this type, the possibility of coexistence of autonomous quasiperiodic oscillations with both periodic cycles and chaotic attractors was shown.

In this work, we will present a study of the details of the formation of self-organized quasiperiodicity, as well as multistability in the above systems: the simplest generator of quasi-periodic oscillations, and two genetic repressilators with quorum-sensing coupling. We provide comparative analysis of the observed phenomenon for models of different nature. First, we describe a relatively simple model of radio-physical generator and then consider the same aspects in the genetic repressilators.

II. The Simplest Radio-Physical Generator

A. Mathematicla model of generator

The generator model is a three-dimensional dynamical system described by the following system of differential equations:

$$\begin{aligned} \dot{x} &= y, \\ \dot{y} &= (z + x^2 - 0.5x^4)y - \omega_0^2 x, \\ \dot{z} &= \mu - x^2 \end{aligned} \qquad (1)$$

This model is a generator with hard excitation hybridized with a generator of relaxation oscillations, which is described by variable z. Formally the system is autonomous, but relaxation oscillations are a kind of external force, which manifests itself as an internal property of the system. Model (1) has a number of features: firstly, it has no equilibrium states, and secondly, it has symmetry with respect to the replacement:

$$(x \to -x,\ y \to -y,\ z \to z). \qquad (2)$$

Let us consider the features of quasiperiodic dynamics and multistability in this model using numerical simulations.

B. Numerical Simulations

In [9] the diversity and richness of the dynamics of model (1) were shown. The tongues of synchronization which is limited only from the one side in the parameter space were presented. In this paper we concentrate on a relatively simple case and consider the model dynamics using as an example the co-existing two-dimensional torus and limit cycle of period-7 limited by two saddle-node bifurcations from both sides on the parameter interval.

Figure 1 shows a fragment of the bifurcation trees near the domain of limit cycle of period-7 (Fig.1*a*) and bifurcation diagram for the limit cycle of period-7 obtained with XPP AUTO (Fig. 1*b*). The trees were constructed with adiabatic initial conditions (which means that for each new parameter value we take the final point of the previous step as the initial conditions for integreation) and different scannng directions of the parameter interval (red and black colors). Thus, we can visualize the co-existence between limit cycle and torus.

Let us discuss the bifurcation tree evolution with decreasing parameter ω_0 (Fig.1*a*, black arrow). For ω_0= 2.95 a two-frequency quasiperiodic oscillations are observed. At $\omega_0 \approx 2.9113$ a limit cycle of period-7 appears as a result of saddle-node bifurcation. In this case limit cycles occur on the torus surface, the invariant curve for this case was described in [8]. Then at $\omega_0 \approx 2.7746$ the limit cycle disappears and the torus emerges again. If the scan direction is reversed (Fig. 1*a*, red arrow), we see that, in addition to the cycle, a two-frequency torus emerges in the system at $\omega_0 \approx 2.8083$. At lower ω_0, the torus coexists with the base limit cycle of period-7. As can be seen from the bifurcation diagram Fig.1*b* the limit cycle of period-7 arises via saddle-node bifurcations (*LP*).

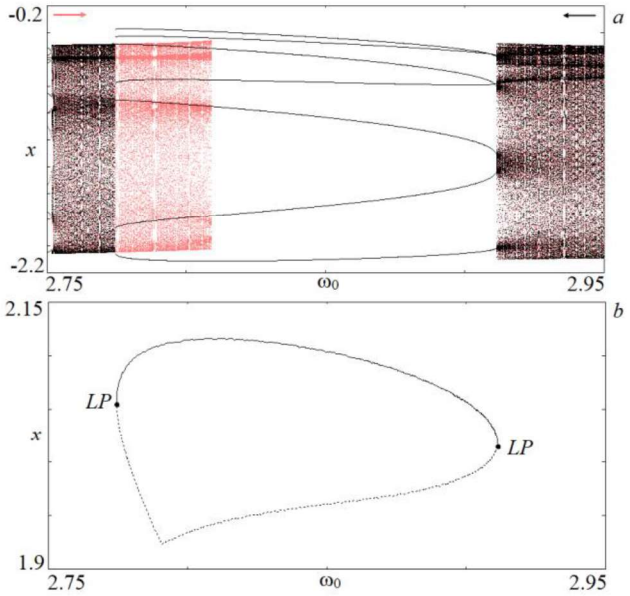

Fig. 1. Bifurcation diagrams of model (1) for μ=0.7. *a*) numerical integration with different scanning of parameter interval; *b*) diagram obtained with XPP AUTO for limit cycle of period-7. *LP* are points of saddle-node bifurcations.

Numerical bifurcation analysis allows us to identify the bifurcations of the cycles; however, only direct numerical integration can be used to locate and analyze the torus. Let us consider the detailed evolution of the Poincaré sections and basins of attractions during torus formation and destruction, taking into account its coexistence with limit cycle.

In [8] we suggested two routes toward torus destruction, one proceeding through synchronization and the other, through crisis of torus. They differ in details of evolution of the torus invariant curve: (i) synchronization on the torus surface is associated with saddle-node bifurcations. When a bifurcation occurs, a pair of limit cycles (stable and unstable) are born. Before bifurcation the phase trajectory is condensed in the vicinity of each fixed point. Thus, before the bifurcation we observe smooth turns of invariant curve near the areas with high density of the phase points; (ii) torus undergoes crisis, which means a collision of the phase trajectory with the basin of attraction of a coexisting regime, or with some unstable cycle. In this case invariant curve breaks down as a result of smoothness loss, and before the crisis sharp bends of the invariant curve are observed.

In Fig. 2, the phase portraits of limit cycle of period-7 (fixed points) and torus (invariant curve) in the Poincaré section are given along with the basins of their attraction (olive) and the basin of torus (grey). Fig. 2*a* corresponds to the value of parameter ω_0 near saddle-node bifurcation point, where torus and limit cycle are co-exist. The torus invariant curve has six smooth-turns. The fixed points of the limit

cycle are situated very close to the boundary of basin of attraction. It means that limit cycle in this case disappears as a result of boundary crisis. In Fig.2b the phase portraits of limit cycle of period-7 and torus in the Poincaré section near the parameter value, at which the co-existing torus disappears. The invariant curve has six sharp bends instead of the seven smooth-turns.The fixed points are located in the center of their basins of attraction. The torus undergoes crisis after the invariant curve touches the basins of attraction of the limit cycles.

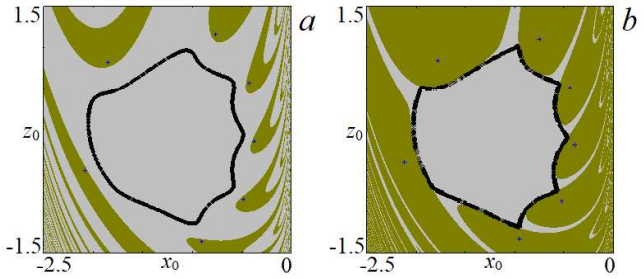

Fig. 2. Phase portaraints in Poincarè section and basins of attraction for co-existing limit cycle of period-7 and two-frequency quasiperiodic regime. μ=0.7, *a*: ω_0=2.7761; *b*: ω_0=2.8083.

III. Two Genetic Represslators with Quorum-Sensing Coupling

A. Mathematical model

We use the reduced version of the model for two three-dimensional repressilators coupled via the production of special signal molecules called "autoinducer". Fig.3 shows the principle scheme of a single repressilator. Here **a**, **b**, **c** are mRNAs, *A*, *B*, *C* are expressed protein repressors. *S* is autoinducer molecule which diffuses through the cell membrane.

The resulting equations for the protein concentrations and the concentration *S* are

$$\begin{aligned}
\dot{A}_i &= \beta_1(-A_i + \frac{\alpha}{1+C_i^n}),\\
\dot{B}_i &= \beta_2(-B_i + \frac{\alpha}{1+A_i^n}),\\
\dot{C}_i &= \beta_3(-C_i + \frac{\alpha}{1+B_i^n} + \frac{\kappa S_i}{1+S_i}),\\
\dot{S}_i &= -k_{S0}S_i + k_{S1}B_i - \eta(S_i - S_{ext}),
\end{aligned} \tag{3}$$

where i = 1,2 for the two repressilators, β_j (j = 1,2,3) are the ratios of the protein decay rate to mRNA decay rate, α accounts for the maximum transcription rate in the absence of an inhibitor, and n is the Hill cooperativity coefficient for inhibition. For the quorum sensing pathway k_{s0} is the ratio of the *S* decay rate to the mRNA decay rate, and as previously mentioned, k_{s1} is the rate of production of *S* and κ gives the strength of *S* activation of protein *C*. The diffusion coefficient η depends on the membrane permeability to the *S* molecule. The concentration of *S* in the external medium S_{ext}

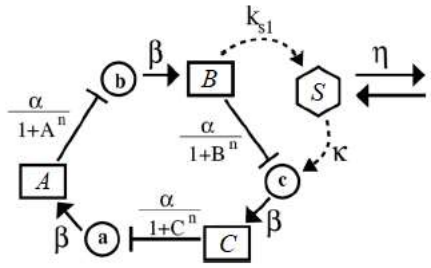

Fig. 3. Principle scheme of repressilator with quorum-sensing feedback.

is determined according to quasi-steadystate approximation by *S* produced by both repressilators (S_1 and S_2) and a dilution factor *Q*:

$$S_{ext} = Q\frac{S_1 + S_2}{2}. \tag{4}$$

The model parameters are fixed in accordance with what was proposed in [7]: β_1 = 0.5, $\beta_2 = \beta_3$ = 0.1, n = 3, k_{S0} = 1, k_{S1} = 0.01, η = 2, κ = 15, α=270. As control parameter, we use the coupling strength *Q*. In [6], it was shown that the coexistence of a torus and a synchronous cycle is possible in model (3).

B. Numerical simulations

In Fig. 4*a* two bifurcation diagrams are presented, constructed with the adiabatic initial conditions, with different scanning directions of the parameter interval. At Q = 0.7618 and Q = 1.0258 we observed the appearance of the symmetric limit cycle with winding numbers 5:5 (Fig. 4*a*), which is not a classical resonance on the torus. For α= 270, the limit cycle of period-5 is continuously stable and coexists with the torus over the extent of the limit cycle.

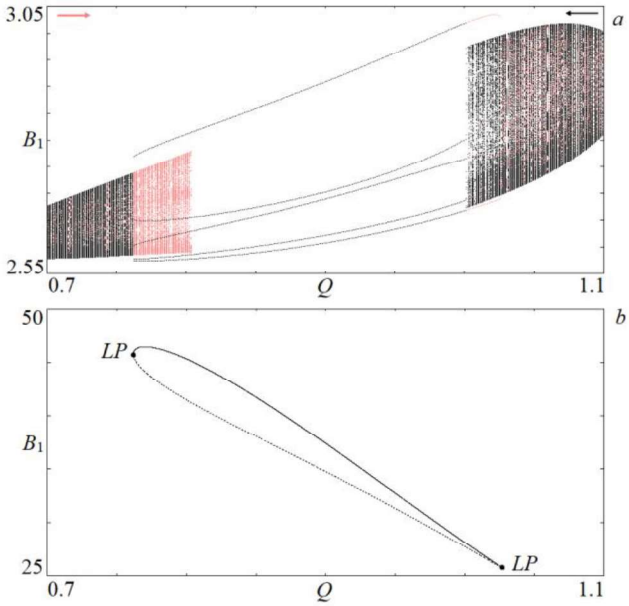

Fig. 4. Bifurcation diagrams of model (3) for β_1 = 0.5, $\beta_2 = \beta_3$ = 0.1, n = 3, k_{S0} = 1, k_{S1} = 0.01, η = 2, κ = 15, α=270. *a*) numerical integration with different scanning directions of parameter interval; *b*) diagram obtained with XPP AUTO for limit cycle of period-5. *LP* are points of saddle-node bifurcations.

In Fig.4*b* bifurcation diagram obtained with XPP AUTO is presented. The limit cycle of period-5 occurs as a result of

saddle-node bifurcations. We also consider a simples case, when limit cycle is stable and doesn't undergo any other bifurcations. As it was for model (1), the coexistence can be observed only within some intervals, however, for model (3) there are two intervals near each point of saddle-node bifurcation.

Let us analyze transformations of the invariant curves near saddle node point and in the area of bistability. In Fig.5 the phase portraits of limit cycle of period-5 (fixed points) and torus (invariant curve) in the Poincaré section are given. Fig. 5*a* corresponds to the value of parameter Q near saddle-node bifurcation point, where torus and limit cycle co-exist. The torus invariant curve has four smooth-turns. Fig.5*b* shows the phase portraits of limit cycle of period-5 and torus in the Poincaré section near point of parameter, where co-existing torus disappears. Invariant curve losses smoothness, and shows five sharp bends instead of the four smooth-turns. The torus undergoes crisis after the invariant curve touches basins of attraction of limit cycles. The structure of the invariant curves near another saddle-node bifurcation point is the same.

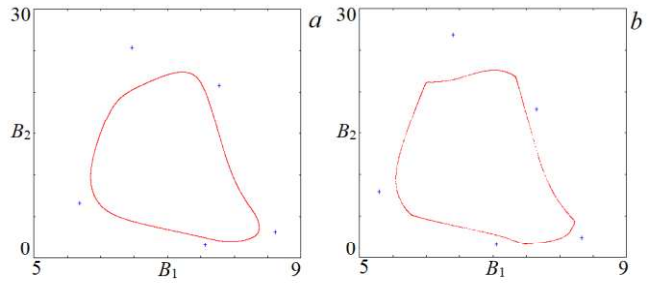

Fig. 5. Phase portaraints in Poincarè section for co-existing limit cycle of period-5 and two-frequency quasiperiodic regime. $\beta_1 = 0.5$, $\beta_2 = \beta_3 = 0.1$, $n = 3$, $k_{S0} = 1$, $k_{S1} = 0.01$, $\eta = 2$, $\kappa = 15$, α=270, *a*: Q=0.8044; *b*: Q=0.7624.

ACKNOWLEDGMENT

The work was carried out with the financial support of the Russian Foundation of Basic Research, grants No. 17-01-00070, No. 19-02-00610.

REFERENCES

[1] P.S. Landa, Nonlinear Oscillations and Waves in Dynamical Systems. Kluwer, Dordrecht, 1996.

[2] N.V. Stankevich, et al., "Exciting Chaotic and Quasi-Periodic Oscillations in a Multicircuit Oscillator with a Common Control Scheme," Technical Physics Letter, vol. 44, No.5, pp. 428-431.

[3] M. Rosenblum, A. Pikovsky, "Self-organized quasiperiodicity in oscillator ensembles with global nonlinear coupling," Phys. Rev. Lett., vol. 98, No.6, 2007, pp. 064101.

[4] Pikovsky, M. Rosenblum, "Self-organized partially synchronous dynamics in populations of nonlinearly coupled oscillators," Physica D: Nonlinear Phenomena, vol. 238, No.1, 2009, pp. 27-37.

[5] M. Rosenblum, A. Pikovsky, "Two types of quasiperiodic partial synchrony in oscillator ensembles," Phys. Rev. E, vol.92, No.1, 2015, pp. 012919.

[6] Ullner, et al., "Multistability and clastering in a population of synthetic genetic oscillators via phase-repulsive cell-to-cell communication," Phys. Rev. Lett., vol.99, 2007, pp. 148103.

[7] E.H. Hellen, E. Volkov, "Flexible dynamics of two quorum-sensing coupled repressilators," Phys. Rev. E, vol.95, 2017, pp.022408.

[8] N.V. Stankevich, E.I. Volkov, "Multistability in a three-dimensional oscillator: tori, resonant cycles and chaos", Nonlinear Dyn. 2018. Vol. 94. No. 4. P. 2455-2467.

[9] A.P. Kuznetsov, S.P. Kuznetsov, E. Mosekilde and N.V. Stankevich, "Generators of quasiperiodic oscillations with three-dimensional phase space," The European Physical Journal Special Topics, vol. 222, No 10, 2013, pp. 2391-2398.

[10]

The emperical mode decomposition for ECG signal preprocessing

Alexander Tychkov
Research Institute for Fundamental and Applied Studies
Penza State University
Penza, Russia
tychkov-a@mail.ru

Alan Alimuradov
Research Institute for Fundamental and Applied Studies
Penza State University
Penza, Russia
alansapfir@yandex.ru

Pyotr Churakov
Data Measuring Equipment and Metrology Department
Penza State University
Penza, Russia
churakov-pp@mail.ru

***Abstract*—Preprocessing of ECG signals allows increasing efficiency and effectiveness of diagnosis of socially significant heart diseases. Development of algorithms and programs for digital processing of ECG signals should ensure preservation of informatively significant components, adaptability to individual features and parameters of a patient, as well as the possibility of using online daily monitoring in mobile systems during human free movement activity. To solve the indicated problems, it is proposed to use the Hilbert-Huang transform, which will allow ensuring the reduction of the level of the most characteristic interference with minimal distortion of the useful component of the ECG signal.**

Keywords—ECG signal; interference; Hilbert-Huang transform; preprocessing

I. INTRODUCTION

Electrocardiogram (ECG) signal is a complexly structured signal consisting of cyclically repetitive pulses, which are combinations of simple impulses of different areas of the heart. Pulses of ECG signal are called waves, and their combinations are called cycles [1].

ECG signal has a structure consisting of three main areas: P wave, QRS complex and T wave. P wave and T wave consist of one or two pulses, and QRS complex can contain

several bipolar pulses [2]. The amplitude and temporal characteristics of the main areas of ECG signal are fairly stable in one patient, but at the same time they may have a large variation of values in other patients. It is associated with individual features of the heart functioning system [3] and the presence of congenital [4] or acquired pathologies [5] in the process of life.

One of the common reasons for ineffective diagnosis of heart diseases, especially in the conditions of daily or multi-day monitoring [6], are interferences different in appearance and intensity [7]. The most characteristic interferences in ECG signals are low frequency (baseline drift and motion artifact shown in Fig. 1), and high frequency (network and muscle interference shown in Fig. 2).

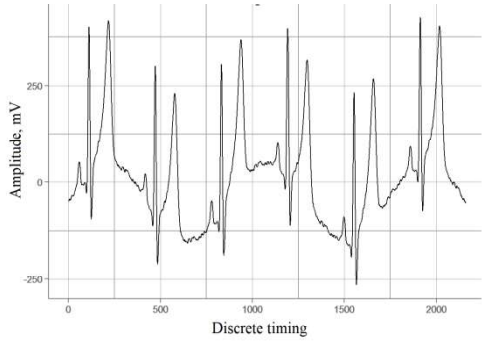

Fig. 1. Low frequency interferences in ECG signal.

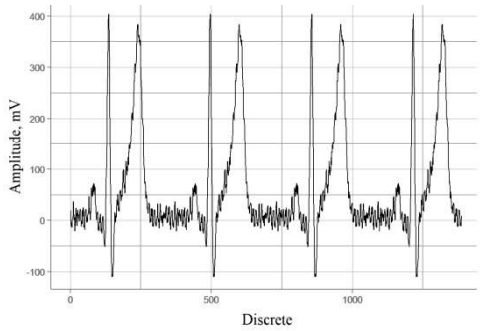

Fig. 2. High frequency interferences in ECG signal.

Effective interference suppression in ECG signals will allow increasing the efficiency of diagnosis of heart diseases. In addition, the technology of signal separation from interferences can be widely applicable in other medical applications, for example, to separate fetal and maternal ECG signals in pregnancy [8].

II. METHODS OF DEVELOPMENT

Despite significant advances in the development of digital data processing methods, there is a problem of their effective implementation related to nonlinearity and non-stationarity of ECG signal, as it's not possible to describe it with a clear analytical function in various time, frequency and energy concepts, and makes it difficult to effectively suppress interferences.

To solve these problems, it is proposed to use the Hilbert-Huang transform (HHT) [9], which will allow ensuring the level reduction of the most characteristic interferences with minimal distortion of the useful component of ECG signal.

The first application of HHT for ECG signal processing was noted in [10] in 2002.

HHT is an integrated approach, which includes the decomposition of ECG signal into amplitude-time components (ATC), and performing of Hilbert spectral analysis (HSA) based on the obtained ATC [9]. A characteristic feature is the signal decomposition only within its extremes at each time point, which does not require the formation of additional analytical functions for the signal under study [11].

III. ANALYSIS OF KNOWN HHT-BASED ALGORITHMS FOR INTERFERENCE SUPPRESSION

An algorithm to remove low-frequency interferences in ECG signals using HHT, carrying out signal decomposition into ATC components, complete removal of individual ATC, corresponding to low-frequency interferences, and reverse restoration of ECG signals, is shown in [12].

The disadvantage of this approach is the removal of the useful component of ECG signal with the complete removal of some ATC. Research results have showed that there is reduction of low-frequency interferences when removing the last three components, but the useful information about the signal is distorted.

According to another algorithm [13], the signal is decomposed into components, one ATC is completely removed and the others are processed with the subsequent recovery of the original signal. Threshold processing in the known method [13] is performed by soft thresholding.

In the known method, ATC with the frequency value which does not exceed 2 Hz, and the threshold processing which does not exceed 30 Hz, are subject to removal. However, in [14], it was proved that from three to five ATC of ECG signal fall into the threshold frequency range from 2 to 30 Hz. It can lead to the selection difficulty of removal or threshold processing of individual components that fall into the specified range.

There is another algorithm [15], the disadvantage of which is the impossibility of simultaneous signal processing for solving problems of robust processing in presence of various high frequency and low frequency interferences. In addition, the known algorithm has limitations concerning duration of the processed original signal (less than 10 s), which is unacceptable for the purposes of long-term online monitoring.

There is an algorithm for ECG signal preprocessing [16], based on the addition of individual ATC, the construction and transformation of the Hilbert spectrum into a binary code, and the calculation of its fractal dimension (FD) [17].

Based on the construction results, the average value of the signal energy is calculated, and the comparison of the obtained value with the threshold value is made, which indicates the presence of high or low frequency interferences in the signal.

The known algorithm is original in terms of detecting interferences but not their suppression in the signal.

The research conducted by the authors of this article regarding the analysis of the amplitude-time components of ECG signal [18] have showed that with the appearance of low-frequency interferences in ECG signal and the subsequent signal decomposition into ATC, new components can be formed that are not characteristic to an ideal ECG signal.

IV. IMPROVING AN ALGORITHM FOR INTERFERENCE SUPPRESSION

To solve the formulated tasks, an original algorithm for ECG signal preprocessing (Fig. 5), based on the allocation of the TP segment of the ECG signal, its decomposition into amplitude-time components and the surface of energy density (SED) using HHT, is proposed.

Let us consider each stage of the algorithm in detail.

Stage 1. Input of the ECG signal is carried out via interface facilities (blocks 1, 2): certified medical devices, a doctor database (DB), and the Internet DB.

Stage 2. The allocation of the TP segment of the ECG signal (block 3) is carried out using the known method [24]. The TP segment is the time period from the end of the T wave to the beginning of the P wave of the next cardiac cycle. During this time period, the electrical activity of the heart is absent. Consequently, the U wave and any other informative signal components are absent in the baseline area [TP/2, P] from the middle of the TP segment to the beginning of the P wave of the next cardiac cycle, and only interferences are present.

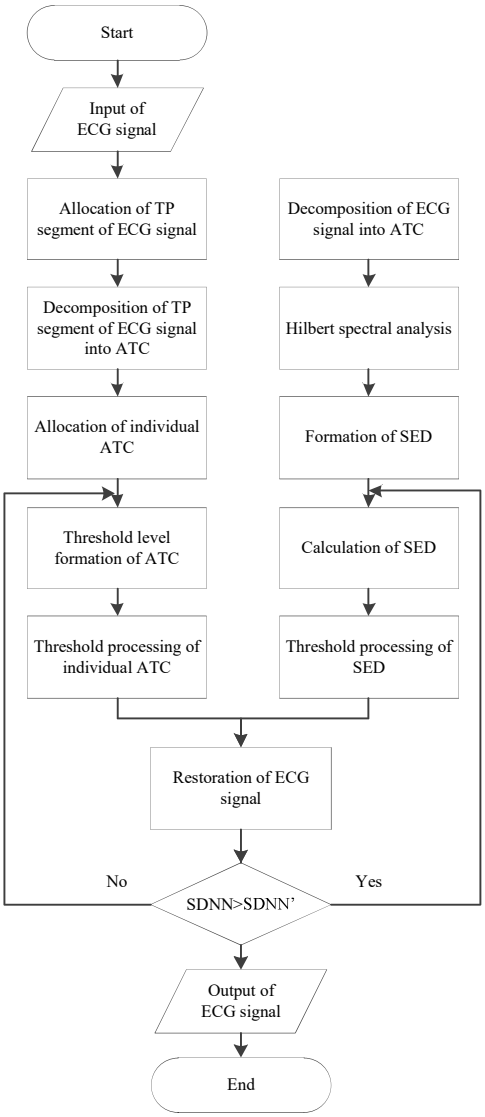

Fig. 3. Algorithm for interference suppression in ECG signal

Stage 3. The decomposition of the ECG signal (block 8) and the TP segment (block 4) into ATC is carried out according to the HHT.

As a result of decomposition of the TP segment of the ECG signal, the final signal envelope is removed from the ECG signal, and the amplitude-time components of the signal are subjected to further analysis to suppress low frequency interferences, which contain frequencies below 30 Hz [13].

Stage 4. Threshold processing of the investigated ECG signal (blocks 9-12) and the TP segment (blocks 5-7). To suppress high frequency interferences in the ECG signal, a volume threshold processing of SED is performed. To do this, the average value of signal energy is calculated:

$$\overline{SED}(t) = \frac{1}{N}\sum_{i=1}^{I} SED(t_i)\cdot$$

Then, the distribution function of the mean value of energy over frequency is calculated:

$$SED(F) = f(\overline{SED}(t))\cdot$$

According to the calculation results of the distribution function of the average value of energy over frequency, a volumetric threshold surface of energy density is constructed:

$$SED_{thr}(t) = \overline{SED}(F)\cdot\Delta t,$$

where Δt is the duration of the ECG signal [t1, tI].

The result of previous calculations is the formed threshold surface.

Stage 5. The ECG signal restoration (block 13), calculation of the level of interferences and the verification of its compliance with the permissible level (block 14) are carried out by determining the statistical criteria. In case of unsatisfactory recovery, there is a change in the cutoff frequency of the filter (blocks 6, 11) and the threshold processing stage of the investigated ECG signal is repeated (blocks 6, 7, 11, 12).

V. EXPERIMENT

To assess the quality of suppression of intensive interferences of various types in ECG signals, it is necessary to use criteria that allow obtaining a calculated characteristic of a difference signal. Such criteria include statistical ones, applied for direct quantitative assessment of interference suppression in the studied signal section at a given signal-to-noise ratio. Statistical criteria for assessing the quality of interference suppression include: SDNN, SDANN, RMSSD, NN50, PNN50, CV, D, As, Ex. A detailed description of these criteria is presented in [20].

Among the above assessment criteria, the standard deviation (SDNN) is the simplest and most sufficient procedure for this case of statistical data analysis/

The calculated SDNN for a signal with high frequency interference is 5%, and it is 8% for a signal with low frequency interference.

Ensuring the effectiveness of interference suppression in ECG signals will lead to an increase in reliable conclusions and an increase in the efficiency of determining BMD signal

markers, especially in patient's free motor activity during long-term monitoring.

VI. CONCLUSION

In the present article, an algorithm for ECG signal preprocessing based on the Hilbert-Huang transform is proposed and developed. It includes the steps of TP segment allocation, decomposition of the recorded signal and TP segment into ATC, threshold processing and SDNN calculation for making a decision that allows reducing the level of the most characteristic high frequency and low frequency interferences to 5 and 8%, respectively. The proposed algorithm can be applied in systems of long-term monitoring, as it is able to make a decision about the level of interferences and intensity of the studied signal.

The Hilbert-Huang transform is capable to perform ECG signal processing recorded with a sampling rate of 500 Hz, with a sliding window of at least 10 s during the period of no more than 8 ms. Therefore, the integrated ECG signal processing is the most promising solution in terms of speed and ensuring a low level of residual interferences in the signal with a minimum level of distortion of useful information.

ACKNOWLEDGMENT

The authors thank the Russian Science Foundation for financial and organizational support of the project "Search for hidden patterns of borderline mental disorders, and the development of a rapid assessment system of human mental health" No. 17-71-20029, 2017-2020.

REFERENCES

[1] V.N. Orlov, Guide to Electrocardiography. Moscow: Medicine, 1984.

[2] A.N. Kalinichenko and O.D. Yuryeva, "Recognition of human psychophysiologic conditions by indices of heart rate variability," Proc. 10th Int. Conf. Pattern Recognition and Image Analysis: New Information Technologies (PRIA-10-2010). St. Petersburg, Russian Federation, December 5-12, 2010, vol. 2, pp. 273-276.

[3] T. Chanwimalueang, W. von Rosenberg, and D.P. Mandic, "Enabling R-peak detection in wearable ECG: Combining matched filtering and Hilbert transform," IEEE Int. Conf. Digit. Signal Process. (DSP). Calgary, Canada, July 2015, pp. 134-138.

[4] T. Tsuda, "Cyanotic congenital heart disease," J Heart Cardiol., 2016, vol. 2(1), pp. 1-5.

[5] Lungand and A. Vahanian, "Epidemiology of acquired valvular heart disease," Can J Cardiol., 2014, vol. 30, no. 9, pp. 962-970. DOI: 10.1016/j.cjca.2014.03.022

[6] F. Agrafioti, ECG in Biometric Recognition: Time Dependency and Application Challenges: University of Toronto, 2011.

[7] M. Blanco-Velasco, B. Weng, and K.E. Barner, "ECG signal denoising and baseline wander correction based on the empirical mode decomposition," Comput Biol Med., 2008, vol. 38, pp. 1-13.

[8] J. Jasper Raj Immanuel, V. Prabhu, V. Jane Christopheraj, D. Sugumar, and Dr. P.T. Vanathi, "Separation of maternal and fetal ECG signals from the mixed source signal using FASTICA," Procedia Engineering, 2012, vol. 30, pp. 356-363.

[9] N.E. Huang, "The empirical mode decomposition and the Hilbert spectrum for nonlinear and non-stationary time series analysis," Proc. R Soc Lond., 1998, pp. 903-995.

[10] Benitez, P.A. Gaydecki, A. Zaidi, and A.P. Fitzpatrick, "The use of Hilbert transform in ECG signal analysis," Comput. Biol. Med., 2001, vol. 31, pp. 399-406.

[11] Z.H. Wu and N.E. Huang, "Ensemble empirical mode decomposition: a noise-assisted data analysis method," Advances in Adaptive Data Analysis, 2009, vol. 1, pp. 1-41.

[12] V.V. Kovtun, R. Dodson, and J.E. Bange, Low Distortion ECG Filter. US Patent 2003/0083583 A1, publ. May 1, 2003.

[13] S. Simake, ECG Filtering. US Patent 2006/0235321, publ. October 19, 2006.

[14] A.Yu. Tychkov, P.P. Churakov, O.N. Bodin, and L.Yu. Krivonogov, Method for Adaptive Noise Suppression in Electrocardiograms. RF Patent 2011147031, publ. October 7, 2013.

[15] R. Heanry, ECG Signal Processor and Method. US Patent 2008/0064971, publ. May 13, 2008.

[16] O.N. Bodin, L.Yu. Krivonogov, A.Yu. Tychkov, and P.P. Churakov, Method for Noise Suppression in Electrocardiogram Signal. RF Patent 2440022 C2, publ. January 20, 2012.

[17] G.N. Dolya, V.K. Ivanov, A.M. Stadnik, and R.E. Pashchenko (Ed.), Fractal Analysis of Processes, Structures and Signals. A collective monograph. Kharkov: EcoPerspective, 2006.

[18] A.Yu. Tychkov and P.P. Churakov, "Application of time-frequency analysis method processing tasks EED," Measurement. Monitoring. Management. Control, 2015, vol. 1, no. 11, pp. 68-72.

[19] A.N. Mitroshin, O.N. Bodin, D.S. Loginov, I.O. Zhulev, and V.V. Proshkin, Method for Isolating the Onset of the Cardiac Cycle, and Device for Its Implementation. RF Patent 2294139, publ. February 27, 2007.

[20] G.R. Arce, Nonlinear Signal Processing: A Statistical Approach. New Jersey: John Wiley & Sons, Inc., Hoboken, 2005.

Designing the neural network for personalization of food products for persons with genetic president of diabetic sugar

Andrey M. Vaskovsky
Department of Information Systems and Technologies
K.G. Razumovsky Moscow State University of technologies and management (the First Cossack University)
Moscow, Russia
mr.helios.a@mail.ru

Marina S. Chvanova
Department of Information Systems and Technologies
K.G. Razumovsky Moscow State University of technologies and management (the First Cossack University)
Moscow, Russia
Department of Mathematical Modeling and Information Technologies
G.R. Derzhavin Tambov State University
Tambov, Russia
tmbtsu@gmail.com

***Abstract*—The article substantiates the relevance of the design of a neural network personalizing food for people with a genetic predisposition to diabetes. Existing models and forecasting methods for solving this problem are considered. When developing an information system for personalizing food products, it is justified that the development focuses on modeling the digital twin of the product and the consumer, as well as defining the technologies that form the basis of a personalized nutrition model to create an accurate, properly functioning system.**

Keywords—neural network, nutrition personalization, susceptibility to diabetes.

I. INTRODUCTION

Currently, the incidence of diabetes has increased significantly, according to the International Diabetes Federation, currently more than 246 million people live in it. In this disease, the pancreas produces an insufficient amount of the hormone insulin, which is necessary for the body to assimilate sugar. Diabetes can develop in obese patients and in older people, who have it more often as a result of stress. In diabetes, nutritional therapy plays an important role, despite the fact that currently there are many medications that reduce blood sugar levels. Proper, rational and carefully balanced diet is a key factor in maintaining a stable systemic compensation of carbohydrate metabolism. When the form of diabetes mellitus is mild, treatment with a diet is generally required. With moderate severity and severe form, therapeutic nutrition should be combined with insulin or other drugs.

Obviously, in the individual selection of food it is necessary to take into account two factors: the effect of food on metabolism and the effect of the genotype on the development of metabolic pathology. And this other knowledge makes sense only in relation to the person to whom recommendations for proper nutrition will be addressed. It is necessary to introduce a food personalization system with the ability to control blood sugar levels. That is why in the modern world the problem of personalizing nutrition for people with a genetic predisposition to diabetes is very relevant.

As a rule, individual nutrition is individual nutritional recommendations aimed at strengthening, maintaining health and preventing diseases. These recommendations take into account the different reactions to individual nutrients that arise as a result of the interaction between nutrients and biological processes. These include interactions between internal factors, such as genetics, microbiomes, metabolic interactions, as well as external factors, such as dietary habits and physical activity.

To understand the basic dynamics of health when considering interpersonal variations and the implementation of personalized interventions related to nutrition, it is important to focus on developing prognostic methods that track a person's health response in a timely manner. A perspective can help doctors adapt targeted treatment, understand the differences in treatment responses, and develop individualized nutritional approaches.

Individual nutritional approaches can initiate the creation of information processing processes for digestion, absorption and metabolism. They provide a link between molecular events and health outcomes through: integrating data of all significant scales; combining multicurrency models with health outcomes using modern machine learning models; generation of non-intuitive hypotheses; experimental testing using preclinical and clinical trials with standardized dietary interventions.

With the advent of big data, you can extract data related to the consumption of standardized products, functional products and beverage sales reports. Medical informatics initiatives can be used to collect and extract data from electronic medical records (EHR) and an insurance claims database. EHR data can be combined with knowledge gained in the field of nutrition and data science to create computational models and synthetic patient groups. These synthetic patients can be used as avatars, which reflect inter-individual variations for preformal predictive analysis and evaluation of the systemic response to personalized nutritional recommendations. These predictive data can be used to determine the complex regulatory mechanisms of food interventions at the border of immunity, metabolism and intestinal microbiome. In general, modern computational

methods and data analysis platforms can help shape healthcare platforms.

The use of artificial intelligence systems for effective decision making in a food personalization system has significant potential. This can significantly reduce the time of normal exercise and the time of choosing food and controlling blood sugar levels. The general idea of using artificial intelligence systems for the food industry was reviewed and reflected in the literature earlier; however, the use of artificial intelligence systems was not considered that way. As a result, it becomes necessary to introduce a system of food personalization using neural network technologies. The scientific novelty of the study lies precisely in the development of a digital food personalization system for people with a genetic predisposition.

II. RESEARCH

A number of scientific publications [1], [2], [3], [4] consider one of the most common forecasting models - an integrated moving average with an external factor (ARIMAX). In work [5] there are more than 100 classes of prediction models. Thus, the intuitive group is used in two cases, if the object of forecasting is very simple or so complex that it is impossible to analyze analytically the influence of external factors. The intuitive group does not develop forecasting models, it reflects the individual judgments of experts regarding the development prospects of the process. This group is based on the mobilization of professional experience and intuition. The methods of the intuitive group are used to analyze the process, the development of which is not amenable to mathematical formalization, the article [6] indicates that such methods include methods of expert assessments, prediction in the image, historical analogies. Currently, the use of expert systems, including the use of odd logic, is widespread [7]. A detailed description of the method of intuitive forecasting is discussed in the article [8]. The review [9] considers models of structural and statistical forecasting. There are also forecasting models for highly specialized tasks. For tasks such as predicting the level of sugar in human blood, models based on differential equations [10] are used, hydrodynamic models [11] are used to predict traffic flow, and models based on nonlinear cells based on external factors are used to predict natural phenomenon. fields that have an internal state that changes over time under the influence of this field [12]. Such models are developed and applied for special systems and processes. In the framework of this work, the last specified class of formalized models is not considered.

Based on the review and comparative analysis of the prediction models, the neural network model was chosen due to its high adaptability, design uniformity, scalability and a wide range of applications.

III. RESULTS OF THE STUDY

When developing an information system for personalizing food for people with a genetic predisposition to diabetes, it is necessary to take into account that the development focuses on modeling the digital twin of the product and the consumer, as well as defining technologies that form the basis of a personalized nutrition model to create an accurate, properly functioning system.

The digital twin is a virtual prototype of a real object, group of objects or processes. This is a complex software product that is created on the basis of a wide variety of data. The digital twin is not limited to collecting data from development projects — it continues to collect and analyze data throughout the entire life cycle of a real object.

In the model of personalized nutrition, a large number of different technologies play an important role, since it is they who ultimately form its basis. To develop such a model, it is necessary to unambiguously identify technologies and their composition.

Food and processing technologies:

- dietary supplements are necessary for a balanced diet, since in most cases a person can receive less of the substances he needs for proper functioning and good health;
- canning technology - designed to process food products to suppress the activity of microorganisms that spoil the products, as well as to increase the shelf life of food products;
- product enrichment - it is necessary to add to the products any missing necessary nutrients and minor components;
- design and construction of products - it is necessary to obtain products that are not only safe for humans, but also their genetic structures, which protect them from the negative impact of the external environment and have healing properties;

Information Technology:

- BigData - tools, approaches and methods for processing huge amounts of data included in the information system of food personalization for people with a genetic predisposition to diabetes;
- personal data protection is necessary to protect consumer data;
- digital twin of the product and the consumer - necessary for virtualization and storage of the product and the consumer in the system.

Service technologies: platform; Delivery; Cooking; escort.

Medical technologies: genomic research; analyzes.

Also in the model of personalized nutrition, it is necessary to remember the individual goals and limitations of the consumer, as they will help to improve the accuracy and functionality of the information system for personalizing food for people with a genetic predisposition to diabetes.

After analysis, it is necessary to form an idea of the model visualization. To begin with, let's write out the main process, which mainly concerns our work, with the help of a special process modeling program - Ramus. The input information model is the consumer's need for personalized nutrition, product information and data on the effects of products and various substances on human health. The governing documents are “Normative-legal acts”, “Regulations of the enterprise” and “Methods of logical inference”. The mechanism used is “Specialist”, “Hardware”, “Software” and “Consumer”.

In order for the model to form the recommended (personalized) food, it is necessary to go through 3 stages:

1. The formation of the digital twin of the consumer, for its further use in the machine logical inference. In order to form a digital twin of a consumer, it is necessary to determine individual limitations of the consumer himself, as a result of which we obtain the values necessary to fill in an electronic medical record. Next, a survey is conducted about the consumer's taste preferences and the identification of his individual goals, to which he aspires. And after all these steps, the data is processed. At the output of such a subprocess, we get a digital analogue of the consumer, which is necessary for the logical inference machine.

2. Formation of a digital twin of a product for its further use in the logical inference machine. Detailing this process is not required, since the formation of the digital twin of the product occurs by entering values into the system database.

3. Inference machine. At this stage, there is a preliminary processing of data obtained from the digital twin of the product and the consumer, and data on the effect of food and various substances on human health. After processing, a trained prediction model is applied to the obtained data, which will be introduced into the digital food personalization system. Next, the forecast results are processed, forming recommendations for nutrition.

When creating medical systems, it is necessary to take into account that the electronic medical record of the patient is not the only category of these systems. There are three categories in total:

- Electronic patient record - this includes what applies to a specific patient. Applications are not limited to keeping patient demographics and patient records.
- Public health information networks — systems of this level abstract away from individual data and aggregate quantitative data from a multitude of patient-oriented systems to predict the development of events such as epidemics and bioterrorism.
- Support for clinical research - this group includes systems for making decisions and modeling drugs.

There is no clear boundary between the categories presented; incoming data is transferred from one to another, processed, supplemented and returned. Using the Health Level 7 (HL7) standard as a database structure will help to store all received messages from any other system.

You can see that RIM is based on 4 main classes: Entity, Role, Participation and Act, and two additional classes for describing relationships: Role Link and Act Relationship. The use of the concept of "class" is connected with the fact that RIM follows the basic principles of inheritance in OOP. The standard clearly states:

- Generalization (generalization) - when the class of the heir includes all the properties of the class of the parent;
- Specialization (specialization) - the class-successor redefines some functions of the parent, and also defines additional properties for even more specialization.

To obtain the required messages, HL7v3 uses the refinement process (refinement process), which leads to the creation of several domain information models (D-MIM) for domains and a set of refined information message models (R-MIM) in each of them. From the R-MIM, following the same rules, get the final description of hierarchical messages (HMD), from which, in turn, messages are built.

Next, you need to describe one of the standards HL7, designed to standardize the structure and ensure the semantic compatibility of medical systems in the exchange of medical information and / or medical documents. This is the standard clinical document architecture (CDA).

The second edition of this standard ensures the availability of seven characteristics of a CDA document, such as:

- the security of the information provided;
- management of the information provided;
- support authentication requirements for all submitted information;
- support of the context of the information provided;
- maintain the integrity of information;
- ability to read information provided by man;
- Support for binary information such as multimedia components, PDF, images and more.

Due to these characteristics, CDA becomes extremely flexible for use in various areas. And, despite the fact that among the developers of medical systems, CDA is considered to be an extremely difficult standard, it has become one of the most successful HL7s designed to integrate medical data. Most medical systems currently encode information in one of nine possible CDA document templates, for example, the Medical Assistance Continuity Document (CCD) is one of these templates.

The Medical Care Continuity Document is an XML-based standard designed to encode the structure and semantics of a patient's medical record for later exchange.

Thus, to create a digital twin model of a consumer, it is necessary to use not only data on individual goals and restrictions of the consumer, but also data from electronic medical records.

As part of the study, the following aspects and processes were reviewed, described, modeled and developed:

- identified problems that may arise in the development of a digital food personalization system;
- an interface has been developed for both users and specialists;
- developed a personalized nutrition model, a digital twin of the product and the consumer;
- describes the database structure of the digital food personalization system for people with a genetic predisposition to diabetes;
- neural network introduced;
- approbation of the model and analysis of the possibilities and limits of its use in practice.

REFERENCES

[1] Boxing J., Jenkins G.M. Time series analysis, forecast and management. M .: Mir, 1974. 406 p.

[2] Norizan M., Maizah Hura A., Zuhaimy I. Short Term Load Forecasting Using Double Seasonal ARIMA Model // Regional Conference on Statistical Sciences, Malaysia, Kelantan, 2010. P. 57 – 73.

[3] Collantes-Duarte J., Rivas-Echeverriat F. Time Series Forecasting usingARIMA, Neural Networks and Neo Fuzzy Neurons // WSEAS InternationalConference on Neural Networks and Applications, Switzerland, 2002

[4] Day-Ahead Electricity Price Forecasting Using the Wavelet Transform and ARIMA Models / A.J. Conejo [at al.] // IEEE transaction on power systems, 2005, Vol. 20, No. 2. P. 1035 – 1042.

[5] Tikhonov E.E. Forecasting in market conditions. Nevinnomyssk, 2006, 221 p.

[6] Normative systems in forecasting the development of the business sector of the economy / L.I. Muratova [et al.] // Management of Economic Systems [electronic resource]. 2009, №20. U

[7] Leonenkov. Fuzzy modeling in MATLAB and fuzzyTECH.SPb: BHW-Petersburg, 2005. 736 p.

[8] Armstrong J.S. Forecasting for Marketing // Quantitative Methods in Marketing. London: International Thompson Business Press, 1999. P. 92 – 119.

[9] Jingfei Yang M. Sc. Power System Short-term Load Forecasting: Thesis for Ph.d degree. Germany, Darmstadt, Elektrotechnik und Informationstechnik der Technischen Universität, 2006. 139 p.

[10] Methods for predicting optimal insulin doses for type I diabetes patients. Review / S.A. Chernetsov [et al.]

[11] Semenov V.V. Mathematical modeling of the dynamics of traffic megalopolis. M .: IPM them. MV Keldysh RAS, 2004. 44 p.

[12] Self-organization in leaky threshold systems: The influence of near-mean field dynamics and its implications for earthquakes, neurobiology, and forecasting / J.B. Rundle [at al.] // Colloquium of the National Academy of Sciences, Irvine, USA, 2002. P. 2514 – 2521

The control of the dynamics of intense electron beams coupled through a common field

Artem Badarin
Neuroscience and cognivite technology Laboratory, Center for Technologies in Robotics and Mechatronics Components
Innopolis University
Innopolis, Russia
Badarin.a.a@mail.ru

***Abstract*— This paper presents the results of a study of the nonlinear dynamics of a system with several electron beams. A review and analysis of the latest results obtained in this area. In this case, the main emphasis in this work is made on controlling the generation characteristics in such a highly nonlinear system. The main dynamic modes typical for this kind of systems are shown.**

Keywords— PIC, non-stationary processes of electron-wave interaction; numerical simulation; optimization; electron-plasma devices;

Introduction

Virtual cathode generators (vircator, reditron, virtod, etc.) are one of the most popular devices in superpowerful beam-plasma microwave electronics and are currently being actively studied [1-11]. One of the main advantages of these devices is the generation of heavy-duty electromagnetic radiation with the extreme simplicity of design. At the same time, this type of microwave devices is characterized by strongly nonlinear dynamics. The disadvantages are low efficiency, usually of the order of one percent, and low generation frequency.

One of the possible mechanisms for increasing the frequency of the generation of vircator systems is to increase the density of the injected electron beam. Recall that the generation frequency of this class of devices is directly proportional to the plasma frequency of the injected electron flow, which is determined by its density. Nevertheless, an increase in the frequency in this way leads to a sharp drop in the generation efficiency, due to the existence of an optimal value of the injected current in all known vircator circuits. What makes it unacceptable to use this method to significantly increase the frequency.

A possible solution to this problem is the development of new oscillator circuits on a virtual cathode. In particular, in [10], the question of the synchronization of several virtual cathodes in the drift space region was studied in detail. At the same time, multipath klystrons are very common. The use of several electrons beams in them in place of one is connected with the aim of improving the grouping and, therefore, efficiency, by reducing the forces of the space charge.

The experimental analysis of such systems causes a number of difficulties associated primarily with the high cost of creating a full-size experimental layout. At the same time, modern numerical methods make it possible to solve these problems with a high degree of accuracy of reliability. Numerical modeling was carried out using the PIC method [12, 13].

Taking into account the peculiarities of such sources of ultrahigh-frequency microwave radiation as devices with a virtual cathode, a circuit is proposed in which the power of each of the oscillating virtual cathodes is added in a common resonator (drift chamber) - a multi-beam vircator circuit in which several beams with supercritical currents are loaded on a common resonator [10]. Such a scheme has shown its effectiveness, in terms of increasing the frequency of generation.

Thus, this work is devoted to the continuation of the study of the processes of interaction of several intense electron flows with supercritical current. In this case, the main emphasis in this work is made on controlling the generation characteristics in such a highly nonlinear system.

Results

When several electron beams with a supercritical current are injected into the general drift space, a Bursianos instability begins to develop in each of the beams, leading to the formation of a virtual cathode (VC).

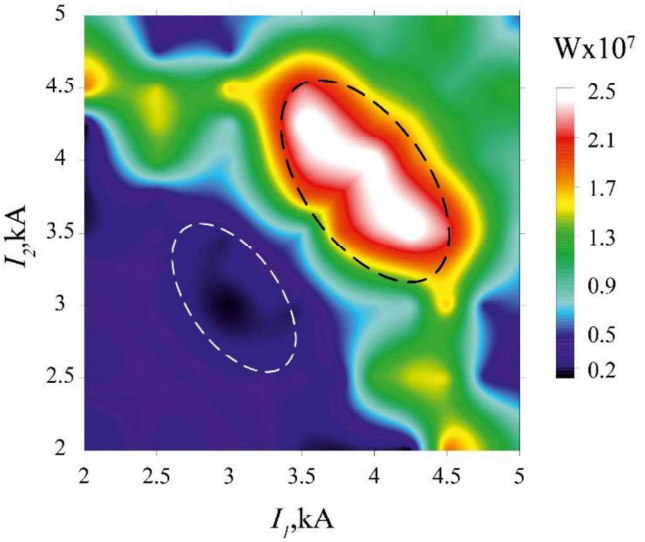

Fig. 1. Dependence of the output power of electromagnetic radiation on the magnitude of the injected currents.

It is well known that the dynamics of a VC is characterized by strong nonlinearity and is determined by the current density [2-4, 13-17]. In the systems under study, electron flows have different current magnitudes. This leads

to the fact that the formed VCs have different temporal and spatial scales, as well as different power of electromagnetic radiation. At the same time, the beams interact with each other through the common field of the drift chamber. In view of the differences in the dynamics of each of the beams and the nonlinear coupling between them, it is possible to implement various collective dynamics modes.

In particular, the interaction of electron flows can lead to synchronization of the oscillations of part of the beams and to an increase in the amplitude of their vibrations. The reverse situation is also possible, namely, desynchronization of VC oscillations and, as a result, suppression of each other's oscillations. Note that it was previously shown that the interaction of several beams due to strong nonlinearity can lead to the randomization of the generated electromagnetic radiation [15].

Figure 1 shows the dependence of the power of electromagnetic radiation on the current value of the injected beams. The black dotted line marks the region characterized by high output power. This area corresponds to the mode of synchronization of oscillations of several VCs. The white dotted line marks the region corresponding to the oscillation desynchronization mode and is characterized by a sharp drop in the output radiation power.

Thus, the control of the oscillation regimes in this system is mainly determined by the ratio between the injected currents.

ACKNOWLEDGMENT

This work has been supported by Russian Foundation for Basic Research (Project 18-32-20135).

References

[6] Booske, J.H. Plasma physics and related challenges of millimeter-wave-to-terahertz and highpower microwave generation / J. H. Booske // Physics of Plasmas. – 2008. – Vol. 15. – P. 055502.

[7] Kurkin, S. A., A. A. Koronovskii, and A. E. Hramov. "Output microwave radiation power of low-voltage vircator with external inhomogeneous magnetic field." Technical Physics Letters 37, no. 4 (2011): 356-359.

[8] Dubinov, Alexander E., Alexey G. Petrik, Semen A. Kurkin, Nikita S. Frolov, Alexey A. Koronovskii, and Alexander E. Hramov. "Beam-plasma instability in charged plasma in the absence of ions." Physics of Plasmas 23, no. 4 (2016): 042105.

[9] Kurkin, S. A., A. E. Hramov, and A. A. Koronovskii. "Nonlinear dynamics and chaotization of virtual cathode oscillations in annular electron beam in uniform magnetic field." Plasma Phys. Rep 35, no. 8 (2009): 628-642.

[10] Shao, H., Liu, G., Yang, Z., Chen, C., Song, Z., & Huang, W. (2006). Characterization of modes in coaxial vircator. Ieee transactions on plasma science, 34(1), 7-13.

[11] Kurkin, S. A., A. A. Koronovskii, and A. E. Hramov. "Formation and dynamics of a virtual cathode in a tubular electron beam placed in a magnetic field." Technical Physics 54, no. 10 (2009): 1520.

[12] Starodubov, A. V., Makarkin, S. A., Galushka, V. V., Pavlov, A. M., Serdobintsev, A. A., Koronovskii, A. A., & Kalinin, Y. A. (2018, April). Higher harmonics generation in low-voltage vircator system. In 2018 IEEE International Vacuum Electronics Conference (IVEC) (pp. 219-220). IEEE.

[13] Kalinin, Y. A., Starodubov, A. V., & Fokin, A. S. (2019). Hybrid Vircator Microwave Oscillator with a Nonlaminar Electron Beam and an Electrodynamic Section. Plasma Physics Reports, 45(8), 770-776.

[14] Parson, J. M., Lynn, C. F., Scott, M. C., Calico, S. E., Dickens, J. C., Neuber, A. A., & Mankowski, J. J. (2015). A frequency stable vacuum-sealed tube high-power microwave vircator operated at 500 Hz. Ieee electron device letters, 36(5), 508-510.

[15] Badarin, A. A., Kurkin, S. A., Koronovskii, A. A., Hramov, A. E., & Rak, A. O. (2018). Processes of virtual cathodes interaction in multibeam system. Physics of Plasmas, 25(8), 083110.

[16] Frolov, N. S., Kurkin, S. A., Khramova, M. V., Badarin, A. A., Koronovskii, A. A., Pavlov, A. N., & Hramov, A. E. (2016, April). Perspective sub-THz powerful microwave generator" nanovircator" for T-rays biomedical diagnostics. In Saratov Fall Meeting 2015: Third International Symposium on Optics and Biophotonics and Seventh Finnish-Russian Photonics and Laser Symposium (PALS) (Vol. 9917, p. 991721). International Society for Optics and Photonics.

[17] Birdsall, C.K. Plasma physics via computer simulation / C.K. Birdsall, A.B. Langdon – Taylor and Francis Group, 2005.

[18] Kurkin, S. A., Badarin, A. A., Koronovskii, A. A., Frolov, N. S., & Hramov, A. E. (2018). Modeling instabilities in relativistic electronic beams in the CST particle studio environment. Mathematical Models and Computer Simulations, 10(1), 59-68.

[19] Egorov, E. N., A. A. Koronovskii, S. A. Kurkin, and A. E. Hramov. "Formation and nonlinear dynamics of the squeezed state of a helical electron beam with additional deceleration." Plasma Physics Reports 39, no. 11 (2013): 925-935.

[20] Badarin, A. A., Kurkin, S. A., Frolov, N. S., Selskii, A. O., Hramov, A. E., & Koronovskii, A. A. (2018). Analyzing Complex Dynamic Modes in Different Modifications of Relativistic Generators on a Virtual Cathode. Bulletin of the Russian Academy of Sciences: Physics, 82(11), 1456-1460.

[21] Badarin, A. A., Kurkin, S. A., & Hramov, A. E. (2015). Multistability in a relativistic electron beam with an overcritical current. Bulletin of the Russian Academy of Sciences: Physics, 79(12), 1439-1442.

[22] Badarin, A. A., Kurkin, S. A., Koronovskii, A. A., & Hramov, A. E. (2015). The effect of the conductivity of drift chamber walls on the dynamics of a relativistic electron beam with a virtual cathode. Technical Physics Letters, 41(12), 1148-1151.

Influence of the sensory information ambiguity on the brain state during the decision-making task

Alexander Kuc
Patent and license department,
Saratov State Technical University,
Saratov, Russia,
kuc1995@mail.ru

Vladimir Nedaivozov
Neuroscience and Cognitive Technology Laboratory,
Center for Technologies in Robotics
and Mechatronics Components,
Innopolis University
Innopolis, Republic of Tatarstan, Russia

Abstract*— The process of visual information classification includes different states of brain activity, such as sensory processing and decision-making. The stage of sensory processing is usually short and occurs in the occipital and parietal areas of the brain, while the decision-making stage is more pronounced over time and includes the parietal and frontal areas. In the current paper, we consider the brain activity during the classification task using ambiguous visual stimuli with varying degrees of ambiguity. We show that with increasing ambiguity of the visual stimulus, the brain engages neuronal populations in the distributed cortical regions in 15-30 Hz frequency band, including the frontal area at the early stages of information processing.

Keywords*— classification task, cortical network, wavelet analysis.

Introduction

The task of visual information classification includes two steps: sensory processing and decision-making [1]. The decision-making is associated with the choice of one option from a set of alternatives based on available sensory data. To make a decision, the received sensory information must be processed and interpreted.

The processes of sensory processing and decision-making are actively studied in rodents and monkeys using implanted microelectrodes [2]. In this paper, we analyze these processes in the human brain using noninvasive electrical activity recordings. The recent review [3] highlights the important role of large-scale cortical interactions in human perceptual decision-making. At the same time, according to a recent review [4], most studies have focused on a limited number of recording sites and therefore the current understanding of how different areas coordinate sensory processing decision-making in the brain is limited.

In the paper we consider the classification task implying classification of bistable visual stimuli with varying degrees of ambiguity. It is clear that increasing the ambiguity of the visual stimulus affects the complexity of the decision. However, it is unclear how the change of ambiguity affects the neural activity dynamics of the brain at the stage of sensory processing.

We focus on the beta (15-30 Hz) frequency bands, since, on the one hand, it is associated with the processing of visual information, and on another hand, the activity of the beta-band plays an important role in human decision-making.

Materials and Methods

Participants

Ten healthy volunteers, twelve males and eight females, between the ages of 20 and 43 with normal or corrected-tonormal visual acuity participated in the experiments. All of them provided informed written consent before participating. The experimental studies were performed in accordance with the Declaration of Helsinki and approved by the local Research Ethics Committee of the Innopolis University.

Visual task

Necker cube was used as bistable visual stimuli [5]. Visual task consisted in the classification of the sequentially presented ambiguous Necker cubes as left- or right-oriented. The Necker cube [6] is a 2D-image which looks like a cube with transparent faces and visible ribs.

An observer without any perception abnormalities perceives the Necker cube as a bistable 3D-object due to the specific position of the inner ribs. The value g defining a contrast of the three middle ribs is usually used as a control parameter. The values g=1 and g=0 correspond, respectively, to 0 (black) and 255 (white) pixels' luminance of the middle lines. Each Necker cube image drawn by black and gray lines was located at the center of the computer screen on a white background. A red dot drawn at the center of the Necker cube was used to attract the attention of subjects and prevent possible perception shifts due to eye movements while observing the image.

Signal Analysis

To analyze time-frequency structure of EEG signals we used continuous wavelet analysis. Wavelet energy spectrum $E^n(f,t) = \sqrt{W_n(f,t)^2}$ was calculated for each EEG channel in the frequency range $f \in [1, 30]$ Hz. Here, $W_n(f,t)$ is the complex-valued wavelet coefficients calculated as

$$W_n(f,t) = \sqrt{f} \int_{t-4/f}^{t+4/f} X_n(t)\psi^*(f,t)dt, \quad (1)$$

where n = 1, …, N is the EEG channel number (N = 31 is the total number of channels used for analysis). The symbol "*" denotes complex conjugation.

The Morlet wavelet was chosen as the mother wavelet. This wavelet is often used to analyze neurophysiological data [7] is defined as

$$\psi(f,t) = \sqrt{f}\pi^{1/4} e^{j\omega_0 f(t-t_0)} e^{f(t-t_0)^2/2}, \quad (2)$$

where $\omega_0 = 2\pi$ is the parameter of the mother wavelet function.

For beta-frequency band the wavelet amplitude $E_\beta^n(t)$ was calculated via the following equation

$$E_\beta^n(t) = \frac{1}{\Delta f_\beta} \int_{\Delta f_\beta} E^n(f',t)df', \quad (3)$$

where $\Delta f_\beta = 15 - 30$ Hz.

All demonstrations of Necker cubes were divided into two groups in the accordance with image ambiguity:

1. Low ambiguity stimuli, including the Necker cube images with $g \in \{15, 25, 75, 85\}$.
2. High ambiguity stimuli, including the Necker cube images with $g \in \{40, 45, 55, 60\}$.

For each value of g we selected I = 20 presentations of Necker cubes. As the result, for each set of cubes (low ambiguity and high ambiguity) the number of Necker cubes presentations was M = 80.

The values of the wavelet energy (3) calculated for the whole time of the experimental session were then averaged over all M presentations of Necker cubes separately for low ambiguity and high ambiguity images as

$$\langle E_\beta \rangle = \frac{1}{M} \sum_{n=1}^{M} \int_{\tau_i,\gamma_i} E_\beta^n(t')dt'. \quad (4)$$

This value was calculated for each EEG channel. After that, were allocated the time intervals τ and γ, where τ - 500 ms before the Necker cube demonstration, γ – 500 ms after the Necker cube demonstration. Using statistical analysis, we identified EEG channels with the most significant changes. Finally, the difference between the number of channels demonstrating increase and decrease of beta-band energy was calculated for the cubes of high and low ambiguity

Results

We have recorded 31 EEG signals via noninvasive electrodes, arranged according to 10-10 layout during human processing of visual information and solving the visual stimuli classification task.

The spectral energy of EEG was averaged for a set of simple Necker cubes (low ambiguity) and for complex ones (high ambiguity). EEG channels with the most significant changes during processing and classification of visual information were identified and the difference between the number of EEG channels exhibiting increase and decrease of the beta-band spectral power was calculated. This difference is shown in Fig 1 (a) for the cubes with low and high ambiguity. Statistical test (Wilcoxon signed rank test for the related samples) demonstrates the significant change of this difference with the increase of the image ambiguity.

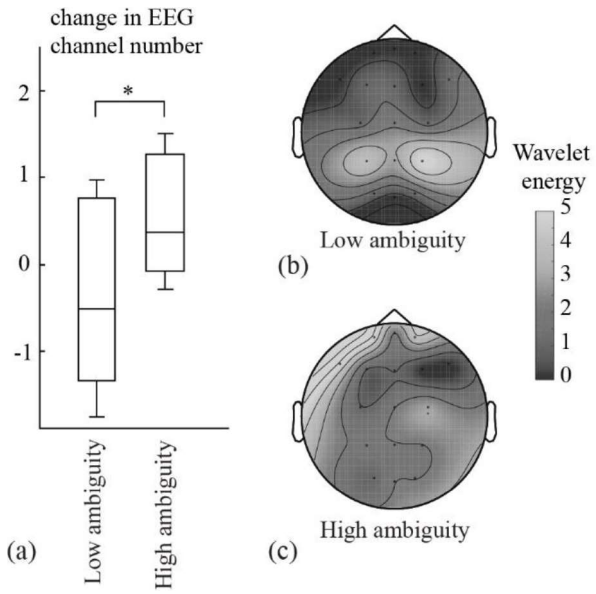

Fig.1. (a) Change of EEG channel number and (b,c) topographical plot of the distribution of EEG spectral power in the beta-band

In Fig. 1 (b, c) the topographical distributions of the beta-band spectral energy are shown for the cubes of low (b) and high (c) ambiguity.

It can be seen, that for the Necker cubes with low ambiguity the beta-band energy increases in the parietal area. For the Necker cubes stimuli with high ambiguity, the beta-band energy increases mostly in the frontal area.

Conclusion

We demonstrate that the spatio-temporal cortical activity in the beta-band during a sensory processing is affected by the ambiguity of visual information.

Acknowledgment

This work is supported by Russian Science Foundation for Basic Research (Grant 18-32-20129) and the President Programm (project MK-992.2018.2). AK thanks the Innovation assistance fund (Ref. 14346GU/2019).

References

[23] H.R. Heekeren, S. Marrett, L.G. Ungerleider, "The neural systems that mediate human perceptual decision making" in Nature reviews neuroscience, vol. 9, 2008, p. 467.

[24] M. Siegel, T. J. Buschman, and E. K. Miller, “Cortical information flow during flexible sensorimotor decisions” in Science vol. 348, 2015, p. 1352 .

[25] M. Siegel, A. K. Engel, and T. H. Donner, “Cortical network dynamics of perceptual decision-making in the human brain” in Frontiers in human neuroscience vol. 5, 2011, p. 21

[26] T. D. Hanks and C. Summereld, “Perceptual decision making in rodents, monkeys, and humans” in Neuron vol. 93, 2017, p. 15.

[27] J. Kornmeier, M. Pfaffle, M. Bach, “Necker cube: stimulus-related (low-level) and percept-related (high-level) EEG signatures early in occipital cortex” in Journal of vision, vol. 11, 2011, p. 12.

[28] L. A. Necker Esq., “LXI. Observations on some remarkable optical phœnomena seen in Switzerland; and on an optical phœnomenon which occurs on viewing a figure of a crystal or geometrical solid,” The London, Edinburgh, and Dublin Philosophical Magazine and Journal of Science, vol. 1, no. 5, pp. 329–337, 1832.

[29] Hramov A. E., Koronovskii A. A., Makarov V. A., Pavlov A. N., Sitnikova E. Wavelets in Neuroscience. Springer Heidelberg New York Dordrecht London, p. 314, 2015.

Trajectory Planning For Biped Walk With Non-instantaneous Double Support Phase

Ramil Khusainov*, Shamil Mamedov*, Popov Dmitry*
Center for Technologies in Robotics and Mechatronics Components, Innopolis University
Innopolis, Russia
Email: * r.khusainov,sh.mamedov,d.popov@innopolis.ru

***Abstract*—In this paper we present a technique for finding periodic gaits for five-link planar bipedal robot with point feet. Unlike most works that are limited to the consideration of only underactuated single support phase (SSP) we show that this phase change condition is state dependant and extend our approach to the presence of double support phase (DSP). The concept of virtual holonomic constraints is used with full set of constraints during SSP and during SSP to DSP change.**

***Index Terms*—five-link biped robot, virtual holonomic constraint, trajectory planning, double support phase**

I. Introduction

The control of planar point contact bipeds as underactuated mechanical systems has been widely studied. Trajectory planning of a biped based on a concept of virtual holonomic constraints [1] and subsequent use of hybrid zero dynamics [2] or transversal linearization [3] allows to investigate orbital stability and design control systems. Parametrization of the virtual constraints allows to choose optimal trajectories in terms of energy consumption or any other cost function.

In most earlier works on the biped robot with point feet trajectory consists of a SSP and an instantaneous switch to the next SSP. However in human like locomotion there is a DSP besides a SSP that improves the stability of robot motion. Furthermore, since in DSP the system is overactuated, it is easier to control robot velocity change in speeding up or slowing down. A few papers considered a DSP for a biped robot with point feet to analyze the influence on stability and time optimality [4], [5]. However these works either are not based on virtual constraints concept, which complicates the further task of orbital stabilization or the full set of physical constraints on SSP and SSP to DSP phase change are not considered.

In this paper, we study the SSP trajectory planning task taking into account the full set of mechanical constraints imposed both during SSP and SSP to DSP phase change moment. Necessary conditions for SSP to SSP transitions are derived. The algorithm to find trajectories with DSP is proposed.

II. Problem Statement

Consider five-link planar biped robot shown in Fig.(1). In general it has seven degrees of freedom (DoF), two of them correspond to position of any point on the robot, for example, point $p_1 = [p_1^x;\ p_1^y]$, which describes position of the robot with respect to inertial frame. While the rest five correspond to angular position of each link, $q = [q_1; \ldots; q_5]$. During walking the robot experiences repetitive SSP, impact and double support DSP. During the SSP the robot is completely defined by q as the stance leg is attached to ground, however has only four actuator (there is no torque applied between ground and the stance leg), therefore the system has underactuation of degree one. During DSP both legs of the robot are attached to ground, thus robot has three DoF and four actuators that makes the system over-actuated, because of that wide range of trajectories can be realized in contrast to SSP. Therefore in this paper we limit our discussion to SSP and impact of the swing leg with ground. The main goal of this paper is to lay out optimization procedure that allows to find the trajectory of the biped during SSP, so that after impact the system enters DSP. The underlying challenge is the presence of underactuation and constraints on torques.

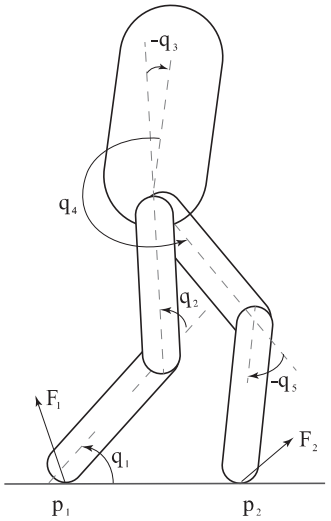

Fig. 1. Schematic drawing of the five-link planar biped robot during the impact

III. Dynamic Model

For dynamic model considered in this paper we have to make the following assumption: the robot is made of five rigid

The reported study was funded by RFBR according to the research project №18-38-00945\18.

links connected by four frictionless and rigid joints. Under this assumption applying Euler-Lagrange method [6] the dynamic model of the robot in SSP is easily obtained

$$D(q)\ddot{q} + C(q,\dot{q})\dot{q} + G(q) = \begin{bmatrix} 0_{1\times 4} \\ I_{4\times 4} \end{bmatrix} \tau, \tag{1}$$

where $D(q)$ is the inertia matrix; $C(q,\dot{q})$ is the Coriolis and Centrifugal matrix; $G(q)$ is the gravity vector; and the matrix on the right hand side, usually denoted as B is input matrix, that has rank four due to underactuation. After SSP when the swing leg contacts the ground an impact occurs that modeled as a contact between two rigid bodies. In the literature, there exist a large number of rigid impact models [7]–[9], and any of them can be used to compute mapping between the generalized velocity just after the impact and generalized velocity and position just before the impact. In this paper we use the model described in [9] that is based on the hypotheses that: the impact is instantaneous; after the impact the swing leg does not slip and stays on the ground; and during the impact the externally applied forces can be represented by impulses.

The derivation of the impact model requires the ground reaction forces at the leg ends, and thus seven- DoF unpinned model of the robot.

$$D_e(q_e)\ddot{q}_e + C_e(q_e,\dot{q}_e)\dot{q}_e + G_e(q_e) = B_e\tau + \delta F_{ext}, \tag{2}$$

By integrating Eq.(2) over the duration of the impact, we obtain

$$D_e(q^+_{e,int})\dot{q}^+_{e,int} - D_e(q^-_e)\dot{q}^-_e = \begin{bmatrix} J^T_{p_1} & 0 \\ 0 & J^T_{p_2} \end{bmatrix} \begin{bmatrix} F_1 \\ F_2 \end{bmatrix}, \tag{3}$$

where J_{p_i} $(i = 1,2)$ is a Jacobian matrix of point p_i; F_i $(i = 1,2)$ is the ground reaction force at point p_i; $\dot{q}^-_e$ is the velocity just before the impact and $\dot{q}^+_{e,int}$ is the velocity just after the impact. Solving together Eq.(3) and velocity constraints at points p_1 and p_2 after the impact, one can obtain $\dot{q}^+_e$, F_i

$$F_1 = \Delta_{F_1}\dot{q}^-, \quad F_2 = \Delta_{F_2}\dot{q}^-, \quad \dot{q}^+_{int} = \bar{\Delta}_{\dot{q}}\dot{q}^- \tag{4}$$

Combined model of SSP and the impact that is of hybrid nature becomes

$$\begin{cases} D(q)\ddot{q} + C(q,\dot{q})\dot{q} + G(q) = Bu, & (q;\dot{q}) \notin \Gamma, \\ q^+_{int} = q^-,\ \dot{q}^+_{int} = \bar{\Delta}_{\dot{q}}\dot{q}^- & (q;\dot{q}) \in \Gamma, \end{cases} \tag{5}$$

where the switching surface is

$$\Gamma = \{(q,\dot{q}) \mid p^x_2(q) = 0,\ p^y_2(q) > 0\}. \tag{6}$$

Notice that if only SSP walking scheme is considered then the angular momentum conservation principle can be applied insted of solving (3). In this case the angular momentum respect to impact point p_2 just before and after collision is conserved. However, commonly it is not mentioned that it is not always possible to realize SSP to SSP change and it depends on the robot state at the moment of collision. Namely, the angular momentum respect to point p_2 before collision is linear function of joint angular velocities and equal to $K_{p_2} = K_{p_1} + \overline{p_2p_1} \times Q = H\dot{q}$, where K_{p_1} is the angular momentum respect to point p_1, $Q = MV_{com}$ is the total linear momentum of the robot. Since after collision K_{p_2} keeps its value, SS to SS transition is realizable only when the sign of K_{p_2} value corresponds to clockwise rotation, that is to moving forward condition. Since K_{p_1} value sign corresponds to the desired direction of rotation, then step length is the parameter which influences the condition of switch between phases. In other words, the bigger the step length, the easier to find trajectory corresponding to SSP to DSP case. Similar result shown for simple compass biped with fixed joint angle [10], where for joint angles more than some certain value SSP to SSP transitions are not possible.

In a classical setting trajectory planning for an underactuated mechanical system boils down to finding $(q^*(t),\ \dot{q}^*(t))$ by solving an optimization problem to obtain feed-forward torques, $U_{ff}(t)$ required to keep the system on the trajectory. There are two main problems associated with this approach. First of all, as state space of the system, $x = [q;\ \dot{q}]$ is large, $x \in \mathbf{R}^{10}$, in addition to constraints, optimization will be very time consuming. Secondly, we assume that the walking of the robot is symmetric and cyclic, therefore it is not important to follow trajectory as a function of time but rather to converge to closest point on the cycle. To overcome these problems we have to introduce kinematic relations between generalized coordinates, usually called virtual holonomic constraints (VHC) [1], [11], [12]. Assume that the angle between the stance leg and the ground q_1 is the generator of motion s, then introduce the following relations

$$q = \Phi(s),\ \dot{q} = \Phi'(s)\dot{s},\ \ddot{q} = \Phi'(s)\ddot{s} + \Phi''(s)\dot{s}^2, \tag{7}$$

where $\phi_i(s)$ can be any function but usually chosen as regular polynomial, Bzier polynomial or trigonometric polynomial of degree n. By substituting (7) into (1) we obtain dynamics written in $(s,\dot{s})$

$$D(s)\Phi'(s)\ddot{s} + \Big(D(s)\Phi''(s) + C(s)\Phi'(s)\Big)\dot{s}^2 + G(s) = Bu \tag{8}$$

In underactuated systems the main challenge is to stabilize passive DoF, whose dynamics for the robot can be obtained by premultiplying both parts of (8) by $B^\perp$ $(B^\perp B = 0)$

$$\alpha(s)\ddot{s} + \beta(s)\dot{s}^2 + \gamma(s) = 0 \tag{9}$$

Resulting dynamics is called reduced dynamics of the system [11], [13] and has set of properties [14] useful for trajectory planning and control design for mechanical systems. Introduction of VHC allows to rewrite dynamics in a form such that new state space of the system, $x_s = [s;\ \dot{s}]$ becomes of dimension two. It greatly reduces search domain of the optimization problem. Moreover, by means of VHC we were able to reparametrize time, therefore solving both problems of "classical" trajectory planning problem for underactuated systems.

IV. Optimization

Initial and final positions of the SSP of the robot can be defined by the following set of parameters: position of the

torso with respect to vertical, σ, vertical position of the hip, p^y_{hip}, step length, L_{step}, and a parameter that defines vertical position of the hip, p^x_{hip}, both in the beginning and in the end of SSP. These parameters allow to uniquely define q^+ and q^-.

In order to get rid of step duration and convert second order differential equation (9) into first order differential equation we introduce $Y(s) = \dot{s}^2$. Reduced dynamics written in terms of $Y(s)$ has the form

$$\alpha(s)\dot{Y}(s) + 2\beta(s)Y(s) + 2\gamma(s) = 0. \tag{10}$$

As optimization requires solving reduced dynamics for each set of parameters, solving first order equation instead of second order facilitates to the reduction of time needed to find optimal trajectory. Optimization parameters are initial velocity of the motion generator, $\dot{s}_0$ and $(m+1)$ coefficients of the $\Phi(s)$. Altogether there are $4\times(m+1)+1$ parameters, P, to optimize. As the posed problem is non-convex with many constraints, we divide it into two subproblems: first one is search for feasible points and the second one is minimization of cost function whether it is cost of transportation (COT), min max of the torques or any other chosen cost. To solve these problems we use MATLAB's built in function *fmincon* with *SQP* solver for finding feasible points and *interior point* for minimization of the cost.

To solve subproblem one we set cost function to zero and try to find parameters, initialized randomly, to satisfy the following constraints on:

- initial and final pose of the robot, $A_{eq}P = [0; q^+; q^-]$;
- angular velocity of the stance leg during SSP, $\dot{s} < 0$;
- GRF of the stance leg during SSP, $F^N_1 > 0$, $\frac{|F^T_1|}{|F^N_1|} < \mu$;
- linear velocity of the swing leg at contact, $v^y_s < 0$;
- GRF at points p_i at the impact, $F^N_i > 0$, $\frac{|F^T_i|}{|F^N_i|} > \mu$;
- angular velocities during SSP, $\dot{q}_{min} < \dot{q} < \dot{q}_{max}$;
- torques, $\tau_{min} < \tau < \tau_{max}$.

Special attention is paid to $F^N_i > 0$ constraints which describe the unilateral nature of contact forces. It turned out that this constraint is a bottleneck for finding trajectories with SSP to DSP transition. Finally by increasing the step length we could eliminate this problem. Once desired number of vectors P are found, second subproblem can be solved by initializing optimization problem at feasible points and minimizing cost function.

V. Conclusion

Planar biped robot motion trajectory search algorithm is presented in the paper with extension to double support phase and utilizing virtual constraints approach. Additional attention is paid on considering the contact force restrictions during SSP to DSP change. Future work will concentrate on DSP continuous dynamics, full cyclic motion and its orbital stabilization.

References

[1] A. Shiriaev, J. W. Perram, and C. Canudas-de Wit, "Constructive tool for orbital stabilization of underactuated nonlinear systems: Virtual constraints approach," *IEEE Transactions on Automatic Control*, vol. 50, no. 8, pp. 1164–1176, 2005.

[2] C. Chevallereau and Y. Aoustin, "Optimal reference trajectories for walking and running of a biped robot," *Robotica*, vol. 19, no. 5, pp. 557–569, 2001.

[3] A. S. Shiriaev, L. B. Freidovich, and S. V. Gusev, "Transverse linearization for controlled mechanical systems with several passive degrees of freedom," *IEEE Transactions on Automatic Control*, vol. 55, no. 4, pp. 893–906, 2010.

[4] M. Scheint, M. Sobotka, and M. Buss, "Virtual holonomic constraint approach for planar bipedal walking robots extended to double support," in *Proceedings of the IEEE Conference on Decision and Control*, 2009.

[5] R. Dehghani, A. Fattah, and E. Abedi, "Cyclic gait planning and control of a five-link biped robot with four actuators during single support and double," 2013.

[6] B. Siciliano, L. Sciavicco, L. Villani, and G. Oriolo, *Robotics: modelling, planning and control*. Springer Science & Business Media, 2010.

[7] R. M. Brach, "Rigid body collisions," *Journal of Applied Mechanics*, vol. 56, no. 1, pp. 133–138, 1989.

[8] V. I. Babitsky, *Theory of vibro-impact systems and applications*. Springer Science & Business Media, 2013.

[9] Y. Hurmuzlu and D. B. Marghitu, "Rigid body collisions of planar kinematic chains with multiple contact points," *The international journal of robotics research*, vol. 13, no. 1, pp. 82–92, 1994.

[10] A. Formalsky, "Moving of the anthropomorphical mechanisms," 1982.

[11] E. R. Westervelt, J. W. Grizzle, C. Chevallereau, J. H. Choi, and B. Morris, *Feedback control of dynamic bipedal robot locomotion*. CRC press, 2018.

[12] M. Maggiore and L. Consolini, "Virtual holonomic constraints for euler–lagrange systems," *IEEE Transactions on Automatic Control*, vol. 58, no. 4, pp. 1001–1008, 2012.

[13] A. Shiriaev, A. Robertsson, J. Perram, and A. Sandberg, "Periodic motion planning for virtually constrained euler–lagrange systems," *Systems & control letters*, vol. 55, no. 11, pp. 900–907, 2006.

[14] A. S. Shiriaev, L. B. Freidovich, and I. R. Manchester, "Can we make a robot ballerina perform a pirouette? orbital stabilization of periodic motions of underactuated mechanical systems," *Annual Reviews in Control*, vol. 32, no. 2, pp. 200–211, 2008.

Vulnerabilities in the vehicle's electronic network equipped with ADAS system

Arthur Kurbanov
Laboratory of autonomous transport system
Innopolis University
Innopolis, Russia
a.kurbanov@innopolis.ru

Sergey Grebennikov
Laboratory of autonomous transport system
Innopolis University
Innopolis, Russia
s.grebennikov@innopolis.ru

Salimzhan Gafurov
Laboratory of autonomous transport system
Innopolis University
Innopolis, Russia
s.gafurov@innopolis.ru

Alexandr Klimchik
Center for Technologies in Robotics and Mechatronics Components
Innopolis University
Innopolis, Russia
a.klimchik@innopolis.ru

***Abstract*—Modern vehicles are distributed systems with numerous Electronic Control Units (ECUs) communicating with each other by means of the standard protocol known as Controller Area Network (CAN-Bus). Such architecture is a basis for Advanced Driver-Assistance Systems (ADAS). ADAS is supposed to take driver's tasks consistently pushing people out of the driving process and decreasing of driver's stress load. Potentially it will result in increasing of vehicles functionality and overall safety on the roads. However, such CAN-bus as a base of ADAS system has a number of significant security limitations. This, the security of such systems plays an important role in their design and operation. This paper gives a brief overview of publications in the field of ADAS systems security. We have conducted a number of experiments on a real car to estimate its vulnerabilities for possible attacks. This article shows how an ADAS-equipped vehicle gives attackers the opportunity to gain control over its critical modules.**

***Keywords*—CAN bus, ADAS, ECU, autonomous vehicle security, car hacking, vulnerabilities**

I. Introduction

ADAS systems usually are represented as separated electronic control units (ECUs) connected via serial buses and communicating with each other with help of a standard protocol called the Controller Area Network (CAN). CAN is a message-based broadcast protocol that runs on two wires: CAN high (CANH) and CAN low (CANL), presenting differential signalling and operating with a bandwidth up to 1 Mb/s. CAN nodes in a vehicle are represented as ECUs that do not send a large block of data; instead, they send short messages with a 64-bit payload. There is no master node in the network because every node initiates sending and arbitration by themselves. Most beneficial features of CAN-bus are message priority defined in its ID and bit-wise arbitration (see CAN message format in Figure 1).

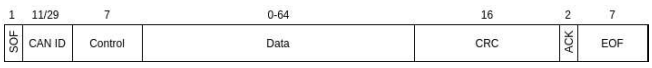

Fig. 1. CAN message format

Methods of protection against sniffing traffic and its spoofing are not built into the CAN protocol, which makes it attractive to intruders. CAN-bus does not have such a security feature as message identification. ADAS-systems interact with important ECUs through the CAN bus, which makes the vehicle highly vulnerable to various attacks.

II. Related works

The potential fragility of the vehicle environment is an urgent topic for research. Several scientific groups were involved in the search for vulnerabilities in vehicles, [1], [2], [3], [4], [5], [6], [7]. In most cases, they address the security issues of the popular CAN bus protocol.

Using wireless and wired physical layer relays, Danev et al. [1] create two attacks that allow an attacker to open and run a car, and to transfer messages between the car and the smart key. They further analyze the critical characteristics of the system.

Charlie Miller and Chris Valasek [2] spoke at the information security conference (DEF CON 22) and made a practical overview of remote attacks on vehicles. Their analysis includes how large the surface of the remote attack on the ECUs and the vehicle features which allow computers to physically control it. In addition, this document describes protection mechanisms, including the intrusion detection and prevention systems.

Phung et al. [4] quite accurately classify cyber attacks on vehicles and the safety-security levels for ECU categories based on remote diagnostics attacks and Firmware updates Over The Air (FOTA) attacks.

Olovsson et al. [6] review a study on the security of a connected vehicle and, in particular, its automotive network. Their goal was to highlight the current state of this situation; identified problems, and what solutions were proposed before. The classification was made into the following five categories: automotive network problems, architectural security functions, intrusion detection systems, lures, threats, and attacks. Also, several areas were identified which, in their opinion, are of immediate concern.

Samuel Woo et al. [7] show that a wireless attack over long distances is physically possible using a real vehicle and a malicious application for smartphones in a related automotive environment. They also proposed a safety protocol for CAN as a countermeasure designed in accordance with the current CAN specifications. Their results show that the proposed security protocol is more efficient than existing security protocols with respect to authentication delay and communication load.

S. Parkinson et al. [8] gives an overview of the most possible attacks on software and hardware of autonomous vehicles and their possible consequences. They tried to answer the question of why

autonomous transport systems are most susceptible to cyber attacks and how to exploit the vulnerabilities in various vehicle sensors.

III. Background

Knowledge of access points and network protocol is necessary to connect to the vehicle CAN. Finding the necessary equipment and utilities that can work with this protocol will be the next step.

A. Vehicle Investigation

The vehicle investigation begins with a search for a data transmission scheme in the official vehicle maintenance repair manual. As a rule, this scheme reflects the number of ECUs with the indication of the connection ports, the data transfer protocol, the information about gateways, the number of isolated buses, bus names, etc. The conceptual diagram of the vehicle network may look like the one shown in Figure 2. Conceptual schemes may vary depending on the manufacturer, but the idea should be clear.

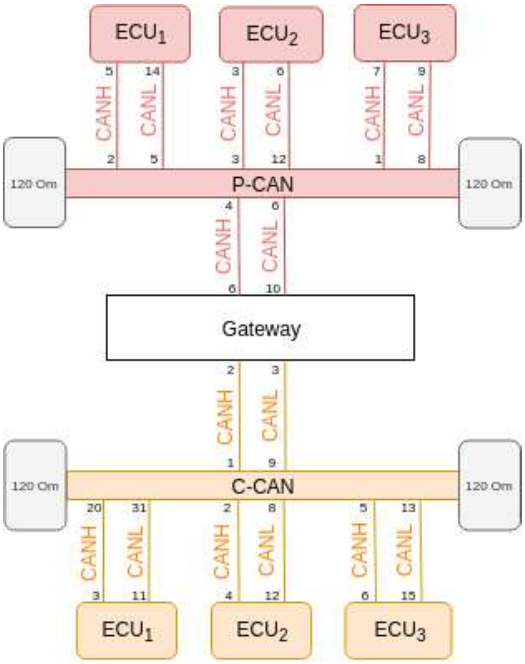

Fig. 2. Conceptual model of an in-vehicle network

To organize physical access to the CAN bus, it is advisable to find a gateway to which various isolated CAN buses are connected, and connect to the desired CAN bus with a CAN device. The Figure 2 shows two buses: P-CAN, which means Powertrain-CAN, and C-CAN, which means Chassis-CAN.

To analyze the network traffic of a CAN bus, there are a few utilities for different operating systems. The following subsections describe which utilities were used in this research.

B. Tools. CAN Devices and Utilities

The choice of the CAN device is dictated by the operating system used and the presence of drivers for it. The authors of the article adhere to open source solutions that are easily integrated with other systems that support the same standard.

At our disposal were two CAN devices: CAN-Hacker and Kvaser. During the tests, the most reliability was shown by Kvaser, the only drawback of which is the price. The operation of these devices was tested in the Linux operating system (Ubuntu 16.04 LTS). For the Linux kernel, the Volkswagen Research Group has developed an open source set of CAN drivers (called SocketCAN) which allows applications to access the CAN bus via the network socket-programming interface. To interact with the CAN network devices, CAN-specific protocols, and the ability to set up a virtual CAN environment the `can-utils` package provides several applications and tools [9].

First of all, in order to understand how the vehicle's embedded systems can be controlled, we have connected to the CAN bus by means of the CAN device and identified which ECUs sent which message by sniffing the bus with `can-utils`.

IV. Practical Attack Experiment

The experiments were carried out on a real car (the brand of which cannot be announced) produced in 2018 with an integrated ADAS system. In this section, the conducted attacks on the wheel steering and acceleration of the vehicle is described.

A. Wheel Steering Attack

On the steering, there are several attack vectors. In some vehicles, the ECU responsible for steering is the MDPS unit. In addition to the direct impact on the Motor Driven Power Steering(MDPS) by the driver, it is possible to influence the system using ADAS systems such as Smart Parking Assist System (SPAS) and Lane Keeping Assist System (LKAS) (see Figure 3).

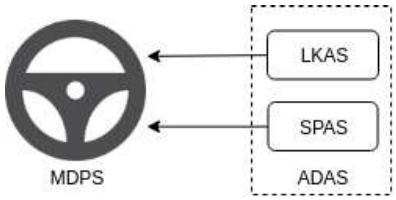

Fig. 3. Steering with LKAS and SPAS

There are several differences between SPAS and LKAS on steering. With SPAS, the steering wheel angle can be set, while LKAS is used to set the torque on the steering wheel. In addition, LKAS can operate at any speed, while SPAS is disabled to operate at a speed of more than 10 km/h. But the SPAS speed limitation can be circumvented by intercepting the package sent from the Engine Control Module (ECM) and spoofing the real speed before sending the packet to the bus.

The above-mentioned systems can be located on the same CAN bus, or, for example, MDPS, SPAS, LKAS are on the C-CAN, and the ECM is on the P-CAN.

B. Acceleration Attack

One of the ECUs that has an accelerating/braking feature is Smart Cruise Control. Figure 4 shows the simplified scheme of components. The Cruise Control module is usually being implemented in the radar unit, thus it turns on and switches to the active mode by related buttons on the steering wheel. Staying active, radar sensor measures all required data as speed, distance and front position of an object. It calculates and sends to the Electronic Stability Control (ESC) the appropriate acceleration and jerk to keep the set speed on or one's distance via C-CAN. Finally, taking management over the brakes and engine, those parameters are applied by ESC.

One should pay attention to curious fact showed on Figure 5: SCC reacts straight after receiving the first "pushed" signal from Cruise button so it's enough only one valid CAN-message from cluster to turn on the Cruise Control. The same thing with turning it to active mode and changing regarded speed.

Hence, there are at least two ways which can entail sudden car acceleration. First, catching and violently sending some cluster messages without unplugging radar unit. Second way implies unplugging radar unit and emulating it messages with accelerating and jerk which intruder wants.

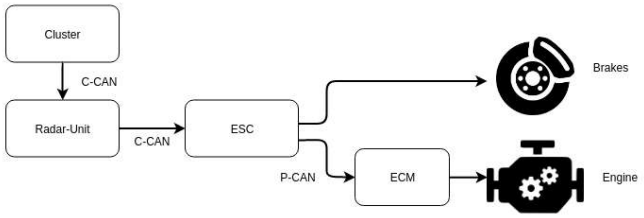

Fig. 4. Components scheme of Smart Cruise Control

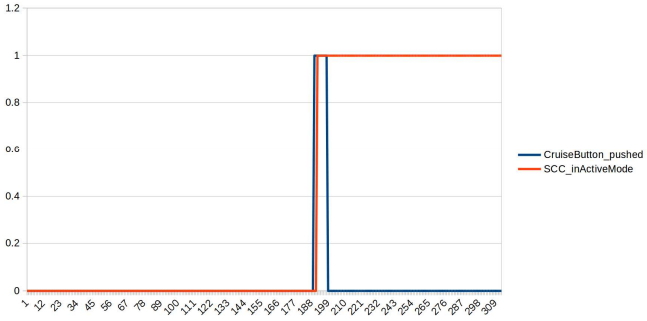

Fig. 5. SCCs behaviour on Cruise button pushed

V. Ethical issues

This research will have to comply with all ethical standards of morality and in its research will not be violated any laws concerning the exploitation of found vulnerabilities in real life.

VI. Conclusion

Provided attacks have shown that an intruder is able to gain a physical access to the CAN bus of the cat and he will be able to gain full control over the vehicle. One of the scenarios of an attack on a vehicle that could be fatal can be summarized: The attacker accelerates the vehicle to high speed and turns the steering wheel sharply, which leads to the vehicle turning over or moving out of the road. In addition to physical access to the bus, theoretically, an attacker can access the control of the vehicle through a multimedia system that contains wireless access modules such as Bluetooth or Wi-Fi (now shown in this article).

Acknowledgment

This research has been supported by the Russian Ministry of Education and Science within the Federal Target Program grant (research grant ID RFMEFI60917X0100).

References

[1] Aurlien Francillon , Boris Danev, and Srdjan Capkun, *Relay Attacks on Passive Keyless Entry and Start Systems in Modern Cars*, Proceedings of the Network and Distributed System Security Symposium, 2011.

[2] Charlie Miller and Chris Valasek, *A Survey of Remote Automotive Attack Surfaces*, DEF CON 22 Hacking Conference Presentation, 2014.

[3] Karl Koscher, Alexei Czeskis and Franziska Roesner, *Experimental Security Analysis of a Modern Automobile*, Proc. of the 31st IEEE Symposium on Security and Privacy, 2010, DOI: 10.1109/SP.2010.34

[4] Dennis K. Nilsson, Phu H. Phung, and Ulf E. Larson, *Vehicle ECU classification based on safety-security characteristics*, Road Transport Information and Control - RTIC 2008 and ITS United Kingdom Members' Conference, IET,2008, DOI: 10.1049/ic.2008.0810

[5] David Oswald, *Wireless Attacks on Automotive Remote Keyless Entry Systems*, TrustED16 - Proceedings of the 6th International Workshop on Trustworthy Embedded Devices, 2016, DOI: 10.1145/2995289.2995297

[6] Pierre Kleberger, Tomas Olovsson, and Erland Jonsson, *Security Aspects of the In-Vehicle Network in the Connected Car*, IEEE Intelligent Vehicles Symposium (IV), 2011, DOI: 10.1109/IVS.2011.5940525

[7] Samuel Woo, Hyo Jin Jo, and Dong Hoon Lee, *A Practical Wireless Attack on the Connected Car and Security Protocol for In-Vehicle CAN*, IEEE Transactions on Intelligent Transportation Systems, 2014, DOI: 10.1109/TITS.2014.2351612.

[8] S. Parkinson, P. Ward, K. Wilson, J. Miller, Cyber threats facing autonomous and connected vehicles: Future challenges, IEEE Transactions on Intelligent Transportation Systems 18 (11)(2017) 28982915, DOI: 10.1109/TITS.2017.2665968

[9] Craig Smith. *The car hacker's handbook: a guide for the penetration tester*. No Starch Press, San Francisco, 2016.

Design of the Parallel Spherical Manipulator for Wrist Rehabilitation

Skvortsova Valeria*, Popov Dmitry†
Center for Technologies in Robotics and Mechatronics Components, Innopolis University
Innopolis, Russia
Email: *v.skvortsova@innopolis.university, †d.popov@innopolis.ru

***Abstract*—This paper presents the most important steps of the wrist rehabilitation robot design. In this work, kinematic synthesis problem of a 3-RRR spherical parallel manipulator is considered including a solution for forward and inverse kinematic problems. In order to maximize dexterity of the parallel manipulator over its workspace, its design is developed by finding o ptimal l ink s hape p arameters. T he C AD d esign for the prototype is obtained based on this optimization.**

***Index Terms*—spherical wrist, rehabilitation, parallel manipulator**

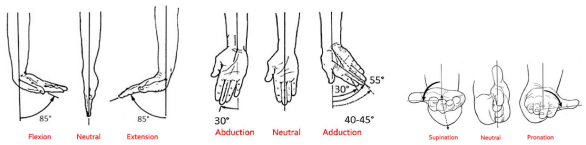

(a) Flexion, Neutral and Extension (b) Abduction, Neutral and Adduction (c) Supination, Neutral and Pronation

Fig. 1: Standard hand movements

I. Introduction

A stroke is the loss of brain function caused by the disturbance, blockage or disruption of the blood vessels. As a result, the affected part of the brain cannot work normally. It can lead to an inability to move one or more limbs. Most patients could have to experience a long time motor injury. Fortunately, after some medical treatment, the vital signs come to stable. However, some injury to the brain cannot be recovered. The part that responds for movement ability can be returned to a normal state if the patients keep receiving dedicated rehabilitation training.

In the context of motion in robotic, spherical 3-degree-of-freedom (DOF) joints are often used. In fact, they are also quite common in biological systems (e.g., shoulder or hip joints) [5]. Parallel manipulators, in which all the actuators are fixed t o t he b ase o f t he r obot, i s p roviding better load-carrying capacity and better dynamic properties. This advantages of parallel spherical manipulator lead to far less intuitive kinematic and dynamic equations than common serial manipulators. Therefore, the lack of advanced analysis and design tools specifically d eveloped f or p arallel mechanisms has hindered their use in many applications. Since a human wrist joint is a 3 DOF joint, it's convenient to use a parallel spherical robot in this case.

In order to clearly understanding the design of wrist rehabilitation robot, it is necessary to describe the geometrical hand references. In anatomy, there are two reference planes of the hand [7]. They are Frontal Plane and Sagittal Plane. The Frontal Plane is the plane that is coplanar with palm. The Sagittal Plane is the plane that goes through with middle finger and perpendicular with the frontal plane.

The movement on the sagittal plane is called as flexion-extension, as shown in fig.1a. The movement is called flexion when the palm goes towards the palm side. When the palm goes towards the dorsal surface, is named extension. The amplitude of flexion and extension can reach up to 85 degrees if the condition exists that there are no abduction and adduction, that will be described in the next paragraph.

Similarly, the movement on the frontal plane contains abduction and adduction, as shown in fig.1b. When the palm goes toward the thumb finger it is called adduction. If it goes toward the little finger, it is named as adduction. he wrist abduction can go to 15 degrees and the adduction to 30 degrees. The third movement comes from the forearm, as shown in fig.1c. Pronation at the forearm is a rotational movement where the hand and upper arm are turned inwards. Supination of the forearm occurs when the forearm or palm are rotated outwards. Supination and pronation are the rotation movement that can rotate 180 degrees of the forearm.

II. Kinematics description

A spherical 3-DOF parallel manipulator with revolute joints is represented schematically in Fig. 2 [2]. A moving platform-represented as an inverted pyramid in Fig. 2 and attached to the base via three kinematic chains, each comprises two intermediate links and three revolute joints. The structure of the manipulator is such that the axes of all 9 revolute joints are intersecting at one common point, which will henceforth be called the center of the mechanism. All moving bodies are in pure rotation with respect to this point. The three actuated joints of the manipulator are represented as cylinders in Fig. 2 and are fixed to the base. Using these actuators, it is possible to control the orientation of the moving platform with three degrees of freedom. All the other revolute joints are underactuated passive joints. Let's denote the frame of end-effector platform as $\Re_2$ [4]

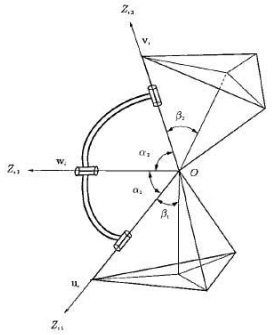

Fig. 2: Kinematics description of parallel spherical manipulator for i-th leg

Firstly, consider the base platform. Denote the frame $OX_0Y_0Z_0$ as $\Re_0$ [6] In this case, we have the following expression:

$$\sin\beta_1 = \frac{2\sqrt{3}}{3}\sin\frac{\gamma_1}{2}; \quad \sin\beta_2 = \frac{2\sqrt{3}}{3}\sin\frac{\gamma_2}{2} \tag{1}$$

The geometry of the end-effector will be a similar to the one of the base platform.

Now, we can define the orientation part of DH-parameters according to description on Fig 2:

TABLE I: DH parameters of the robot

Frame	α_n	θ_n
Base platform (BP)	$\beta_1 + \pi$	$-\eta_i$
Link 1 (L1)	α_1	θ_i
Link 2 (L2)	α_2	μ_{1_i}
End-effector platform (EEP)	0	μ_{2_i}

where α_1 and α_2 - first and second bend angle, θ_i - rotation angle of active joint, μ_{1_i} - rotation angle of first passive joint, μ_{2_i} - rotation angle of the second passive joint and $\eta_i = \frac{2(i-1)\pi}{3}$ where $i = 1, 2, 3$

The rotation matrix for DH-convention is:

$$Q(\alpha_n, \theta_n) = \begin{bmatrix} c\theta_n & -c\alpha_n s\theta_n & s\alpha_n s\theta_n \\ s\theta_n & c\alpha_n c\theta_n & -s\alpha_n c\theta_n \\ 0 & s\alpha_n & c\alpha_n \end{bmatrix} \tag{2}$$

The $Q_{EE_{i(\Re_0)}}$ transformation for end-effector will be looks like inverted DH-convention transformation when $\alpha_n = -\beta_2$ and $\theta_n = -\eta_i$, then:

$$Q_{EE_{i(\Re_0)}} = R_x(\beta_2)R_z(\eta_i) \tag{3}$$

Joints orientation in $\Re_2$ frame, could be found using:

$$Q_{EE_{i(\Re_2)}} = R_x^T(\beta_2)R_z^T(\eta_i) \tag{4}$$

Then we can describe the rotation part of the robot:

$$Q = Q_{Base}\prod_{i=1}^{3}\left(Q_{BP_i}Q_{L1_i}Q_{L2_i}Q_{EEP_i}Q_{EE_{i(\Re_0)}}\right) \tag{5}$$

The End-effector orientation will be described according to the ZYZ convention where ϕ_1, ϕ_2 and ϕ_3 is the angle of rotation frame, respectively. Then rotation matrix from frame $\Re_0$ to $\Re_2$ is:

$$R = R_z(\phi_1)R_y(\phi_2)R_z(\phi_3) \tag{6}$$

Forward kinematic problem

The orientation of end-effector will be expressed using three Euler angles, which will be noted ϕ_1, ϕ_2 and ϕ_3, respectively [1].

At the start, find a solution for the first leg. Therefore, solving the direct kinematics problem for this leg gives a solution for the whole manipulator. Find the Q transformation matrix by the formula (5) for the first leg. Then the solution for forward kinematics will have a two case:

Case 1: $Q_{33} = \pm 1$, then:

$$\phi_1 = 0; \quad \phi_2 = 0; \quad \phi_3 = atan2(Q_{21}, Q_{11}) \tag{7}$$

Case 2: $Q_{33}^2 < 1$, then:

$$\phi_1 = atan2(Q_{23}, -Q_{13}) \tag{8}$$

$$\phi_2 = atan2(\sqrt{1 - Q_{33}^2}, Q_33) \tag{9}$$

$$\phi_3 = atan2(Q_{32}, -Q_{31}) \tag{10}$$

Inverse kinematics problem

The inverse kinematics problem of the spherical parallel manipulator is finding each rotation angles for joints (passive and active) [8].

The first angle θ_i we will find by the vectors v_i and w_i according to the frame $\Re_0$. Let the vectors v'$_i$ and be defined as:

$$\text{v'}_i = RQ_{EE_{i(\Re_2)}}e_z = \begin{bmatrix} \text{v'}_{ix} & \text{v'}_{iy} & \text{v'}_{iz} \end{bmatrix}^T \tag{11}$$

$$\text{w}_i = Q_{BP_i}Q_{L1_i}e_z \tag{12}$$

where $e_z = \begin{bmatrix} 0 & 0 & 1 \end{bmatrix}^T$

So, we know, that the scalar product of vectors is equal to the cosine of the angle between them [10]. Then:

$$\text{w}_i \cdot \text{v'}_i = \cos(\alpha_2) \tag{13}$$

According to the formula (5) and (6) this equation can be expressed as:

$$A_{\theta_i}T_{\theta_i}^2 + 2B_{\theta_i}T_{\theta_i} + C_{\theta_i} = 0; \quad i = 1, 2, 3 \tag{14}$$

where

$$T_{\theta_i} = \tan(\frac{\theta_i}{2}); \quad i = 1, 2, 3$$

Now we can find the angle θ_i by solving the quadratic equation (14). We can find the other angles in passive joints by a similar way by using the scalar product of appropriates vectors. The formulas for finding these values are too large and they are available on request. In results, we have the 8 available solutions but not all of this is useful. We compare the solution of the direct kinematics problem for orientation part according to the formula (5) at the found angles θ, μ_1 and μ_2 with the result by ZYZ-parametrization by formula (6).

III. Workspace analysis

The robot workspace is representing all points that are reachable for the robot end-effector in a 3D Cartesian space. In the case of 3DOF orientation the only robot, these three dimensions are reflected end-effector orientation in ZYZ representation. Though workspace without constraints is not meaningful in the real application, it can help one to have a brief landscape of the workspace. In this section, we carried out α_1 and α_2 parameters optimization of the manipulator. These angles could take values from 0 to 180 degrees in increments of 15 degrees. Parameters $\beta_1 = 0$ and $\beta_2 = \pi/2$ was chosen in accordance with other studies and in terms of a more simple implementation [3] and [9]. The workspace was calculated according to the fact whether the solution has inverse kinematics for calculating the lower link (we found the θ angle for each leg):

$$B_{\theta_i}^2 - 4A_{\theta_i}C_{\theta_i} > 0; \quad i = 1, 2, 3 \tag{15}$$

Geometric constraints was also taken into account. In case when $\beta_1 = 0$ the difference between the corners in the lower platform should not exceed value of 10 degrees.

$$|\theta_1 - \theta_2| > 10^\circ; \quad |\theta_1 - \theta_3 + 2\pi| > 10^\circ; \quad |\theta_3 - \theta_2| > 10^\circ \tag{16}$$

In the optimization of the working space, we calculated the angles for all possible orientations of the end effector in the upper half-plane of the sphere. That is, if expressed in terms of parametrization, angles rotating around an Z-axis could take values from 0 to 360 degrees in increments of 5 degrees, and angles when rotating around an Y-axis could take values from -90 to 90 degrees in increments of 5 degrees.

The following parameters of the robot was chosen: $\beta_1 = 0$, $\beta_2 = \pi/2$, $\alpha_1 = \pi/2$ and $\alpha_2 = \pi/2$, because this configuration has more available orientations that other ones. The result of workspace calculation for this configuration is shown on Fig. 3

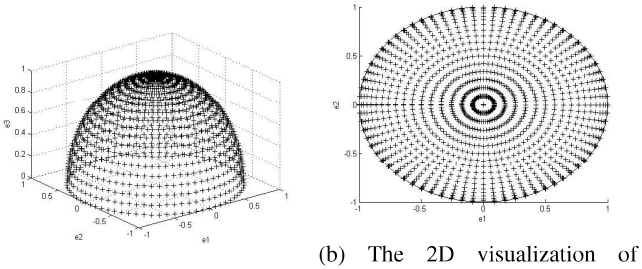

(a) The 3D visualization of workspace analysis

(b) The 2D visualization of workspace analysis (view from above)

Fig. 3: Result of the workspace analysis

Based on all calculations, a prototype of a parallel spherical robot was created. The 3D CAD model of the prototype is presented on the Fig. 4

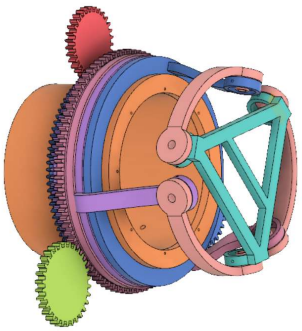

Fig. 4: Prototype of parallel spherical manipulator for rehabilitation

IV. Conclusion

In this paper, we consider the forward and inverse kinematics problem and workspace calculation of spherical parallel manipulator represented by the 3 degree-of-freedom 3RRR wrist rehabilitation parallel robot. The main point of SPM is that its 2 rotation centers are coincident with each other. After analyzing the forward and inverse kinematics of this system, the calculation of optimal parameters was conducted by solving the optimization problem in order to maximize robot workspace. Future work will include prototype development and kinematic, dynamic, elastostatic modeling and calibration.

V. Acknowledgments

This research has been supported by the grant of Russian Science Foundation 17-19-01740.

References

[1] Gosselin, C. M. and Sefrioui, J. and Richard, M. J. On the Direct Kinematics of Spherical Three-Degree-of-Freedom Parallel Manipulators of General Architecture In *Journal of Mechanical Design*, DOI:*10.1115/1.2919419*, 2008.

[2] Gosselin, Clement M. Simulation and computeraided kinematic design of threedegreeoffreedom spherical parallel manipulators In *Journal of Robotic Systems*, DOI:*10.1002/rob.4620121209*, pages 857–869, 1995.

[3] Wu, Guanglei Multiobjective optimum design of a 3-RRR spherical parallel manipulator with kinematic and dynamic dexterities In *Modeling, Identification and Control*, DOI:*10.4173/2012.3.3*, pages 111–122, 2012.

[4] Bonev, IA and Zlatanov, D and Gosselin, C.M Advantages of the modified Euler angles in the design and control of PKMs In *Proceeding of Parallel Kinematic Machines International Conference*, pages 171–188, 2002.

[5] Enferadi, Javad and Tootoonchi, Alireza Akbarzadeh Accuracy and stiffness analysis of a 3-RRP spherical parallel manipulator In *Robotica*, DOI:*10.1017/S0263574710000032*, pages 193–209, 2011.

[6] Gosselin, Clement M. and Lavoie, Eric On the kinematic design of spherical three-degree-of-freedom parallel manipulators In *International Journal of Robotics Research*, DOI:*10.1177/027836499301200406*, pages 394–402, 1993.

[7] Wang, Mirui Design and Analysis of an Adjustable Wrist Rehabilitation Robot 2014.

[8] Bai, Shaoping and Hansen, Michael R. and Andersen, Torben O. Modelling of a special class of spherical parallel manipulators with Euler parameters In *Robotica*, DOI:*10.1017/S0263574708004402*, pages 161–170, 2009.

[9] Bonev, Ilian A. and Gosselin, Clement M. Analytical Determination of the Workspace of spherical parallel mechanisms In *IEEE Transactions on Robotics*, pages 1011–1017, 2006.

[10] Gosselin, Clement Kinematic Analysis Optimization and Programming of Parallel Robotic Manipulators 1985.

Augmentation-Based Object Detection for Winter Time Applications

Rauf Yagfarov
Autonomous Transportation Systems Lab
Innopolis University
Innopolis, Russia
Email: r.yagfarov@innopolis.ru

Vladislav Ostankovich
Autonomous Transportation Systems Lab
Innopolis University
Innopolis, Russia
Email: v.ostankovich@innopolis.ru

Salimzhan Gafurov
Autonomous Transportation Systems Lab
Innopolis University
Innopolis, Russia
Email: s.gafurov@innopolis.ru

***Abstract*—Despite the significant advancements in object detection, there is still a number of detection tasks that are challenging and difficult. To eliminate them and to push forward the research in this area a technological "IceVision" Challenge was organized in Russia in 2019. The main objective of this Challenge is to develop new approaches for object detection in severe weather conditions focusing on winter time. The obtained results are supposed to be implemented for autonomous driving. This paper reports the approach that was used by our team in this competition. The approach is based on a Cascade R-CNN model in combination with data augmentation. It allowed us to take fourth place among 187 participants on the preliminary stage of the completion.**

***Keywords*—object detection, traffic signs, autonomous driving, winter time, icevision**

I. Introduction

Object detection has run the gamut from simple computer detection algorithms (see, [1], [2] and others) to highly sophisticated deep learning based detection (see, [3], [4] and others). A thorough survey on object detection is presented in paper [5]. Nowadays object detection is known to be one the most significant task in computer vision allowing to identify objects on digital images as well as to find their positions and orientations. It has been extensively used in a great number of application spheres such as navigation, localization, vision, surveillance and others. Such a great interest in object detection and its extensive usage in recent 5 years were inspired by advances in deep learning techniques that have initiated a new era of this area of research. Developing advanced computer vision algorithms requires large datasets. Their building was forced by a number of Challenges that were organized in the last 15 years. Nowadays a number of well-known datasets have been released, including the datasets of PASCAL VOC Challenges [6], ImageNet Large Scale Vision Recognition Challenge [7], MS-COCO Detection Challenge [8]. However, there is a lack on Challenges and datasets focusing on object detection for winter time implementation. This is a crucial factor limiting the progress of computer vision algorithms. To propose new ideas and approaches for such tasks a technological "IceVision" Challenge was organized in Russia by National University of Science and Technology MISIS (Moscow) and Scientific Production Association "StarLine" (Moscow). The main objective of this competition is to develop software allowing to detect various objects in the winter time accurately and effectively based on camera images. This paper describes the experience of our team gained from participating in the preliminary stage of this Challenge. This stage focused on traffic signs detection in winter time. The paper describes the approach used by our team for such a task.

II. Challenge Task

The main purpose of the preliminary stage of IceVision Challenge is to estimate the content of digital images for the purpose of detecting traffic signs from 10 categories (see Table I). Training images were presented with initial annotation. Developed algorithms should provide labelling specifying what kind of traffic sign is present in the image. The storage of training images includes about 4 000 images. This storage was collected and labelled especially for the IceVision Challenge and has not been published ever before. This task initiates the challenge accompanied by such common for computer vision difficulties as illuminations, intraclass variations, objects rotation and scale variation, objects localization, dense and occluded objects detection and speed of detection. To deal with these difficulties a robust and effective computer vision approach should be chosen.

III. Method

We realized our model by means of an open source toolbox based on PyTorch for object detection called "mmdetection" [9]. It includes a number of models. Among them we have chosen the following three cascade-based R-CNN models as they have shown the best results on object detection tasks on COCO dataset [8]:

- Cascade R-CNN [10] with ResNeXt101 (64x4d setting) with FPN (Feature Pyramid Network) [11] as a backbone of the network FPN is based on Faster RCNN [12] and proposes great advances for detecting objects with a wide variety of scales. ;
- a modification of previous one with an addition of GC (Global Context) block after 1x1 convolutional layers of backbone [13];
- Cascade R-CNN with ResNet50 as a backbone of the network and deformable convolutions in ResNet stages from 3 to 5

To increase the amount of data for neural networks training and thus increase the accuracy, various data augmentation techniques were used. Used techniques can be divided into two groups: classical approaches and Generative Adversarial Networks (GAN) based augmentation. The classical methods of augmentation include pixel-level transforms and spatial-level transforms. Pixel-level transformations affect only on an input image and leave rest data such as bounding boxes, feature points and masks unchanged. Examples of such transformations are blur, noise, colour shift, brightness/contrast change etc. Spatial-level transformations affect on images as well as on bounding boxes, masks and feature points. Examples of such transformations are flip, crop, rotation, translation etc. In this work, we used the library for classical augmentation called Albumentations [14], which provides a large number of different classical augmentation transformations. For our experiments, we used the following transformations: Blur, RandomGamma, HueSaturationValue, RGBShift, RandomBrightness RandomContrast, MedianBluer, CLAHE, GaussianNoise, HorizontalFlip. We used only one geometric

TABLE I
TRAFFIC SIGNS CLASSES

2.1	2.4	3.1	3.24	3.27	4.1	4.2	5.19	5.20	8.22
	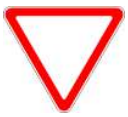								

TABLE II
AUGMENTATION TYPES

Original image	Classical augmentation	CycleGAN augmentation
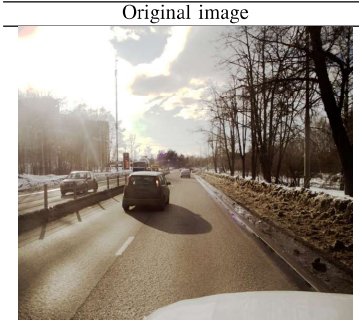	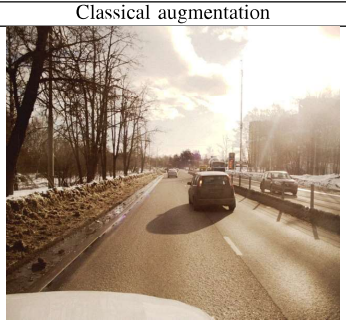	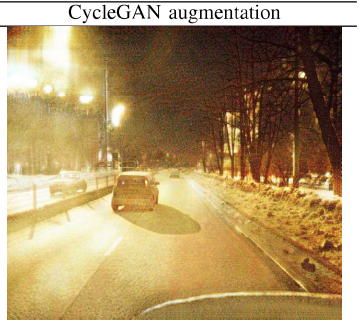

TABLE III
RESULTS

Model	2.1	2.4	3.1	3.24	3.27	4.1	4.2	5.19	5.20	8.22	Total
Cascade R-CNN (ResNeXt 101)	+225.377 -54 171.377	+66.761 -32 34.761	+19.952 -44 24.048	+205.521 -44 161.521	+69.92 -46 23.92	+61.165 -80 18.835	+75.058 -12 63.058	+893.264 -34 859.264	+68.519 -18 50.519	+64.825 -8 56.825	+1750.36 -372 1378.36
Cascade R-CNN (ResNeXt 101) + GC	+201.405 -38 163.405	+64.827 -16 48.827	+16.047 -24 7.953	+196.892 -24 172.892	+62.367 -36 26.367	+50.567 -52 1.433	+65.532 -4 61.532	+838.657 -12 826.657	+65.545 -4 61.545	+56.749 -2 54.749	+1618.59 -212 1406.59
Cascade R-CNN (ResNet 50) + DCN	+214.52 -56 158.52	+57.887 -28 29.887	+13.894 -32 18.106	+195.872 -40 155.872	+68.544 -44 24.544	+47.183 -62 14.817	+64.484 -10 54.484	+829.654 -92 737.654	+37.413 -6 31.413	+45.884 -4 41.884	+1575.34 -374 1201.34
Cascade R-CNN (ResNeXt 101) (aug.)	+295.157 -64 231.157	+109.038 -30 79.038	+36.251 -6 30.251	+235.369 -34 201.369	+106.461 -32 74.461	+69.281 -38 31.281	+84.636 -22 62.636	+944.4 -20 924.4	+107.137 -8 99.137	+70.902 -2 68.902	+2058.63 -256 1802.63

transformation (HorizontalFlip), as the road signs in the image are always in approximately the same areas on images and are not turned over.

The testing set of IceVision competition contained big number of night images, while the training set didn't contain any of those. GAN-based augmentation was applied to let the network additionally train on artificially generated night images. For this purpose, Image-to-Image Translation using Cycle-Consistent Adversarial Networks (a.k.a. CycleGAN) was applied [15]. We trained the CycleGAN on thousand day images and thousand night images of size 1024x896 for 70 epochs. An example of day to night conversion is shown in Table II.

IV. RESULTS AND CONCLUSION

For the evaluation of results, organizers of the competition selected intersection over union (IoU) metric which is used to measure the accuracy of object detection. IoU defines positives and negatives. Detection is said to be successful if IoU $\geq$ 0.5 and the class is predicted correctly. If traffic sign is detected twice, then the detection with the smallest IoU is considered as False Positive (FP). Each FP results in a penalty of two points. Each correct detection with IoU $>$ 0.85 results in a reward of 1 point. Otherwise, the amount of points is calculated as follows:

$$Reward = (\frac{IoU-0.5}{0.35})^{0.25}$$

The total score is computed as a sum of all correct detection points minus all penalties. It worth to mention that IoU equivalent to 0.5 leads to noisy detection. However, increasing of this parameter degrades the overall detection performance. Such a situation is caused by the following factors: i) exponentially vanishing positive samples result in over-fitting during training and ii) inference-time mismatch between the IoUs for which the detector is optimal and those of the input hypotheses. To address these problems we implement a multi-stage object detection architecture,the Cascade R-CNN. Our results for different models are shown in Table III.

ACKNOWLEDGMENT

This research was supported by the Russian Education Ministry under the Agreement No. 075-10-2018-017 on granting a subsidy from 11.26.2018 Development of a commercial urban transport with the intellectual driver assistance system City Pilot. The customer is a federal target program. The unique identifier of the project RFMEFI60918X0005. Industrial partner - KAMAZ

REFERENCES

[1] P. Viola and M. Jones, "Rapid object detection using aboosted cascade of simple features," *Computer Vision and Pattern Recognition*, pp. 1–1, 2001.

[2] P. Viola and M. Jones, "Robust real-time face detection," *International journal of computer vision*, vol. 57, no. 2, pp. 137–154, 2004.

[3] T. D. R. Girshick, J. Donahue and J. Malik, "Rich feature hierarchies for accurate object detection and semantic segmentation," in *IEEE conference on computer vision and pattern recognition*, pp. 580–587, IEEE, 2014.

[4] R. G. J. Redmon, S. Divvala and A. Farhadi, "You only look once: Unified, real-time object detection," in *IEEE conference on computer vision and pattern recognition*, pp. 779–788, IEEE, 2016.

[5] Z. S. Zhengxia Zou, "Object detection in 20 years: A survey," *arXiv preprint arXiv:1905.05055v2*, 2019.

[6] C. K. W. J. W. M. Everingham, L. Van Gool and A. Zisserman, "The pascal visual object classes (voc)challenge," *International journal of computer vision*, vol. 88, no. 2, pp. 303–338, 2010.

[7] H. S. J. K. S. S. S. M. Z. H. A. K. A. K. M. B. a. O. Russakovsky, J. Deng, "Imagenet large scale visual recognition challenge," *International Journal of Computer Vision*, vol. 115, no. 3, pp. 211–252, 2015.

[8] T.-Y. Lin, M. Maire, S. Belongie, J. Hays, P. Perona, D. Ramanan, P. Dollár, and C. L. Zitnick, "Microsoft coco: Common objects in context," in *European conference on computer vision*, pp. 740–755, Springer, 2014.

[9] J. P. Y. C. Y. X. X. L. S. S. W. F. Z. L. J. X. Z. Z. D. C. C. Z. T. C. Q. Z. B. L. X. L. R. Z. Y. W. J. D. J. W. J. S. W. O. C. C. L. D. L. Kai Chen, Jiaqi Wang, "MMDetection: Open mmlab detection toolbox and benchmark," *arXiv preprint arXiv:1906.07155*, 2019.

[10] Z. Cai and N. Vasconcelos, "Cascade r-cnn: Delving into high quality object detection," *arXiv preprint arXiv:1712.00726v1*, 2017.

[11] R. B. G. K. H. B. H. a. S. J. B. T.-Y. Lin, P. Doll ar, "Feature pyramid networks for object detection," *CVPR*, vol. 1, no. 2, 2017.

[12] R. G. Ren, K. He and J. Sun, "Faster r-cnn: Towards real-time object detection with region proposal networks," *Advances in neural information processing systems*, vol. 1, no. 2, 2015.

[13] Y. Cao, J. Xu, S. Lin, F. Wei, and H. Hu, "Gcnet: Non-local networks meet squeeze-excitation networks and beyond," *arXiv preprint arXiv:1904.11492*, 2019.

[14] E. K. V. I. I. A. Buslaev, A. Parinov and A. A. Kalinin, "Albumentations: fast and flexible image augmentations," *ArXiv e-prints*, 2018.

[15] J.-Y. Zhu, T. Park, P. Isola, and A. A. Efros, "Unpaired image-to-image translation using cycle-consistent adversarial networks," in *Proceedings of the IEEE international conference on computer vision*, pp. 2223–2232, 2017.

Investigation of complex nonlinear processes in systems with intense relativistic electron beams

Semen Kurkin
Neuroscience and Cognitive Techology Lab, Center for Technologies in Robotics and Mechatronics Components
Innopolis University
Innopolis, Russia
Saratov State University
Saratov, Russia
kurkinsa@gmail.com

***Abstract*—The following novel schemes of relativistic generators with virtual cathode were proposed and investigated in terms of nonlinear dynamics analysis, enhancing output power, efficiency and generation frequency: multibeam vircator, vircator with elliptical resonator, vircator with photonic crystal. The carried-out analysis and obtained results have shown efficiency of the proposed vircator schemes.**

Keywords—vircator, virtual cathode, high-power microwaves, relativistic electron beam, photonic crystal, multibeam vircator

I. Introduction

Relativistic generators with virtual cathode (vircators, virtodes, reditrons, etc.) are one of the most promising and actively investigated extremely high-power sources of electromagnetic signals in the microwave and sub-THz ranges. Such devices can be used in systems for acceleration of ion beams, for studying electromagnetic compatibility, probing the atmosphere, etc. [1]. The main advantages of vircators are very high output power, easy control of spectral characteristics, low requirements for the electron beam quality, in certain modes – wide frequency band of generated signals, and simplicity of design, including the possibility of operating without external magnetic field.

However, the main disadvantages of generators with relativistic electron beams with supercritical current are their low efficiency and relatively low generation frequency. Many researchers have been making constant attempts to enhance the energy conversion efficiency of vircators [2-9].

One of the possible solutions to the problem of low efficiency and advancement to the millimeter-wave band is the development of novel vircator schemes and the modification of old ones. This paper is devoted to the presentation of the results of investigation of complex nonlinear processes in the following prospective systems with intense relativistic electron beams: multibeam vircator, vircator with elliptical resonator, vircator with photonic crystal.

II. Main Results

A three-dimensional particle-in-cell (PIC) electromagnetic code was used to simulate complex non-stationary processes of electron-wave interaction in the considered systems.

A. Vircator with Elliptical Resonator

The scheme of vircator with elliptical resonator is shown in Fig. 1a. The dynamics of electron beam in this scheme was analyzed. The results of global optimization were obtained by changing the control parameters of the system. We have studied the influence of the electron beam current and the geometric parameters of the elliptical resonator (radii of semiaxes) on output power of the vircator on the working mode. We have found the optimal values of these parameters.

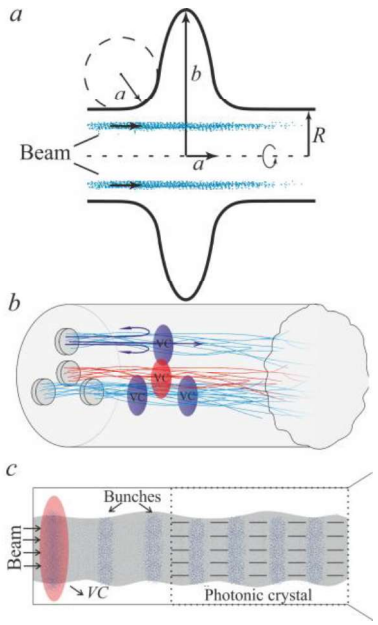

Fig. 1. Schemes of the proposed vircators. (a) Multibeam vircator. (b) Vircator with elliptical resonator. (c) Vircator with photonic crystal.

We have carried out optimization of power output of the vircator and proposed a variant of matching of cylindrical working chamber of the vircator with coaxial power output based on a smooth increase of the inner conductor radius from 0 in the chamber to R_c in the waveguide (R_c is the inner radius of the coaxial waveguide), thus enhancing vircator efficiency. We have investigated the dependence of output power of the vircator with elliptical resonator on R_c at the presence of the matching that demonstrates also the existence of optimum.

Also, we have analyzed dynamics of relativistic electron beam in the proposed scheme. We observed a significant increasing of spatial amplitude of virtual cathode (VC) oscillations in the investigated model compared to the classical vircator. This effect is caused by the intense interaction of virtual cathode with high-Q eigenmode of the electrodynamical structure. We have found out that virtual

cathode should be formed directly in the resonator to achieve maximum output power.

We have shown that elliptical type of the resonator makes it possible to provide a better efficiency of interaction of the relativistic electron beam with electromagnetic field due to better localization of the field being excited in elliptical resonator. It leads to a significant increase in the efficiency of the vircator up to 5-7%. At the same time, vircator with elliptical resonator demonstrates the regimes with intense higher harmonics of the fundamental frequency of virtual cathode oscillations.

B. Multibeam Vircator

Multibeam scheme of vircator is the system, in which several electron beams with supercritical currents are loaded onto common resonator (Fig. 1b). This scheme is considered as promising for increasing generation power and frequency [10]. The possibility of effective interaction of several virtual cathodes in a single interaction space was analyzed, and conditions of effective addition of powers of each beam at the output load were determined.

The effect of synchronization of virtual cathodes in the model of a multibeam relativistic vircator [11] was discovered for the first time. This effect is important both from the fundamental and applied points of view because it can allow shifting relativistic vircators to a higher frequency range without substantially increasing the total current in the system. This result can be achieved using one relativistic electron beam with the highest current as the beam that determines the frequency, and the remaining (N-1) beams with lower currents as supporting beams, which "pump" the necessary energy into the system.

Thus, to increase the vircator generation frequency (which is determined by the plasma frequency) and the power at a given frequency, it is not necessary to increase the total current injected into the system, compared with the single beam. However, it is sufficient to increase only the current of one of the N beams (base beam). As a result, due to synchronization, VCs in all electron beams will oscillate at one frequency, which is set by the VC oscillations frequency in the base beam, which will lead to an increase in the output signal power at this frequency (Fig. 2).

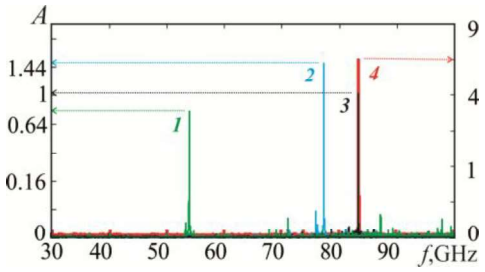

Fig. 2. The normalized power spectra of the signal at the waveguide port output in the model of multibeam relativistic vircator when one electron beam is injected into the system with a current of 12 kA (green spectrum 1), 14 kA (blue spectrum 2), or 16 kA (black spectrum 3) and when three electron beams are injected with currents of 12 kA, 14 kA, and 16 kA (red spectrum 4, right scale). The spectra are normalized to the power of the main spectral component of the output signal generated in a single-beam system with a current of 16 kA. The value of the induction of an external magnetic field is B = 1 T; the energy of the injected electron beams W_e = 1 MeV.

C. Vircator with Photonic Crystal

The scheme of vircator with photonic crystal is shown in Fig. 1c. We have studied the properties of microwave generation in a virtual cathode oscillator with a photonic crystal composed of metal grids. Our simulation results show the high efficiency of photonic crystal structure utilization in comparison with the standard scheme of an axial virtual cathode oscillator: operation efficiency reaches 20% at the optimal parameters [12]. We have shown that the dispersion characteristics of the photonic crystal make it possible to synchronize the phase velocity of electromagnetic wave with electron beam propagating after a virtual cathode, that increases substantially the efficiency of vircator generation.

We have revealed that photonic crystal located in the drift tube of the axial vircator permits us to significantly improve the efficiency of microwave generation due to a number of factors: (i) high interaction impedance with passing REB, (ii) distributed electromagnetic feedback with VC, and (iii) efficient electromagnetic energy output compared to the traditional cylindrical waveguide.

The obtained results demonstrate that the virtual cathode oscillator with a photonic crystal can be considered as a prospective high-power microwave source where the vircator operation mechanism and photonic crystal properties complement each other to produce high-power electromagnetic radiation.

In conclusion, the carried-out analysis and obtained results have shown efficiency of the proposed vircator schemes in terms of increasing of efficiency and generation frequency [13]. Actually, relativistic vircator with elliptical resonator or photonic crystal demonstrate efficiency up to 10-20 %. Operation at higher harmonics in these devices or using the virtual cathodes synchronization effect in the multibeam vircator allow to achieve generation frequency of 80-100 GHz.

ACKNOWLEDGMENT

This work has been supported by Russian Foundation for Basic Research (Project 18-32-20135) and the Ministry of Education and Science of the Russian Federation (Project 3.859.2017/4.6).

REFERENCES

[1] J. Benford, J. A. Swegle and E. Schamiloglu, "High Power Microwaves," 3rd Edition, CRC Press, Taylor and Francis Group, 2016.

[2] Mumtaz, S., Lim, J.S., Ghimire, B., Lee, S.W., Choi, J.J. and Choi, E.H. Enhancing the power of high power microwaves by using zone plate and investigations for the position of virtual cathode inside the drift tube. Physics of Plasmas, 25(10), p.103113, 2018.

[3] Badarin, A. A., Kurkin, S. A., Koronovskii, A. A., & Hramov, A. E. The effect of the conductivity of drift chamber walls on the dynamics of a relativistic electron beam with a virtual cathode. Technical Physics Letters, 41(12), 1148-1151, 2015.

[4] Badarin, A. A., Kurkin, S. A., & Hramov, A. E. Multistability in a relativistic electron beam with an overcritical current. Bulletin of the Russian Academy of Sciences: Physics, 79(12), 1439-1442, 2015.

[5] Frolov, N. S., Kurkin, S. A., Khramova, M. V., Badarin, A. A., Koronovskii, A. A., Pavlov, A. N., & Hramov, A. E. Perspective sub-THz powerful microwave generator" nanovircator" for T-rays biomedical diagnostics. In Saratov Fall Meeting 2015: Third International Symposium on Optics and Biophotonics and Seventh Finnish-Russian Photonics and Laser Symposium (PALS)(Vol. 9917, p. 991721). International Society for Optics and Photonics, 2016.

[6] Kurkin, S. A., Badarin, A. A., Koronovskii, A. A., Frolov, N. S., & Hramov, A. E. Modeling instabilities in relativistic electronic beams in the CST particle studio environment. Mathematical Models and Computer Simulations, 10(1), 59-68, 2018.

[7] Kurkin, S.A., Koronovskii, A.A. and Hramov, A.E. Output microwave radiation power of low-voltage vircator with external inhomogeneous magnetic field. Technical Physics Letters, 37(4), pp.356-359, 2011.

[8] Kurkin, S.A. and Hramov, A.E. Virtual cathode formation in annular electron beam in an external magnetic field. Technical Physics Letters, 35(1), pp.23-25, 2009.

[9] Kurkin, S.A., Hramov, A.E. and Koronovskii, A.A. Nonlinear dynamics and chaotization of virtual cathode oscillations in annular electron beam in uniform magnetic field. Plasma Phys. Rep, 35(8), pp.628-642, 2009.

[10] Badarin, A.A., Kurkin, S.A., Koronovskii, A.A., Hramov, A.E. and Rak, A.O. Processes of virtual cathodes interaction in multibeam system. Physics of Plasmas, 25(8), p.083110, 2018.

[11] Danziger, M.M., Moskalenko, O.I., Kurkin, S.A., Zhang, X., Havlin, S. and Boccaletti, S. Explosive synchronization coexists with classical synchronization in the Kuramoto model. Chaos: An Interdisciplinary Journal of Nonlinear Science, 26(6), p.065307, 2016.

[12] Frolov, N.S., Kurkin, S.A., Koronovskii, A.A., Hramov, A.E. and Rak, A.O. High-efficiency virtual cathode oscillator with photonic crystal. Applied Physics Letters, 113(2), p.023503, 2018.

[13] Dubinov, A.E., Petrik, A.G., Kurkin, S.A., Frolov, N.S., Koronovskii, A.A. and Hramov, A.E. Beam-plasma instability in charged plasma in the absence of ions. Physics of Plasmas, 23(4), p.042105, 2016.

Динамика сложных сетей и их применение в интеллектуальной робототехнике (Dynamics of Complex Networks and their Application in Intellectual Robotics)